

Donor-Acceptor Assemblies Formed Between BODIPY or Ferrocene-BODIPY  
Hybrids and Nanocarbon Materials for Light Harvesting

by

Tanner Blesener

A Thesis submitted to the Faculty of Graduate Studies of  
The University of Manitoba  
in partial fulfilment of the requirements of the degree of

DOCTOR OF PHILOSOPHY

Department of Chemistry

University of Manitoba

Winnipeg

Copyright © 2020 by Tanner Blesener

## Abstract

The energy crisis is a major problem the world is currently facing with many scientists working on ways to solve it. The development of new renewable energy resources has been studied extensively in recent years with intense interest in the development of new solar cell devices. This research has led to the development of new third generation photovoltaic devices such as dye-sensitized, organic, perovskite, and quantum dot solar cells. The research explored here focused on the development of new boron azadipyrromethane (aza-BODIPY) and boron dipyrromethane (BODIPY) dyes for use in organic and dye sensitized solar cells. The reason for using aza-BODIPY and BODIPY dyes is due to their high absorptivity and fluorescence quantum yields. We designed and synthesized four different types of aza-BODIPY and BODIPY compounds starting with  $\beta$ -pyrrolic dipyrrene aza-BODIPYs, followed by  $\alpha$ -pyrrolic pyrene BODIPYs, third was a ferrocene-BODIPY-C<sub>60</sub> fullerene triad, and the final design was a dipyridine BODIPY. These compounds were studied using UV-vis and steady-state fluorescence spectroscopy as well as X-ray crystallography. In order to investigate the interaction between donors and acceptors both absorption and fluorescence titration experiments along with transient absorption spectroscopy was also conducted. The goal was to determine what type of architecture works best for the formation of supramolecular arrays between donors and acceptors: non-covalent, covalent, or coordination. The results of the experiments with dipyrrene aza-BODIPY and BODIPY compounds showed that non-covalent interaction occurred between our dyes and nanocarbon material in the solid state with stronger interactions occurring with graphene and single walled carbon nanotubes. The ferrocene-BODIPY-C<sub>60</sub> triad complexes revealed that rapid excited state deactivation caused by catechol bridging group can be subverted via rapid charge transfer from ferrocene to the BODIPY thus extending its excited state lifetime. Dipyridine BODIPY acceptors were able to successfully mimic pyridine C<sub>60</sub> acceptors and form charge separated states with zinc tetra-tertbutyl phthalocyanine via coordination of pyridine linking group to the metal center. Since photoinduced electron transfer was only seen in our coordination complexes, this has become our preferred architecture for the preparation of light harvesting devices.

## Acknowledgments

I would like to start by expressing my deepest appreciation and respect for my advisor professor Viktor Nemykin for not only being the greatest teacher I have ever had with an abundance of knowledge and enthusiasm for chemistry but also for his support and guidance throughout my graduate studies.

I am also extremely thankful to all of the other people in the Nemykin lab who helped teach me everything I would need to be successful when working in the lab especially our postdoc Yura Zatsikha for his assistance doing synthesis.

I would also like to thank all the people I collaborated with on my projects such as Professor David Herbert and Gregory Rhode for running crystallography experiments on my compounds as well as Professor David Blank and his research group Rachel Swedin, Andrew Healy, and Philip Goff for their work running and helping interpret the transient absorption data. I would also like to thank Dr. Belosludov for his help with DFT calculations for non-covalent interactions between pyrene aza-BODIPY and pyrene BODIPY complexes with nanocarbon material.

The completion of my graduate studies would also not have been possible without the help of my advisory committee: David Herbert, Georg Schreckenbach, and Derek Oliver who provided invaluable advice, encouragement, and support.

Lastly I would like to thank the University of Manitoba as well as NSERC and the Canadian Foundation for Innovation for funding this important research and providing me with this opportunity.

## Contribution of Authors

### Tanner Blesener (Author of Thesis)

Since most scientific research is performed by teams that continue to grow in size and specialty of its members it becomes increasingly important to include what areas of the research you contributed to. Here I will list my contribution on the research reported in chapters 2-4 of the thesis. I was involved in the design, synthesis, and characterization of all compounds which includes running NMR, high resolution mass spectrometry, UV-Vis, and fluorescence spectroscopy. I also investigated the redox properties of all target compounds by running cyclic voltammetry and differential pulse voltammetry. In order to determine the spectroscopic signatures of the redox-active species I also conducted spectroelectrochemical oxidation experiments. To determine the interaction and potential complex formation with nanocarbon materials for Chapter 2 I also ran UV-vis and fluorescent titration experiments where I calculated the quenching constant  $K_{SV}$  for compounds **2.5a-d**, **2.6**, and **2.8-2.9**. I calculated the estimated free energy for electron transfer  $\Delta G_{ET}$  for all target compounds in Chapter 2. I also ran the solid state absorption spectrum on our compounds alone and in a mixture of compound with C<sub>60</sub> fullerene for chapter 2. In Chapter 4 I also ran all absorption and fluorescence titration experiments between the pyridine acceptors and corresponding porphyrin and phthalocyanines. I generated all figures and tables that display the results from all parts of the experiments that I contributed to. I also generated the plots using the data obtained from the computational experiments that were ran. I also contributed to the interpretation and conclusion drawn from our results for all of the experiments done on these compounds. I contributed to the writing of all work in this thesis that was published.

### Viktor Nemykin

Assisted with direction of research and design of molecules as well as collected most of the computational data. He also ran x-ray crystallography on many of the BODIOPY compounds. He helped interpret all results for the experiments and contributed to the writing of all published papers.

**Yura Zatsikha (postdoctoral associate)**

He assisted with the design, synthesis, and characterization of all compounds such as running absorption, fluorescence, and NMR spectroscopy. He helped with interpretation of results that he worked on as well as the writing of any work that was published in the thesis that he did.

**David Blank and research group (Philip C. Goff, Andrew Healy, Rachel Swedin)**

David Blank and his research group performed all transient absorption experiments on our compounds at the University of Minnesota for us.

**David E. Herbert**

David Herbert ran X-ray crystallography on some of the BODIPY compounds that crystal structures were obtained in the thesis.

## List of Abbreviations

DCM – dichloromethane

DMF – dimethylformamide

ACN - acetonitrile

BODIPY – boron-dipyrromethane

NIR – near infrared

CV – cyclic voltammetry

DPV – differential pulse voltammetry

HRMS – high resolution mass spectrometry

TBAP – tetrabutylammonium perchlorate

TFAB – tetrabutylammonium-tetrakis(pentafluorophenyl)borate

NMR – nuclear magnetic resonance

UV-Vis – ultraviolet-visible

IVCT – intervalence charge transfer

DFT – density functional theory

TDDFT – time dependent density functional theory

MO – molecular orbital

APCI – atmospheric-pressure chemical ionization

OPV – organic photovoltaic

HOMO – highest occupied molecular orbital

LUMO – lowest unoccupied molecular orbital

SWCNT – single walled carbon nanotubes

D- $\pi$ -A – donor- $\pi$ -acceptor

MLCT – metal to ligand charge transfer

DIPEA – diisopropylethylamine

DBU – 1,8-diazabicyclo[5.4.0]undec-7-ene

PPV – poly(phenylenevinylene)

PCBM – [6,6]phenyl-C<sub>61</sub>-butyric acid methyl ester

P3HT – poly(3-hexylthiophene-2,5-diyl)

SCE – saturated calomel electrode

NHE – normal hydrogen electrode

## Table of Contents

<b>Abstract</b>	i
<b>Acknowledgments</b>	ii
<b>Contribution of Authors</b>	iii
<b>Abbreviations</b>	v
<b>List of Tables</b>	ix
<b>List of Figures</b>	x
<b>Chapter 1: Introduction</b>	
Solar Energy	1
Third Generation Solar Devices	2
Design of Organic and Dye Sensitized Photovoltaic Devices	5
Organic Solar Cell Research	12
Dye Sensitized Solar Cell Research	16
Techniques Used to Investigate Donor/Acceptor Chromophores	19
<b>Chapter 2: Pyrene aza-BODIPY and BODIPYs for non-covalent interaction with nanocarbon material</b>	
Introduction	29
Synthesis and Characterization of 2.5a - 2.5e	31
Interaction and Potential Complex Formation of Pyrene-aza-BODIPYs with Nanocarbon Materials	58
Fully Conjugated Pyrene-BODIPY and Pyrene-BODIPY-Ferrocene Dyads and Triads	81
	<b>vii</b>

Interaction and Potential Complex Formation of Pyrene-BODIPYs with Nanocarbon materials	95
Experimental Section	102
Conclusion	113
<b>Chapter 3: Investigation of Ferrocene-BODIPY-C<sub>60</sub> triads covalently linked by a catechol linker</b>	
Introduction	129
Synthesis, Characterization, and Electron-Transfer Properties of Ferrocene-BODIPY-Fullerene NIR Absorbing Triads	132
Rapid Excited State Deactivation of BODIPY Derivatives by a Catechol Linker	158
Experimental Section	188
Conclusion	196
<b>Chapter 4: Pyridine-BODIPY a new type of non-fullerene acceptor for coordination to metal centers of porphyrins and phthalocyanines</b>	
Introduction	207
Synthesis and Characterization of Pyridine-BODIPY	210
Interaction and complex formation with Porphyrins and Phthalocyanines	218
Experimental Section	231
Conclusion	232
<b>Conclusion</b>	<b>236</b>

## List of Tables

<b>Table 2.1. Selected photophysical properties of aza-BODIPYs 2.5a–2.5e and the reference compound 2.6.</b>	43
<b>Table 2.2. Redox properties of aza-BODIPYs 2.5a – 2.5e and the reference compound 2.6.</b>	49
<b>Table 2.3. Estimated quenching constants for non-covalent complexes formation between aza-BODIPYs 2.5a – 2.5e and 2.6 and C<sub>60</sub> or C<sub>70</sub> fullerenes.</b>	65
<b>Table 2.4. DFT-predicted interaction energies for the formation of non-covalent complexes between pyrene and nanocarbon materials</b>	78
<b>Table 2.5. Absorption and emission data on BODIPYs 2.8 – 2.10 in DCM.</b>	88
<b>Table 2.6. Electrochemical data on BODIPYs 2.8–2.10 in DCM/0.1M TBAP system.</b>	90
<b>Table 3.1. UV-vis spectra of the target compounds in DCM.</b>	144
<b>Table 3.2. Redox properties of target compounds in DCM/0.05M TFAB system.</b>	146
<b>Table 3.3. Exponential time constants for recovery of the ground state (transient bleach) following photoexcitation. Data and fits presented in Figure 3.28.</b>	158
<b>Table 3.4. First order time constants</b>	170
<b>Table 3.5. Redox properties of compounds 3.5a-3.5d and 3.6a-3.6e in DCM/0.1M TBAP system</b>	172
<b>Table 3.6. Energetics</b>	175
<b>Table 4.1. Selected photophysical properties of acceptor compounds 4.3 – 4.5 and Donor porphyrins and phthalocyanines 4.6 – 4.14.</b>	217
<b>Table 4.2. Electrochemical data on acceptors and donor</b>	218
<b>Table 4.3. Estimated quenching constants for coordination complex formation between electron acceptors 4.3 and 4.4 and electron donors 4.6-4.9 and 4.12-4.14</b>	220

## List of Figures

<b>Figure 1.1: Cubic perovskite crystal structure</b>	3
<b>Figure 1.2: Schematic for basic perovskite solar cell</b>	3
<b>Figure 1.3: Schematic for general quantum dot solar cell</b>	4
<b>Figure 1.4: Solar spectrum outside earth's atmosphere AM0 and average solar Spectrum accounting for atmospheric interference AM1.5</b>	6
<b>Figure 1.5: 1 chlorophyll-a, 2 metal phthalocyanine, and 3 merocyanine dye are organic chromophores for use in photovoltaic devices</b>	6
<b>Figure 1.6: Representation of the ground and excited state energy levels</b>	7
<b>Figure 1.7: Electron flow in a single layer organic photovoltaic device</b>	8
<b>Figure 1.8: Two separate pathways for generation of electricity in solar cells</b>	9
<b>Figure 1.9: Electron flow in n-type dye sensitized solar cell</b>	10
<b>Figure 1.10: Current voltage curve for a photovoltaic device</b>	10
<b>Figure 1.11: Schematic of a typical bulk heterojunction solar cell</b>	12
<b>Figure 1.12: 1 porphyrin, 2 phthalocyanine, and 3 subphthalocyanine are chromophoric systems for use in photovoltaic devices</b>	13
<b>Figure 1.13: 1 [6,6]phenyl-C61-butyric acid methyl ester (PCBM), 2 Indene C60, and 3 C60 are fullerene electron acceptors for photovoltaic devices</b>	14
<b>Figure 1.14: Structures of non-fullerene acceptor materials for different bandgaps used in photovoltaic devices</b>	15
<b>Figure 1.15: Lattice structures (a) graphene and (b) single walled carbon nanotubes.</b>	16
<b>Figure 1.16: Schematic diagram of a typical dye sensitized solar cell</b>	17
<b>Figure 1.17: Ruthenium dyes for dye sensitized solar cells</b>	17
<b>Figure 1.18: Dyes 1-3 are examples of metal free indoline derivatives for photovoltaic applications</b>	18
<b>Figure 1.19: Panchromatic Porphyrin sensitizer with record high 13% efficiency</b>	19
<b>Figure 1.20: Absorption/Fluorescence schematic and sample spectrum</b>	20
<b>Figure 1.21: Jablonski diagram depicting electronic states and transitions</b>	20
<b>Figure 1.22: Transient absorption spectrometer optical layout</b>	21
<b>Figure 1.23: Cyclic voltammetry graph of a reversible oxidation process</b>	22
<b>Scheme 2.1: Synthetic pathway for preparation of the aza-BODIPYs 2.5a-2.5e</b>	31

<b>Scheme 2.2: The synthesis of pyrene-BODIPYs 2.7-2.10</b>	81
<b>Figure 2.1: <sup>1</sup>H NMR spectrum of compound 2.5a in CDCl<sub>3</sub></b>	32
<b>Figure 2.2: <sup>13</sup>C NMR spectrum of compound 2.5a in CDCl<sub>3</sub></b>	33
<b>Figure 2.3: <sup>1</sup>H NMR spectrum of compound 2.5b in CDCl<sub>3</sub></b>	33
<b>Figure 2.4: <sup>13</sup>C NMR spectrum of compound 2.5b in CDCl<sub>3</sub></b>	34
<b>Figure 2.5: <sup>1</sup>H NMR spectrum of compound 2.5c in CDCl<sub>3</sub></b>	34
<b>Figure 2.6: <sup>13</sup>C NMR spectrum of compound 2.5c in CDCl<sub>3</sub></b>	35
<b>Figure 2.7: <sup>1</sup>H NMR spectrum of compound 2.5d in CDCl<sub>3</sub></b>	35
<b>Figure 2.8: <sup>13</sup>C NMR spectrum of compound 2.5d in CDCl<sub>3</sub></b>	36
<b>Figure 2.9: <sup>1</sup>H NMR spectrum of compound 2.5e in CDCl<sub>3</sub></b>	36
<b>Figure 2.10: <sup>13</sup>C NMR spectrum of compound 2.5e in CDCl<sub>3</sub></b>	37
<b>Figure 2.11: HRMS spectra of compounds 2.4a (left) and 2.5a (right)</b>	37
<b>Figure 2.12: HRMS spectra of compounds 2.4b (left) and 2.5b (right)</b>	38
<b>Figure 2.13: HRMS spectra of compounds 2.4c (left) and 2.5c (right)</b>	38
<b>Figure 2.14: HRMS spectra of compounds 2.4d (left) and 2.5d (right)</b>	39
<b>Figure 2.15: HRMS spectra of compounds 2.4e (left) and 2.5e (right)</b>	39
<b>Figure 2.16: CAMERON representation of aza-BODIPYs</b>	41
<b>Figure 2.17: UV-Vis spectra of compounds 2.5a – 2.5e and 2.6 in DCM</b>	42
<b>Figure 2.18: Fluorescence spectra of aza-BODIPYs</b>	44
<b>Figure: 2.19: Fluorescence spectrum at 275 nm excitation of compounds 2.5a-2.5d in DCM</b>	44
<b>Figure 2.20: Pump-probe data for 2.5a in a DCM solution</b>	45
<b>Figure 2.21: Pump-probe data for 2.5b in a DCM solution</b>	45
<b>Figure 2.22: Pump-probe data for 2.5c in a DCM solution</b>	46
<b>Figure 2.23: Pump-probe data for 2.5d in a DCM solution</b>	46
<b>Figure 2.24: Pump-probe response for 2.5e</b>	48
<b>Figure 2.25: CV/DPV of compound 2.5a and 2.5d in DCM</b>	50
<b>Figure 2.26: CV and DPV data for aza-BODIPYs 2.5b and 2.5e in DCM</b>	50
<b>Figure 2.27: CV/DPV of compound 2.5c and 2.6 in DCM</b>	51
<b>Figure 2.28: Spectroelectrochemical oxidation of compound 2.5e in DCM/0.15 M TFAB solvent system</b>	52

<b>Figure 2.29: IVCT band deconvolution analysis for [2.5e]<sup>+</sup></b>	52
<b>Figure 2.30: DFT-predicted compositions of frontier orbitals for compounds 2.5a–2.5e and 2.6</b>	54
<b>Figure 2.31: DFT-predicted energy diagram for the frontier MOs in 2.5a – 2.5e and 2.6</b>	54
<b>Figure 2.32: DFT-predicted frontier molecular orbitals for 2.5a – 2.5e and 2.6</b>	55
<b>Figure 2.33: Experimental (top) and TDDFT-predicted (bottom) UV-vis spectra of aza-BODIPYs 2.5a – 2.5e and 2.6</b>	57
<b>Figure 2.34: Steady-state and difference absorption spectra of the aza-BODIPY 2.5a upon stepwise addition of the C<sub>60</sub> or C<sub>70</sub> fullerenes</b>	59
<b>Figure 2.35: Steady-state and difference absorption spectra of the aza-BODIPY 2.5b upon stepwise addition of the C<sub>60</sub> or C<sub>70</sub> fullerenes</b>	60
<b>Figure 2.36: Steady-state and difference absorption spectra of the aza-BODIPY 2.5c upon stepwise addition of the C<sub>60</sub> or C<sub>70</sub> fullerenes</b>	61
<b>Figure 2.37: Steady-state and difference absorption spectra of the aza-BODIPY 2.5d upon stepwise addition of the C<sub>60</sub> or C<sub>70</sub> fullerenes</b>	62
<b>Figure 2.38: Steady-state and difference absorption spectra of the aza-BODIPY 2.6 upon stepwise addition of the C<sub>60</sub> or C<sub>70</sub> fullerenes</b>	63
<b>Figure 2.39: Difference absorption spectra of the aza-BODIPY 2.5e upon stepwise addition of the C<sub>60</sub> or C<sub>70</sub> fullerenes</b>	64
<b>Figure 2.40: Pump-probe transients for 2.5e, a mixture of 2.5e and C<sub>60</sub>, and C<sub>60</sub> in solution</b>	66
<b>Figure 2.41: Steady-state emission and difference absorption spectra of the aza-BODIPY 2.5a upon stepwise addition of the (6,5)-SWCNT or graphene</b>	67
<b>Figure 2.42: Steady-state emission and difference absorption spectra of the aza-BODIPY 2.5b upon stepwise addition of the (6,5)-SWCNT or graphene</b>	68
<b>Figure 2.43: Steady-state emission and difference absorption spectra of the aza-BODIPY 2.5c upon stepwise addition of the (6,5)-SWCNT or graphene</b>	69
<b>Figure 2.44: Steady-state emission and difference absorption spectra of the aza-BODIPY 2.5d upon stepwise addition of the (6,5)-SWCNT or graphene</b>	70

<b>Figure 2.45: Steady-state emission and difference absorption spectra of the aza-BODIPY 2.6 upon stepwise addition of the (6,5)-SWCNT or graphene</b>	71
<b>Figure 2.46: Difference absorption spectra of the aza-BODIPY 2.6 upon stepwise addition of the (6,5)-SWCNT or graphene</b>	72
<b>Figure 2.47: Time-dependent changes in absorption and fluorescence spectra of 2.5b in the presence of excess of (6,5)-SWCNT</b>	72
<b>Figure 2.48: Time-dependent changes in absorption and fluorescence spectra of 2.5b in the presence of excess of graphene</b>	73
<b>Figure 2.49: Solid-state (KBr matrix) UV-vis spectra of 2.5b and 2.5e without and in the presence of C<sub>60</sub> fullerene</b>	74
<b>Figure 2.50: Solid-state (KBr matrix) UV-vis spectra of 2.5a, 2.5c, and 2.5d without and in the presence of C<sub>60</sub> fullerene.</b>	74
<b>Figure 2.51: Representative images of the X-ray crystal structure of 2.5b·C<sub>60</sub></b>	76
<b>Figure 2.52: Representative images of the X-ray crystal structure of 2.5d·2C<sub>60</sub></b>	77
<b>Figure 2.53: Predicted geometries and charge density isosurfaces of intramolecular interaction calculated at LC-wPBE level of theory</b>	80
<b>Figure 2.54: <sup>1</sup>H NMR spectra of compound 2.8 in CDCl<sub>3</sub></b>	82
<b>Figure 2.55: <sup>1</sup>H COSY NMR spectra of compound 2.8 in CDCl<sub>3</sub></b>	82
<b>Figure 2.56: <sup>13</sup>C NMR spectra of compound 2.8 in CDCl<sub>3</sub></b>	83
<b>Figure 2.57: <sup>1</sup>H NMR spectra of compound 2.9 in CDCl<sub>3</sub></b>	83
<b>Figure 2.58: <sup>1</sup>H COSY NMR spectra of compound 2.9 in CDCl<sub>3</sub></b>	84
<b>Figure 2.59: <sup>13</sup>C NMR spectra of compound 2.9 in CDCl<sub>3</sub></b>	84
<b>Figure 2.60: <sup>1</sup>H NMR spectra of compound 2.10 in CDCl<sub>3</sub></b>	85
<b>Figure 2.61: <sup>1</sup>H COSY NMR spectra of compound 2.10 in CDCl<sub>3</sub></b>	85
<b>Figure 2.62: <sup>13</sup>C NMR spectra of compound 2.10 in CDCl<sub>3</sub></b>	86
<b>Figure 2.63: HRMS spectra of compound 2.8, 2.9, and 2.10</b>	86
<b>Figure 2.64: CAMERON drawings of BODIPYs 2.8 and 2.9</b>	87
<b>Figure 2.65: Absorption and TDDFT-predicted spectra of pyrene-BODIPYs 2.8, 2.9, and 2.10 in DCM</b>	88

<b>Figure 2.66: Normalized emission spectra of pyrene-BODIPYs 2.8 and 2.9 in toluene and fluorescence intensity increase upon oxidation of BODIPY 2.10 with FeCl<sub>3</sub> in DCM/MeOH</b>	90
<b>Figure 2.67: CV and DPV data for compound 2.10 in DCM/0.1M TBAP system</b>	91
<b>Figure 2.68: Spectroelectrochemical oxidation of compound 2.10 in DCM/0.3M TBAP system</b>	92
<b>Figure 2.69: Chemical oxidation of BODIPY 2.10 with Fe(ClO<sub>4</sub>)<sub>3</sub> in DCM/MeOH System</b>	92
<b>Figure 2.70: DFT-predicted compositions of frontier orbitals for pyrene-BODIPYs 2.8 – 2.10</b>	93
<b>Figure 2.71: DFT-predicted energy diagram for the frontier MOs in pyrene-BODIPYs 2.8 – 2.10</b>	94
<b>Figure 2.72: DFT-predicted images of frontier orbitals for pyrene-BODIPYs 2.8 – 2.10</b>	94
<b>Figure 2.73: Difference absorption spectra of the BODIPYs 2.8 – 2.10 observed upon titrations with C<sub>60</sub> (top) and C<sub>70</sub> (bottom) fullerenes in DCM/toluene</b>	97
<b>Figure 2.74: Changes in steady-state fluorescence of the BODIPYs 2.8 and 2.9 observed upon titrations with C<sub>60</sub> (top) and C<sub>70</sub> (bottom) in DCM/toluene</b>	97
<b>Figure 2.75: Difference absorption spectra of the BODIPYs 2.8 – 2.10 observed upon titrations with (6,5)-SWCNT and graphene fullerenes in DCM/toluene</b>	98
<b>Figure 2.76: Changes in steady-state fluorescence of the BODIPYs 2.8 and 2.9 observed upon titrations with (6,5)-SWCNT and graphene in DCM/toluene</b>	99
<b>Figure 2.77: Transient absorption spectra of BODIPY 2.8</b>	100
<b>Figure 2.78: Transient absorption spectra of C<sub>60</sub> fullerene with 410 nm pump</b>	101
<b>Figure 2.79: Transient absorption spectra of BODIPY 2.8 mixture with C<sub>60</sub> (1:10 mol/mol) pumped at 560 and 410 nm.</b>	101
<b>Scheme 3.1: Synthetic pathway for preparation of the ferrocene-BODIPY-fullerene triads 3.3a – 3.3d</b>	130
<b>Scheme 3.2: Synthetic pathway for preparation of the reference BODIPY-fullerene dyad 3.3e and (2,3)-3.3b</b>	131
<b>Scheme 3.3: Synthesis of compounds 3.5a-d, 3.6a-e and 3.7</b>	132
<b>Figure 3.1: <sup>1</sup>H NMR spectrum of compound 3.2a in CDCl<sub>3</sub></b>	133

<b>Figure 3.2: <math>^1\text{H}</math> NMR spectrum of compound (3,4)-3.2b in <math>\text{CDCl}_3</math></b>	134
<b>Figure 3.3: <math>^1\text{H}</math> NMR spectrum of compound (2,3)-3.2b in <math>\text{CDCl}_3</math></b>	134
<b>Figure 3.4: <math>^1\text{H}</math> NMR spectrum of compound 3.2c in <math>\text{CDCl}_3</math></b>	135
<b>Figure 3.5: <math>^1\text{H}</math> NMR spectrum of compound 3.2d in <math>\text{CDCl}_3</math></b>	135
<b>Figure 3.6: <math>^1\text{H}</math> NMR spectrum of compound 3.2e in <math>\text{CDCl}_3</math></b>	136
<b>Figure 3.7: <math>^1\text{H}</math> NMR spectrum of compound 3.3a in <math>\text{C}_6\text{D}_6</math></b>	136
<b>Figure 3.8: <math>^1\text{H}</math> NMR spectrum of compound (3,4)-3.3b in <math>\text{C}_6\text{D}_6</math></b>	137
<b>Figure 3.9: <math>^1\text{H}</math> NMR spectrum of compound (2,3)-3.3b in <math>\text{C}_6\text{D}_6</math></b>	137
<b>Figure 3.10: <math>^1\text{H}</math> NMR spectrum of compound 3.3c in <math>\text{C}_6\text{D}_6</math></b>	138
<b>Figure 3.11: <math>^1\text{H}</math> NMR spectrum of compound 3.3d in <math>\text{C}_6\text{D}_6</math></b>	138
<b>Figure 3.12: <math>^1\text{H}</math> NMR spectrum of compound 3.3e in <math>\text{C}_6\text{D}_6</math></b>	139
<b>Figure 3.13: APCI high-resolution mass spectrum of compound 3.2a and 2.2c</b>	139
<b>Figure 3.14: APCI high-resolution mass spectrum of compound (3,4)-3.2b and (2,3)-3.2</b>	140
<b>Figure 3.15: APCI high-resolution mass spectrum of compound 3.2d and 3.2e</b>	140
<b>Figure 3.16: APCI high-resolution mass spectrum of compound 3.3a and 3.3c</b>	141
<b>Figure 3.17: APCI high-resolution mass spectrum of compound (3,4)-3.3b and (2,3)-3.3</b>	141
<b>Figure 3.18: APCI high-resolution mass spectrum of compound 3.3d (left) and 3.3e</b>	142
<b>Figure 3.19: CAMERON drawing of the X-ray structure of Fc-BODIPY-<math>\text{C}_{60}</math> triad (2,3)-3.3b and packing motifs observed in the X-ray crystal structure of (2,3)-3.3b.</b>	143
<b>Figure 3.20: Overlapped UV-Vis spectra of 3.3a – 3.3e and 3.4 in DCM</b>	145
<b>Figure 3.21: Room-temperature CV and DPV data for 3.4 (a), 3.3e (b), 3.3a (c), (3,4)-3.3b (d), (2,3)-3.3b (e), 3.3c (f), and 3.3d (g) in DCM/0.05 M TFAB system</b>	146
<b>Figure 3.22: Spectroelectrochemical oxidation of triad (3,4)-3.3b in 0.15 M DCM/TFAB solvent system</b>	148
<b>Figure 3.23: DFT-predicted compositions of frontier orbitals for 3.3a–3.3e</b>	150
<b>Figure 3.24: DFT-predicted energy diagram for the frontier MOs in 3.3a – 3.3d and 3.4</b>	150
<b>Figure 3.25: DFT-predicted frontier molecular orbitals for 3.3a – 3.3e</b>	151

<b>Figure 3.26: Experimental and TDDFT-predicted UV-vis spectra of triads 3.3a – 3.3d and dyad 3.3e</b>	151
<b>Figure 3.27: Pump-probe spectra for the BODIPY-C<sub>60</sub> dyad, Fc<sub>2</sub>-BODIPY-C<sub>60</sub> triad and Fc<sub>2</sub>-BODIPY</b>	155
<b>Figure 3.28: Recovery of the ground state bleach for the Fc<sub>2</sub>-BODIPY, BODIPY-C<sub>60</sub> dyad Fc<sub>2</sub>-BODIPY-C<sub>60</sub> triad, and Fc<sub>2</sub>-BODIPY-C<sub>60</sub> triad</b>	156
<b>Figure 3.29: Molecular structures and labels</b>	158
<b>Figure 3.30: <sup>1</sup>H NMR spectrum of compound 3.6a in CDCl<sub>3</sub></b>	159
<b>Figure 3.31: <sup>13</sup>C NMR spectrum of compound 3.6a in CDCl<sub>3</sub></b>	160
<b>Figure 3.32: <sup>1</sup>H NMR spectrum of compound 3.6b in CDCl<sub>3</sub></b>	160
<b>Figure 3.33: <sup>13</sup>C NMR spectrum of compound 3.6b in CDCl<sub>3</sub></b>	161
<b>Figure 3.34: <sup>1</sup>H NMR spectrum of compound 3.6c in CDCl<sub>3</sub></b>	161
<b>Figure 3.35: <sup>13</sup>C NMR spectrum of compound 3.6c in CDCl<sub>3</sub></b>	162
<b>Figure 3.36: <sup>1</sup>H NMR spectrum of compound 3.6d in CDCl<sub>3</sub></b>	162
<b>Figure 3.37: <sup>13</sup>C NMR spectrum of compound 3.6d in CDCl<sub>3</sub></b>	163
<b>Figure 3.38: <sup>1</sup>H NMR spectrum of compound 3.6e in CDCl<sub>3</sub></b>	163
<b>Figure 3.39: <sup>13</sup>C NMR spectrum of compound 3.6e in CDCl<sub>3</sub></b>	164
<b>Figure 3.40: <sup>1</sup>H NMR spectrum of compound 3.7 in CDCl<sub>3</sub></b>	164
<b>Figure 3.41: HRMS spectrum of compound 3.6a-e and 3.7</b>	165
<b>Figure 3.42: Absorption spectra for 3.5a-d and 3.6a-e in toluene</b>	166
<b>Figure 3.43: Absorption and emission spectra of compounds 3.5a and 3.6a</b>	166
<b>Figure 3.44: Absorption and emission spectra of compounds 3.5b and 3.6b</b>	167
<b>Figure 3.45: Absorption and emission spectra of compounds 3.5c and 3.6c</b>	167
<b>Figure 3.46: Absorption and emission spectra of compounds 3.5d and 3.6d</b>	168
<b>Figure 3.47: Absorption and emission spectra of compounds 3.5d and 3.6e</b>	168
<b>Figure 3.48: Pump-probe measurements on 3.6a in toluene excited at 530 nm</b>	170
<b>Figure 3.49: DPV spectra of compounds 3.5a and 3.6a</b>	172
<b>Figure 3.50: DPV spectra of compounds 3.5b and 3.6b</b>	172
<b>Figure 3.51: DPV spectra of compounds 3.5c (green) and 3.6c</b>	173
<b>Figure 3.52: DPV spectra of compounds 3.5d (green) and 3.6d</b>	173
<b>Figure 3.53: DPV spectra of compounds 3.5d (green) and 3.6e</b>	174

<b>Figure 3.54: TPSSh SP DFT-predicted molecular orbital composition of compounds 3.5a and 3.6a</b>	175
<b>Figure 3.55: TPSSh SP DFT-predicted molecular orbital composition of compounds 3.5b (left) and 3.6b</b>	175
<b>Figure 3.56: TPSSh SP DFT-predicted molecular orbital composition of compounds 3.5c (left) and 3.6c</b>	176
<b>Figure 3.57: TPSSh SP DFT-predicted molecular orbital composition of compounds 3.5d (left) and 3.6d</b>	176
<b>Figure 3.58: TPSSh SP DFT-predicted molecular orbital composition of compounds 3.5d and 3.6e</b>	176
<b>Figure 3.59: B3LYP SP DFT-predicted molecular orbital composition of compounds 3.5a (left) and 3.6a</b>	177
<b>Figure 3.60: B3LYP SP DFT-predicted molecular orbital composition of compounds 3.5b and 3.6b</b>	177
<b>Figure 3.61: B3LYP SP DFT-predicted molecular orbital composition of compounds 3.5c and 3.6c</b>	177
<b>Figure 3.62: B3LYP SP DFT-predicted molecular orbital composition of compounds 3.5d and 3.6d</b>	178
<b>Figure 3.63: B3LYP SP DFT-predicted molecular orbital composition of compounds 3.5d (left) and 3.6e</b>	178
<b>Figure 3.64: TD DFT-predicted and experimental absorption spectra of compounds 3.5a and 3.6a</b>	179
<b>Figure 3.65: TD DFT-predicted and experimental absorption spectra of compounds 3.5b and 3.6b</b>	180
<b>Figure 3.66: TD DFT-predicted and experimental absorption spectra of compounds 3.5c and 3.6c</b>	180
<b>Figure 3.67: TD DFT-predicted and experimental absorption spectra of compounds 3.5d and 3.6d</b>	181
<b>Figure 3.68: TD DFT-predicted and experimental absorption spectra of compounds 3.5d and 3.6e</b>	181

<b>Figure 3.69: TD DFT-predicted and experimental absorption spectra of compounds 3.5a and 3.6a</b>	182
<b>Figure 3.70: TD DFT-predicted and experimental absorption spectra of compounds 3.5b and 3.6b</b>	182
<b>Figure 3.71: TD DFT-predicted and experimental absorption spectra of compounds 3.5c and 3.6c</b>	183
<b>Figure 3.72: TD DFT-predicted and experimental absorption spectra of compounds 3.5d and 3.6d</b>	183
<b>Figure 3.73: TD DFT-predicted and experimental absorption spectra of compounds 3.5d and 3.6e</b>	184
<b>Figure 3.74: DFT computational predictions of orbital energies for compounds in Figure 3.29. Energetics relative to the initial optically excited <math>\pi^*</math> state derived from experimental optical and electrochemical values in table 3.6</b>	186
<b>Figure 3.75: TPSSh DFT-predicted frontier molecular orbitals of compounds 3.5a-d and 3.6a-e</b>	187
<b>Scheme 4.1: Synthetic pathway for preparation of BODIPY-pyridine compounds</b>	208
<b>Figure 4.1: Reference compounds fulleropyrrolidine 4.4 and 4.5</b>	208
<b>Figure 4.2: Electron donor porphyrins and phthalocyanine</b>	209
<b>Figure 4.3: Electron donor zinc octaethylporphyrins</b>	210
<b>Figure 4.4: <math>^1\text{H}</math> NMR spectrum of compound 4.3 <math>\text{CDCl}_3</math></b>	211
<b>Figure 4.5: <math>^{13}\text{C}</math> NMR spectrum of compound 4.3 <math>\text{CDCl}_3</math></b>	211
<b>Figure 4.6: HRMS spectra of compound 4.3</b>	212
<b>Figure 4.7: UV-Vis spectra of compound 4.3 in DCM</b>	213
<b>Figure 4.8: UV-Vis spectra of 4.6, 4.7, 4.8, and 4.9 in DCM</b>	213
<b>Figure 4.9: UV-Vis spectra of 4.10, 4.11, 4.12, 4.13, and 4.14 in DCM</b>	214
<b>Figure 4.10: Fluorescence spectra of compound 4.3 at an excitation wavelength of 605 nm in DCM</b>	214
<b>Figure 4.11: Fluorescence spectra of compounds 4.6 - 4.8 in DCM</b>	215
<b>Figure 4.12: Fluorescence spectra of zinc octaethylporphyrins 4.10 - 4.14 in DCM</b>	215
<b>Figure 4.13: CV/DPV of compound 4.3 in DCM</b>	217
<b>Figure 4.14: CV/DPV of compound 4.3 + 4.11 in DCM</b>	218

<b>Figure 4.15: Absorption titration of 4.3 into solution of 4.6 and absorption titration of 4.4 into solution of 4.6 in DCM</b>	220
<b>Figure 4.16: Fluorescence titration of 4.6 into solution of 4.3 excitation: 530 nm and Fluorescence titration of 4.4 into solution of 4.6 excitation: 550 nm in DCM</b>	220
<b>Figure 4.17: Absorption titration of 4.3 into solution of 4.7 and absorption titration of 4.4 into solution of 4.7 in DCM</b>	221
<b>Figure 4.18: Fluorescence titration of 4.7 into solution of 4.3 excitation: 530 nm and Fluorescence titration of 4.4 into solution of 4.7 excitation: 540 nm in DCM</b>	221
<b>Figure 4.19: Absorption titration of 4.8 into solution of 4.3 and absorption titration of 4.4 into solution of 4.8 in DCM</b>	222
<b>Figure 4.20: Fluorescence titration of 4.8 into solution of 4.3 excitation: 550 nm and fluorescence titration of 4.4 into solution of 4.8 excitation: 610 nm in DCM</b>	222
<b>Figure 4.21: Absorption titration of 4.9 into solution of 4.3 and absorption titration of 4.4 into solution of 4.9 in DCM.</b>	223
<b>Figure 4.22: Fluorescence titration of 4.9 into solution of 4.3 excitation: 610 nm in DCM</b>	223
<b>Figure 4.23: Absorption titration of 4.3 into solution of 4.10 and absorption titration of 4.4 into solution of 4.10 in DCM</b>	224
<b>Figure 4.24: Fluorescence titration of 4.3 into solution of 4.10 excitation: 530 nm and fluorescence titration of 4.4 into solution of 4.10 excitation 530 nm in DCM</b>	225
<b>Figure 4.25: Absorption titration of 4.3 into solution of 4.11 and absorption titration of 4.4 into solution of 4.11 in DCM</b>	225
<b>Figure 4.26: Fluorescence titration of 4.3 into solution of 4.11 excitation: 410 nm and fluorescence titration of 4.4 into solution of 4.11 excitation 550 nm in DCM</b>	226
<b>Figure 4.27: Absorption titration of 4.3 into solution of 4.12 and absorption titration of 4.4 into solution of 4.12 in DCM</b>	226
<b>Figure 4.28: Fluorescence titration of 4.3 into solution of 4.12 excitation: 410 nm and fluorescence titration of 4.4 into solution of 4.12 excitation 550 nm in DCM</b>	227
<b>Figure 4.29: Absorption titration of 4.3 into solution of 4.13 and absorption titration of 4.4 into solution of 4.13 in DCM</b>	227

<b>Figure 4.30: Fluorescence titration of 4.13 into solution of 4.3 excitation: 595 nm and fluorescence titration of 4.4 into solution of 4.13 excitation 580 nm in DCM</b>	228
<b>Figure 4.31: Absorption titration of 4.3 into solution of 4.14 and absorption titration of 4.4 into solution of 4.14 in DCM</b>	228
<b>Figure 4.32: Fluorescence titration of 4.14 into solution of 4.3 excitation: 560 nm and fluorescence titration of 4.4 into solution of 4.14 excitation 600 nm in DCM</b>	229
<b>Figure 4.33: Transient absorption of 4.3 and 4.8 1:1 in DCM at 665nm 100uW</b>	230
<b>Figure 4.34: Transient absorption of 4.4 and 4.8 1:1 in DCM at 665nm 100uW</b>	230

# Chapter 1

## Introduction

### Solar Energy

One of the greatest problems the World is currently facing can be summed up best by a quote from Nobel prize winner Richard Smalley, “After a little bit of conversation in any group of American citizens, and probably any group of citizens in the world, I believe you will find that pretty much everyone will agree that energy is the single most important problem”.<sup>1</sup> This energy crisis is due to increasing energy demand, dependence on non-renewable resources such as fossil fuels, and an increasing World population. It is estimated that energy consumption will increase by 20-35% from the years 2010 to 2035 according to the international energy agency.<sup>2</sup> The increasing energy demand is a problem, because most of the World’s current energy production comes from fossil fuels which are not only a finite resource, but also cause serious harm to our environment.

When fossil fuels such as coal, oil, and natural gas are combusted they release CO<sub>2</sub> into our environment. Carbon dioxide along with other heat absorbing gases linger in the atmosphere and act as an insulator for thermal energy. These gases act as a barrier to heat radiation and prevents it from passing back through the atmosphere into space. This is commonly referred to as the greenhouse effect.<sup>3</sup> If the concentration of greenhouse gases in the atmosphere continues to increase it will substantially change how much heat energy is absorbed and will have a long lasting effect on the climate of the planet. This means if we want to continue energy production at this scale we will not only need to find a renewable energy source, but one that is less impactful on our environment.

Many avenues have been pursued for finding the best renewable energy source to replace the use of fossil fuels such as wind, hydroelectric, geothermal, biofuels, and solar energy. The solution will most likely be contribution from all these renewable sources. The one major problem that many of these renewable energy sources have is that they struggle to produce the quantity needed to meet the energy demand.<sup>4</sup> The amount of energy produced by all renewable energy sources in 2011 was estimated to be about 19% of the total energy being consumed.<sup>5</sup> This means

that at least one of these renewable energy sources production would need to be increased drastically to meet the World's energy demand. A promising candidate for this is solar energy. The reason for this is because the total amount of solar irradiation per year on the Earth's surface equals roughly 10000 times the World's yearly energy needs.<sup>6</sup> This means even if we can gather only a small fraction of this energy it would be enough to meet the World's needs. However additional technological advances will need to happen for this to be an economically viable option.

The most developed and well-known area of photovoltaic devices for energy production are silicon-based solar cells. Since the very first silicon solar cell with efficiencies lower than 1% was made advances in the field have led to efficiencies of 25%.<sup>7</sup> However even with these strides in the field of photovoltaic devices the generation cost of these devices are still not competitive with conventional energy sources for it to become widely commercialized. Many strategies have been employed to achieve this such as thinning down crystalline silicon to reduce material cost as well as using thin films of more highly absorbent material. The problem is that all of these ideas lead to lower efficiencies so further techniques would also need to be developed to retain desired efficiencies well keeping the cost down. An alternative to silicon solar cells that has garnered a lot of interest in recent years are the series of third generation photovoltaic devices.

### **Third generation solar devices**

Third generation thin film photovoltaic devices are perovskite, quantum dot, organic, and dye sensitized solar cells. They have desirable properties over their silicon counterparts such as mechanical flexibility, low temperature processing, and abundance of cheap organic material all allowing for reduced production costs. The problems of third generation solar cells vary between each one with some suffering from lower efficiencies while others have poor stability and life times compared to silicon devices. However the field of these thin film photovoltaic devices is still relatively new. With the wide range of molecules and possibilities of chemical modifications with these organic based compounds there are still many unexplored avenues of research that could lead to the desired efficiencies needed for these devices to become commercially viable. Here I will attempt to give a broad overview of third generation perovskite and quantum dot solar cells.

Perovskite based photovoltaic devices consist of a compound that has a perovskite based crystal structure that is usually an organic-inorganic lead or tin halide substance that absorbs light

and acts as a charge carrier conductor. They typically have a chemical formula  $ABX_3$  where A and B are cations and X is an anion.<sup>8</sup> Figure 1.1 depicts the crystal structure of a typical perovskite where the anions are mobile and can wander due to vacancies in the crystal.<sup>9</sup>

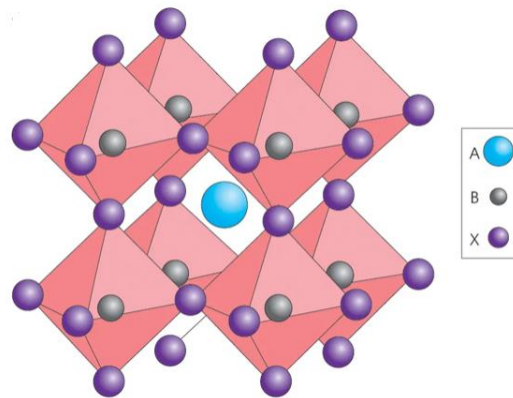


Figure 1.1: Cubic perovskite crystal structure<sup>63</sup>

This crystal structure provides favorable properties such as greater charge-carrier mobility, longer exciton diffusion length, and low exciton binding energy compared to the organic based photovoltaic devices.<sup>10</sup> Excitons consist of a bound electron and electron hole pair an example being when an electron is excited via absorption. Perovskites having high excitation diffusion and exciton binding allows for separation of the electron and electron hole pair which result in better efficiency. Perovskites also still maintain high light absorptivity and easily tunable bandgaps which have allowed them to achieve power conversion efficiencies higher than 20% making them a promising alternative to silicon based solar cells. A schematic for typical perovskite solar cell can be seen in Figure 1.2

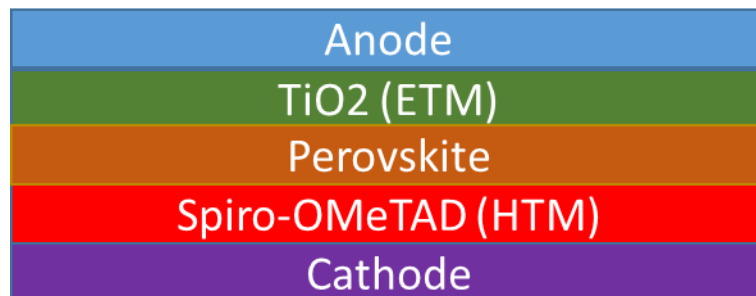


Figure 1.2: Schematic for basic perovskite solar cell. ETM: electron transport material HTM: hole-transport material

The major issue with these devices is their stability in the presence of moisture. Perovskites are prone to hydrolysis when moisture is introduced due to their hygroscopic nature resulting in cell lifetimes far shorter than feasible for industrial applications. An additional problem with perovskite materials is the toxicity of the heavy metals present in the perovskite crystals.<sup>11, 12</sup> This can become an even larger problem when the perovskites degrade as they form harmful compounds containing heavy metals such as lead.<sup>13</sup>

Colloidal quantum dots are semiconductor nanocrystals that are chemically prepared with diameters less than twice the Bohr radius.<sup>14</sup> The energy levels and thus the bandgap of these quantum dots become tunable by changing their size. Sizes of the quantum dots are typically controlled by varying the temperature or reaction time of the synthesis. This means various bandgaps can be achieved without changing the material or using different construction techniques.<sup>15</sup> This unique property allows them to reach a wide range of wavelengths especially into the near infrared spectrum. These devices can also be assembled using a solution processing method.

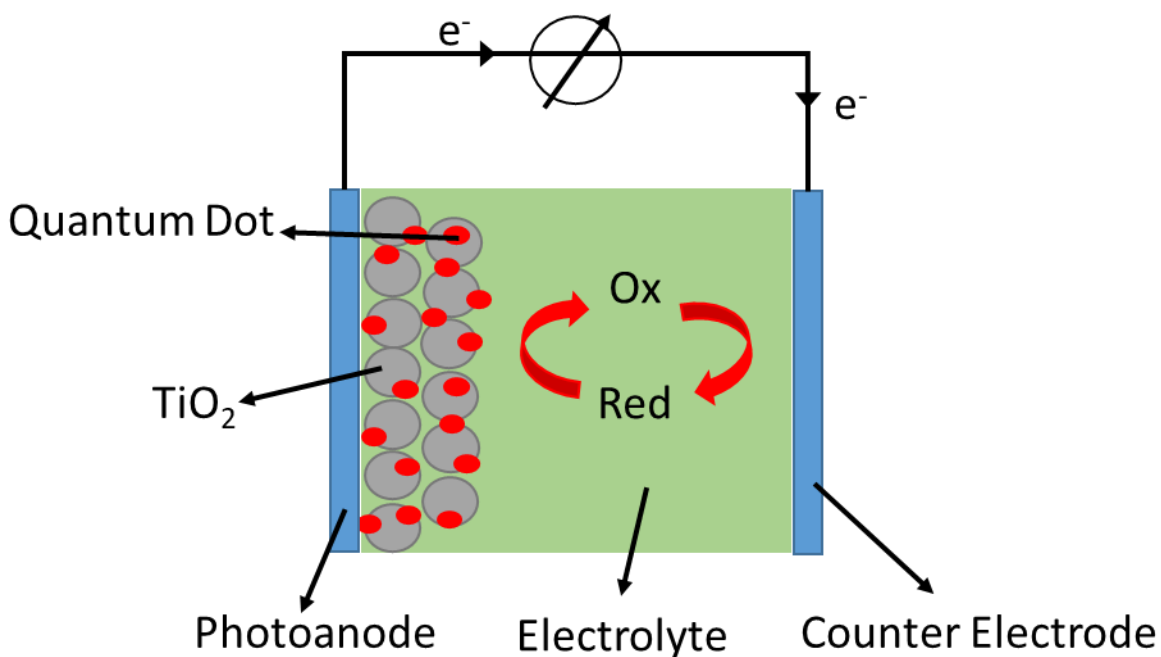


Figure 1.3: Schematic for general quantum dot solar cell

These properties have garnered quantum dot photovoltaic devices a lot of attention since they all help drive down the cost of production while maintaining efficiencies.<sup>16</sup>

The disadvantages of colloidal quantum dot devices are toxicity, stability, and electronic trap states. Electronic trap states are when electrons or electron holes become stuck inside defects in the material that require much more energy to remove than they have resulting in localized electronic states which leads to a lower efficiency. Quantum dots are commonly made using copper indium gallium selenide, cadmium telluride, lead selenide, and lead sulfide. These compounds all have some level of toxicity and due to degradation in air these toxic compounds would find their way into the environment. The performance of these cells is also affected by electronic trap states that occur from surface defects on the quantum dots that then trap electrons or their hole pairs leading to reduced efficiencies.

Since perovskite and quantum dot based photovoltaic devices both suffer from poor stability and contain toxic chemicals that can leach into the environment they appear to be less promising replacements for silicon solar cells. Organic and dye sensitized solar cells however are more promising as they don't suffer from the same stability and toxicity problems while with clever design can still be able to achieve high efficiencies. Here I will go into a more in depth explanation on the development of organic and dye sensitized solar cells.

## **Design of Organic and Dye Sensitized Photovoltaic Devices**

The basis of a photovoltaic device is to convert energy from the sun in the form of light into electrical energy that we can use. The intensity of light from the sun that reaches the earth just before it reaches our atmosphere is known as the solar constant with a value of  $1353 \text{ W/m}^2$ . As the solar radiation passes through our atmosphere it experiences light scattering and absorption. This changes the spectrum and intensity of the solar radiation at the Earth's surface with a total value scaled to  $1000 \text{ W/m}^2$  (Figure 1.4). A light absorbing material is used to capture this energy which is then converted into electricity.<sup>17</sup>

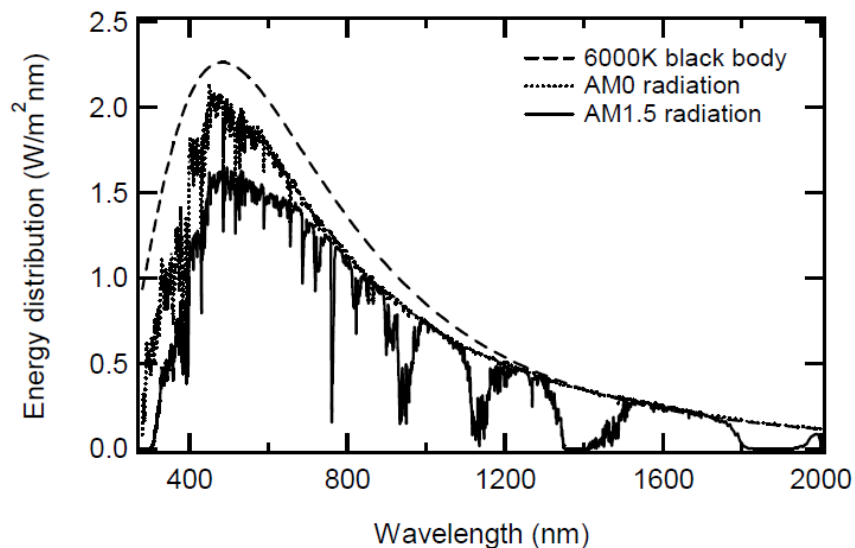


Figure 1.4: Solar spectrum outside the earth's atmosphere AM0 and average solar spectrum accounting for atmospheric interference AM1.5<sup>66</sup>

Organic photovoltaic devices use carbon-based molecules with semiconducting properties as their light absorbing material. These semiconducting molecules all belong to a class of planar aromatic compounds that have delocalization of their  $\pi$  electrons across the entire conjugated system. Examples of some of the first materials used for OPV are chlorophyll-a (1), metal phthalocyanine (2), and merocyanine dye (3) figure 1.5.<sup>18,19,20</sup>

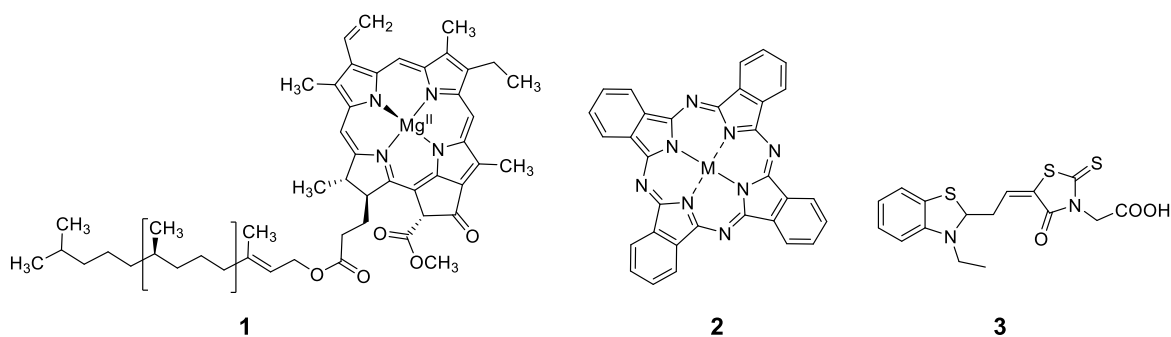


Figure 1.5: **1** chlorophyll-a, **2** metal phthalocyanine, or, and **3** merocyanine dye are organic chromophores for use in photovoltaic devices. M in phthalocyanines can be typical metals used in phthalocyanines such as Zn, Cu, or Ru.

Delocalization in these systems is possible due to a single unhybridized p-orbital oriented perpendicular to the  $sp^2$  hybridized orbitals formed by the carbon atoms. The overlapping  $sp^2$

orbitals interact and form  $\sigma$ -bonds while the lone p orbital forms  $\pi$ -bonds between neighboring carbons. This configuration results in the highest occupied molecular orbital (HOMO) belonging to the  $\pi$ -bonding orbital leaving the lowest unoccupied molecular orbital (LUMO) on the  $\pi^*$ -antibonding orbital. The HOMO and LUMO act as the valence band and conduction bands in typical semiconducting material with the energy difference between the HOMO and LUMO equal to the band gap  $E_g$ .

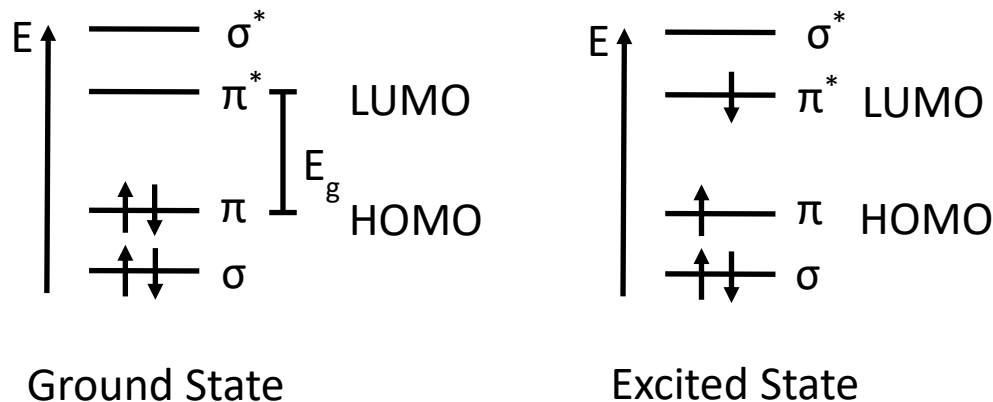


Figure 1.6: Simplified representation of the ground and excited state energy levels

When the molecule is excited with sufficient energy of photons electrons can move from the  $\pi$ -bonding orbital to the  $\pi^*$ -antibonding orbital. This excited electron can then be injected into an electrode surface and generate electricity.<sup>21</sup>

First we will examine a simple single layer organic photovoltaic device that consists of an organic light absorbing semiconducting molecule or polymer sandwiched between two different conducting electrodes. One electrode must consist of a conductor with a high work function such as indium tin oxide (ITO) while the second electrode must have a low work function like aluminum. The light absorbing material can then absorb energy from sunlight exciting one of its electrons from the HOMO to LUMO creating an excited electron and electron hole pair called an exciton.<sup>65</sup> The difference in the work function of the two conducting electrodes pulls the electron to the higher work function material while the hole moves toward the one with the lower work function due to the potential difference created by the two electrodes as can be seen in Figure 1.7.<sup>22,23</sup>

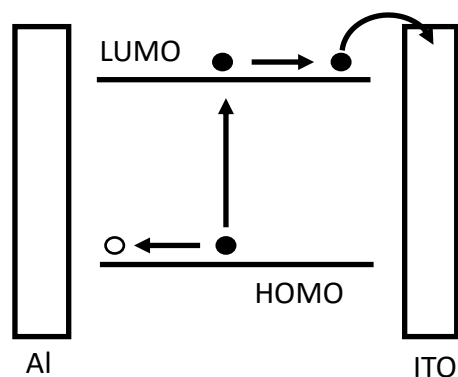


Figure 1.7: Electron flow in a single layer organic photovoltaic device

One of the main drawbacks for OPV unfortunately is that these excitons have short lifetimes typically in the nanosecond regime after which they recombine. This leads to poor exciton diffusion lengths around 5-10nm. What this means is that even if excitons are formed throughout the entire active area of the photovoltaic cell only the area within the diffusion length distance from the metal contacts will dissociate into free charge carriers generating photocurrent. All other excitons formed away from the metal contacts will be unable to diffuse to the metal surface before recombining. With collection only occurring at metal contacts instead of the entire absorbing film this reduces the effectiveness of single layer devices.<sup>24</sup>

To account for the poor diffusion of generated excitons in organic photovoltaic devices a new model was designed. The bulk heterojunction solar cell was designed to assist in efficient generation of free charges to prevent recombination of the excited electrons and extend the photoactive region through the entire active layer. To do this a new electron accepting molecule with a higher electron affinity is introduced into the active layer of the cell along with the electron donating absorption material making up a new donor/acceptor system. This allows the excited electron from the donor to undergo charge transfer to the acceptor as long as there is an energy level offset between the two and the ionization potential of the HOMO and LUMO is large enough to break up the Coulomb interaction at the donor/acceptor interface.<sup>25</sup>

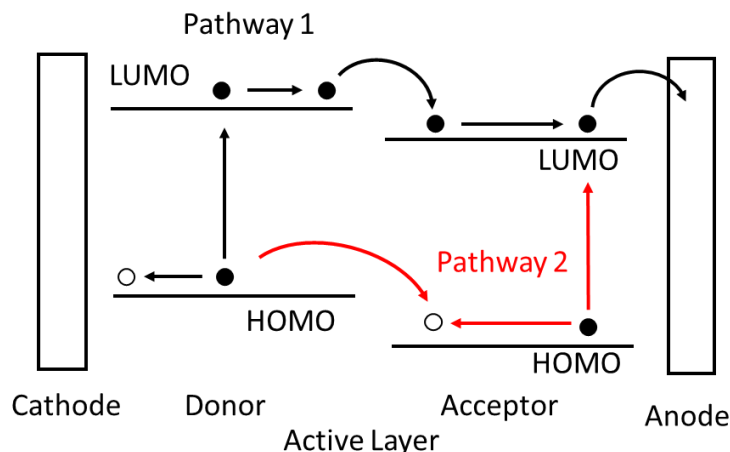


Figure 1.8: Two separate pathways for generation of electricity in solar cells. Pathway 1 in black is excitation of donor molecule while pathway 2 in red is excitation of acceptor.

The acceptor molecule can also have its electron excited by absorbing light and then an electron can be donated from the HOMO of the donor to the HOMO of the acceptor. Once this charge transfer has occurred you have effectively separated the electron and hole pairs on the acceptor and donor molecules respectively which results in a reduced charge recombination rate leading to better free charge generation. In this example the donor is a p-type semiconductor as it has excess holes generated in the HOMO orbital or valence band while the acceptor is an n-type semiconductor with excess electrons in the LUMO orbital or conduction band. Since the electron accepting molecule is mixed in with the electron donating absorption material it allows for charge collection to occur throughout the active layer and be transported to the metal contacts for collection.

Dye sensitized solar cells function similarly with an organic compound to absorb light and donate electrons, however the process in how this is done is slightly different than a normal organic solar cell. In the organic solar cell both the donor and acceptor act as semiconductors and shuttle electron or electron hole pairs to their corresponding electrodes. In a dye sensitized solar cell redox reactions are also used to shuttle electrons. A dye sensitized solar cell consists of a dye, semiconductor, electrolyte, and a counter electrode. There are two types of dye sensitized solar cells, n-type and p-type depending on what kind of semiconductor is used. N-type solar cells are more common due to higher achieved efficiencies which typically use titanium dioxide ( $\text{TiO}_2$ ) as their n-type semiconductor. In n-type dye sensitized solar cell the dye absorbs light exciting an

electron that is then donated to the acceptor undergoing an oxidation process. Electrolyte, typically iodide/triiodide then regenerates the dye by providing an electron through a reduction reaction. The donated electron travels through the semiconducting material to the electrode surface where it is transported to the counter electrode. At the counter electrode the electrolyte regains its lost electron via an oxidation process completing the cycle.<sup>26</sup>

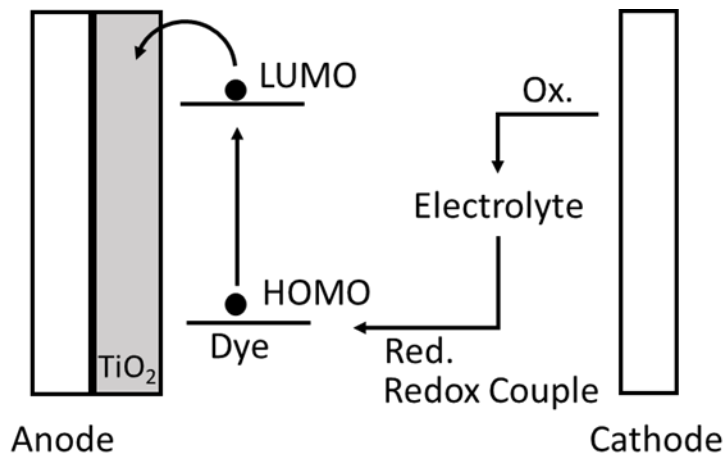


Figure 1.9: Electron flow in n-type dye sensitized solar cell

The performance of a photovoltaic device is determined by the measurement of an external electrical current taken as a function of an externally applied voltage. Results of these measurements are then usually depicted in a current-voltage (*IV*) graph. A typical *IV* graph is shown in Figure 1.10 for a photovoltaic cell when light is shining on it.

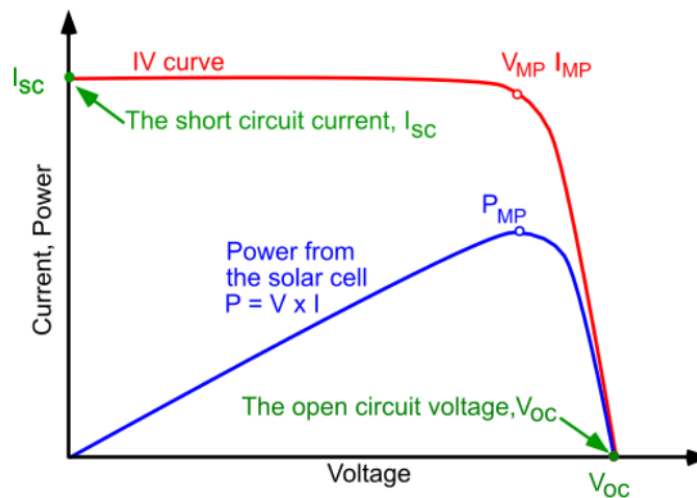


Figure 1.10: Current voltage curve for a photovoltaic device

There are three important points on the graph that represent specific parameters for the photovoltaic device.<sup>27,28,29</sup> First there is the short circuit current  $I_{SC}$  which is the current running through the device when no external voltage is applied. The second point is the open circuit voltage  $V_{OC}$ . This is the voltage required such that no external current is flowing through the illuminated device. The final point on the  $IV$  graph is the maximum power point  $P_{mp}$  where the power output of the photovoltaic device is maximized.

$$\text{eq 1.1 } P_{mp} = I_{mp} \times V_{mp}$$

An additional characteristic used in determining the effectiveness of photovoltaic devices called fill factor (FF) can also be derived from the  $IV$  graph.

$$\text{eq 1.2 } FF = \frac{I_{mp} \times V_{mp}}{I_{SC} \times V_{OC}}$$

Fill factor is a ratio of the actual maximum power compared to the theoretical upper limit. As can be seen in figure 1.10 the more rectangular the  $IV$  curve is the higher the FF will be so it is often referred to as the quality of the shape of the  $IV$  curve.

The parameters from the  $IV$  curve allow you to determine the energy conversion efficiency  $\eta_e$ .

$$\text{eq 1.3 } \eta_e = \frac{P_{mp}}{P_{in}} = \frac{V_{mp} \times I_{mp}}{p_{in}}$$

The conversion efficiency is a ratio of the total power from the light incident on the photovoltaic device  $P_{in}$  and the total electrical power generated by the device  $P_{mp}$ .<sup>8</sup> Since this ratio is dependent on the characteristic of the light illuminating your photovoltaic device it is important to be careful when comparing performances of different devices. For any photovoltaic device the light can be across a large range of wavelengths or focused on one specific value with the same light intensity and in both cases the resulting efficiencies will be very different.<sup>30,31</sup> That is why when stating energy conversion efficiencies a spectral distribution is always specified for the incoming light which is usually a monochromatic light source or a reference to a standardized illumination.<sup>32</sup>

The efficiency of photovoltaic devices is affected greatly by the loss of  $V_{oc}$  due to recombination. There are three different recombination mechanisms that lead to  $V_{oc}$  loss. The first being radiative recombination due to absorption of light of higher energy than the HOMO-

LUMO energy bandgap of your light absorbing material. This loss is unavoidable for all photovoltaic devices where the extra energy absorbed by the electron is lost as radiative energy as it travels toward the LUMO energy level. The second form of  $V_{oc}$  loss is due to radiative recombination due to energy below the band gap of your absorption material which does not lead to excitation of an electron.<sup>33</sup> These two forms of recombination make up the bulk of the loss of efficiency determined by the Shockley-Queisser limit which states that the maximum efficiency for any photovoltaic device consisting of a single p-n junction under normal sunlight conditions with an optimal band gap of 1.34 eV is 33.7%. The final recombination factor to consider is the non-radiative recombination occurring when an electron recombines with an electron hole. This can happen when the donor fails to inject an electron into the acceptor or at the surface contacts where the electron and hole pairs can come into contact during diffusion toward electrodes. In dye sensitized solar cells recombination can occur at contacts between the dye and semiconductor as well as with the semiconductor and electrolyte.

## Organic Solar Cell Research

Organic solar cells have been researched heavily in recent years with the focus on bulk heterojunction solar cells due to their small diffusion lengths. As mentioned above, these solar cells contain both an organic electron donating and accepting semiconducting material in the active layer that can absorb light and generate photocurrent. One of the first organic photovoltaic device using this model contained copper phthalocyanine as the donor and a perylene tetracarboxylic derivative as the acceptor that obtained an efficiency of approximately 1%.<sup>34</sup>

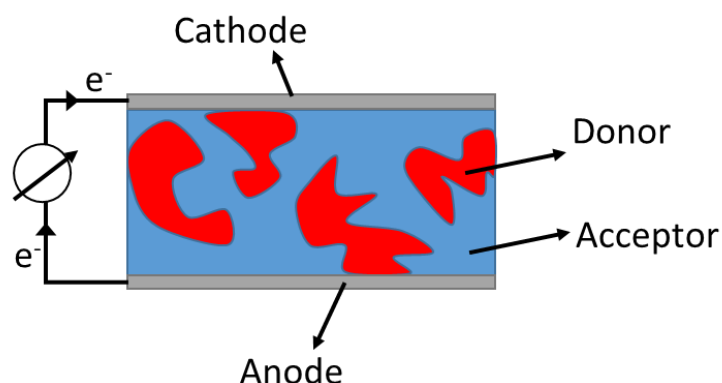


Figure 1.11: Schematic of a typical bulk heterojunction solar cell

Phthalocyanines and porphyrins along with their derivatives are one of the more widely developed electron donors for organic solar cells. This is due to their outstanding light harvesting properties such as absorption and charge transfer.

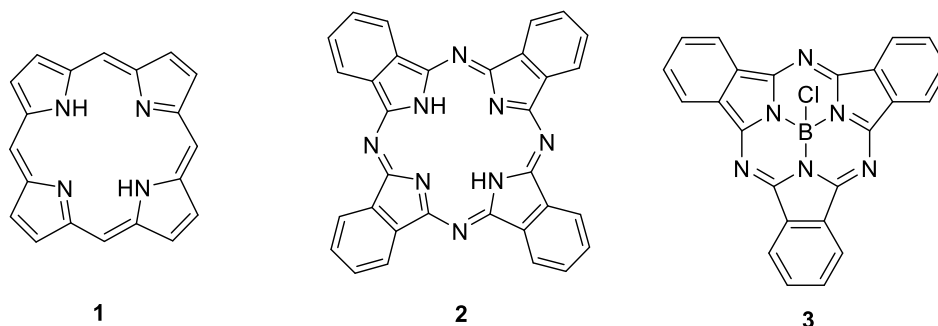


Figure 1.12: **1** porphyrin, **2** phthalocyanine, and **3** subphthalocyanine are chromophoric systems that are promising for use in photovoltaic devices.

Subphthalocyanines (SubPc) specifically garnered great interest due to their larger  $V_{oc}$  and better energy alignment. Efficiencies of 2.1% were achieved using subphthalocyanine and fullerene, approximately double the efficiency of copper phthalocyanine and fullerene.<sup>35</sup>

Polymer based semiconductors are also promising electron donors due to easy bandgap tunability and cost effective fabrication. One of the first series of polymers investigated was poly(phenylenevinylene) (PPV) derivatives. This started with the report of the first PPV solar cell which was a mixture of poly[2-methoxy-5-(2'-ethylhexyloxy)-p-phenylene vinylene and fullerene.<sup>36</sup> PPV polymers were further developed with the addition of substituents onto the polymer backbone to modify energy levels. It was found that introducing electron withdrawing groups such as CN groups lowered both the HOMO and LUMO levels without changing the band gap. It was also discovered that electron rich dialkoxy thiophene units raised the HOMO with little effect on the LUMO resulting in narrower band gaps.<sup>37</sup> With the need to produce donors with even smaller band gaps, research shifted away from PPV toward polythiophenes especially poly(3-hexylthiophene-2,5-diyl) (P3HT). This was due to its lower band gap of 1.9 eV compared to PPV-derivatives which typically have greater than 2 eV. Upon optimization of device fabrication and donor pairing, a power conversion efficiency of 7.4% was achieved using P3HT.<sup>38</sup> To further improve charge transfer, new donor-acceptor oligomers with low band-gap energies were developed. These donor-acceptor systems allow for easier control of the HOMO and LUMO

energies as typically they are determined by the HOMO of the donor and LUMO of the acceptor. This allows for tuning of the HOMO and LUMO levels to be done separately by modifying the donor or acceptor units. It also leads to more rapid injection of electrons from the electron donating semiconductor to the electron accepting semiconductor. This advance in polymer design has led to power conversion efficiencies as high as 11%.

Photovoltaic devices also require an electron acceptor component, however development of new electron acceptors has not changed significantly until recent years. The most prominent electron acceptors for organic solar cells have been soluble fullerene derivatives with the most common one being [6,6]phenyl-C<sub>61</sub>-butyric acid methyl ester (PCBM).<sup>39,40</sup> Other fullerene derivatives using C<sub>70</sub> for its higher absorption and indene-C<sub>60</sub> were also made.

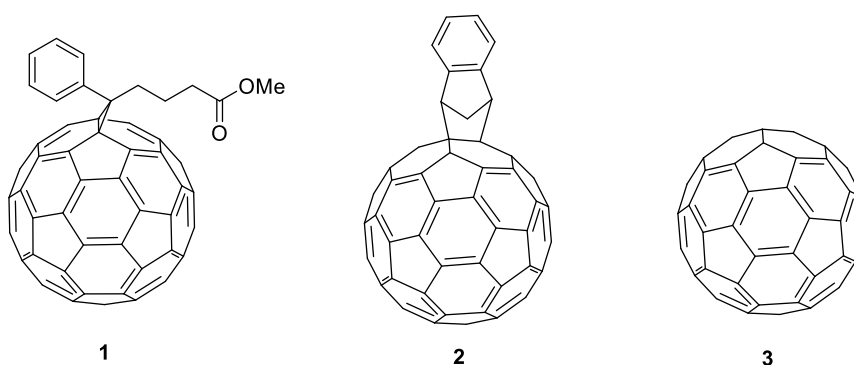


Figure 1.13: **1** [6,6]phenyl-C<sub>61</sub>-butyric acid methyl ester (PCBM), **2** Indene C<sub>60</sub>, and **3** C<sub>60</sub> are fullerene electron acceptors for photovoltaic devices

These Fullerenes made for promising electron acceptors due to their electron mobility, exciton splitting, and isotropic charge transfer properties. Isotropic charge transfer means that charge can diffuse evenly in all directions. These properties allowed fullerene acceptor based systems to reach efficiencies upward of 10% but due to several shortcomings they have had limited performance.<sup>41</sup> The major issue with Fullerene acceptors is their low absorption in the visible and near-infrared region of the solar spectrum resulting in poor energy capture. This means the donor molecule must be the primary light absorber for this type of system and the fullerene acceptor can't contribute to exciton generation via excitation of its own electrons as described above. Fullerene acceptors are also limited by their ability for further modification as it is difficult to add additional substituents. This means that the physical properties of fullerenes can't be tuned making it difficult to maximize V<sub>oc</sub> for these systems. Considering the shortcomings of fullerene acceptors development of new

acceptors materials with higher absorption and higher  $V_{oc}$  potentials is an important step in obtaining competitive efficiencies for organic solar cells.

In recent years there has been rapid development of new non-fullerene acceptor materials due to their distinct advantages over fullerene acceptors. Advantages of non-fullerene acceptors are tunable bandgaps, higher absorption in the UV-Vis and NIR region, tunable energy levels so proper energy alignment between donor and acceptor can be achieved for high  $V_{oc}$ , increased planarity and crystallinity for improved morphology and stability. The current field of new acceptor materials can be split into wide bandgap, medium bandgap, and narrow bandgap acceptors.

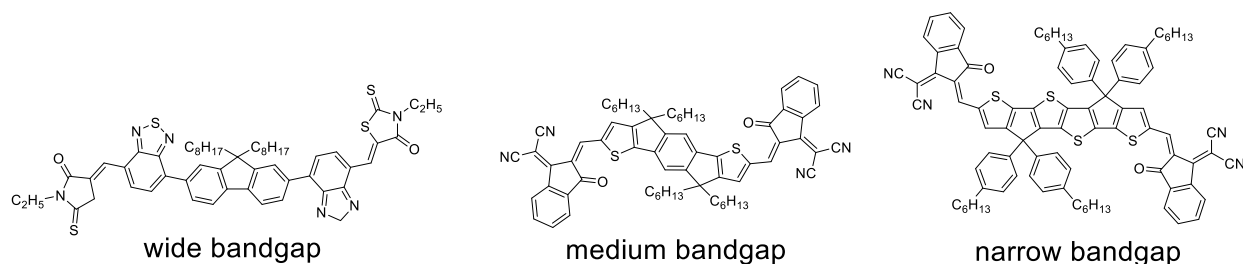


Figure 1.14: Structures of non-fullerene acceptor materials for different bandgaps used in photovoltaic devices

Wideband gap acceptors with a band gap greater than 1.9 eV have been synthesized and achieved efficiencies of 9%.<sup>43</sup> These wide bandgap acceptors absorb at higher energies so they suffer from poor absorption in the NIR region. They also tend to have significant absorption overlap with donor molecules that limits their exciton generation. Medium band gap acceptors with a band gap between 1.5-1.9 eV have achieved even higher efficiencies of 11%.<sup>44</sup> This is due to their higher absorption in the NIR region and lower absorption overlap with wide bandgap donor molecules. Low band gap acceptors, with bandgaps of less than 1.5 eV, have achieved efficiencies of 11-12%.<sup>45</sup> These lower band gap energies allow for strong absorption in the NIR region and have even less overlap with donor molecules that absorb strongly in the UV-VIS spectrum. This indicates that the direction for the design of new acceptors should be on medium and narrow band gap acceptors due to their absorption in the UV and NIR region.

Single-walled carbon nanotubes (SWCNT) are a promising electron accepting material. This is due to their strong absorption, high carrier mobility, and chemical stability. One of the

major drawbacks to organic solar cells is the low carrier mobility in organic semiconductors which could potentially be addressed through the use of SWCNT. Careful consideration, however must be taken when using SWCNT as they can be metallic or semiconducting in nature. Metallic SWCNT are not useful for photovoltaic applications as they promote electron recombination. This means that semiconducting SWCNT must be purified from metallic ones or selectively prepared to obtain pure semiconducting SWCNT. The properties of the SWCNT can be determined by their chirality SWCNT with armchair configuration being metallic, zigzag being semiconducting, and chiral carbon nanotubes which are defined by their chiral indices (n,m) being metallic for all values of (n-m)/3 being an integer and all non-integer values being semiconducting.

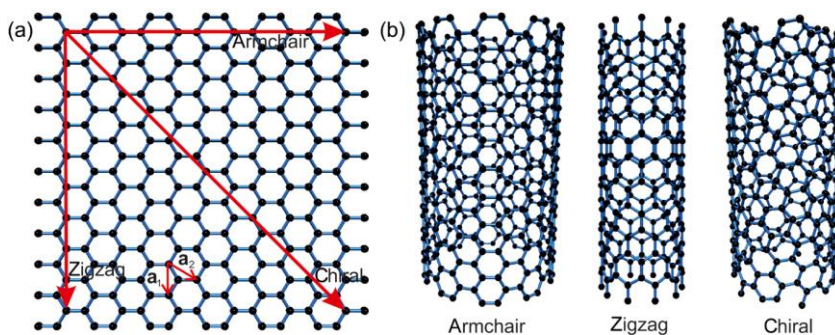


Figure 1.15: Lattice structures (a) graphene and (b) single walled carbon nanotubes.<sup>42</sup>

## Dye Sensitized Solar Cell Research

Here I will discuss the development of dye sensitized solar cells including the research effort being done to improve stability and efficiency. The light harvesting dye is one of the most crucial parts of the solar cell and therefore careful consideration must be taken when deciding on an appropriate dye. Here is a summary of important properties the dye should have.<sup>46</sup>

1. Panchromatic absorption ( $\lambda_{\text{abs}} = 300\text{-}800\text{ nm}$ ) with the optimum absorption band overlapped with sunlight for efficient light harvesting.
2. Covalent or strong non-covalent interaction between the dye and semiconductor.
3. Appropriate energy levels of the HOMO and LUMO to promote charge transfer and redox reaction with electrolyte for regeneration.
4. Thermal and chemical stability.

The first dye sensitized solar cell was made using a ruthenium dye on  $\text{TiO}_2$  film with  $\text{I}^-/\text{I}_3^-$  electrolyte and Pt-FTO cathode. The solar cell achieved an efficiency of 7.12% under full sunlight irradiation with a fill factor of 0.685.<sup>47</sup> An example of dye sensitized solar cell can be seen in figure 1.16.

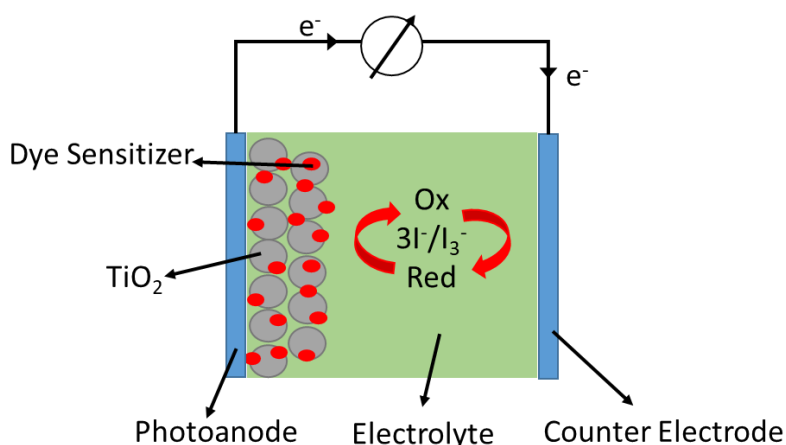


Figure 1.16: Schematic diagram of a typical dye sensitized solar cell

Research into ruthenium dyes was extensively investigated and further efficiencies up to 11.29% was achieved via addition of electron donating alkylthiophene moieties as seen in figure 1.17.<sup>48</sup>

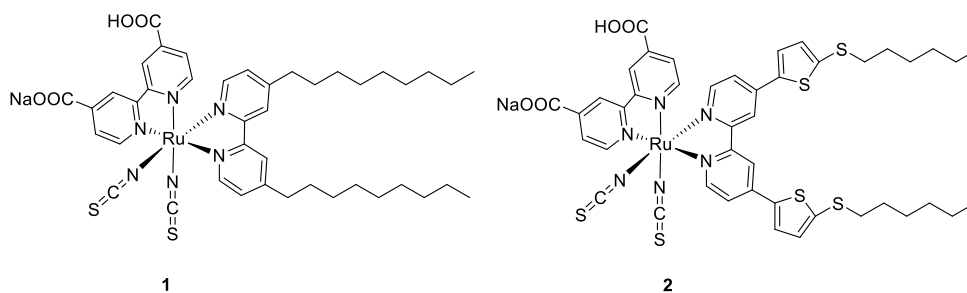


Figure 1.17: Ruthenium dyes for dye sensitized solar cells

This increased the extinction coefficient as well as red shifted the metal to ligand charge transfer band so it can capture more of the NIR region boosting the efficiency.<sup>49,50</sup> Although these advancements with ruthenium dyes are promising they still use toxic and expensive metals therefore research into alternative organic based dyes was pursued.

Organic dyes have tunable optoelectronic properties by simply making structural adjustments along with higher molar absorptivities with some over  $100,000 \text{ M}^{-1}\text{cm}^{-1}$ .<sup>51</sup> The

limitations of organic dyes compared to ruthenium arise from narrow and sharp absorption bands that don't span the visible spectrum, aggregation due to planarity of the chromophores that inhibit electron transfer, weak absorption in the near infrared, and lower stability.<sup>52</sup> The initial high performing organic dyes that were synthesized were indoline based derivatives that were able to achieve efficiencies of 9.03% however they suffered from poor stability.<sup>53,54</sup>

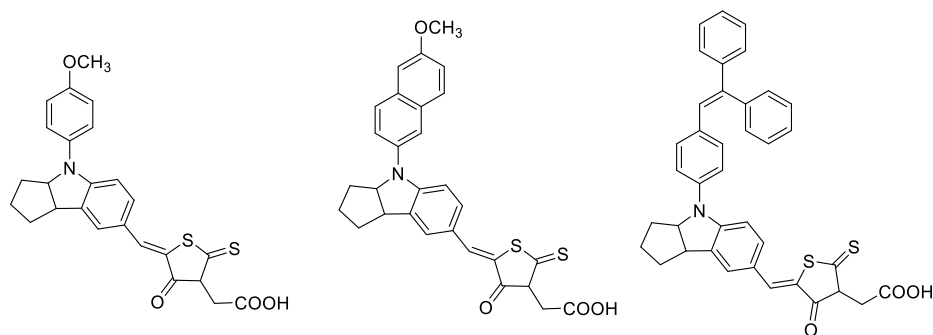


Figure 1.18: These are examples of metal free indoline derivatives for photovoltaic applications

Since these initial dyes suffered from low stability researches began looking at robust dyes containing donor- $\pi$  bridge-acceptor systems (D- $\pi$ -A). Careful consideration must be given when assembling these D- $\pi$ -A dyes as the HOMO orbital must be centered at the electron donating substituent while the LUMO is centered on the electron accepting group. This means that once excited the electron travels from the electron donating group through the  $\pi$  bridge into the electron accepting group, resulting in strong coupling with the conduction band of the semiconducting material.<sup>64</sup> The coupling promotes rapid electron transfer from the excited state of the dye to the conduction band of the semiconductor. Using D- $\pi$ -A dye systems a series of dyes containing diaryl amine group as the electron donor, cyanoacrylate group as acceptor group, and a thiophene moiety as the  $\pi$ -conducting bridge were synthesized.<sup>55</sup> Efficiencies of 10.1% under standard air mass 1.5 spectra illumination was achieved while the dyes showed remarkable robustness, resisting degradation over 1000 hours of light soaking at full solar intensity and elevated temperatures.<sup>53, 56</sup>

Donor  $\pi$ -bridge-acceptor sensitizers often have limited absorption in the near infrared region leading to lower conversion efficiencies. To improve this type of sensitizer porphyrins and phthalocyanines are interesting candidates as they are both photo- and electrochemical stable compounds. The absorption spectrum of a porphyrin has a Soret band at 400 nm with a high

absorption coefficient and moderately strong Q-bands at 600 nm. Phthalocyanines have similar absorption however their Q-bands are more intense and are red shifted to around 700 nm. Due to the high symmetry of unsubstituted porphyrins and phthalocyanines their frontier molecular orbitals are distributed all over the molecule which give them poor electron donating capabilities making them unsuitable for photovoltaic devices. Early work done using phthalocyanine for photovoltaics exhibited poor power conversion efficiencies of 3.5% using a tri-tert-butyl carboxylic zinc phthalocyanine.<sup>57</sup> Using the D- $\pi$ -bridge-A system porphyrins and phthalocyanines were incorporated as the  $\pi$ -bridge between donors and acceptors.<sup>58</sup> Doing this a record high efficiency of 13% was achieved using a zinc porphyrin core with bis(2',4'-bis(hexyloxy)-[1,1'-biphenyl]-4-yl)amine donor and proquinoidal benzothiadiazole substituents.<sup>59</sup>

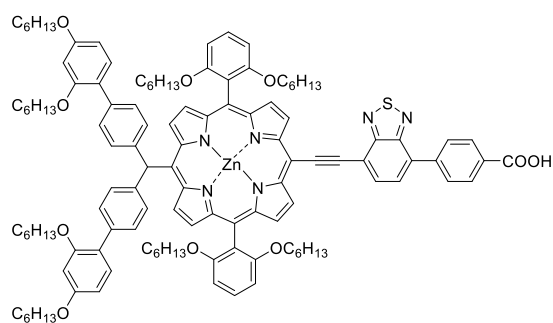


Figure 1.19: Panchromatic porphyrin sensitizer with record high 13% efficiency<sup>59</sup>

Characterization of these light absorbing chromophores and investigating their electron transfer processes is important for understanding how these photovoltaic systems work so that proper direction can be taken when designing new chromophores for more efficient devices. There are many different spectroscopy techniques that are used for probing chromophores such as absorption, fluorescence, transient absorption, and electrochemistry. These different techniques allow for determination of energy levels of the HOMO and LUMO orbitals as well as their capability for exciton generation.

## Techniques Used to Investigate Donor/Acceptor Chromophores

Two important techniques used for probing the ground and excited states of these chromophores are absorption and fluorescence spectroscopy. Absorption spectroscopy is used to probe the ground state of a chromophore and determine what wavelengths of the ultraviolet, visible, and near infrared spectrum light is absorbed. Fluorescence probes the excited state and

measures any photons given off during radiative relaxation of the electron from excited state to the ground state.

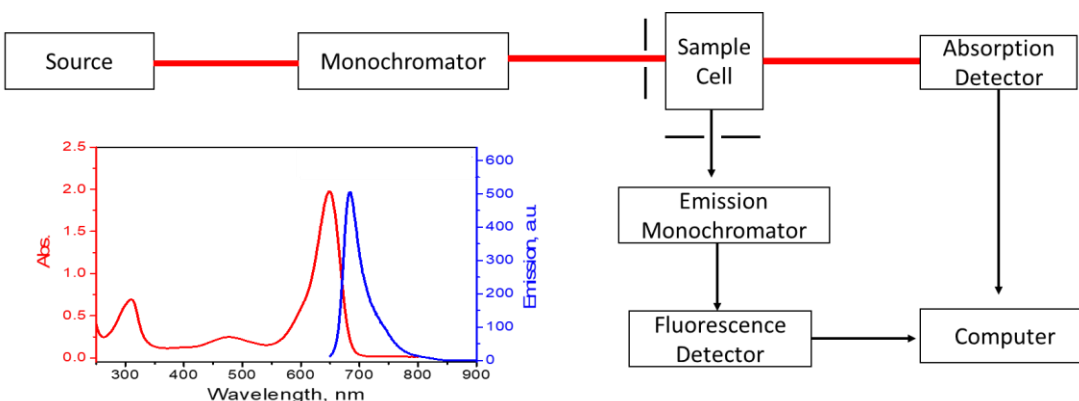


Figure 1.20: Absorption/Fluorescence schematic and sample spectrum.

Fluorescence spectroscopy is useful when determining if electron transfer occurs between electron donors and acceptors. If electron transfer occurs the molecule has its fluorescence quenched since the electron no longer undergoes radiative relaxation when it is donated to the electron acceptor. These processes can be visualized by a Jablonski diagram showing the electronic states of your chromophore and the transitions between them as seen in Figure 1.21. The  $S_0$  state is the ground electronic energy state and the  $S_1$  is the first electronic state above ground state. Each electronic energy state also has additional vibrational energy levels as denoted by 0, 1, 2, and 3.

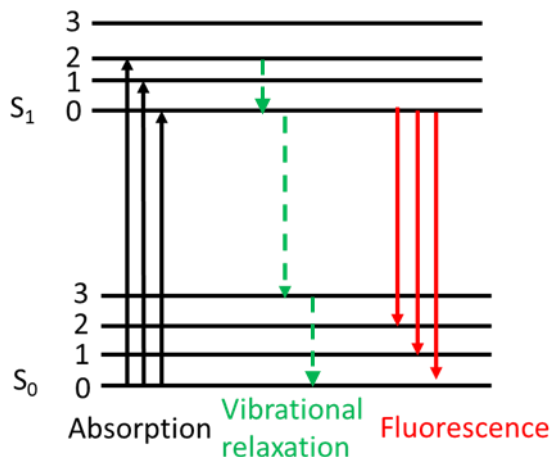


Figure 1.21: Jablonski diagram depicting electronic states and transitions.

An additional absorption technique used for characterizing these chromophore systems is transient absorption spectroscopy. This technique measures the change in absorption of an excited state generated by excitation of a ground-state molecule over time typically in the femtosecond to millisecond timescale. This is done by using a pump and probe laser pulse system in which first the sample is excited by a pump pulse and then after a delay the sample is excited again by a probe pulse usually in the femtosecond timescale. This ensures that the molecule is in an excited state and then the absorption spectrum is repeatedly measured over time. The difference between the pump and probe absorption vs the probe absorption alone is then taken which gives you  $\Delta A$ . This can be taken as the change in absorption as a function of time or wavelength.<sup>60</sup>

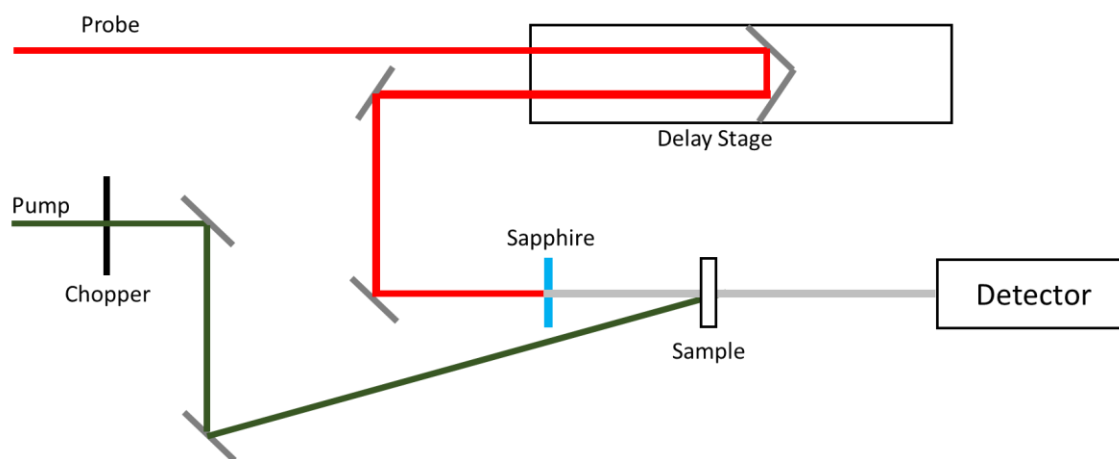


Figure 1.22: Transient absorption spectrometer optical layout.

This allows us to monitor the intermediate states of the electron transfer processes occurring between our electron donors and acceptors.<sup>61</sup> Monitoring the change in absorption across wavelengths shows if there is a formation of a charge separated state between our donor and acceptor molecules while monitoring it over time at a specific wavelength will show the number of decay processes along with the rate at which the decay processes occur.<sup>62</sup> This provides the lifetime of the charge separated states of the donor and acceptor molecules which is an important factor in how likely charge recombination is to occur in photovoltaic devices.

Electrochemistry is another technique used when investigating chromophores for use in photovoltaic devices as it can probe the oxidation and reduction potentials of these molecules and estimate the HOMO and LUMO energies. Cyclic voltammetry is the common electrochemical method used for determining oxidation and reduction potentials for these systems. Using a

working electrode, counter electrode, reference electrode, electrolyte, and a potentiostat a sweep of potentials can be applied to the system while measuring the current generated. The current will increase if there is an electron transfer process occurring at the electrode surface indicating that an oxidation or reduction process occurs at that applied potential.

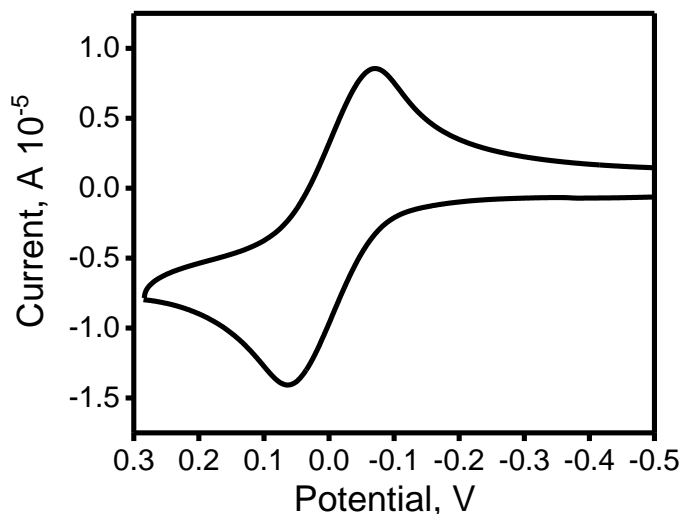


Figure 1.23: Cyclic voltammetry graph of a reversible oxidation process.

The potential from these experiments tells us the amount of energy required to either remove an electron from the HOMO orbital (oxidation) or add an electron to the LUMO orbital (reduction) of our compound. Knowing these energies an approximation of the HOMO and LUMO energy levels can be made which is important for determining what types of acceptors and donors will work well together in a photovoltaic device.

One must be careful when correlating electrochemical measurements to orbital energies as there is a series of challenges that must be considered. One such issue is that the reference compound can be affected by environmental effects such as solvent or supporting electrolyte which can make it difficult to compare results with other research groups with a high level of accuracy. Research groups also use different references such as saturated calomel electrode (SCE) and Ag/AgCl so care must be taken to make sure when comparing data or converting into orbital energies that similar systems were used. Another major issue that arises when determining orbital energy values from electrochemistry oxidation and reduction potentials is that the measurements are done in solution and not in the gas phase which needs to correct for the gas phase ionization

potential so it can be compared with normal hydrogen electrode or (NHE). When converting oxidation and reduction potentials calibrated with ferrocene equations 1.4 and 1.5 below can be used however it is important to remember that these conversions don't take into consideration the solvent and supporting electrolyte effects.<sup>67</sup>

$$\text{eq 1.4 } E_{\text{HOMO}} = (E_{[\text{onset,ox vs. Fc}^+/\text{Fc}]} + 5.39) \text{ eV}$$

$$\text{eq 1.5 } E_{\text{LUMO}} = (E_{[\text{onset,red vs. Fc}^+/\text{Fc}]} + 5.39) \text{ eV}$$

Computational chemistry is an additional tool that can be used to help analyze favorable properties of chromophores for potential use in photovoltaic applications. There are many different methods used in computational chemistry such as molecular mechanics, ab initio, semi empirical, density functional theory (DFT), and molecular dynamics. These methods are based in the theory of quantum mechanics and many of them are approximations to the solution of the Schrödinger equation from a variety of different approaches. Density functional theory is particularly useful for analyzing chromophores for photovoltaic applications as it predicts the electron density of a molecule. The exact expression for determining the energy of the electron density isn't however known and so a variety of different functionals are used and then compared with experimental results until good agreement is found. Hybrid functionals are combinations of electronic density and wave function calculations made to obtain better approximations for the exchange and correlation energy component of the total energy of the DFT calculation. A common hybrid functional that is used is B3LYP which is a combination of the Hartree-Fock method with DFT and is used to make up for the less than ideal approximation of the exchange correlation from the DFT calculations alone. Using these complex functionals many properties of a molecule can be modeled such as their ground state geometry, energy, optical, and magnetic properties. Time dependent density functional theory (TDDFT) is an addition to DFT that investigates the properties of systems in the presence of time-dependent potentials. This method allows for the determination of excitation energies, frequency-dependent response properties, and photoabsorbtion spectrum.

Overall, when donor acceptor assemblies for light harvesting are considered, there are three major architectures. The first architecture utilizes supramolecular arrays that are formed as a result of non-covalent interactions between donor and acceptor molecules. In general the driving forces for such interactions include van der Waals, dipole-dipole, or ionic forces. These are in general weaker than regular covalent bonds and thus study of these supramolecular arrays in

solution is quite challenging. However, such intramolecular forces are strong enough to form well-ordered 3D structures in the solid state and thus (since the organic photovoltaic solar cells are solid state devices) are quite useful for the design of light harvesting models for organic photovoltaics. This approach is also the cheapest from the commercial point of view when compared to the other two mentioned below. In the second extreme the donor and acceptor parts of the supramolecular assembly are connected by covalent bonds. In this approach both direct connection between donor and acceptor and the connection between the donor and acceptor through a linking group are possible. This approach allows strict control for the donor and acceptor distances geometry and electronic structure. From the commercial application point of view however, preparation of such donor acceptor models with additional covalent bonds is potentially more expensive. Finally the third approach for formation of supramolecular arrays utilizing interaction between donor and acceptor fragments uses coordination bonds. Such bonds are typically strong enough to clearly define donor acceptor distances and electron transfer pathways but, come without extra cost for the formation of covalent bonds. The coordination approach also allows us to screen a large number of donor acceptor blocks to fine tune the optical redox and electron transfer properties that are useful for light harvesting. Thus in chapters 2-4 I will discuss all three of these approaches in a systematic way. In chapter 2 we will focus on the formation, photophysics, and photoinduced electron transfer in the non-covalent light harvesting arrays formed between a variety of BODIPYs and aza-BODIPYs and nanocarbon acceptors. In chapter 3 we will investigate BODIPY fullerene donor acceptor assemblies that are covalently linked using the most common catechol bridge at the boron hub. Finally in chapter 4 I will screen a large number of donor acceptor assemblies formed between electron donating porphyrin and phthalocyanines axially coordinated through the coordination bond to the array of the pyridine containing fullerenes and BODIPYs.

## References

1. Smalley, R. Nanotechnology, Energy, and People, 2003.
2. IEA, World Energy Outlook 2010 (Paris, IEA: 2010).
3. “Svante Arrhenius (1859–1927),” NASA Earth Observatory, last modified 2013, <http://earthobservatory.nasa.gov/Features/Arrhenius/>.
4. Green MA Photovoltaics: Technology Overview. Energy Policy 28(14):989–998 2000
5. 87REN21, Renewables 2013 Global Status Report (Paris: REN21 Secretariat, 2013).
6. N.S. Lewis, D.G. Nocera, *Proc. Natl. Acad. Sci. USA* **2006**, 103(43), 15729-15735.
7. M. A. Green, The path to 25% silicon solar cell efficiency: History of silicon cell evolution. Prog. Photovolt: Res. Appl., **2009**, 17, 183
8. G.E. Eperon, S.D. Stranks, C. Menelaou, M.B. Johnston, L.M. Herz, H.J. Snaith, *Energy Environ Sci* **2014**, 7, 982–988
9. C. Eames, J. M. Frot, P. R. F. Barnes, B. C. O’Regan, A. Walsh, M. S. Islam, *Nat. Commun.* 6 (**2015**) 7497
10. A. Kojima, K. Teshima, Y. Shirai, T. Miyasaka, *J Am Chem Soc* **2009**, 131(17), 6050–6051
11. G. Niu, W. Li, F. Meng, L. Wang, H. Dong, Y. Qiu, *J Mater Chem A* **2014**, 2(3), 705–710
12. T. Leijtens, GE. Eperon, NK. Noel, SN. Habisreutinger, A. Petrozza, HJ Snaith *Adv Energy Mater.* **2015**, 5(20), article number 1500963
13. J. Yang, B.D. Siempelkamp, D. Liu, T. L. Kelly, *Am Chem Soc Nano* **2015**, 9, 1955–1963.
14. AJ. Nozik, *Physica E* **2002**, 14, 115–120.
15. S. Baskoutas, T. Andreas F. *Journal of Applied Physics* **2006**, (1) 99.
16. I. Robel, V. Subramanian, M. Kuno, PV. Kamat, *J Am Chem Soc* **2006**, 128:2385–93.
17. KM. Coakley, MD. McGehee, *Chem Mater* **2004**, 16(23):4533–4542
18. C. W. Tang, A. C. Albrecht, *J. Chem. Phys.* **1975**, 62, 2139.
19. A. K. Ghosh, T. Feng, *J. Appl. Phys.* **1978**, 49, 5982.
20. G. A. Chamberlain, *Solar Cells* **1983**, 8, 47
21. JL. Bredas, JP. Calbert, DA. da Silva Filho, J. Cornil, (2002) *Nat Acad Sci* **2002**, 99(9), 5804–5809

22. Kymissis I (2009) The physics of organic semiconductors. In: Organic Field Effect Transistors. Integrated Circuits and Systems, Springer, US, pp 1-12
23. D. Hu, J. Yu, G. Padmanaban, S. Ramakrishnan, PF. Barbara, *Nano Lett* **2002**, 2(10), 1121–1124
24. VC. Sundar, J. Zaumseil, V. Podzorov, E. Menard, RL. Willett, T. Someya, ME. Gershenson, JA. Rogers, *Science* **2004**, 303(5664), 1644–1646
25. SH. Park, A. Roy, S. Beaupre, S. Cho, N. Coates, JS. Moon, D. Moses, M. Leclerc, K. Lee, AJ Heeger, (2009) *Nat Photon* **2009**, 3(5):297–302
26. J. Gong, J. Liang, K. Sumathy, **2012**, 16, 5848–60.
27. M. Grätzel, *Nature* **2001**, 414(6861), 338–344
28. M. Grätzel, *Acc Chem Res* **2009**, 42 (11), 1788–1798
29. A. Hagfeldt, G. Boschloo, L. Sun, L. Kloo, H. Pettersson, *Chem Rev* **2010**, 110(11), 6595–6663
30. J. Desilvestro, M. Gratzel, L. Kavan, J. Moser, *J. Am. Chem. Soc.* **1985**, 107, 2988
31. J. Rostalski, D. Meissner, *Sol. En. Mat. Sol. Cells* **2000**, 61, 87
32. R. J. Van Overstraten, R. P. Mertens, *Physics, Technology and Use of Photovoltaics*, Adam Hilger Ltd, Bristol and Boston (1986)
33. MC. Scharber, D. Muhlbacher, M. Koppe, P. Denk, C. Waldauf, AJ. Heeger, CJ. Brabec, *Adv Mater* **2006**, 18, 789–794.
34. C. W. Tang, *Appl. Phys. Lett.* **1986**, 48, 183–185
35. K.L. Mutolo, E.I. Mayo, B.P. Rand, S.R. Forrest, M.E. Thompson, *J. Am. Chem. Soc.* **2006**, 128, 8108.
36. G. Yu, J. Gao, J. C. Hummelen, F. Wudl, A. J. Heeger, *Science* **1995**, 270, 1789–1791.
37. B. C. Thompson, Y.-G. Kim, T. D. McCarley, J. R. Reynolds, *J. Am. Chem. Soc.* **2006**, 128, 12714–12725.
38. X. Guo, C. Cui, M. Zhang, L. Huo, Y. Huang, J. Hou, Y. Li, *Energy Environ. Sci.* **2012**, 5, 7943–7949.
39. Y-J. Cheng, S-H. Yang, C-S Hsu, *Chem Rev* **2009**, 109(11), 5868–5923
40. A. Mishra, P. Bäuerle, *Angew Chem Int Ed* **2012**, 51(9), 2020–2067

41. B. Kan, M. Li, Q. Zhang, F. Liu, X. Wan, Y. Wang, W. Ni, G. Long, X. Yang, H. Feng, Y. Zuo, M. Zhang, F. Huang, Y. Cao, TP. Russell, Y. Chen, *J Am Chem Soc* **2015**, 137(11):3886–3893
42. Jozef Bocko, Pavol Lengvarský, Róbert Huňady, and Juraj Šarloši, *Mech. Sci.* **2018**, 9, 349–358.
43. M. T. Dang, L. Hirsch, G. Wantz, *Adv. Mater.* **2011**, 23, 3597–3602
44. Y. Lin, Y. et al. *Adv. Mater.* **2015**, 27, 1170–1174.
45. W. Zhao, et al. *J. Am. Chem. Soc.* **2017**, 139, 7148–7151.
46. JN. Clifford, E. Martínez-Ferrero, A. Viterisi, E. Palomares, (2011) *Chem Soc Rev* **2011**, 40 (3):1635–1646
47. B. O'Regan, M. A. Grätzel, *Nature* **1991**, 353 (6346), 737–740.
48. Y. Cao, Y. Bai, Q. Yu, Y. Cheng, S. Liu, D. Shi, F. Gao, P. Wang, *J Phys Chem C* **2009**, 113(15), 6290–6297
49. MK. Nazeeruddin, P. Péchy, T. Renouard, SM. Zakeeruddin, R. Humphry-Baker, P. Comte, P. Liska, L. Cevey, E. Costa, V. Shklover, L. Spiccia, GB Deacon, CA. Bignozzi, M. Grätzel, (2001) *J Am Chem Soc* **2001**, 123(8), 1613–1624
50. Y. Chiba, A. Islam, Y. Watanabe, R. Komiya, N. Koide, L. Han, *Jpn J Appl Phys* **2006**, 45(2), 24–28
51. GK. Mor, S. Kim, M. Paulose, OK Varghese, K. Shankar, J. Basham, CA. Grimes, *Nano Lett* **2009**, 9(12), 4250–4257
52. K. Hara, T. Sato, R. Katoh, A. Furube, Y. Ohga, A. Shinpo, S. Suga, K. Sayama, H. Sugihara, H. Arakawa, *J Phys Chem B* **2003b**, 107(2), 597–606
53. T. Horiuchi, H. Miura, S. Uchida, *Chem Commun* **2003**, 0(24), 3036–3037
54. S. Ito, H. Miura, S. Uchida, M. Takata, K. Sumioka, P. Liska, P. Comte, P. Péchyb, M. Grätzel, *Chem Commun* **2008**, 0(41), 5194–5196
55. W. Zeng, Y. Cao, Y. Bai, Y. Wang, Y. Shi, M. Zhang, F. Wang, C. Pan, P. Wang *Chem Mater* **2010**, 22(5), 1915–1925
56. J-H Yum, DP. Hagberg, S-J Moon, KM. Karlsson, T. Marinado, L. Sun, A. Hagfeldt, MK. Nazeeruddin, M. Grätzel, *Angew Chem Int Ed* **2009**, 48(9), 1576–1580

57. JJ. Cid, M. Garcia-Iglesias, JH. Yum, A. Forneli, J. Albero, E. Martinez-Ferrero, P. Vazquez, M. Grätzel, MK. Nazeeruddin, E. Palomares, T. Torres, *Chem Eur J* **2009**, 15(20), 5130–5137
58. WM. Campbell, KW. Jolley, P. Wagner, K. Wagner, PJ. Walsh, KC. Gordon, L. Schmidt-Mende, MK Nazeeruddin, Q. Wang, M. Grätzel, DL. Officer, (2007) *J Phys Chem C* **2007**, 111(32), 11760–11762
59. S. Mathew, A. Yella, P. Gao, R. Humphry-Baker, BFE Curchod, N. Ashari-Astani, I. Tavernelli, U. Rothlisberger, MK. Nazeeruddin, M. Grätzel, *Nat Chem* **2014**, 6 (3), 242–247
60. S. Yamamoto, J. Guo, H. Ohkita, S. Ito, *Adv Funct Mater* **2008**, 18, 2555–2562
61. J. Guo, H. Ohkita, H. Benten, S. Ito *J Am Chem Soc* **2009**, 131, 16869–16880
62. RA. Marsh, JM. Hodgkiss, S. Albert-Seifreid, RH. Friend, *Nano Lett* **2010**, 10, 923–930
63. M. A. Green, A. Ho-Baillie, H. J. Snaith, *Nat Photonics* **2014**, 8, 506-514
64. G. Zhang, H. Bala, Y. Cheng, D. Shi, X. Lv, Q. Yu, P. Wang, *Chem Commun* **2009**, 0(16), 2198–2200
65. AC. Mayer, SR. Scully, BE. Hardin, MW. Rowell, MD. McGehee, *Mater Today* **2007**, 10, 28–33
66. C.A. Gueymard, D. Myers, K. Emery, *Solar Energy*, **2002**, 73, 6, 443-467
67. C.M. Cardona, W. Li, A.E. Kaifer, D. Stockdale, G.C. Bazan, *adv. Mater.*, **2011**, 23, 2367-2371

## Chapter 2

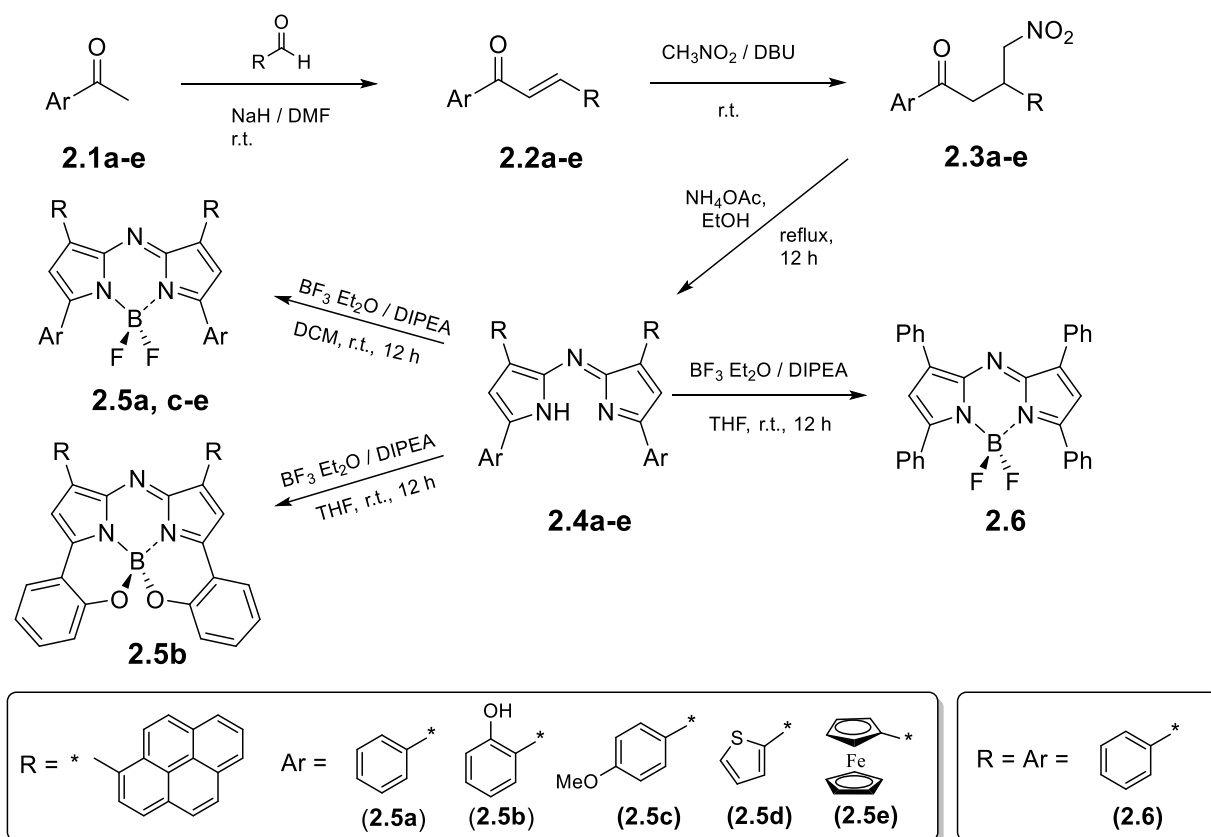
### Pyrene aza-BODIPYs and BODIPYs for non-covalent interaction with nanocarbon material

#### Introduction

Formation of stable long-lived charge-separated states is an important initial step in the preparation of efficient organic solar cells.<sup>1-5</sup> Although there are many examples of covalently bound donor-acceptor systems,<sup>6-19</sup> formation of non-covalent donor-acceptor systems with long-lived charge-separated states have only recently been studied extensively.<sup>1-5,20-32</sup> The potential advantage of a non-covalent systems is the ability to self-assemble upon simple mixing; however, the weaker non-covalent interactions can lead to a decrease in stability and additional conformational disorder. The various forces that make up non-covalent interactions can be divided into electrostatic forces, van der Waals forces, and  $\pi$ - $\pi$  interactions. It is difficult to control relative D-A geometries and orientation, which tunes the degree of electronic coupling between the donor and acceptor.<sup>33-44</sup> There are some examples demonstrating efficient formation of long-lived photo-induced charge transfer between conjugated chromophore donors and non-covalently associated fullerenes, carbon nanotubes, and graphene.<sup>43-52</sup> Formation and stability of these non-covalent D-A assemblies relies on enhancement of dispersion forces and electronic coupling provided by  $\pi$ - $\pi$  interactions, and topology that facilitates strong spatial overlap.

Chromophores that have demonstrated to be effective and stable assemblies for initial light absorption and charge separation are porphyrins<sup>54-64</sup>, phthalocyanines<sup>65-73</sup>, subphthalocyanines<sup>75-81</sup>, BODIPYs<sup>81-87</sup>, and aza-BODIPYs<sup>88-93</sup>. The functionalization of electron donating groups capable of intramolecular electron-transfer generates donor- $\pi$ -acceptor chromophores that facilitates electron injection between extended  $\pi$ -systems. Organic amines<sup>94-105</sup> and ferrocene<sup>106-121</sup> are examples of effective electron-donating groups capable of facilitating photoinduced intramolecular electron-transfer.

To enhance the non-covalent interaction of the above-mentioned chromophores through electronic coupling of  $\pi$ - $\pi$  interactions, polyaromatic fragments that are either conjugated or not conjugated into the chromophore's  $\pi$ -system could be introduced in these donor-acceptor assemblies.<sup>123-130</sup> Polyaromatic pyrene group have been shown to facilitate non-covalent interactions with nanocarbon surfaces. These type of assemblies have demonstrated photoinduced electron-transfer between organic chromophores and a nanocarbon surface following excitation around 400 nm.<sup>131-137</sup> To investigate these non-covalent formations a series of pyrene substituted aza-BODIPYs and BODIPYs and their interaction with nanocarbon materials was explored in order to determine their photoinduced electron-transfer properties. The first chromophores explored was a series of 1,7-dipyrene aza-BODIPYs (**2.5a-2.5e**, Scheme 2.1) with two covalently linked pyrene groups at the  $\beta$ -position of the aza-BODIPYs that are not conjugated into the  $\pi$ -system of the chromophore. The pyrene groups were hypothesized to facilitate non-covalent interactions via a chelate effect with nanocarbon materials such as C<sub>60</sub> and C<sub>70</sub> and (6,5)-single walled carbon nanotubes (SWCNT). The electron density distribution in the aza-BODIPYs were modulated by changing the electron-donating groups at the  $\alpha$ -position of the aza-BODIPY core.



Scheme 2.1. Synthetic pathway for preparation of the aza-BODIPYs **2.5a** – **2.5e**.

The second set of chromophores explored was a series of pyrene-BODIPYs (**2.8-2.10**, Scheme 2.2) where the pyrene is substituted at the  $\alpha$ -position of the BODIPY and is conjugated into the  $\pi$ -system of the chromophore.

### Synthesis and characterization of **2.5a** - **2.5e**

We have used a typical chalcone-based synthetic strategy<sup>138-140</sup> for the preparation of pyrene-containing aza-BODIPYs **2.5a** – **2.5e** and the reference 1,3,5,7-tetraphenyl-aza-BODIPY **2.6** (Scheme 2.1). A variety of aryl-substituents located at the  $\alpha$ -positions were chosen to modulate electron density at the aza-BODIPY core. Chalcones **2.2a-2.2e** were synthesized by the condensation reaction of 1-pyrenecarboxaldehyde and the corresponding ketones **2.1a-2.1e** with subsequent nitromethylation to form products **2.3a-2.3e**. Nitromethyl derivatives **2.3a-2.3e** were converted to the corresponding azadipyrromethanes **2.4a-2.4e** by reaction with ammonium acetate, and then to the final pyrene-containing aza-BODIPYs **2.5a-2.5e** by reaction with boron trifluoride solution. All new compounds were characterized by <sup>1</sup>H and <sup>13</sup>C NMR spectroscopy, high-

resolution mass spectrometry, and UV-vis spectroscopy (Figure 2.1-2.15). The NMR spectra of all target compounds confirm their symmetric nature, while high-resolution mass spectra are in full agreement with their elemental composition.

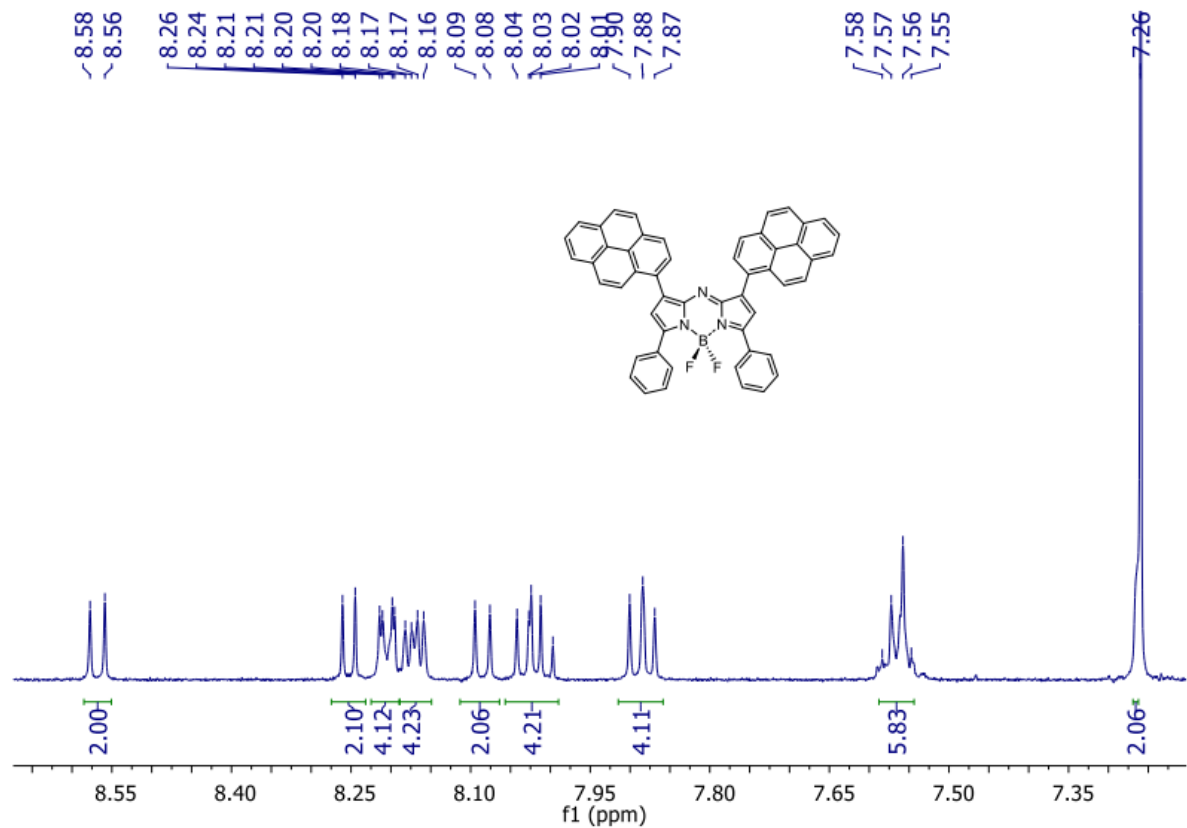


Figure 2.1:  $^1\text{H}$  NMR spectrum of compound **2.5a** in  $\text{CDCl}_3$ .

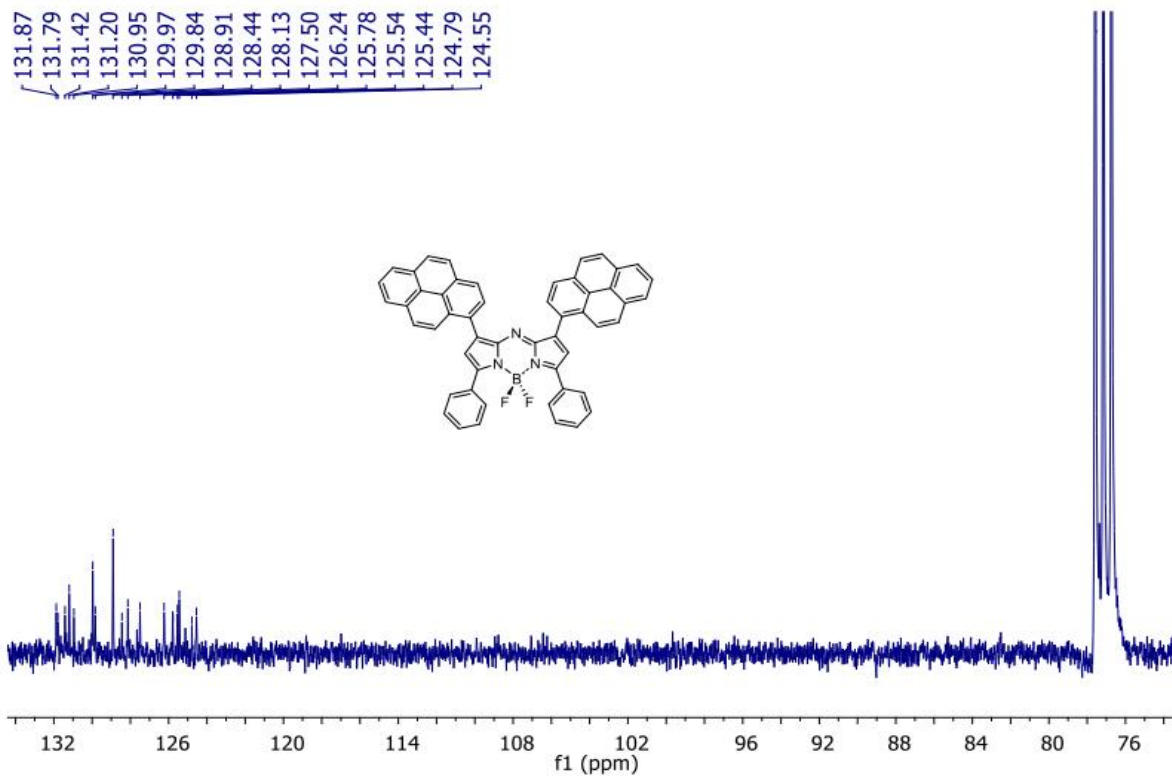


Figure 2.2:  $^{13}\text{C}\{^1\text{H}\}$  NMR spectrum of compound **2.5a** in  $\text{CDCl}_3$ .

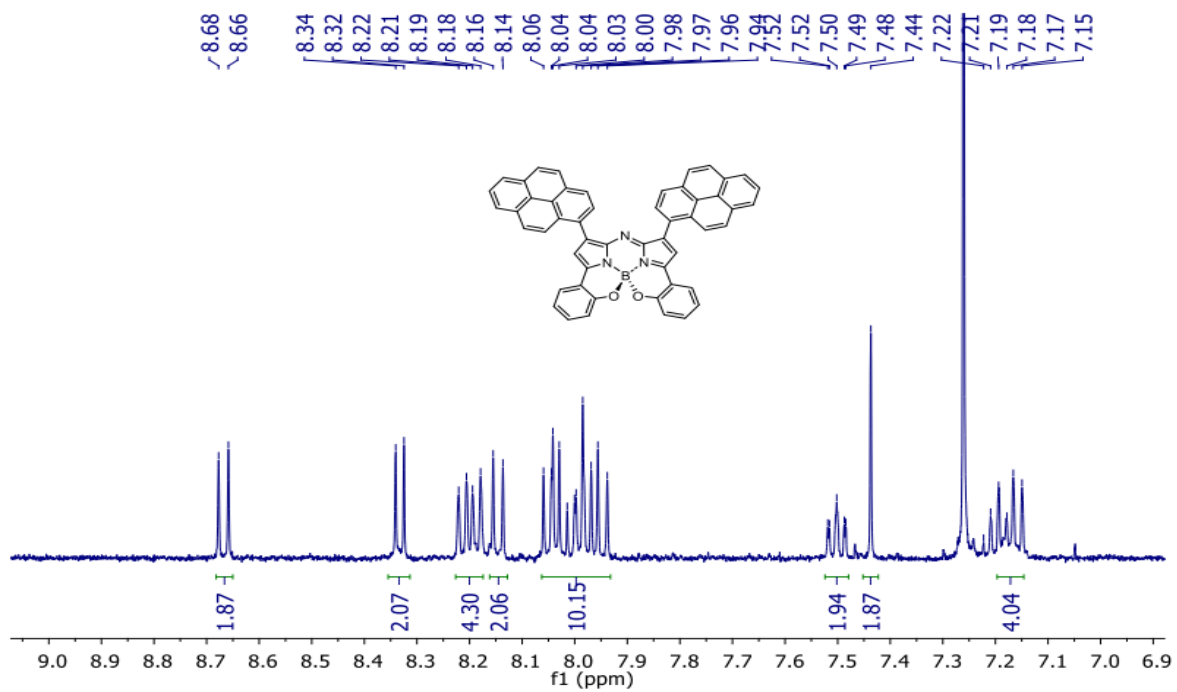


Figure 2.3:  $^1\text{H}$  NMR spectrum of compound **2.5b** in  $\text{CDCl}_3$ .

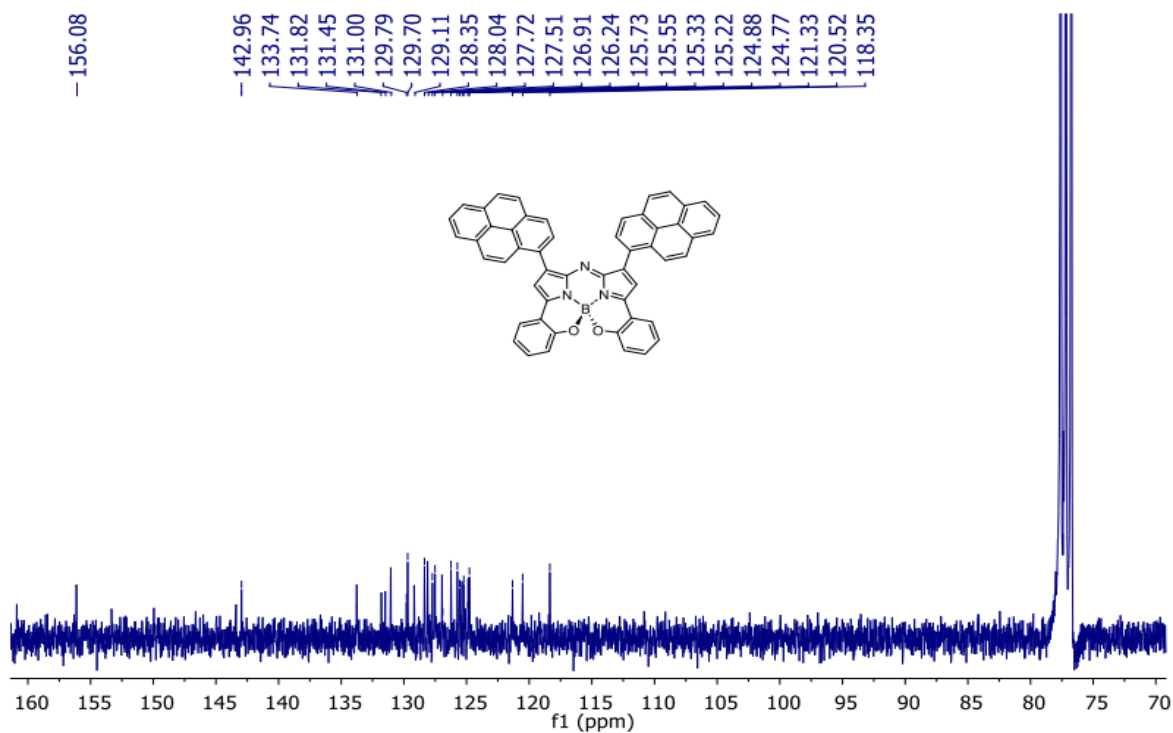


Figure 2.4:  $^{13}\text{C}\{^1\text{H}\}$  NMR spectrum of compound **2.5b** in  $\text{CDCl}_3$ .

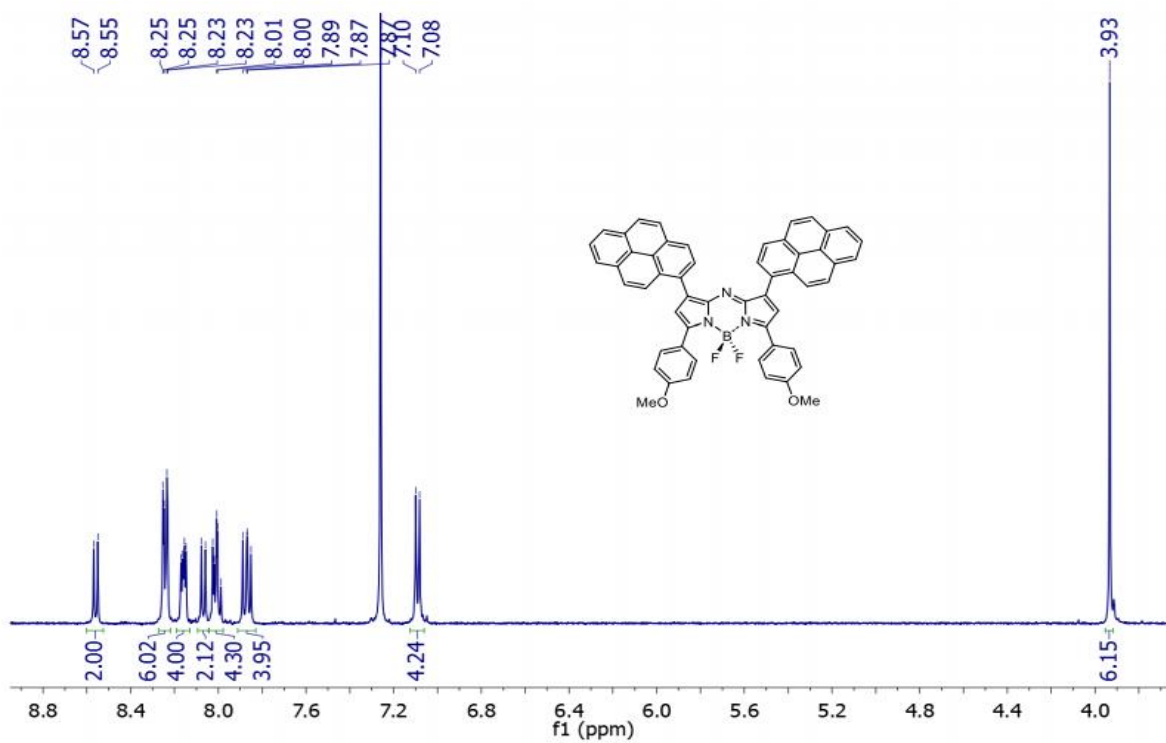


Figure 2.5:  $^1\text{H}$  NMR spectrum of compound **2.5c** in  $\text{CDCl}_3$ .

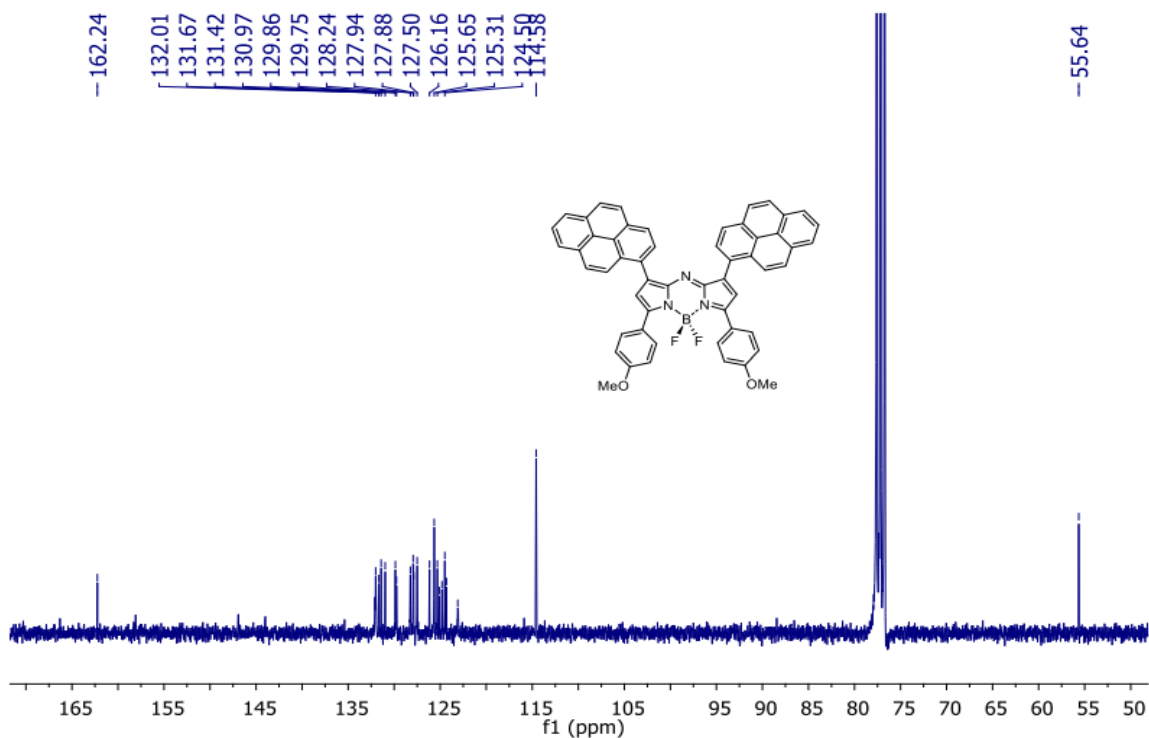


Figure 2.6:  $^{13}\text{C}\{^1\text{H}\}$  NMR spectrum of compound **2.5c** in  $\text{CDCl}_3$ .

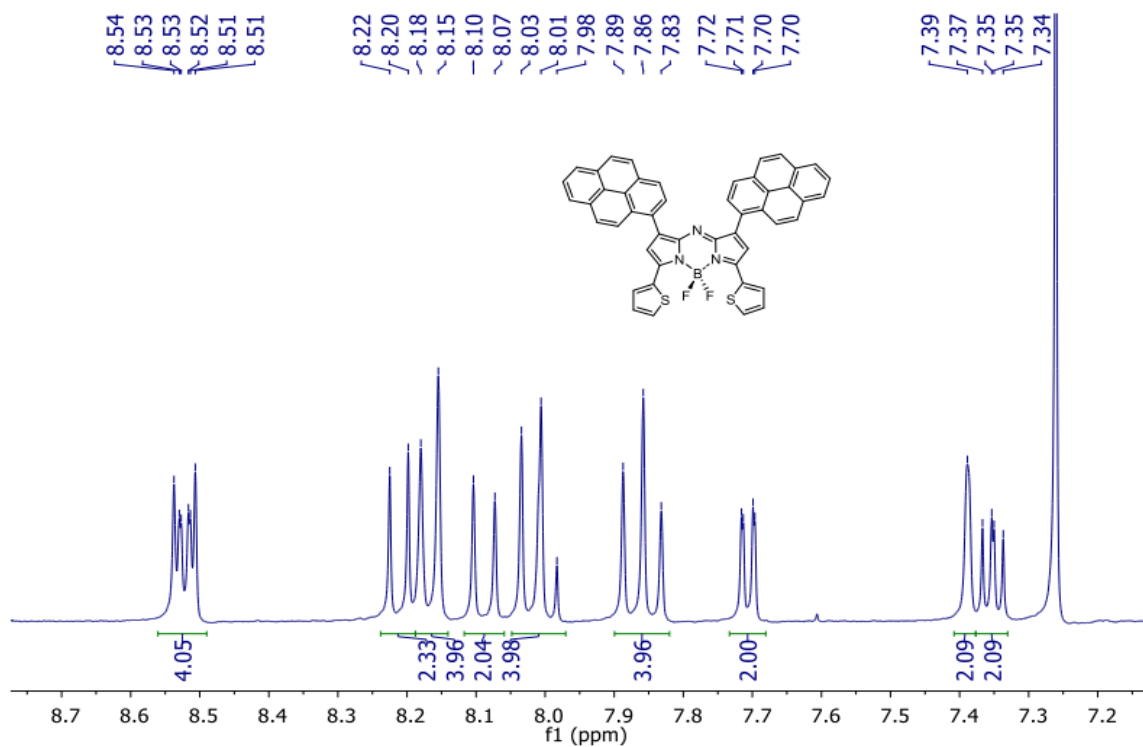


Figure 2.7:  $^1\text{H}$  NMR spectrum of compound **2.5d** in  $\text{CDCl}_3$ .

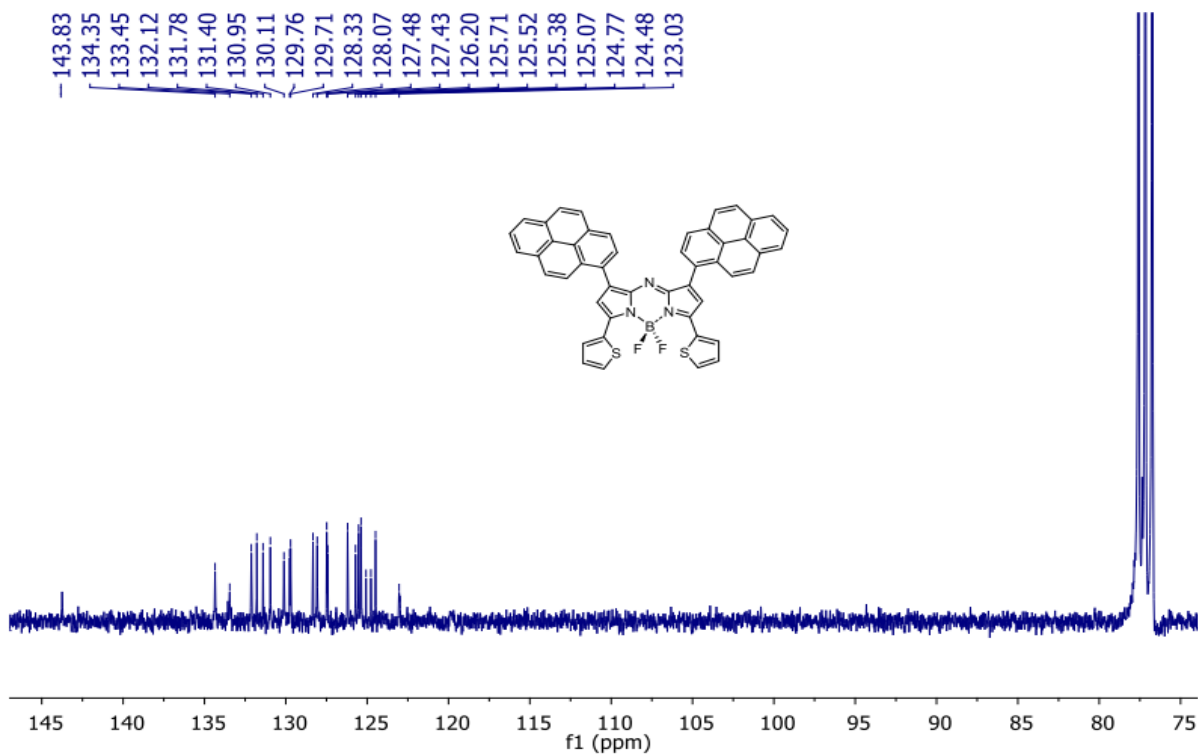


Figure 2.8:  $^{13}\text{C}\{^1\text{H}\}$  NMR spectrum of compound **2.5d** in  $\text{CDCl}_3$ .

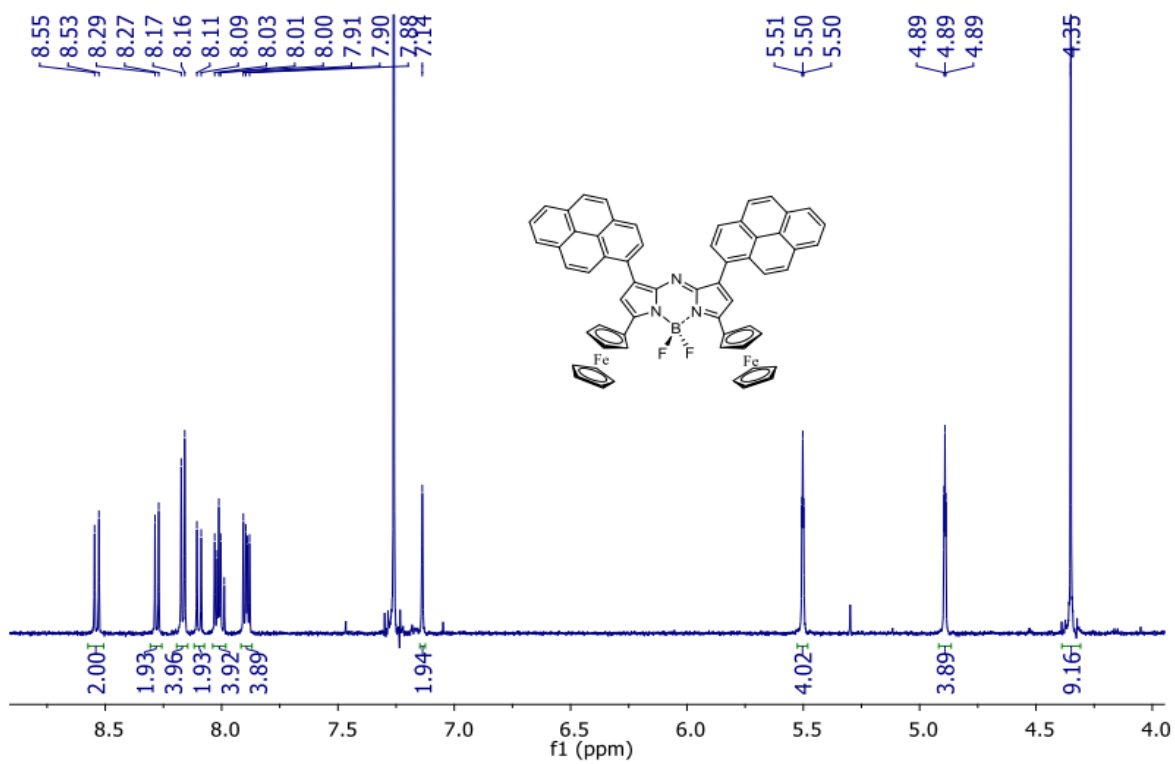


Figure 2.9:  $^1\text{H}$  NMR spectrum of compound **2.5e** in  $\text{CDCl}_3$ .

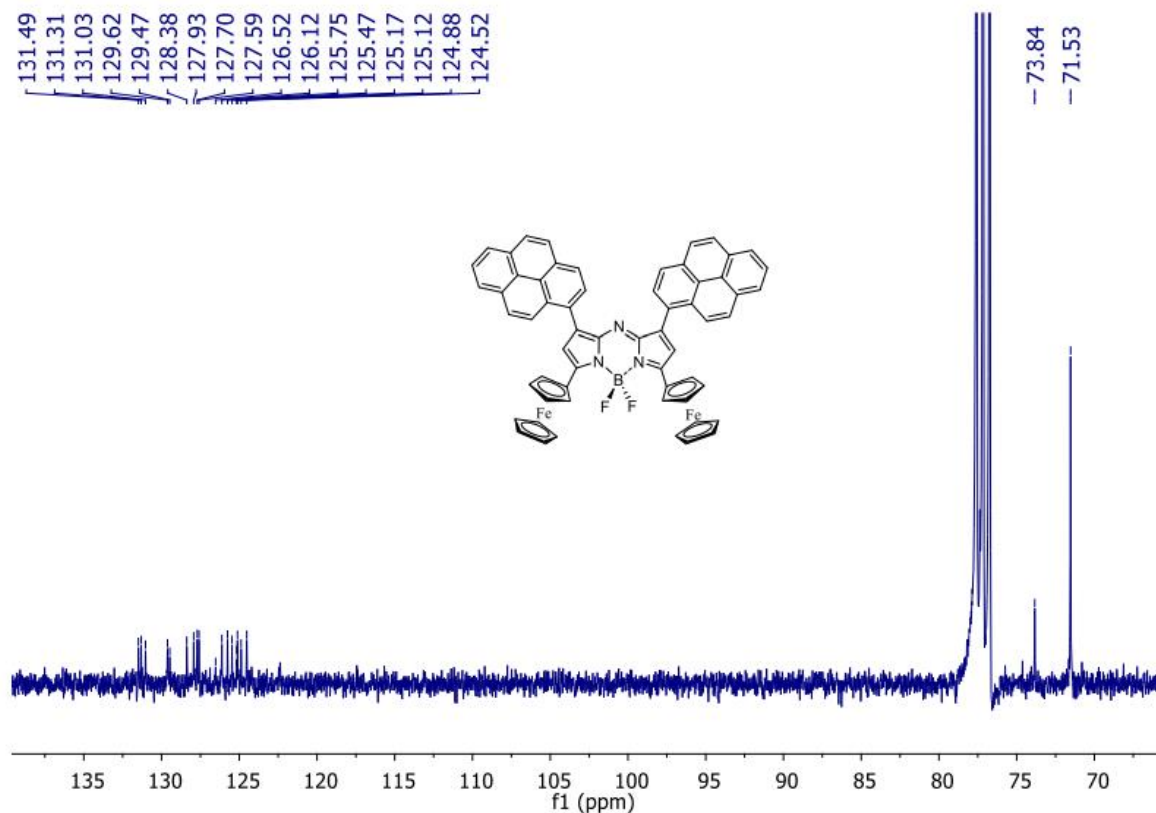


Figure 2.10:  $^{13}\text{C}\{^1\text{H}\}$  NMR spectrum of compound **2.5e** in  $\text{CDCl}_3$ .

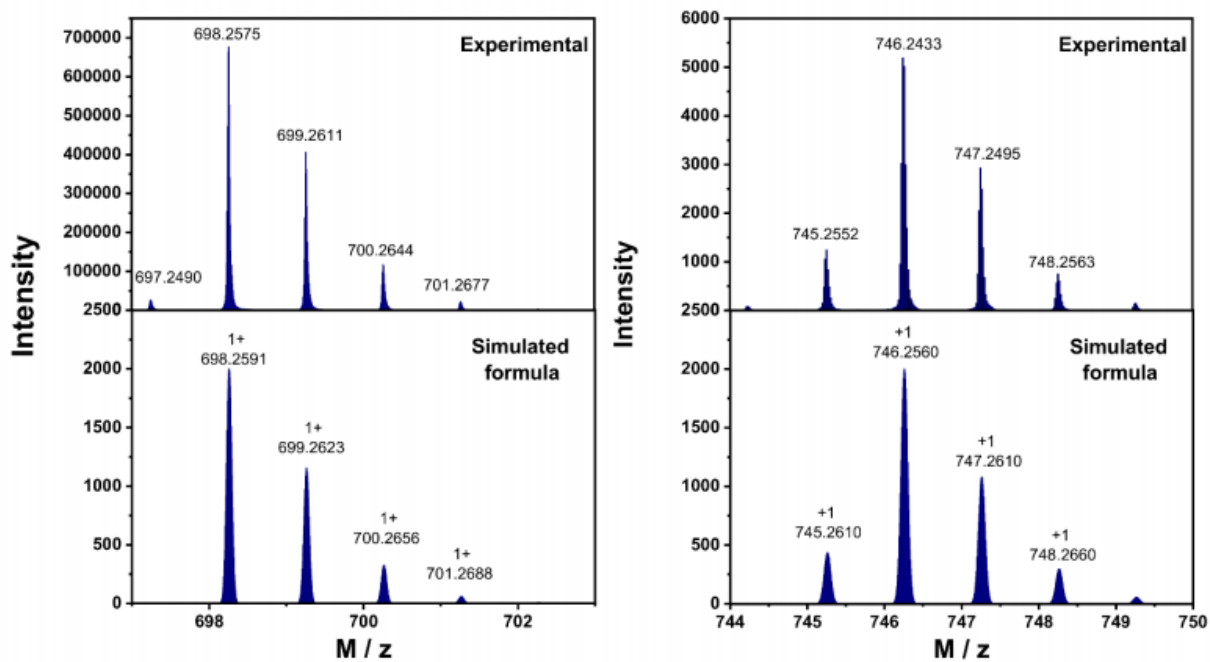


Figure 2.11: HRMS spectra of compounds **2.4a** (left) and **2.5a** (right).

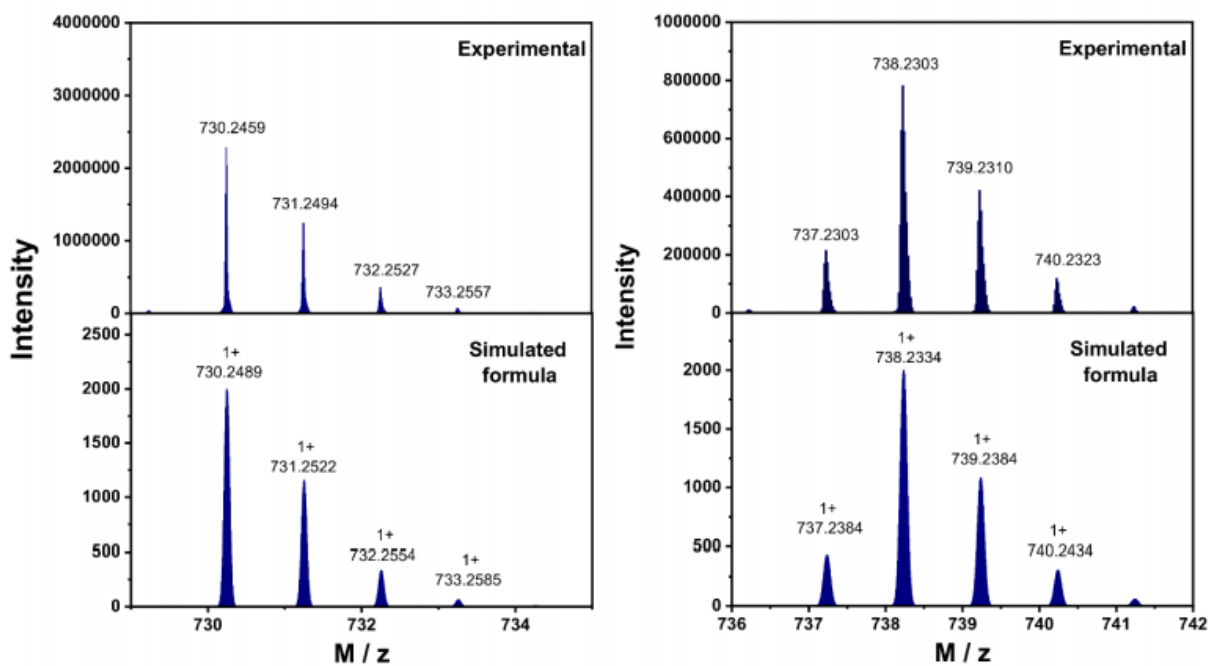


Figure 2.12: HRMS spectra of compounds **2.4b** (left) and **2.5b** (right).

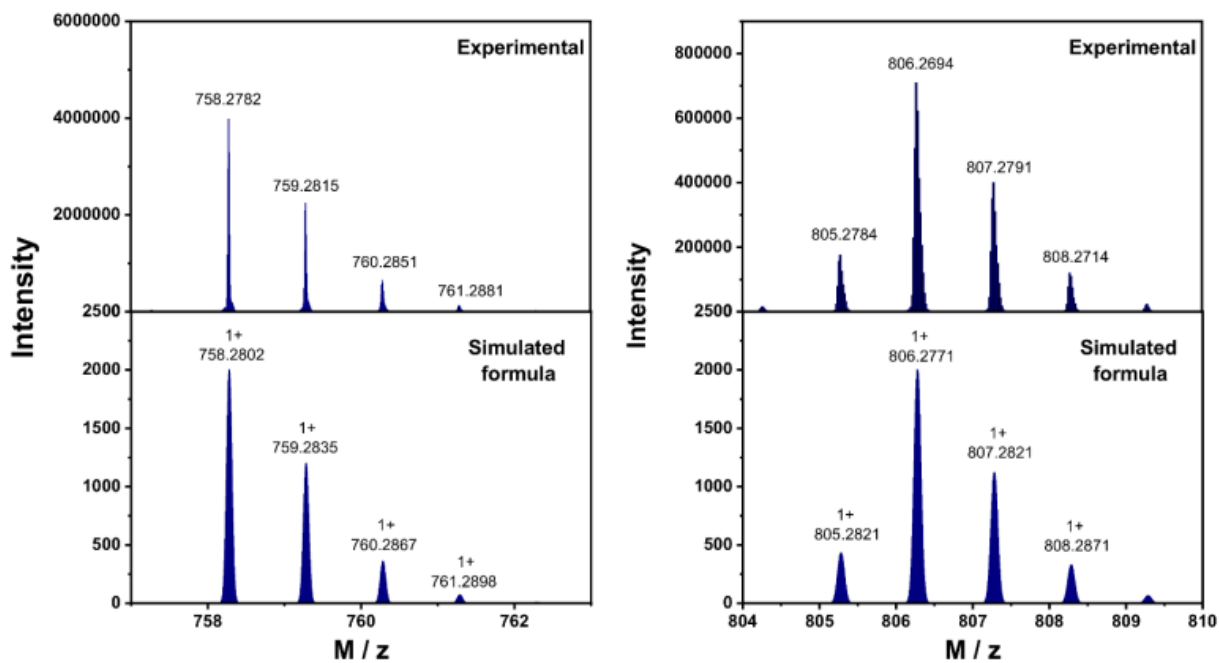


Figure 2.13: HRMS spectra of compounds **2.4c** (left) and **2.5c** (right).

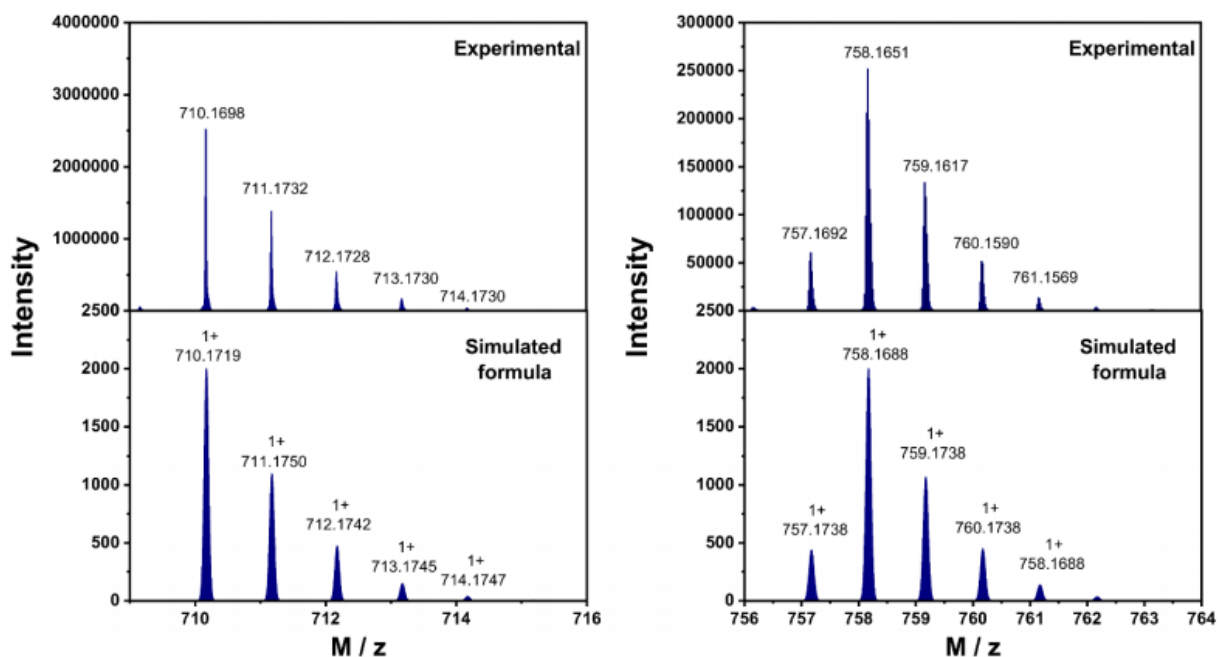


Figure 2.14: HRMS spectra of compounds **2.4d** (left) and **2.5d** (right).

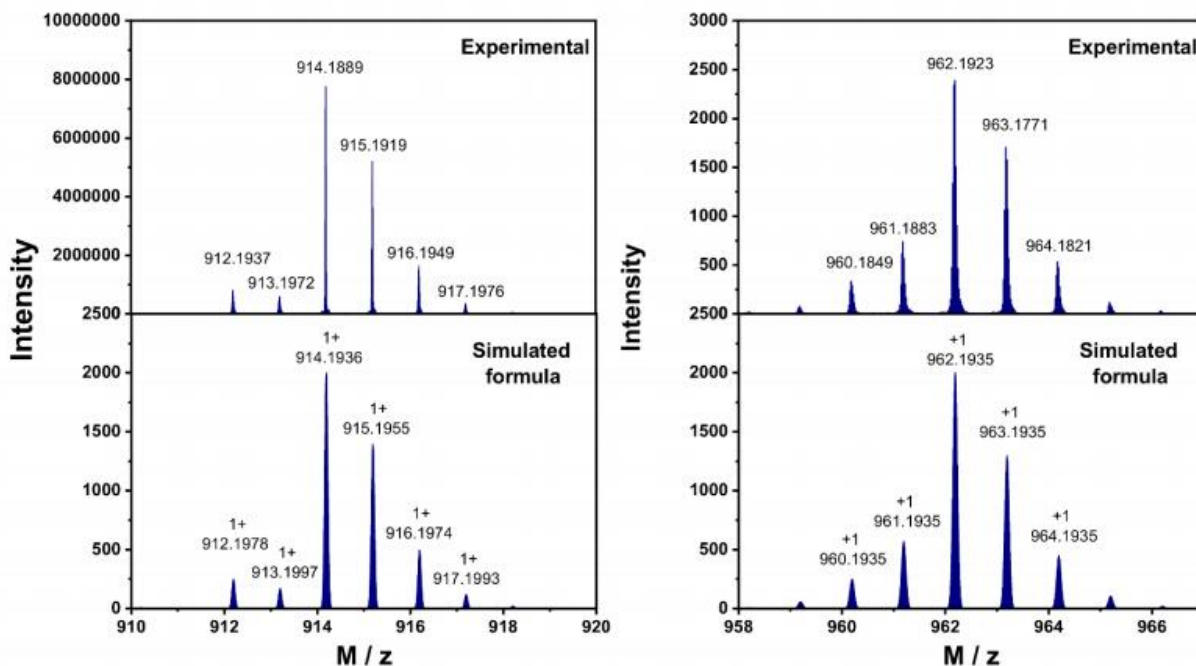


Figure 2.15: HRMS spectra of compounds **2.4e** (left) and **2.5e** (right).

The molecular structures of **2.4e**, **2.5a**, **2.5d**, and **2.5e** were confirmed by the X-ray crystallography (Figure 2.16). Relatively large torsional angles between the two phenyl substituents and the aza-BODIPY core in **2.5a**,  $\sim 35.84^\circ$  and  $\sim 43.10^\circ$ , inhibit conjugation between

the substituents and the chromophore's  $\pi$ -system. The torsional angles were much smaller in **2.5d** and **2.5e**. Crystal structures of **2.5d** had torsion angles between the thiophene group and aza-BODIPY core that varied between  $\sim 0.90^\circ$  and  $\sim 29.94^\circ$ , and with **2.5e** the torsion angles between the ferrocene group and aza-BODIPY core varied between  $6.64^\circ$  and  $17.10^\circ$ . The observation of a nearly coplanar arrangement between the aza-BODIPY core and the ferrocene substituents in **2.5e**, and the relatively short Fe-Fe distance ( $\sim 8.13$  Å), should facilitate electron-transfer between the ferrocene donor and the aza-BODIPY acceptor as previously observed in the phenyl analogue of **2.5e**.<sup>141</sup>

In the crystal structures of **2.4e**, **2.5a**, **2.5d**, and **2.5e**, both pyrene groups are rotated away from the aza-BODIPY  $\pi$ -system (the torsion angles are vary between  $\sim 33.82^\circ$  and  $\sim 44.78^\circ$  for **2.5a**,  $\sim 36.64$  and  $\sim 53.68^\circ$  for **2.5d**, and  $\sim 48.04^\circ$  and  $\sim 51.62^\circ$  for **2.5e**), which reflects the steric bulk. Interestingly, the pyrene fragments in **2.5a** do not form the typical intermolecular  $\pi$ - $\pi$  stacking motif. Rather, they form close slipped-stack type contacts with both the aza-BODIPY core and pyrene group from a neighboring molecule of **2.5a**. The closest pyrene-pyrene intermolecular contact observed in the crystal structure of **2.5a** is  $\sim 3.35$  Å, which is close to the pyrene- $\beta$ -pyrrolic ( $\sim 3.34$  Å) and pyrene- $\alpha$ -pyrrolic ( $\sim 3.32$  Å) intermolecular contacts. In the ferrocene-containing **2.5e**, both slipped-stack ( $\sim 3.19$  to  $\sim 3.26$  Å) and H-type ( $\sim 3.35$  to  $\sim 3.36$  Å) close pyrene-pyrene contacts were observed in the crystal structure. With the thiophene-containing **2.5d**, only H-type ( $\sim 3.34$  to  $\sim 3.39$  Å) pyrene-pyrene stacking was observed in the crystal structure. In contrast to the X-ray crystal structures of **2.5d** and **2.5e**, the aza-BODIPY core in the crystal structure of **2.5a** adopts an unusual, slightly domed conformation. Doming occurs away from the two bulky pyrene fragments. Important for the potential to form non-covalent complexes with nanocarbon partners, the X-ray crystallography data on **2.5a**, **2.5d**, and **2.5e** suggest a large enough cavity between two pyrene groups to accommodate both fullerene and (6,5)-SWCNT in a chelate-type geometry.

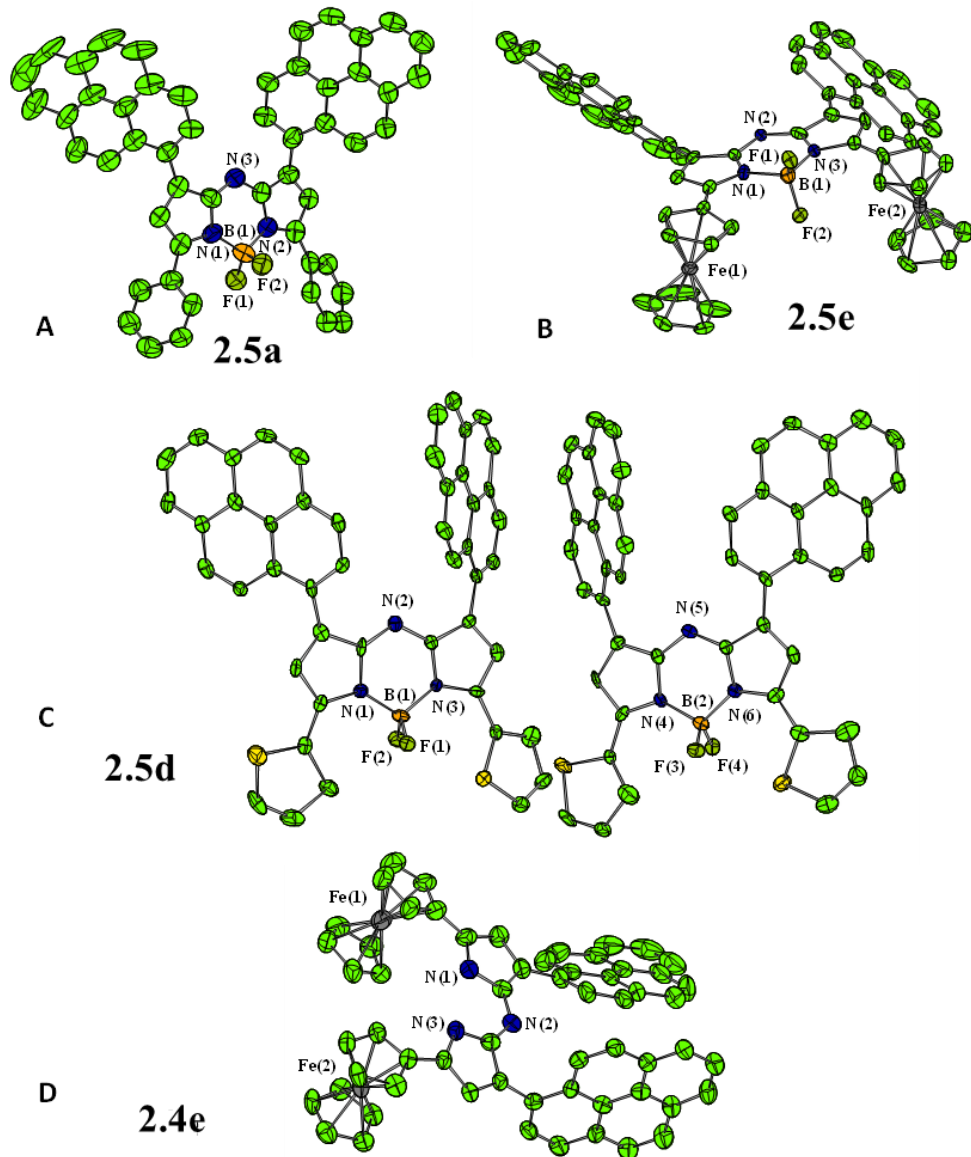


Figure 2.16: CAMERON representation of aza-BODIPYs **2.5a** (A), **2.5e** (B), two crystallographically independent molecules of **2.5d** (C), and aza-DIPY **2.4e** (D) with thermal ellipsoids shown at 50% probability level. All hydrogen atoms are omitted for clarity.

The UV-vis spectra of **2.5a–2.5e** are presented in Figure 2.17 and can be separated into three general categories. The first consists of **2.5b – 2.5d**, with UV-vis spectra that are typical for this class of compounds, dominated by a single narrow band in the visible range followed by several lower intensity components.<sup>138-140</sup> The key differences between UV-vis spectra of **2.5b – 2.5e** and **2.6**, which lacks the pyrene unit, are the broader low-intensity bands in the visible range and the presence of intense and characteristic absorption bands at ~275 nm and ~345 nm that are

associated with the pyrene constituents in **2.5b** – **2.5e**. The second category is represented by the phenyl derivative **2.5a** that has a broad and intense single low-energy band in the visible region and narrow bands at wavelengths shorter than 400 nm primarily localized on the pyrene fragments. The last category is represented by the ferrocene derivative **2.5e**. It has two intense low-energy bands observed at 638 nm and 856 nm that are in good agreement with a previously reported diphenyl-ferrocene analogue.<sup>141</sup> The low-energy broad band observed at 856 nm was assigned to the metal-to-ligand charge-transfer (MLCT) transitions, and the narrower band observed at 638 nm was assigned to an aza-BODIPY centered  $\pi$ - $\pi^*$  transition. In general, the energy of the most intense  $\pi$ - $\pi^*$  transition observed in **2.5a** – **2.5d** correlates well with the DFT-predicted (discussed below) electron donating ability of the substituents located at the  $\alpha$ -positions of BODIPY core,  $2.5a < 2.5c < 2.5b \sim 2.5d$ .

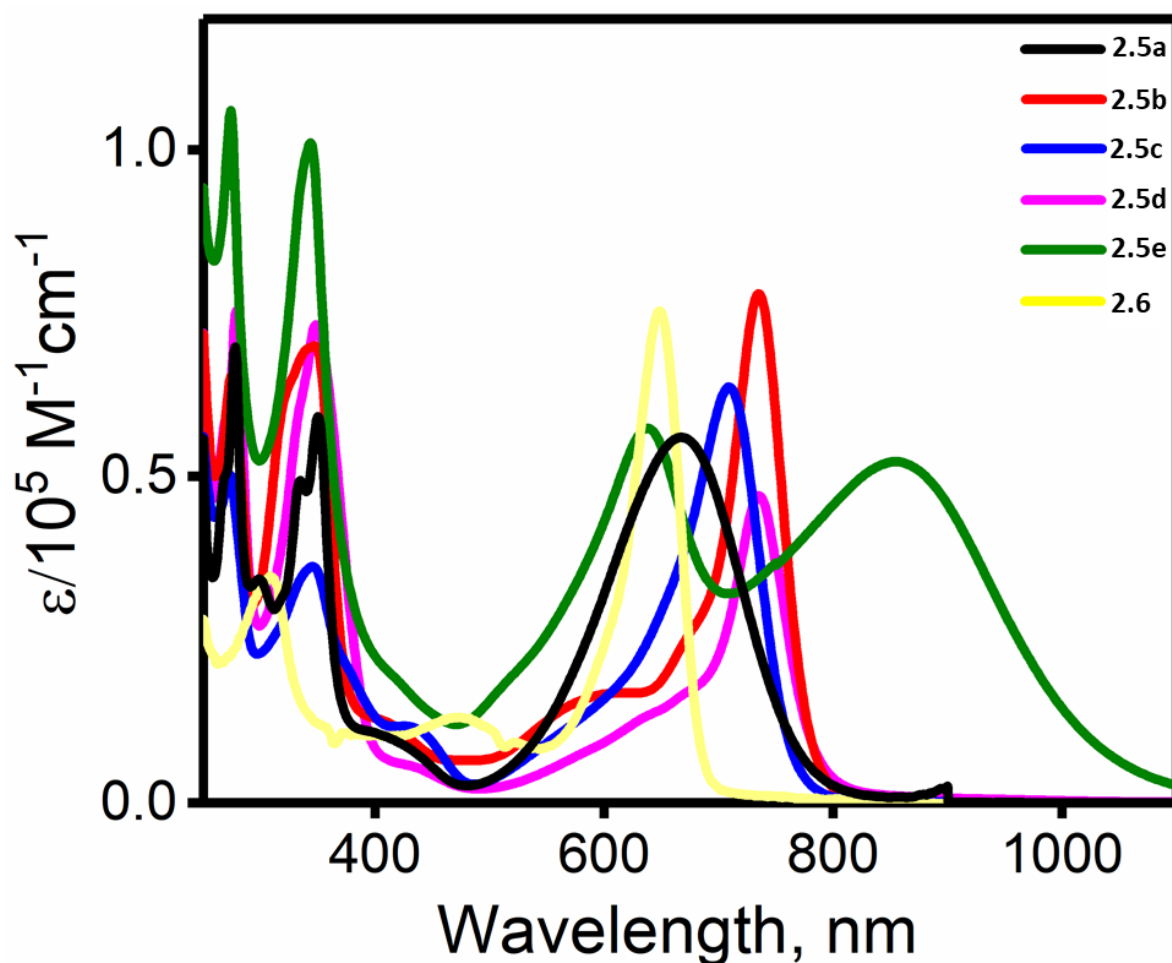


Figure 2.17: UV-Vis spectra of compounds **2.5a** – **2.5e** and **2.6** in Dichloromethane (DCM).

Steady-state fluorescence spectra are in Figure 2.18 and Figure 2.19. Fluorescence from the ferrocene-containing **2.5e** was completely quenched, which is typical for ferrocene-containing BODIPYs<sup>142-146</sup> and aza-BODIPYs.<sup>141,147,148</sup> The fluorescence quantum yields for **2.5a** – **2.5d** were significantly smaller than other BODIPY compounds,<sup>149,150</sup> reflecting the electron-donating role played by the installed pyrene substituents. The fluorescence spectrum of **2.5a** was an approximate mirror image of its absorption spectrum with a significant Stokes shift of 2570 cm<sup>-1</sup> (Table 2.1). Following excitation at 275 nm and 345 nm, predominantly centered on the pyrene substituents, emission was observed from **2.5a** – **2.5d** in the visible and near IR regions, clearly indicating energy transfer from pyrene substituents to the aza-BODIPY core, see figure 2.19. In the case of thiophene-containing compound **2.5d** the pyrene-centered fluorescence peak is much stronger than the aza-BODIPY emission peak, while the opposite trend was observed for **2.5a**–**2.5c** upon excitation at 275 and 345 nm, which is indicative of much better energy transfer from pyrene fragments to the aza-BODIPY core in compounds **2.5a**–**2.5c** (Figure 2.19).

Table 2.1. Selected photophysical properties of aza-BODIPYs **2.5a**–**2.5e** and the reference compound **2.6**. Lifetimes were determined by transient absorption for all compounds. Data presented in Figure 2.24 and 2.20-2.23.

Compound	$\lambda_{\text{abs}}$ [nm] ( $\epsilon$ [ $\text{M}^{-1}\text{cm}^{-1}$ ])	Emission [nm] ( $\Phi$ )	$\tau$ [ns]
<b>2.5a</b>	335 (49000), 351 (59000), 667 (55000)	805 (0.006)	0.87±0.07
<b>2.5b</b>	347 (70000), 735 (78000)	436, 782 (0.0076)	1.6±0.1
<b>2.5c</b>	346 (36000), 709 (64000)	398, 760 (0.0167)	1.1±0.1
<b>2.5d</b>	347 (73000), 735 (47000)	421, 778 (0.0142)	1.3±0.1
<b>2.5e</b>	344 (101000), 638 (57000), 854 (52000)	not detected	1.7±0.2
<b>2.6</b>	308 (35000), 648 (75000)	674(0.34)	

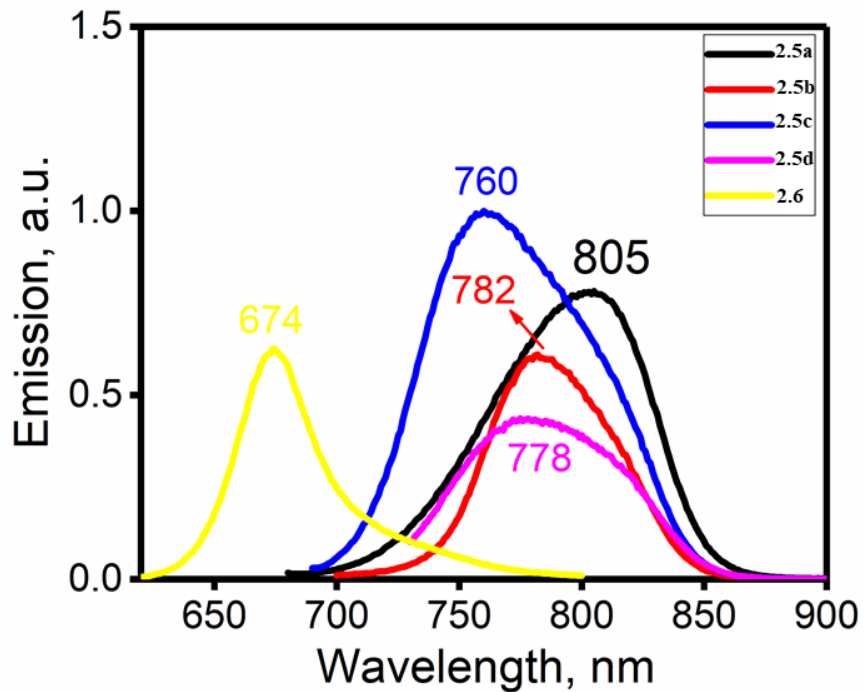


Figure 2.18: Fluorescence spectra of aza-BODIPYs **2.5a** – **2.5d** and **2.6** in DCM. Excitation wavelengths are: 650 nm (**2.5a**), 680 nm (**2.5b**), 670 nm (**2.5c**), 700 nm (**2.5d**), and 600 nm (**2.6**).

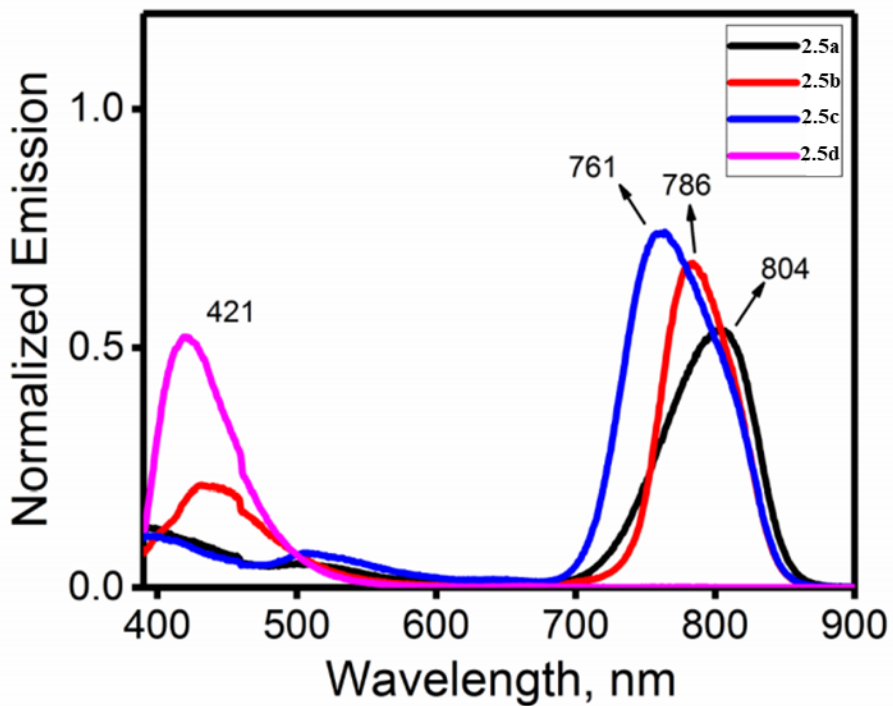


Figure: 2.19: Fluorescence spectrum at 275 nm excitation of compounds **2.5a**–**2.5d** in DCM

Excited state lifetimes are reported in Table 2.1. At 1 – 2 ns, the lifetimes for **2.5a** – **2.5d** are all similar to reported values for analogous BODIPYs and aza-BODIPYs systems.<sup>149,150</sup> The data and fits are presented in Figures 2.20-2.23. The data were well fitted with a single exponential decay. No longer lived emission was found within the signal to noise of the experiments, leaving no evidence for the formation of a triplet state. This is in contrast with the reports of triplet state formation following excitation of *meso*-pyrene BODIPYs.<sup>151-152</sup>

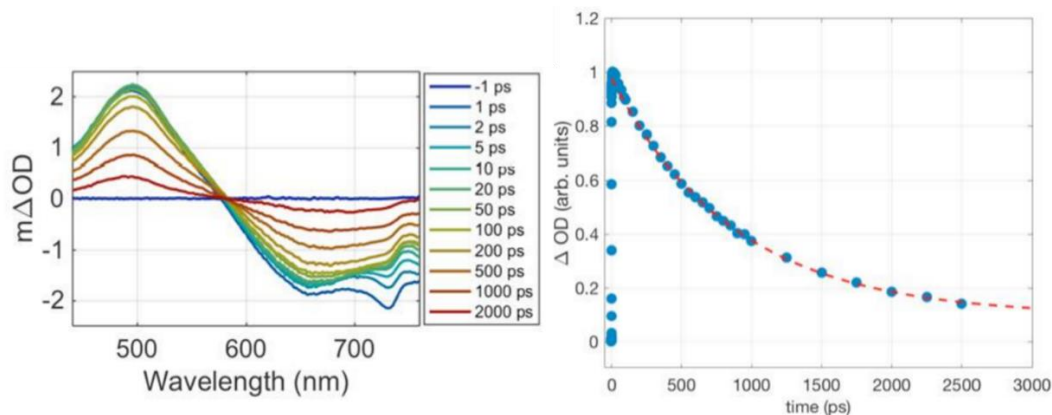


Figure 2.20: Pump-probe data for **2.5a** in a DCM solution. Sample was excited at 650 nm. Top is full frequency transient pump-probe. Bottom is the time dependence probed at 500 nm, the circles are the raw data and the dashed line is a single exponential fit. Fitting parameters are presented in Table 2.1.

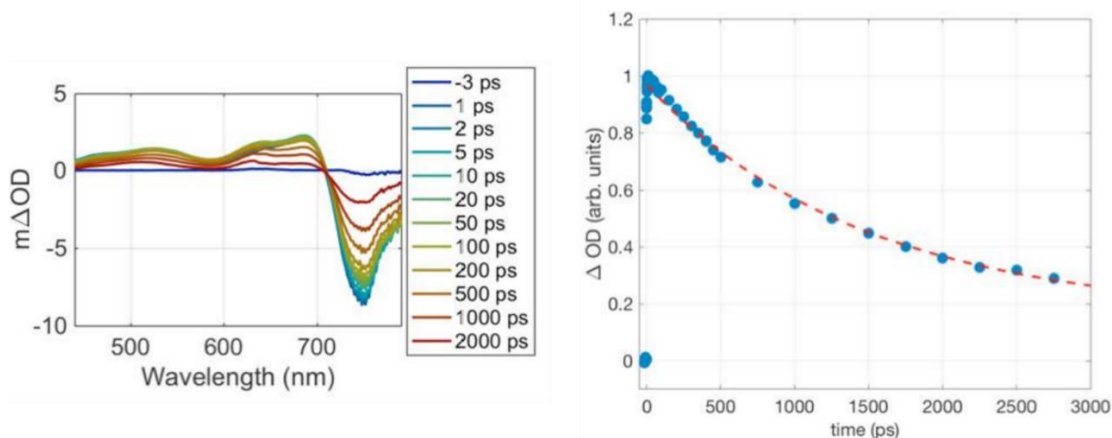


Figure 2.21: Pump-probe data for **2.5b** in a DCM solution. Sample was excited at 640 nm. Top is full frequency transient pump-probe. Bottom is the time dependence probed at 525 nm, the circles are the raw data and the dashed line is a single exponential fit. Fitting parameters are presented in Table 2.1.

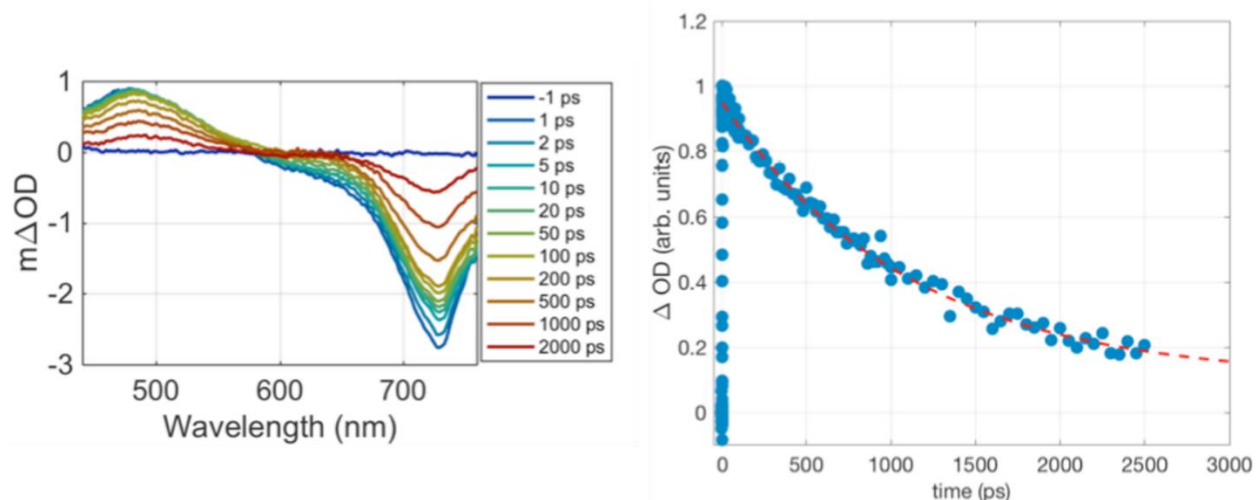


Figure 2.22: Pump-probe data for **2.5c** in a DCM solution. Sample was excited at 650 nm. Top is full frequency transient pump-probe. Bottom is the time dependence probed at 480 nm, the circles are the raw data and the dashed line is a single exponential fit. Fitting parameters are presented in Table 2.1.

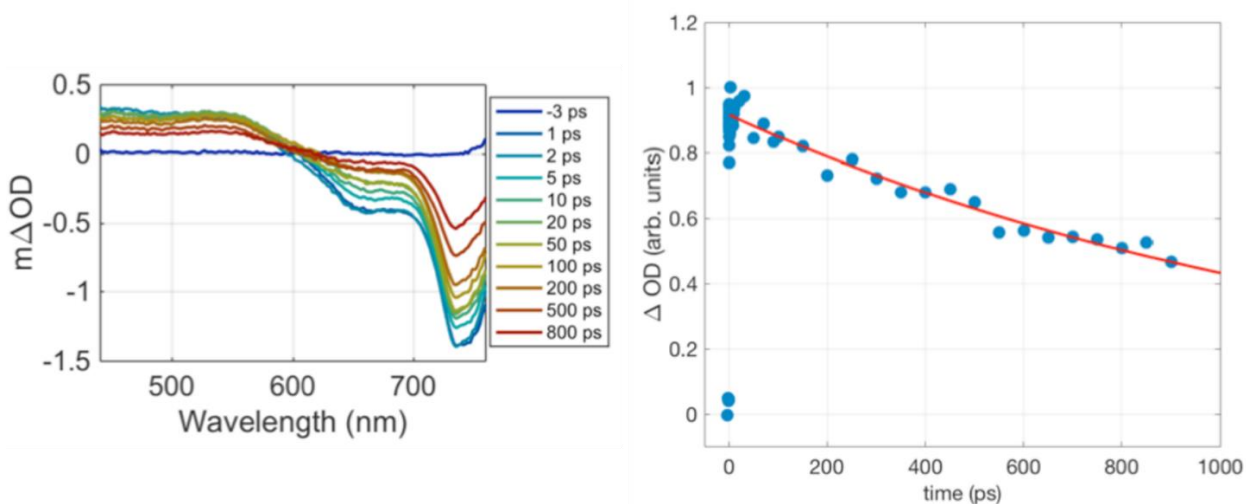


Figure 2.23: Pump-probe data for **2.5d** in a DCM solution. Sample was excited at 650 nm. Top is full frequency transient pump-probe. Bottom is the time dependence probed at 500 nm, the circles are the raw data and the dashed line is a single exponential fit. Fitting parameters are presented in Table 2.1.

Time-resolved pump-probe transients for the non-fluorescent ferrocene containing **2.5e** are shown in Figure 2.24. The decay of the transient absorption feature centered at 475 nm was well fitted with a single exponential having a time constant of 1.7 ns (Table 2.1). This is consistent with

the excited state lifetimes of **2.5a** – **2.5d**, and we assign this state to a  $\pi^*$  excited state involving both the aza-BODIPY core and the pyrenes. It is interesting to note that the lifetime of this state is substantially longer than the 176 ps excited state lifetime we previously reported for the analogous BODIPY diphenyl ferrocene system.<sup>153-155</sup> In that system we assigned the excited state lifetime to charge recombination following excitation that immediately produced a charge transfer from the ferrocene to the aza-BODIPY core. As shown in Figure 2.24, unlike the transient absorption at 475 nm that decayed as a single exponential, in order to obtain a reasonable fit to recovery of the ground state bleach probed at 650 nm, a second exponential decay component with a time constant of ca. 100 ps becomes statistically significant in the data, Figure 2.24. Addition of the faster component is consistent with overlapping transitions in the excitation that includes both the pyrene centered excitation and ferrocene to aza-BODIPY core charge transfer. The shorter time constant is consistent with the time scales for charge recombination that we reported in similar ferrocene appended BODIPY systems.<sup>153</sup> Increase in the amplitude and subtle change in shape of the transient difference spectra with excitation at 920 nm compared to 640 nm is also consistent with the expectation that there should be an increase in the contribution from the charge transfer transition as the excitation moves to longer wavelength.

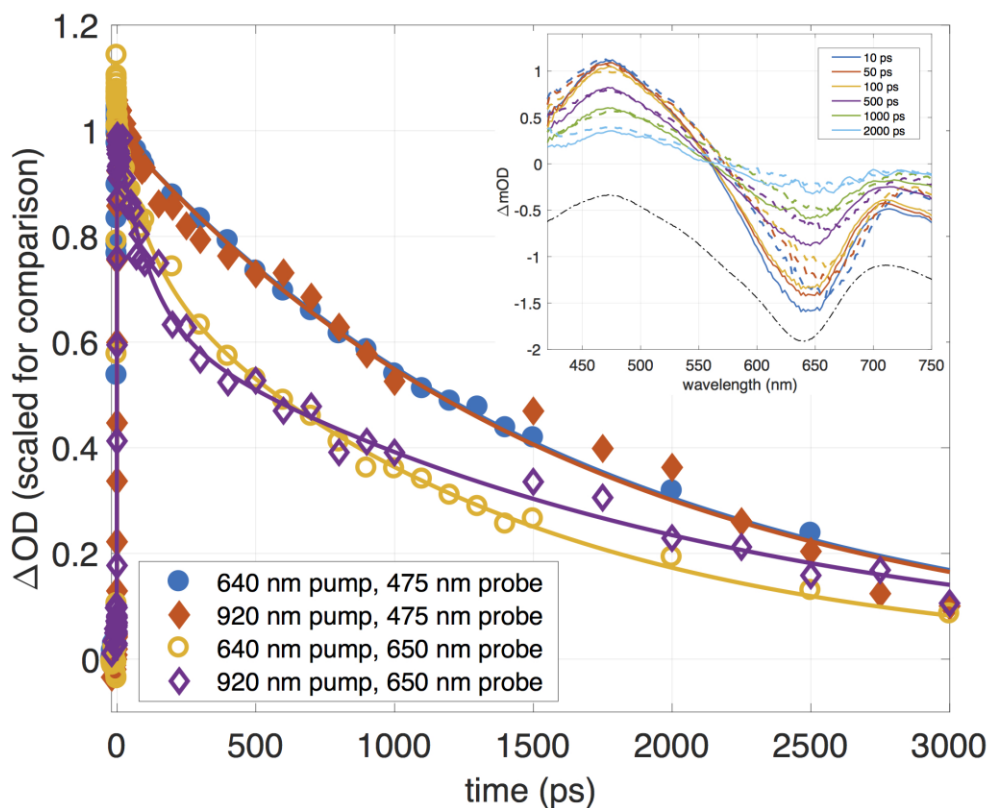


Figure 2.24: Pump-probe response for **2.5e**. Symbols are the data, lines are fits as described in the text. Data probed at 650 nm has been inverted for comparison with data probed at 475 nm. Inset: transient full frequency spectra at indicated pump-probe delay times. The solid lines were pumped at 640 nm, the dashed lines were pumped at 920 nm. The dash-dot line is the absorption spectrum inverted as a guide to the shape of the bleach component in the pump-probe spectra.

The redox properties of **2.5a** – **2.5e** were investigated by electrochemical methods (cyclic voltammetry, CV and differential pulse voltammetry, DPV) The data are summarized in Table 2.2 and shown in Figure 2.25-2.27. In the cases of **2.5a** – **2.5d** and the reference compound **2.6**, one oxidation and two reduction processes associated with the aza-BODIPY core were observed. Both reduction processes were quasi-reversible, in agreement with the literature data.<sup>153-155</sup> The first reduction potentials were all within 100 mV of each other, indicating limited influence of the substituents located at the  $\alpha$ -position of the corresponding aza-BODIPY. This is consistent with the significant contribution from the nitrogen atoms to the LUMO in aza-BODIPY as discussed below. The first oxidation process is quasi-reversible in **2.5a** – **2.5c** and irreversible in **2.5d**. The larger range of oxidation potentials across the series is consistent with the significant contribution from the  $\alpha$ -pyrrolic carbon atoms to the HOMO in aza-BODIPYs. Irreversible oxidation of the

pyrene groups in **2.5a** – **2.5d** was observed at higher potentials (Table 2.2, Figure 2.25-2.27). A single broad two-electron oxidation wave was observed in the CV and DPV experiments on **2.5b** – **2.5d**. With **2.5a**, two one-electron oxidation waves associated with a stepwise oxidation of the pyrene groups were clearly resolved in the DPV experiments. In the case of the ferrocene-containing **2.5e**, the first and second reduction processes remained reversible and were attributed to the reduction of the aza-BODIPY core. The first reduction potential is more negative in **2.5e** than **2.5a** – **2.5d**. The first and second single-electron oxidations were assigned to the stepwise oxidation of two ferrocene groups in **2.5e**. Both of these oxidations were quasi-reversible and the difference between them, 460 mV, is similar to that observed for the phenyl analogue of **2.5e**.<sup>141</sup> More interestingly, three additional single-electron oxidation waves were observed in CV and DPV experiments on **2.5e**. The first quasi-reversible oxidation in **2.5e**, Ox<sub>3</sub> in Table 2.2, was assigned to oxidation of the aza-BODIPY core, while the other two, closely spaced at the higher potentials, Ox<sub>4</sub> and Ox<sub>5</sub>, were attributed to the stepwise irreversible oxidation of the pyrene fragments.

**Table 2.2.** Redox properties of aza-BODIPYs **2.5a** – **2.5e** and the reference compound **2.6**.

Compound	E <sup>4</sup> <sub>Ox</sub> (V)	E <sup>3</sup> <sub>Ox</sub> (V)	E <sup>2</sup> <sub>Ox</sub> (V)	E <sup>1</sup> <sub>Ox</sub> (V)	E <sup>1</sup> <sub>Red</sub> (V)	E <sup>2</sup> <sub>Red</sub> (V)
<b>2.5a</b>			1.0*	0.7	-0.86	-1.6*
<b>2.5b</b>			1.0*	0.62	-0.91	-1.5*
<b>2.5c</b>			1.05*	0.57	-0.91	-1.63*
<b>2.5d</b>			0.95*	0.57*	-0.81	-1.55*
<b>2.5e</b>	1.1*	0.85	0.44	0	-1.16	-1.84
<b>2.6</b>				0.84	-0.85	-1.65
<b>2.6</b> <sup>93</sup>				0.76	-0.79	-1.54

All potentials are referenced to the FcH/FcH<sup>+</sup> couple in DCM/0.05M TFAB. “\*” denotes irreversible or partially reversible process.

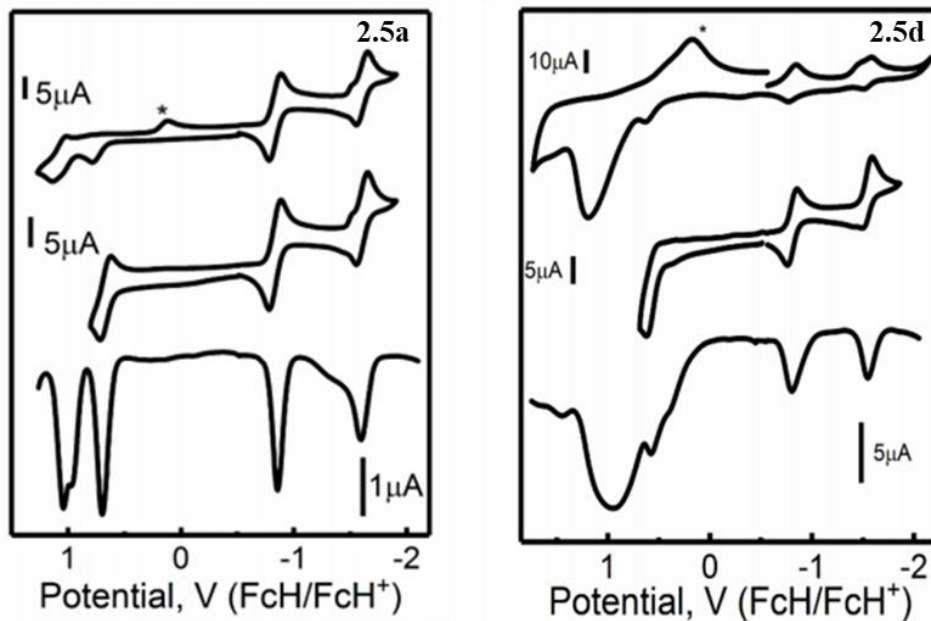


Figure 2.25: CV/DPV of compound **2.5a** and **2.5d** in DCM. \*Indicates degradation products originated from the irreversible oxidation processes.

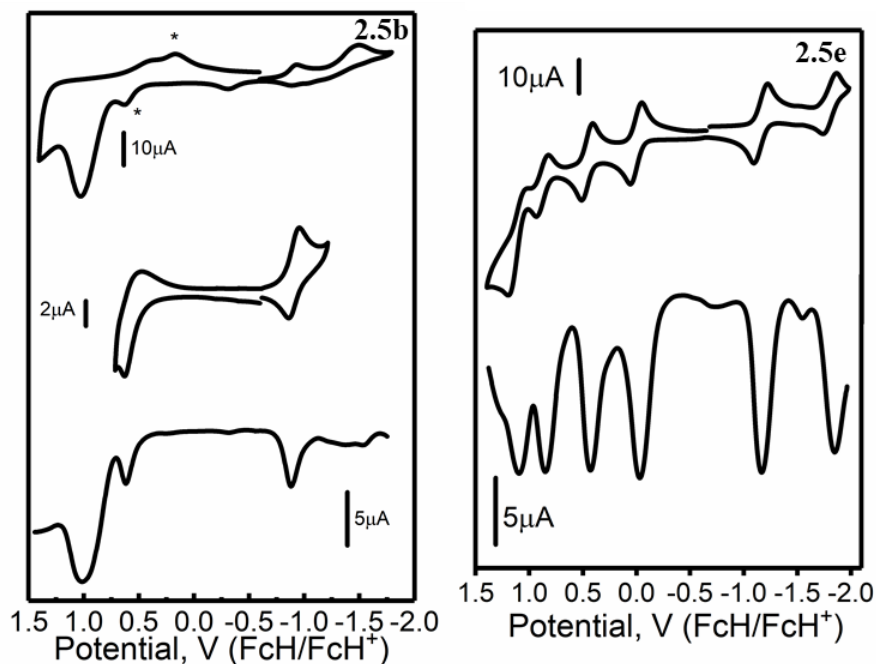


Figure 2.26: CV and DPV data for aza-BODIPYs **2.5b** and **2.5e** in DCM. \*Indicates degradation products originated from the irreversible oxidation processes

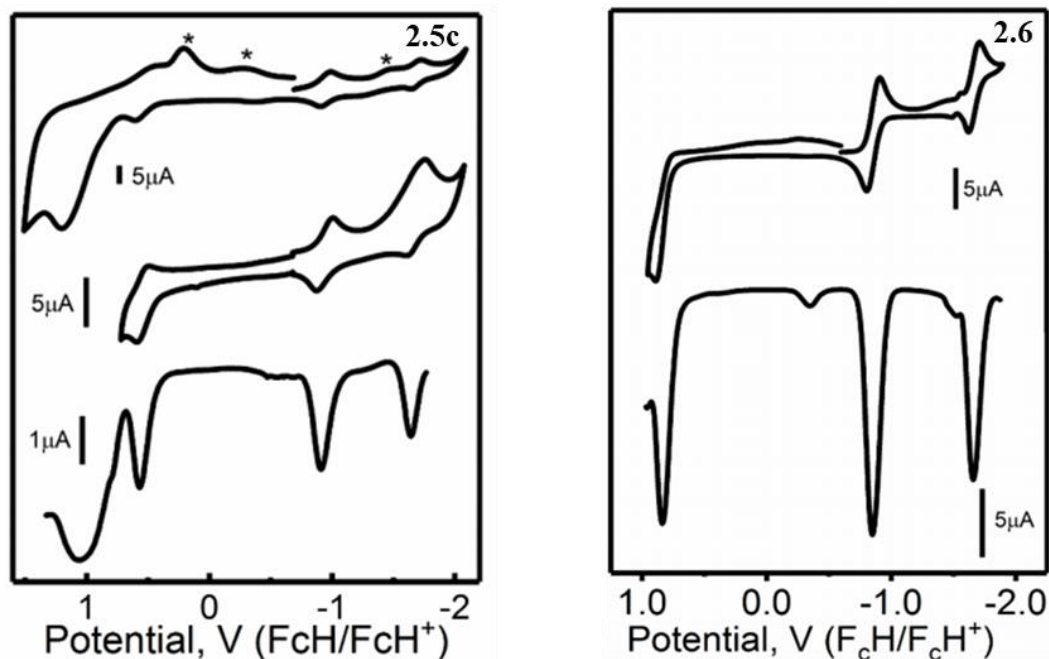


Figure 2.27: CV/DPV of compound **2.5c** and **2.6** in DCM. \*Indicates degradation products originated from the irreversible oxidation processes.

In order to characterize spectroscopic signatures of the redox-active species generated upon stepwise oxidation of the ferrocene groups in **2.5e**, we conducted spectroelectrochemical oxidation experiments (Figure 2.28). Similar to the phenyl analogue of the **2.5e**,<sup>141</sup> during the first oxidation process, two new broad bands appeared in the NIR region peaked at ~1000 and ~2500 nm. Simultaneously, the initial bands at 557 nm and 685 nm were transformed into a single broad band observed at 577 nm. The broad band at ~2500 nm is characteristic of mixed-valence diferrocenyl-<sup>141</sup> and tetraferrocenyl-containing<sup>156</sup> aza-BODIPYs and is indicative of formation of the mixed-valence [**2.5e**]<sup>+</sup>. Band deconvolution analysis of the NIR region of UV-Vis-NIR spectrum of [**2.5e**]<sup>+</sup> is suggestive of the Class II (weakly coupled) behavior of this mixed-valence compound (Figure 2.29).<sup>157-159</sup> During the second oxidation process, the NIR bands are diminished and the final spectrum is dominated by a very characteristic strong aza-BODIPY centered  $\pi-\pi^*$  transition observed at 593 nm. The presence of this band in doubly oxidized [**2.5e**]<sup>2+</sup> indicates that the aza-BODIPY chromophore is not significantly affected upon stepwise oxidation of **2.5e**, which is consistent with a stepwise oxidation of the two ferrocene groups.

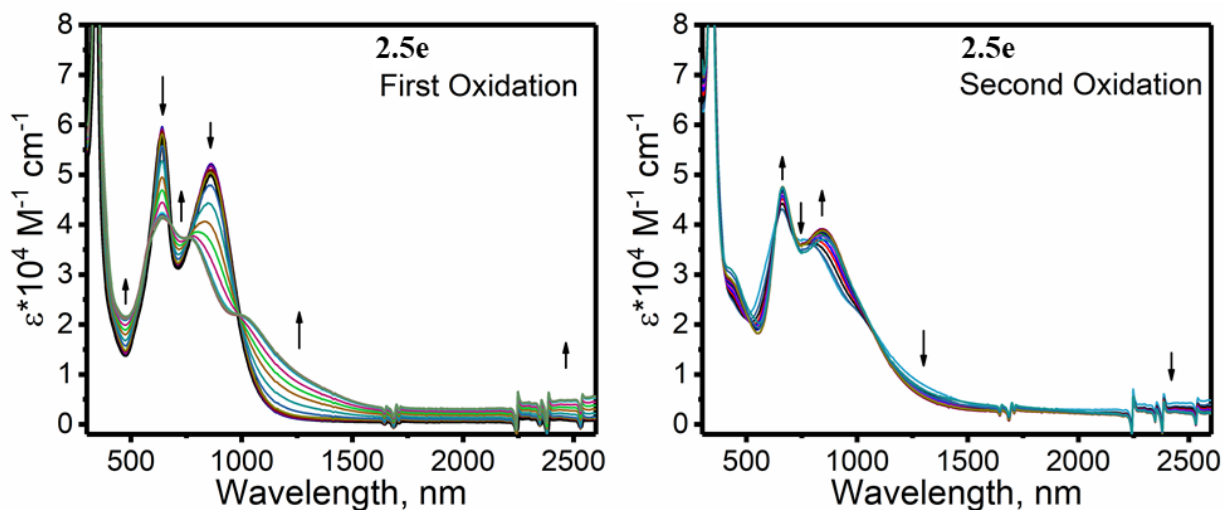


Figure 2.28: Spectroelectrochemical oxidation of compound **2.5e** in DCM/0.15 M TFAB solvent system: the first oxidation process (left); the second oxidation process (right).

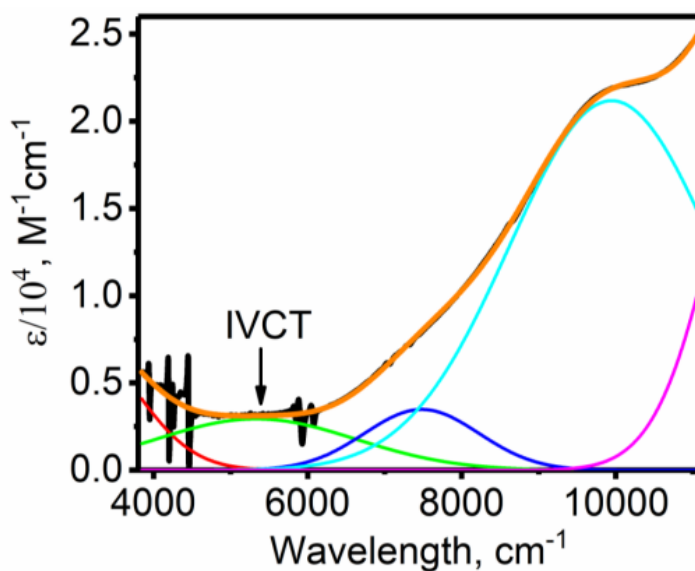


Figure 2.29: Intervalence charge transfer (IVCT) band deconvolution analysis for  $[2.5e]^+$ . Selected parameters: IVCT energy is  $5330\text{ cm}^{-1}$ ,  $\epsilon = 2944\text{ M}^{-1}\text{ cm}^{-1}$ ; FWHM =  $3049\text{ cm}^{-1}$ ,  $H_{ab} = 554.5\text{ cm}^{-1}$ .

In order to correlate experimentally observed spectroscopic and redox properties with electronic structure, DFT and TDDFT calculations were performed on **2.5a** – **2.5e** using B3LYP exchange correlation functional. The predicted frontier orbital compositions are shown in Figure

2.30, an energy level diagram is presented in Figure 2.31, and the important frontier orbitals are pictured in Figure 2.32. In the case of reference 1,3,5,7-tetraphenyl-aza-BODIPY **2.6**, DFT predicts the HOMO is primarily localized at the  $\alpha$ - and  $\beta$ -position of the chromophore's core, which is typical for BODIPYs and aza-BODIPYs.<sup>142-146</sup> In addition to this, **2.5a** – **2.5d** have significant (~20- 50%) HOMO contributions from the pyrene fragments, while HOMO-1 and HOMO-2 were predicted to have dominant pyrene character. DFT predicts that the LUMO in **2.5a** – **2.5d** is localized on the pyrrolic- and *meso*-nitrogen atoms, which is common for aza-BODIPY chromophores.<sup>142-146</sup> The energy of the HOMO follows the electron-donating ability of the functional group attached at the  $\alpha$ -position of aza-BODIPY, as one might expect. A large contribution from the pyrene fragments to the HOMO, HOMO-1, and HOMO-2 of **2.5a** – **2.5d** is indicative of the potential electron-donating character of the pyrene  $\pi$ -system. This adds partial pyrene-to-aza-BODIPY charge-transfer character to the HOMO  $\rightarrow$  LUMO single-electron excitation and explains significant decreases in fluorescence quantum yields observed in **2.5a**–**2.5d** when compared to **2.6**. In all compounds studied, pyrene-centered LUMO+1 and LUMO+2 were predicted to be ~1.5 eV higher in energy than the LUMO. In **2.5e**, the DFT-predicted HOMO is ferrocene-centered, while the highest energy occupied  $\pi$ -type molecular orbital is HOMO-1. This electronic structure correlates well with the experimentally observed CV and DPV oxidation of the ferrocene groups in **2.5e** at low potential. Overall, the DFT-predicted electronic structures of **2.5a** – **2.5e** are suggestive of a large contribution from the pyrene fragments to the HOMO energy region, which is expected to be exhibited by disappearance of the aza-BODIPY core-centered  $\pi$ – $\pi^*$  transitions observed in the reference compound **2.6** and appearance of the significant pyrene-to-aza-BODIPY charge-transfer character in transitions observed at the low-energy region of the corresponding UV-vis spectra.

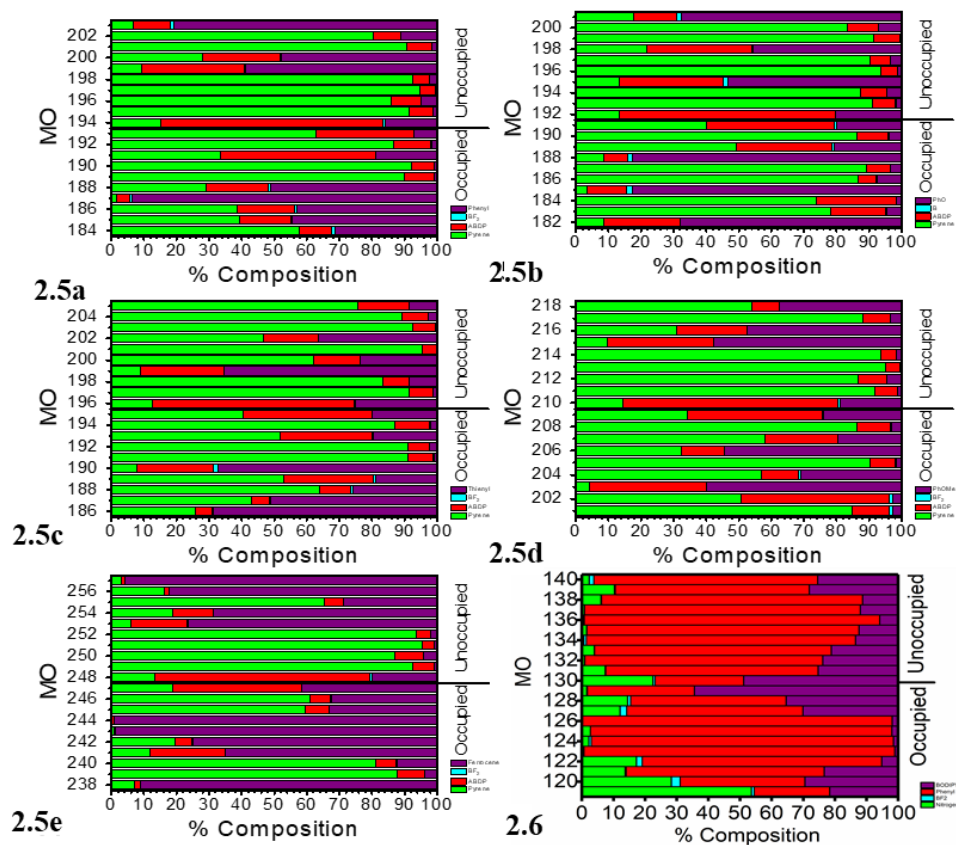


Figure 2.30: DFT-predicted compositions of frontier orbitals for compounds **2.5a–2.5e** and **2.6**. purple=alpha substituent ex. ferrocene, red=aza-BODIPY, light blue=BF<sub>2</sub>, green=pyrene

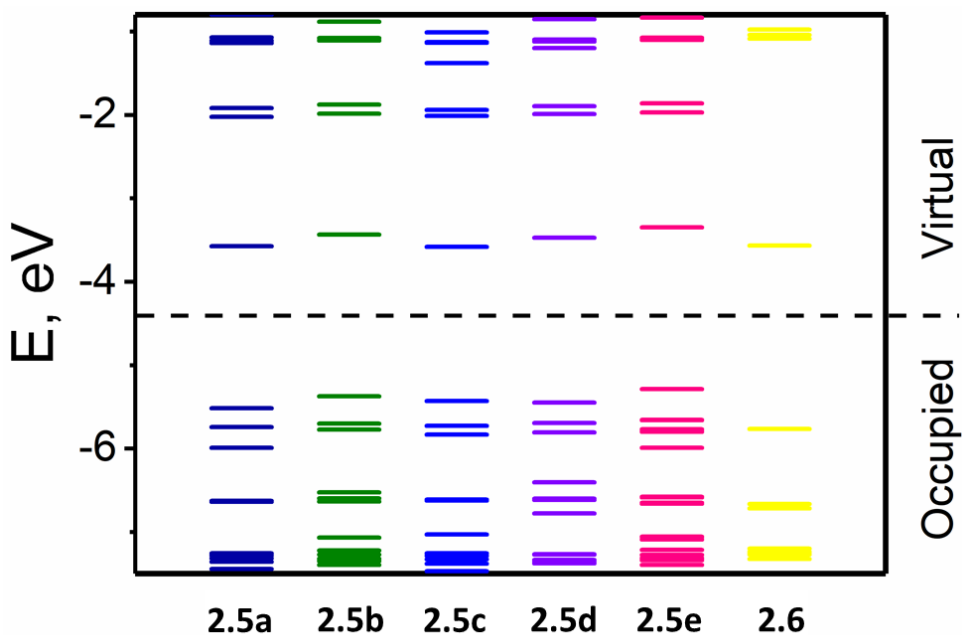


Figure 2.31: DFT-predicted energy diagram for the frontier MOs in **2.5a – 2.5e** and **2.6**.

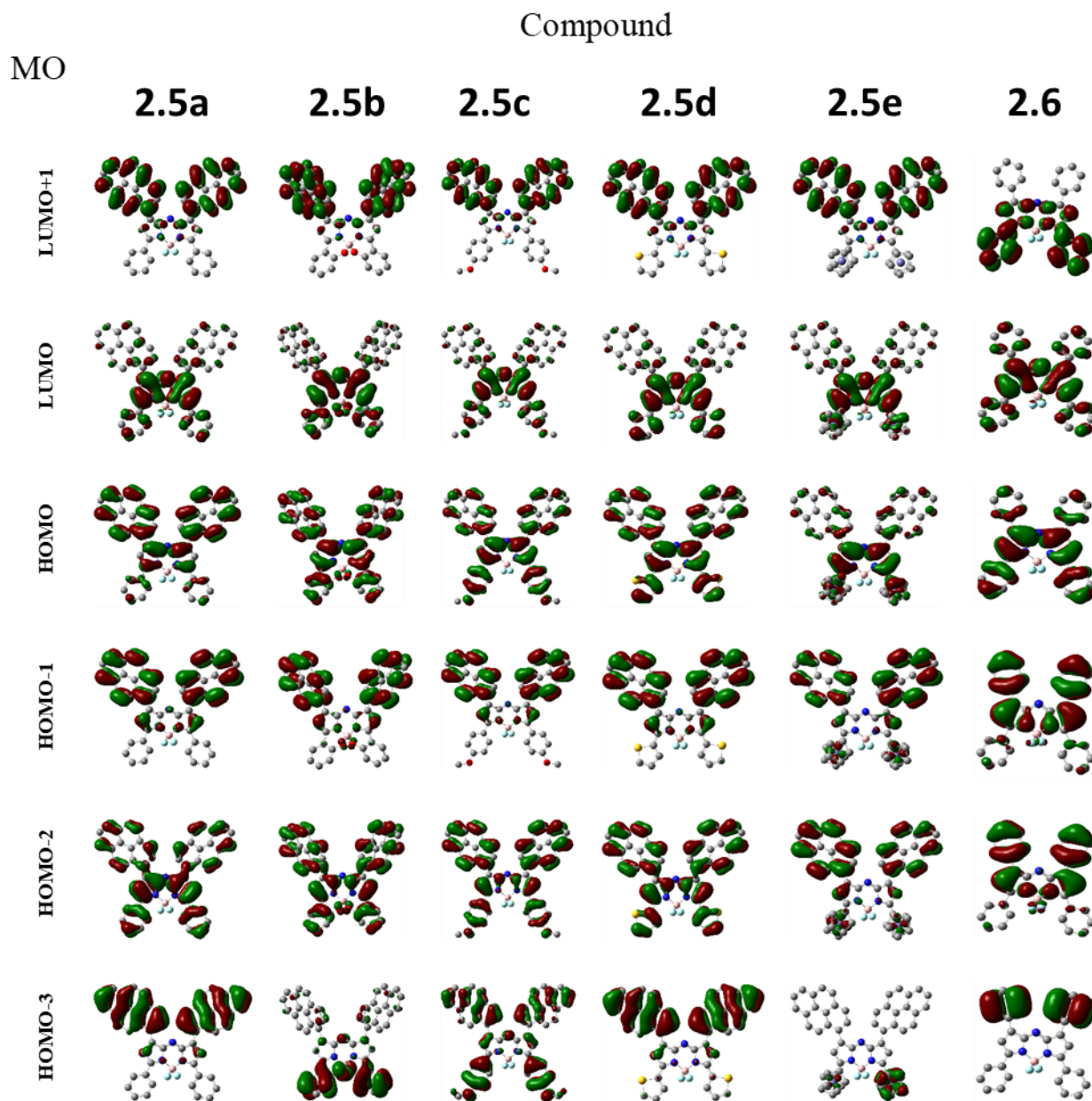


Figure 2.32. DFT-predicted frontier molecular orbitals for **2.5a** – **2.5e** and **2.6**.

Energies, oscillator strengths, and theoretical UV-vis spectra predicted by the TDDFT calculations for aza-BODIPYs **2.5a** – **2.5e** and **2.6** along with experimental UV-Vis spectra are shown in Figure 2.33. In the case of **2.5a** – **2.5d**, the TDDFT-predicted UV-Vis spectra in the low-energy region (550 – 900 nm) are dominated by three intense bands, which correlate well with the experimental data. Indeed, in the case of **2.5b**, three bands can be clearly seen in the low-energy

region. In the cases of **2.5c** and **2.5d**, the most intense band in the 600 – 720 nm region is accompanied by a lower-intensity broad shoulder, and in the case of **2.5a**, a broad asymmetric band spans the entire low-energy range. DFT predicts that the lowest-energy transition should be dominated by the HOMO-LUMO single-electron excitation, which has aza-BODIPY/pyrene ( $\pi$ )  $\rightarrow$  aza-BODIPY ( $\pi^*$ ) character. The other two intense transitions predicted by the TDDFT calculations in the 550 nm – 900 nm region are dominated by the pyrene ( $\pi$ , HOMO-1 and HOMO-2)  $\rightarrow$  aza-BODIPY ( $\pi^*$ , LUMO) excitations. Due to the significant charge-transfer (pyrene-to-aza-BODIPY) character, B3LYP-based TDDFT calculations may overestimate the pyrene-to-aza-BODIPY transition intensities. The predicted locations in energy are in good agreement with the experimental data. In case of the ferrocene-containing **2.5e**, TDDFT predicts five transitions with significant MLCT character for the longer wavelength band experimentally observed between 670 nm and 1100 nm. These transitions are dominated by HOMO – HOMO-5  $\rightarrow$  LUMO single-electron excitations. TDDFT calculations predicted the pyrene-to-pyrene  $\pi$ - $\pi^*$  transitions observed in the UV. Overall, the TDDFT calculations correctly predicted trends in energies and intensities of the most intense transitions observed experimentally for **2.5a** – **2.5e**.

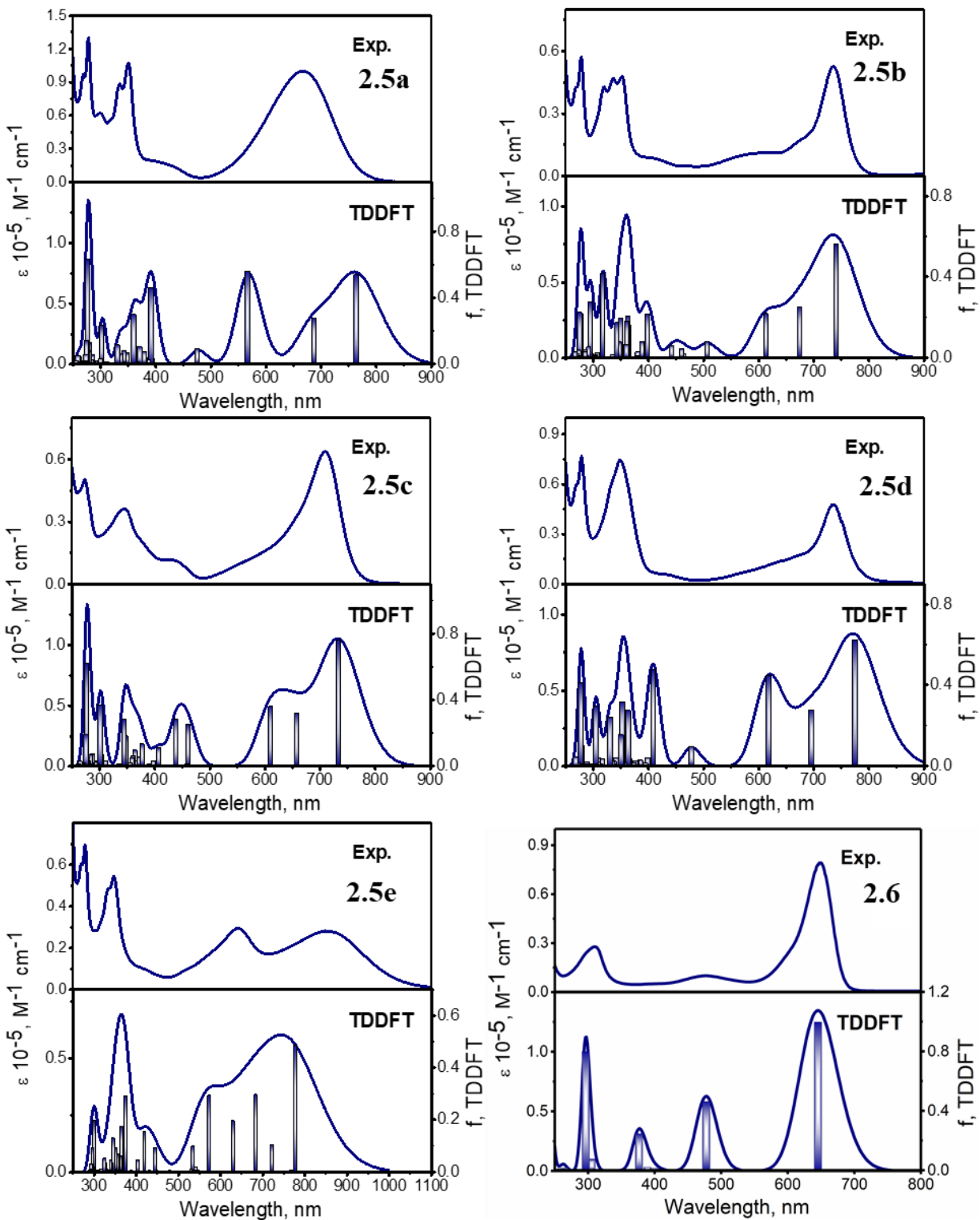


Figure 2.33: Experimental (top) and TDDFT-predicted (bottom) UV-vis spectra of aza-BODIPYs 2.5a – 2.5e and 2.6.

## Interaction and Potential Complex Formation of Pyrene-aza-BODIPYs with Nanocarbon Materials

Installation of the pyrene substituents into **2.5a–2.5e** was motivated by the potential to promote assembly of intermolecular complexes with nanocarbon electron acceptors. The hypothesis that the pyrene motif would successfully provide an effective conduit for association and charge transfer was based on prior reports of other donor-acceptor complexes observed in solution.<sup>160-167</sup> The energetics of electron transfer from the **2.5a–2.5e** photo-excited states to a nano-carbon acceptor can be estimated from the spectroscopic and electrochemical measurements following a standard approach.<sup>168-172</sup> One-electron transfer is energetically favorable in all cases, with  $\Delta G$  ranging from -0.2 eV for **2.5d** to -0.5 eV for **2.5e**. Changes in static and time resolved absorption, and static fluorescence, with addition of C<sub>60</sub>, C<sub>70</sub>, (6,5)-SWCNT, and graphene were measured as potential indicators of charge transfer and quantitative evidence of complex formation.

Titration of **2.5a – 2.5d** and the reference compound **2.6** with solutions of C<sub>60</sub> and C<sub>70</sub> fullerenes reveal identical results (Figure 2.34-2.39). No significant reduction in fluorescence was observed with addition of fullerenes when exciting at the most intense low-energy band (first excited state). A reduction in both the pyrene and aza-BODIPY emission bands were observed with addition of fullerenes when exciting at 275 nm and 345 nm. Accounting for the significant absorption at these wavelengths by both C<sub>60</sub> and C<sub>70</sub> to first order, a Stern-Volmer analysis of the titrations taking into consideration a competitive absorption of aza-BODIPY and C<sub>60</sub>/C<sub>70</sub> chromophores was carried out.<sup>173</sup> The resulting quenching constants are shown in Table 2.3 and suggest the possibility of weakly associating and/or interacting complexes. However, the need to correct for substantial interference from direct absorption of the fullerenes at these wavelengths<sup>173</sup> when quantifying the reduction in emission leaves significant uncertainty in the evidence for complex formation. The fact that the quenching constants for **2.5a – 2.5e** are smaller or comparable to that for reference **2.6**, demonstrates a lack of any specific enhancement from the pyrene substituents in the formation of complexes at room temperature in solution.

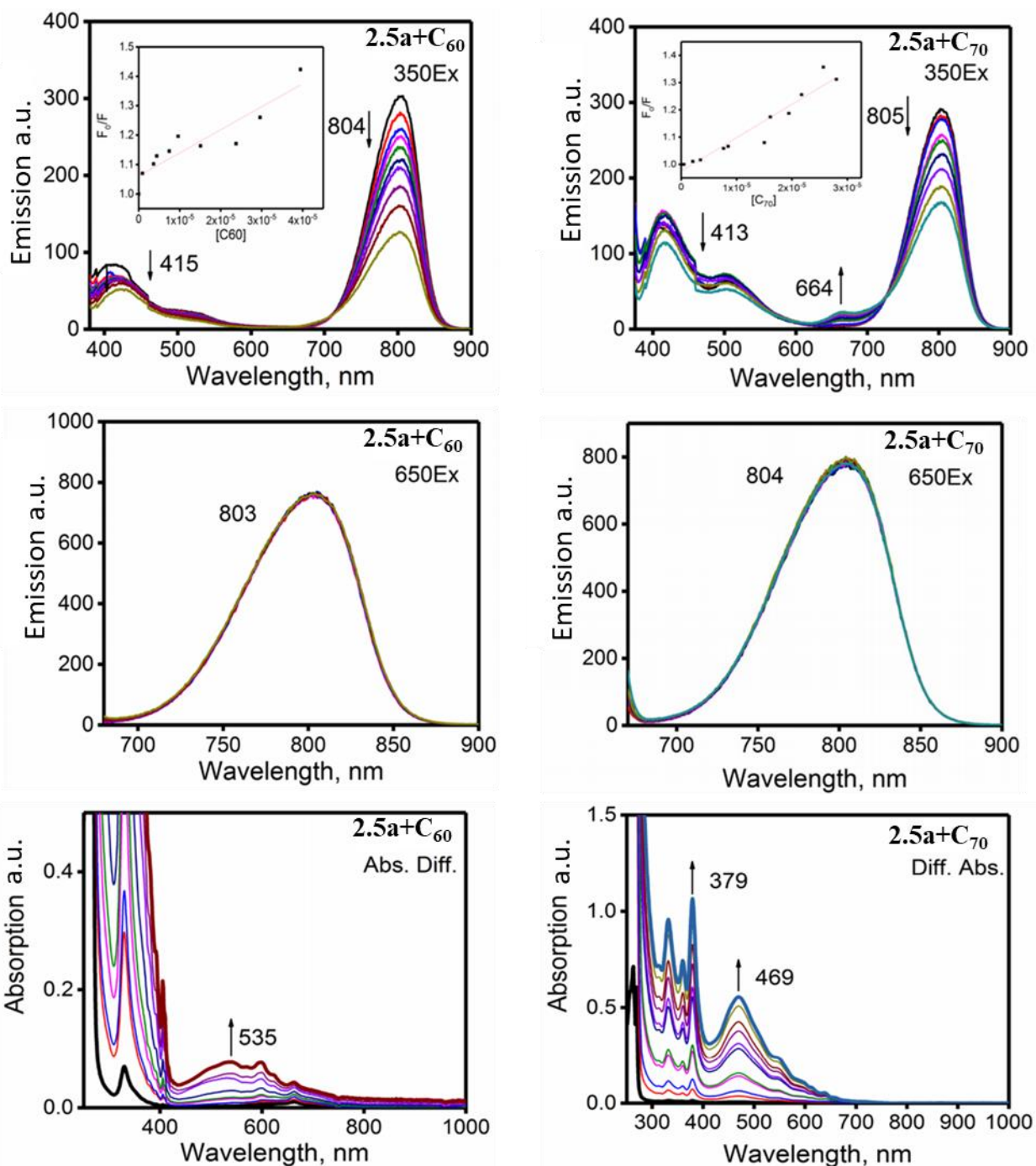


Figure 2.34: Steady-state (top and middle) and difference absorption (bottom) spectra of the azabodipy **2.5a** upon stepwise addition of the C<sub>60</sub> (left panel) or C<sub>70</sub> (right panel) fullerenes. Excitation wavelengths are shown in the upper right corners of each figure.

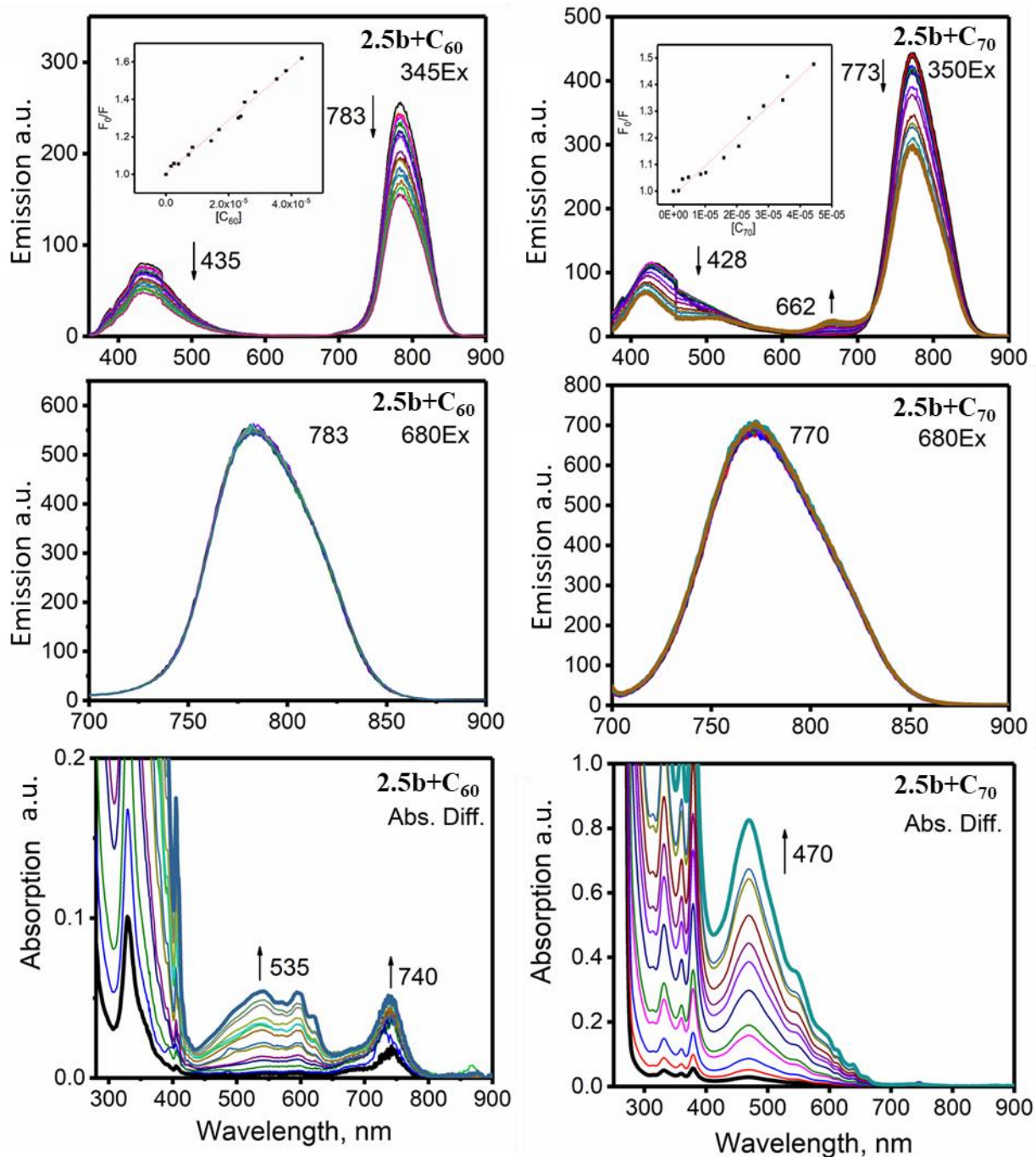


Figure 2.35: Steady-state (top and middle) and difference absorption (bottom) spectra of the aza-BODIPY **2.5b** upon stepwise addition of the C<sub>60</sub> (left panel) or C<sub>70</sub> (right panel) fullerenes. Excitation wavelengths are shown in the upper right corners of each figure.

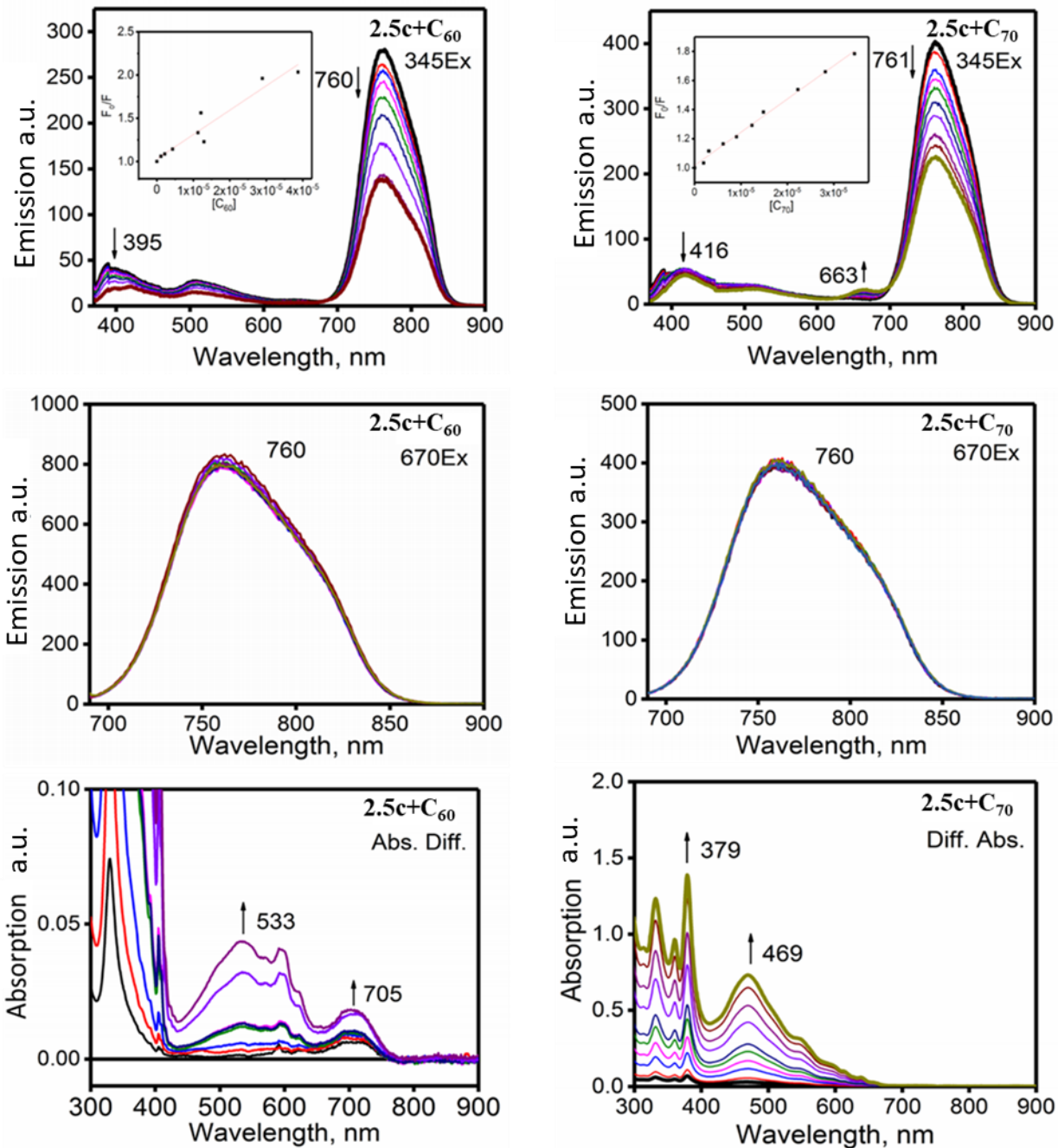


Figure 2.36: Steady-state (top and middle) and difference absorption (bottom) spectra of the aza-BODIPY **2.5c** upon stepwise addition of the C<sub>60</sub> (left panel) or C<sub>70</sub> (right panel) fullerenes. Excitation wavelengths are shown in the upper right corners of each figure.

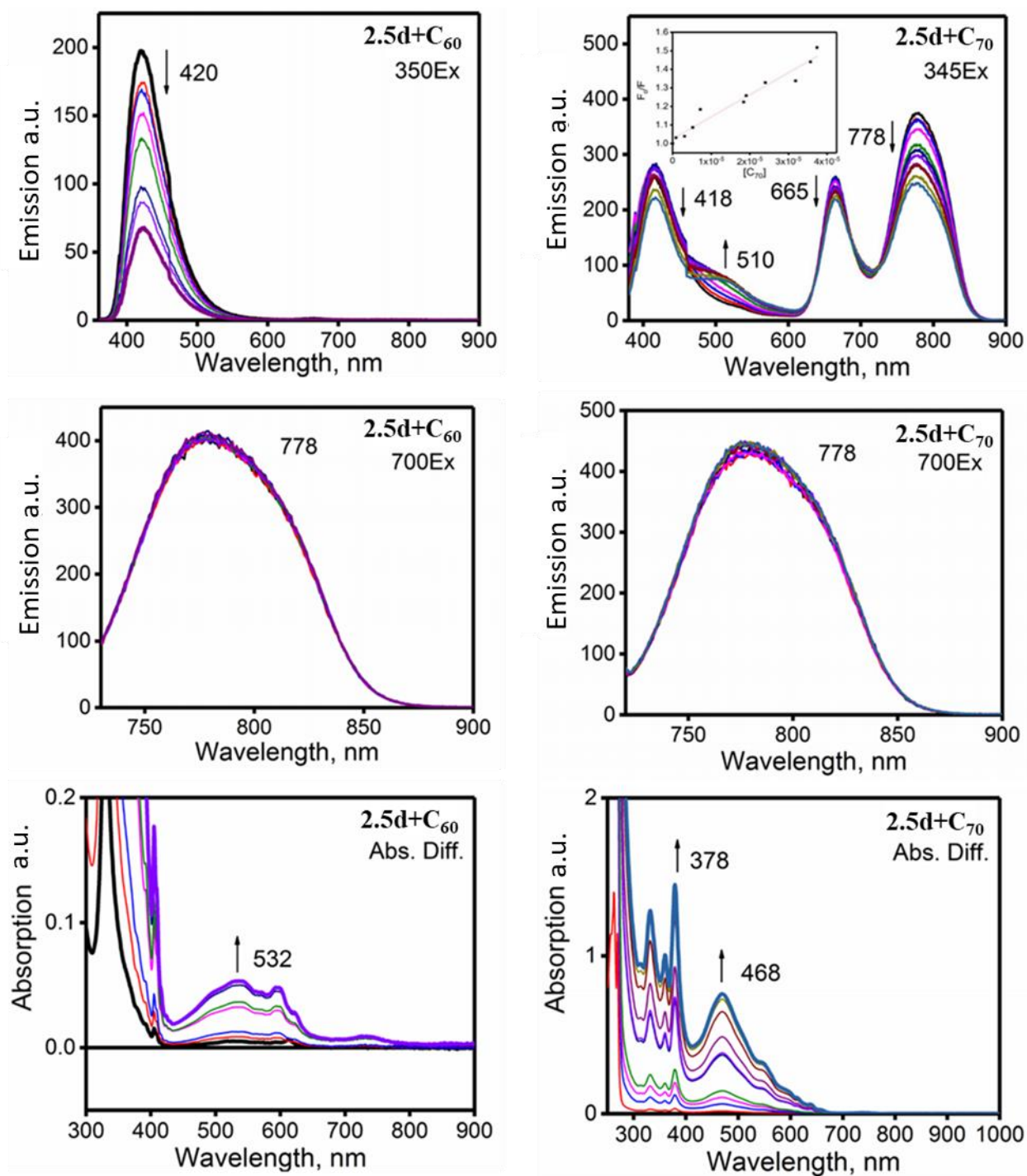


Figure 2.37: Steady-state (top and middle) and difference absorption (bottom) spectra of the aza-BODIPY **2.5d** upon stepwise addition of the C<sub>60</sub> (left panel) or C<sub>70</sub> (right panel) fullerenes. Excitation wavelengths are shown in the upper right corners of each figure.

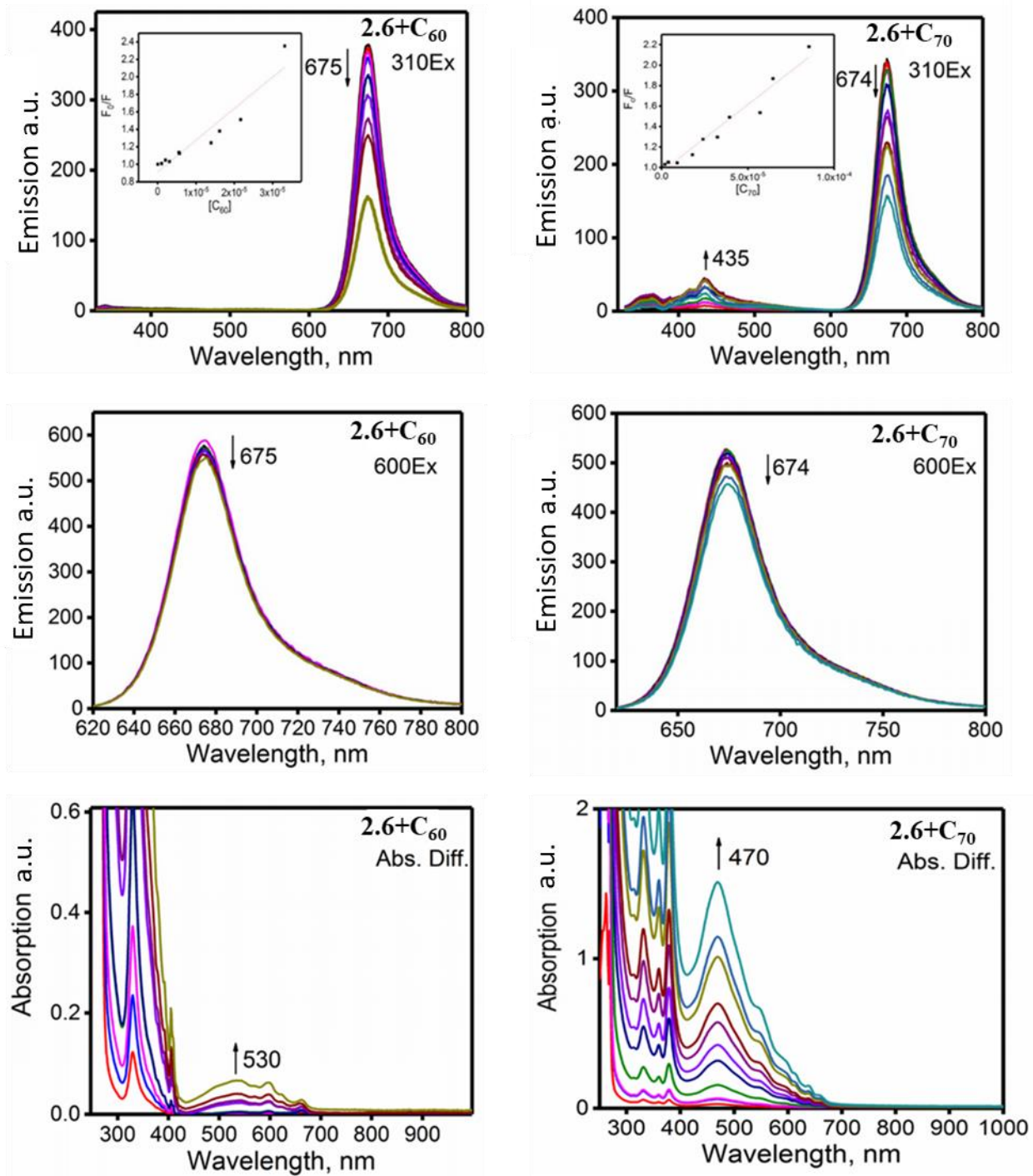


Figure 2.38: Steady-state (top and middle) and difference absorption (bottom) spectra of the aza-BODIPY **2.6** upon stepwise addition of the  $C_{60}$  (left panel) or  $C_{70}$  (right panel) fullerenes. Excitation wavelengths are shown in the upper right corners of each figure.

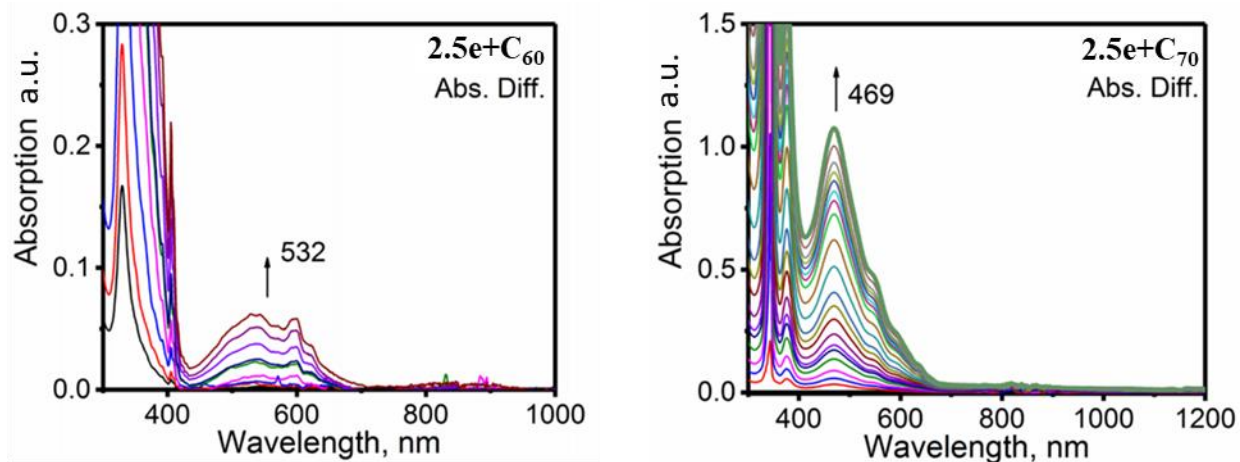


Figure 2.39: Difference absorption spectra of the aza-BODIPY **2.5e** upon stepwise addition of the C<sub>60</sub> (left panel) or C<sub>70</sub> (right panel) fullerenes.

Upon titration of the aza-BODIPYs with fullerenes, all spectral changes in the UV-Vis absorption could be accounted for by independent absorption of the added fullerene (Figure 2.34-2.39). No low-energy absorption bands characteristic of charge-transfer were observed. The lack of evidence for electron transfer is consistent with recent reports on non-covalent complexes formed between functionalized subphthalocyanines and fullerene.<sup>174-177</sup> We conclude that if there was any residual emission quenching when exciting in the UV region, it was the result of energy transfer rather than charge transfer. Using covalently linked subphthalocyanine-fullerene dyads, Torres and co-workers demonstrated a strong distance dependence to the donor-acceptor quenching mechanism.<sup>178-180</sup> Shorter distances ( $\sim 3.1$  Å) between the donor and acceptor facilitated electron-transfer, while small increases in separation ( $\sim 3.3$  Å) favored energy transfer.

Transient absorption was used to investigate the possibility of photoinduced electron transfer between the electron rich, non-fluorescent **2.5e** and C<sub>60</sub>, Figure 2.40 compares transient absorption for solutions of **2.5e**, C<sub>60</sub>, and a 1:10 molar ratio of **2.5e**:C<sub>60</sub>. Transient absorption was measured following excitation at 410 nm, where absorption is a combination of **2.5e** and C<sub>60</sub>, and at 650 nm, where the absorption is dominated by **2.5e**. Figure 2.40a and 2.40b compare excitation at 650 nm with and without C<sub>60</sub> present. Within the signal-to-noise of the experiments, there was no detectable difference between the shapes or time evolution of the spectra with the addition of C<sub>60</sub>. The transient spectra are a combination of a ground state bleach that mirrors the absorption spectrum (negative  $\Delta OD$ ) and excited state absorption on both the short and long wavelength sides

of the bleach (positive  $\Delta OD$ ). The spectra appear within the time resolution of the experiment,  $\sim 100$  fs, and decay in both the visible and near-IR portion of the spectrum with the lifetime reported in Table 2.1. The absence of electron transfer is supported by the unperturbed decay of the initial excited state of **2.5e** in the presence of  $C_{60}$  and the lack of any new absorption features in the near-IR consistent with the anion of  $C_{60}$ .

When exciting at a shorter wavelength, 410 nm, the transient spectra for **2.5e** alone are nearly identical to the spectra when exciting at 650 nm. The addition of  $C_{60}$  significantly changes the shape and decay of the spectra, Figure 2.40c, with strong, broad absorption in the near-IR peaked around 980 nm. However, the new features are all well accounted for by direct absorption of  $C_{60}$ , as presented in Figure 2.40d. The pump-probe spectra for the 1:10 molar ratio of **2.5e**: $C_{60}$  are a linear combination of independent **2.5e** and  $C_{60}$  spectra. There is no evidence for charge transfer. We note that transient absorption features in the near-IR reported here are very similar to other reports that have interpreted the signals as indicator of energy and charge transfer in analogous systems.<sup>74,75,88,181</sup> Our results demonstrate the potential for dominance of the near-IR transient absorption by direct excitation of independent  $C_{60}$  in these types of titrations studies. This indicates that even at low  $C_{60}$  concentrations and longer wavelengths in the tail of the  $C_{60}$  absorption, signals originating from direct fullerene absorption must still be carefully accounted for prior to any conclusions associated with energy or charge transfer.

Table 2.3. Estimated quenching constants for non-covalent complexes formation between aza-BODIPYs **2.5a** – **2.5e** and **2.6** and  $C_{60}$  or  $C_{70}$  fullerenes.

Compound	$K_{sv} C_{60}$	$K_{sv} C_{70}$
<b>2.5a</b>	4600	11500
<b>2.5b</b>	19500	15700
<b>2.5c</b>	22900	18700
<b>2.5d</b>	9230	15800
<b>2.6</b>	12800	18200

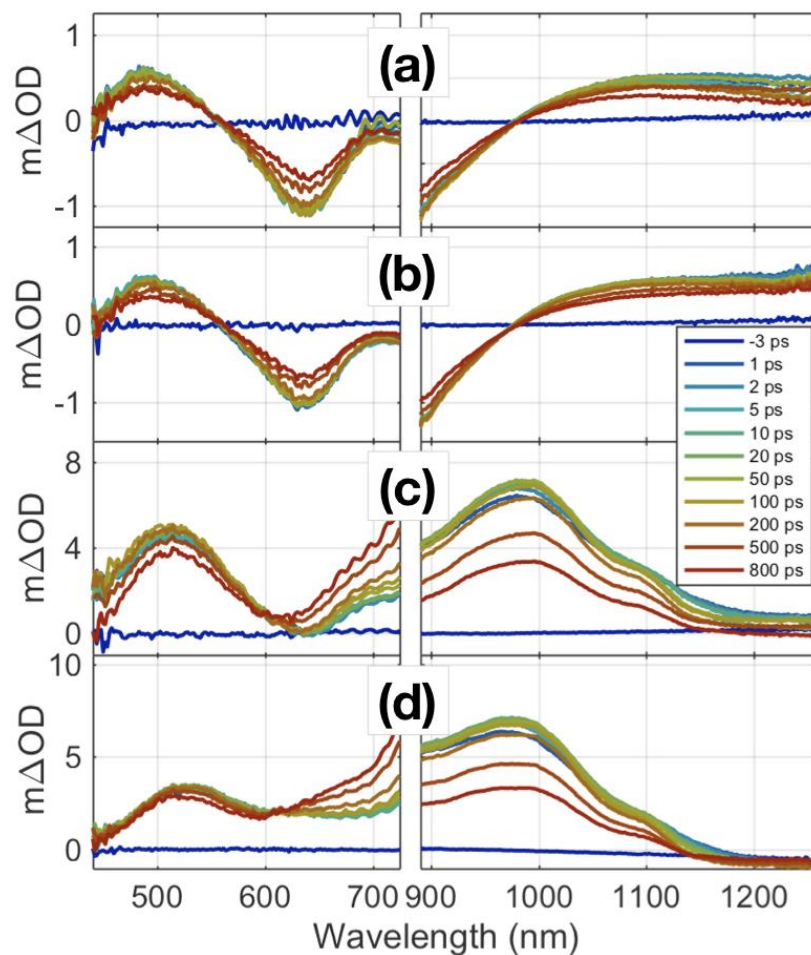


Figure 2.40: Pump-probe transients for **2.5e**, a mixture of **2.5e** and  $C_{60}$ , and  $C_{60}$  in solution. (a) **2.5e** excited at 650 nm. (b) **2.5e**: $C_{60}$  1:10 mole ratio excited at 650 nm. (c) **2.5e**: $C_{60}$  1:10 mole ratio excited at 410 nm. (d)  $C_{60}$  excited at 410 nm.

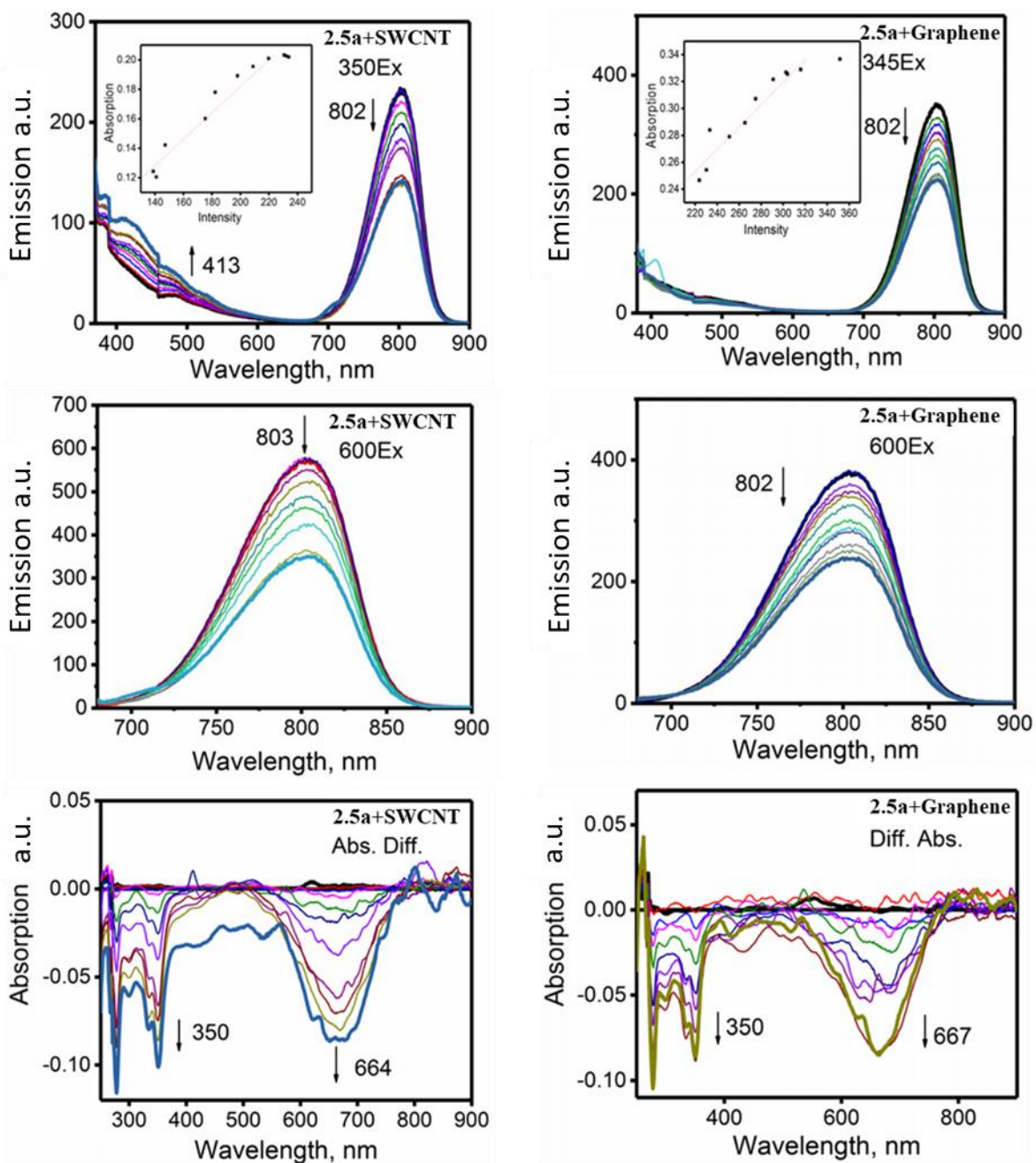


Figure 2.41: Steady-state emission (top and middle), and difference absorption (bottom) spectra of the aza-BODIPY **2.5a** upon stepwise addition of the (6,5)-SWCNT (left panel) or graphene (right panel). Excitation wavelengths are shown at the upper right corners of each graph.

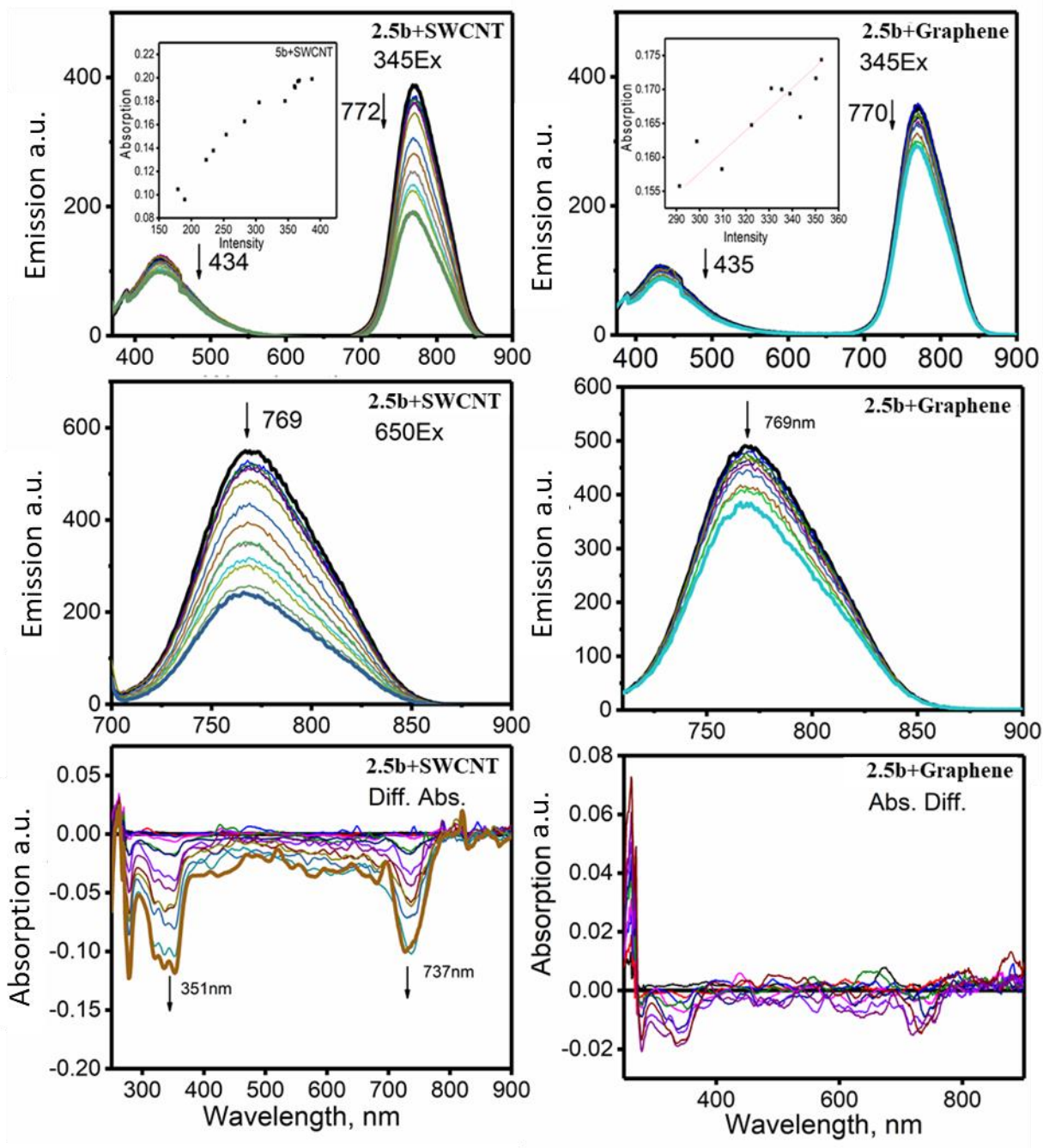


Figure 2.42: Steady-state emission (top and middle), and difference absorption (bottom) spectra of the aza-BODIPY **2.5b** upon stepwise addition of the (6,5)-SWCNT (left panel) or graphene (right panel). Excitation wavelengths are shown at the upper right corners of each graph.

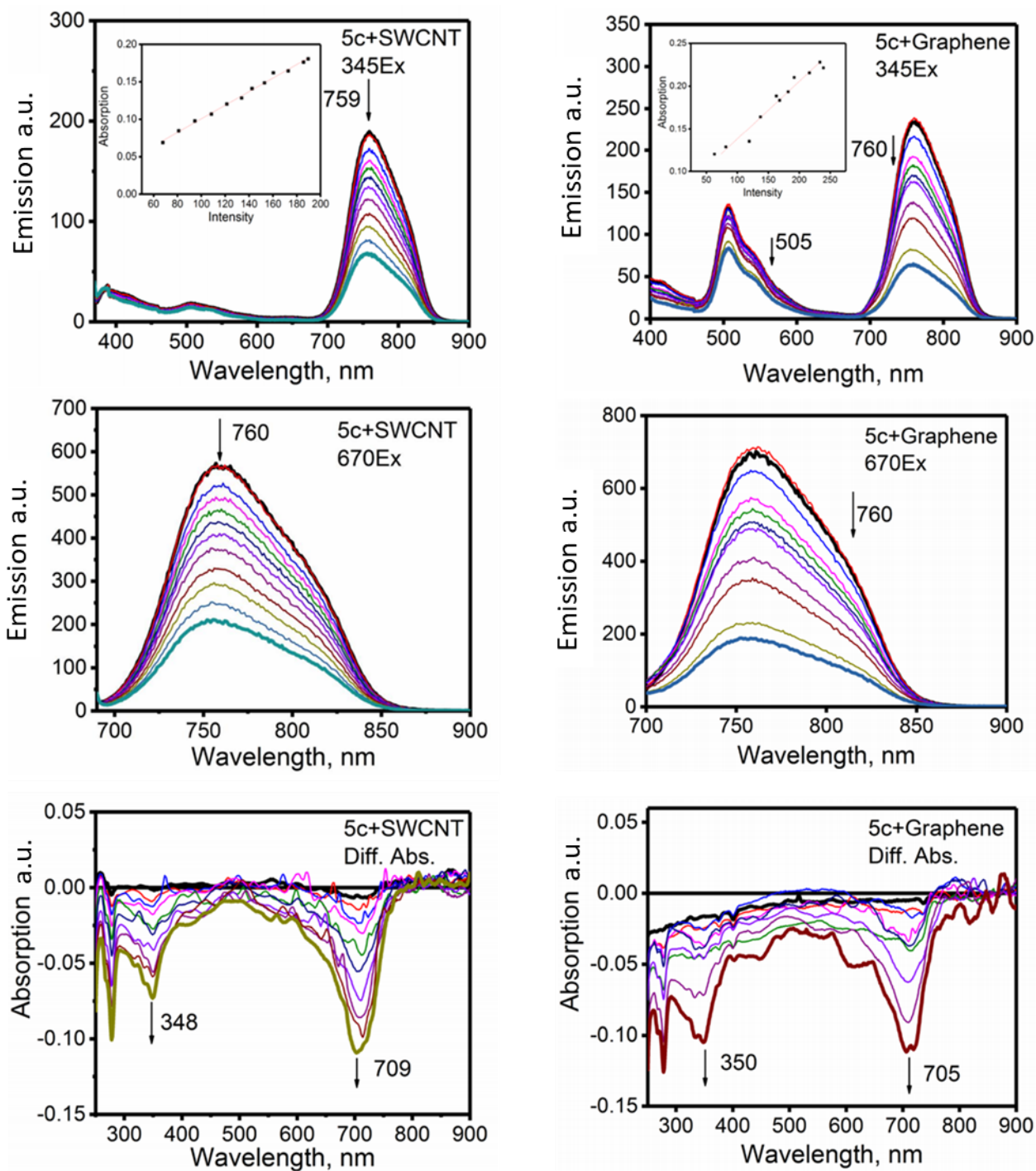


Figure 2.43: Steady-state emission (top and middle), and difference absorption (bottom) spectra of the aza-BODIPY **2.5c** upon stepwise addition of the (6,5)-SWCNT (left panel) or graphene (right panel). Excitation wavelengths are shown at the upper right corners of each graph.

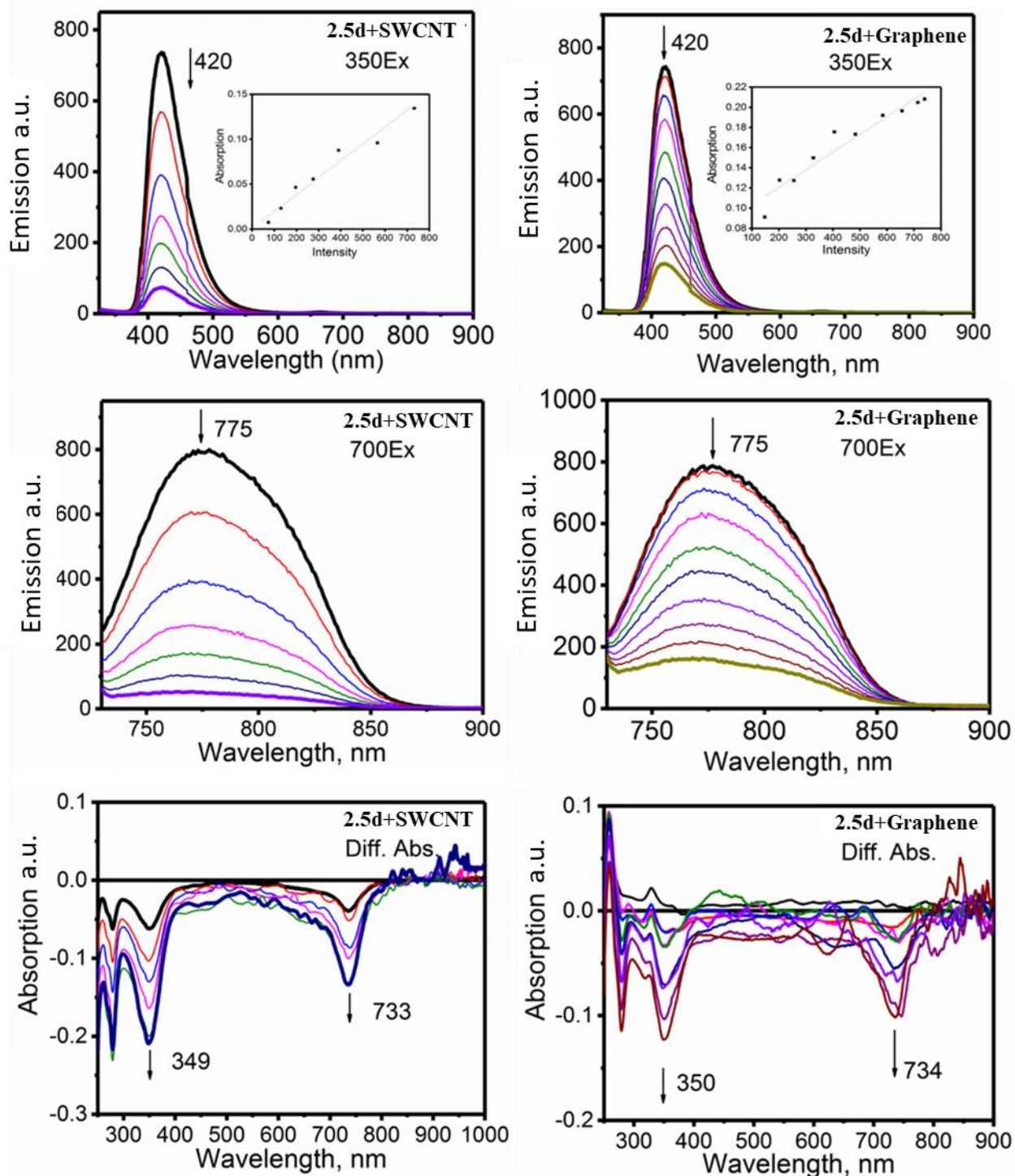


Figure 2.44: Steady-state emission (top and middle), and difference absorption (bottom) spectra of the aza-BODIPY **2.5d** upon stepwise addition of the (6,5)-SWCNT (left panel) or graphene (right panel). Excitation wavelengths are shown at the upper right corners of each graph.

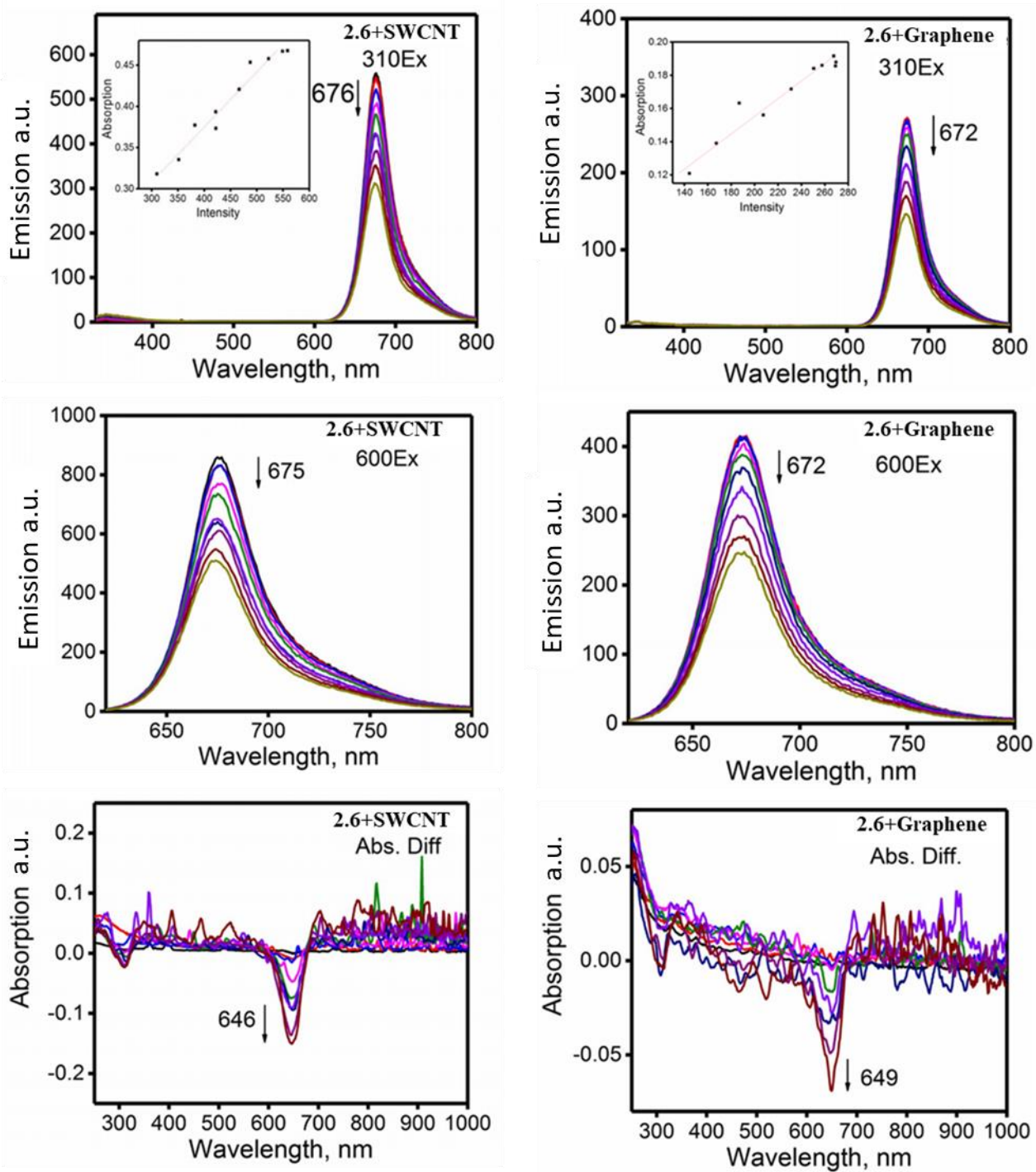


Figure 2.45: Steady-state emission (top and middle), and difference absorption (bottom) spectra of the aza-BODIPY **2.6** upon stepwise addition of the (6,5)-SWCNT (left panel) or graphene (right panel). Excitation wavelengths are shown at the upper right corners of each graph.

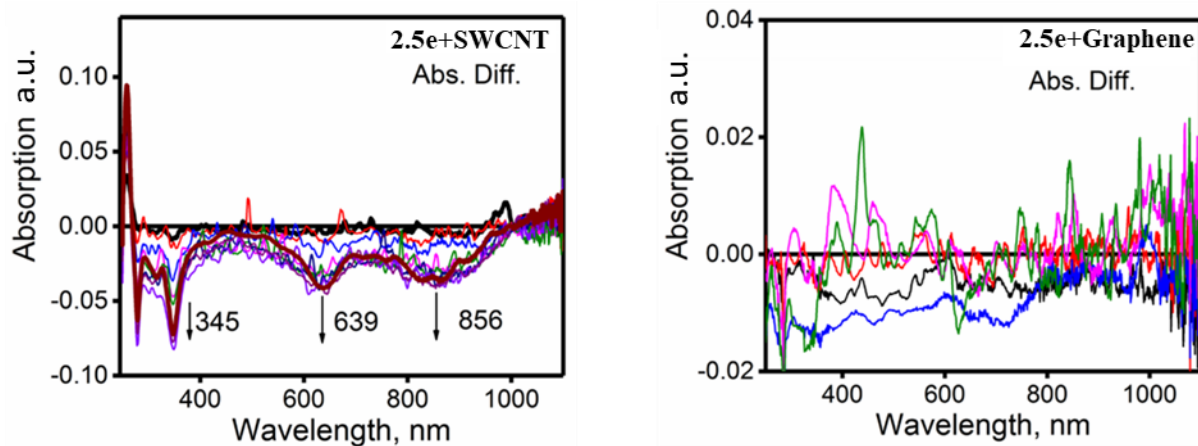


Figure 2.46: Difference absorption spectra of the aza-BODIPY **2.6** upon stepwise addition of the (6,5)-SWCNT (left panel) or graphene (right panel).

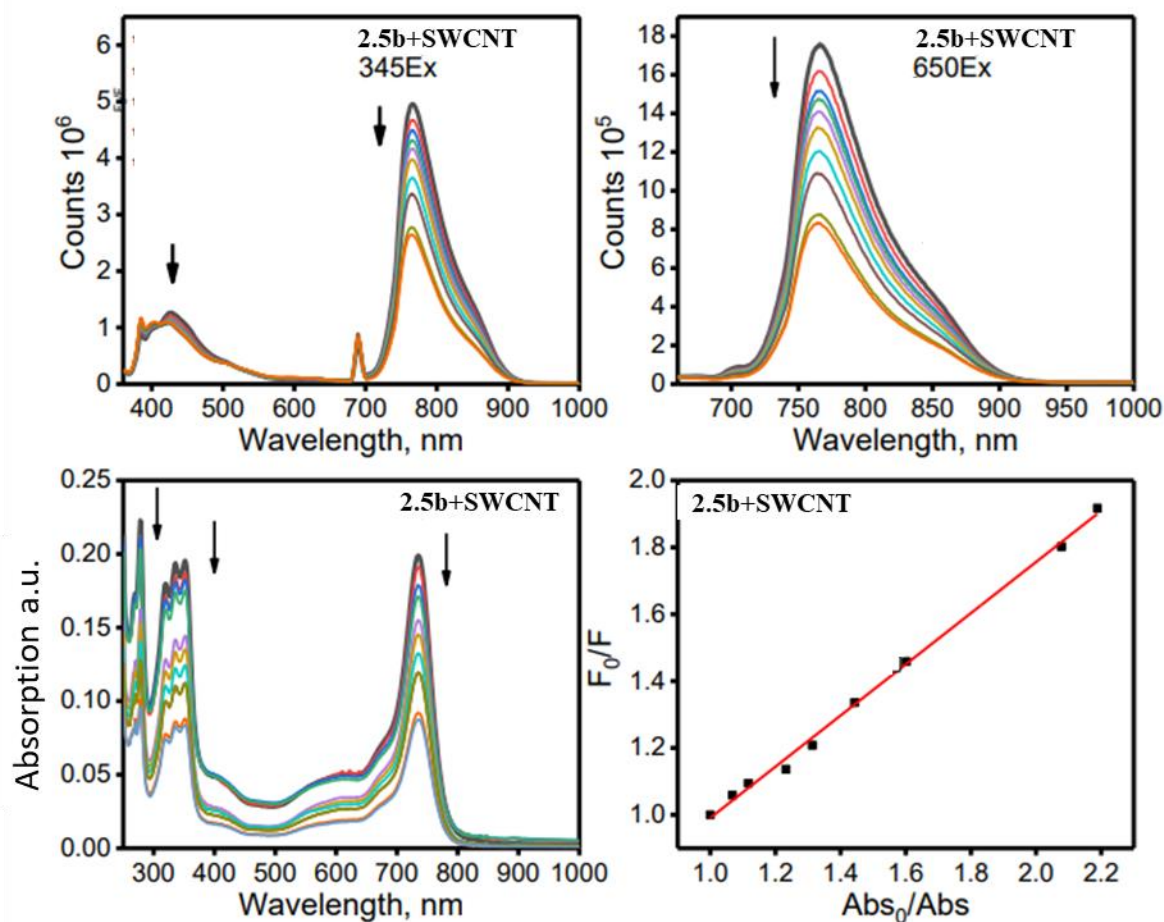


Figure 2.47: Time-dependent changes in absorption and fluorescence spectra of **2.5b** in the presence of excess of (6,5)-SWCNT

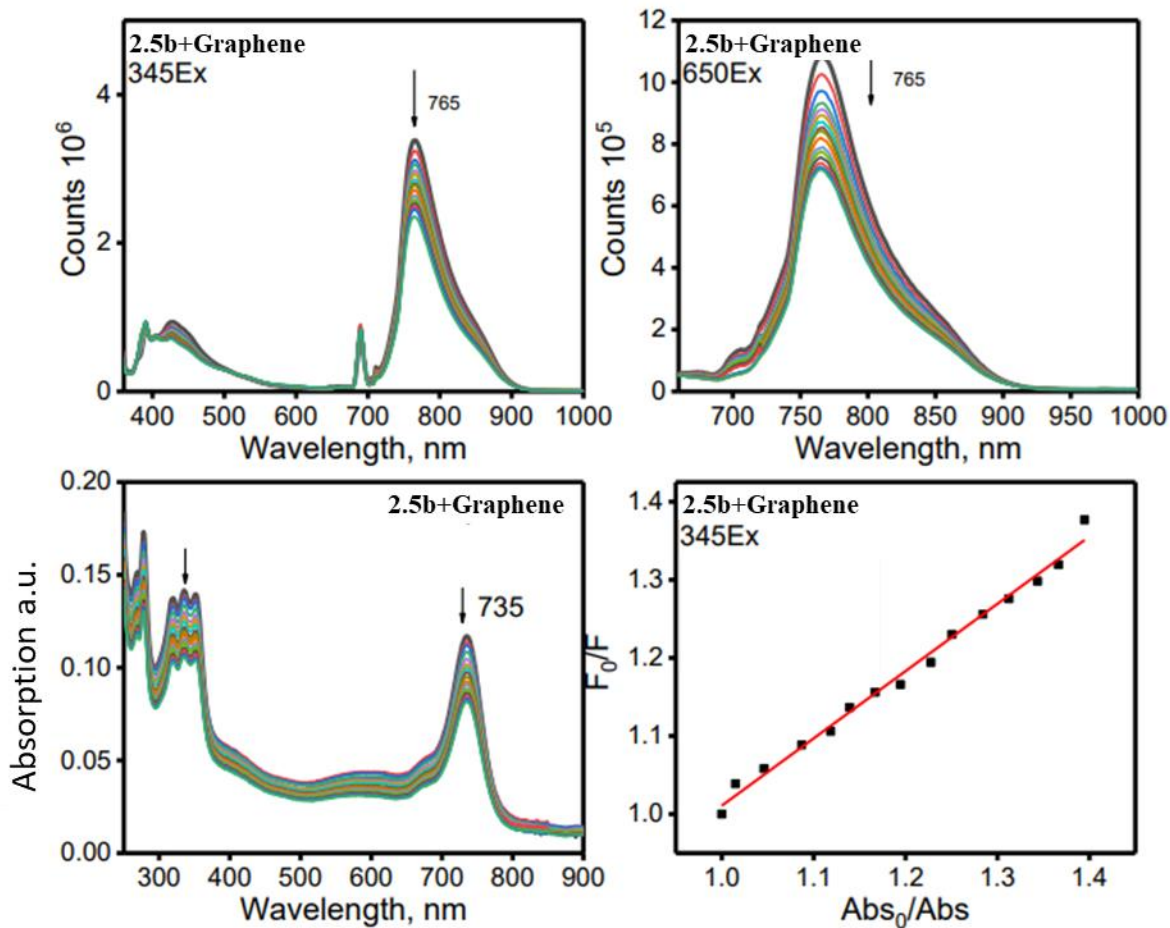


Figure 2.48: Time-dependent changes in absorption and fluorescence spectra of **2.5b** in the presence of excess of graphene

Titration of aza-BODIPYs **2.5a** – **2.5d**, and the reference compound lacking the pyrene ligands, **2.6**, with (6,5)-SWCNT and graphene all resulted in reduction in the observed fluorescence intensity independent of the excitation wavelength (Figures 2.40-2.46). However, loss of fluorescence was always accompanied by a linearly correlated loss in absorption of the aza-BODIPY, Figures 2.40-2.48. The lack of solubility of (6,5)-SWCNT and graphene complicated the experiments with interference from scattering and changes in the background that limited quantitative confidence when correlating the emission and absorption losses. Within error, the slope of emission vs absorption with addition of SWCNT and graphene was always close to 1. When solutions of **2.5a** – **2.5e** and **2.6** were treated with an excess of (6,5)-SWCNTs or graphene, time-dependent loss of absorption was also observed (Figure 2.47 and 2.48). We conclude that loss of emission, and absorption, predominantly reflected removal of the chromophores from the excitation volume via physical adsorption and loss of solubility as SWCNT or graphene were

added. The observation indicated association between the aza-BODIPY compounds and the nanocarbon materials. However, there was no observed enhancement in that interaction with installation of the pyrene ligands. The emission and absorption losses were comparable with, **2.5a-2.5d**, and without the pyrenes, **2.6**. The indirect nature of the measurement and the complexity imposed by the limited solubility of the acceptors, which is likely to change dynamically with donor association, and the potential for larger scale aggregation, limits the interpretation of these observations to the presences of association without characterization of the strength of the interaction.

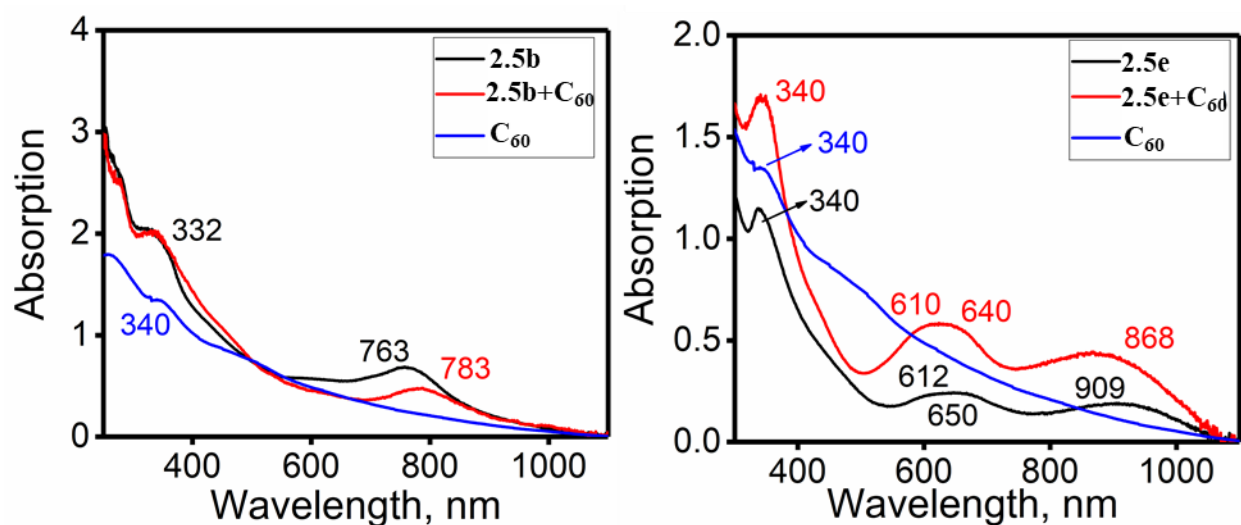


Figure 2.49: Solid-state (KBr matrix) UV-vis spectra of **2.5b** and **2.5e** without and in the presence of C<sub>60</sub> fullerene. Spectra of C<sub>60</sub> fullerene are also provided for comparison.

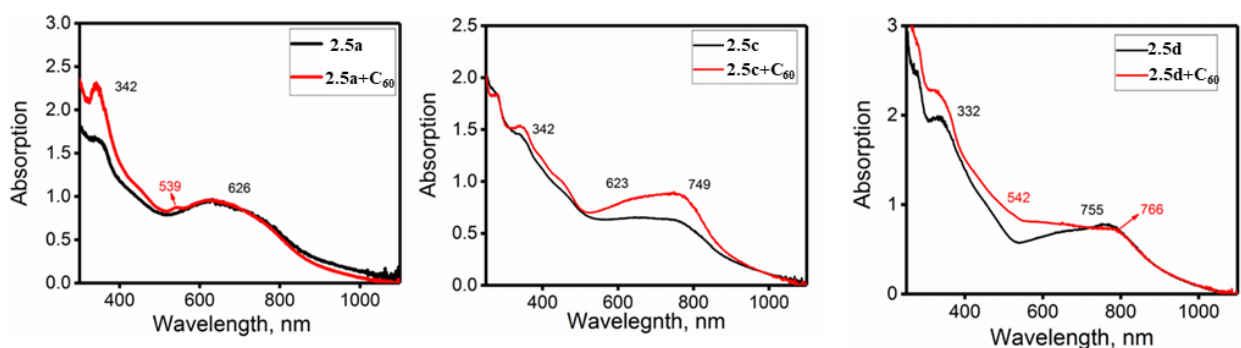


Figure 2.50: Solid-state (KBr matrix) UV-vis spectra of **2.5a**, **2.5c**, and **2.5d** without and in the presence of C<sub>60</sub> fullerene.

Although there was only minimal evidence for spontaneous association between **2.5a**–**2.5e** and fullerenes in solution, assuming some degree of mixing, proximity is forced in the solid state. Several porphyrins and subphthalocyanines have been shown to co-crystallize with C<sub>60</sub> forming well-ordered light-harvesting/electron-accepting layers potentially useful for photovoltaics application.<sup>174-177,182-191</sup> Multilayer combination of the subphthalocyanines and fullerenes have demonstrated decent photovoltaic performance despite a lack of electron-transfer between these components in solution.<sup>192-195</sup> We have compared UV-Vis spectra of solid-state samples of **2.5a**–**2.5e** with and without equimolar amount of C<sub>60</sub> (Figures 1.49-1.50). Peak broadening in some cases did not allow clear observation of co-crystallization with the fullerene. However, in all cases some interaction between aza-BODIPYs and C<sub>60</sub> was observed. The clearest examples were **2.5b** and **2.5e**, presented in Figure 1.49. In the case of ferrocene-containing **2.5e**, the NIR MLCT and visible  $\pi$ – $\pi^*$  transitions were shifted to higher energy by ~30 nm and ~10 nm, respectively, in the **2.5e**·C<sub>60</sub> complex compared to the same bands in pure **2.5e**. A shift of ~20 nm in the opposite direction, to lower energy, was observed in **2.5b**·C<sub>60</sub> complexes. Spectral shifts for the other aza-BODIPYs were less evident, Figure 1.50, and a significant change in the overall absorption profile throughout the longer wavelength region (550 nm – 1000 nm) was found for the systems. These results suggest the possibility of different modes of interactions between **2.5a**–**2.5e** and C<sub>60</sub> that would not reflect a single favored pyrene/C<sub>60</sub> chelate interaction motif.

area; (D) pyrene-pyrene interaction motif; (E) view along crystallographic *b*-axis; (F) view along crystallographic *c*-axis.

In order to support our hypothesis, we attempted co-crystallization of equimolar amounts of the individual aza-BODIPYs **2.5a**–**2.5e** and C<sub>60</sub> fullerenes. In the majority of cases, the crystals obtained were either too small and/or too poorly diffracting (typically only up to 3 Å), which is common for non-covalent complexes between functional dyes and fullerenes. We were able to obtain relatively good quality crystals suitable for X-ray diffraction for assemblies of **2.5b**·C<sub>60</sub> and **2.5d**·C<sub>60</sub>. The solid-state structure of **2.5b**·C<sub>60</sub> shows formation of a 1:1 complex. The B,O-chelating motif can be clearly seen from the experimental X-ray structure. In addition, a single disordered toluene solvent molecule was also observed in the unit cell (Figure 2.51). The fullerenes do not form close contacts with the pyrene fragments. Instead, fullerenes are located above the electron-rich B,O-fragment of **2.5b**, and form a one-dimensional (1D) channeled structure with the closest contact between two C<sub>60</sub> molecules at a distance of ~3.87 Å. The closest contact between

**2.5b** and  $C_{60}$  is  $\sim 3.34$  Å, which is similar to non-covalent complexes between subphthalocyanines and  $C_{60}$ .<sup>174-177,192-195</sup> The X-ray structure of the non-covalent complex between **2.5b** and  $C_{60}$  also contains intermolecular pyrene-pyrene interactions with short contacts typical of  $\pi$ - $\pi$  complexes ( $\sim 3.17 - 3.34$  Å). These non-covalent interactions lead to the formation of 1D aza-BODIPY chains of **2.5b**. The pyrene-pyrene intermolecular non-covalent contacts were shorter than expected and the aza-BODIPY: $C_{60}$  contacts were longer than expected.

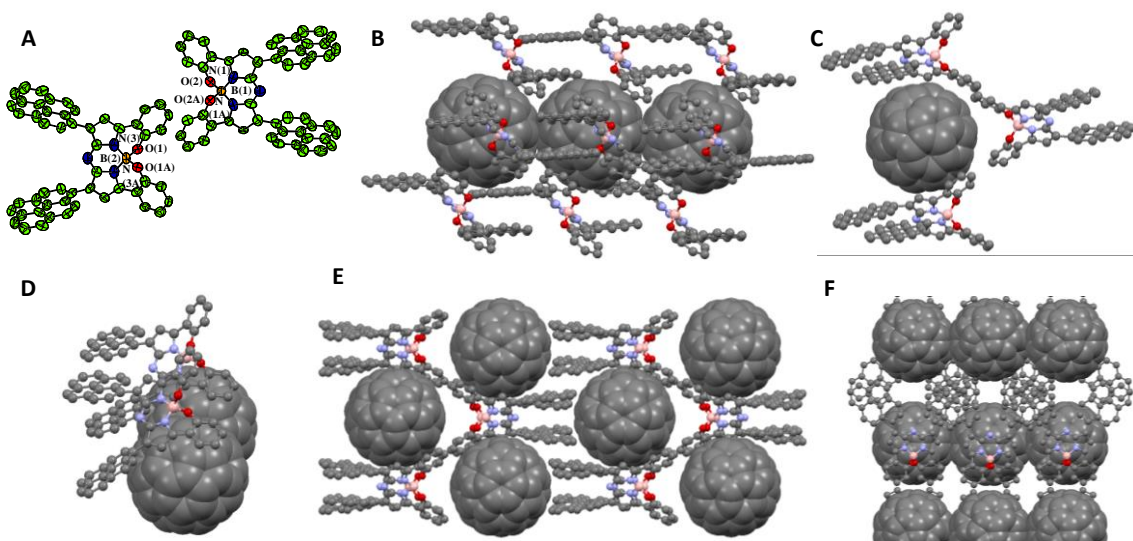


Figure 2.51: Representative images of the X-ray crystal structure of **2.5b**· $C_{60}$  (in all cases hydrogen atoms are omitted for clarity): (A) two independent molecules on **2.5b** observed in the unit cell; (B) view along crystallographic  $a$ -axis; (C)  $C_{60}$  interacting motif with the electron-rich B,O-chelated area; (D) pyrene-pyrene interaction motif; (E) view along crystallographic  $b$ -axis; (F) view along crystallographic  $c$ -axis.

Similar to the X-ray structure of **2.5a**, the pyrene fragments in the solid-state structure of **2.5b**· $C_{60}$  are rotated away from the aza-BODIPY  $\pi$ -system. A general motif in the X-ray structure of non-covalent complexes between **2.5b** and  $C_{60}$  is two independent chains: one consisting of  $C_{60}$ , and the other of aza-BODIPY **2.5b** molecules. The electron-deficient fullerenes prefer to interact with the electron-rich part of **2.5b**, which is localized at the phenolic rather than the pyrenyl fragment of the aza-BODIPY core.

In comparison, crystallization of the equimolar amounts of **2.5d** and  $C_{60}$  fullerene results in formation of a **2.5d**· $2C_{60}$  aggregate and needles characteristic of **2.5d** (Figure 2.52). A key difference with the solid-state structure of **2.5b**· $C_{60}$  is the presence of shorter contacts ( $\sim 3.1$  Å)

between the pyrene moieties of **2.5d** and  $C_{60}$ . The aggregate appears to be held together by close pyrene- $C_{60}$  contacts between one **2.5d** and two fullerenes ( $\sim 3.08, 3.31 \text{ \AA}$ ; Figure 2.52b), with an additional close contact between a third  $C_{60}$  and an electron-rich thiophene ring ( $\sim 3.32 \text{ \AA}$ ) similar to in **2.5b**· $C_{60}$ . Each thiophene is situated close to a second  $C_{60}$  ( $\sim 3.38 \text{ \AA}$ ), though offset at an angle that significantly reduces any  $\pi$ - $\pi$  interactions. Pyrene/pyrene interactions ( $\sim 3.48 \text{ \AA}$ ) are retained between neighboring molecules of **2.5d**. One of two pyrene fragments in each **2.5d** forms a well aligned H-type aggregate with a neighboring **2.5d** molecule (Figure 2.52c). Six molecules of **2.5d** form a “cage” around two fullerene molecules (Figure 2.52d). On the other hand, there are four closely spaced fullerene molecules wrapped around single molecule of **2.5d** (Figure 2.52e). The closest contact between two  $C_{60}$  molecules is  $\sim 3.23 \text{ \AA}$ , with pairs of fullerenes forming a 2x2 ribbon running through the crystal lattice. Overall, X-ray data on **2.5b**· $C_{60}$  and **2.5d**· $2C_{60}$  complexes clearly suggest that the electron density at the BODIPY core can be easily tuned to compete with the pyrene group for non-covalent interaction with the nanocarbon materials. Such competitive interactions can be used to control the desired architecture in non-covalent assemblies formed between aza-BODIPY or BODIPY chromophores and fullerenes.

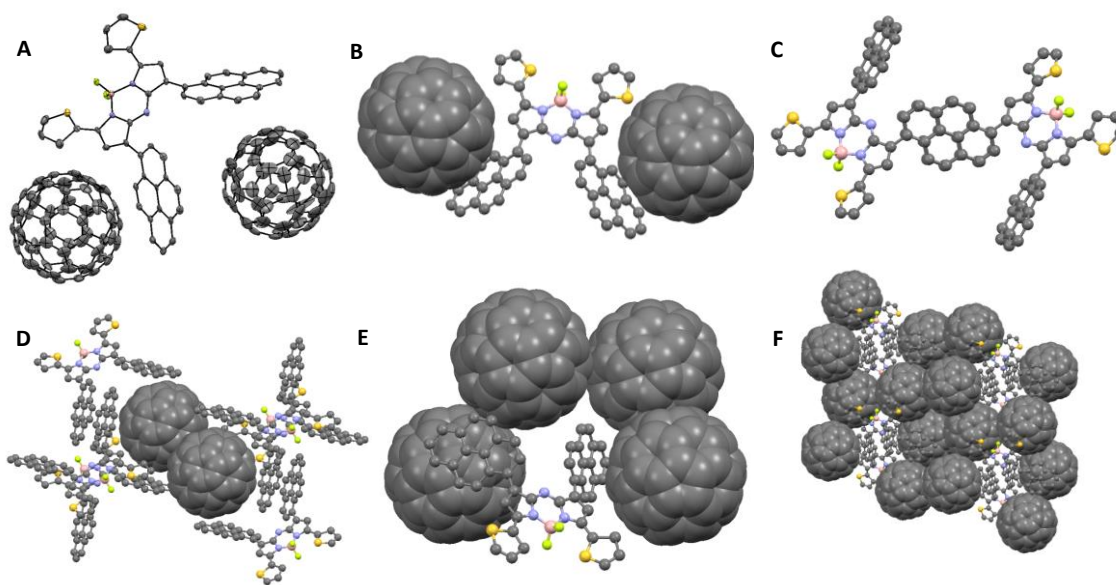


Figure 2.52: Representative images of the X-ray crystal structure of **2.5d**· $2C_{60}$  (in all cases hydrogen atoms are omitted for clarity): (A) independent molecules observed in the unit cell; (B) close contacts formed between two fullerene molecules and pyrene fragments in **2.5d**; (C) pyrene-pyrene interactions in **2.5d**; (D) “six pyrene – two fullerene” cage; (E) four fullerene molecules forming close contacts around **2.5d**; (F) view along crystallographic *a*-axis.

Table 2.4. DFT-predicted interaction energies for the formation of non-covalent complexes between pyrene and nanocarbon materials.<sup>a,b</sup>

Functional	pyrene:pyrene	pyrene:C <sub>60</sub>	pyrene:(6,5)- SWCNT	pyrene:graphene
LC-wPBE	-1.91 (-1.63)	-2.23 (-1.87)	-3.30(-1.34)	-4.21 (-4.38)
CAM-B3LYP	-1.55 (-1.39)	-1.59 (-1.45)	-2.18(-1.30)	-2.62 (-2.85)
LC-wPBE-D3	-14.53 (-13.69)	-13.45 (-12.71)	-22.61 (-21.81)	-30.25 (-29.68)
CAM-B3LYP- D3	-10.77 (-10.21)	-10.87 (-10.28)	-17.93 (-17.46)	-23.34 (-22.95)
B3LYP-D3	-12.34 (-11.60)	-11.69 (-11.09)	-20.23 (-18.24)	-26.79 (-26.19)
B97D	-13.31 (-12.33)	-14.00 (-13.75)	-23.26 (-20.71)	-30.03 (-28.99)
xB97XD	-15.94 (-14.68)	-15.41 (-14.60)	-27.49 (-23.23)	-32.34 (-31.45)

<sup>a</sup> Values in parentheses belongs to ZPE corrected; <sup>b</sup> all energies in kcal/mol.

In order to explore energies for the formation of non-covalent  $\pi$ - $\pi$  complexes between pyrene and nanocarbon materials, we have conducted set of the DFT calculations for pyrene-pyrene, pyrene-C<sub>60</sub>, pyrene-(6,5)-SWCNT, and pyrene-graphene assemblies (Table 2.4, Figure 2.53). Since it is expected that the DFT-predicted interaction energies for such weakly-interacting complexes should have significant dependence on the exchange-correlation functional, we have compared two functionals the incorporate long-range corrections (CAM-B3LYP<sup>196</sup> and LC-wPBE<sup>197-200</sup>) and several functionals with dispersion corrections (B97D,<sup>201</sup> wB97-XD,<sup>202</sup> CAM-B3LYP-D3,<sup>203</sup> B3LYP-D3,<sup>203</sup> and LC-wPBE-D3,<sup>203</sup> Figure 2.53). The DFT-predicted interaction energies for non-covalent pyrene-pyrene dimers show a clear dependence on exchange-correlation (Table 2.4). Long-range corrected functionals predict small interaction energies (~1.4–1.6 kcal/mol) between two pyrene molecules, while dispersion-corrected functionals predict higher

interaction energies (~10-14 kcal/mol). In all cases, pyrene molecules remained planar and the pyrene-pyrene complexes have slipped-stack geometries (Figure 2.53). Geometries also remain planar for the pyrene-graphene complexes calculated by all tested exchange-correlation functionals. Similarly, in the case of pyrene-C<sub>60</sub> complexes, long-range corrected functionals predict rather small formation energies (~1.4–1.9 kcal/mol), while dispersion-corrected functionals predict much higher interaction energies (~10–13 kcal/mol). It should be noted, however, that dispersion-corrected functionals predict geometries of the pyrene-C<sub>60</sub> complexes with rather short intermolecular distances, which were not observed in the experimental X-ray structures of the pyrene-containing compounds.<sup>204-207</sup> No difference was predicted by DFT when energies of complex formation for pyrene/pyrene and pyrene/C<sub>60</sub> pairs were compared between exchange-correlation functionals ( $\pm 0.5$  kcal/mol for each pair). This similarity in energy is indicative of a lack of preference for pyrene/C<sub>60</sub> over pyrene/pyrene interactions, and correlates well with the experimental data. DFT-predicted geometries and interaction energies for the pyrene-(6,5)-SWCNT complexes exhibit the same trends as pyrene-C<sub>60</sub> complexes. Long-range corrected functionals predict smaller interaction energies and planar pyrene geometries, while dispersion-corrected functionals predict much higher interaction energies and slightly distorted pyrene geometries (Table 2.4 and Figure 2.53). When the complex formation energies are compared between pyrene/(6,5)-SWCNT and pyrene/graphene, we found no clear trend across the different exchange-correlation functionals (Table 2.4). Overall, it seems that the dispersion-corrected functionals overestimate interaction energies for the formation of pyrene-nanocarbon complexes. Such a large interaction, 15-30 kcal/mol, is not consistent with the experimental observations. The DFT calculations predict a lack of the energetic preference for selective pyrene-C<sub>60</sub> non-covalent complex formation when compared to competing pyrene/pyrene interactions, which correlates well with the experimental X-ray crystal structure of the **2.5b**·C<sub>60</sub> and **2.5d**·2C<sub>60</sub> systems. DFT-predicted non-covalent complex formation energies for pyrene-(6,5)-SWCNT and pyrene-graphene were higher, in agreement with the experimental data. Overall, DFT calculations are indicative of weak pyrene-nanocarbon interaction energies that are not strong enough to facilitate structural assembly or photoinduced electron-transfer processes.

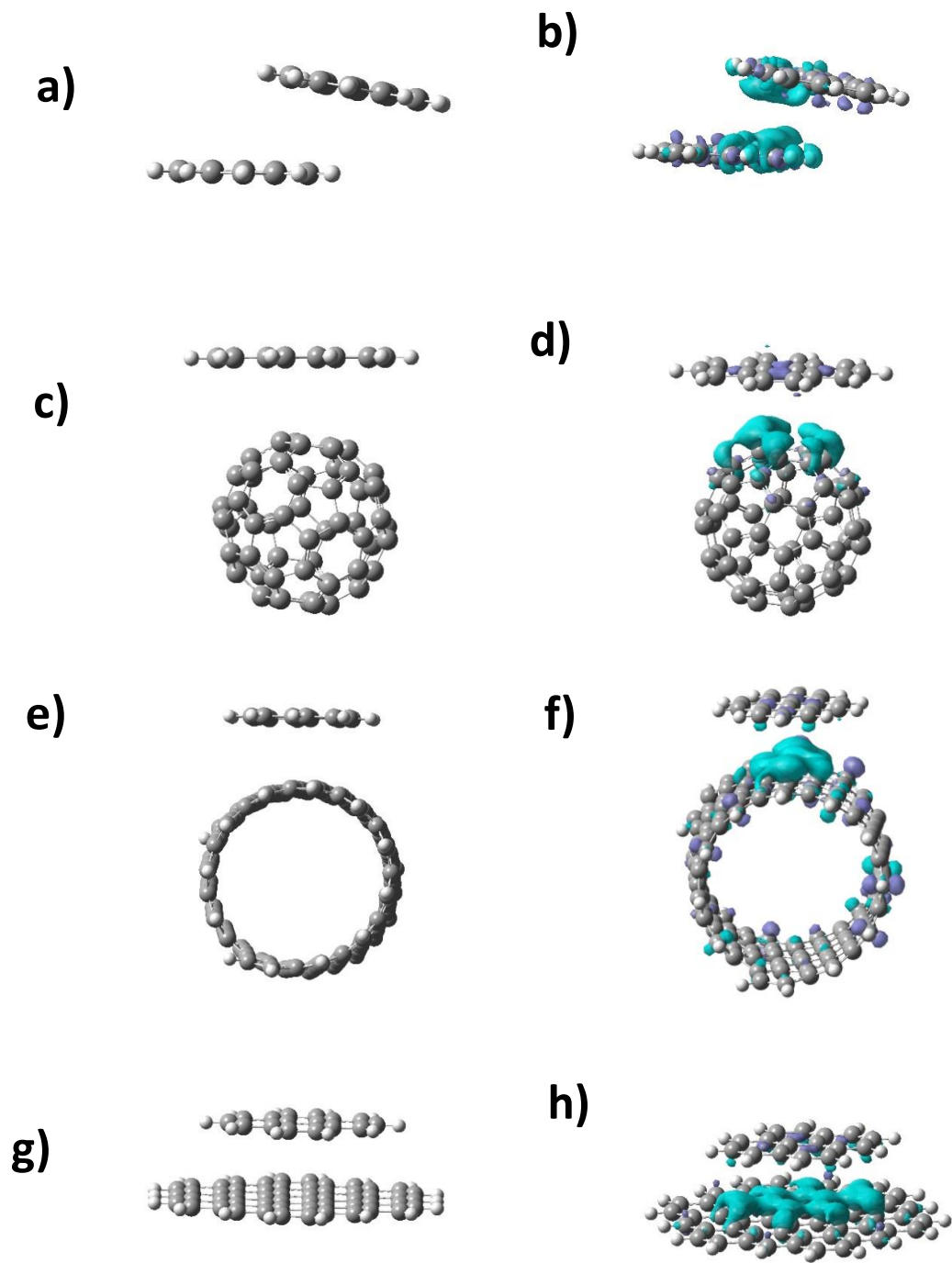
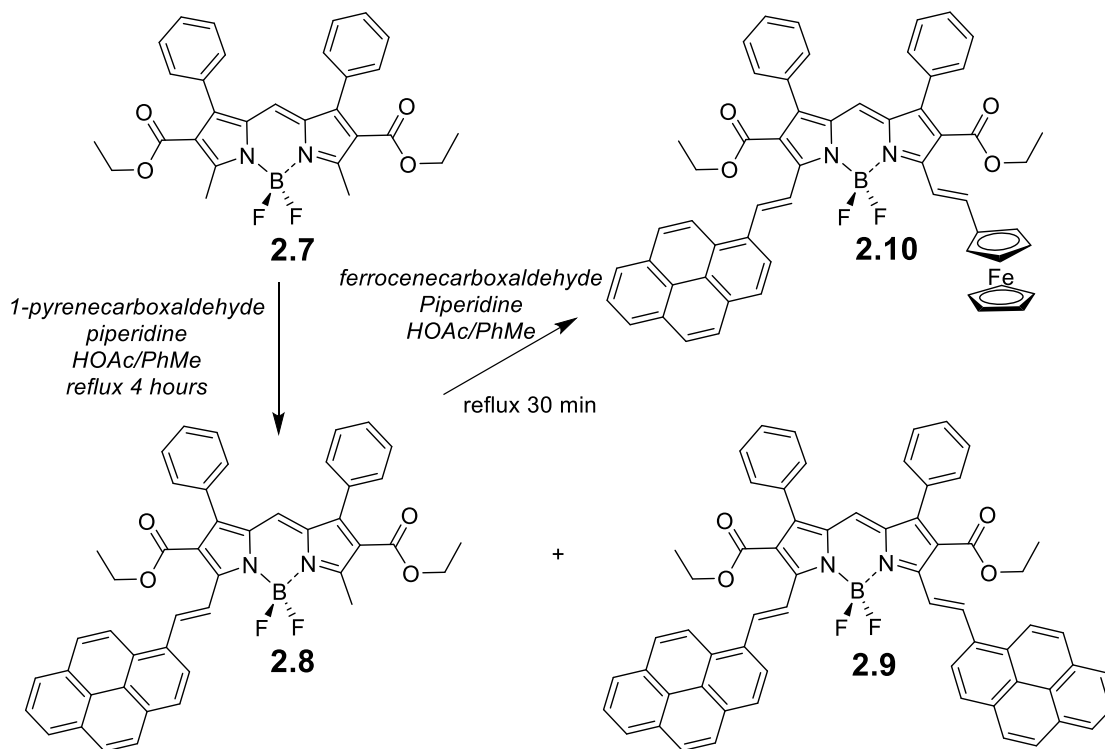


Figure 2.53: Predicted geometries (a, c, e, and g) and charge density isosurfaces (b, d, f, and h) of intramolecular interaction calculated at LC-wPBE level of theory for pyrene-pyrene (a and b), pyrene-C<sub>60</sub> (c and d), pyrene-(6,5)-SWCNT (e and f), pyrene-graphene (g and h), respectively.

## Fully conjugated pyrene-BODIPY and pyrene-BODIPY-ferrocene dyads and triads

All new pyrene-BODIPYs **2.8** – **2.10** were prepared using Knoevenagel condensation reaction approach.<sup>18</sup> Reaction between starting BODIPY **2.7** and 1-pyrenecarboxaldehyde leads to the formation of mono- and dipyrene-containing BODIPYs **2.8** and **2.9**, respectively, which can be easily separated using standard purification techniques. Further reaction between pyrene-BODIPY **2.8** and ferrocenecarboxaldehyde leads to the formation of ferrocene-containing pyrene-BODIPY **2.10** (Scheme 2.2).



Scheme 2.2: The synthesis of pyrene-BODIPYs **2.8** – **2.10**.

New pyrene-BODIPYs **2.8**–**2.10** were characterized by <sup>1</sup>H, <sup>13</sup>C, and 2D NMR as well as UV-Vis spectroscopy and high-resolution mass spectrometry (Figure 2.54-2.63). The presence of a single set of vinylic protons and a methyl group at the  $\alpha$ -position in BODIPY **2.8**, equivalent set of vinylic protons in symmetric BODIPY **2.9**, and two non-equivalent sets of vinylic protons along with the characteristic ferrocene protons in BODIPY **2.10** correlate well with their respective structures.

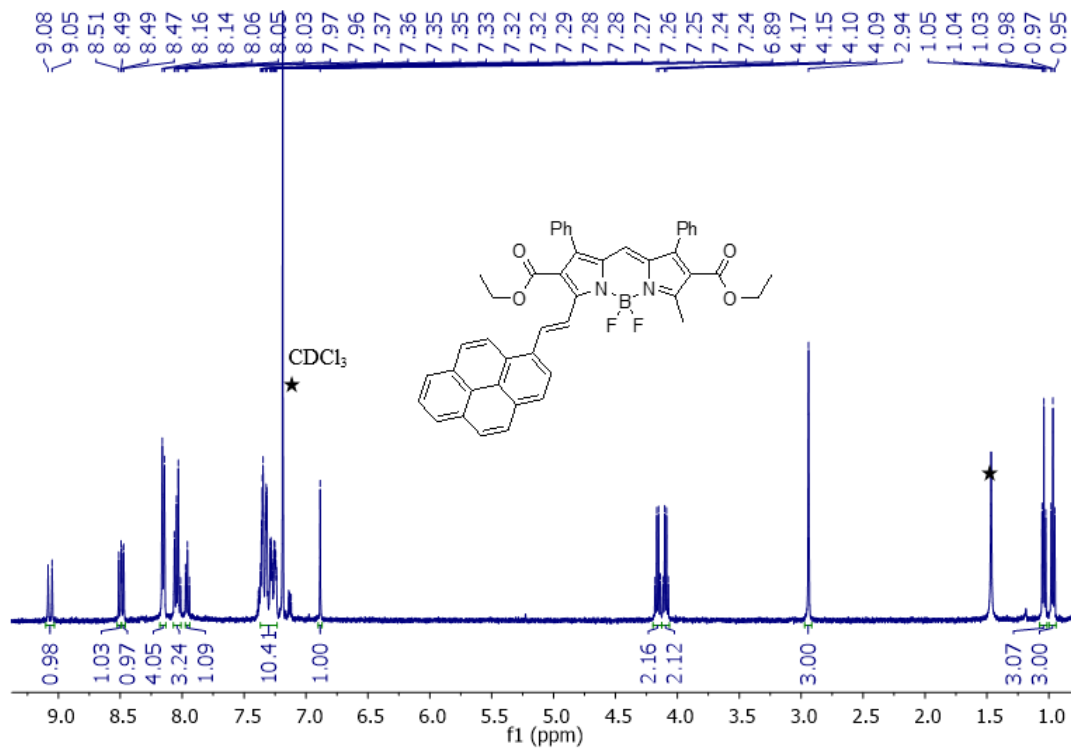


Figure 2.54:  $^1\text{H}$  NMR spectra of compound **2.8** in  $\text{CDCl}_3$ . (★ denotes solvent residues.)

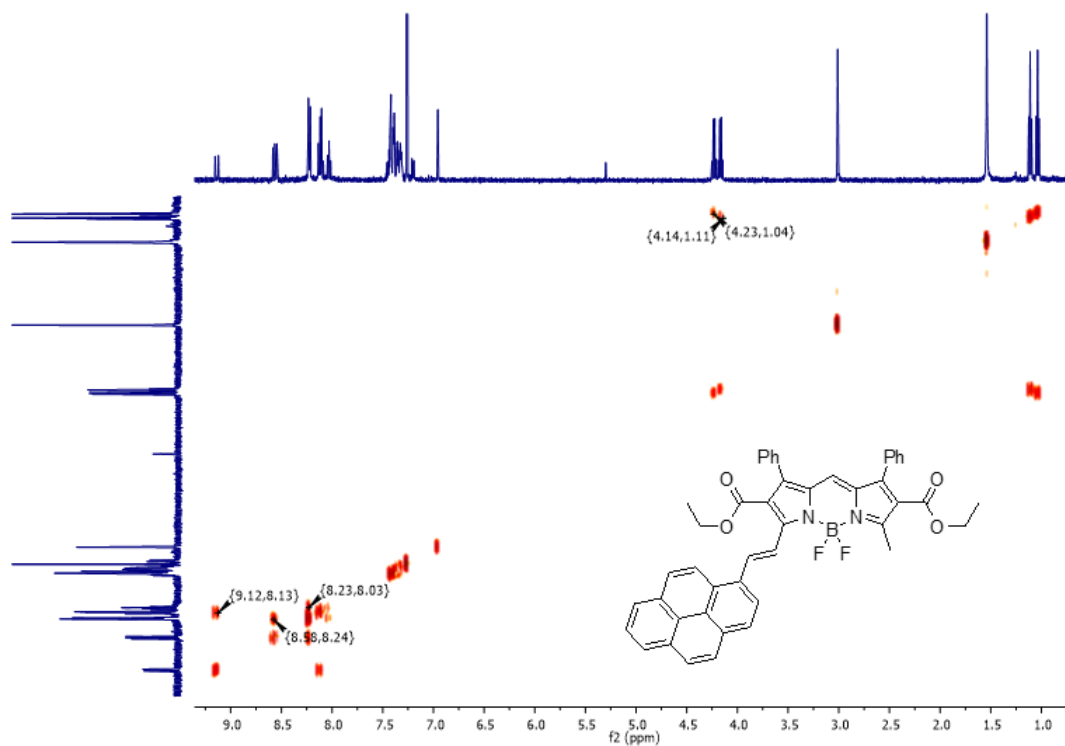


Figure 2.55:  $^1\text{H}$  COSY NMR spectra of compound **2.8** in  $\text{CDCl}_3$ .

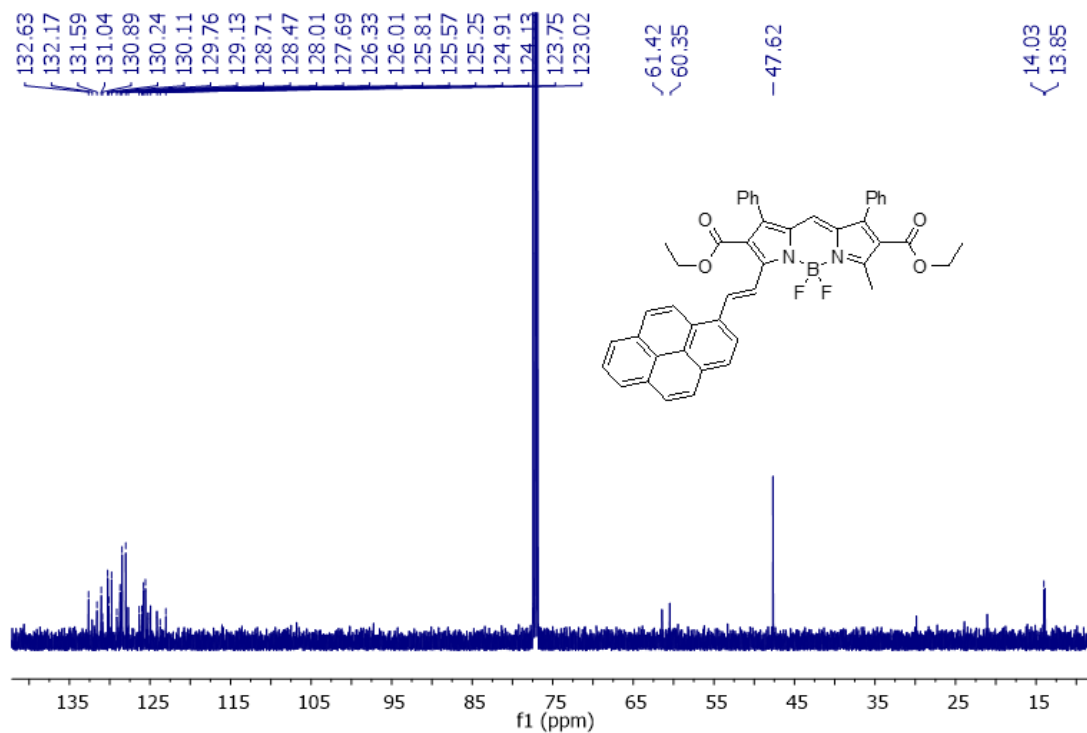


Figure 2.56:  $^{13}\text{C}$  NMR spectra of compound **2.8** in  $\text{CDCl}_3$ .

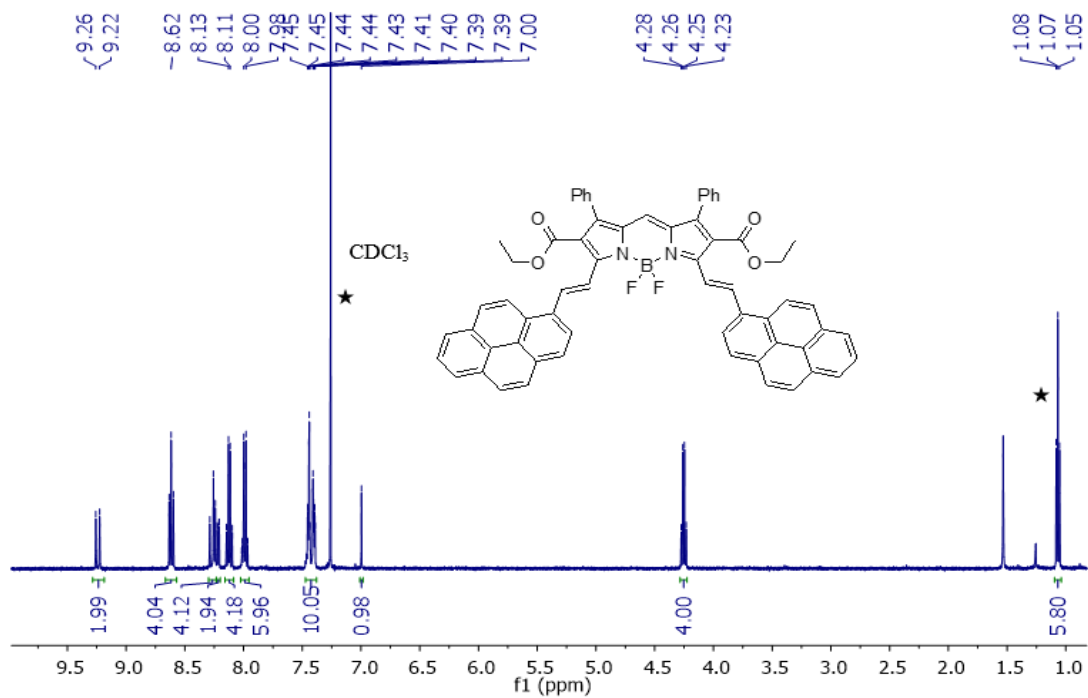


Figure 2.57:  $^1\text{H}$  NMR spectra of compound **2.9** in  $\text{CDCl}_3$ . (★denotes solvent residues.)

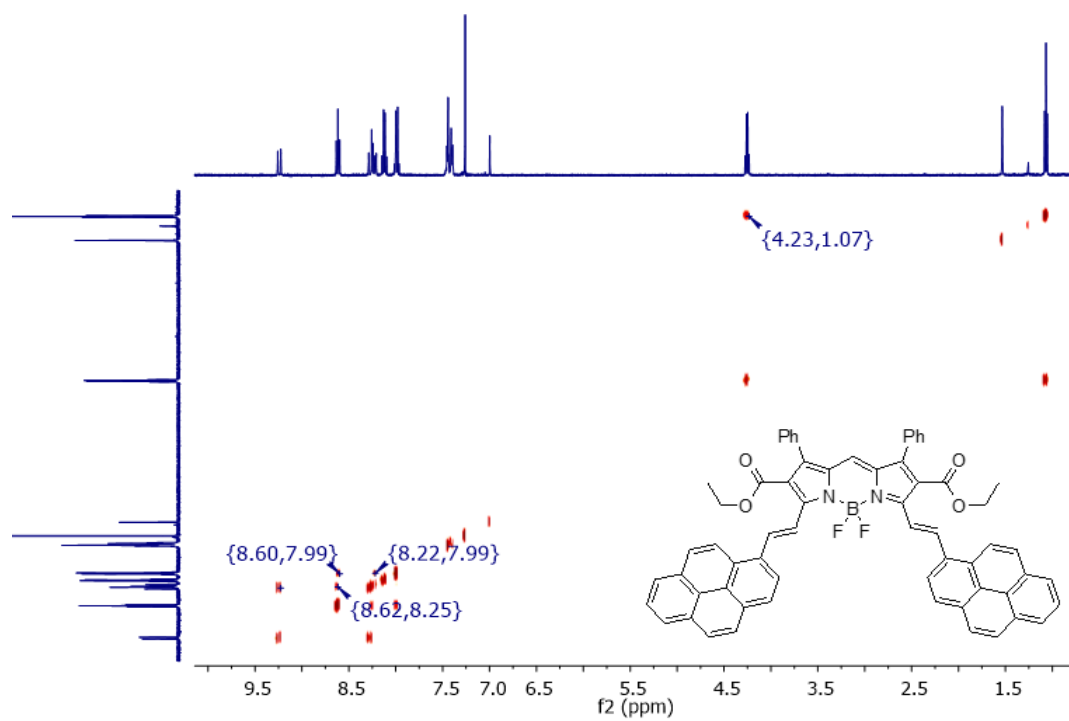


Figure 2.58:  $^1\text{H}$  COSY NMR spectra of compound **2.9** in  $\text{CDCl}_3$ .

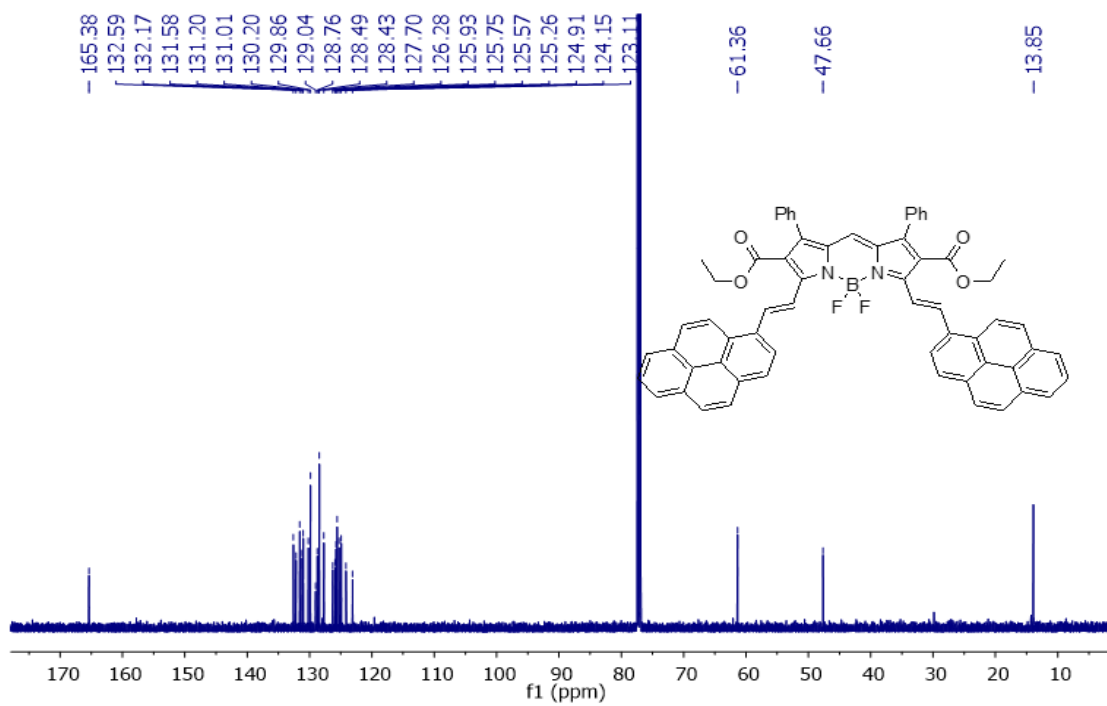


Figure 2.59:  $^{13}\text{C}$  NMR spectra of compound **2.9** in  $\text{CDCl}_3$ .

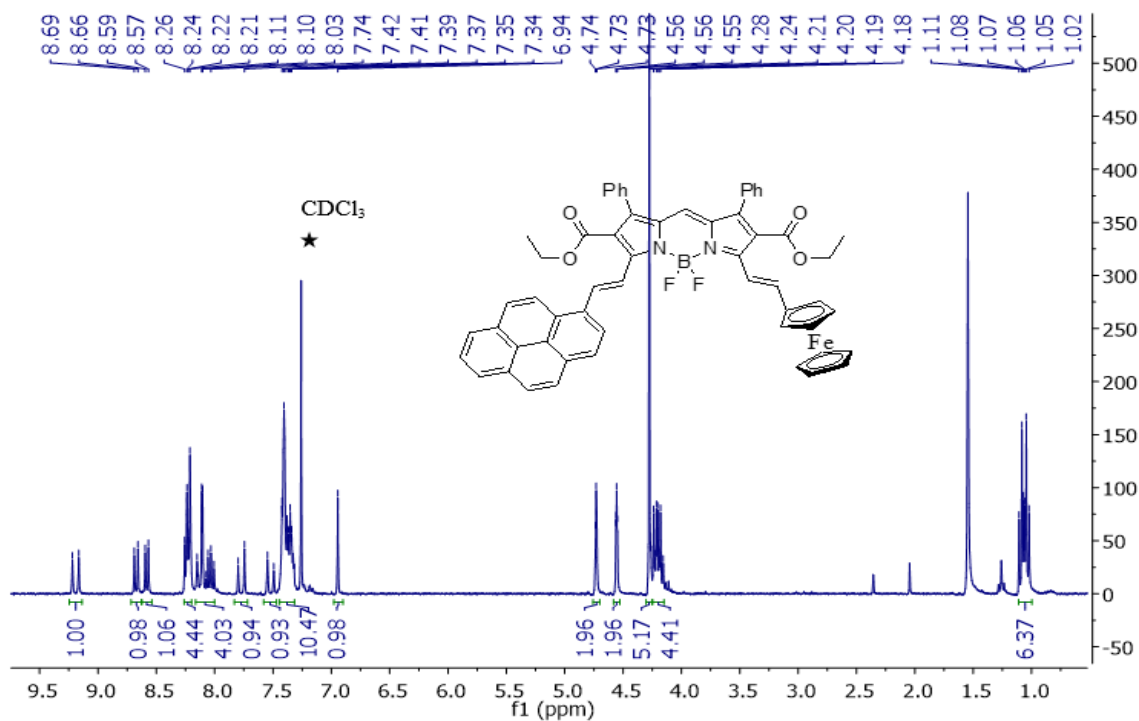


Figure 2.60:  $^1\text{H}$  NMR spectra of compound **2.10** in  $\text{CDCl}_3$ . (★ denotes solvent residues.)

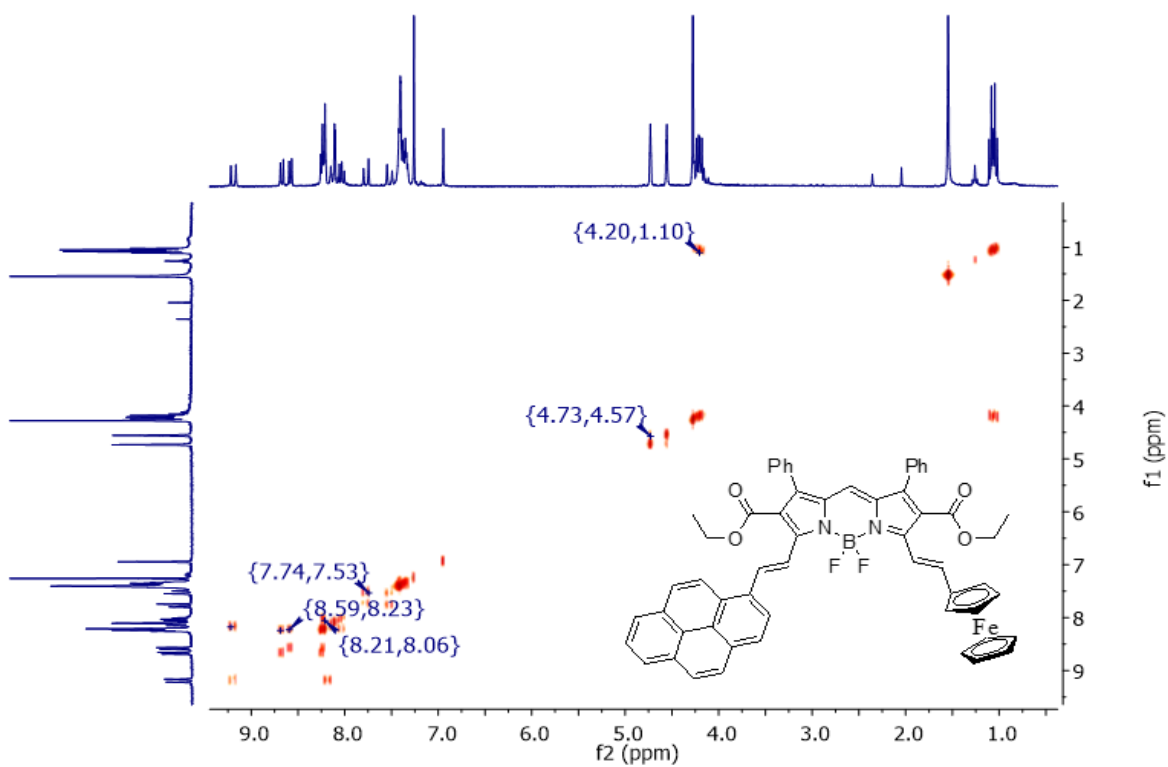


Figure 2.61:  $^1\text{H}$  COSY NMR spectra of compound **2.10** in  $\text{CDCl}_3$ .

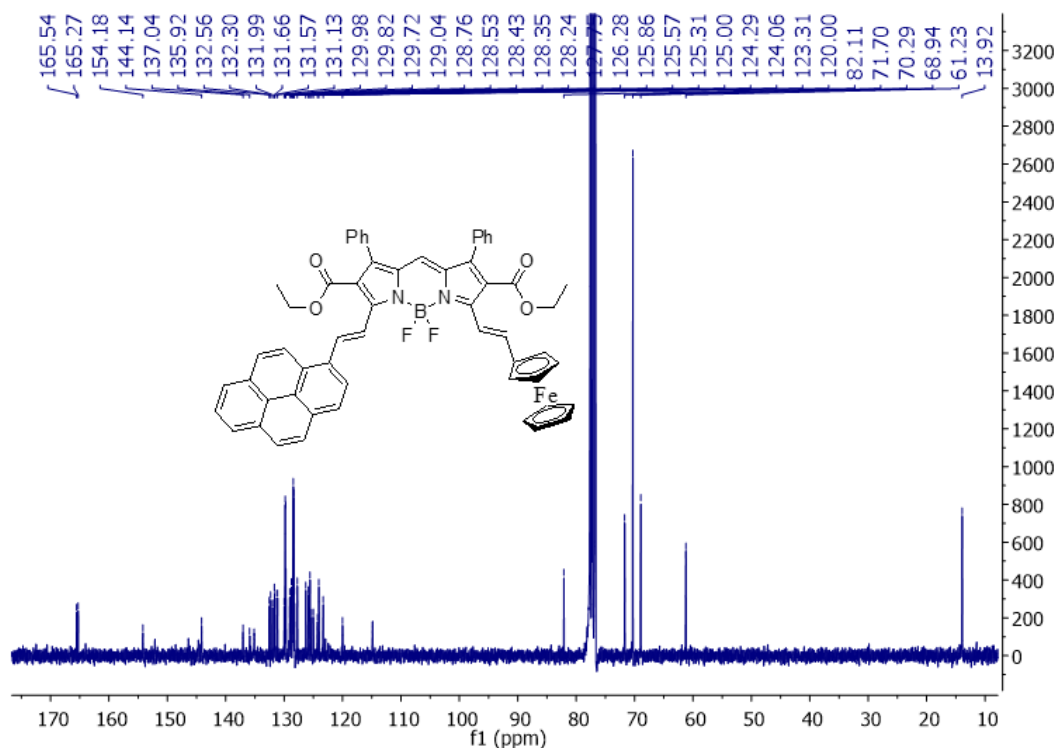


Figure 2.62:  $^{13}\text{C}$  NMR spectra of compound **2.10** in  $\text{CDCl}_3$ .

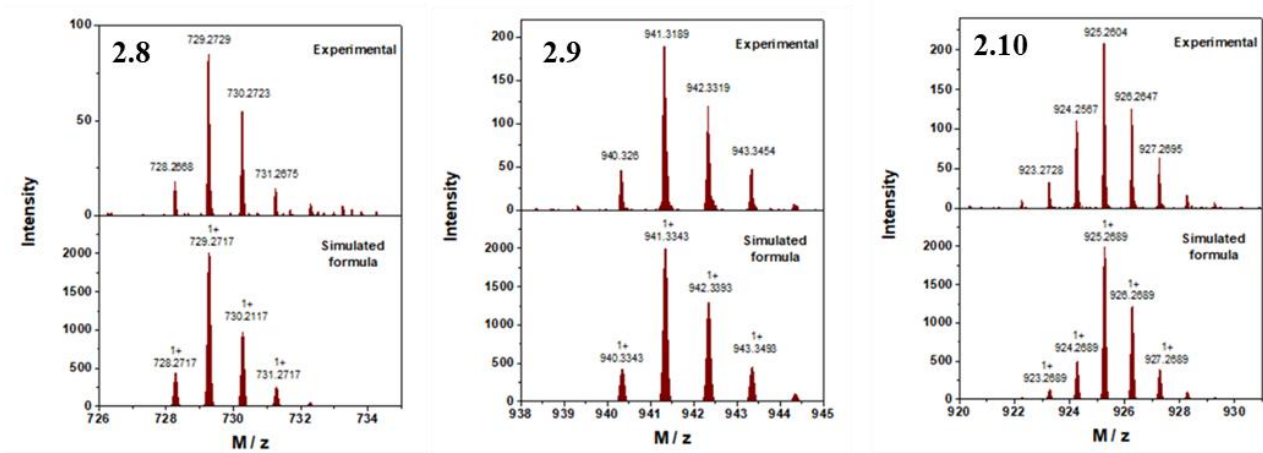


Figure 2.63: HRMS spectra of compound **2.8**, **2.9**, and **2.10**.

In addition to the spectroscopic data, the ultimate structures of BODIPYs **2.8** and **2.9** were established by X-ray crystallography (Figure 2.64). In both compounds, the  $\text{C}_{\alpha\text{-pyrrole}}\text{-CH=CH-C}_{\text{pyrene}}$  bonds clearly alternate between single and double bonds, which is evident from their bond distances. The pyrene fragment is well conjugated into the BODIPY-vinyl  $\pi$ -system with observed  $\text{N-C}_{\alpha\text{-pyrrole}}\text{-CH=CH-}$ ,  $\text{C}_{\alpha\text{-pyrrole}}\text{-CH=CH-C}_{\text{pyrene}}$ , and  $\text{-CH=CH-C}_{\text{pyrene}}\text{-C}_{\text{pyrene}}$  torsion angles in

mono-pyrene BODIPY **2.8** ( $10.19^\circ$ ,  $3.95^\circ$ , and  $1.39^\circ$ , respectively) and dipyrene BODIPY **2.8** ( $15.41/19.19^\circ$ ,  $0.22/4.20^\circ$ , and  $6.60/20.97^\circ$ , respectively) close to the expected values. In contrary, the phenyl groups located at the positions 1 and 7 of BODIPYs **2.8** and **2.9** are rotated away from the BODIPY  $\pi$ -system as evident from the corresponding  $C_{\alpha\text{-pyrrole}}\text{-}C_{\beta\text{-pyrrole}}\text{-}C_{\text{ipso}}\text{-}C_{\text{ortho}}$  torsion angles that varies between  $39.78$  and  $56.81^\circ$ . The BODIPY core in **2.8** is slightly domed, while it is planar in the case of BODIPY **2.9**.

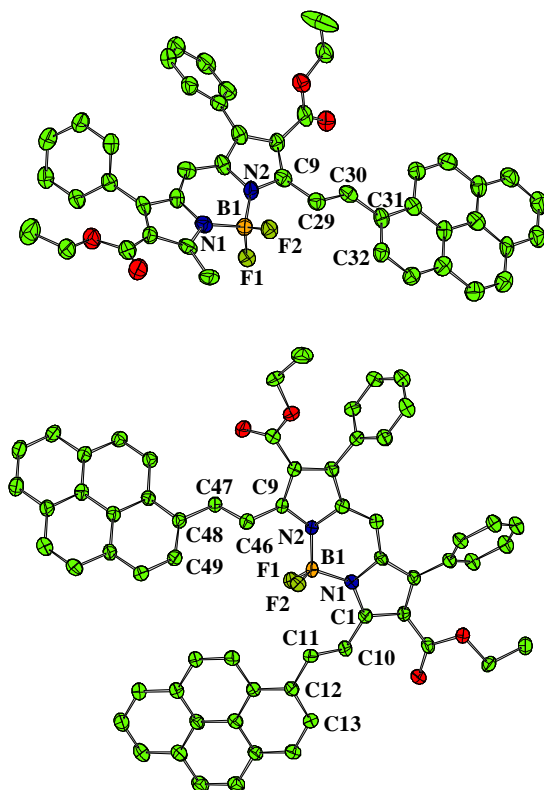


Figure 2.64: CAMERON drawings of BODIPYs **2.8** (top) and **2.9** (bottom) with ellipsoids shown at 50% probability level with side-chain atom labels and all hydrogen atoms omitted for clarity. Selected bond distances ( $\text{\AA}$ ) and angles ( $^\circ$ ): **2.8**: F(1)-B(1) 1.371(9), B(1)-F(2) 1.392(10), B(1)-N(1) 1.564(10), B(1)-N(2) 1.564(10), C(9)-C(29) 1.468(11), C(29)-C(30) 1.349(11), C(30)-C(31) 1.470(11), F(1)-B(1)-F(2)  $110.3(7)$ , N(1)-B(1)-N(2)  $107.0(6)$ , C(9)-C(29)-C(30)  $123.5(7)$ , C(29)-C(30)-C(31)  $124.6(7)$ ; **2.9**: F(1)-B(1) 1.402(6), B(1)-F(2) 1.387(5), B(1)-N(1) 1.555(6), B(1)-N(2) 1.553(6), C(1)-C(10) 1.435(6), C(10)-C(11) 1.347(6), C(11)-C(12) 1.447(5), C(9)-C(46) 1.433(6), C(9)-C(8) 1.433(6), C(46)-C(47) 1.351(6), C(47)-C(48) 1.451(6), F(1)-B(1)-F(2)  $109.5(4)$ , N(1)-B(1)-N(2)  $108.5(3)$ , C(1)-C(10)-C(11)  $129.1(4)$ , C(10)-C(11)-C(12)  $125.4(4)$ , C(9)-C(46)-C(47)  $126.3(4)$ , C(46)-C(47)-C(48)  $126.6(4)$ .

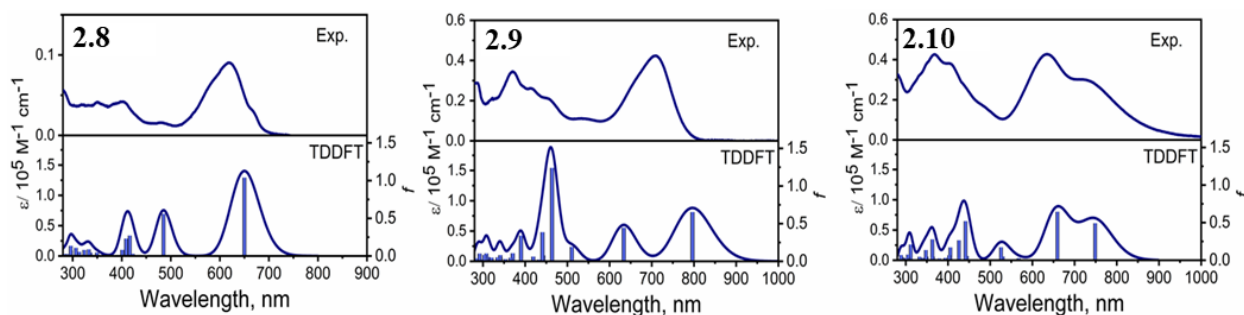


Figure 2.65: Absorption (top) and TDDFT-predicted (bottom) spectra of pyrene-BODIPYs **2.8** (left), **2.9** (middle), and **2.10** (right) in DCM. TDDFT-predicted excitation energies are shown by vertical bars.

Table 2.5. Absorption and emission data on BODIPYs **2.8** – **2.10** in DCM.

Compound	$\lambda_{\text{abs}}$ [nm] ( $\epsilon$ [ $\text{M}^{-1}\text{cm}^{-1}$ ])	Emission [nm] ( $\Phi$ )	$\tau$ [ns]	$\kappa_{\text{SV}}$ C <sub>60</sub>	$\kappa_{\text{SV}}$ C <sub>70</sub>
<b>2.8</b>	403(15960), 484(7630), 634(48600)	707 (0.11)	3.92±0.02	21440	13500
<b>2.9</b>	373(38190), 550(13920), 724(54400)	766 (0.119)	2.41±0.01	18700	16000
<b>2.10</b>	369(35500), 634(35580), 713(25140)	ND	0.268±0.017	ND	ND

ND: not determined.

The UV-vis spectra of new pyrene-BODIPYs **2.8–2.10** are shown in Figure 2.65 and summarized in Table 2.5. As was observed in the X-ray crystallography, conjugation of the pyrene fragment into the  $\pi$ -system of BODIPY core is obvious from the comparison of the UV-Vis spectra of the pyrene-BODIPYs **2.8** and **2.9** with the parent BODIPY **2.7**. Indeed, stepwise addition of one and two conjugated pyrene fragments to the BODIPY core results in  $\sim 100$  nm low-energy shift of the most intense  $\pi$ - $\pi^*$  transition from 520 nm in **2.7** to 634 nm in **2.8** to 724 nm in **2.9**. Similar to the reported earlier ferrocene-BODIPY systems with BODIPY-CH=CH-Fc motif<sup>153</sup>, the UV-vis spectrum of **2.10** has an additional, lower intensity broad metal-to-ligand (MLCT) band in the low-energy region observed at 713 nm. The steady-state fluorescence spectra of pyrene-BODIPYs **2.8** and **2.9** are shown in Figure 2.66. The observed Stokes shifts for **2.8** and **2.9** are in

the typical range for BODIPYs between 10-20nm. It is interesting to mention that since pyrene fragments in BODIPYs **2.8** and **2.9** are conjugated to the BODIPY core, their individual electron-donating properties are suppressed and thus measured fluorescence quantum yields in these compounds (Table 2.5) are in the typical range for BODIPYs with extended  $\pi$ -systems. This observation is in contrast with the pyrene-BODIPY systems in which pyrene fragments are located at *meso*-<sup>208</sup> or  $\beta$ -pyrrolic<sup>243</sup> position and behave as effective quenchers of the BODIPY's singlet excited state. Steady-state fluorescence of the ferrocene-containing BODIPY **2.10** is quenched, which is similar to the other ferrocene-BODIPY systems in which electron-transfer process from the ferrocene donor to the photoexcited BODIPY core is thought to be the major contribution to the quenching mechanism.<sup>148,153</sup> This was further confirmed by the oxidation of the BODIPY **2.10** with  $\text{Fe}(\text{ClO}_4)_3$  or  $\text{FeCl}_3$  as the oxidation of the ferrocene to ferrocenium leads to the partial restoration of the fluorescence of BODIPY core (Figure 2.66) and similar behavior was observed in numerous ferrocene-chromophore systems.<sup>153</sup>

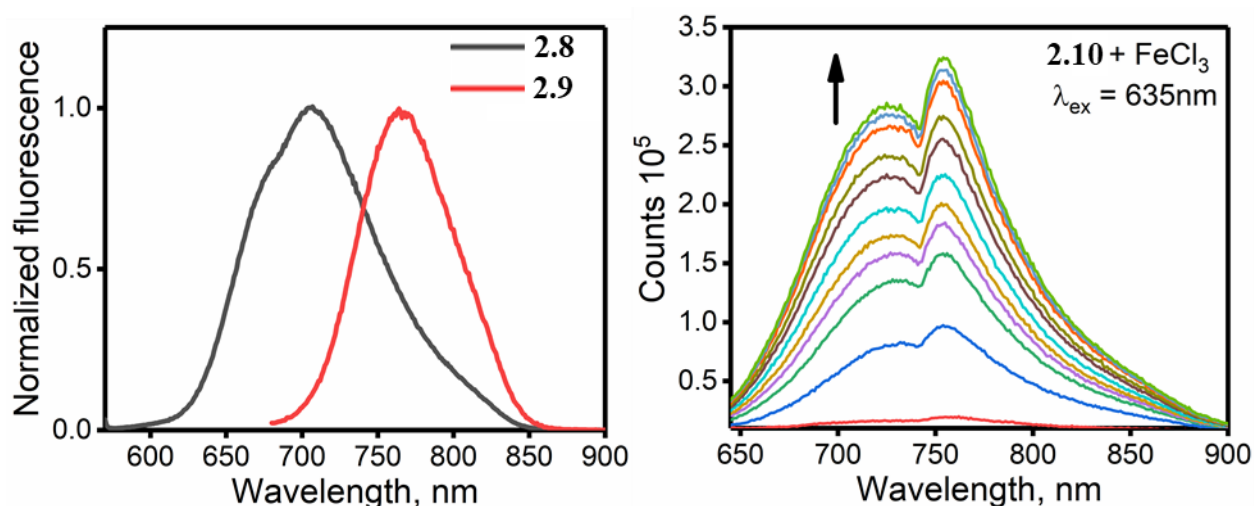


Figure 2.66. Normalized emission spectra of pyrene-BODIPYs **2.8** and **2.9** in toluene (left) and fluorescence intensity increase upon oxidation of BODIPY **2.10** with  $\text{FeCl}_3$  in DCM/MeOH (right).

The redox properties of pyrene-BODIPYs **2.8** – **2.10** were studied by electrochemical (cyclic voltammetry, CV, and differential pulse voltammetry, DPV, Figure 2.67 and Table 2.6) approaches. In the case of organic systems **2.8** and **2.9** all oxidation processes were found to be

irreversible, while the first reduction process in both compounds is quasi-reversible. In the case of ferrocene-containing system **2.10**, reversible oxidation of the ferrocene group and quasi-reversible reduction of the pyrene-BODIPY core were observed in the electrochemical experiments along with several irreversible oxidations observed at the higher potentials.

Table 2.6. Electrochemical data on BODIPYs **2.8–2.10** in DCM/0.1M TBAP system.

Compound	E <sup>3</sup> <sub>Ox</sub> (V)	E <sup>2</sup> <sub>Ox</sub> (V)	E <sup>1</sup> <sub>Ox</sub> (V)	E <sup>1</sup> <sub>Red</sub> (V)
<b>2.8</b>	-	1.1*	0.74*	-1.04
<b>2.9</b>	1.1*	0.74*	0.56*	-1.04
<b>2.10</b>	1.1**	0.74*	0.1	-1.04

All potentials are referenced to Fc/Fc<sup>+</sup> couple. \*Irreversible processes. \*\*Broad, probably multi-electron oxidation process

We have used a standard approach for the estimation of the possible photoinduced electron-transfer processes in non-covalent assemblies formed between BODIPYs **2.8 – 2.10** and C<sub>60</sub> fullerene, which are provided by the formula:<sup>168,169,171,209</sup>

$$\Delta G_{ET}^0 = e \left[ E^0 \left( \frac{D^+}{D} \right) - E^0 \left( \frac{A}{A^-} \right) \right] - E_{00} - \left( \frac{e^2}{4\pi\epsilon_0} \right) \left( \frac{1}{\epsilon_S R_{DA}} \right) - \left( \frac{e^2}{4\pi\epsilon_0} \right) \left( \frac{1}{2r^+} + \frac{1}{2r^-} \right) \left( \frac{1}{\epsilon_{EC}} - \frac{1}{\epsilon_S} \right) \quad (2.1)$$

Where E<sup>0</sup>(D<sup>+</sup>/D) and E<sup>0</sup>(A/A<sup>-</sup>) are oxidation potential of a donor and reduction potential of an acceptor, respectively; E<sub>00</sub> excitation energy at the BODIPY; R<sub>DA</sub> is a donor-accepted distance estimated on a basis of DFT calculations and X-ray data available for non-covalent complexes formed between aza-BODIPYs and C<sub>60</sub>;<sup>243</sup> ε<sub>s</sub> and ε<sub>EC</sub> are the dielectric constants of the solvents used in photochemical and electrochemical studies; r<sup>+</sup> and r<sup>-</sup> are the effective ionic radii of the donor and acceptor, respectively, that are estimated on the basis of DFT calculations. The estimated ΔG<sup>0</sup><sub>ET</sub> values were found between -0.31 and -0.80 eV, which is suggestive of the potential photoinduced electron-transfer in non-covalent assemblies formed between BODIPYs **2.8–2.10** and C<sub>60</sub> fullerene.

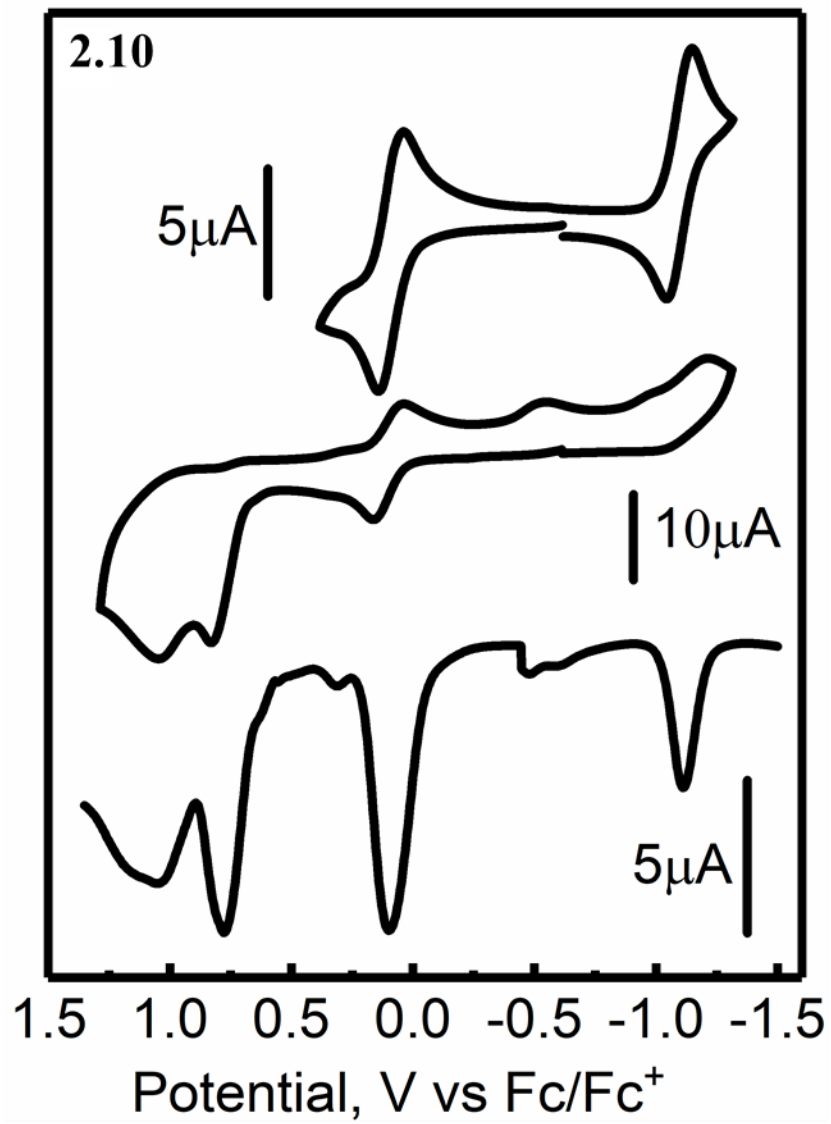


Figure 2.67: CV and DPV data for compound **2.10** in DCM/0.1M TBAP system. Top CV reversible oxidation and reduction process, middle CV irreversible 2<sup>nd</sup> oxidation process, bottom DPV oxidation processes.

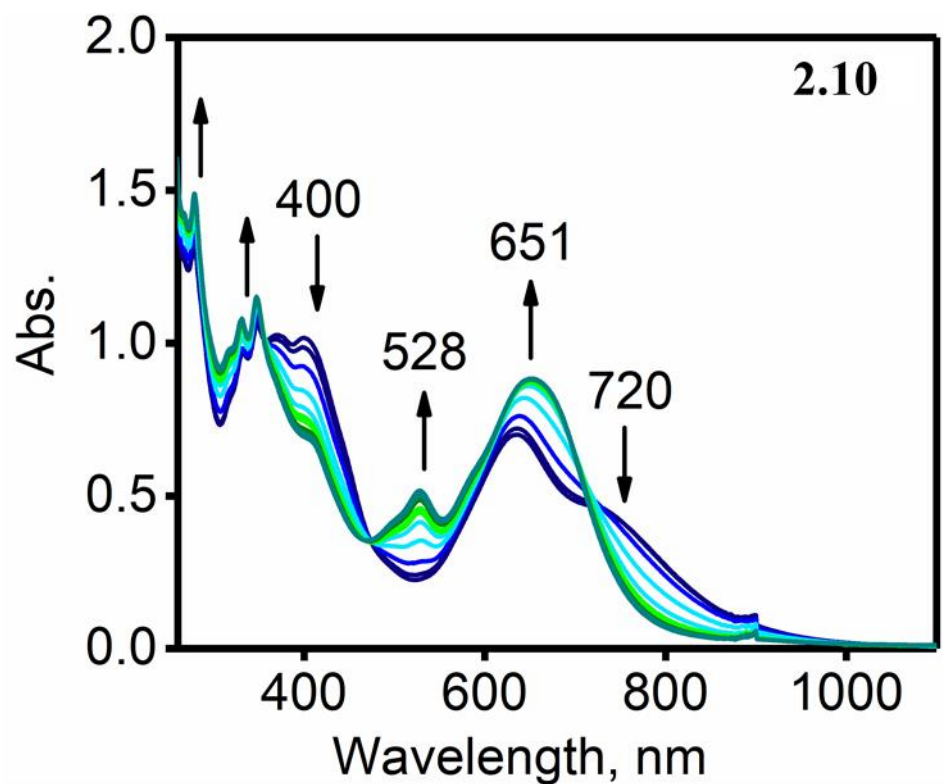


Figure 2.68: Spectroelectrochemical oxidation of compound **2.10** in DCM/0.3M TBAP system.

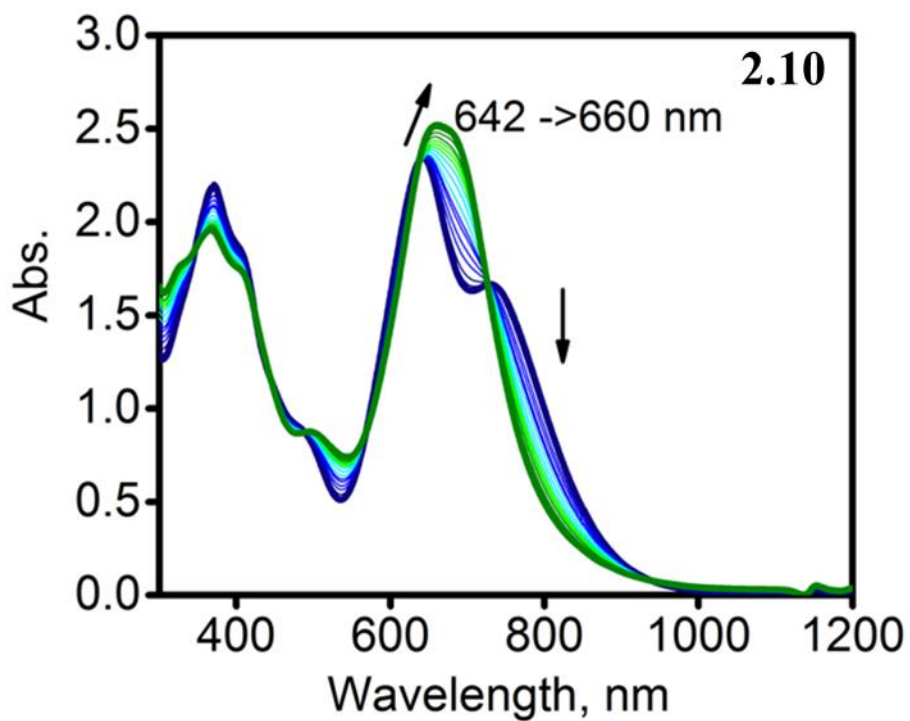


Figure 2.69: Chemical oxidation of BODIPY **2.10** with  $\text{Fe}(\text{ClO}_4)_3$  in DCM/MeOH system.

To confirm the origin of the first oxidation process in ferrocene-BODIPY **2.10**, we conducted spectroelectrochemical oxidation experiments on this compound (Figure 1.68). During the bulk electrolysis, the lower-intensity MLCT band at 720 nm disappears, while the initial BODIPY-centered  $\pi$ - $\pi^*$  transition at 635 nm undergoes a small low-energy shift to 651 nm and a new band at 528 nm appears in the UV-vis spectrum of  $[\mathbf{2.10}]^+$ , this is very typical for ferrocene-BODIPY compounds and indicative of the ferrocene oxidation.<sup>153</sup> Spectroelectrochemical data correlate well with the chemical oxidation data on BODIPY **2.10** as both oxidations result in the formation of  $[\mathbf{2.10}]^+$  (Figure 2.69).

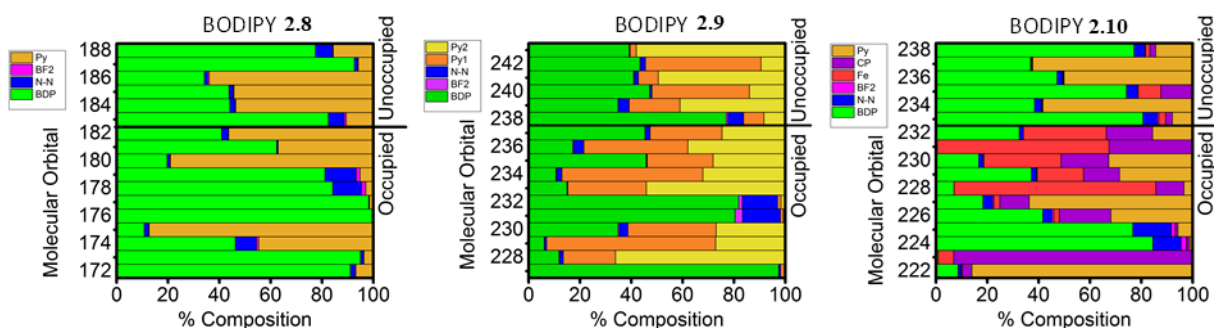


Figure 2.70: DFT-predicted compositions of frontier orbitals for pyrene-BODIPYs **2.8** – **2.10**. Abbreviation: “Py” = pyrene group; “N-N” = nitrogen atoms in BODIPY core; “BDP” = BODIPY fragment except nitrogen atoms; “CP” = cyclopentadienyl ligands.

In order to correlate observed photophysical and electrochemical behavior of pyrene-BODIPY systems **2.8** – **2.10** with their respective electronic structures, we conducted DFT and TDDFT calculations on all new compounds. The compositions for frontier molecular orbitals predicted by DFT calculations is shown in Figure 2.70, the comparative DFT-predicted energy diagram is presented in Figure 2.71 and selected frontier orbitals are shown in Figure 2.72.

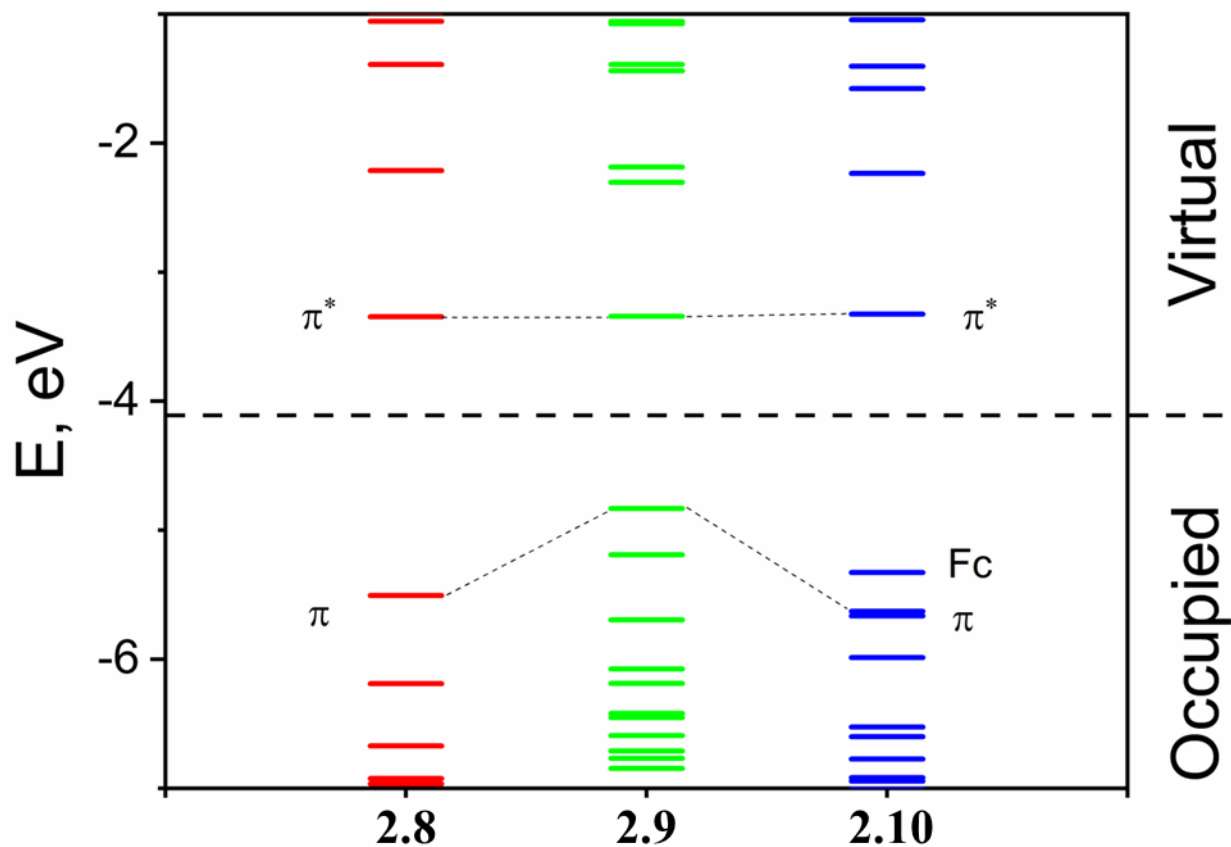


Figure 2.71: DFT-predicted energy diagram for the frontier MOs in pyrene-BODIPYs **2.8** – **2.10**.

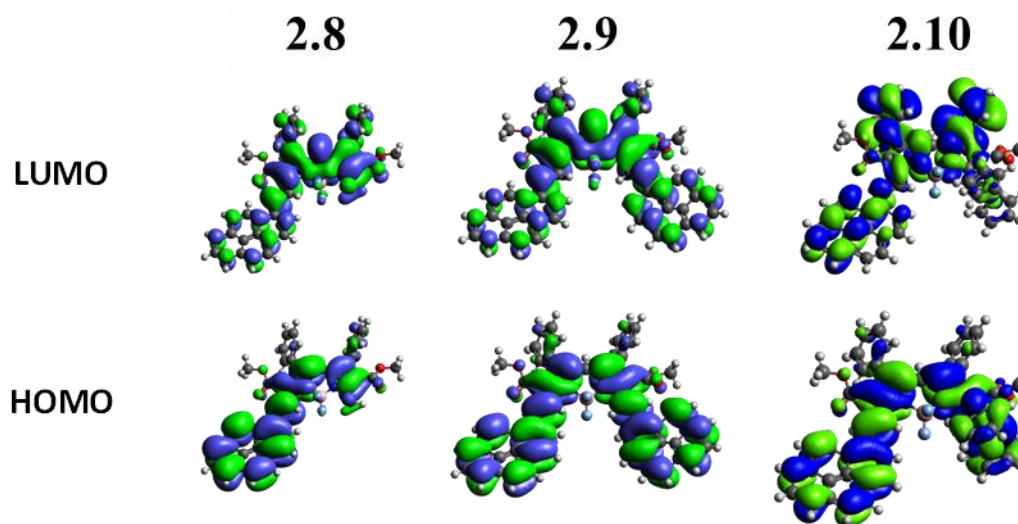


Figure 2.72: DFT-predicted images of frontier orbitals for pyrene-BODIPYs **2.8** – **2.10**.

DFT-predicted orbital energies and orbitals order correlate well with the experimental observations. In the case of mono- and dipyrene-BODIPYs **2.8** and **2.9** the DFT-predicted HOMO

is clearly delocalized over both BODIPY core and pyrene fragments confirming formation of the extended  $\pi$ -system in these compounds. In agreement with electrochemical and spectroelectrochemical data, the HOMO in ferrocene-containing pyrene-BODIPY **2.10** has predominant ferrocene character, while the HOMO-1 is a delocalized pyrene-BODIPY centered  $\pi$ -orbital. Similarly, the LUMO in all new pyrene-BODIPY compounds **2.8** – **2.10** is delocalized over organic chromophore and energies correlate well with electrochemical data. The DFT-predicted LUMO energy in BODIPYs **2.8** – **2.10** is nearly constant, which correlate well with the values for the first reduction potential in these compounds. The DFT-predicted HOMO energy in BODIPY **2.8** is significantly lower than that in BODIPY **2.9**, which again correlate well with the experimental electrochemical data.

Comparison between experimental and TDDFT-predicted UV-Vis spectra of pyrene-BODIPYs **2.8** – **2.10** is shown in Figure 2.65. In agreement with experimental data, the most intense low-energy band in purely organic compounds **2.8** and **2.9** is associated with a single excited state that predominantly originates from the HOMO  $\rightarrow$  LUMO single-electron excitations. In the case of ferrocene-containing pyrene-BODIPY **2.10** TDDFT predicts that the first excited state should have a predominant MLCT character with lower intensity, while the pyrene-BODIPY centered predominantly  $\pi$ - $\pi^*$  transition should be more intense and will have a higher energy compared to the MLCT band. Importantly, TDDFT correctly predicts low-energy for BODIPY-centered predominantly  $\pi$ - $\pi^*$  transition going from pyrene-BODIPY **2.8** to **2.9**, which correlates well with the stepwise increase of the respective  $\pi$ -system in these compounds. Overall, TDDFT calculations on pyrene-BODIPYs **2.8** – **2.10** reproduce both energies and intensities of the experimental UV-vis spectra of these compounds that provides an additional confidence in an interpretation of the respective photophysical data.

## **Interaction and Potential Complex Formation of Pyrene-BODIPYs with Nanocarbon Materials**

As discussed in previous literature,<sup>122-130,132,210-214</sup> the presence of a polarizable and electron-rich extended  $\pi$ -systems in light-harvesting chromophores can facilitate non-covalent  $\pi$ - $\pi$  interactions between such systems and nanocarbon electron-acceptor materials. Thus, we have investigated non-covalent complexes formation between pyrene-BODIPYs **2.8** – **2.10** and

nanocarbon materials (C<sub>60</sub> and C<sub>70</sub> fullerenes, (6,5)-SWCNT, and graphene) using UV-vis and steady-state fluorescence approaches. When titrations with fullerene (C<sub>60</sub> and C<sub>70</sub>) acceptors are considered, the difference absorption spectra of pyrene-BODIPYs **2.8** – **2.10** are reflective of only concentration increase of the electron acceptor, while formation of the expected low-energy charge-transfer band was not observed (Figure 2.73). In agreement with this observation, no quenching of the steady-state fluorescence in pyrene-BODIPYs **2.8** and **2.9** was observed upon excitation of the BODIPY chromophore at the respective low-energy bands (Figure 2.74). In contrary, clear quenching of the fluorescence was observed when 350 nm excitation was used in fluorescence experiments (Figure 2.74). Careful analysis of the fluorescence quenching observed upon 350 nm excitation was conducted using following formula, which takes into consideration competitive absorption of the fullerene acceptor:<sup>215</sup>

$$F = F_0 * \frac{1 - e^{-\varepsilon_1 * C_1 * l}}{\varepsilon_1 * C_1} * \frac{\varepsilon_1 * C_1 + \varepsilon_2 * C_2}{1 - e^{-(\varepsilon_1 * C_1 + \varepsilon_2 * C_2) * l}} * \frac{\varepsilon_3 * C_2 * l}{1 - e^{-\varepsilon_3 * C_2 * l}}$$

Where  $F$  is a corrected fluorescence,  $F_0$  is an experimentally observed fluorescence,  $\varepsilon_1$  is a molar extinction coefficient of fluorophore at excitation (BODIPY),  $C_1$  is a concentration of fluorophore (BODIPY),  $l$  is a path length,  $\varepsilon_2$  is a molar extinction coefficient of quencher at excitation (Fullerene),  $C_2$  is a concentration of quencher (fullerene),  $\varepsilon_3$  is a molar extinction coefficient of quencher (fullerene) at emission of fluorophore (BODIPY).

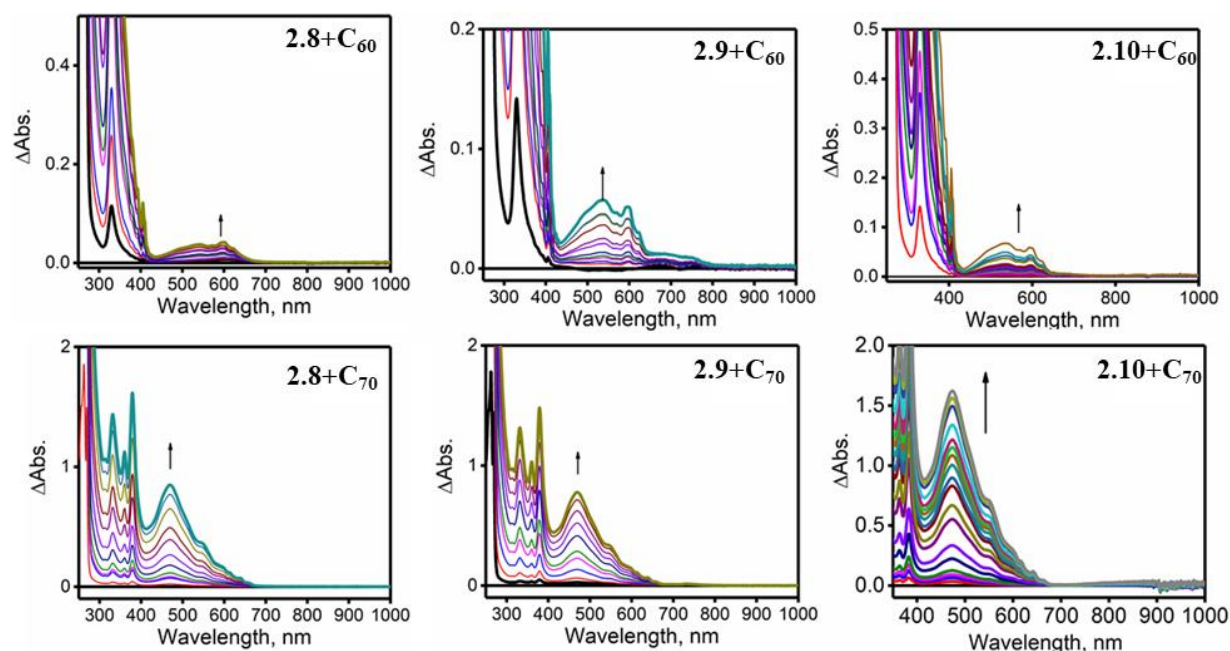


Figure 2.73: Difference absorption spectra of the BODIPYs **2.8** – **2.10** observed upon titrations with  $C_{60}$  (top) and  $C_{70}$  (bottom) fullerenes in DCM/toluene.

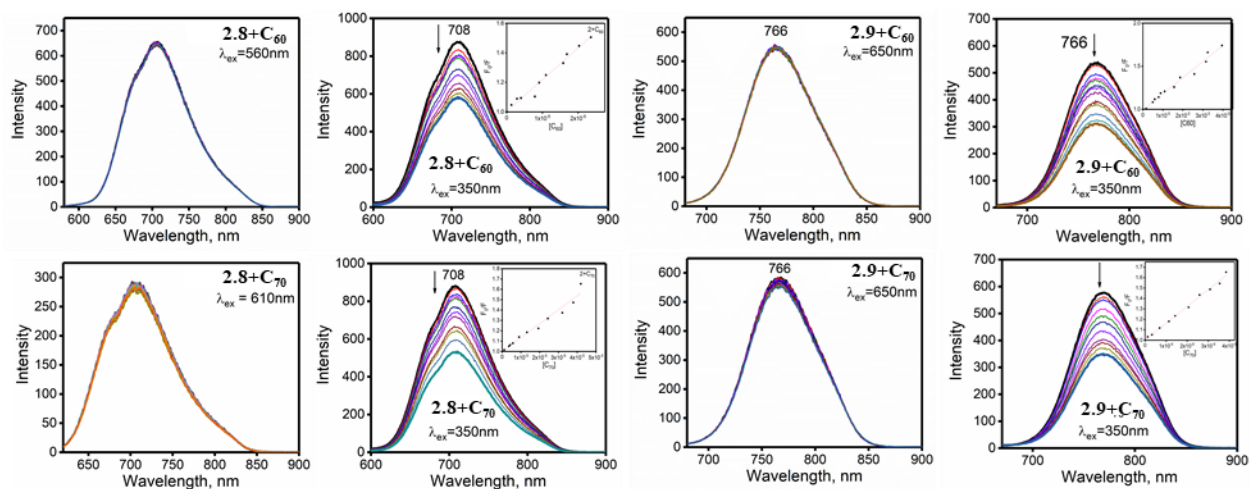


Figure 2.74: Changes in steady-state fluorescence of the BODIPYs **2.8** and **2.9** observed upon titrations with  $C_{60}$  (top) and  $C_{70}$  (bottom) in DCM/toluene. Excitation wavelengths are shown for each graph along with quenching constant analyses given as insets.

Analysis of the data (Table 2.5) is indicative of a rather weak non-covalent interaction between pyrene-BODIPY **2.8** or **2.9** and  $C_{60}$  or  $C_{70}$  fullerenes. The lack of the fluorescence quenching for **2.8** :  $C_{60}$  and **2.9** :  $C_{60}$  mixtures upon selective photoexcitation of the BODIPY core at low energy

and clear fluorescence quenching upon photoexcitation at 350 nm when both BODIPY and fullerene are photoexcited is indicative of the potential energy- or electron-transfer processes in which fullerene plays a role of acceptor. In contrast, to the fullerene titration data stepwise addition of the (6,5)-SWCNT or graphene to a solution of pyrene-BODIPYs **2.8** and **2.9** leads to decrease of fluorescence at all tested wavelengths (Figure 2.76). Such fluorescence decrease, however, is associated with the overall decrease of absorption of pyrene-BODIPYs and thus (Figure 2.75), taking into consideration the heterogeneous nature of the final solutions, it is difficult to clearly state if the fluorescence decrease is associated with physical adsorption of the chromophores on the (6,5)-SWCNT or graphene surface or it is a result of the effective electron- or energy-transfer from the photoexcited chromophore to the nanocarbon material. Overall, the UV-vis and steady-state fluorescence data are indicative of the rather weak interactions between fullerenes and pyrene-BODIPYs **2.8** – **2.10**, while stronger interactions between these chromophores and (6,5)-SWCNT or graphene was observed that does not exclude potential electron-transfer from the photoexcited chromophores to the nanocarbon surface.

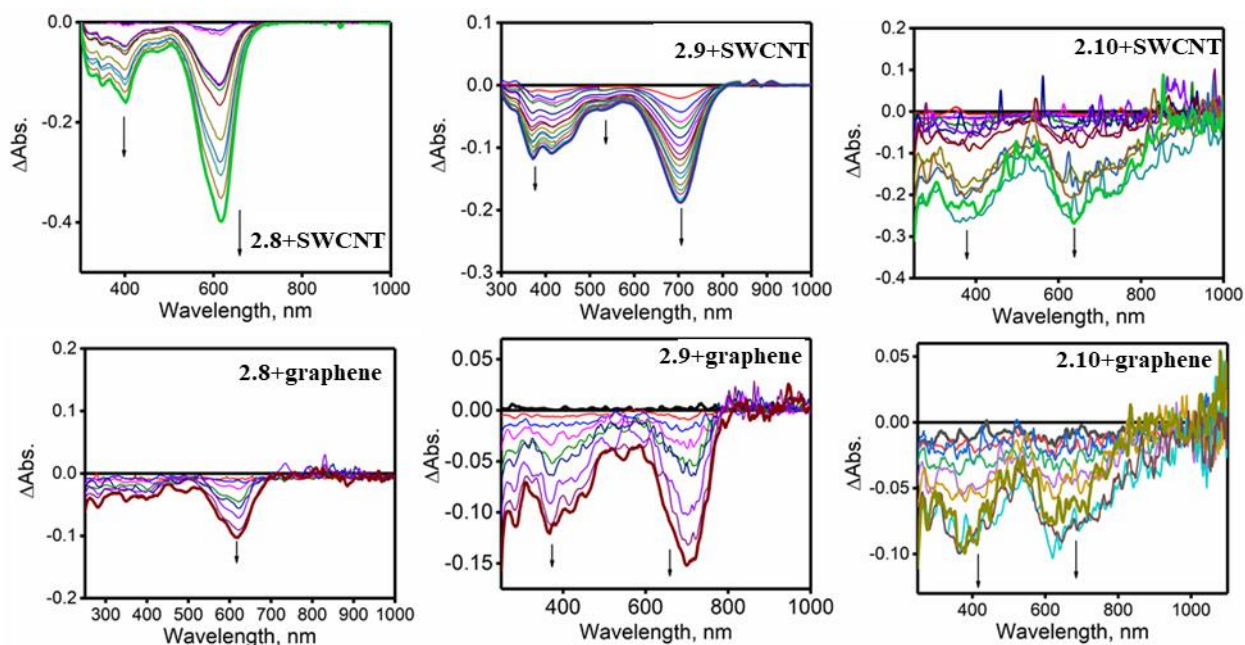


Figure 2.75: Difference absorption spectra of the BODIPYs **2.8** – **2.10** observed upon titrations with (6,5)-SWCNT (top) and graphene (bottom) fullerenes in DCM/toluene.

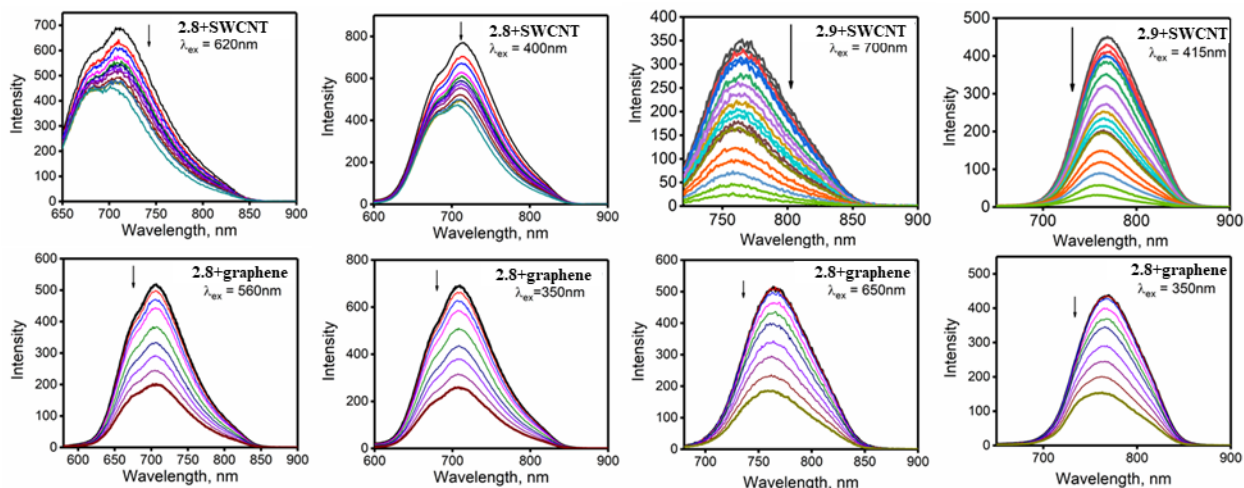


Figure 2.76: Changes in steady-state fluorescence of the BODIPYs **2.8** and **2.9** observed upon titrations with (6,5)-SWCNT (top) and graphene (bottom) in DCM/toluene. Excitation wavelengths are shown for each graph as insets.

In order to further investigate a potential electron-transfer processes in non-covalent assemblies formed between pyrene-BODIPYs **2.8** – **2.9** and  $C_{60}$  fullerene, we conducted time-resolved photophysical experiments. First, fluorescence lifetimes for organic pyrene-BODIPYs **2.8** and **2.9** were found in the typical for BODIPY chromophores range of  $\sim 2 - 4$  ns (Table 2.5). In contrary, the first excited state lifetime for organometallic BODIPY **2.10** is 268 ps, which is close to that observed earlier in vinylferrocene-BODIPY compounds.<sup>153</sup> Such lifetime shortening is indicative of the usual electron-transfer process from the ferrocene donor to the photoexcited BODIPY antennae. As a typical example, transient absorption spectra of pyrene-BODIPY **2.8** are shown in Figure 2.77. The transient absorption spectra of this compound are independent of the excitation wavelength and consists of two peaks at 510 and 760 nm in the visible region and two prominent peaks at 1100 and 1270 nm in the NIR region (Figure 2.77). In agreement with the steady-state fluorescence data, when excited at 650 nm, transient absorption spectra of the 1 : 10 mol/mol mixture of **2.8** and  $C_{60}$  is indistinguishable (both in spectra profiles and lifetimes) from the transient absorption spectra of BODIPY **2.8** (Figure 2.79). Since in majority of publications on similar systems, researchers use 390 – 410 nm excitation wavelength for investigation of the photoinduced electron-transfer from the photoexcited chromophore to the nano-carbon materials, we also studied the transient absorption spectra of the 1 : 10 mol/mol mixture of **2.8** and  $C_{60}$  upon 410 nm excitation wavelength (Figure 2.79). At first glance, there are two new features that appear in the

spectra. The first one is observed at 880 nm and the second one is located at 1000 nm. Careful analysis of the transient absorption data on **2.8** : C<sub>60</sub> mixture, however, is indicative of the superposition of the spectra of BODIPY **2.8** (Figure 2.77) and C<sub>60</sub> fullerene (Figure 2.78). In particular, transient absorption spectra of C<sub>60</sub> fullerene have both 880 and 980 nm bands accompanied by the prominent shoulder at 1100 nm. More importantly, excited state lifetimes for 880, 980, and 1100 nm signals of the pure C<sub>60</sub> fullerene are very close to those observed in **2.8** : C<sub>60</sub> mixture thus excluding any significant photoinduced electron-transfer from the BODIPY **2.8** to C<sub>60</sub> fullerene in solution. Thus, an extra caution should be taken when interpreting transient absorption data from covalent or non-covalent chromophore: fullerene assemblies that are photoexcited at ~400 nm wavelength as the excited state absorption of fullerene or its derivatives in the NIR region can be easily mistaken with the photoinduced electron-transfer from the photoexcited organic chromophore to fullerene acceptor.

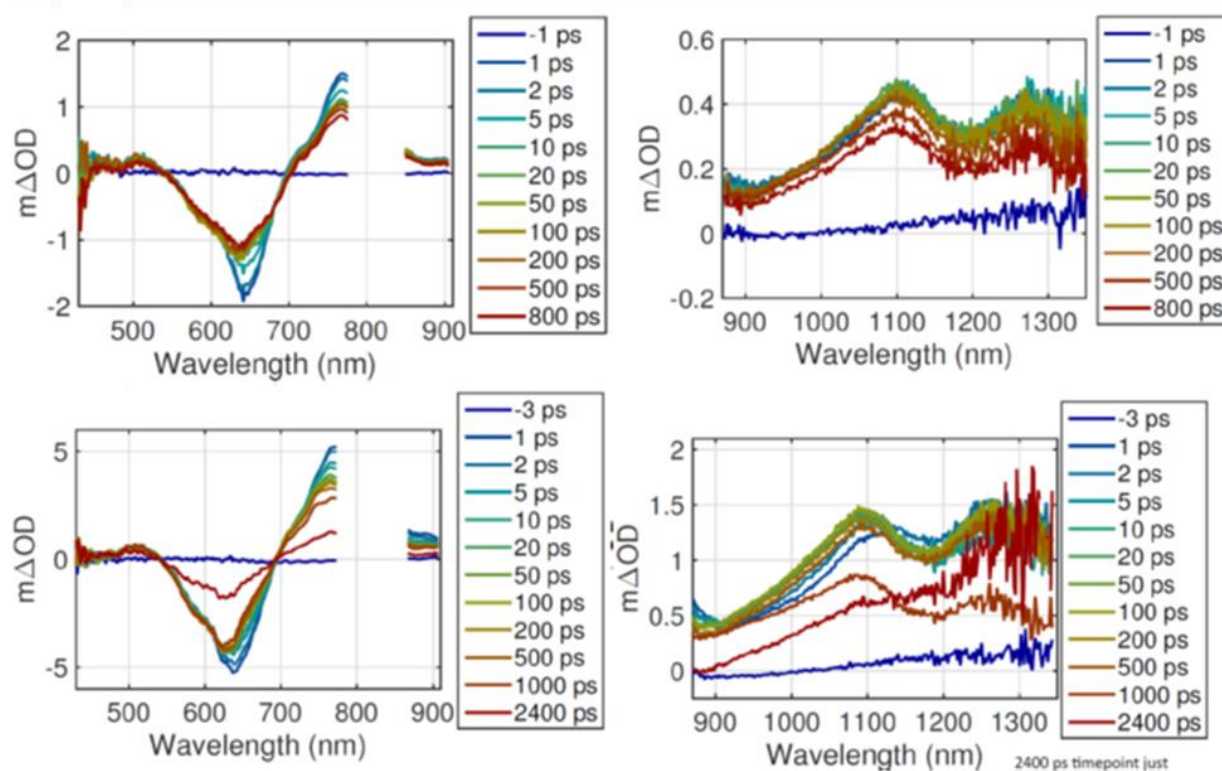


Figure 2.77: Transient absorption spectra of BODIPY **2.8**. Top: 560 nm pump. Bottom: 410 nm pump.

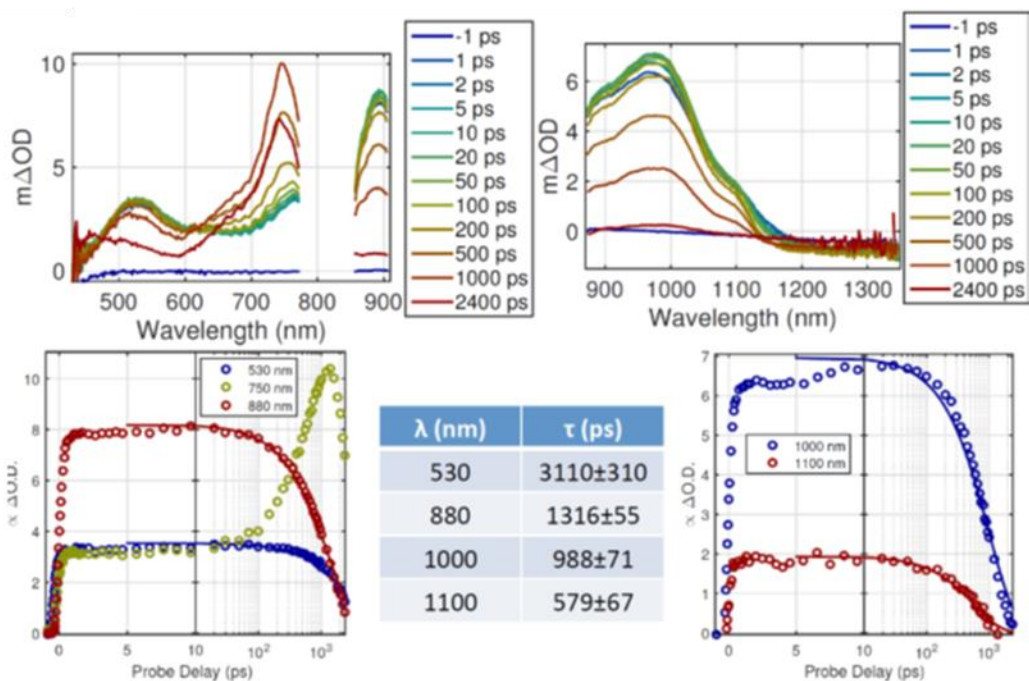


Figure 2.78: Transient absorption spectra of C<sub>60</sub> fullerene with 410 nm pump.

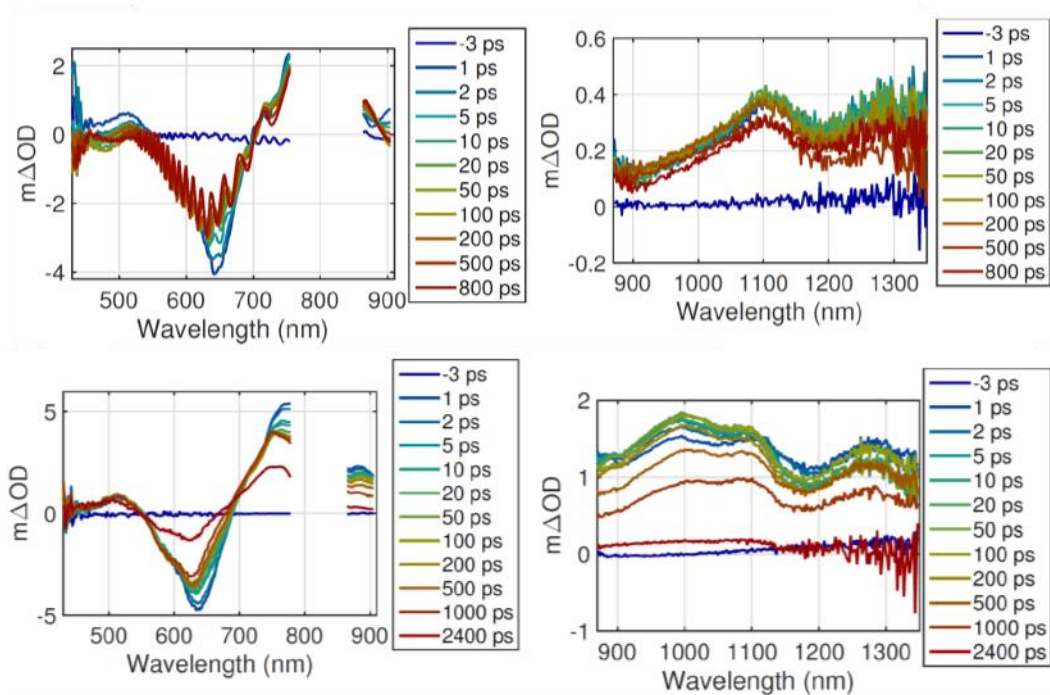


Figure 2.79: Transient absorption spectra of BODIPY **2.8** mixture with C<sub>60</sub> (1:10 mol/mol) pumped at 560 (top) and 410 nm (bottom).

## Experimental Section

**Reagents and materials.** Solvents were purified using standard approaches: toluene and THF were dried over sodium metal, DCM and chloroform were dried over calcium hydride. Fullerenes C<sub>60</sub> and C<sub>70</sub>, (6,5)-SWCNT (95% purity), and graphene were purchased from Sigma Aldrich, BODIPY derivative **2.3a**,<sup>216</sup> Dimethyl BODIPY derivative **1.7**,<sup>242</sup> acetyl ferrocene,<sup>217</sup> chalcones **2.3a**,<sup>218</sup> **2.3b**,<sup>219</sup> **2.3c**,<sup>220</sup> and **2.3d**<sup>221</sup> were prepared as described earlier. SWCNT were additionally purified following the literature procedure.<sup>222</sup>

**Spectroscopy Measurements.** Jasco-720 and Agilent spectrophotometers were used to collect UV-Vis data. Fluorescence spectra were recorded on a Cary Eclipse spectrometer. Electrochemical cyclic voltammetry (CV) and differential pulse voltammetry (DPV) measurements were conducted using a CH Instruments electrochemical analyser utilizing a three-electrode scheme with platinum working, auxiliary and Ag/AgCl reference electrodes. DCM was used as solvents and 0.1 M solution of tetrabutylammonium perchlorate (TBAP) or 0.05M tetrabutylammonium tetrakis(pentafluorophenyl)borate (TFAB) were used as supporting electrolytes. In all cases, experimental redox potentials were corrected using decamethylferrocene (Fc\*H) as an internal standard. NMR spectra were recorded on a Varian INOVA instrument with a 500 MHz frequency for protons and 125 MHz frequency for carbons and on a Bruker Avance instrument with a 300 MHz frequency for protons and 75 MHz frequency for carbons. Chemical shifts are reported in parts per million (ppm) and referenced to tetramethylsilane (Si(CH<sub>3</sub>)<sub>4</sub>) as an internal standard. <sup>13</sup>C NMR spectra for compounds **2.4a-d** were not recorded due to the low solubility. High-resolution mass spectra of compounds **2.4a-e**, **2.5a-e**, and **2.8-2.10** were recorded using a Bruker micrOTOF-QIII.

Fluorescence lifetimes were measured using time correlated single photon counting (TCSPC). Samples in a 1 cm quartz cuvette were excited with a 650 nm, 40 MHz diode laser (Driver: Picoquant PDL 800-B; Head: Picoquant LDH-P-470). Emission was directed through a double monochromator (Jobin-Yvon DH-10), detected using an avalanche photodiode (Picoquant MPD PDM), and time resolved using a Time-Harp 300 TCSPC system. The instrument response of the system is approximately 500 ps FWHM.<sup>244</sup> Non-emissive samples were measured with pump-probe spectroscopy. A home-built laser system consisting of a Ti:sapphire oscillator (powered by a Spectra Physics Millennia Pro) and regenerative amplifier (powered by a Spectra

Physics Empower 15) generated 75 fs (FWHM), 0.8-1.0 mJ, 815 nm pulses at a repetition rate of 1 kHz. A portion of this light was directed into a home-built noncollinear optical parametric amplifier (NOPA) to create excitation pulses at 640 nm, 650 nm and 920 nm. Continuum probe pulses of 420-750 nm and 850-1400 nm were created by focusing a small fraction of the 815 nm light (~20  $\mu$ W) into a 2 mm sapphire window and Yttrium Aluminium Garnet (YAG) crystal, respectively. The excitation light was polarized at 54.7 degrees relative to the probe polarization (the magic angle) to isolate the isotropic dynamics of the excited state. Time delay between the excitation and probe pulses was controlled by a mechanical delay stage (Newport UTM150PP.1). Pump and probe pulses were focused and spatially overlapped in 1 mm quartz cuvette containing the sample. The probe beam emerging from the sample was collimated, directed through a monochromator and detected on an array. A Princeton Instruments SP2150i monochromator (150 lines/mm, 500 nm blaze) with an attached 256-pixel diode array (Hamamatsu S3902-256Q) was used for visible light. A Princeton Instruments SP2150 monochromator (150 lines/mm, 1200nm blaze) with an attached 256 linear pixel InGaAs diode array (Hamamatsu G9213-256S)) was used for infra-red light. The pump beam was modulated at half the laser repetition rate while the probe beam was measured for every laser pulse and the change in optical density,  $\Delta$ OD, induced by the pump was calculated and recorded for each pulse pair. Typically, 20,000-40,000 pulse pairs were averaged for each time point presented in the pump-probe data. The dependence of the  $\Delta$ OD signal for pump pulse energies between 20-100 nJ was found to be linear. Data shown was collected with pump pulse energies of 60 nJ and 120 nJ. Samples had an optical density of <0.25 at the excitation wavelength and were held in a 1 mm path length cell during data collection. Absorption spectra taken before and after the pump probe experiments were indistinguishable, indicating no evidence of sample degradation.

**Computational Details.** The starting geometries of compounds **2.5a-2.5e**, **2.6**, **2.7-2.10** were optimized using a B3LYP exchange-correlation functional.<sup>223,224</sup> B3LYP exchange-correlation functional was found to result in good agreement between calculated and experimentally determined bond distances and angles in ferrocene-containing compounds.<sup>225-230</sup> Energy minima in optimized geometry was confirmed by the frequency calculations (absence of the imaginary frequencies). Solvent effect was calculated using the polarized continuum model (PCM).<sup>231</sup> In all calculations, DCM was used as the solvent. In PCM-TDDFT calculation, the first 50 states were

calculated. Full-electron Wachter's basis set<sup>232</sup> was utilized for iron atoms, while all other atoms were modelled using 6-311G(d)<sup>233</sup> basis set. Gaussian 09 software was used in all calculations.<sup>234</sup> QMForge program was used for molecular orbital analysis.<sup>235</sup> In DFT calculations on the formation energies of pyrene-pyrene, pyrene-C<sub>60</sub>, pyrene-(6,5)-SWCNT, and pyrene-graphene non-covalent complexes long-range corrected CAM-B3LYP and LC-wPBE exchange-correlation functionals and several functionals with dispersion correction (wB97, wB97-X2 CAM-B3LYP-D3, and LC-wPBE-D3) have been tested. For pyrene-pyrene, pyrene-C<sub>60</sub>, pyrene-(6,5)-SWCNT, and pyrene-graphene systems, 6-31+G(d) basis set was used for all atoms. (6,5)-SWCNT was modelled by the 134 atoms truncated geometry with terminal hydrogen atoms located at the edges. The length of such (6,5)-SWCNT model was 13.568 Å, which is sufficient enough for an accurate descriptions of pyrene-(6,5)-SWCNT interactions. Graphene was modelled by the repeated translation of the six-membered carbon units (54 total carbon atoms). The terminal carbon atoms in graphene model were terminated by hydrogens. The final model had a 14.48x14.48 Å size, which is sufficient to model pyrene-graphene interactions.

**X-ray crystallography.** Single crystals of aza-BODIPY **2.4e**, **2.5a**, **2.5d**, **2.5e**, **2.5b·C<sub>60</sub>**, **2.5d·2C<sub>60</sub>**, **2.8**, and **2.9** complex suitable for X-ray crystallographic analysis were obtained by slow evaporation from their DCM (**2.4e**, **2.5a**, **2.5d**, and **2.5e**) or DCM/toluene (**2.5b·C<sub>60</sub>**, and **2.5d·2C<sub>60</sub>**) solutions. X-ray diffraction data for **2.5a** and **2.5b·C<sub>60</sub>** were collected on Rigaku RAPID II Image Plate system using graphite-monochromated Cu-K $\alpha$  radiation ( $\lambda = 1.54187$  Å) at 123 K. Data for **2.5d**, **2.5e** and **2.5d·2C<sub>60</sub>** compounds were obtained on a Bruker D8 QUEST ECO CMOS diffractometer using graphite-monochromated Mo-K $\alpha$  radiation ( $\lambda = 0.71073$  Å) at 150 K. Data for **2.4e** were obtained on a Bruker APEX-II diffractometer using graphite-monochromated Cu-K $\alpha$  radiation ( $\lambda = 1.54187$  Å) at 150 K. All diffractometer manipulations, including data collection, integration and scaling were carried out using the Bruker APEX3 software suite. Absorption corrections were applied using SADABS. The structures were solved by direct methods<sup>236</sup> (**2.5a**, **2.5d**, **2.5e**, **2.5d·2C<sub>60</sub>**) or by the SuperFlip method<sup>237,238</sup> (**2.5b·C<sub>60</sub>**) and refined by full-matrix least-squares refinement using Crystals for Windows<sup>239</sup> (**2.5a**) or SHELXL-2014/7<sup>240,241</sup> (**2.5b·C<sub>60</sub>**, **2.5d**, **2.5e**, **2.5d·2C<sub>60</sub>**) programs. No obvious missed symmetry was reported by PLATON. All non-hydrogen atoms were refined with anisotropic thermal parameters. Hydrogen atoms were placed in idealized positions and refined using a riding model.

The solvent toluene molecule in **2.5b**•**C**<sub>60</sub> complex was found to be disordered over two sites. In **2.5d**•**2C**<sub>60</sub>, disorder in one of two C<sub>60</sub> molecules in the asymmetric unit could not be satisfactorily modelled, leading to higher than desirable thermal parameters for the carbon sites in this unit. “Flip”-type disorder was observed for thiophenyl side chains in **2.5d** and **2.5d**•**2C**<sub>60</sub>, wherein different types of atoms (sulfur and carbon) occupy positions that are close to each other. This disorder influences the thermal parameters of the respective sulfur and carbon atoms, which were therefore equated for each pair of disordered atoms in the disordered rings.

Crystal data for **2.4e** C<sub>60</sub> H<sub>39</sub> Fe<sub>2</sub> N<sub>3</sub>: MW = 913.64, monoclinic, space group *P*2<sub>1</sub>/*n*, *a* = 7.3960(4), *b* = 45.697(3), *c* = 12.5412(7) Å,  $\alpha = 90^\circ$ ,  $\beta = 94.623(5)^\circ$ ,  $\gamma = 90^\circ$ , *V* = 4224.82 Å<sup>3</sup>, *Z* = 4,  $\mu = 5.864 \text{ mm}^{-1}$ , 35657 reflections, (3810 *I* > 2 $\sigma$ (*I*)), 2 $\theta_{\text{max}}$  = 125.54; final *R*<sub>1</sub> = 0.0845, *R*<sub>w</sub> (all) = 0.1494. Crystal data for **2.5a** C<sub>52</sub>H<sub>30</sub>B<sub>1</sub>F<sub>2</sub>N<sub>3</sub>: MW = 745.64, monoclinic, space group *P*2<sub>1</sub>/*c*, *a* = 12.8265(2), *b* = 20.1233(4), *c* = 14.4166(10) Å,  $\alpha = 90^\circ$ ,  $\beta = 105.552(7)^\circ$ ,  $\gamma = 90^\circ$ , *V* = 3584.9(2) Å<sup>3</sup>, *Z* = 4,  $\mu = 0.697 \text{ mm}^{-1}$ , 12889 reflections, (1665 *I* > 2 $\sigma$ (*I*)), 2 $\theta_{\text{max}}$  = 58.935; final *R*<sub>1</sub> = 0.0782, *R*<sub>w</sub> (all) = 0.1874. Crystal data for **2.5b**•**C**<sub>60</sub>: C<sub>119</sub>H<sub>36</sub>B<sub>1</sub>O<sub>2</sub>N<sub>3</sub>: MW = 1458.28, monoclinic, space group *C*<sub>2</sub>/*c*, *a* = 19.7995(4), *b* = 47.3003(9), *c* = 14.7939(10) Å,  $\alpha = 90^\circ$ ,  $\beta = 106.263(7)^\circ$ ,  $\gamma = 90^\circ$ , *V* = 13300.4(11) Å<sup>3</sup>, *Z* = 8,  $\mu = 0.677 \text{ mm}^{-1}$ , 6927 reflections, (3569 *I* > 2 $\sigma$ (*I*)), 2 $\theta_{\text{max}}$  = 50.427; final *R*<sub>1</sub> = 0.1203, *R*<sub>w</sub> (all) = 0.2665. Crystal data for **2.5d** C<sub>49</sub>H<sub>28</sub>BCl<sub>2</sub>F<sub>2</sub>N<sub>3</sub>S<sub>2</sub>: M 842.57, monoclinic, space group *P*2<sub>1</sub>/*c*, *a* = 29.1647(15), *b* = 7.7468(3), *c* = 33.4875(16) Å,  $\alpha = 90^\circ$ ,  $\beta = 96.487(3)^\circ$ ,  $\gamma = 90^\circ$ , *V* = 7517.5(6) Å<sup>3</sup>, *Z* = 8,  $\mu = 0.337 \text{ mm}^{-1}$ , 12828 reflections, (6009 *I* > 2 $\sigma$ (*I*)), 2 $\theta_{\text{max}}$  = 49.556; final *R*<sub>1</sub> = 0.0966, *wR*<sub>2</sub> (all) = 0.1880. Crystal data for **2.5d**•**C**<sub>60</sub>: C<sub>169</sub>H<sub>26</sub>BF<sub>2</sub>N<sub>3</sub>OS<sub>2</sub>: MW = 2226.86, triclinic, space group *P*-1, *a* = 13.2973(10), *b* = 16.7957(12), *c* = 22.0745(16) Å,  $\alpha = 101.739(4)^\circ$ ,  $\beta = 105.539(3)^\circ$ ,  $\gamma = 99.699(4)^\circ$ , *V* = 4518.7(6) Å<sup>3</sup>, *Z* = 2,  $\mu = 0.143 \text{ mm}^{-1}$ , 15469 reflections, (7504 *I* > 2 $\sigma$ (*I*)), 2 $\theta_{\text{max}}$  = 49.658; final *R*<sub>1</sub> = 0.1075, *wR*<sub>2</sub> (all) = 0.2836. Crystal data for **2.5e**: C<sub>60</sub>H<sub>38</sub>BF<sub>2</sub>Fe<sub>2</sub>N<sub>3</sub>: MW = 961.44, monoclinic, space group *P*2<sub>1</sub>/*c*, *a* = 21.490(2), *b* = 9.7500(10), *c* = 19.997(2) Å,  $\alpha = 90^\circ$ ,  $\beta = 96.947(4)^\circ$ ,  $\gamma = 90^\circ$ , *V* = 4159.2(7) Å<sup>3</sup>, *Z* = 4,  $\mu = 0.756 \text{ mm}^{-1}$ , 7127 reflections, (4418 *I* > 2 $\sigma$ (*I*)), 2 $\theta_{\text{max}}$  = 49.514; final *R*<sub>1</sub> = 0.1036, *wR*<sub>2</sub> (all) = 0.2078. crystal data for BODIPY **2.8**: *a* = 11.8942(2) Å, *b* = 24.6471(4) Å, *c* = 14.7953(10) Å,  $\alpha = 90^\circ$ ,  $\beta = 110.060(8)^\circ$ ,  $\gamma = 90^\circ$ , *V* = 4074.2(3) Å<sup>3</sup>, cell symmetry is monoclinic, space group *P*2<sub>1</sub>/*n*, *Z* = 4, total reflections: 22435, goodness of fit = 0.9563, *wR*(all) = 0.2312, *R*(*I* > 2 $\sigma$ (*I*)) = 0.1027 (CCDC 1825658). crystal data for BODIPY **2.9**: *a* = 12.1367(6) Å, *b* = 14.2874(6) Å, *c* = 14.5167(10) Å,

$\alpha = 112.536(8)^\circ$ ,  $\beta = 98.382(7)^\circ$ ,  $\gamma = 90.203(6)^\circ$ ,  $V = 2295.30(16) \text{ \AA}^3$ , cell symmetry is triclinic, space group  $P-1$ ,  $Z = 2$ , total reflections: 20401, goodness of fit = 1.0069,  $wR(\text{all}) = 0.2016$ ,  $R(I > 2\sigma I) = 0.0628$  (CCDC 1825657) Additional crystallographic information for all compounds are accessible from the Cambridge Structural Database: CCDC-1582584 (**2.5a**), CCDC-1582586 (**2.5d**), CCDC-1582588 (**2.5e**), CCDC-1582585 (**2.5b·C<sub>60</sub>**), and CCDC-1582587 (**2.5d·2C<sub>60</sub>**).

## EXPERIMENTAL PROCEDURE

**Compound 2.2e.** To the solution of acetyl ferrocene (8.7 mmol, 2000 mg) and pyrenecarboxaldehyde (8.7 mmol, 2017 mg) in dry DMF (20 mL) sodium hydride (8.7 mmol, 209 mg) was added portion wise. The resulting mixture was stirred for 5 min at room temperature and then quenched with iced water (20 mL). The resulting precipitate was filtered, washed with water and dried. Yield 3600 mg (90 %).  $^1\text{H NMR}$  (300 MHz,  $\text{CDCl}_3$ )  $\delta$  8.99 (d,  $J_{H,H} = 15.6$  Hz, 1H), 8.64 (d,  $J_{H,H} = 9.3$  Hz, 1H), 8.44 (d,  $J_{H,H} = 8.0$  Hz, 1H), 8.26 – 8.21 (m, 4H), 8.16 – 8.02 (m, 3H), 7.44 (d,  $J_{H,H} = 15.6$  Hz, 1H), 5.02 – 5.01 (m, 2H), 4.65 – 4.64 (m, 2H), 4.28 (s, 5H);  $^{13}\text{C NMR}$  {1H} (75 MHz,  $\text{CDCl}_3$ )  $\delta$  137.73, 132.79, 131.53, 130.98, 130.38, 129.38, 128.72, 128.66, 127.50, 126.46, 126.07, 125.95, 125.49, 125.16, 124.24, 123.01, 81.03, 73.00, 70.32, 69.99.

**Compound 2.3a.** To the solution of compound **2.2a** (2.69 mmol, 896 mg) in nitromethane (10 ml) DBU (2.69 mmol, 410 mg) was added. The resulting mixture was refluxed for 5 min. The resulting colorless solution was cooled down to room temperature, diluted with water (10 mL), then methanol was added until white solid precipitated. The product was collected by filtration yielding 990 mg (93 %) of **2.3a**.  $^1\text{H NMR}$  (500 MHz,  $\text{CDCl}_3$ )  $\delta$  8.51 (d,  $J_{H,H} = 9.4$  Hz, 1H), 8.23 – 8.20 (m, 3H), 8.17 (d,  $J_{H,H} = 8.0$  Hz, 1H), 8.09 (d,  $J_{H,H} = 11.6$  Hz, 1H), 8.05 – 8.01 (m, 2H), 7.95 – 7.93 (m, 3H), 7.58 – 7.55 (m, 1H), 7.46 – 7.43 (m, 2H), 5.52 – 5.47 (m, 1H), 5.08 (dd,  $J_{H,H} = 12.6, 7.0$  Hz, 2H), 3.76 (dd,  $J_{H,H} = 6.8, 3.1$  Hz, 2H);  $^{13}\text{C}$  {1H} NMR (75 MHz,  $\text{CDCl}_3$ )  $\delta$  197.05, 136.49, 133.74, 132.61, 131.51, 130.96, 130.87, 128.89, 128.78, 128.21, 127.90, 127.39, 126.36, 125.72, 125.49, 125.26, 122.04, 79.59, 42.15.

**Compound 2.3b.** To the solution of compound **2.2b** (4.02 mmol, 1400 mg) in nitromethane (15 mL) DBU (4.02 mmol, 611 mg) was added. The resulting mixture was stirred for 10 min at room temperature. Then the resulting colorless solution was acidified with acetic acid (1 mL) and diluted

with water. The product was extracted with chloroform. The organic layer was washed with water (2×40 mL), brine solution, dried over MgSO<sub>4</sub>, and evaporated to dryness yielding 1478 mg (89 %) of pure **2.3b**. <sup>1</sup>H NMR (500 MHz, CDCl<sub>3</sub>) δ 11.85 (s, 1H), 8.43 (d, *J*<sub>H,H</sub> = 9.3 Hz, 1H), 8.18 – 8.14 (m, 3H), 8.11 (d, *J*<sub>H,H</sub> = 8.0 Hz, 1H), 8.03 (d, *J*<sub>H,H</sub> = 8.9 Hz, 1H), 7.99 – 7.95 (m, 2H), 7.86 (d, *J*<sub>H,H</sub> = 8.0 Hz, 1H), 7.70 (dd, *J*<sub>H,H</sub> = 8.1, 1.5 Hz, 1H), 7.42 – 7.38 (m, 1H), 6.89 – 6.88 (m, 1H), 6.83 – 6.80 (m, 1H), 5.44 – 5.39 (m, 1H), 4.99 (dd, *J*<sub>H,H</sub> = 11.8, 6.5 Hz, 2H), 3.78 (dd, *J*<sub>H,H</sub> = 17.8, 6.5 Hz, 2H); <sup>13</sup>C{<sup>1</sup>H} NMR (75 MHz, CDCl<sub>3</sub>) δ 202.73, 162.62, 136.99, 132.05, 131.47, 131.01, 130.79, 129.66, 128.87, 128.78, 127.97, 127.34, 126.40, 125.80, 125.54, 125.42, 125.26, 124.86, 123.31, 121.83, 119.25, 119.18, 118.87, 79.51, 41.53, 29.85.

**Compound 2.3c.** To the solution of compound **2.2c** (1.82 mmol, 660 mg) in nitromethane (10 mL) DBU (1.82 mmol, 276 mg) was added. The resulting mixture was stirred for 10 min at room temperature. Then the resulting colorless solution was diluted with water and the product was extracted with chloroform. The organic layer was dried over MgSO<sub>4</sub>, and evaporated to dryness yielding 694 mg (90 %) of pure **2.3c**. <sup>1</sup>H NMR (300 MHz, CDCl<sub>3</sub>) δ 8.52 (d, *J*<sub>H,H</sub> = 9.4 Hz, 1H), 8.23 – 8.14 (m, 4H), 8.00 – 8.004 (m, 3H), 7.96 – 7.91 (m, 3H), 6.93 – 6.88 (m, 2H), 5.52 – 5.43 (m, 1H), 5.09 (dd, *J*<sub>H,H</sub> = 12.6, 6.8 Hz, 2H), 3.85 (s, 3H), 3.70 – 3.67 (m, 2H); <sup>13</sup>C{<sup>1</sup>H} NMR (75 MHz, CDCl<sub>3</sub>) δ 195.48, 163.99, 132.84, 131.49, 130.88, 130.86, 130.51, 129.57, 128.83, 128.70, 127.83, 127.39, 126.32, 125.66, 125.44, 125.23, 124.93, 79.60, 55.68, 41.77.

**Compound 2.3d.** To the solution of compound **2.2d** (3.50 mmol, 1193 mg) in nitromethane (15 mL) DBU (3.50 mmol, 532 mg) was added. The resulting mixture was stirred for 10 min at room temperature. Then the resulting colorless solution was diluted with water and the product was extracted with chloroform. The organic layer was dried over MgSO<sub>4</sub>, and evaporated to dryness yielding 1281 mg (91 %) of pure **2.3d**. <sup>1</sup>H NMR (300 MHz, CDCl<sub>3</sub>) δ 8.50 (d, *J*<sub>H,H</sub> = 9.4 Hz, 1H), 8.23 – 8.15 (m, 4H), 8.09 – 8.00 (m, 3H), 7.95 (d, *J*<sub>H,H</sub> = 8.0 Hz, 1H), 7.71 – 7.70 (m, 1H), 7.64 – 7.62 (m, 1H), 7.11 – 7.08 (m, 1H), 5.50 – 5.41 (m, 1H), 5.13 (dd, *J*<sub>H,H</sub> = 12.6, 6.9 Hz, 2H), 3.74 – 3.70 (m, 2H); <sup>13</sup>C{<sup>1</sup>H} NMR (75 MHz, CDCl<sub>3</sub>) δ 189.85, 143.61, 134.48, 132.42, 132.28, 131.47, 130.96, 130.83, 128.82, 128.78, 128.37, 127.90, 127.36, 126.35, 125.72, 125.49, 125.41, 125.24, 124.89, 123.43, 121.97, 79.40, 42.70.

**Compound 2.3e.** To the solution of compound **2.2e** (8.10 mmol, 3580 mg) in nitromethane (25 mL) DBU (8.10 mmol, 1230 mg) was added. The resulting mixture was refluxed for 10 min. The resulting colorless solution was cooled down to room temperature, diluted with water (20 mL), the product was extracted with chloroform, washed with water, brine, dried over Na<sub>2</sub>SO<sub>4</sub> and evaporated to dryness. Yield 3260 mg (80 %) of **2.3e**. <sup>1</sup>H NMR (300 MHz, CDCl<sub>3</sub>) δ 8.57 (d, *J*<sub>H,H</sub> = 9.4 Hz, 1H), 8.26 – 8.19 (m, 4H), 8.09 – 7.96 (m, 4H), 5.48 – 5.39 (m, 1H), 5.12 (dd, *J*<sub>H,H</sub> = 12.6, 7.0 Hz, 2H), 4.77 – 4.73 (m, 2H), 4.49 – 4.48 (m, 2H), 4.01 (s, 5H), 3.57 (dd, *J*<sub>H,H</sub> = 17.5, 6.3 Hz, 2H); <sup>13</sup>C{<sup>1</sup>H} NMR (75 MHz, CDCl<sub>3</sub>) δ 201.05, 132.89, 131.53, 130.97, 130.91, 128.95, 128.77, 127.90, 127.41, 126.36, 125.71, 125.49, 125.18, 124.97, 122.21, 79.61, 78.51, 72.73, 72.69, 69.95, 69.41, 43.11.

#### **General procedure for the synthesis of compounds 2.4a-e:**

The mixture of appropriate nitrobutanone derivative **2.3a-d** and ammonium acetate (50 eq.) was refluxed in ethanol or *n*-butanol (30 mL) for 12-24 h. After cooling to room temperature, the precipitate was filtered, washed with ethanol and dried.

**Compound 2.4a.** The mixture was refluxed for 24 h. Yield 280 mg (35 %). <sup>1</sup>H NMR (500 MHz, CDCl<sub>3</sub>) δ 8.53 (d, *J*<sub>H,H</sub> = 9.4 Hz, 2H), 8.18 (d, *J*<sub>H,H</sub> = 7.6 Hz, 2H), 8.15 – 8.13 (m, 2H), 8.10 – 8.06 (m, 6H), 7.98 – 7.95 (m, 6H), 7.81 (d, *J*<sub>H,H</sub> = 8.9 Hz, 2H), 7.69 (d, *J*<sub>H,H</sub> = 7.6 Hz, 2H), 7.63 – 7.60 (m, 4H), 7.55 – 7.52 (m, 2H), 7.38 (s, 2H); HRMS (APCI positive) calcd for C<sub>52</sub>H<sub>31</sub>N<sub>3</sub> [M + H]<sup>+</sup>: 698.2591, found 698.2575.

**Compound 2.4b.** The mixture was refluxed for 12 h. Yield 330 mg (25 %). <sup>1</sup>H NMR (300 MHz, DMSO-d<sub>6</sub>) δ 8.41 (d, *J*<sub>H,H</sub> = 9.3 Hz, 1H), 8.26 – 8.25 (m, 2H), 8.22 – 8.18 (m, 4H), 8.12 – 8.05 (m, 8H), 7.81 (d, *J*<sub>H,H</sub> = 9.1 Hz, 2H), 7.75 (s, 1H), 7.69 – 7.68 (m, 1H), 7.43 – 7.40 (m, 2H), 7.21 – 7.19 (m, 2H), 7.08 – 7.05 (m, 2H); HRMS (APCI positive) calcd for C<sub>52</sub>H<sub>31</sub>N<sub>3</sub>O<sub>2</sub> [M + H]<sup>+</sup>: 730.2489, found 730.2459.

**Compound 2.4c.** The mixture was refluxed for 12 h. Yield 182 mg (27 %). <sup>1</sup>H NMR (300 MHz, CDCl<sub>3</sub>) δ 8.54 (d, *J*<sub>H,H</sub> = 9.3 Hz, 2H), 8.19 (d, *J*<sub>H,H</sub> = 7.9 Hz, 2H), 8.14 – 8.11 (m, 2H), 8.07 – 7.93 (m, 12H), 7.80 (d, *J*<sub>H,H</sub> = 8.9 Hz, 2H), 7.68 (d, *J*<sub>H,H</sub> = 7.9 Hz, 2H), 7.29 (s, 2H), 7.14 (d, *J*<sub>H,H</sub> = 8.7

Hz, 4H), 3.96 (s, 6H); HRMS (APCI positive) calcd for C<sub>54</sub>H<sub>35</sub>N<sub>3</sub>O<sub>2</sub> [M + H]<sup>+</sup>: 758.2802, found 758.2782.

**Compound 2.4d.** The mixture was refluxed for 20 h in *n*-butanol. Yield 166 mg (26 %). <sup>1</sup>H NMR (300 MHz, CDCl<sub>3</sub>) δ 8.51 (d, *J*<sub>H,H</sub> = 9.2 Hz, 2H), 8.16 – 8.12 (m, 7H), 8.08 – 8.03 (m, 4H), 7.99 – 7.95 (m, 7H), 7.80 – 7.77 (m, 2H), 7.71 – 7.70 (m, 1H), 7.68 – 7.65 (m, 2H), 7.60 – 7.58 (m, 1H); HRMS (APCI positive) calcd for C<sub>48</sub>H<sub>27</sub>N<sub>3</sub>S<sub>2</sub> [M + H]<sup>+</sup>: 710.1719, found 710.1698.

**Compound 2.4e.** The mixture was refluxed for 24 h in *n*-butanol under argon atmosphere. After cooling to room temperature, the product was filtered, washed with ethanol, dried. The crude product was purified by column chromatography on Al<sub>2</sub>O<sub>3</sub> using toluene as the solvent. Dark violet fraction was collected, evaporated to dryness yielding 260 mg (15 %) of pure **2.4e**. <sup>1</sup>H NMR (300 MHz, CDCl<sub>3</sub>) δ 8.56 (d, *J*<sub>H,H</sub> = 9.3 Hz, 2H), 8.23 (d, *J*<sub>H,H</sub> = 8.0 Hz, 2H), 8.14 (d, *J*<sub>H,H</sub> = 7.4 Hz, 2H), 8.08 (d, *J*<sub>H,H</sub> = 6.9 Hz, 2H), 7.98 – 7.93 (m, 6H), 7.83 (d, *J*<sub>H,H</sub> = 8.9 Hz, 2H), 7.72 (d, *J*<sub>H,H</sub> = 8.0 Hz, 2H), 6.98 (s, 2H), 4.99 (t, *J*<sub>H,H</sub> = 1.9 Hz, 4H), 4.68 (t, *J*<sub>H,H</sub> = 1.9 Hz, 4H), 4.33 (s, 10H); <sup>13</sup>C NMR (75 MHz, CDCl<sub>3</sub>) δ 156.45, 150.41, 140.97, 131.48, 131.08, 130.65, 129.75, 129.72, 129.31, 127.59, 127.35, 127.02, 126.25, 125.84, 125.05, 125.01, 124.95, 124.72, 124.28, 119.38, 71.48, 70.52, 69.81, 67.92; HRMS (APCI positive) calcd for C<sub>60</sub>H<sub>39</sub>Fe<sub>2</sub>N<sub>3</sub> [M + H]<sup>+</sup>: 914.1919, found 914.1889.

**Compound 2.5a.** The solution of compound **2.4a** (0.143 mmol, 100mg) in DCM (10 mL) was treated with DIPEA (0.717 mmol, 92 mg) and stirred for 10 min at room temperature. Then the solution of BF<sub>3</sub>·Et<sub>2</sub>O (1.43 mmol, 203 mg) was added dropwise and the mixture was stirred overnight at room temperature. Then the reaction mixture was slowly quenched with methanol (10 mL) and the resulting precipitate was filtered yielding 87 mg (81%) of pure dye **2.5a**. <sup>1</sup>H NMR (500 MHz, CDCl<sub>3</sub>) δ 8.58 (d, *J*<sub>H,H</sub> = 9.3 Hz, 2H), 8.26 (d, *J*<sub>H,H</sub> = 8.0 Hz, 2H), 8.21 – 8.20 (m, 4H), 8.18 – 8.16 (m, 4H), 8.09 (d, *J*<sub>H,H</sub> = 9.3 Hz, 2H), 8.04 – 8.00 (m, 4H), 7.90 – 7.87 (m, 4H), 7.58 – 7.55 (m, 6H), 7.27 (m, 2H); <sup>13</sup>C NMR (75 MHz, CDCl<sub>3</sub>) δ 131.87, 131.79, 131.42, 131.20, 130.95, 129.97, 129.84, 128.91, 128.44, 128.13, 127.50, 126.24, 125.78, 125.54, 125.44, 124.79, 124.55; HRMS (APCI positive) calcd for C<sub>52</sub>H<sub>30</sub>BF<sub>2</sub>N<sub>3</sub> [M + H]<sup>+</sup>: 746.2560, found 746.2433.

**Compound 2.5b.** The solution of compound **2.4b** (0.137 mmol, 100mg) in dry THF (10 mL) was treated with DIPEA (2.05 mmol, 264 mg) and stirred for 10 min at room temperature. Then the solution of  $\text{BF}_3 \cdot \text{Et}_2\text{O}$  (2.74 mmol, 390 mg) was added dropwise and the mixture was stirred overnight at room temperature. Then the reaction mixture was slowly quenched with water (20 mL), product was extracted with EtOAc, dried over  $\text{Na}_2\text{SO}_4$ , and evaporated to dryness. The crude product was purified by column chromatography on silica gel using toluene as a solvent yielding 20 mg (20 %) of pure dye **2.5b**.  $^1\text{H}$  NMR (500 MHz,  $\text{CDCl}_3$ )  $\delta$  8.68 (d,  $J_{H,H} = 9.3$  Hz, 2H), 8.34 (d,  $J_{H,H} = 8.0$  Hz, 2H), 8.22 – 8.18 (m, 4H), 8.16 (d,  $J_{H,H} = 9.3$  Hz, 2H), 8.06 – 7.94 (m, 10H), 7.52 – 7.58 (m, 2H), 7.44 (s, 2H), 7.22 – 7.15 (m, 4H);  $^{13}\text{C}$  NMR (75 MHz,  $\text{CDCl}_3$ )  $\delta$  156.08, 142.96, 133.74, 131.82, 131.45, 131.00, 129.79, 129.70, 129.11, 128.35, 128.04, 127.72, 127.51, 126.91, 126.24, 125.73, 125.55, 125.33, 125.22, 124.88, 124.77, 121.33, 120.52, 118.35; HRMS (APCI positive) calcd for  $\text{C}_{52}\text{H}_{28}\text{BN}_3\text{O}_2$   $[\text{M} + \text{H}]^+$ : 738.2334, found 738.2303.

**Compound 2.5c.** The solution of compound **2.4c** (0.132 mmol, 100mg) in DCM (10 mL) was treated with DIPEA (1.32 mmol, 170 mg) and stirred for 10 min at room temperature. Then the solution of  $\text{BF}_3 \cdot \text{Et}_2\text{O}$  (1.98 mmol, 281 mg) was added dropwise and the mixture was stirred overnight at room temperature. Then the reaction mixture was slowly quenched with methanol (10 mL) and the resulting precipitate was filtered yielding 90 mg (85%) of pure dye **2.5c**.  $^1\text{H}$  NMR (500 MHz,  $\text{CDCl}_3$ )  $\delta$  8.57 (d,  $J_{H,H} = 9.3$  Hz, 2H), 8.25 - 8.23 (m, 6H), 8.17 – 8.15 (m, 4H), 8.08 (d,  $J_{H,H} = 9.3$  Hz, 2H), 8.03 – 7.99 (m, 4H), 7.89 – 7.85 (m, 4H), 7.10 (d,  $J_{H,H} = 8.9$  Hz, 4H), 3.93 (s, 6H);  $^{13}\text{C}$  NMR (75 MHz,  $\text{CDCl}_3$ )  $\delta$  162.24, 132.01, 131.67, 131.42, 130.97, 129.86, 129.75, 128.24, 127.94, 127.88, 127.50, 126.16, 125.65, 125.31, 125.10, 124.81, 124.50, 124.32, 123.09, 114.58, 55.64; HRMS (APCI positive) calcd for  $\text{C}_{54}\text{H}_{34}\text{BF}_2\text{N}_3\text{O}_2$   $[\text{M} + \text{H}]^+$ : 806.2771, found 806.2694.

**Compound 2.5d.** The solution of compound **2.4d** (0.473 mmol, 336mg) in DCM (20 mL) was treated with DIPEA (4.73 mmol, 610 mg) and stirred for 10 min at room temperature. Then the solution of  $\text{BF}_3 \cdot \text{Et}_2\text{O}$  (9.46 mmol, 1.39 g) was added dropwise and the mixture was stirred overnight at room temperature. Then the reaction mixture was slowly quenched with water (20 mL), organic layer was washed with water, dried over  $\text{Na}_2\text{SO}_4$  and evaporated to dryness. The crude product was purified by column chromatography using chloroform as a solvent yielding 129

mg (36 %) of pure dye **2.5d**.  $^1\text{H}$  NMR (300 MHz,  $\text{CDCl}_3$ )  $\delta$  8.54 – 8.51 (m, 4H), 8.21 (d,  $J_{H,H} = 8.0$  Hz, 2H), 8.18 – 8.15 (m, 4H), 8.10 (d,  $J_{H,H} = 9.3$  Hz, 2H), 8.03 – 7.98 (m, 4H), 7.89 – 7.83 (m, 4H), 7.72 (dd,  $J_{H,H} = 5.0, 0.8$  Hz, 2H), 7.39 (s, 2H), 7.37 – 7.34 (m, 2H);  $^{13}\text{C}$  NMR (75 MHz,  $\text{CDCl}_3$ )  $\delta$  143.83, 134.35, 133.45, 132.12, 131.78, 131.40, 130.95, 130.11, 129.76, 129.71, 128.33, 128.07, 127.48, 127.43, 126.20, 125.71, 125.52, 125.38, 125.07, 124.77, 124.48, 123.03; HRMS (APCI positive) calcd for  $\text{C}_{48}\text{H}_{26}\text{BF}_2\text{N}_3\text{S}_2$   $[\text{M} + \text{H}]^+$ : 758.1688, found 758.1651.

**Compound 2.5e.** The solution of compound **2.4d** (0.109 mmol, 100mg) in DCM (10 mL) was treated with DIPEA (1.09 mmol, 141 mg) and stirred for 10 min at room temperature under argon atmosphere. Then the solution of  $\text{BF}_3 \cdot \text{Et}_2\text{O}$  (2.18 mmol, 312 mg) was added dropwise and the mixture was stirred overnight at room temperature under argon atmosphere. Then the reaction mixture was slowly quenched with methanol (10 mL) and the resulting precipitate was filtered yielding 87 mg (67%) of pure dye **2.5e**.  $^1\text{H}$  NMR (500 MHz,  $\text{CDCl}_3$ )  $\delta$  8.55 (d,  $J = 9.3$  Hz, 2H), 8.29 (d,  $J = 8.0$  Hz, 2H), 8.17 (d,  $J = 7.6$  Hz, 4H), 8.11 (d,  $J = 9.3$  Hz, 2H), 8.03 – 7.99 (m, 4H), 7.91 – 7.88 (m, 4H), 7.14 (s, 2H), 5.51 – 5.50 (m, 4H), 4.90 – 4.89 (m, 4H), 4.35 (s, 10H).  $^{13}\text{C}$  NMR (75 MHz,  $\text{CDCl}_3$ )  $\delta$  131.49, 131.31, 131.03, 129.62, 129.47, 128.38, 127.93, 127.70, 127.59, 126.52, 126.12, 125.75, 125.47, 125.17, 125.12, 124.88, 124.52, 73.84, 71.53; HRMS (APCI positive) calcd for  $\text{C}_{60}\text{H}_{38}\text{BF}_2\text{N}_3\text{Fe}_2$   $[\text{M} + \text{H}]^+$ : 962.1935, found 962.1923.

**1,7-Diphenyl-2,6-dicarbethoxy-3-(2-(pyrenyl)vinyl)-5-methyl-4,4-difluoro-4-bora-3a,4a,-diazas-indacene (2.8) and 1,7-diphenyl-2,6-dicarbethoxy-3,5-bis-(2-(pyrenyl)vinyl)-4,4-difluoro-4-bora-3a,4a,-diazas-indacene (2.9).** A mixture of 400 mg (0.775 mmol) of BODIPY **2.7**,<sup>242n</sup> b 267 mg (1.162 mmol) of 1-pyrenecarboxaldehyde, 321 mg (3.77 mmol) of piperidine and 651 mg (10.85 mmol) of acetic acid was refluxed in 50 mL of toluene for 4 h. After cooling, the solution was washed with water, dried over  $\text{Na}_2\text{SO}_4$  and evaporated to dryness. The residue was purified by column chromatography on silica using DCM as eluent yielding 141 mg (25%) of monopyrene-containing BODIPY **2.8** and 262 mg (36%) of dipyrene-containing BODIPY **2.9**.

**Compound 2.8.**  $^1\text{H}$  NMR (500 MHz,  $\text{CDCl}_3$ )  $\delta$  9.07 (d,  $J = 16.0$  Hz, 1H), 8.50 (d,  $J = 9.4$  Hz, 1H), 8.48 (d,  $J = 8.1$  Hz, 1H), 8.16 - 8.14 (m, 4H), 8.06 - 8.04 (m, 3H), 7.96 (t,  $J = 7.6$  Hz, 1H), 7.37 –

7.23 (m, 10H), 6.89 (s, 1H), 4.16 (q,  $J = 7.1$  Hz, 2H), 4.10 (q,  $J = 7.1$  Hz, 2H), 2.94 (s, 3H), 1.04 (t,  $J = 7.1$  Hz, 3H), 0.97 (t,  $J = 7.1$  Hz, 3H);  $^{13}\text{C}$  NMR (125 MHz,  $\text{CDCl}_3$ )  $\delta$  132.63, 132.17, 131.59, 131.04, 130.89, 130.24, 130.11, 129.76, 129.13, 128.71, 128.47, 128.01, 127.69, 126.33, 126.01, 125.81, 125.57, 125.25, 124.91, 124.13, 123.75, 123.02, 61.42, 60.35, 47.62, 14.03, 13.85. HRMS (APCI positive) calcd for  $\text{C}_{46}\text{H}_{35}\text{BF}_2\text{N}_2\text{O}_4$   $[\text{M} + \text{H}]^+$ : 729.2731, found 729.2729.

**Compound 2.9.**  $^1\text{H}$  NMR (500 MHz,  $\text{CDCl}_3$ )  $\delta$  9.24 (d,  $J = 16.0$  Hz, 2H), 8.63 – 8.60 (m, 4H), 8.29 – 8.24 (m, 4H), 8.22 (dd,  $J = 6.9, 1.7$  Hz, 2H), 8.15 – 8.10 (m, 4H), 8.02 – 7.96 (m, 6H), 7.45 – 7.39 (m, 10H), 7.00 (s, 1H), 4.25 (q,  $J = 7.1$  Hz, 4H), 1.07 (t,  $J = 7.1$  Hz, 6H);  $^{13}\text{C}$  NMR (125 MHz,  $\text{CDCl}_3$ )  $\delta$  165.38, 132.59, 132.17, 131.58, 131.20, 131.01, 130.20, 129.86, 129.04, 128.76, 128.49, 128.43, 127.70, 126.28, 125.93, 125.75, 125.57, 125.26, 124.91, 124.15, 123.11, 61.36, 47.66, 13.85; HRMS (APCI positive) calcd for  $\text{C}_{63}\text{H}_{43}\text{BF}_2\text{N}_2\text{O}_4$   $[\text{M} + \text{H}]^+$ : 941.3357, found 941.3338.

**1,7-Diphenyl-2,6-dicarbethoxy-3-(2-(pyrenyl)vinyl)-5-(2-(ferrocenyl)vinyl)-4,4-difluoro-4-bora-3a,4a,-diazas-indacene (2.10).**

A mixture of 80 mg (0.11 mmol) of compound **2.8**, 26 mg (0.12 mmol) ferrocenecarboxaldehyde, 30 mg of piperidine, and 30 mg of acetic acid was refluxed in 10 mL of dry toluene for 30 min. After cooling to room temperature the solution was washed with water, dried over  $\text{Na}_2\text{SO}_4$  and evaporated to dryness. The crude product was refluxed with hot methanol and filtered. Yield 72 mg (71%) of BODIPY **2.10**.

**Compound 2.10.**  $^1\text{H}$  NMR (300 MHz,  $\text{CDCl}_3$ )  $\delta$  9.22 (d,  $J = 16.4$  Hz, 1H), 8.69 (d,  $J = 9.4$  Hz, 1H), 8.59 (d,  $J = 8.2$  Hz, 1H), 8.26 – 8.21 (m, 4H), 8.15 – 8.01 (m, 4H), 7.80 (d,  $J = 16.2$  Hz, 1H), 7.52 (d,  $J = 16.2$  Hz, 1H), 7.42 – 7.34 (m, 10H), 6.94 (s, 1H), 4.74 – 4.73 (m, 2H), 4.56 – 4.55 (m, 2H), 4.28 (s, 5H), 4.24 – 4.16 (m, 4H), 1.11 – 1.02 (m, 6H);  $^{13}\text{C}$  NMR (75 MHz,  $\text{CDCl}_3$ )  $\delta$  165.54, 165.27, 154.18, 144.14, 137.04, 135.92, 135.13, 132.56, 132.30, 131.99, 131.66, 131.57, 131.13, 129.98, 129.82, 129.72, 129.04, 128.76, 128.53, 128.43, 128.35, 128.24, 127.75, 126.28, 125.86,

125.69, 125.57, 125.31, 125.00, 124.29, 124.06, 123.31, 120.00, 82.11, 71.70, 70.29, 68.94, 61.23, 13.92; HRMS (APCI positive) calcd for C<sub>57</sub>H<sub>43</sub>BF<sub>2</sub>FeN<sub>2</sub>O<sub>4</sub> [M + H]<sup>+</sup>: 925.2706, found 925.2714.)

## Conclusion

A synthetic strategy was demonstrated for preparation of a 1,7-dipyrene-aza-BODIPY and 1,7-dipyrene-3,5-diferrocene-aza-BODIPY derivatives with pyrene substituted at the  $\beta$ -position (**2.5a-2.5e**) along with three new pyrene-BODIPY systems with pyrene substituted at the  $\alpha$ -position (**2.8-2.10**). Full structural and electronic characterization of new aza-BODIPY **2.5a-2.5e** and BODIPY compounds **2.8-2.10** was done using 1D and 2D NMR, UV-Vis, fluorescence spectroscopy, high-resolution mass spectrometry as well as X-ray crystallography. Installation of the  $\alpha$  and  $\beta$ -pyrene substituents was motivated by the hypothesis that they would provide an effective intermolecular binding motif to drive complex formation with nanocarbon based electron acceptors. This hypothesis was based, in part, on prior reports of analogous applications creating intermolecular charge transfer complexes that appeared to spontaneously assemble in solution.<sup>1-5,60-67</sup> The  $\beta$ -substituted aza-BODIPY compounds show classical pyrene-centered absorption bands at 375 and 345 nm in the UV-vis spectra of **2.5a – 2.5e** indicating that the pyrene fragments are not conjugated into the chromophores  $\pi$ -system however, the  $\alpha$ -substituted BODIPYs **2.8 – 2.10** show a prominent low-energy shift and an absence of the pyrene peaks at 375 and 345 nm clearly indicative of conjugation of the pyrene groups. The  $\alpha$ -pyrene BODIPYs **2.8 – 2.10** show regular NIR-emitting BODIPYs fluorescence quantum yields and small Stokes energy shifts. Consequently the aza-BODIPYs **2.5a – 2.5e** with the pyrene groups decoupled from the chromophores  $\pi$ -system show reduced fluorescence quantum yields and larger Stokes energy shifts. This result has contributed to the pyrene group facilitating unwanted pyrene-to-chromophore electron transfer processes. Formation of weakly-bonded non-covalent complexes between our new pyrene-aza-BODIPYs and pyrene-BODIPYs and nanocarbon material (C<sub>60</sub>, C<sub>70</sub>, SWCNT, and graphene) was studied by UV-Vis, steady-state fluorescence, and time-resolved transient absorption spectroscopy. Experiments titrating nanocarbon based acceptors into solutions containing our new compounds **2.5a-2.5e** and **2.8-2.10** resulted in significant reduction of measured emission from the chromophores and the appearance of new absorption features in the transient absorption following photoexcitation. However, careful accounting of the interference of the nanocarbon acceptors with the excitation light left only limited, residual

evidence of weak interactions with nanocarbon acceptors in solution. Solid state structures and DFT predictions supported the relatively weak and somewhat non-specific interaction between our aza-BODIPY and BODIPY compounds and the nanocarbon acceptors. Direct comparison to the aza-BODIPY control compound, **2.6**, demonstrated no significant enhancement in the interaction with nanocarbon acceptors with the addition of the pyrene ligands. The pyrene substituents were demonstrated to be ineffective as a motif to promote and direct intermolecular complex formation with fullerenes and SWCNTs, disproving the initial hypotheses. In the absence of a dominant pyrene-nanocarbon driven association, tuning the electron-donating groups at the  $\alpha$ -positions of the aza-BODIPY core was observed to play a role in the relatively weak non-covalent complex formation between **2.5a–2.5e** and fullerenes. This work draws into question conclusions that pyrenes are generally effective ligands in the construction of organic donor-nanocarbon-based-acceptor assemblies, and it highlights the care that must be taken when interpreting some commonly employed approaches to measuring complex formation. With no enhanced interaction observed via the addition of pyrene group to the BODIPY I believe future direction of this work would be best directed toward alternative methods of enhancing the non-covalent interaction of the BODIPY with the nanocarbon material. Since we observed interaction between C<sub>60</sub> and **2.5b** in crystal structures the addition of new electron donating groups to increase electron density on the BODIPY core could be a promising direction to take this work. However we decided to investigate a different approach for the interaction of our BODIPY's with fullerenes in chapter 3 where we investigate the photoinduced electron properties in the donor acceptor arrays formed between covalently linked ferrocene BODIPYs and C<sub>60</sub> fullerene. In my architecture conjugated to the BODIPY chromophore ferrocene donors should transfer electrons to the photoexcited antenna. Next the photoreduced BODIPY chromophore should transfer electrons to the terminal fullerene acceptor. As the linking group between the BODIPY and fullerene we chose the most popular catechol linker located at the boron hub.

## References

1. F. D'Souza, O. Ito, *Handbook of Porphyrin Science*, **2010**, 1, 307 – 438.
2. M. E. El-Khouly, O. Ito, P. M. Smith, F. D'Souza, *J. Photochem. Photobiol., C* **2004**, 5, 79–104.
3. S. Fukuzumi, *Phys. Chem. Chem. Phys.* **2008**, 10, 2283–2297.
4. F. D'Souza, O. Ito, *Organic Electronics and Photonics*, **2008**, 1, Chap. 13.
5. K. Ohkubo, S. Fukuzumi, *Bull. Chem. Soc. Japan* **2009**, 82, 303–315.
6. D. Gonzalez-Rodriguez, T. Torres, D. M. Guldi, J. Rivera, M. A. Herranz, L. Echegoyen, D. González-Rodríguez, *J. Am. Chem. Soc.* **2004**, 126, 6301-6313.
7. M. Rudolf, O. Trukhina, J. Perles, L. Feng, T. Akasaka, T. Torres, D. M. Guldi, *Chem. Science* **2015**, 6, 4141-4147.
8. D. Gonzalez-Rodriguez, T. Torres, D. M. Guldi, J. Rivera, L. Echegoyen, *Org. Lett.* **2002**, 4, 335-338.
9. S. Fukuzumi, *Phys. Chem. Chem. Phys.* **2008**, 10, 2283-2297.
10. Ikemoto, K. Takimiya, Y. Aso, T. Otsubo, M. Fujitsuka, O. Ito, *Org. Lett.* **2002**, 4, 309–311.
11. H. Gotfredsen, M. Jevric, A. Kadziola, M. B. Nielsen, *Eur. J. Org. Chem.* **2016**, 2016, 17-21.
12. G. M. A. Rahman, A. Troeger, V. Sgobba, D. M. Guldi, N. Jux, M. N. Tchoul, W. T. Ford, A. Mateo-Alonso, M. Prato, *Chem. Eur. J.* **2008**, 14, 8837-8846
13. I. A. Mochalov, A. N. Lapshin, V. A. Nadtochenko, V. A. Smirnov, N. F. Goldshleger, *Russ. Chem. Bull.* **2006**, 55, 1598-1604.
14. A. Vecchi, E. Gatto, B. Floris, V. Conte, M. Venanzi, V. N. Nemykin, P. Galloni, *Chem. Commun.* **2012**, 48, 5145-5147.
15. H. Imahori, Y. Mori, Y. Matano, *J. Photochem. Photobiol. C* **2003**, 4, 51–83.
16. H. Imahori, K. Tamaki, Y. Araki, Y. Sekiguchi, O. Ito, Y. Sakata, S. Fukuzumi, *J. Am. Chem. Soc.* **2002**, 124, 5165–5174.
17. F. D'Souza, R. Chitta, S. Gadde, D.-M. S. Islam, A. L. Schumacher, M. E. Zandler, Y. Araki, O. Ito, *J. Phys. Chem. B* **2006**, 110, 25240–25250.

18. J. Springer, G. Kodis, L. De La Garza, A. L. Moore, T. A. Moore, D. Gust, *J. Phys. Chem. A* **2003**, *107*, 3567–3575.
19. D. González-Rodríguez, G. Bottari, *J. Porphyrins Phthalocyanines* **2009**, *13*, 624–636.
20. N. Aratani, A. Osuka, in: *Handbook of Porphyrin Science*. K. M. Kadish, K. M. Smith, R. Guilard, (Eds.); World Scientific Publishing Co. Pte. Ltd. **2010**, *Vol. 1*, pp 1 – 132.
21. T. S. Balaban, in: *Handbook of Porphyrin Science*. K. M. Kadish, K. M. Smith, R. Guilard, (Eds.); World Scientific Publishing Co. Pte. Ltd. **2010**, *Vol. 1*, pp 221 – 306.
22. B. Verreet, B. P. Rand, D. Cheyens, A. Hadipour, T. Aernouts, P. Heremans, A. Medina, C. G. Claessens, T. Torres, *Adv. Energy Mater.* **2011**, *1*, 565-568.
23. W. A. Luhman, R. J. Holmes, *Adv. Funct. Mater.* **2011**, *21*, 764-771.
24. A. Della Pia, M. Riello, D. Stassen, T. S. Jones, D. Bonifazi, A. De Vita, G. Costantini, *Nanoscale* **2016**, *8*, 19004-19013.
25. K. Saito, Y. Kashiwagi, K. Ohkubo, S. Fukuzumi, *J. Porphyrins Phthalocyanines* **2006**, *10*, 1371-1379.
26. A. Vecchi, N. R. Erickson, J. R. Sabin, B. Floris, V. Conte, M. Venanzi, P. Galloni, V. N. Nemykin, *Chem. Eur. J.* **2015**, *21*, 269-279.
27. C. B. Kc, F. D'Souza, *Coord. Chem. Rev.* **2016**, *322*, 104-141.
28. V. S. R. Krishna, M. Samanta, S. Pal, N. P. Anurag, S. Bandyopadhyay, *Org. Biomol. Chem.* **2016**, *14*, 5744-5750.
29. Z. Xu, F. Gao, E. A. Makarova, A. A. Heikal, V. N. Nemykin, *J. Phys. Chem. C* **2015**, *119*, 9754-9761.
30. D. Gust, *Faraday Discussions* **2015**, *185*, 9-35.
31. J. Guo, Y. Liang, S. Xiao, J. M. Szarko, M. Sprung, M. K. Mukhopadhyay, J. Wang, L. Yu, L. X. Chen, *New J. Chem.* **2009**, *33*, 1497-1507.
32. A. Das, S. Ghosh, *Angew. Chem., Int. Ed.* **2014**, *53*, 2038-2054;
33. S. J. Dammer, P. V. Solntsev, J. R. Sabin, V. N. Nemykin, *Inorg. Chem.* **2013**, *52*, 9496-9510.
34. F. Scarel, C. Ehli, D. M. Guldi, A. Mateo-Alonso, *Chem. Commun.* **2013**, *49*, 9452-9454.
35. M. Ince, A. Hausmann, M. V. Martinez-Diaz, D. M. Guldi, T. Torres, *Chem. Commun.* **2012**, *48*, 4058-4060.
36. M. Amelia, A. Credi, *Inorg. Chim. Acta* **2012**, *381*, 247-250.

37. D. Linton, P. Driva, B. Sumpter, I. Ivanov, D. Geohegan, C. Feigerle, M. D. Dadmun, *Soft Matter* **2010**, *6*, 2801-2814.
38. B. Sun, Z. Ou, D. Meng, Y. Fang, Y. Song, W. Zhu, P. V. Solntsev, V. N. Nemykin, K. M. Kadish, *Inorg. Chem.* **2014**, *53*, 8600-8609.
39. M. R. Rao, S.-S. Sun, *Langmuir* **2013**, *29*, 15146-15158.
40. K. Jalani, M. Kumar, S. J. George, *Chem. Commun.* **2013**, *49*, 5174-5176.
41. A. Ghosh, K. V. Rao, R. Voggu, S. J. George, *Chem. Phys. Lett.* **2010**, *488*, 198-201.
42. E. M. Perez, B. M. Illescas, M. A. Herranz, N. Martin, *New J. Chem.* **2009**, *33*, 228-234.
43. K. Dirian, M. A. Herranz, G. Katsukis, J. Malig, L. Rodriguez-Perez, C. Romero-Nieto, V. Strauss, N. Martin, D. M. Guldi, *Chem. Sci.* **2013**, *4*, 4335-4353.
44. Y. Shen, J. S. Reparaz, M. R. Wagner, A. Hoffmann, C. Thomsen, J.-O. Lee, S. Heeg, B. Hatting, S. Reich, A. Saeki, *Chem. Sci.* **2011**, *2*, 2243-2250.
45. W. Seitz, A. Kahnt, D. M. Guldi, T. Torres, *J. Porphyrins Phthalocyanines* **2009**, *13*, 1034-1039.
46. A. S. D. Sandanayaka, O. Ito, *J. Porphyrins Phthalocyanines* **2009**, *13*, 1017-1033.
47. M. Zannotti, R. Giovannetti, C. A. D'Amato, E. Rommozzi, *Spectrochim. Acta, Part A* **2016**, *153*, 22-29.
48. D. I. Schuster, J. D. Jr. Megiatto, *Nat. Chem.* **2009**, *1*, 182-183.
49. A. S. D. Sandanayaka, N. K. Subbaiyan, S. K. Das, R. Chitta, E. Maligaspe, T. Hasobe, O. Ito, F. D'Souza, *ChemPhysChem* **2011**, *12*, 2266-2273.
50. J. Bartelmess, A. R. M. Soares, M. V. Martinez-Diaz, M. G. P. M. S. Neves, A. C. Tome, J. A. S. Cavaleiro, T. Torres, D. M. Guldi, *Chem. Commun.* **2011**, *47*, 3490-3492.
51. M.-E. Ragoussi, J. Malig, G. Katsukis, B. Butz, E. Spiecker, G. de la Torre, T. Torres, D. M. Guldi, *Angew. Chem., Int. Ed.* **2012**, *51*, 6421-6425.
52. G. Bottari, G. de la Torre, D. M. Guldi, T. Torres, *Chem. Rev.* **2010**, *110*, 6768-6816.
53. D. H. Hochmuth, S. L. J. Michel, A. J. P. White, D. J. Williams, A. G. M. Barrett, B. M. Hoffman, *Eur. J. Inorg. Chem.* **2000**, 593-596.
54. D. M. Eichhorn, S. L. Yang, W. Jarrell, T. F. Baumann, L. S. Beall, A. J. P. White, D. J. Williams, A. G. M. Barreyy, B. M. Hoffman, *J. Chem. Soc. Chem. Commun.* **1995**, 1703-1704.

55. T. Higashino, K. Sugiura, Y. Tsuji, S. Nimura, S. Ito, H. Imahori, *Chem. Lett.* **2016**, *45*, 1126-1128.
56. M. Adineh, P. Tahay, W.-K. Huang, H.-P. Wu, E. W.-G. Diau, N. Safari, *RSC Adv.* **2016**, *6*, 102979-102983.
57. T. Higashino, K. Kawamoto, K. Sugiura, Y. Fujimori, Y. Tsuji, K. Kurotobi, S. Ito, H. Imahori, *ACS Appl. Mater. Interfaces* **2016**, *8*, 15379-15390.
58. T. Higashino, Y. Fujimori, K. Sugiura, Y. Tsuji, S. Ito, H. Imahori, *J. Porphyrins Phthalocyanines* **2015**, *19*, 140-149.
59. R. B. Ambre, G.-F. Chang, M. R. Zanwar, C.-F. Yao, E. W.-G. Diau, C.-H. Hung, *Chem. Asian J.* **2013**, *8*, 2144-2153.
60. S. H. Kang, I. T. Choi, M. S. Kang, Y. K. Eom, M. J. Ju, J. Y. Hong, H. S. Kang, H. K. Kim, *J. Mater. Chem. A* **2013**, *1*, 3977-3982.
61. H. Hayashi, A. S. Touchy, Y. Kinjo, K. Kurotobi, Y. Toude, S. Ito, H. Saarenpaeae, N. V. Tkachenko, H. Lemmetyinen, H. Imahori, *ChemSusChem* **2013**, *6*, 508-517.
62. S. Mathew, H. Iijima, Y. Toude, T. Umeyama, Y. Matano, S. Ito, N. V. Tkachenko, H. Lemmetyinen, H. Imahori, *J. Phys. Chem. C* **2011**, *115*, 14415-14424.
63. C.-F. Lo, S.-J. Hsu, C.-L. Wang, Y.-H. Cheng, H.-P. Lu, E. W.-G. Diau, C.-Y. Lin, *J. Phys. Chem. C* **2010**, *114*, 12018-12023.
64. C. P. Hsieh, H.-P. Lu, C.-L. Chiu, C.-W. Lee, S.-H. Chuang, C.-L. Mai, W.-N. Yen, S.-J. Hsu, E. W.-G.; Diau, C.-Y. Yeh, *J. Mater. Chem.* **2010**, *20*, 1127-1134.
65. D. Molina, M. E. El-Khouly, M. El-Kemary, S. Fukuzumi, F. Fernandez-Lazaro, A. Sastre-Santos, *Chem. Eur. J.* **2016**, *22*, 17800-17807.
66. S. Yamamoto, A. Zhang, M. J. Stillman, N. Kobayashi, M. Kimura, *Chem. Eur. J.* **2016**, *22*, 18760-18768.
67. M. E. El-Khouly, S. Fukuzumi, *Photochem. Photobiol. Sci.* **2016**, *15*, 1340-1346.
68. H. Yang, S. Pan, D. Ma, D. He, Y. Wang, S. Xie, Y. Peng, *J. Luminescence* **2016**, *179*, 588-594.
69. S. Yamamoto, T. Ikeuchi, S. Mori, M. Kimura, *Asian J. Org. Chem.* **2014**, *3*, 1083-1088.
70. T. Ikeuchi, H. Nomoto, N. Masaki, M. J. Griffith, S. Mori, M. Kimura, *Chem. Commun.* **2014**, *50*, 1941-1943.

71. M. Vengris, D. S. Larsen, L. Valkunas, G. Kodis, C. Herrero, D. Gust, T. Moore, A. Moore, R. van Grondelle, *J. Phys. Chem. B* **2013**, *117*, 11372-11382.
72. Y. Ishida, T. Shimada, S. Takagi, *J. Phys. Chem. C* **2013**, *117*, 9154-9163.
73. M. Kimura, H. Nomoto, H. Suzuki, T. Ikeuchi, H. Matsuzaki, T. N. Murakami, A. Furube, N. Masaki, M. J. Griffith, S. Mori, *Chem. Eur. J.* **2013**, *19*, 7496-7502.
74. C. B. Kc, G. N. Lim, F. D'Souza, *Chem. Asian J.* **2016**, *11*, 1246-1256.
75. C. B. Kc, G. N. Lim, M. E. Zandler, F. D'Souza, *Org. Lett.* **2013**, *15*, 4612-4615.
76. F. A. Sari, A. Yuzer, W. Cambarau, M. Ince, *J. Porphyrins Phthalocyanines* **2016**, *20*, 1114-1121.
77. T. Weidner, J. E. Baio, J. Seibel, U. Siemeling, *Dalton Trans.* **2012**, *41*, 1553-1561.
78. K. Sakamoto, S. Yoshino, M. Takemoto, K. Sugaya, H. Kubo, T. Komoriya, S. Kamei, S. Furukawa, *Amer. J. Anal. Chem.* **2014**, *5*, 1037-1045.
79. E. Ohno-Okumura, K. Sakamoto, T. Kato, T. Hatano, K. Fukui, T. Karatsu, A. Kitamura, T. Urano, *Dyes Pigments* **2002**, *53*, 57-65.
80. J. Fernandez-Ariza, R. M. Krick Calderon, J. Perles, M. S. Rodriguez-Morgade, D. M. Guldi, T. Torres, *Chem. Commun.* **2017**, *53*, 8525-8528.
81. X.-D. Jiang, T. Fang, X. Liu, D. Xi, *Eur. J. Org. Chem.* **2017**, *2017*, 5074-5079.
82. C. Yu, Q. Wu, J. Wang, Y. Wei, E. Hao, L. Jiao, *J. Org. Chem.* **2016**, *81*, 3761-3770.
83. Y. V. Zatsikha, V. P. Yakubovskiy, M. P. Shandura, Y. P. Kovtun, *RSC Adv.* **2013**, *3*, 24193-24201.
84. A. Martin, C. Long, R. J. Forster, T. E. Keyes, *Chem. Commun.* **2012**, *48*, 5617-5619.
85. O. Buyukcakir, O. A. Bozdemir, S. Kolemen, S. Erbas, E. U. Akkaya, O. Buyukcakir, *Org. Lett.* **2009**, *11*, 4644-4647.
86. X. Qi, S. K. Kim, E. J. Jun, L. Xu, S.-J. Kim, J. A. Yoon, *Bull. Korean Chem. Soc.* **2007**, *28*, 2231-2234.
87. M. P. Shandura, V. P. Yakubovskiy, A. O. Gerasov, O. D. Kachkovsky, Y. M. Poronik, Y. P. Kovtun, *Eur. J. Org. Chem.* **2012**, *2012*, 1825-1834.
88. N. Adarsh, M. S. Krishnan, D. Ramaiah, *Anal. Chem.* **2014**, *86*, 9335-9342.
89. W. Sheng, J. Cui, Z. Ruan, L. Yan, Q. Wu, C. Yu, Y. Wei, E. Hao, L. Jiao, *J. Org. Chem.* **2017**, *82*, 10341-10349.
90. H. Yamane, S. Ohtani, K. Tanaka, Y. Chujo, *Tetr. Lett.* **2017**, *58*, 2989-2992.

91. E. V. Antina, N. A. Bumagina, *Chem. Heterocyclic Comp.* **2017**, *53*, 39-41.
92. S. Shimizu, T. Iino, A. Saeki, S. Seki, N. Kobayashi, *Chem. Eur. J.* **2015**, *21*, 2893-2904.
93. V. Bandi, H. B. Gobeze, F. D'Souza, *Chem. Eur. J.* **2015**, *21*, 11483-11494.
94. A. Cidlina, M. Miletin, M. Fathi-Rasekh, V. N. Nemykin, P. Zimcik, V. Novakova, *Chem. Eur. J.* **2017**, *23*, 1795-1804.
95. S. A. Majeed, B. Ghazal, D. E. Nevenon, P. C. Goff, D. A. Blank, V. N. Nemykin, S. Makhseed, *Inorg. Chem.* **2017**, *56*, 11640-11653.
96. M. Maiuri, J. J. Snellenburg, I. H. M. van Stokkum, S. Pillai, K. WongCarter, D. Gust, T. A. Moore, A. L. Moore, R. van Grondelle, G. Cerullo, D. Polli, *J. Phys. Chem. B* **2013**, *117*, 14183-14190.
97. G. de la Torre, G. Bottari, M. Sekita, A. Hausmann, D. M. Guldi, T. Torres, *Chem. Soc. Rev.* **2013**, *42*, 8049-8105.
98. M.-E. Ragoussi, M. Ince, T. Torres, *Eur. J. Org. Chem.* **2013**, *2013*, 6475-6489.
99. M. Kloz, S. Pillai, G. Kodis, D. Gust, T. A. Moore, A. L. Moore, R. van Grondelle, J. T. M. Kennis, *Chem. Sci.* **2012**, *3*, 2052-2061.
100. C. Romero-Nieto, J. Guilleme, J. Fernandez-Ariza, M. S. Rodriguez-Morgade, D. Gonzalez-Rodriguez, T. Torres, D. M. Guldi, *Org. Lett.* **2012**, *14*, 5656-5659.
101. E. Lager, J. Liu, A. Aguilar-Aguilar, B. Z. Tang, E. Pena-Cabrera, *J. Org. Chem.* **2009**, *74*, 2053-2058.
102. P. Verwilst, H.-R. Kim, J. Seo, N.-W. Sohn, S.-Y. Cha, Y. Kim, S. Maeng, J.-W. Shin, J. H. Kwak, C. Kang, J. S. Kim, *J. Am. Chem. Soc.* **2017**, *139*, 13393-13403.
103. Z. Biyiklioglu, T. Keles, *Inorg. Chim. Acta* **2017**, *466*, 130-138.
104. K. B. Petrushenko, I. K. Petrushenko, O. V. Petrova, L. N. Sobenina, B. A. Trofimov, *Dyes Pigments* **2017**, *136*, 488-495.
105. Y. Gawale, N. Adarsh, S. K. Kalva, J. Joseph, M. Pramanik, D. Ramaiah, N. Sekar, *Chem. Eur. J.* **2017**, *23*, 6570-6578.
106. Y. V. Zatsikha, D. B. Nemez, R. L. Davis, S. Singh, D. E. Herbert, A. J. King, C. J. Ziegler, V. N. Nemykin, *Chem. Eur. J.* **2017**, *23*, 14786-14796.
107. N. R. Erickson, C. D. Holstrom, H. M. Rhoda, G. T. Rohde, Y. V. Zatsikha, P. Galloni, V. N. Nemykin, *Inorg. Chem.* **2017**, *56*, 4717-4728.

108. N. O. Didukh, Y. V. Zatsikha, G. T. Rohde, T. S. Blesener, V. P. Yakubovskiy, Y. P. Kovtun, V. N. Nemykin, *Chem. Commun.* **2016**, 52, 11563-11566.
109. E. Maligaspe, M. R. Hauwiler, Y. V. Zatsikha, J. A. Hinke, P. V. Solntsev, D. A. Blank, V. N. Nemykin, *Inorg. Chem.* **2014**, 53, 9336-9347.
110. P. V. Solntsev, K. L. Spurgin, J. R. Sabin, A. A. Heikal, V. N. Nemykin, *Inorg. Chem.* **2012**, 51, 6537-6547.
111. P. V. Solntsev, J. R. Sabin, S. J. Dammer, N. N. Gerasimchuk, V. N. Nemykin, *Chem. Commun.* **2010**, 46, 6581-6583.
112. V. N. Nemykin, G. T. Rohde, C. D. Barrett, R. G. Hadt, C. Bizzarri, P. Galloni, B. Floris, I. Nowik, R. H. Herber, A. G. Marrani, R. Zanoni, N. M. Loim, *J. Am. Chem. Soc.* **2009**, 131, 14969-14978.
113. A. K. Burrell, W. M. Campbell, G. B. Jameson, D. L. Officer, P. D. W. Boyd, Z. Zhao, P. A. Cocks, K. C. Gordon, K. C. *Chem. Commun.* **1999**, 637-638.
114. P. Galloni, B. Floris, L. De Cola, E. Cecchetto, R. M. Williams, *J. Phys. Chem. C* **2007**, 111, 1517-1523.
115. Z. Jin, K. Nolan, C. R. McArthur, A. B. P. Lever, C. C. Leznoff, *J. Organomet. Chem.* **1994**, 468, 205-212.
116. G. Pomarico, A. Vecchi, F. Mandoj, O. Bortolini, D. O. Cicero, P. Galloni, R. Paolesse, *Chem. Commun.* **2014**, 50, 4076-4978.
117. O. Galangau, I. Fabre-Francke, S. Munteanu, C. Dumas-Verdes, G. Clavier, R. Meallet-Renault, R. B. Pansu, F. Hartl, F. Miomandre, *Electrochim. Acta* **2013**, 87, 809-815.
118. R. Misra, B. Dhokale, T. Jadhav, S. M. Mobin, *Dalton Trans.* **2013**, 42, 13658-13666.
119. X. Yin, Y. Li, Y. Li, Y. Zhu, X. Tang, H. Zheng, D. Zhu, *Tetrahedron* **2009**, 65, 8373-8377.
120. R. Misra, B. Dhokale, T. Jadhav, S. M. Mobin, *Organometallics* **2014**, 33, 1867-1877.
121. X. Yin, Y. Li, Y. Zhu, X. Jing, Y. Li, D. Zhu, *Dalton Trans.* **2010**, 39, 9929-9935.
122. E. M. Cabaleiro-Lago, J. Rodríguez-Otero, J. A. Carrazana-García, *Phys. Chem. Chem. Phys.* **2017**, 19, 26787-26798.
123. J. Bartelmess, M. Frasconi, P. B. Balakrishnan, A. Signorelli, L. Echegoyen, L.; T. Pellegrino, S. Giordani, *RSC Adv.* **2015**, 5, 50253-50258.
124. A. Sygula, M. Yanney, W. P. Henry, F. R. Fronczek, A. V. Zabula, M. A. Petrukhina, *Cryst. Growth Design* **2014**, 14, 2633-2639.

125. A. S. Filatov, M.V. Ferguson, S.N. Spisak, B. Li, C. F. Campana, M. A. Petrukhina, *Cryst. Growth Design* **2014**, *14*, 756-762.
126. A. S. Filatov, M. A. Petrukhina, *Coord. Chem. Rev.* **2010**, *254*, 2234-2246.
127. N. Martín, *Adv. Energy Mater.* **2017**, *7*, 1601102.
128. F. Lodermeier, R. D. Costa, D. M. Guldi, *Adv. Energy Mater.* **2017**, *7*, 1601883.
129. S. M. Ryno, M. K. Ravva, X. Chen, H. Li, J.-L. Brédas, *Adv. Energy Mater.* **2017**, *7*, 1601370.
130. G. de la Torre, G. Bottari, T. Torres, *Adv. Energy Mater.* **2017**, *7*, 1601700.
131. Y. Li, H. M. Rhoda, A. M. Wertish, V. N. Nemykin, *J. Porphyrins Phthalocyanines* **2016**, *20*, 1098-1113.
132. S. Nakano, Y. Kage, H. Furuta, N. Kobayashi, S. Shimizu, *Chem. Eur. J.* **2016**, *22*, 7706-7710.
133. C. B. Kc, G. N. Lim, F. D'Souza, *Angew. Chem., Int. Ed.* **2015**, *54*, 5088-5092.
134. L. Ji, Y. Wu, L. Ma, X. Yang, *Composites, Part A: Applied Science and Manufacturing* **2015**, *72*, 32-39.
135. W. Hayes, B. W. Greenland, *Adv. Polymer Sci.* **2015**, *268*, 143-166.
136. T. Umeyama, J. Baek, J. Mihara, N. V. Tkachenko, H. Imahori, *Chem. Commun.* **2017**, *53*, 1025-1028.
137. D. Didier, E. Schulz, *Tetr. Asymmetry* **2013**, *24*, 769-775.
138. L. P. Jameson, S. V. Dzyuba, *Bioorg. Med. Chem. Lett.* **2013**, *23*, 1732-1735.
139. H. Klifout, A. Stewart, M. Elkhailifa, H. He, *ACS Appl. Mater. Interfaces* **2017**, *9*, 39873-39889.
140. X.-D. Jiang, S. Li, J. Guan, T. Fang, X. Liu, L.-J. Xiao, *Curr. Org. Chem.* **2016**, *20*, 1736-1744.
141. C. J. Ziegler, K. Chanawanno, A. Hasheminsasab, Y. V. Zatsikha, E. Maligaspe, V. N. Nemykin, *Inorg. Chem.* **2014**, *53*, 4751-4755.
142. V. N. Nemykin, T. S. Blesener, C. J. Ziegler, *Macroheterocycles*, **2017**, *10*, 9-26, DOI: 10.6060/mhc170188n.
143. A. Vecchi, P. Galloni, B. Floris, V. N. Nemykin, *J. Porphyrins Phthalocyanines* **2013**, *17*, 165-196.

144. K. Ladomenou, V. Nikolaou, G. Charalambidis, A. Charisiadis, A. G. Coutsolelos, *Comptes Rendus Chimie* **2017**, *20*, 314-322.
145. S. P. Singh, T. Gayathri, *Eur. J. Org. Chem.* **2014**, *2014*, 4689-4707.
146. F. L. Arbeloa, J. M. V. Banuelos, T. Arbeloa, I. L. Arbeloa, *Trends Phys. Chem.* **2008**, *13*, 101-122.
147. Y. V. Zatsikha, N. O. Didukh, D. Nemez, A. C. Schlachter, P.-L. Karsenti, Y. P. Kovtun, P. D. Harvey, V. N. Nemykin, *Chem. Commun.* **2017**, *53*, 7612-7615.
148. Y. V. Zatsikha, N. O. Didukh, T. Blesener, M. P. Kayser, Y. P. Kovtun, D. A. Blank, V. N. Nemykin, *Eur. J. Inorg. Chem.* **2017**, *2017*, 318-324.
149. E. Maligaspe, T. J. Pundsack, L. M. Albert, Y. V. Zatsikha, P. V. Solntsev, D. A. Blank, V. N. Nemykin, *Inorg. Chem.* **2015**, *54*, 4167-4174.
150. H. M. Rhoda, K. Chanawanno, A. J. King, Y. V. Zatsikha, C. J. Ziegler, V. N. Nemykin, *Chem. Eur. J.* **2015**, *21*, 18043-18046.
151. M. A. Filatov, S. Karuthedath, P. M. Polestshuk, H. Savoie, K. J. Flanagan, C. Sy, E. Sitte, M. Telitchko, F. Laquai, R. W. Boyle, M. O. Senge, *J. Am. Chem. Soc.* **2017**, *139*, 6282-6285.
152. J. Zhao, K. Xu, W. Yang, Z. Wang, F. Zhong, *Chem. Soc. Rev.* **2015**, *44*, 8904-8939.
153. Y. V. Zatsikha, E. Maligaspe, A. A. Purchel, N. O. Didukh, Y. Wang, Y. P. Kovtun, D. A. Blank, V. N. Nemykin, *Inorg. Chem.* **2015**, *54*, 7915-7928.
154. A. Vecchi, P. Galloni, B. Floris, S. V. Dudkin, V. N. Nemykin, *Coord. Chem. Rev.* **2015**, *291*, 95-171.
155. N. Boens, V. Leen, W. Dehaen, *Chem. Soc. Rev.* **2012**, *41*, 1130-1172.
156. Y. V. Zatsikha, C. D. Holstrom, K. Chanawanno, A. J. Osinski, C. J. Ziegler, V. N. Nemykin, *Inorg. Chem.* **2017**, *56*, 991-1000.
157. M. B. Robin, P. Day, *Advances Inorganic Chemistry and Radiochemistry* **1967**, *10*, 247-422.
158. N. S. Hush, *Prog. Inorg. Chem.* **1967**, *8*, 391-444.
159. N. S. Hush, *Coord. Chem. Rev.* **1985**, *64*, 135-157.
160. H. L. C. Feltham, K. Dankhoff, C. J. Meledandri, S. Brooker, *ChemPlusChem* **2018**, *Ahead of Print*.

161. Y. Zhang, R. Ma, X. V. Zhen, Y. C. Kudva, P. Buhlmann, S. J. Koester, *ACS Appl. Mater. Inter.* **2017**, *9*, 38863-38869.
162. X. Zhang, C. Jia, Y. Xue, *Mater. Res. Bull.* **2018**, *98*, 53-58.
163. D. Zaharie-Butucel, M. Potara, A. M. Craciun, R. Boukherroub, S. Szunerits, S. Astilean, *Phys. Chem. Chem. Phys.* **2017**, *19*, 16038-16046.
164. M. Hinnemo, J. Zhao, P. Ahlberg, C. Haegglund, V. Djurberg, R. H. Scheicher, S.-L. Zhang, Z.-B. Zhang, *Langmuir* **2017**, *33*, 3588-3593.
165. G. De Filpo, F. P. Nicoletta, L. Ciliberti, P. Formoso, G. Chidichimo, *J. Power Sources* **2015**, *274*, 274-279.
166. C. Bosch-Navarro, B. Matt, G. Izzet, C. Romero-Nieto, K. Dirian, A. Raya, S. I. Molina, A. Proust, D. M. Guldi, C. Marti-Gastaldo, E. Coronado, *Chem. Sci.* **2014**, *5*, 4346-4354.
167. E. K. Apartsin, M. Yu. Buyanova, D. S. Novopashina, E. I. Ryabchikova, A. V. Filatov, M. A. Zenkova, A. G. Venyaminova, *ACS Appl. Mater. Interfaces* **2014**, *6*, 1454-1461.
168. H. Oevering, M. N. Paddon-Row, M. Heppener, A. M. Oliver, E. Cotsaris, J. W. Verhoeven, N. S. Hush, *J. Am. Chem. Soc.* **1987**, *109*, 3258-3269.
169. A. Weller, *Z. Phys. Chem.* **1982**, *133*, 93-98.
170. D. Rehm, A. Weller, *Isr. J. Chem.* **1970**, *8*, 259-271.
171. J. Kroon, J. W. Verhoeven, M. N. Paddon-row, A. M. Oliver, *Angew. Chem.* **1991**, *30*, 1358-1361.

172.  $\Delta G_{ET}$  was estimated by the following formula:

$$\Delta G_{ET}^0 = e \left[ E^0 \left( \frac{D^+}{D} \right) - E^0 \left( \frac{A}{A^-} \right) \right] - E_{00} - \left( \frac{e^2}{4\pi\epsilon_0} \right) \left( \frac{1}{\epsilon_S R_{DA}} \right) - \left( \frac{e^2}{4\pi\epsilon_0} \right) \left( \frac{1}{2r^+} + \frac{1}{2r^-} \right) \left( \frac{1}{\epsilon_{EC}} - \frac{1}{\epsilon_S} \right)$$

Where  $E^0(D^+/D)$  and  $E^0(A/A^-)$  are oxidation potential of a donor and reduction potential of an acceptor, respectively;  $E_{00}$  excitation energy at the BODIPY;  $R_{DA}$  is a donor-accepted distance estimated on a basis of DFT calculations and X-ray data available for non-covalent complexes formed between aza-BODIPYs and  $C_{60}$ ;  $\epsilon_S$  and  $\epsilon_{EC}$  are the dielectric constants of the solvents used in photochemical and electrochemical studies;  $r^+$  and  $r^-$  are the effective ionic radii of the donor and acceptor, respectively, that are estimated on the basis of DFT calculations.

173. M. Zheng, F. Bai, F. Li, Y. Li, D. Zhu, *J. Appl. Polym. Sci.*, **1998**, *70*, 599-603.

174. H. M. Rhoda, M. P. Kayser, Y. Wang, A. Y. Nazarenko, R. V. Belosludov, P. Kiprof, D. A. Blank, V. N. Nemykin, *Inorg. Chem.* **2016**, *55*, 9549-9563.
175. D. V. Konarev, S. I. Troyanov, R. N. Lyubovskaya, *CrystEngComm* **2015**, *17*, 3923-3926.
176. I. Sanchez Molina, M. Ince, G. Bottari, C. G. Claessens, M. V. Martinez-Diaz, T. Torres, *Turk. J. Chem.* **2014**, *38*, 1006-1012.
177. X.-S. Ke, T. Kim, V. M. Lynch, D. Kim, J. L. Sessler, *J. Am. Chem. Soc.* **2017**, *139*, 13950-13956.
178. D. Gonzalez-Rodriguez, E. Carbonell, D. M. Guldi, T. Torres, *Angew. Chem., Int. Ed.* **2009**, *48*, 8032-8036, S8032/1-S8032/54
179. I. Sanchez-Molina, B. Grimm, R. M. Krick Calderon, C. G. Claessens, D. M. Guldi, T. Torres, *J. Am. Chem. Soc.* **2013**, *135*, 10503-10511.
180. D. Gonzalez-Rodriguez, E. Carbonell, G. M. Rojas, C. A. Castellanos, D. M. Guldi, T. Torres, *J. Am. Chem. Soc.* **2010**, *132*, 16488-16500
181. R. Cantu, H. B. Gobeze, F. D'Souza, *J. Porphyrins Phthalocyanines* **2016**, *20*, 987-996; b) C. B. Kc, G. N. Lim, F. D'Souza, *Chem. Eur. J.* **2016**, *22*, 13301-13311.
182. K. L. Mutolo, E. I. Mayo, B. P. Rand, S. R. Forrest, M. E. Thompson, *J. Am. Chem. Soc.* **2006**, *128*, 8108-8109.
183. Z. Ma, S. Liu, S. Hu, J. Yu, *J. Luminescence* **2016**, *169*(Part\_A), 29-34.
184. S. E. Morris, M. Shtein, *Org. Electronics* **2014**, *15*, 3795-3799.
185. D. Credgington, S.-W. Liu, J. Nelson, J. R. Durrant, *J. Phys. Chem. C* **2014**, *118*, 22858-22864.
186. W.-C. Su, C.-C. Lee, S.-W. Liu, C.-F. Lin, C.-C. Chou, B.-Y. Huang, C.-W. Cheng, *Japan. J. Appl. Phys.* **2014**, *53*, 03CE02/1-03CE02/5.
187. J. Y. Kim, J. Kwak, S. Noh, C. Lee, *J. Nanosci. Nanotech.* **2012**, *12*, 5724-5727.
188. D. S. Josey, S. R. Nyikos, R. K. Garner, A. Dovijarski, J. S. Castrucci, J. M. Wang, G. J. Evans, T. P. Bender, *ACS Energy Lett.* **2017**, *2*, 726-732.
189. C. Duan, G. Zango, M. Garcia Iglesias, F. J. M. Colberts, M. M. Wienk, M. V. Martinez-Diaz, R. A. J. Janssen, T. Torres, *Angew. Chem., Int. Ed.* **2017**, *56*, 148-152.
190. J. S. Castrucci, D. S. Josey, E. Thibau, Z.-H. Lu, T. P. Bender, *J. Phys. Chem. Lett.* **2015**, *6*, 3121-3125.

191. D. E. Wilcox, M. H. Lee, M. E. Sykes, A. Niedringhaus, E. Geva, B. D. Dunietz, M. Shtein, J. P. Ogilvie, *J. Phys. Chem. Lett.* **2015**, *6*, 569-575.
192. I. Sanchez-Molina, C. G. Claessens, B. Grimm, D. M. Guldi, T. Torres, *Chem. Sci.* **2013**, *4*, 1338-1344.
193. R. S. Iglesias, C. G. Claessens, T. Torres, G. M. A. Rahman, D. M. Guldi, *Chem. Commun.* **2005**, 2113-2115.
194. S. Shimizu, S. Nakano, T. Hosoya, N. Kobayashi, *Chem. Commun.* **2011**, *47*, 316-318.
195. F. Camerel, G. Ulrich, P. Retailleau, R. Ziessel, *Angew. Chem., Int. Ed.* **2008**, *47*, 8876-8880.
196. T. Yanai, D. Tew, N. Handy, *Chem. Phys. Lett.* **2004**, *393*, 51-57.
197. Y. Tawada, T. Tsuneda, S. Yanagisawa, T. Yanai, K. Hirao, *J. Chem. Phys.* **2004**, *120*, 8425.
198. O. A. Vydrov, G. E. Scuseria, *J. Chem. Phys.* **2006**, *125*, 234109.
199. O. A. Vydrov, J. Heyd, A. Krukau, G. E. Scuseria, *J. Chem. Phys.* **2006**, *125*, 074106.
200. O. A. Vydrov, G. E. Scuseria, J. P. Perdew, *J. Chem. Phys.* **2007**, *126*, 154109.
201. S. Grimme, *J. Comp. Chem.* **2006**, *27*, 1787-1799.
202. J.-D. Chai, M. Head-Gordon, *Phys. Chem. Chem. Phys.* **2008**, *10*, 6615-6620.
203. S. Grimme, J. Antony, S. Ehrlich, S. Krieg, *J. Chem. Phys.* **2010**, *132*, 154104.
204. J.-Y. Hu, M. Era, M. R. J. Elsegood, T. Yamato, *Eur. J. Org. Chem.* **2010**, 72-79.
205. P. S. Salini, S. K. Rajagopal, M. Hariharan, *Cryst. Growth Design* **2016**, *16*, 5822-5830.
206. M. Kobayashi, N. Hayakawa, T. Matsuo, B. Li, T. Fukunaga, D. Hashizume, H. Fueno, K. Tanaka, K. Tamao, *J. Am. Chem. Soc.* **2016**, *138*, 758-761.
207. T.-C. Chou, C.-L. Hwa, J.-J. Lin, K.-C. Liao, J.-C. Tseng, *J. Org. Chem.* **2005**, *70*, 9717-9726.
208. Z. Wang, J. Zhao, *Org. Lett.* **2017**, *19*, 4492-4495.
209. D. Rehm, A. Weller, *Israel J. of Chem.* **1970**, *8*, 259-271.
210. Y. Zhang, S. Yuan, W. Zhou, J. Xu, Y. Li, *J. Nanosci. Nanotech.* **2007**, *7*, 2366-2375.
211. P. Leyton, J. S. Gomez-Jeria, S. Sanchez-Cortes, C. Domingo, M. Campos-Vallette, *J. Phys. Chem. B* **2006**, *110*, 6470-6474.
212. S. G. Stepanian, V. A. Karachevtsev, A. Glamazda, Yu, U. Dettlaff-Weglikowska, L. Adamowicz, *Mol. Phys.* **2003**, *101*, 2609-2614.

213. J. Lu, S. Liu, H. Li, Y. Shen, J. Xu, Y. Cheng, M. Wang, *J. Mater. Chem. A* **2014**, *2*, 17495-17501.
214. C. Ehli, G. M. A. Rahman, N. Jux, D. Balbinot, D. M. Guldi, F. Paolucci, M. Marcaccio, D. Paolucci, M. Melle-Franco, F. Zerbetto, S. Campidelli, M. Prato, *J. Am. Chem. Soc.* **2006**, *128*, 11222-11231.
215. M. Zheng, F. Bai, F. Li, Y. Li, D. Zhu, *J. Appl. Polym. Sci.* **1998**, *70*, 599-603.
216. J. Killoran, L. Allen, J. F. Gallagher, W. M. Gallagher, D. F. O'Shea, *Chem. Commun.*, **2002**, 1862-1863.
217. D. E. Bublitz, K. L. Rinehart, *Organic Reactions*, **1969**, *17*, 1-154.
218. A. D'Aléo, A. Karapetyan, V. Heresanu, M. Giorgi, F. Fages, *Tetrahedron*, **2015**, *71*, 2255-2259.
219. A. D'Aléo, D. Gachet, V. Heresanu, M. Giorgi, F. Fages, *Chem. Eur. J.*, **2012**, *18*, 12764-12772.
220. Q. Feng, M. Wang, B. Dong, C. Xu, J. Zhao, H. Zhang, *CrystEngComm*, **2013**, *15*, 3623-3629.
221. Z. Xiao, Y. Shi, R. Sun, J. Ge, Z. Li, Y. Fang, X. Wu, J. Yang, M. Zhao, Y. Song, *J. Mater. Chem. C*, **2016**, *4*, 4647-4653.
222. P.-X. Hou, C. Liu, H.-M. Cheng, *Carbon*, **2008**, *46*, 2003-2025.
223. A. D. Becke, *J. Chem. Phys.* **1993**, *98*, 5648-5652.
224. C. Lee, W. Yang, R. G. Parr, *Phys. Rev. B* **1988**, *37*, 785-789.
225. M. Tamada, T. Iino, Y. Wang, M. Ide, A. Saeki, H. Furuta, N. Kobayashi, S. Shimizu, *Tetr. Lett.* **2017**, *58*, 3151-3154.
226. Y. Liu, J. Duan, F. Qi, D. Tian, X. Wang, Z. Liu, W. Huang, *Dalton Trans.* **2017**, *46*, 10332-10338.
227. N. Epelde-Elezcano, E. Palao, H. Manzano, A. Prieto-Castaneda, A. R. Agarrabeitia, A. Tabero, A. Villanueva, S. de la Moya, I. Lopez-Arbeloa, V. Martinez-Martinez, M. J. Ortiz, *Chem. Eur. J.* **2017**, *23*, 4837-4848.
228. N. Zhao, S. Xuan, F. R. Fronczek, K. M. Smith, M. G. H. Vicente, *J. Org. Chem.* **2017**, *82*, 3880-3885.
229. A. M. Christianson, F. P. Gabbai, *Chem. Commun.* **2017**, *53*, 2471-2474.

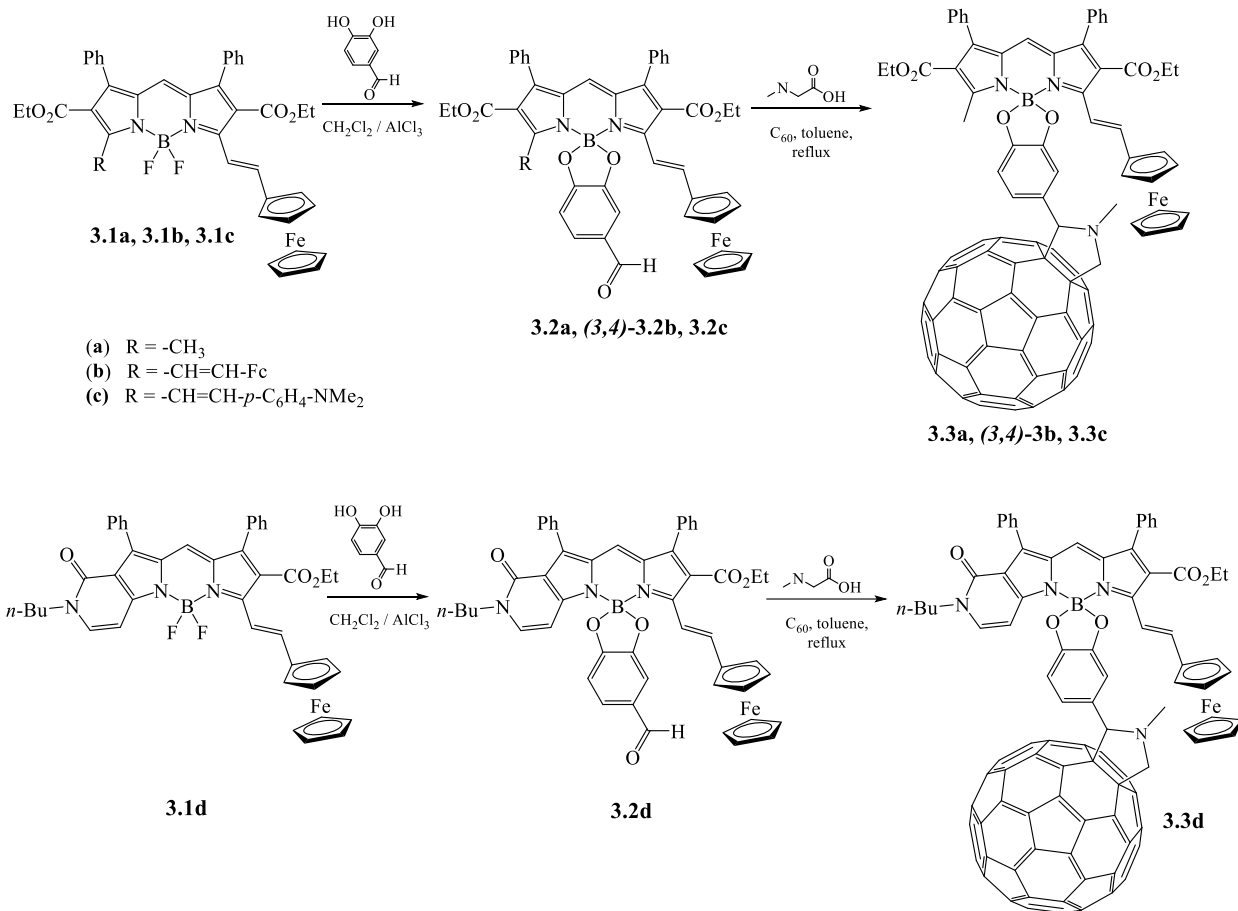
230. W. R. Goetsch, P. V. Solntsev, C. Van Stappen, A. A. Purchel, S. V. Dudkin, V. N. Nemykin, *Organometallics* **2014**, *33*, 145-157.
231. G. Scalmani, M. J. Frisch, B. Mennucci, J. Tomasi, R. Cammi, V. Barone, *J. Chem. Phys.* **2006**, *124*, 094107: 1-15.
232. A. J. H. Wachters, *J. Chem. Phys.* **1970**, *52*, 1033-1036.
233. A. D. McLean, G. S. Chandler, *J. Chem. Phys.* **1980**, *72*, 5639-5648.
234. Gaussian 09, Revision D.1, M. J. Frisch, G. W. Trucks, H. B. Schlegel, G. E. Scuseria, et al Gaussian, Inc., Wallingford CT, **2009**
235. A. L. Tenderholt, QMForge, Version 2.1. Stanford University, Stanford, CA, USA. <http://qmforge.sourceforge.net/>
236. A. Altomare, G. Cascarano, C. Giacovazzo, A. Guagliardi, M. C. Burla, G. Polidori, M. Camalli, *J. Appl. Cryst.* **1994**, *27*, 435.
237. M. Bellizzi, P. C. D. Foss, R. Pelto, G. Crundwell, C. Brueckner, J. B. III Updegraff, M. Zeller, A. D. Hunter, *Zeitschrift fuer Kristallographie* **2004**, *219(2)*, 129-131.
238. P. Wagner, D. L. Officer, M. Kubicki, *Acta Cryst., Section E.* **2006**, *62(12)*, o5745-o5747.
239. P. W. Betteridge, J. R. Carruthers, R. I. Cooper, K. Prout, D. J. Watkin, *J. Appl. Cryst.*, **2003**, *36*, 1487.
240. Bruker-AXS APEX3 v2016.1-0, Madison, Wisconsin, USA, **2016**.
241. G. M. Sheldrick, *Acta Cryst.* **2008**, *A64*, 112-122; c) A. L. Spek, *Acta Cryst.* **2009**, *D65*, 148-155.
242. M. P. Shandura, V. P. Yakubovskiy, Y. P. Kovtun, *J. Heterocyclic Chem.* **2009**, *46*, 1386-1391.
243. Y. V. Zatsikha, T. S. Blesener, P. C. Goff, A. T. Healy, R. K. Swedin, D. E. Herbert, G. T. Rohde, K. Chanawanno, C. J. Ziegler, R. V. Belosludov, D. A. Blank, V. N. Nemykin, *J. Phys. Chem. C*, **2018**, *122*, 27893-27916
244. N. P. Wells, B. W. Boudouris, M. A. Hillmyer, D. A. Blank, *J. Phys. Chem. C* **2007**, *111*, 15404-15414

## Chapter 3

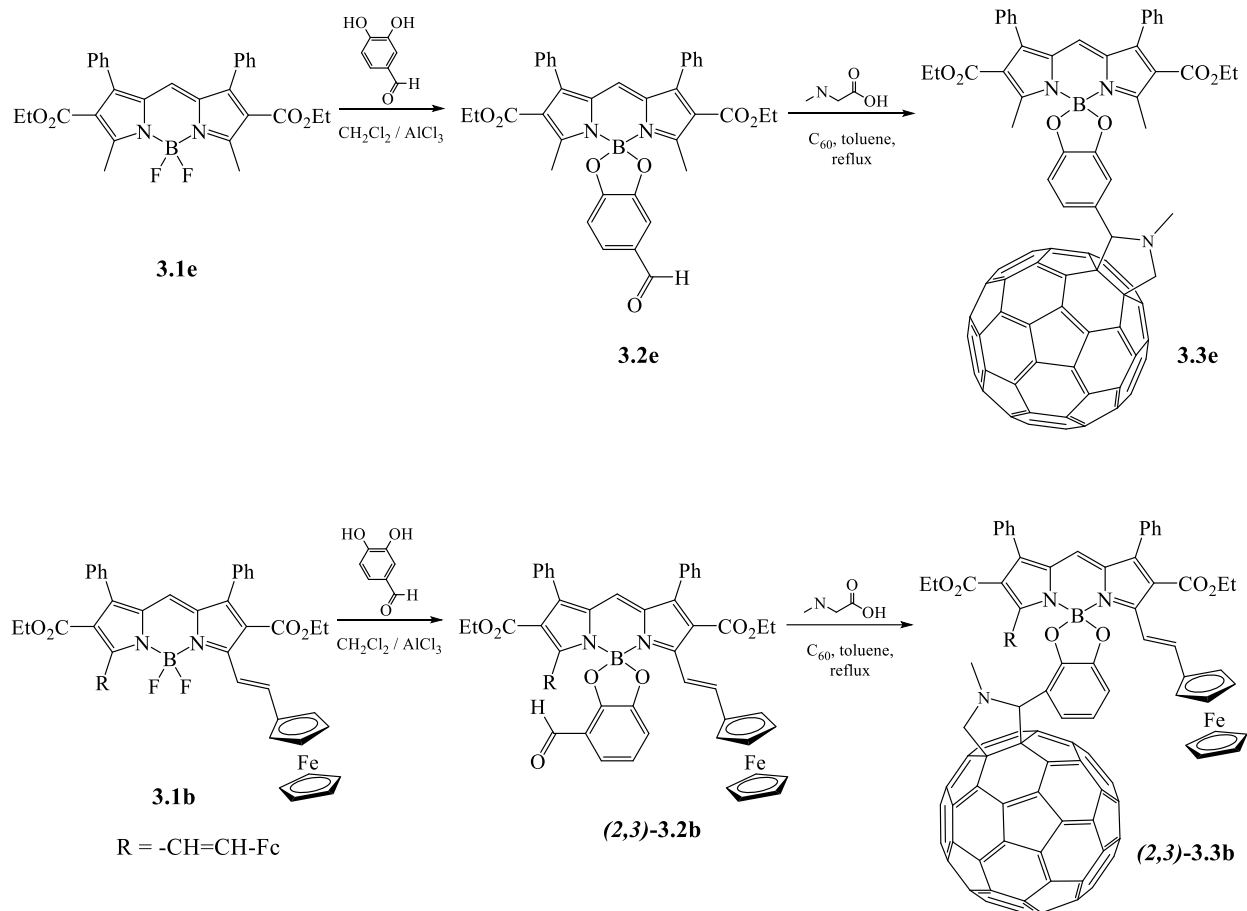
### Investigation of ferrocene-BODIPY-C<sub>60</sub> triads covalently linked via catechol linker

#### Introduction

The photoinduced electron-transfer properties of chromophore-acceptor and donor-chromophore-acceptor molecular assemblies have attracted substantial interest as the basis for potential applications in organic photovoltaic and dye-sensitized solar cells.<sup>1-7</sup> Initial formation of long-lived charge-separated states is one of many important aspects in the design of efficient light-harvesting assemblies.<sup>8</sup> Due to their combined optical properties and stability, porphyrins,<sup>9-15</sup> phthalocyanines,<sup>16-29</sup> subphthalocyanines,<sup>30-47</sup> and more recently BODIPYs,<sup>48-53</sup> aza-BODIPYs,<sup>54,55</sup> and BOPHYs<sup>56-65</sup> have gained significant attention as chromophores in donor-acceptor (D-A) systems targeted at light-harvesting. With readily accessible functionalization and well-known redox properties that make them a robust electron acceptor, fullerene derivatives have often been employed as an excited state charge transfer partner.<sup>66-68</sup> Additional electron-donating ligands such as amines<sup>69-79</sup> and ferrocene<sup>80-88</sup> can be added to facilitate photoinduced charge transfer, extend the absorption spectrum, and extend the charge separation distance to inhibit recombination in D-A assemblies. Although a large number of BODIPY-fullerene D-A systems were published in the literature,<sup>89-91</sup> covalently linked ferrocene-BODIPY-fullerene assemblies in which the ferrocene donor is fully conjugated to the BODIPY  $\pi$ -system have not been reported. Building on our previous work from chapter 2 with ferrocene-BODIPY,<sup>92-95</sup> ferrocene-aza-BODIPY,<sup>96-99</sup> and ferrocene-BOPHY<sup>100-101</sup> dyads, we present the synthesis, electrochemical and photophysical characterization of covalently linked ferrocene-BODIPY-fullerene assemblies **3.3a-e** that employ a catechol based bridge between the BODIPY and fullerene (scheme 3.1-3.3).

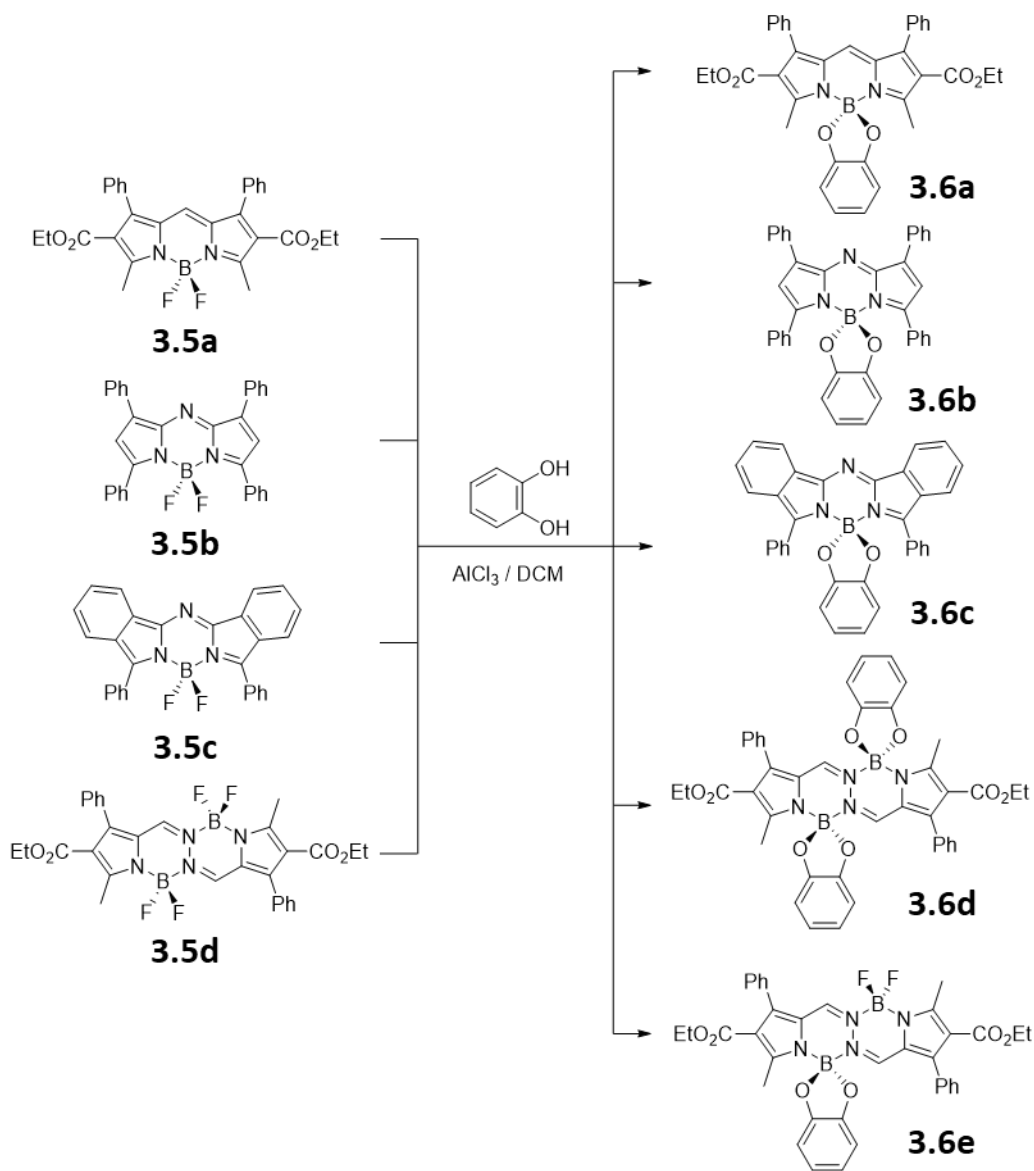


Scheme 3.1: Synthetic pathway for preparation of the ferrocene-BODIPY-fullerene triads **3.3a** – **3.3d**.



Scheme 3.2: Synthetic pathway for preparation of the reference BODIPY-fullerene dyad **3.3e** and **(2,3)-3.3b**.

While I found the parent BODIPY derivatives exhibited large fluorescence quantum yields, no fluorescence was observed in the BODIPY-catechol dyad precursor without ferrocene **3.2e** leading to the hypothesis that the initial photo-excited state on BODIPY derived chromophores were rapidly quenched by the catechol linker. To better understand the underlying dynamics of the catechol linker a series of difluoro and catechol substituted BODIPY complexes (**3.5a-e** and **3.6a-e**) were prepared and characterized.



Scheme 3.3: Synthesis of compounds **3.5a-d**, **3.6a-e** and **3.7**

### Synthesis, Characterization, and Electron-Transfer Properties of Ferrocene-BODIPY-Fullerene NIR Absorbing Triads

Starting from previously reported ferrocene-BODIPY dyads **3.2a** – **3.2d**,<sup>92</sup> ferrocene-BODIPY-fullerene triads **3.3a** – **3.3d** were prepared as outlined in Scheme 3.1. The choice of a catecholpyrrolidine-bridged fullerene as the terminal electron acceptor was based primarily on three factors. First, this architecture was reported to be effective in promoting the desired excited state electron transfer.<sup>102-105</sup> Second, by interrupting conjugation, the bridge is expected to limit

electronic coupling between the ferrocene-BODIPY donor and the fullerene acceptor, with the potential to extend the lifetime of the targeted charge separate state. Third, catecholpyrrolidine-bridged fullerene bridge can be easily installed from the synthetic point of view. Triads **3.3a** – **3.3d** were prepared in two steps. First, a catecholaldehyde fragment was introduced by ligand-exchange between BODIPYs **3.2a** – **3.2d** and the catechol.<sup>106</sup> Then the Prato reaction<sup>107</sup> was used to covalently bond the fullerene to the ferrocene-BODIPY. To investigate the influence of the fullerene-to-BODIPY distance and orientation on the photoinduced electron-transfer processes, two isomeric Fc-BODIPY-C<sub>60</sub> triads, (**2,3**)-**3.3b** and (**3,4**)-**3.3b** were prepared, which differed by the catechol group linkage to fullerene acceptor. Two reference compounds were also prepared as illustrated in Scheme 3.2. One was the BODIPY-fullerene dyad **3.3e**, which lacks the ferrocene (Fc) fragment. The other was the phenylpyrrolidine fullerene reference acceptor **3.4** prepared by Prato reaction between benzaldehyde and C<sub>60</sub> fullerene. All new compounds were characterized by NMR spectroscopy, high-resolution mass spectrometry, and UV-vis spectroscopy (Figures 3.1-3.18). The NMR spectra of all target compounds **3.3a-e** have characteristic diastereotopic signals for protons located at the *N*-methylpyrrolidine fragment. High-resolution mass spectra on **3.3a** – **3.3e** were found to be in full agreement with their elemental composition although in some cases both [M]<sup>+</sup> and [M+1]<sup>+</sup> ion were simultaneously observed.

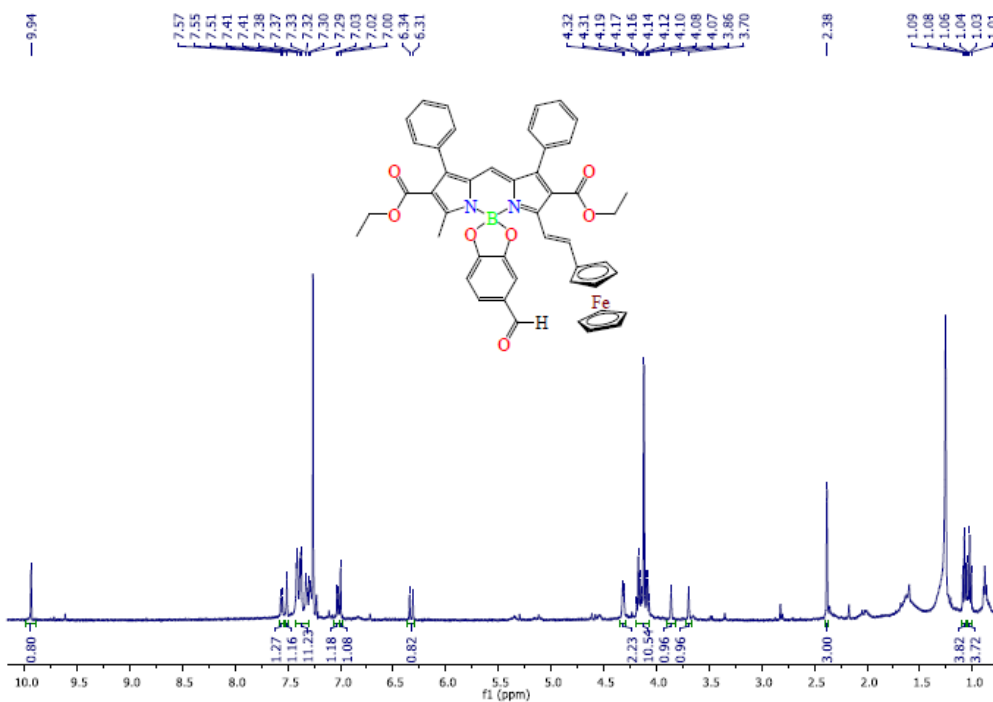


Figure 3.1: <sup>1</sup>H NMR spectrum of compound **3.2a** in CDCl<sub>3</sub>.

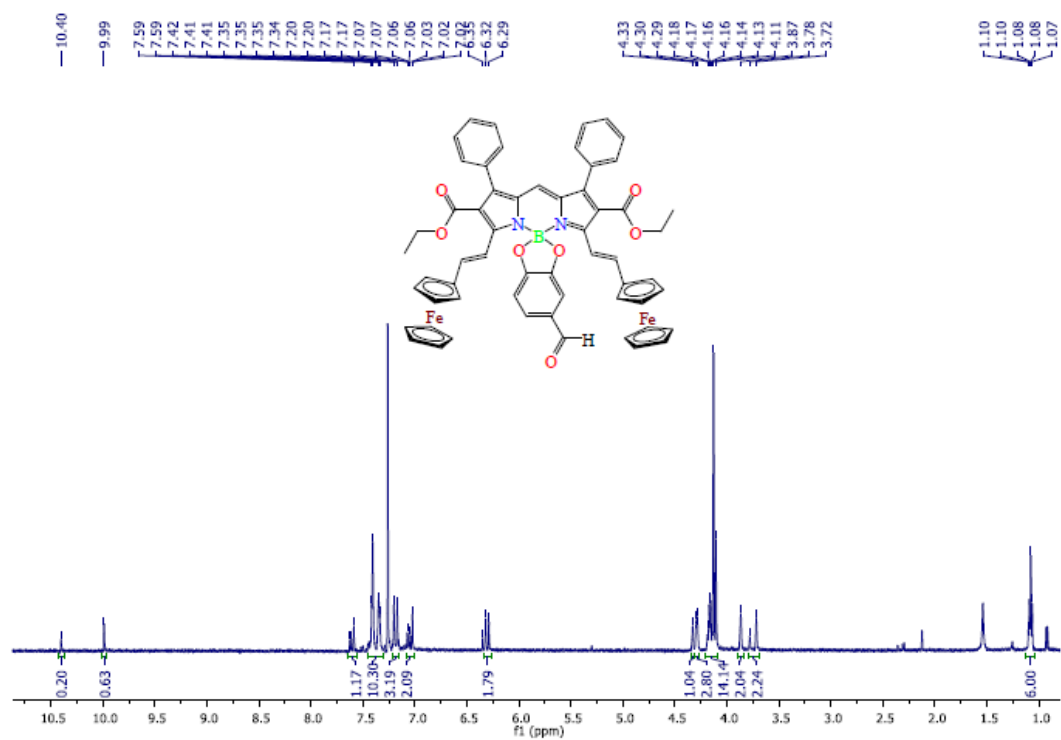


Figure 3.2:  $^1\text{H}$  NMR spectrum of compound (3,4)-**3.2b** in  $\text{CDCl}_3$ .

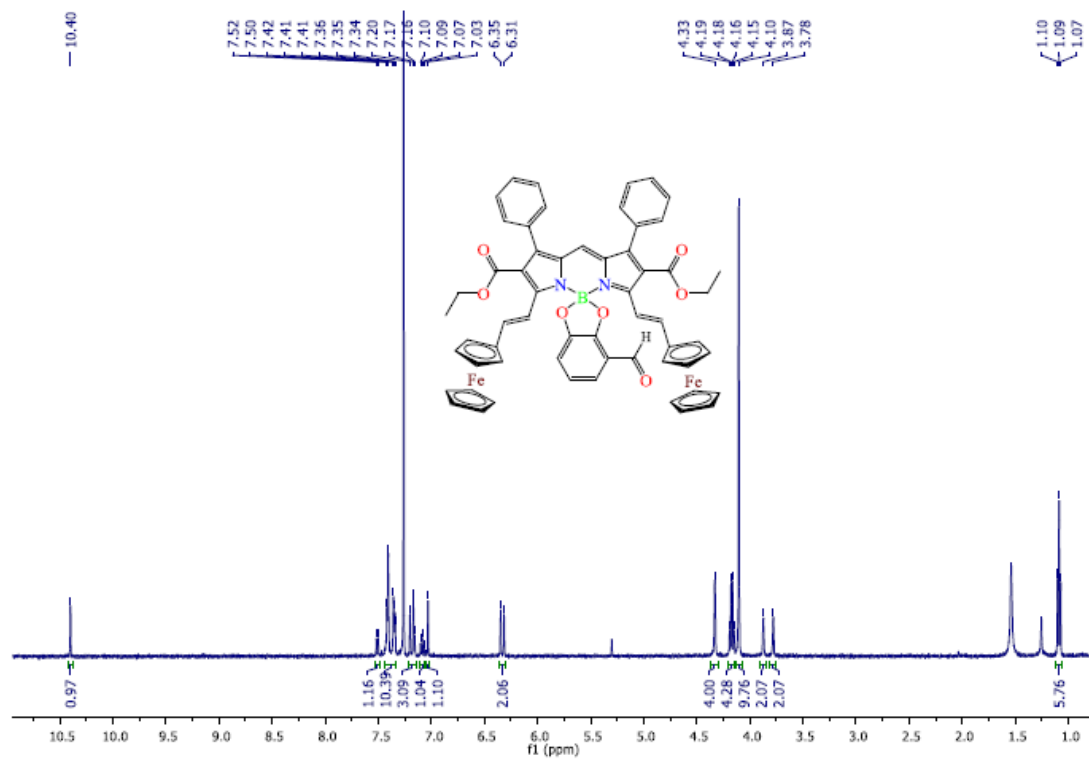


Figure 3.3:  $^1\text{H}$  NMR spectrum of compound (2,3)-**3.2b** in  $\text{CDCl}_3$ .

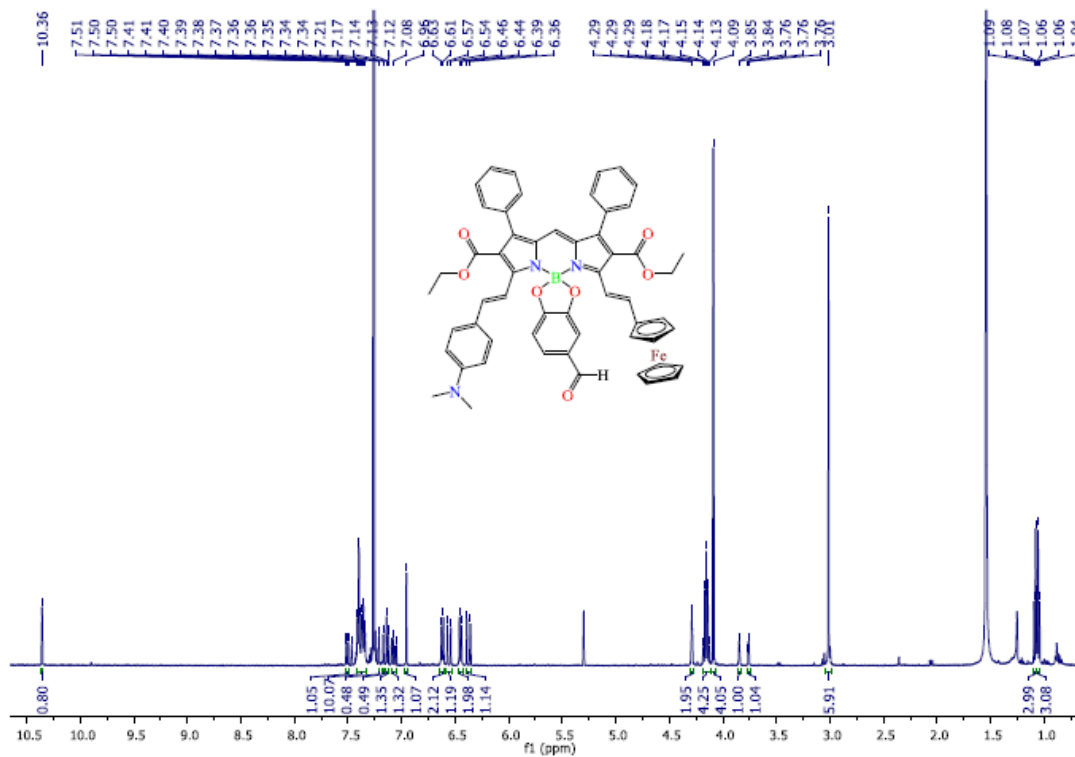


Figure 3.4:  $^1\text{H}$  NMR spectrum of compound **3.2c** in  $\text{CDCl}_3$ .

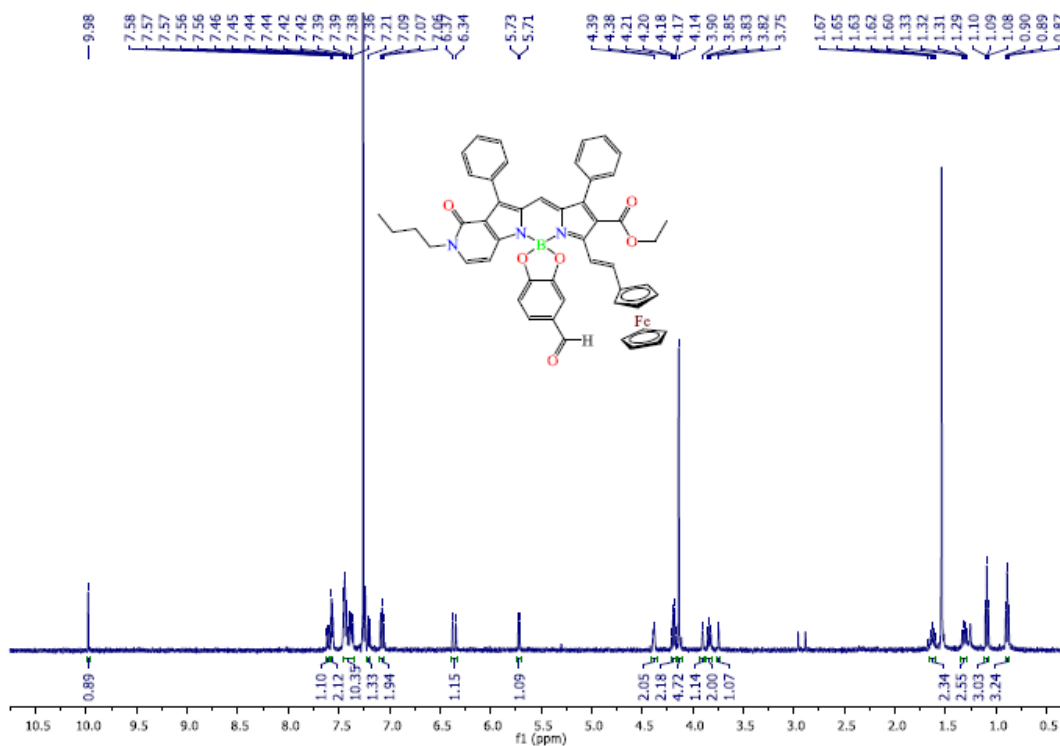


Figure 3.5:  $^1\text{H}$  NMR spectrum of compound **3.2d** in  $\text{CDCl}_3$ .

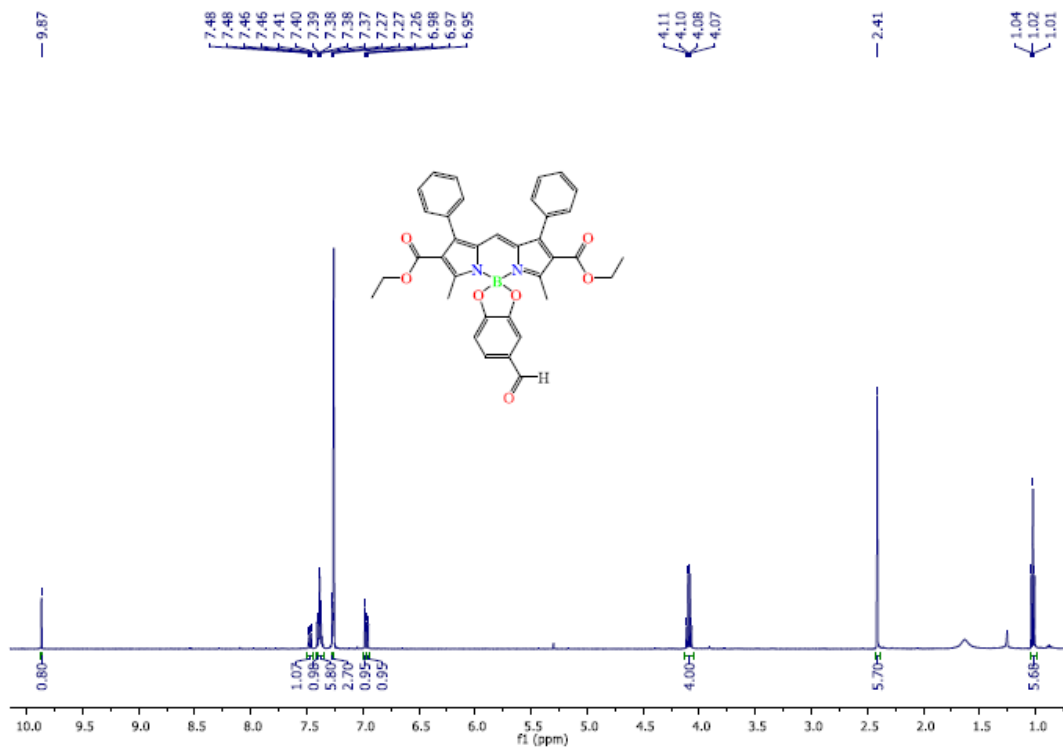


Figure 3.6:  $^1\text{H}$  NMR spectrum of compound **3.2e** in  $\text{CDCl}_3$ .

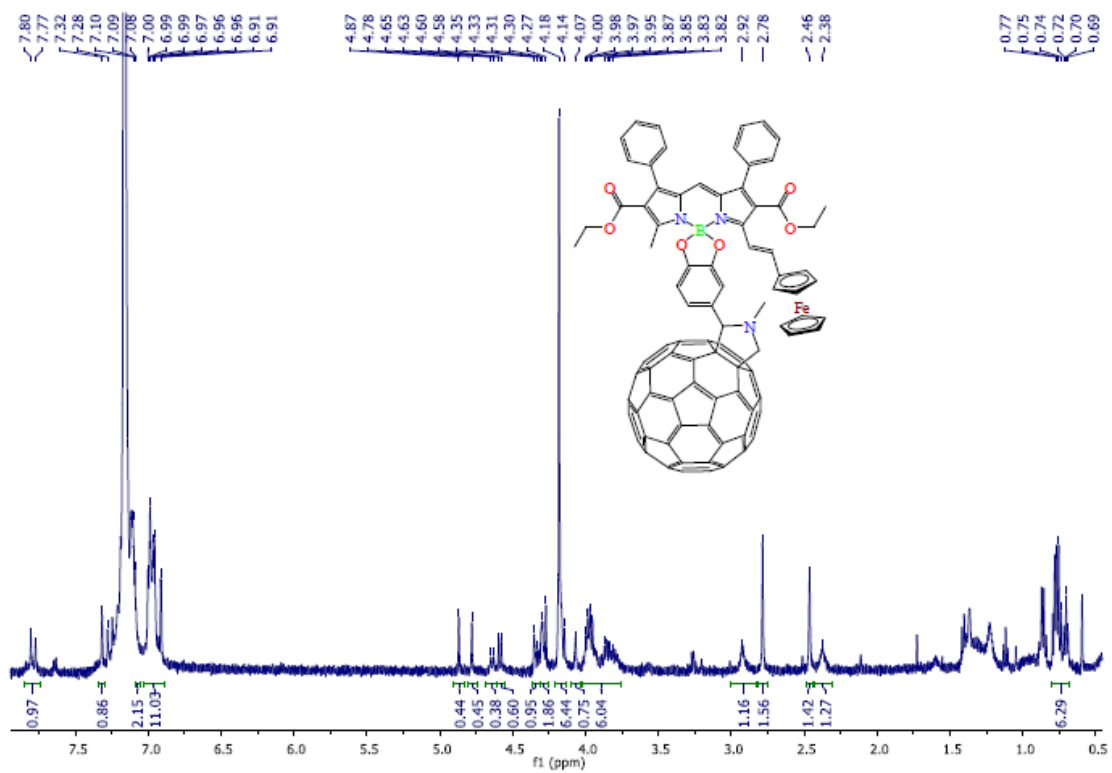


Figure 3.7:  $^1\text{H}$  NMR spectrum of compound **3.3a** in  $\text{C}_6\text{D}_6$ .

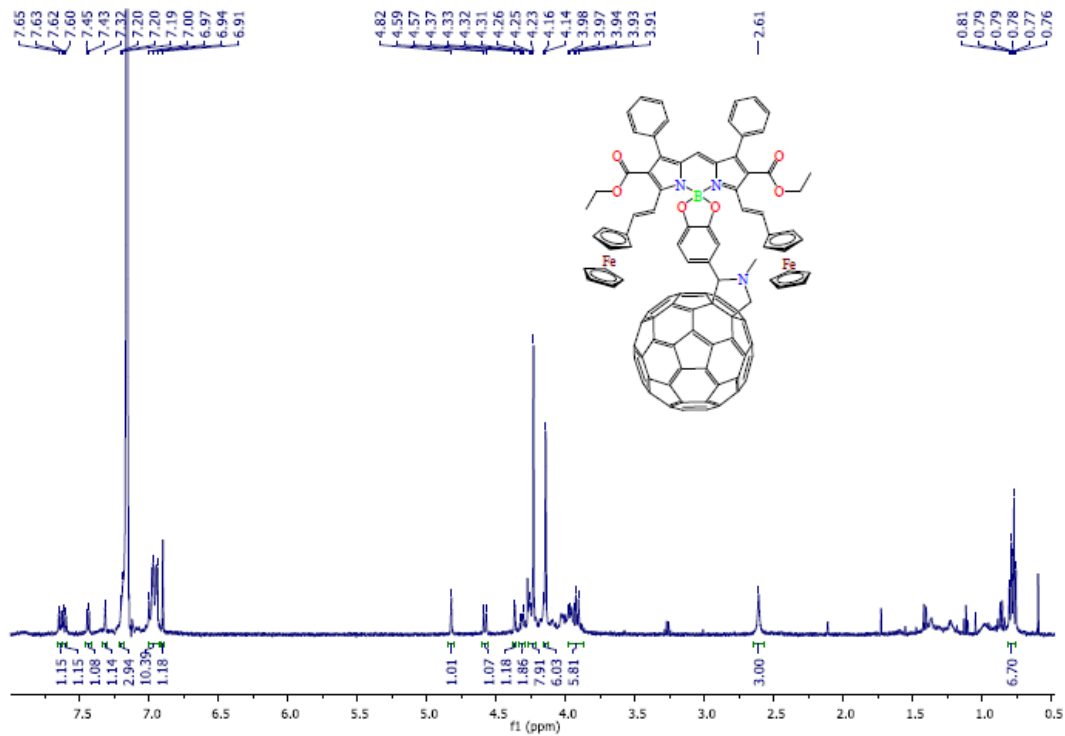


Figure 3.8:  $^1\text{H}$  NMR spectrum of compound (3,4)-**3.3b** in  $\text{C}_6\text{D}_6$ .

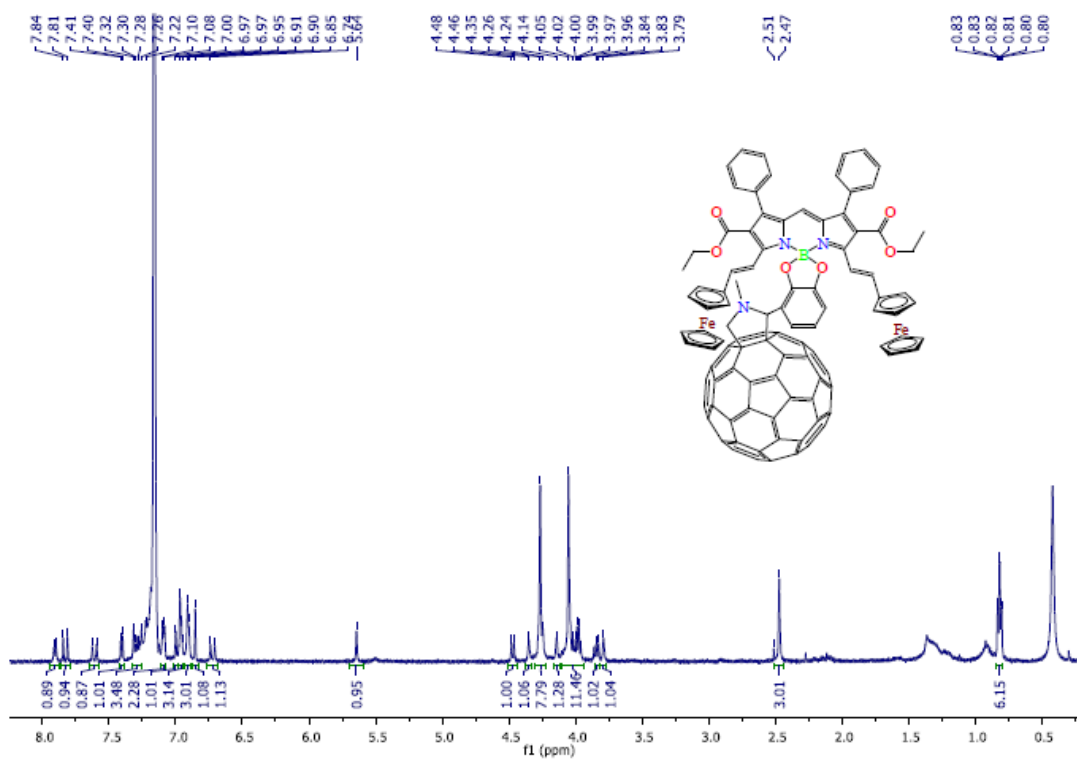


Figure 3.9:  $^1\text{H}$  NMR spectrum of compound (2,3)-**3.3b** in  $\text{C}_6\text{D}_6$ .

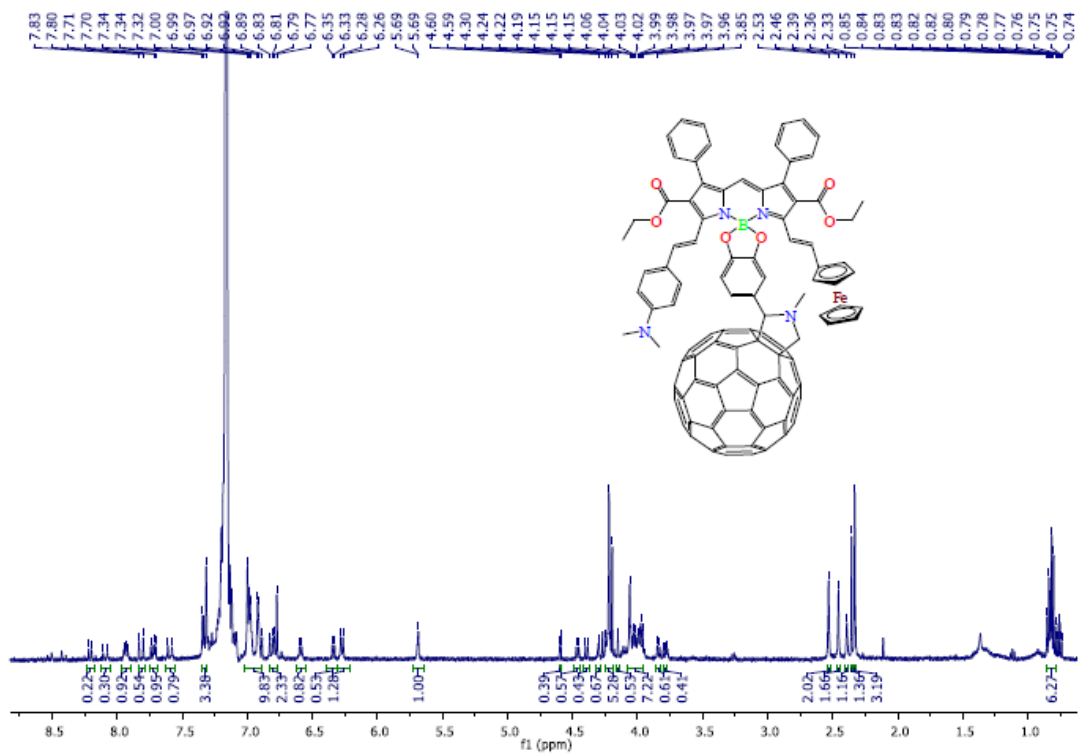


Figure 3.10:  $^1\text{H}$  NMR spectrum of compound **3.3c** in  $\text{C}_6\text{D}_6$ .

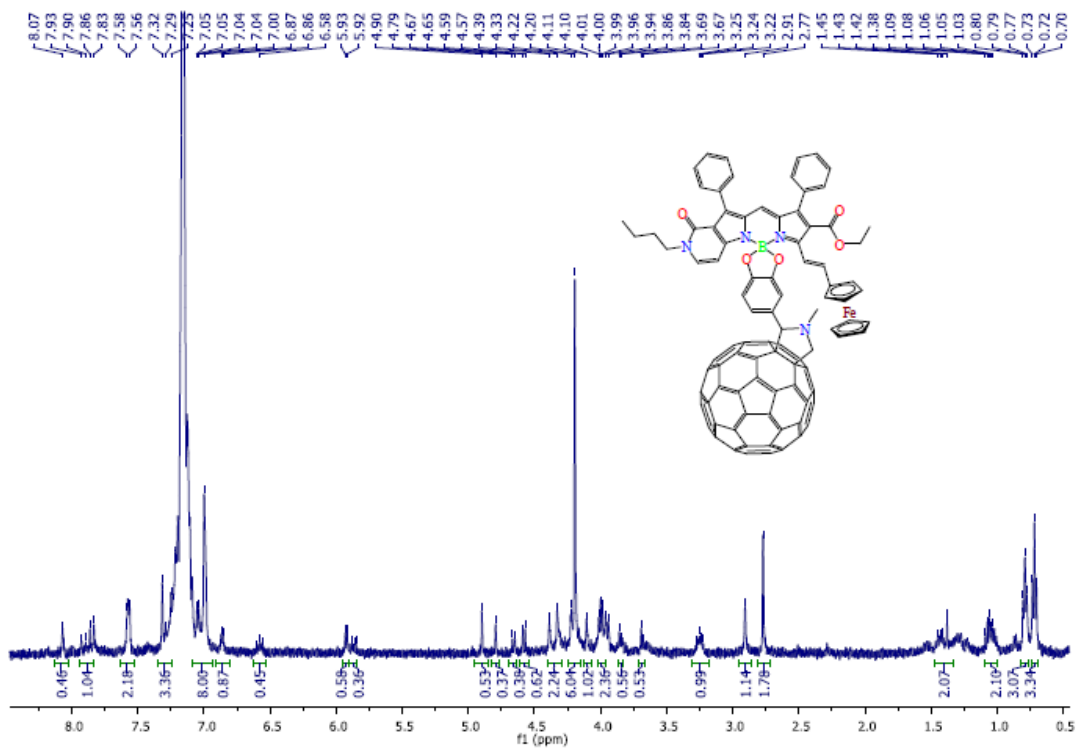


Figure 3.11:  $^1\text{H}$  NMR spectrum of compound **3.3d** in  $\text{C}_6\text{D}_6$ .

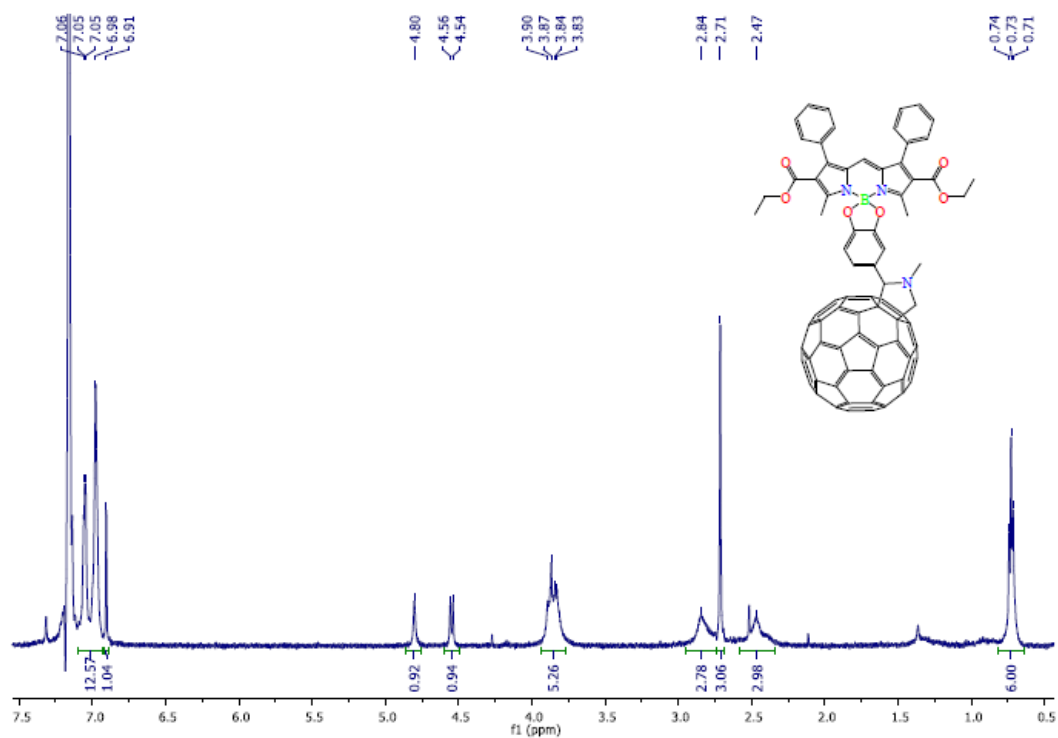


Figure 3.12: <sup>1</sup>H NMR spectrum of compound **3.3e** in C<sub>6</sub>D<sub>6</sub>.

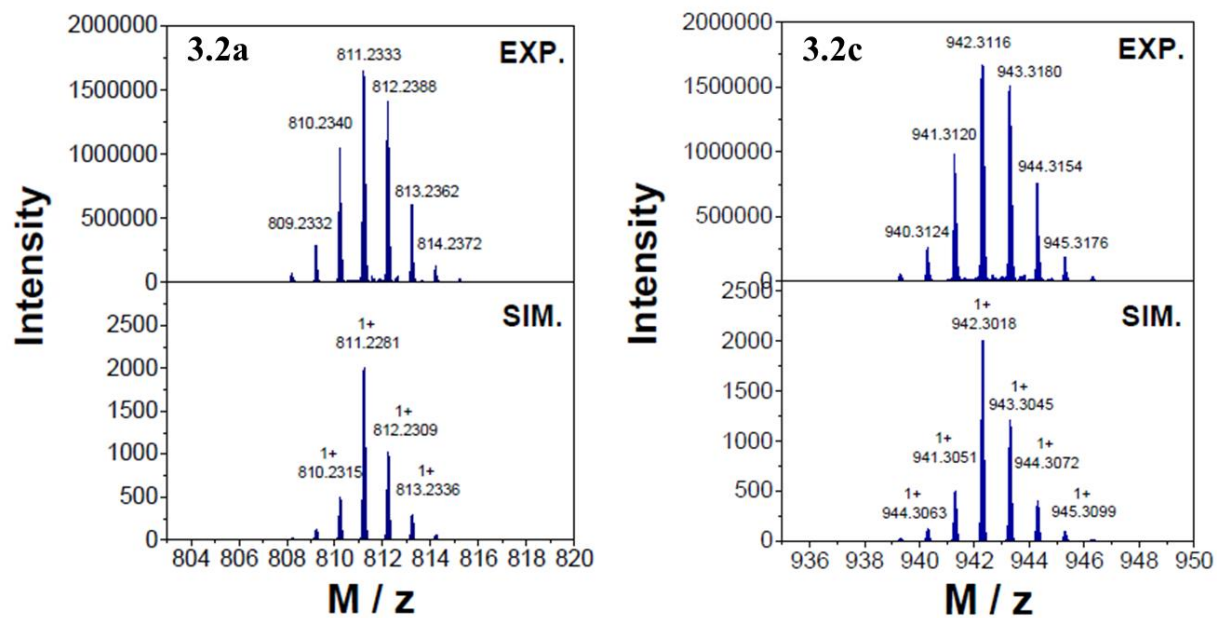


Figure 3.13: APCI high-resolution mass spectrum of compound **3.2a** (left) and **2.2c** (right).

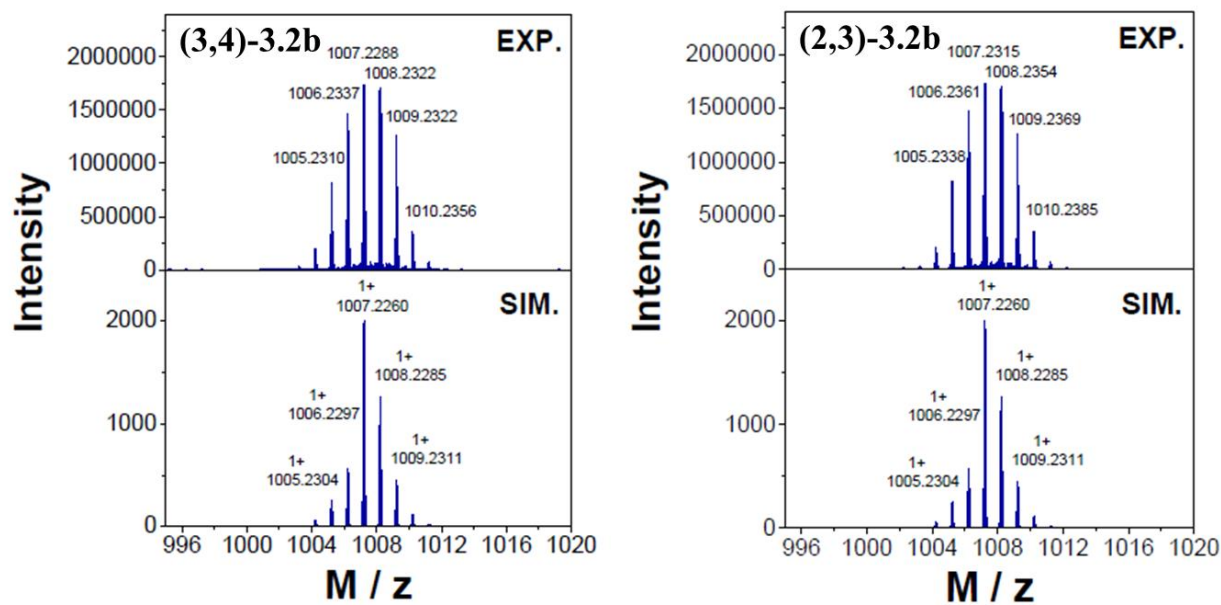


Figure 3.14: APCI high-resolution mass spectrum of compound (3,4)-3.2b (left) and (2,3)-3.2 (right).

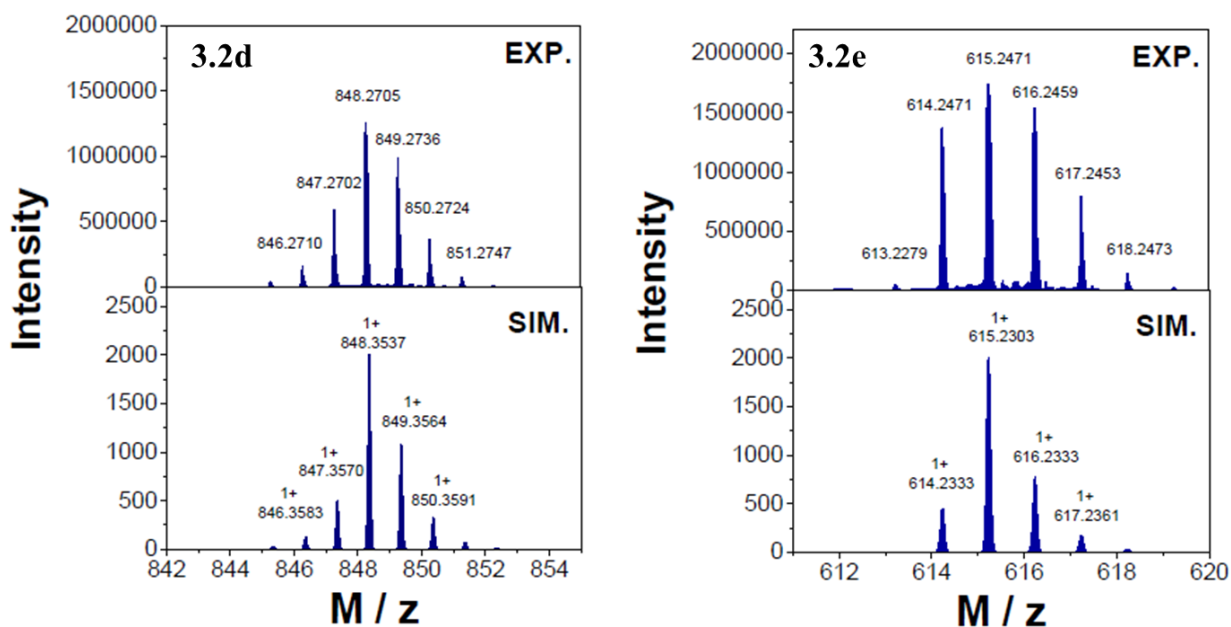


Figure 3.15: APCI high-resolution mass spectrum of compound 3.2d (left) and 3.2e (right).

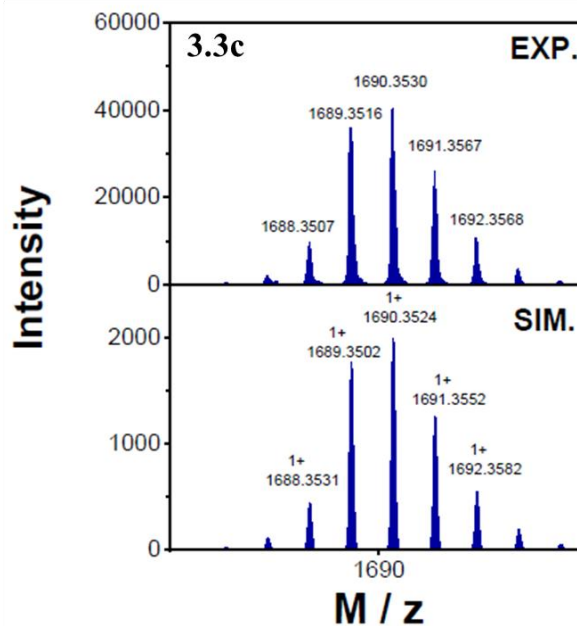
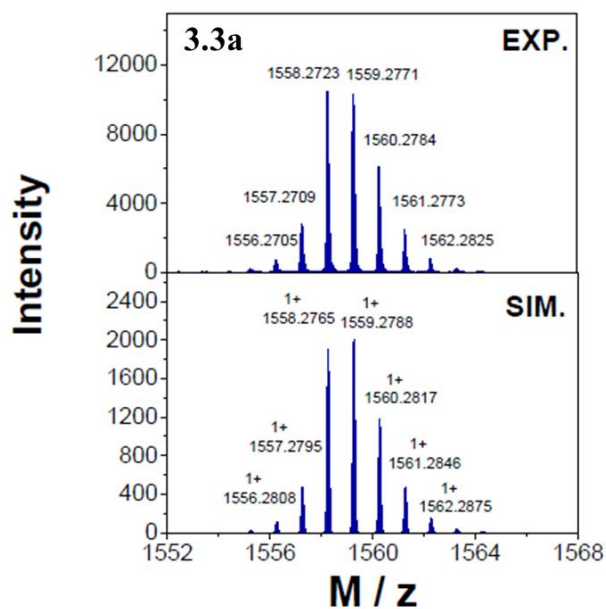


Figure 3.16: APCI high-resolution mass spectrum of compound **3.3a** (left) and **3.3c** (right).

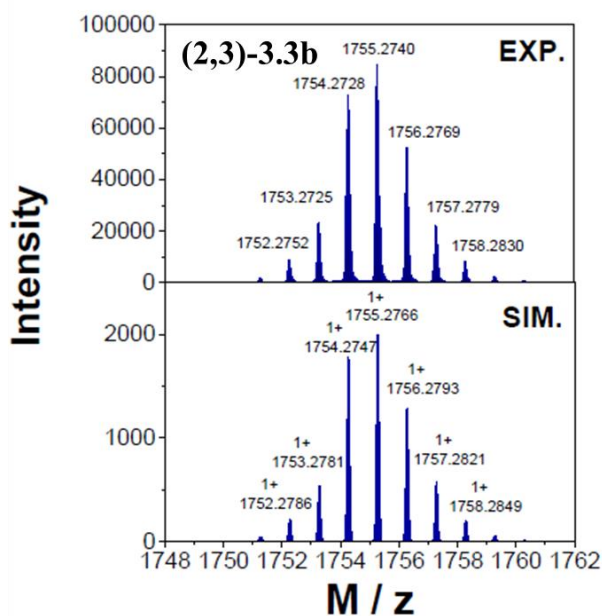
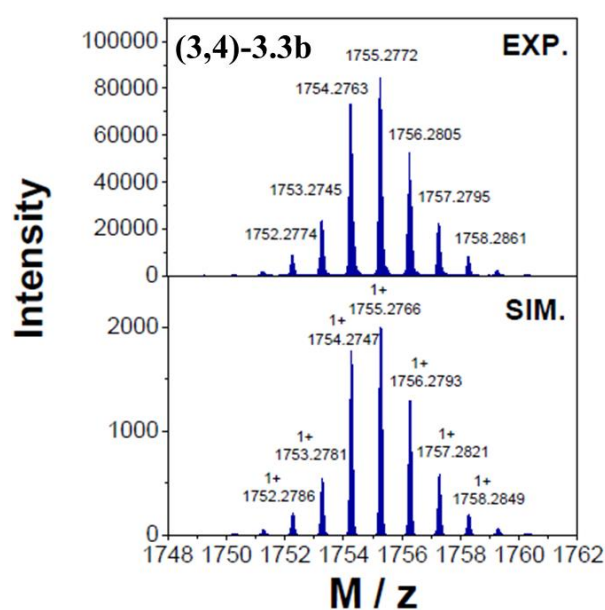


Figure 3.17: APCI high-resolution mass spectrum of compound (3,4)-**3.3b** (left) and (2,3)-**3.3b** (right).

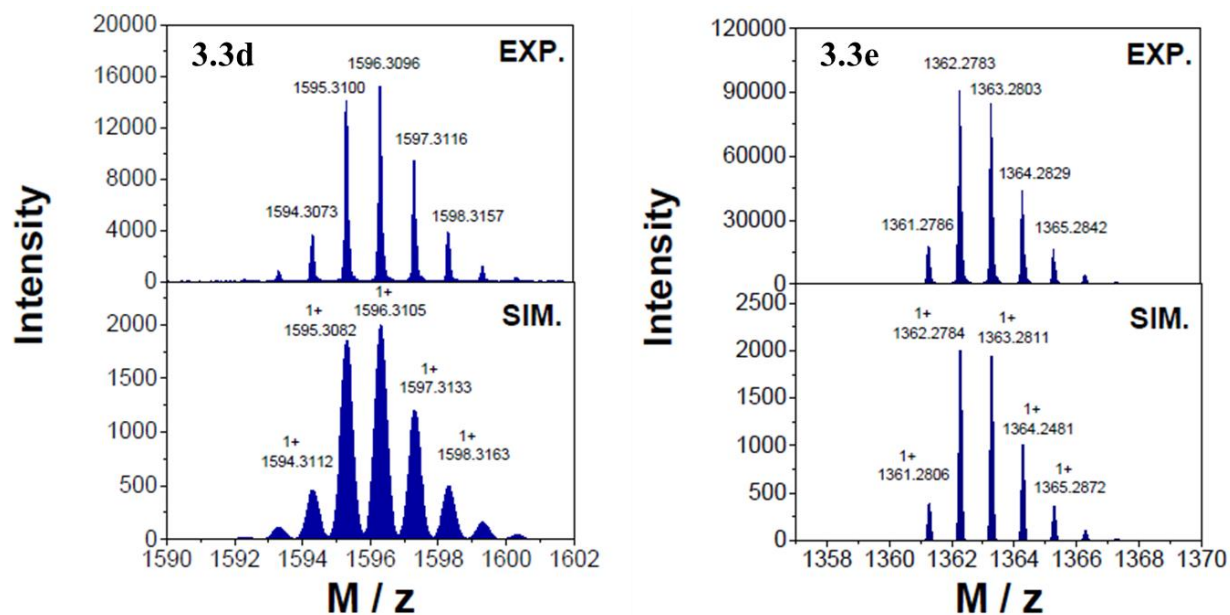


Figure 3.18: APCI high-resolution mass spectrum of compound **3.3d** (left) and **3.3e** (right).

We attempted to obtain single crystals of triads **3.3a–3.3d**. In the majority of cases, crystals were too small for X-ray crystallographic measurements, with typical reflection data limited to  $\sim 3$  Å resolution. However, in the case of triad **(2,3)-3.3b** reliable X-ray data with up to 1.1 Å resolution was obtained, which allowed direct confirmation of the structure (Figure 3.19). In the crystal structure of **(2,3)-3.3b**, two ferrocene fragments were found in a *syn*-conformation with an Fe-Fe distance of  $\sim 10.51$  Å. Torsion angles between the ferrocenes and the BODIPY core were  $\sim 18.44^\circ$  and  $\sim 42.84^\circ$ , the catechol group was perpendicular to the BODIPY plane, and the N-methylpyrrolidine group was racemic. The fullerene in **(2,3)-3.3b** has two sets of close contacts. One set is oriented towards the neighbor fullerene fragment with the closest intermolecular contacts observed at  $\sim 3.15$  and  $\sim 3.19$  Å. The other set of the close intermolecular contacts is roughly perpendicular to the fullerene-fullerene interaction and associated with fullerene-BODIPY interactions. In this case, the fullerene on **(2,3)-3.3b** is located above the BODIPY core with the closest intermolecular contacts observed between fullerene-O(catechol) at  $\sim 2.85$  Å, fullerene-C(BODIPY-*meso*) at  $\sim 3.34$  Å, fullerene-B at  $\sim 3.51$  Å, and fullerene-N(BODIPY) at  $\sim 3.18$  Å (Figure 3.19). As shown by Torres and co-workers for covalently linked subphthalocyanine-fullerene dyads and triads,<sup>[9a,b]</sup> the short fullerene-fullerene ( $\sim 3.1$  Å) and fullerene-BODIPY ( $\sim 3.2$

Å) intermolecular contacts observed in the crystal structure of (2,3)-3.3b have the potential to facilitate an intermolecular electron-transfer processes in triads 3.3a – 3.3d in the solid state.

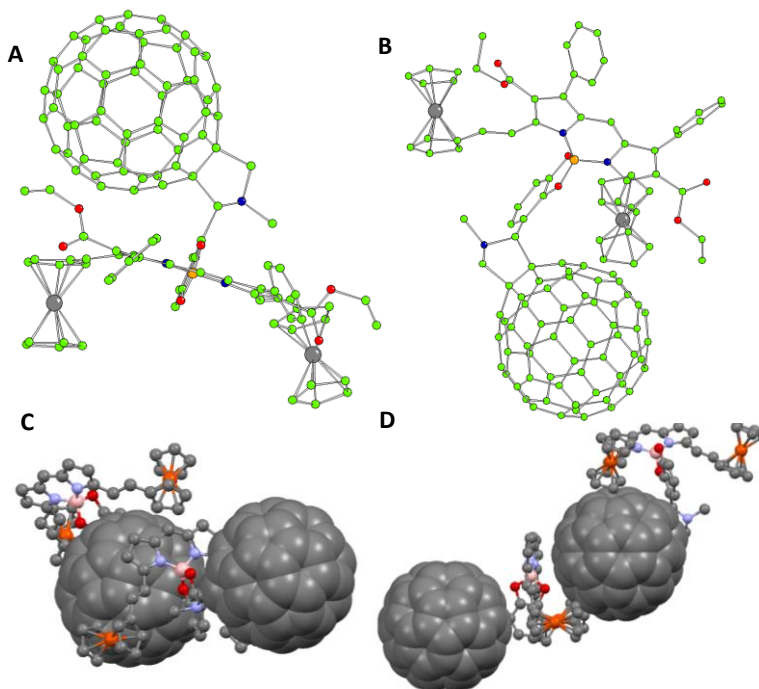


Figure 3.19: (A and B) CAMERON drawing of the X-ray structure of ferrocene-BODIPY-fullerene triad (2,3)-3.3b. All hydrogen atoms are omitted for clarity. (C and D) Packing motifs observed in the X-ray crystal structure of (2,3)-3.3b.

Table 3.1. UV-vis spectra of the target compounds in DCM.

Compound	$\lambda_{\text{abs.}}$ , nm ( $\epsilon \cdot 10^{-4}$ , $\text{M}^{-1} \cdot \text{cm}^{-1}$ )
<b>3.3a</b>	325(3.6), 559(4.2), 680(1.4)
<b>(3,4)-3.3b</b>	325(3.5), 578(2.1), 755(1.8)
<b>(2,3)-3.3b</b>	325(3.5), 585(2.0), 766(1.8)
<b>3.3c</b>	331(3.6), 670(2.3), 764(3.3)
<b>3.3d</b>	315(3.7), 621(3.5), 726(1.6)
<b>3.3e</b>	321(3.3), 522(8.6)
<b>3.4</b>	327(3.5), 430(0.3)

The UV-vis-NIR spectra of the Fc-BODIPY-C<sub>60</sub> triads **3.3a** – **3.3d** and reference compounds **3.3e** and **3.4** are presented in Figure 3.20. The spectra are very similar to those observed in the respective Fc-BODIPY dyads **3.2a** – **3.2d** in the vis-NIR region (Table 3.1).<sup>92</sup> This reflects the lack of conjugation and limited electronic coupling from the BODIPY and the ferrocene to the fullerene. Specifically, in triads **3.3a** – **3.3c**, the low-energy, less intense broad band in the NIR region can be attributed to the predominant metal(Fc)-to-ligand(BODIPY) charge-transfer (MLCT) transition, while the narrow and more intense band in the visible region can be assigned to the BODIPY-centered  $\pi \rightarrow \pi^*$  transition. The fullerene ligand in **3.3a** – **3.3d** can be clearly seen in the UV region. There is a strong absorption typical of fullerenes at 330 nm<sup>107</sup> and similar to that observed in the N-methyl-2-phenyl-fulleropyrrolidine reference compound **3.4** (Figure 3.20). No difference was observed between the UV-vis-NIR spectra of the differocene-containing triads (2,3)-**3.3b** and (3,4)-**3.3b**, which only differ by the connectivity of the fullerene ligand. Similarly, the UV-vis spectrum of reference **3.3e** is very close to the parent BODIPY, **3.1e**, except for the presence of the additional fullerene-centered transition in the UV region of the spectrum (Figure 3.20). Overall, the UV-vis-NIR spectra of compounds **3.3a** – **3.3e** are indicative of the limited electronic communication between Fc-BODIPY core and C<sub>60</sub>. Similar to the parent ferrocene-containing dyads **3.2a** – **3.2d**,<sup>92</sup> steady-state fluorescence is completely quenched in the Fc-BODIPY-C<sub>60</sub> triads **3.3a** – **3.3d**. Fluorescence is also quenched in the reference BODIPY-C<sub>60</sub> dyad **3.3e** as well as catecholaldehyde precursor **3.2e**. In the case of the N-methyl-2-phenyl-fulleropyrrolidine reference, **3.4**, a weak steady-state fluorescence was observed in the NIR region in toluene. Addition of the trifluoroacetic acid to toluene solution of **3.4** does not lead to significant enhancement of the fluorescence, suggests coupling of the lone pair of electrons located at the nitrogen atom into the fullerene  $\pi$ -system.<sup>108f</sup>

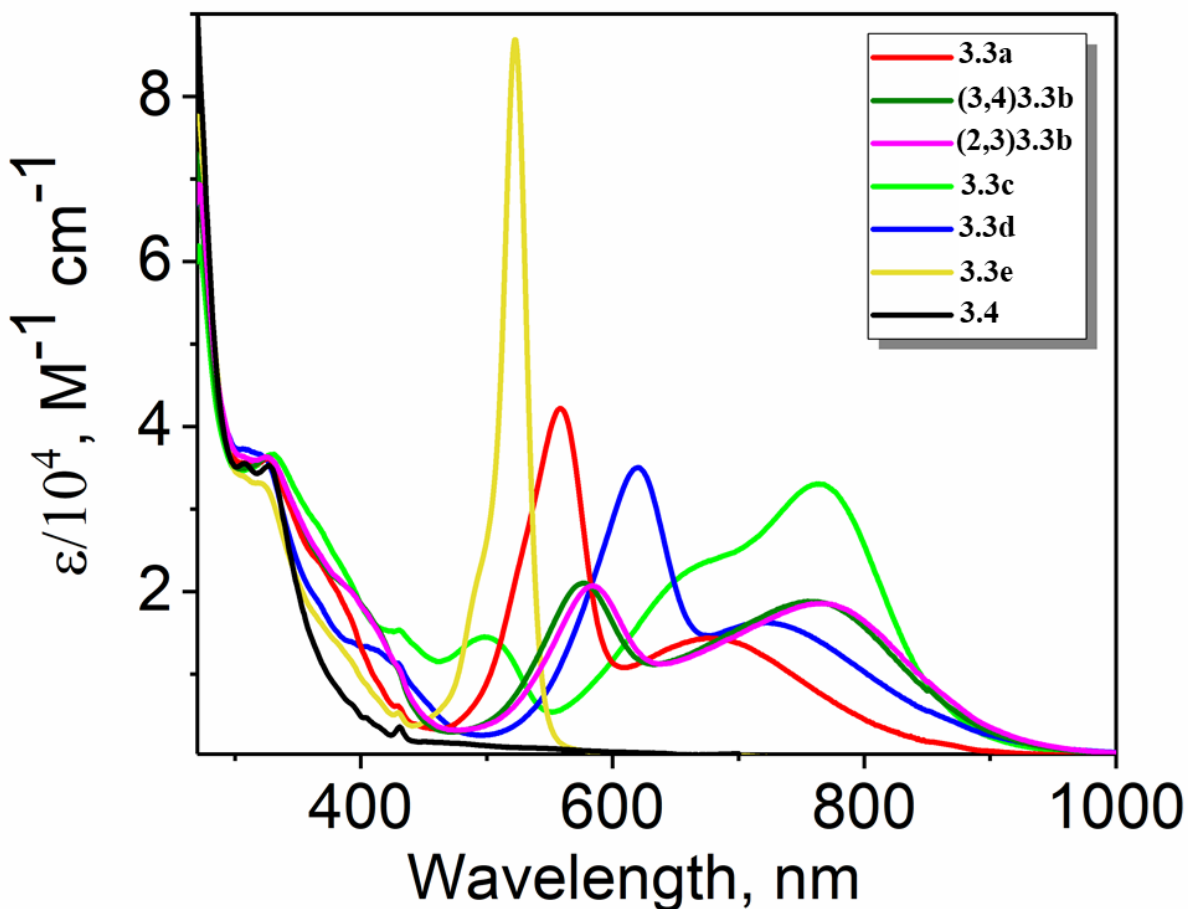


Figure 3.20: Overlapped UV-Vis spectra of **3.3a** – **3.3e** and **3.4** in DCM.

Redox properties of the Fc-BODIPY- $C_{60}$  triads **3.3a** – **3.3d**, as well as reference BODIPY- $C_{60}$  dyad **3.3e** and fullerene **3.4** and in DCM were investigated by electrochemical CV and DPV methods using an electrolyte with a low ion-pairing strength ( $NBu_4[B(C_6F_5)_4]$ , TFAB, Figure 3.21). In all cases, the oxidation processes and potentials in **3.3a**–**3.3d** and **3.3e** are very close to those observed in Fc-BODIPY dyads **3.2a**–**3.2d** and the starting BODIPY **3.1e** (Table 3.2).<sup>92</sup> In particular, the first oxidation process in triads **3.3a**–**3.3d** is always reversible and is associated with the oxidation of ferrocene. In the case of isomeric diferrocene triads **(2,3)-3.3b** and **(3,4)-3.3b** ~150 mV difference in potentials was observed for the first and the second ferrocene-centered oxidation processes similar to that observed earlier for the parent  $Fc_2$ -BODIPY dyad, **3.2b**.<sup>92</sup> This is indicative of the potential electronic coupling between the two iron centers. The BODIPY-centered oxidation in all Fc-BODIPY- $C_{60}$  triads **3.3a**–**3.3d** was irreversible, similar to that observed in the respective Fc-BODIPY dyads **3.2a**–**3.2d**.<sup>92</sup> The irreversible single-electron oxidation process

observed in the reference **3.3e** had a much lower oxidation potential compared to the other BODIPY systems. This potential was close to the oxidation of the catechol bridge, as observed in BODIPY-catechol dyads.<sup>109,110</sup> We assign the first irreversible oxidation in **3.3e** to the catechol-centered oxidation. The reduction side of the electrochemical data on triads **3.3a–3.3d** is indicative of a superposition of reversible (or quasi-reversible) reduction processes centered on the BODIPY core and fullerene fragment. For all triads **3.3a–3.3d** as well as dyad **3.3e**, the first BODIPY-centered and fullerene-centered reduction processes were closely spaced, with the largest separation observed in the pyridone-containing triad **3.3d** (Figure 3.21).

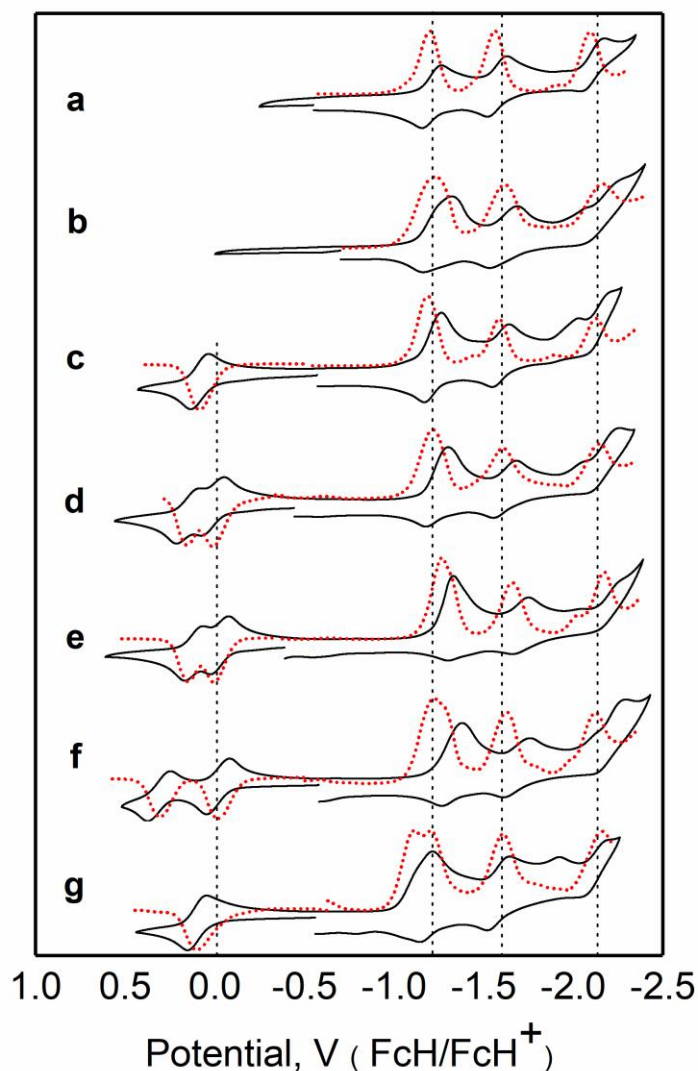


Figure 3.21: Room-temperature CV (black) and DPV (red) data for **3.4** (a), **3.3e** (b), **3.3a** (c), **(3,4)-3.3b** (d), **(2,3)-3.3b** (e), **3.3c** (f), and **3.3d** (g) in DCM/0.05 M TFAB system.

Table 3.2: Redox properties of target compounds in DCM/0.05M TFAB system.

Dye	Ox <sub>4</sub> (V)	Ox <sub>3</sub> (V)	Ox <sub>2</sub> (V)	Ox <sub>1</sub> (V)	Red <sub>1</sub> (V)	Red <sub>2</sub> (V)	Red <sub>3</sub> (V)	Red <sub>4</sub> (V)
<b>3.4</b>			~1.2	~0.8	-1.20	-1.57	-2.09	
<b>3.3e</b>			1.27	0.75	~ -1.2 <sup>a</sup>	-1.61	-2.18	
<b>3.3a</b>		1.2	0.8	0.09	~ -1.2 <sup>a</sup>	-1.60	-2.14	
<b>(3,4)-3.3b</b>	1.3	0.9	0.16	0.01	~ -1.23 <sup>a</sup>	-1.62	-2.10	
<b>(2,3)-3.3b</b>	1.3	0.85	0.15	0.05	~ -1.24 <sup>a</sup>	-1.66	-2.17	
<b>3.3c</b>	1.3	0.8	0.3	-0.018	~ -1.27 <sup>a</sup>	-1.63	-2.16	
<b>3.3d</b>		1.2	0.8	0.10	-1.11	-1.19	-1.61	-2.15

<sup>a</sup> broad, two-electron wave.

In order to gain insight into spectroscopic signatures of the mixed-valence species generated upon stepwise oxidation of the ferrocene groups in the triad **(3,4)-3.3b**, we conducted spectroelectrochemical experiments in the UV-Vis-NIR region (Figure 3.22). From the electrochemical measurements we expect that the phenyl-fulleropyrrolidine fragment ligand will have very little influence on the oxidative behavior of ferrocenes, and this is reflected in the fact that the stepwise oxidation of the ferrocene groups in triad **(3,4)-3.3b** very closely resembled earlier reports for dyad **3.2b**.<sup>92</sup> During the first oxidation, the broad MLCT absorption band at 780 nm drops in intensity, while the more intense band in the visible region increases in intensity and shifts to lower energy. Increase in the broad absorption across the NIR region is characteristic of the inter-valence charge-transfer (IVCT) band previously detected in poly(ferrocenyl)-containing systems following one electron oxidation.<sup>111-114</sup> Formation of the IVCT band is indicative of a mixed-valence character and metal-metal coupling in **[(3,4)-3.3b]<sup>+</sup>**. Our attempts to deconvolute the broad NIR absorption and identify inter-valence charge-transfer band (IVCT) in the mixed-valence **[(3,4)-3.3b]<sup>+</sup>** were unsuccessful because of the broad and featureless nature of the NIR

band. During the second oxidation the IVCT band disappears, and the MLCT band was dramatically reduced in intensity. Both changes are characteristic of complete oxidation of both iron centers in the triad [(3,4)-3.3b]<sup>2+</sup>.

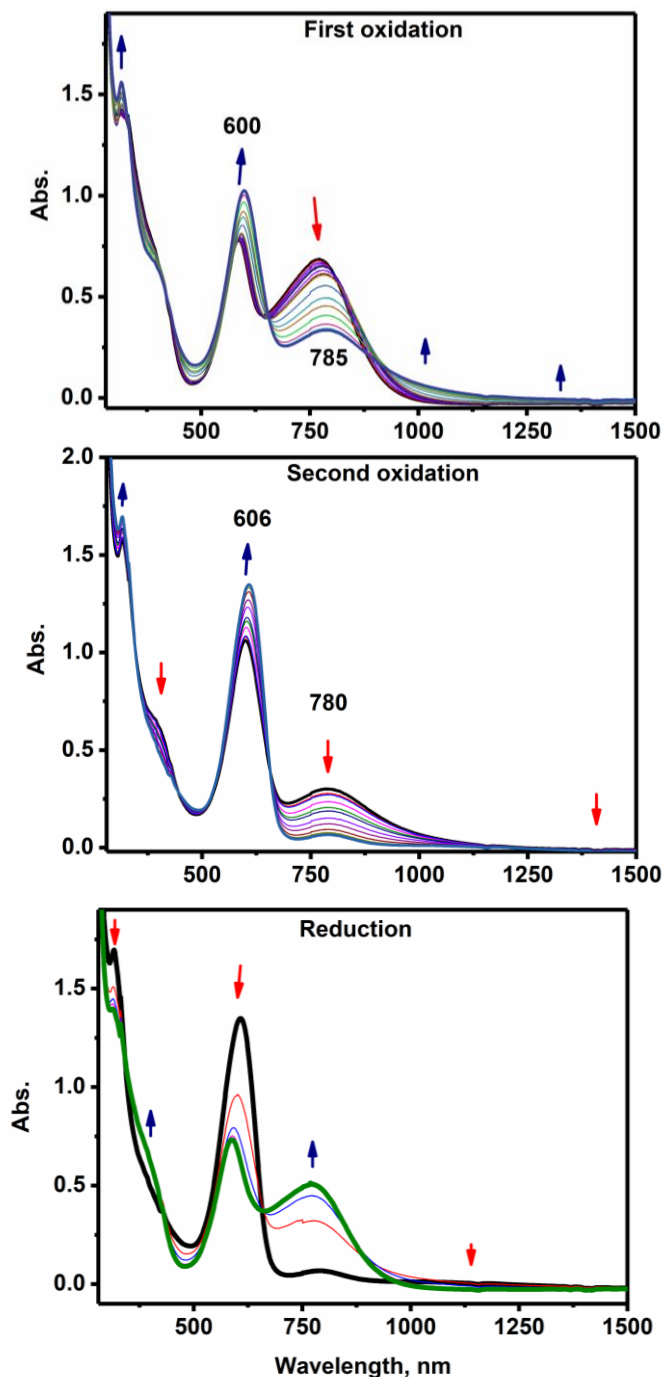


Figure 3.22: Spectroelectrochemical oxidation of triad (3,4)-3.3b in 0.15 M DCM/TFAB solvent system: the first oxidation process (top); the second oxidation process (middle); reduction (bottom).

In order to investigate the electronic structure of the triads **3.3a–3.3d** and correlate their experimentally observed spectroscopic and redox properties with their electronic structure, we conducted a set of DFT and TDDFT calculations on all target compounds. Compositions of the frontier orbitals predicted by the DFT calculations are presented in Figure 3.23, a corresponding energy diagram is presented in Figure 3.24, and selected DFT-predicted frontier orbitals are presented in Figure 3.25. In the case of reference dyad **3.3e**, DFT predicted that the HOMO will be localized on the catechol, in agreement with the experimental data and DFT calculations on BODIPY-catechol, aza-BODIPY-catechol, and BOPHY-catechol dyads.<sup>102-106,109,110</sup> Localization of the HOMO on the catechol agreed well with the low electrochemical potential for the first irreversible oxidation process observed in **3.3e** and the near complete lack of observed steady-state fluorescence in all of the BODIPY-catechol systems.<sup>109,110</sup> In contrast, the HOMO predicted by DFT calculations in Fc-BODIPY-C<sub>60</sub> triads **3.3a–3.3d** was delocalized over the ferrocene-BODIPY core, while the catechol-centered orbitals were lower in energy. The analogous ferrocene-BODIPY delocalization HOMO was previously observed in the absence of the phenyl-fulleropyrrolidine group with the respective Fc-BODIPY dyads, **3.2a–3.2d**.<sup>92</sup> This assignment agrees with the electrochemical and transition absorption data on triads **3.3a–3.3d**. DFT calculations predicted that the LUMO and LUMO+1 in all triads **3.3a–3.3d** and dyad **3.3e** are fullerene-centered, while the LUMO+2 was centered on the BODIPY core. The predicted electronic structures agreed well with the electrochemical data on all target compounds, which were indicative of a fullerene-centered first reduction process close in potential to the first reduction of the BODIPY core. Overall, DFT-calculations on all target Fc-BODIPY-fullerene triads **3.3a – 3.3d** indicated an electronic structure consistent with the following possible transitions in the UV-vis-NIR: (i) predominantly ferrocene-to-fullerene metal-to-ligand charge-transfer (MLCT), (ii) predominantly ferrocene-to-BODIPY MLCT transitions, (iii) predominant BODIPY-to-fullerene intra-ligand charge-transfer (ILCT), (iv) predominant BODIPY-to-BODIPY  $\pi-\pi^*$  excitations, (v) predominant catechol-to-fullerene ILCT transitions, (vi) predominant catechol-to-BODIPY ILCT transitions. In addition to these, fullerene-centered

$\pi-\pi^*$  transitions are expected in the higher-energy region.

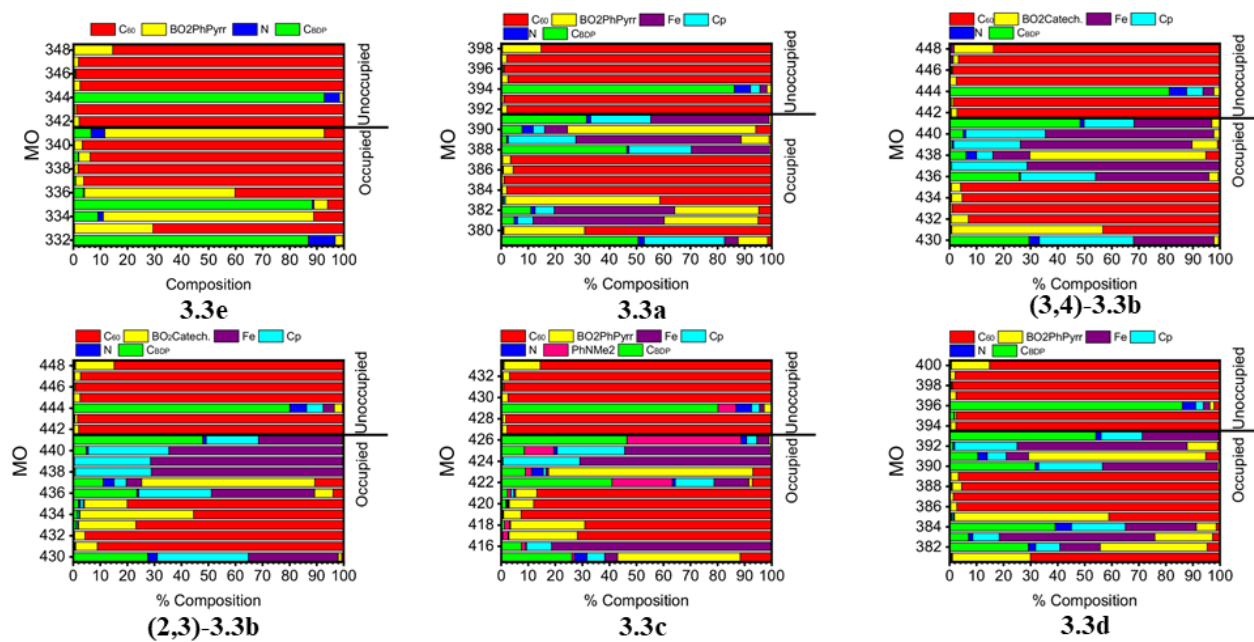


Figure 3.23: DFT-predicted compositions of frontier orbitals for **3.3a–3.3e**

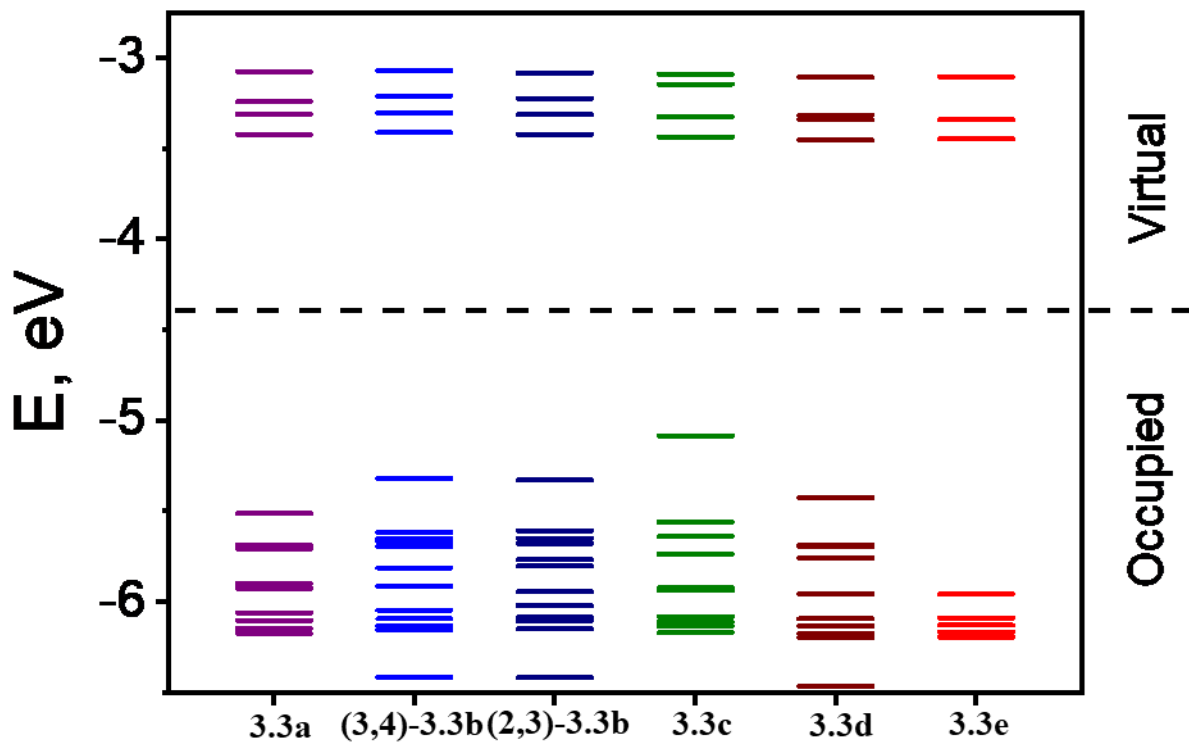


Figure 3.24: DFT-predicted energy diagram for the frontier MOs in **3.3a – 3.3d** and **3.4**.

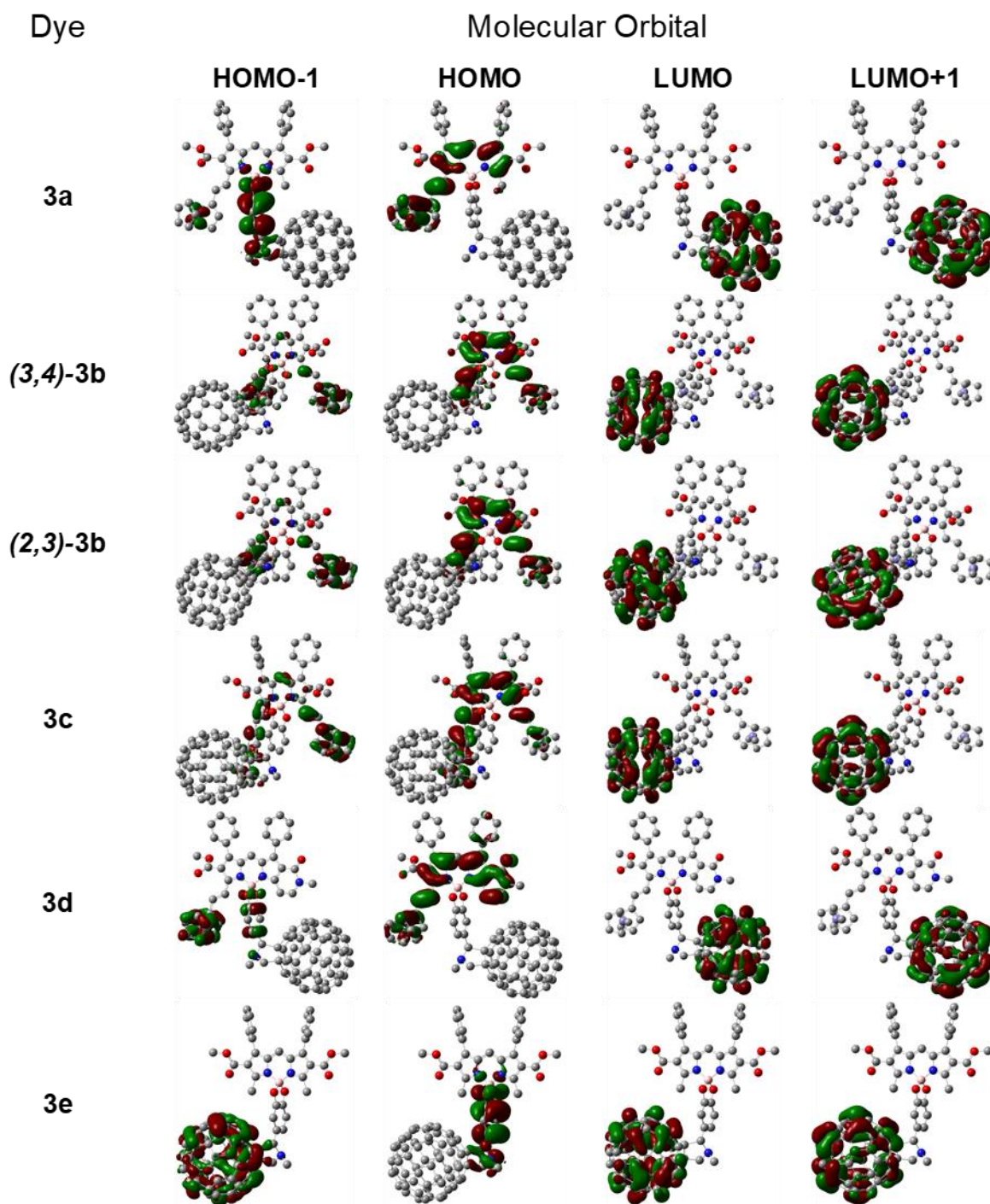


Figure 3.25: DFT-predicted frontier molecular orbitals for **3.3a** – **3.3e**.

Figure 3.26 presents a comparison between experimental and theoretical TDDFT-predicted UV-Vis-NIR spectra of triads **3.3a** – **3.3d** and dyad **3.3e**. The low-energy region of the spectra

consists of the relatively intense, predominantly ferrocene-to-BODIPY MLCT and BODIPY-to-BODIPY  $\pi\text{-}\pi^*$  transitions, analogous to the dyads **3.2a** – **3.2d**.<sup>92</sup> The ferrocene-to-fullerene, BODIPY-to-fullerene, and catechol-to-fullerene charge-transfer transitions were all predicted to have low intensities and are not expected to contribute significantly to absorption in the visible and NIR regions. In general, TDDFT reproduces well both energies and intensities of the experimental transitions observed in the UV-Vis-NIR spectra of triads **3.3a** – **3.3d**. The predicted presence of low-energy charge-transfer transitions supports deactivation pathways that are consistent with the lack of steady-state fluorescence in triads **3.3a** – **3.3d** and dyad **3.3e**.

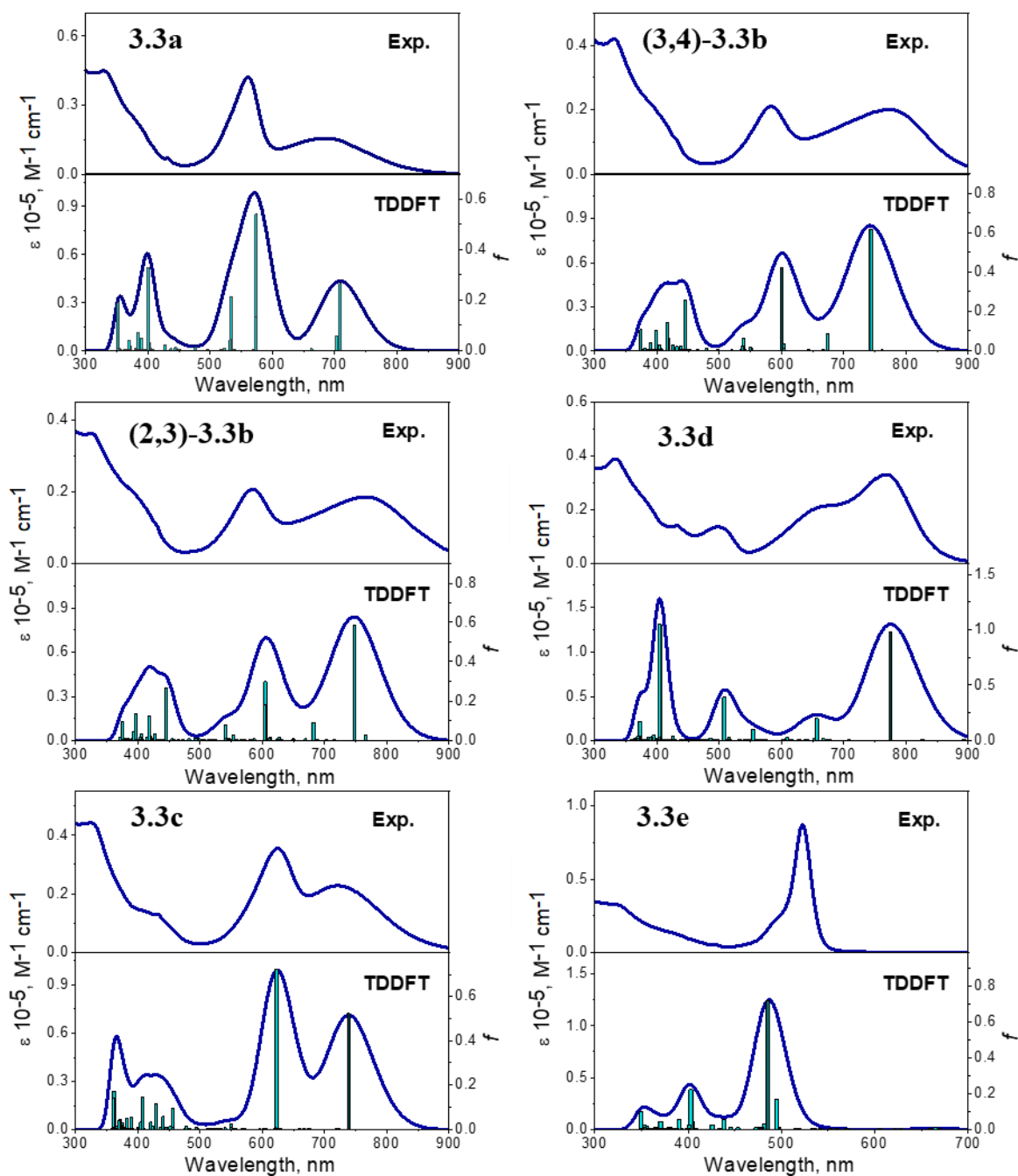


Figure 3.26: Experimental (top) and TDDFT-predicted (bottom) UV-vis spectra of triads **3.3a** – **3.3d** and dyad **3.3e**.

Using the electrochemical and absorption data, and predictions of donor-acceptor distances and radii from DFT calculations, it is possible to estimate the free energy for electron transfer,  $\Delta G_{ET}$ , using equation (3.1).<sup>115</sup>

$$\Delta G_{ET}^0 = e \left[ E^0 \left( \frac{D^{+\cdot}}{D} \right) - E^0 \left( \frac{A}{A^{\cdot-}} \right) \right] - E_{00} - \left( \frac{e^2}{4\pi\epsilon_0} \right) \left( \frac{1}{\epsilon_S R_{DA}} \right) - \left( \frac{e^2}{4\pi\epsilon_0} \right) \left( \frac{1}{2r^+} + \frac{1}{2r^-} \right) \left( \frac{1}{\epsilon_{EC}} - \frac{1}{\epsilon_S} \right) \quad (2.1)$$

In Eq 3.1  $E^0(D^{+}/D)$  and  $E^0(A/A^{\cdot-})$  are the oxidation potential of the donor and reduction potential of the acceptor, respectively;  $E_{00}$  is the excitation energy at the either MLCT or BODIPY-centered transition;  $R_{DA}$  is the donor-acceptor distance, which was estimated from DFT calculations and X-ray data available for triads **3.3a - e**;  $\epsilon_S$  and  $\epsilon_{EC}$  are the dielectric constants of the solvents used in the photochemical and electrochemical studies;  $r^+$  and  $r^-$  are the effective ionic radii of the donor and acceptor, respectively, and were estimated from the DFT calculations. Both BODIPY and fullerene were considered as electron acceptors that can form  $Fc^+$ -BODIPY $^{\cdot-}$ -fullerene and  $Fc^+$  BODIPY-fullerene $^-$  charge separated states. Estimated  $\Delta G_{ET}$  values are modest and negative for toluene (-0.11 – -0.36 eV), and become more negative with an increase in polarity with DCM (-0.22 – -0.82 eV). In both solvents photoinduced electron-transfer is thermodynamically favorable.

Time resolved pump-probe spectroscopy was used to investigate excited state dynamics and potential photoinduced electron-transfer (Figures 3.27, 3.28 and Tables 3.3). The excited state dynamics are consistent across all triads studied, **3.3a-3.3e**. The pump wavelengths were longer than 525 nm to excite the BODIPY core and avoid direct excitation of the fullerene fragment. As an illustrative example, we compare BODIPY- $C_{60}$  (**3.3e**),  $Fc_2$ -BODIPY- $C_{60}$  (**(3,4)-3.3b**), and  $Fc_2$ -BODIPY (**3.1b**). First, consider the BODIPY- $C_{60}$  dyad. The parent BODIPY, **3.1e**, has an excited state lifetime of 6 ns.<sup>92</sup> Addition of the phenyl-fulleropyrrolidine group resulted in a 1000-fold reduction in the lifetime. Very rapid relaxation of the initially excited state took place with a time constant of 4 ps for full recovery of the ground state bleach. There was no evidence for transient absorption around 1100 nm, Figure 3.27b, where the anion-radical of  $C_{60}$  is known to absorb.<sup>119</sup> Addition of the catechol ligand to the parent BODIPY, in the absence of  $C_{60}$ , has been demonstrated to produce sub-ps deactivation of the excited state via charge-transfer between the catechol and BODIPY, followed by vibrational cooling of the ground state on a ~10 ps time scale.<sup>109</sup> Based on these observations, we conclude that rather than electron transfer to the  $C_{60}$ , the

dynamics were dominated by rapid deactivation of the excited state mediated by the catechol bridge.

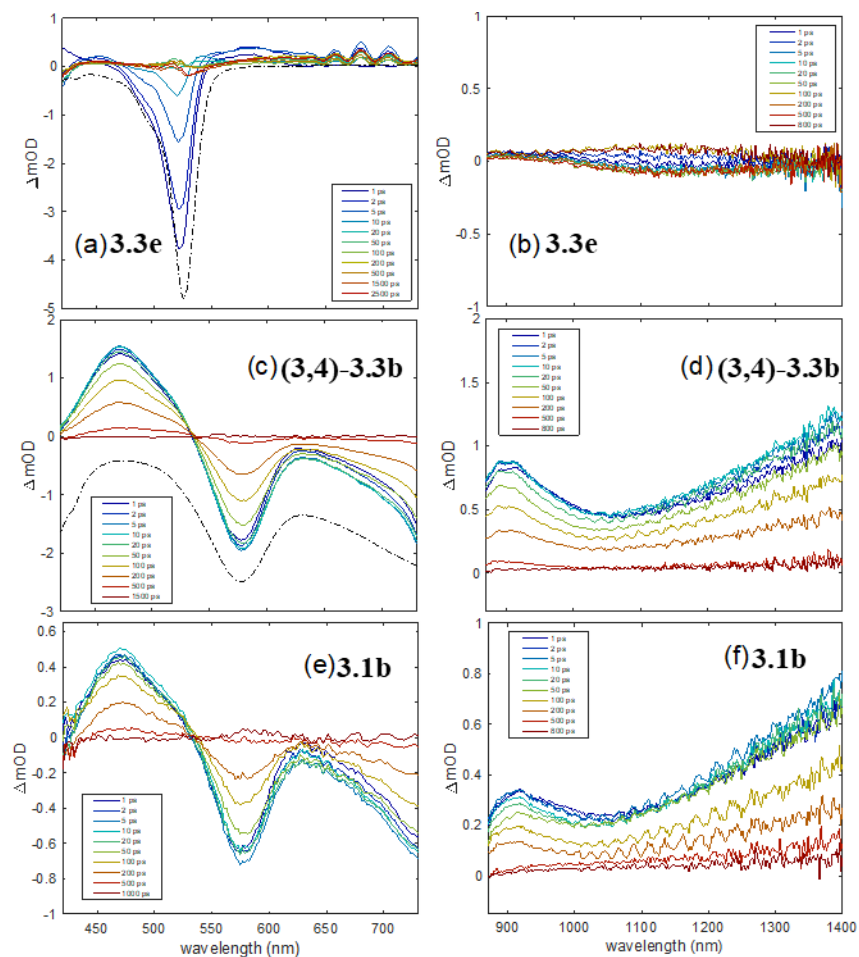


Figure 3.27: Pump-probe spectra for the BODIPY- $C_{60}$  dyad (**3.3e**, excited at 530 nm), the  $Fc_2$ -BODIPY- $C_{60}$  triad (**(3,4)-3.3b**, excited at 570 nm), and  $Fc_2$ -BODIPY (**3.1b**, excited at 570 nm).

The pump-probe spectra for the  $Fc_2$ -BODIPY- $C_{60}$  triad are presented in Figures 3.27c and 3.27d. There is stark contrast with the spectra for the BODIPY- $C_{60}$  dyad. Despite the presence of the catechol bridge, the lifetime was much longer,  $184 \pm 8$  ps, and the excited state includes a broad absorption in the near-IR. The spectra and dynamics are nearly identical to those measured for  $Fc_2$ -BODIPY, Figures 3.27e, 3.27f, 3.28 and Tables 3.3. Addition of ferrocene groups to the BODIPY core, **3.1b**, creates a charge transfer state, with electron density moved from the ferrocene to the BODIPY.<sup>92</sup> This substantially reduces the excited state lifetime when compared to the parent BODIPY, **3.1e**, and in the  $Fc_2$ -BODIPY- $C_{60}$  triad, creation of the  $Fc_2$ -BODIPY charge transfer state preceded and supplanted the catechol mediated deactivation pathway.

We have reported a previous pump-probe measurement on **3.1b**, probed in the visible region of the spectrum,<sup>92</sup> and the results reported here in Figure 3.27e reproduce the prior results to within experimental error. We had not previously reported the transient absorption in the near-IR, Figure 3.27f. The decay of the broad absorption, with a minimum around 1050 nm, is correlated with the decay of the transient absorption and ground state bleach in the visible region, and we assign it to the same charge transfer state in both **3.1b** and the Fc<sub>2</sub>-BODIPY-C<sub>60</sub> triad. Within the experimental uncertainty, there is no evidence in the near-IR for any absorption other than the Fc<sub>2</sub>-BODIPY charge transfer state. In particular, there is no evidence for electron transfer to the C<sub>60</sub> via additional absorption from the anion-radical around 1000 nm, and the near-IR signals all return to the baseline with the lifetime of the initial charge transfer state. Figure 3.28 directly compares recovery of the ground state bleach for **3.1b**, **3.3e**, (3,4)-**3.3b**, and (2,3)-**3.3b**. The excited state dynamics of Fc<sub>2</sub>-BODIPY dyad and the Fc<sub>2</sub>-BODIPY-C<sub>60</sub> triad were effectively indistinguishable, Figure 3.28 and Table 3.3. Analogous dynamics were observed for all triads investigated. Ferrocene groups were effective at providing an initial, rapid charge transfer to the BODIPY, and this had the additional advantage of avoiding the sub-ps catechol mediated deactivation of the excited state. However, despite efficient electron transfer to the BODIPY, no subsequent transfer to the fullerene acceptor was observed during the ~200 ps lifetime of the initially created charge transfer state.

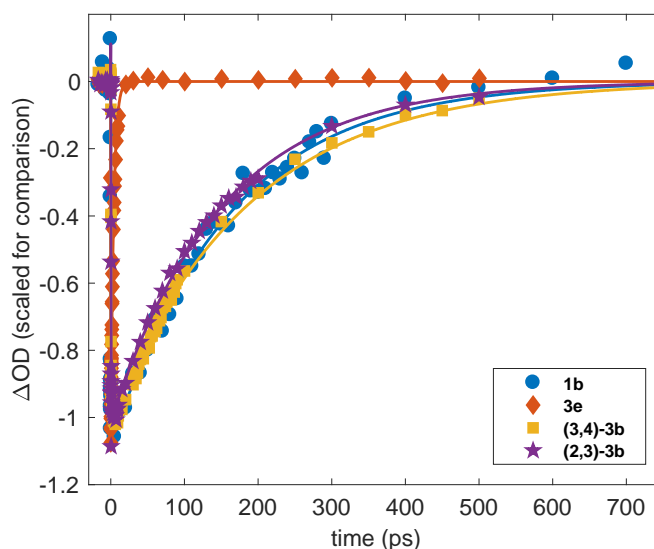


Figure 3.28: Recovery of the ground state bleach for the Fc<sub>2</sub>-BODIPY (**3.1b**, excited at 570 nm, probed at 575 nm), the BODIPY-C<sub>60</sub> dyad (**3.3e**, excited at 530 nm, probed at 525 nm), the Fc<sub>2</sub>-

BODIPY-C<sub>60</sub> triad ((**3,4**)-**3.3b**, excited at 570 nm, probed at 575 nm), and the Fc<sub>2</sub>-BODIPY-C<sub>60</sub> triad ((**2,3**)-**3.3b**, excited at 570 nm, probed at 575 nm). Solid symbols are the data and lines are the exponential decay fits with time constants listed in Table 3.3. Data and fits were scaled for comparison.

Table 3.3. Exponential time constants for recovery of the ground state (transient bleach) following photoexcitation. Data and fits presented in Figure 3.28.

compound	pump $\lambda$ (nm)	Probe $\lambda$ (nm)	$\tau$ (ps)
<b>3.1b</b>	570	575	160 $\pm$ 10
<b>3.3a</b>	570	650	109 $\pm$ 10
( <b>3,4</b> )- <b>3.3b</b>	570	575	184 $\pm$ 8
( <b>2,3</b> )- <b>3.3b</b>	570	575	150 $\pm$ 9
<b>3.3c</b>	650	725	380 $\pm$ 20
<b>3.3d</b>	650	625	200 $\pm$ 20
<b>3.3e</b>	530	525	4.1 $\pm$ 0.15

Investigations that provide suggested evidence for photo-induced charge transfer in analogous systems, employing a fullerene as the electron acceptor, commonly use shorter wavelength light around 400 nm that directly excites the fullerene in addition to the donor antenna.<sup>102-105</sup> While there is the potential for subsequent hole transfer following excitation of the fullerene, absorption of directly excited states of the fullerene dominate the transient spectra and hinder elucidation of any charge transfer. In the absence of longer wavelength excitation, evidence for charge transfer from the excited antenna is lacking in comparable studies.<sup>102-105</sup> By exciting at longer wavelengths, the results reported here isolate excitation of the BODIPY antenna. Inaccessibility of charge transfer from the excited antenna to the fullerene acceptor is likely one of the contributing factors to the lack of reports on well-performing organic photovoltaics devices based on these types of systems.

## Rapid Excited State Deactivation of BODIPY Derivatives by a Catechol Linker

To determine the cause of deactivation of BODIPY fluorescence a series of difluoro (**3.5a-e**) and catechol substituted (**3.6a-e**) BDP derivatives (Figure 3.29) were prepared, purified, and characterized (Figures 3.30-3.41). These compounds were synthesized in order to investigate if the catechol linker is the cause for the lack of photo induced transfer due to the electron rich nature of the catechol group.

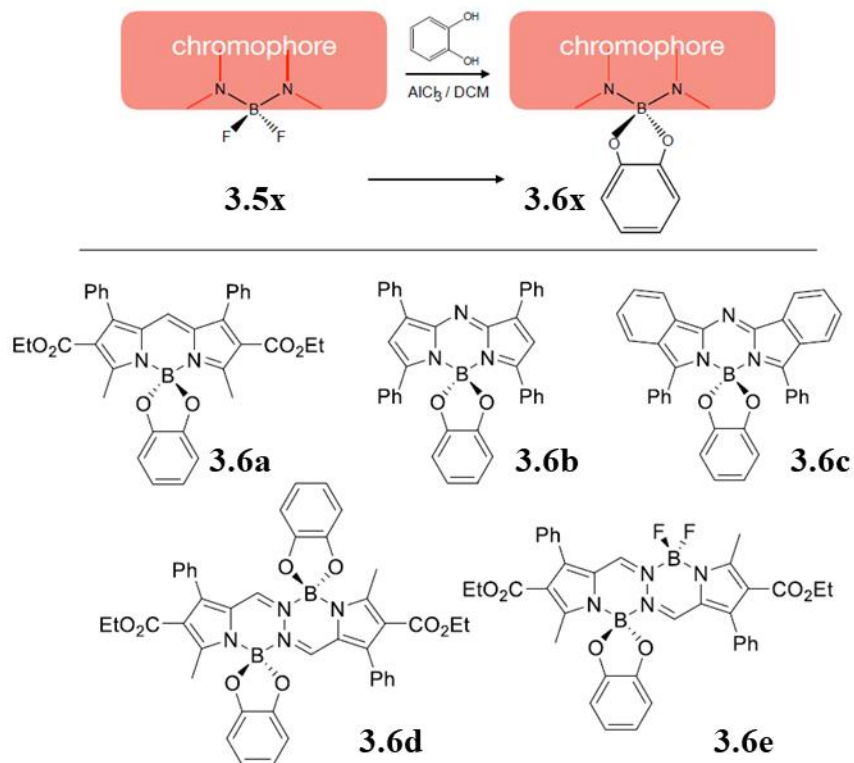


Figure 3.29: Molecular structures and labels

The structures and absorption spectra are presented in Figures 3.29 and 3.42 respectively. UV-vis spectra of all catechol-containing compounds in the low-energy spectral envelope are similar to their precursors (Figures 3.43–3.47). The most intense low energy BODIPY-centered  $\pi\text{-}\pi^*$  transition in **3.5a** and **3.6a** was observed at the same energy. A similar transition in catechol-containing **3.6b** and **3.6c** is slightly shifted to higher energy, and a similar band in BOPHYs **3.6d** and **3.6e** are slightly shifted to lower energy compared to the parent  $\text{BF}_2$ -containing compounds. The most intense band in the aza-BODIPYs **3.5b** and **3.6b** is significantly red-shifted compared to that in BODIPYs **3.5a** and **3.6a** and BOPHYs **3.5d**, **3.6d**, and **3.6e**, while a further red-shift of the

low-energy band was observed upon benzoannulation of the aza-BODIPY core (compounds **3.5c** and **3.6c**). Introduction of one or two catechol fragments at the boron hub in BOPHY **3.5d** also does not significantly change the vibronic profile in UV-vis spectra of **3.6d** and **3.6e**. Once carefully purified, catechol-containing BODIPY, aza-BODIPY, and BOPHYs **3.6a–3.6e** exhibit no steady-state fluorescence when compared to the parent compounds **3.5a–3.5d** (Figures 3.43–3.47). The **3.5x** compounds all exhibited strong, roughly mirror-image fluorescence with Stokes shifts of 20–40 nm. After addition of the catechol, there was no measurable fluorescence observed from any of the **3.6x** compounds, Figures 3.43–3.47, indicating a lack of any residual **3.5x** parent compound in the samples and a significant change in the excited state dynamics. Pump-probe spectroscopy was used to measure the time constants associated with the excited state dynamics. The pump excitation was set at a wavelength near the absorption maximum for each compound. All transient spectra for the **3.5x** compounds consisted of a ground state bleach (GSB,  $\Delta OD < 0$ ), stimulated emission (SE,  $\Delta OD < 0$ ), and excited state absorption (ESA,  $\Delta OD > 0$ ). The transient spectra appeared within the time resolution of the experiments,  $\sim 50$  fs, did not change shape during the full range of time delays probed, and were well fitted by a first-order decay of the amplitude at all probe wavelengths. The fitted time constants are listed in Table 3.4 and assigned to the initial optically excited state relaxing directly back to the ground state.

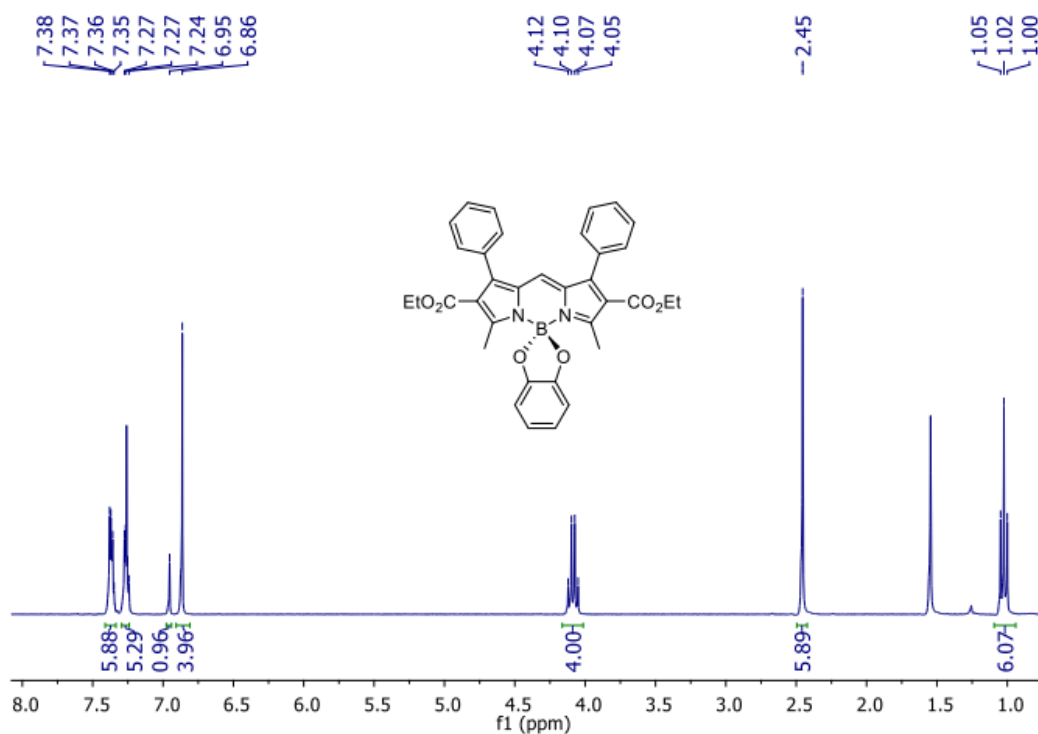


Figure 3.30:  $^1\text{H}$  NMR spectrum of compound **3.6a** in  $\text{CDCl}_3$ .

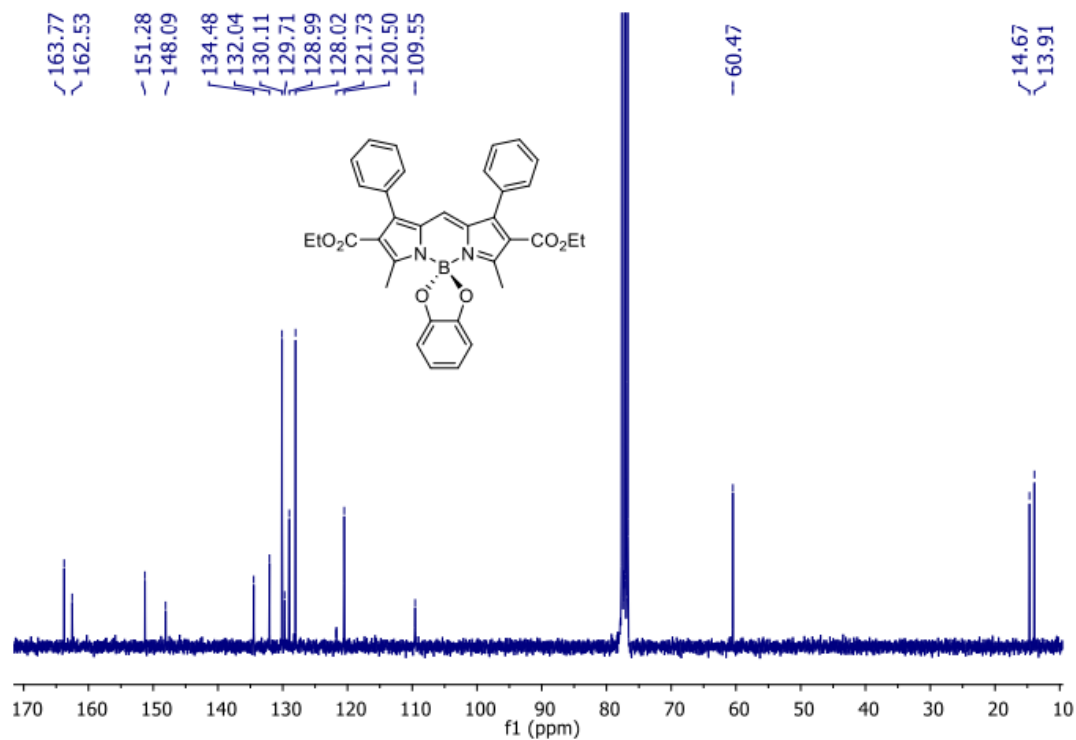


Figure 3.31:  $^{13}\text{C}$  NMR spectrum of compound **3.6a** in  $\text{CDCl}_3$ .

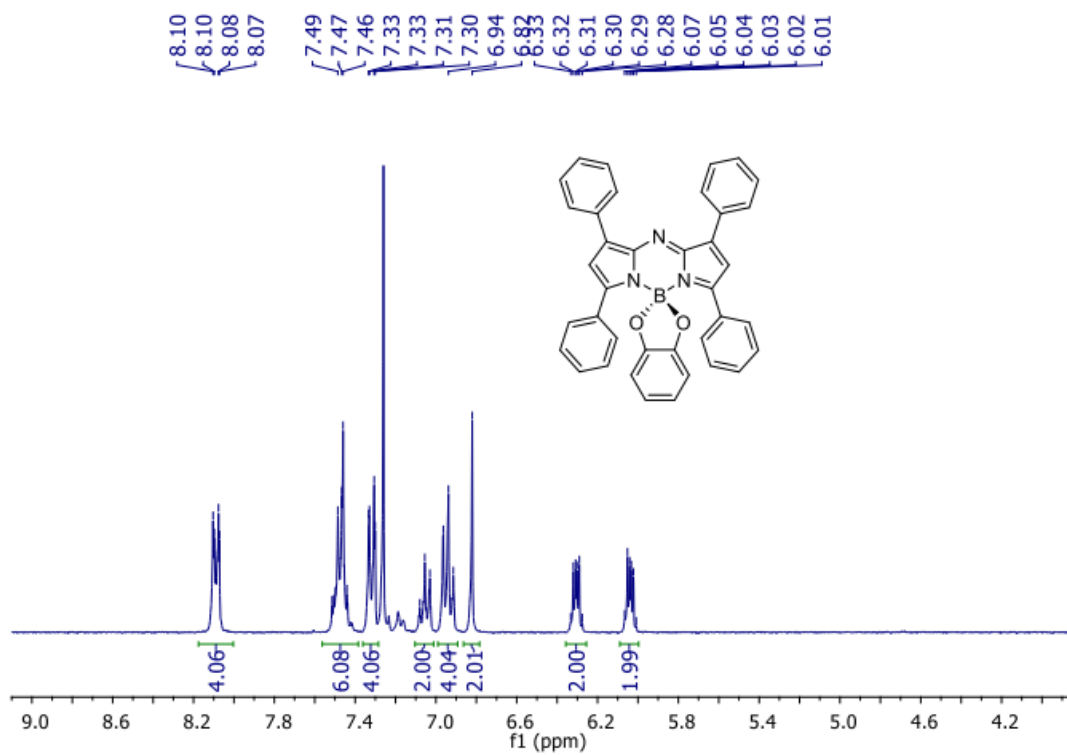


Figure 3.32:  $^1\text{H}$  NMR spectrum of compound **3.6b** in  $\text{CDCl}_3$ .

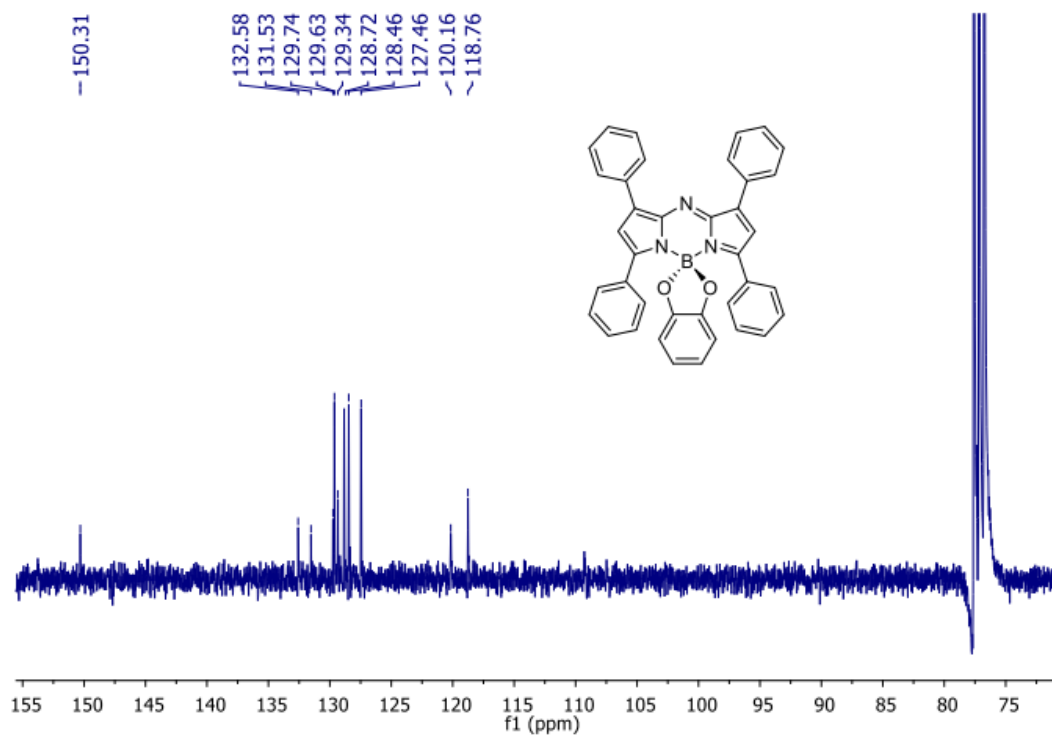


Figure 3.33:  $^{13}\text{C}$  NMR spectrum of compound **3.6b** in  $\text{CDCl}_3$ .

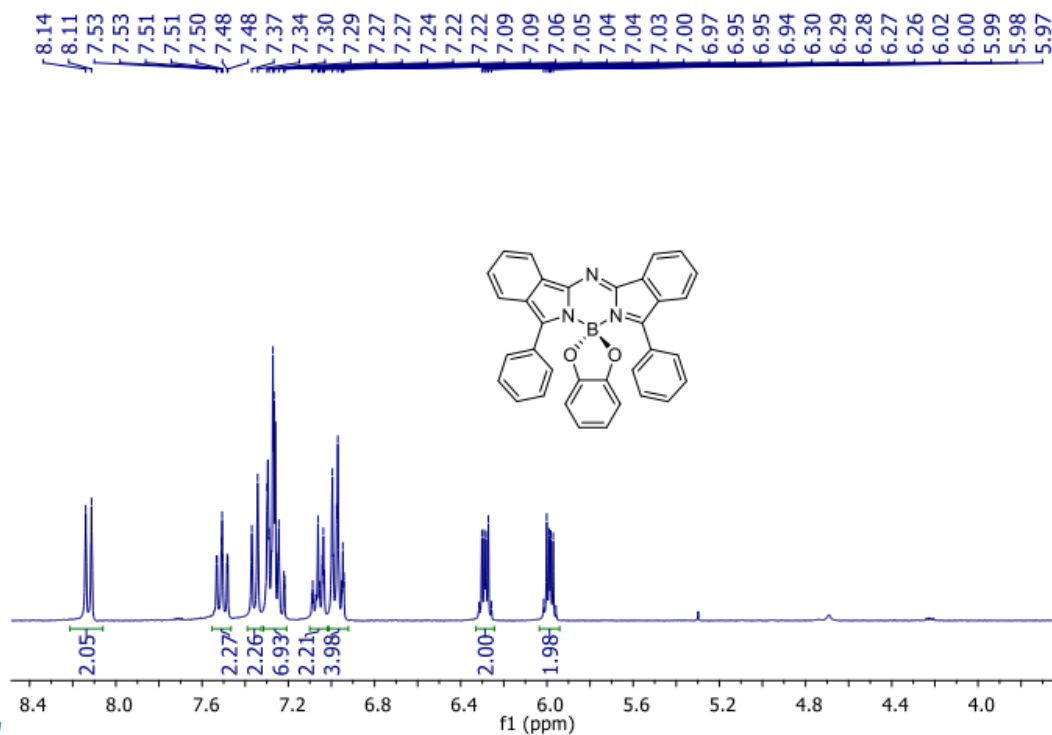


Figure 3.34:  $^1\text{H}$  NMR spectrum of compound **3.6c** in  $\text{CDCl}_3$ .

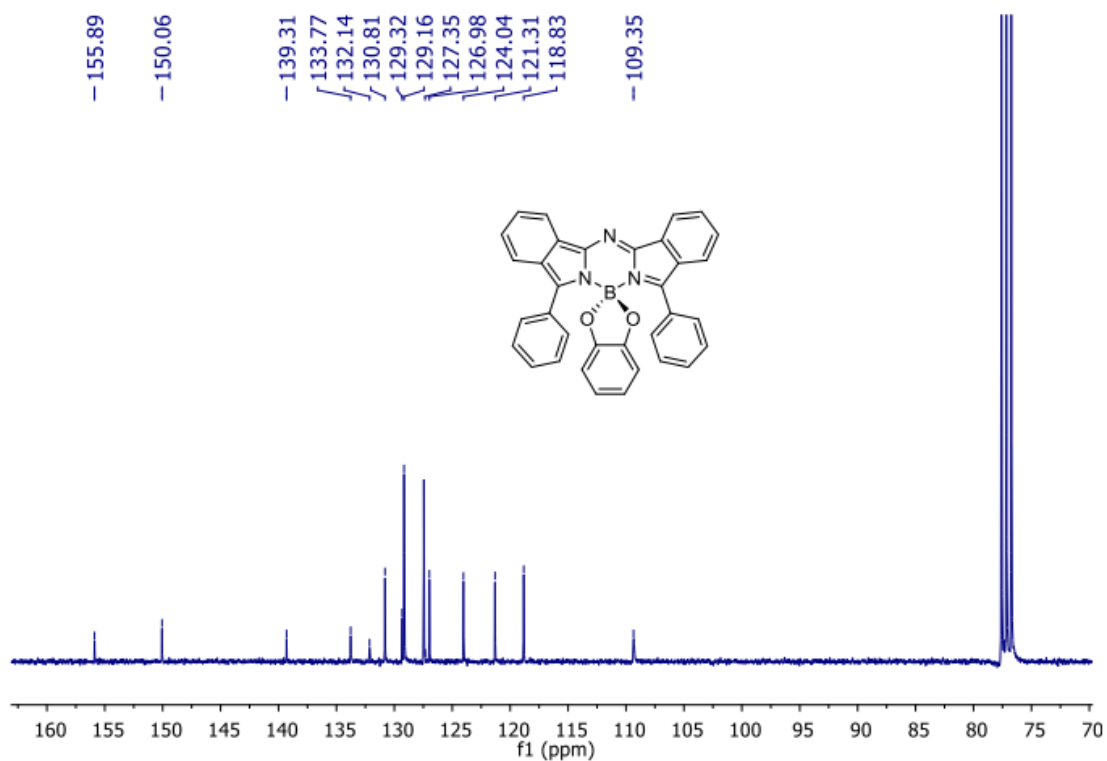


Figure 3.35: <sup>13</sup>C NMR spectrum of compound **3.6c** in CDCl<sub>3</sub>.

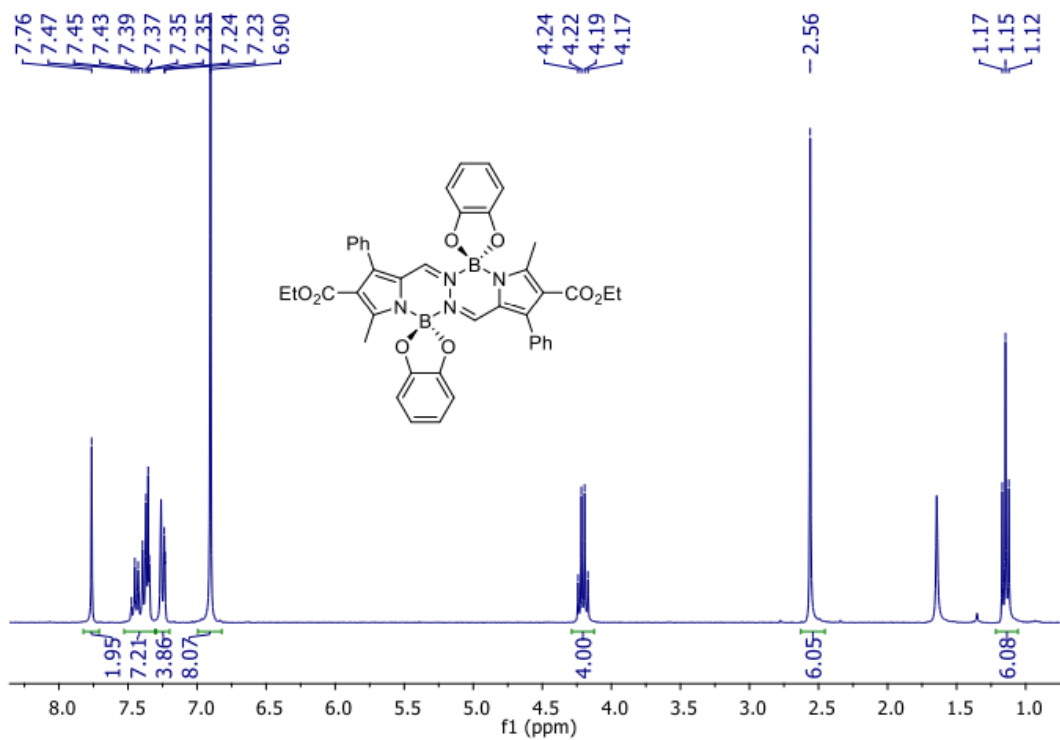


Figure 3.36: <sup>1</sup>H NMR spectrum of compound **3.6d** in CDCl<sub>3</sub>.

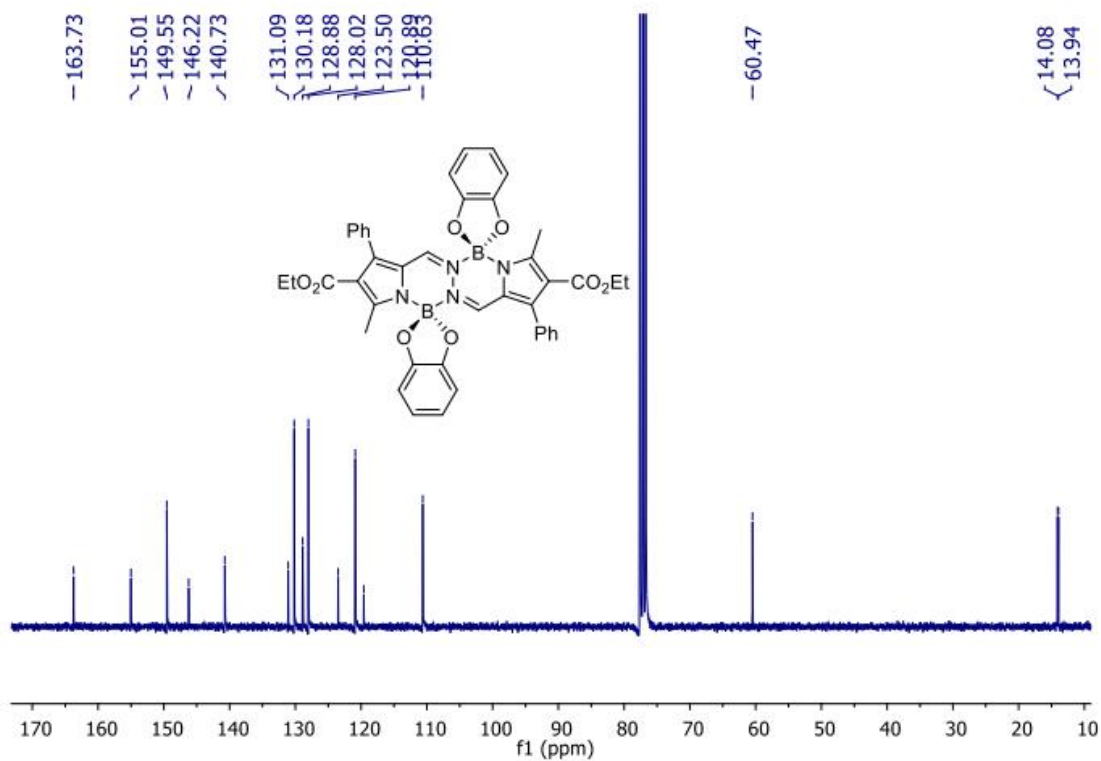


Figure 3.37: <sup>13</sup>C NMR spectrum of compound **3.6d** in CDCl<sub>3</sub>.

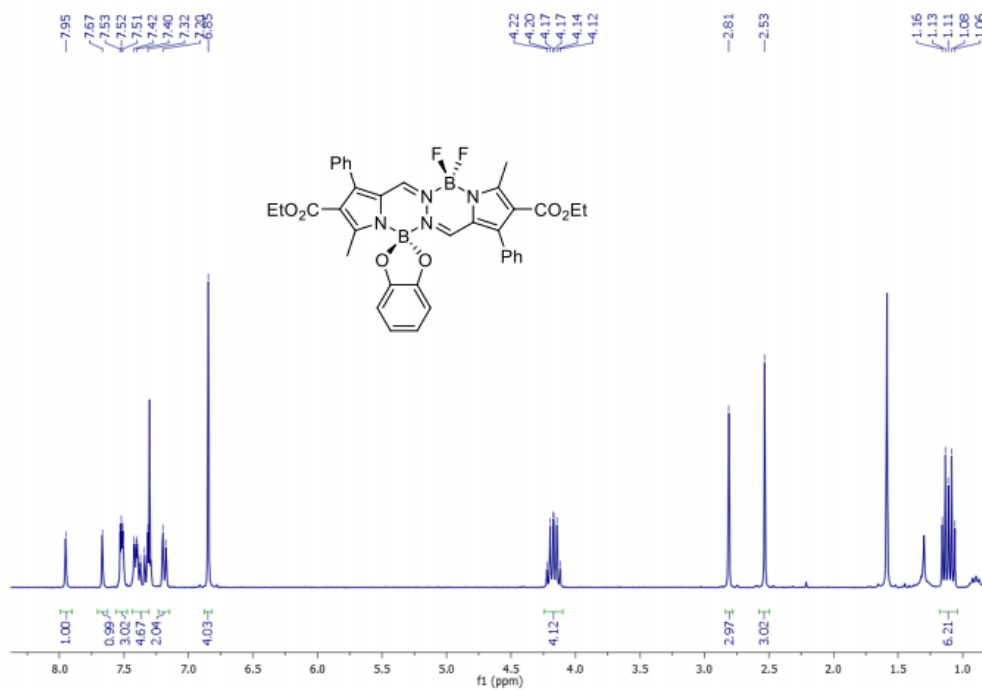


Figure 3.38: <sup>1</sup>H NMR spectrum of compound **3.6e** in CDCl<sub>3</sub>.

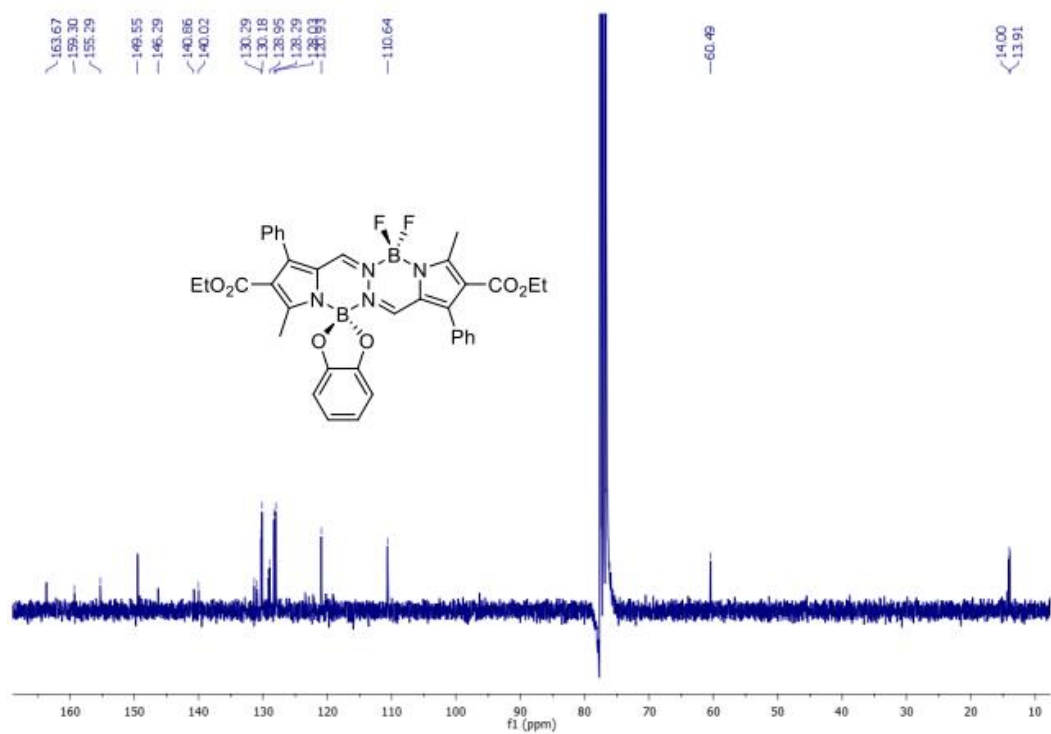


Figure 3.39:  $^{13}\text{C}$  NMR spectrum of compound **3.6e** in  $\text{CDCl}_3$ .

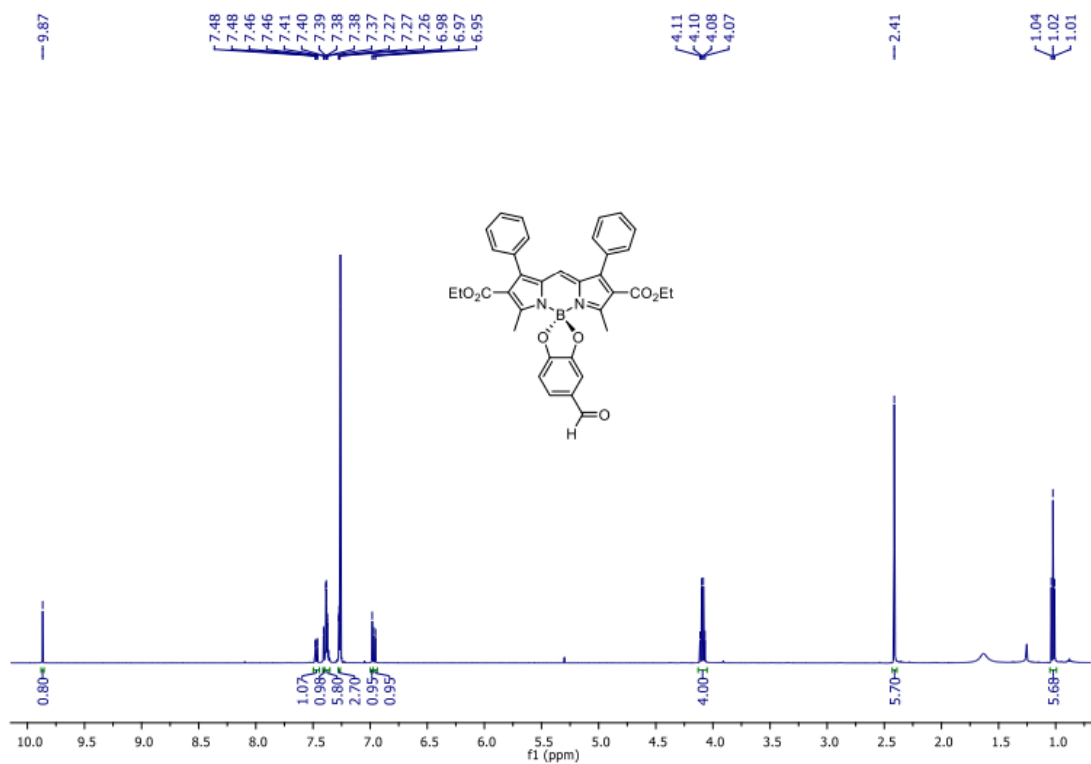


Figure 3.40:  $^1\text{H}$  NMR spectrum of compound **3.7** in  $\text{CDCl}_3$ .

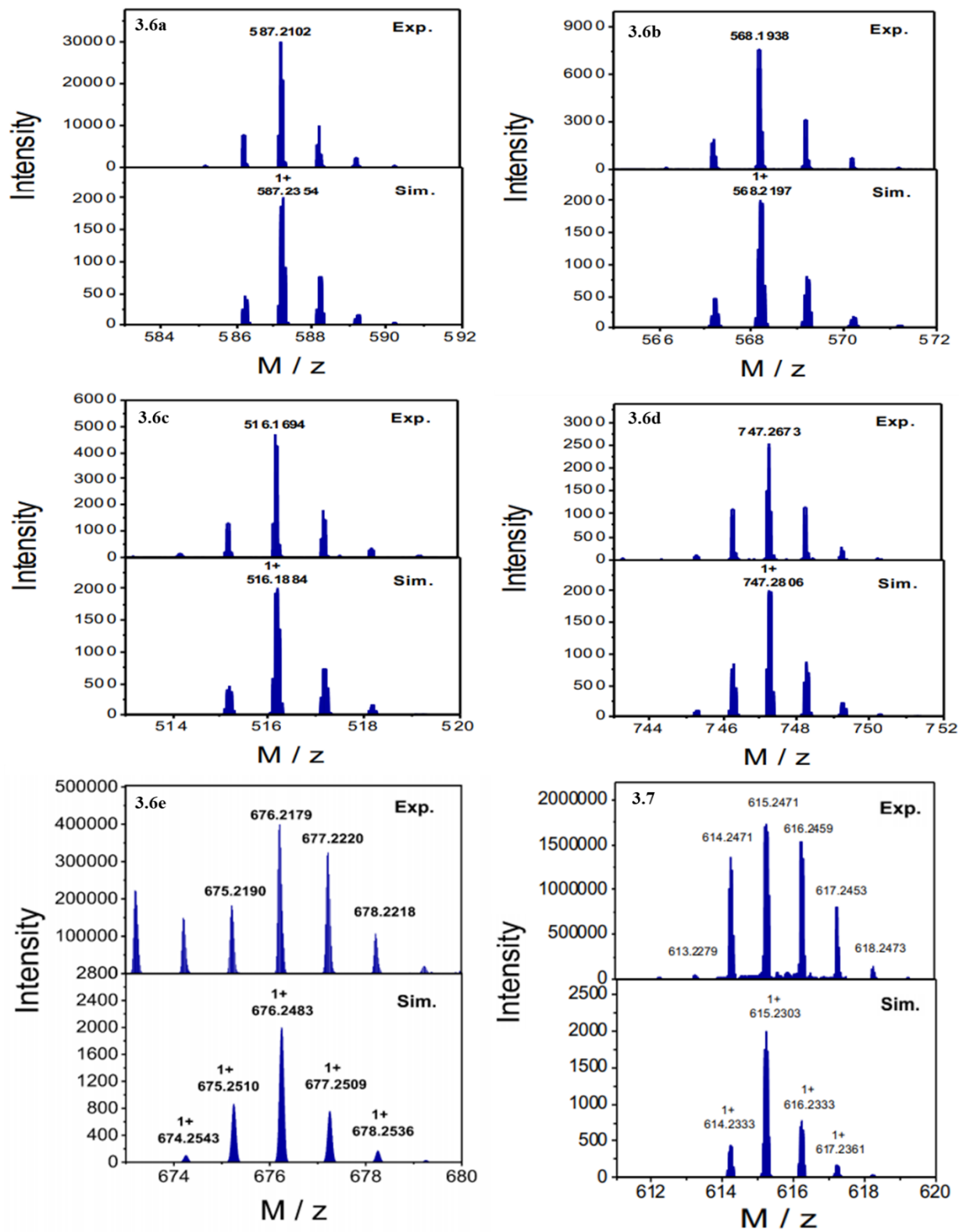


Figure 3.41: HRMS spectra of compounds **3.6a-e** and **3.7**.

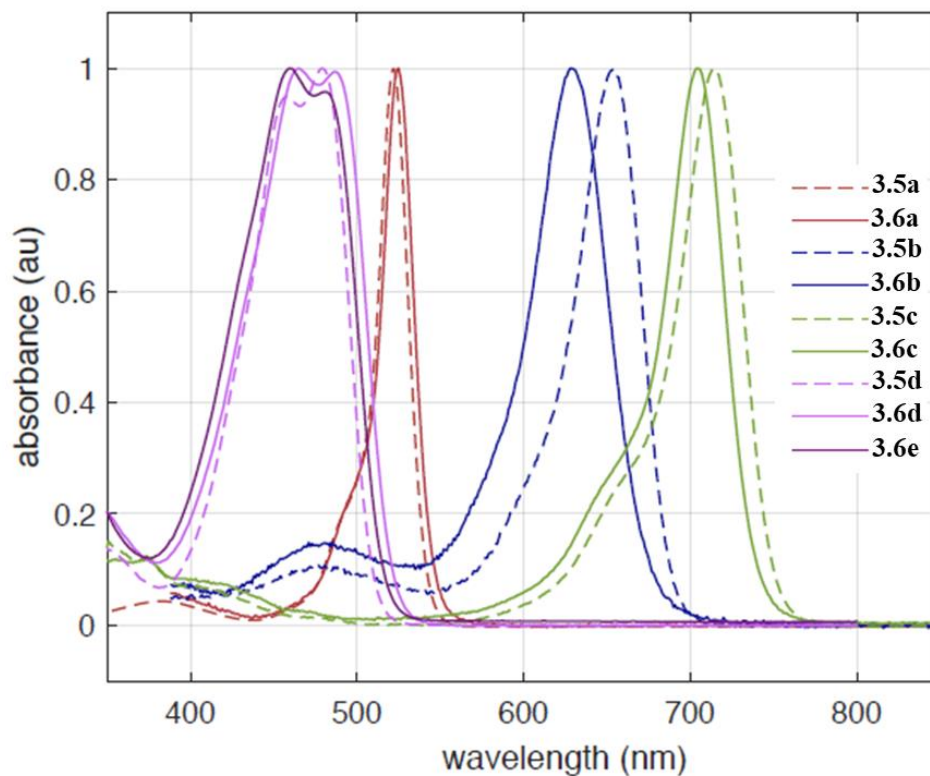


Figure 3.42: Absorption spectra for **3.5a-d** and **3.6a-e** in toluene.

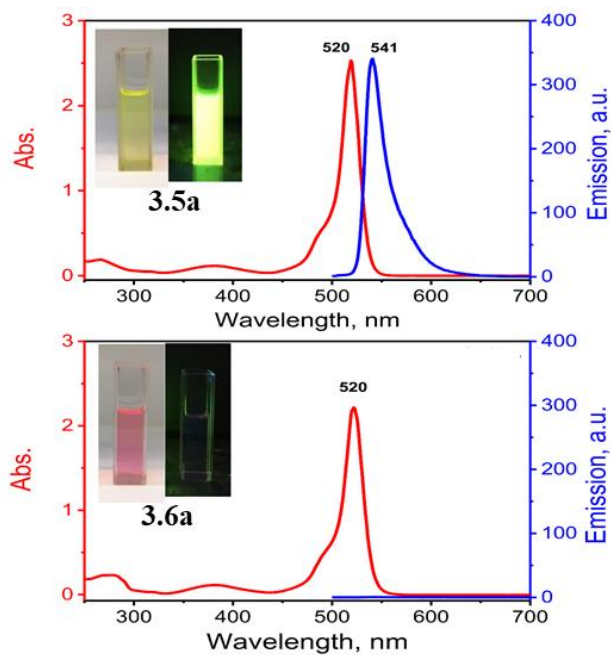


Figure 3.43: Absorption (red) and emission (blue) spectra of compounds **3.5a** (top) and **3.6a** (bottom).

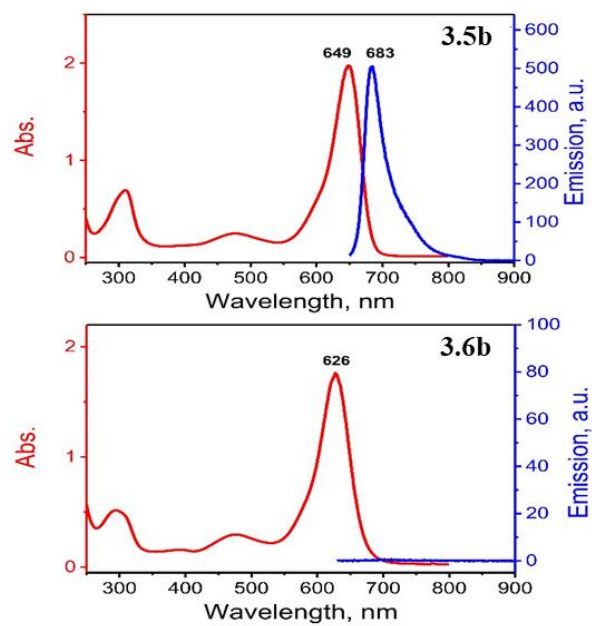


Figure 3.44: Absorption (red) and emission (blue) spectra of compounds **3.5b** (top) and **3.6b** (bottom).

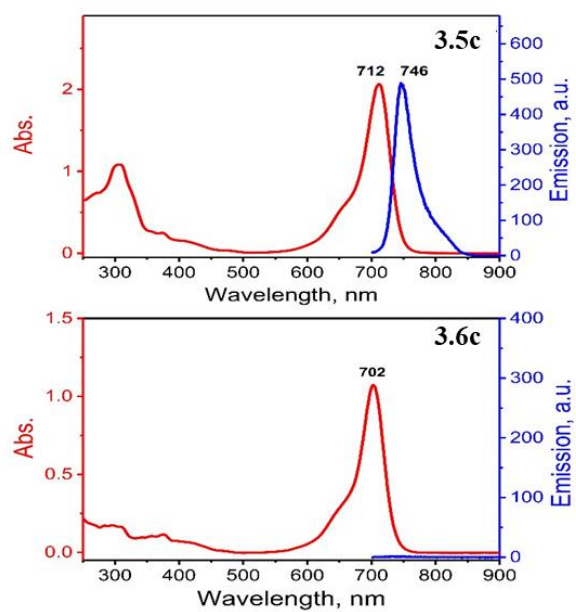


Figure 3.45: Absorption (red) and emission (blue) spectra of compounds **3.5c** (top) and **3.6c** (bottom).

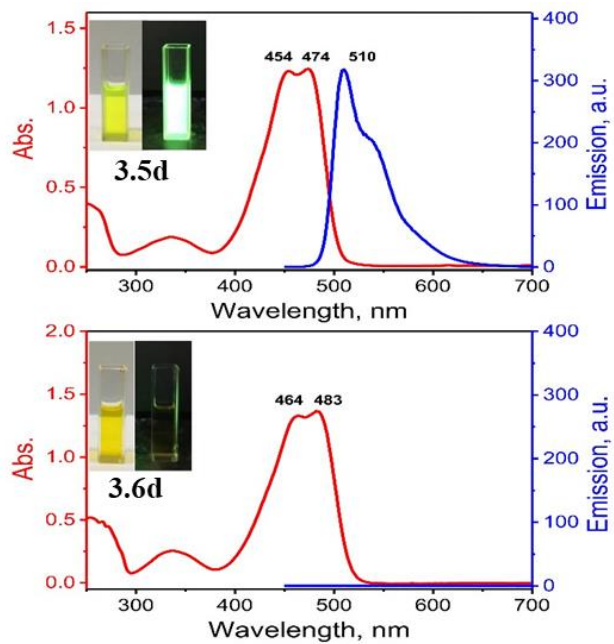


Figure 3.46: Absorption (red) and emission (blue) spectra of compounds **3.5d** (top) and **3.6d** (bottom).

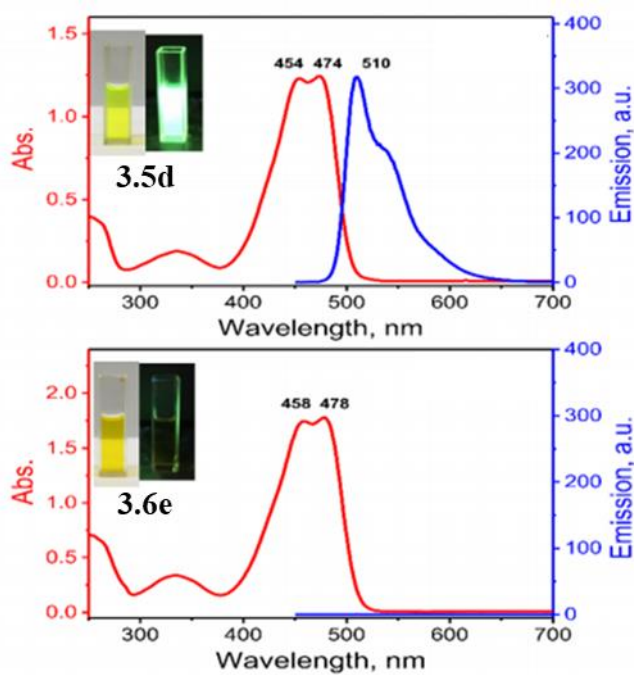


Figure 3.47: Absorption (red) and emission (blue) spectra of compounds **3.5d** (top) and **3.6e** (bottom).

Table 3.4. First order time constants

	$\tau_{\pi^* \rightarrow \text{gs}}$ (ns)		$\tau_{\pi^* \rightarrow \text{CT}}$ (fs)	$\tau_{\text{CT} \rightarrow \text{gs}}$ (ps)
<b>3.5a</b>	3.1±0.1	<b>3.6a</b>	100±6	2.9±0.2
<b>3.5b</b>	1.9±0.1	<b>3.6b</b>	150±20	4.3±0.9
<b>3.5c</b>	1.8±0.1	<b>3.6c</b>	< 500	1.8±0.1
<b>3.5d</b>	1.8±0.2	<b>3.6d</b>	< 500	15.1±0.5
		<b>3.6e</b>	< 500	14.0±0.1

$\pi^*$  is the optically excited state, CT is the charge transfer state, and gs is the electronic ground state.

Pump-probe spectra for the **3.6x** compounds differed significantly from the **3.5x** precursors. The shape of the spectra changed within the first picosecond, and the transient spectra recovered to the baseline, *ie* the original ground state, with time constants that were ca. 1000 times smaller than for the analogous **3.5x** compounds. Pump-probe data for **3.6a** is presented in Figure 3.48. A GSB and SE appeared within the time resolution of the experiment. The negative SE around 580 nm evolves into a positive ESA within the first 100 fs, followed by subsequent return to the baseline. The data probed at 580 nm was fitted as two sequential first-order events with time constants of  $100 \pm 6$  fs and  $2.9 \pm 0.2$  ps, Figure 3.48(b). The GSB around 520 nm recovered to the base line on a comparable time scale to the loss of the intermediate ESA, with a time constant of  $3.5 \pm 0.3$  ps. The data demonstrated very rapid deactivation of the photo-excited state via an intermediate that is accessed on a sub-ps time scale.

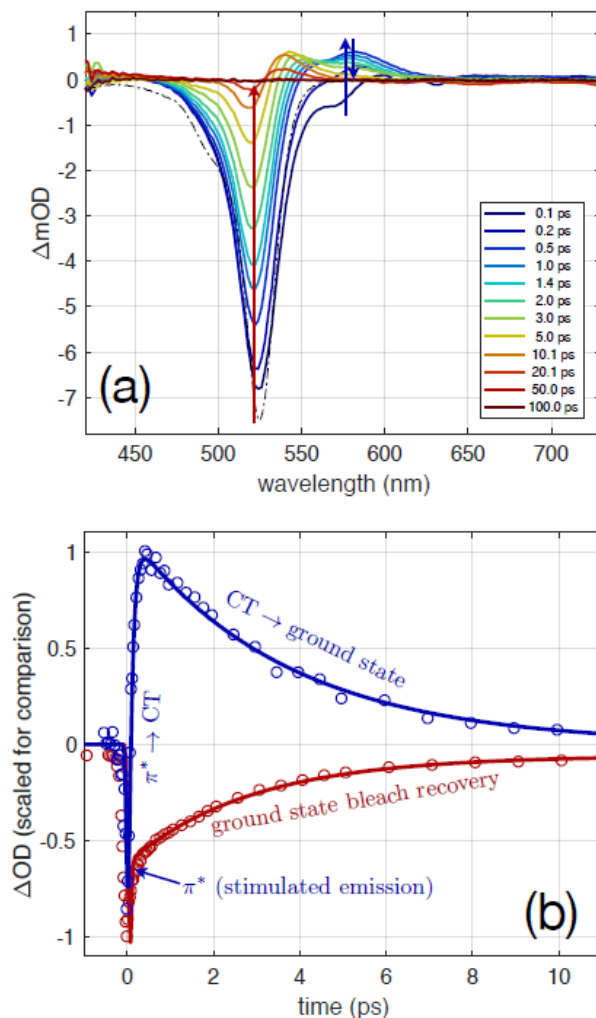


Figure 3.48: Pump-probe measurements on **3.6a** in toluene excited at 530 nm. (a) Transient change in optical density across the visible spectrum. The black dash-dot line is the absorption spectrum inverted and scaled for comparison. (b) Time dependence of the change in optical density at probe wavelengths of 520 nm (red) and 580 nm (blue). The open circles are the data and the solid lines are the fits described in the text.

Similar excited state dynamics were observed for all **3.6x** compounds. Time constants for the two sequential deactivation events are listed in Table 3.4. The time constants for **3.6b** were determined in the same manner as **3.6a**. Evidence for loss of initial SE and creation of new ESA features in the first picosecond was present for all **3.6x** compounds, however, the transition from initial photo-excited state to intermediate was not as well resolved at any single point within transient spectra for **3.6c**, **3.6d**, and **3.6e**. An upper limit of 500 fs for the time constant of this first

step was determined as a conservative estimate based on the delay time when the overall shape of the transient spectrum stopped changing. The time constants for the second step, return to the ground electronic state, were determined by fits to wavelengths in the probe spectrum dominated by ESA of the intermediate in all cases.

The electron-donating ability of the catechol fragment was further investigated by the electrochemical cyclic voltammetry (CV) and differential pulse voltammetry (DPV) data (Figures 3.49-3.52 and Table 3.5). Except dibenzo-aza-BODIPY compound **3.6c**, CV and DPV data are suggestive of superposition of the chromophore and catechol redox signatures. The superposition of catechol and chromophore redox potentials is indicative of rather small electronic coupling between catechol and chromophore fragment in the ground state, which is in agreement with their UV-vis data. In the case of BODIPY **3.6a** and BOPHYs **3.6d** and **3.6e**, electrochemical data are suggestive of the oxidation of catechol fragment during the first oxidation process. In the case of aza-BODIPY **3.6b**, oxidation processes associated with catechol fragment and aza-BODIPY core are closely spaced and thus it is difficult to assign these as both oxidation of catechol and azaBODIPY core are expected to be irreversible. In the case of dibenzo aza-BODIPY **3.6c**, the first oxidation process was observed at potential significantly lower than the oxidation of catechol, which is indicative of the aza-BODIPY chromophore oxidation prior to oxidation of the catechol fragment.

Table 3.5. Redox properties of compounds **3.5a – 3.5d** and **3.6a-3.6e** in DCM/0.1M TBAP system.

Dye	Ox <sub>3</sub>	Ox <sub>2</sub>	Ox <sub>1</sub>	Red <sub>1</sub>	Red <sub>2</sub>
<b>3.5a</b>	-	1.20	-	-1.19	-
<b>3.6a</b>	-	1.20	~0.90	-1.18	-
<b>3.5b</b>	-	-	~0.90	-0.84	-1.66
<b>3.6b</b>	-	0.90	0.74	-0.83	-1.65
<b>3.5c</b>	-	-	0.41	-1.08	-
<b>3.6c</b>	-	~0.80	0.44	-1.11	-
<b>3.5d</b>	-	-	1.40	-1.28	-1.40
<b>3.6d</b>	1.66	1.40	1.14	-1.23	-1.40
<b>3.6e</b>	1.40	1.17	1.09	-1.31	-1.52

All values are relative to Fc/Fc<sup>+</sup> couple

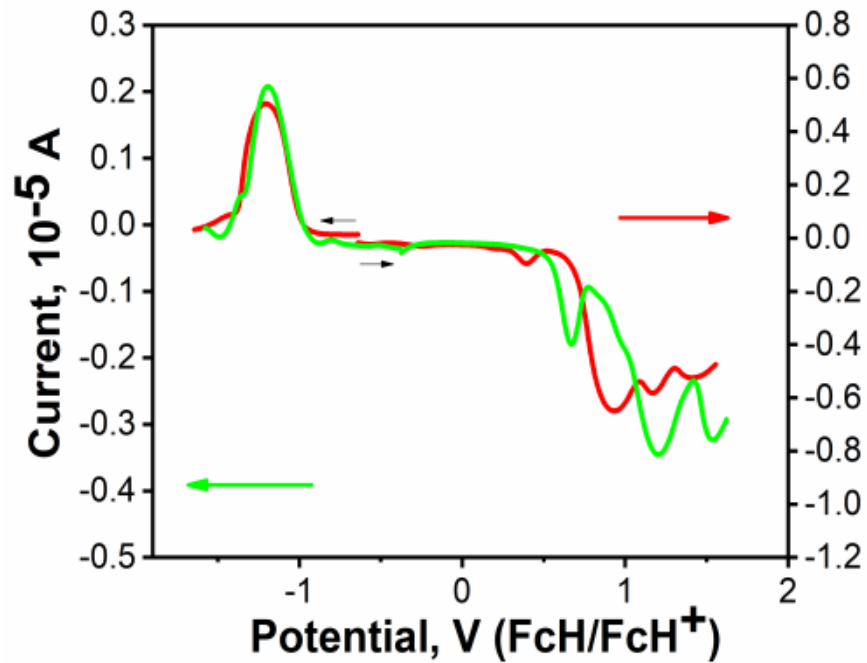


Figure 3.49: DPV spectra of compounds **3.5a** (green) and **3.6a** (red)

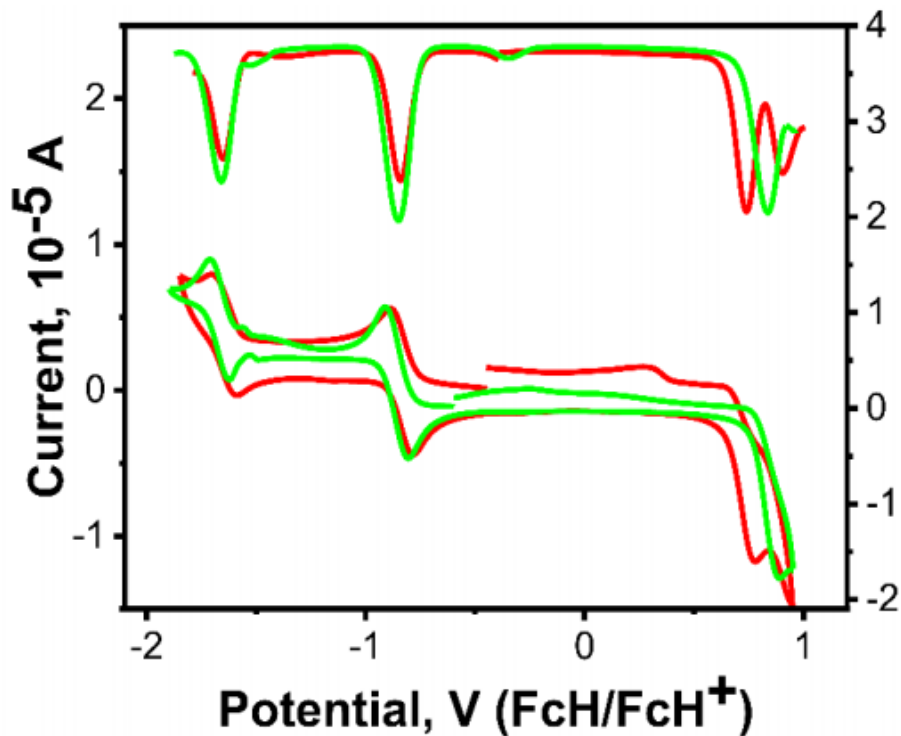


Figure 3.50: DPV spectra of compounds **3.5b** (green) and **3.6b** (red)

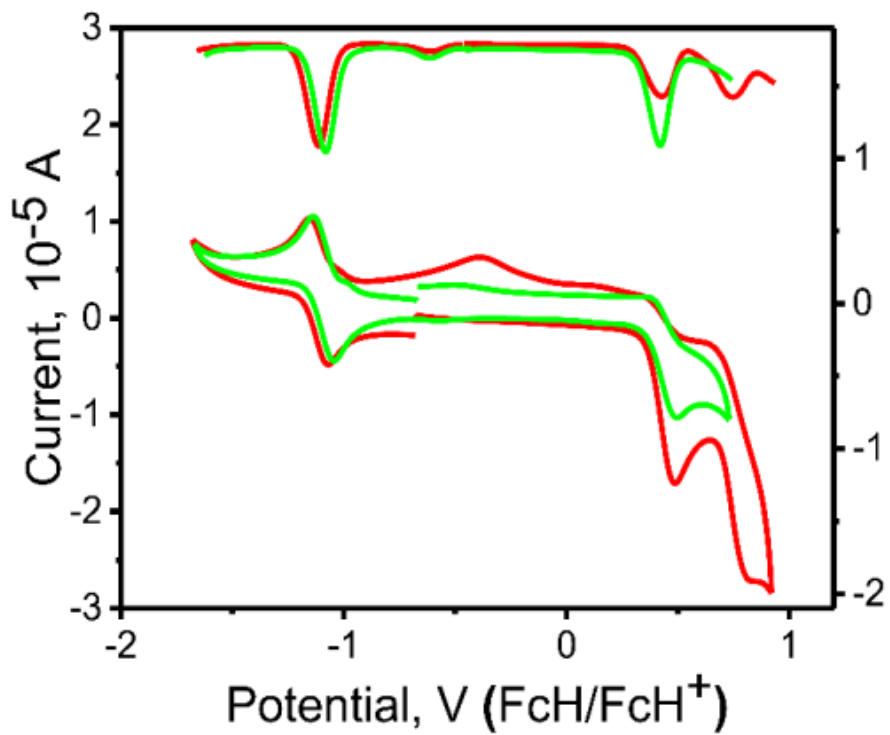


Figure 3.51: DPV spectra of compounds **3.5c** (green) and **3.6c** (red)

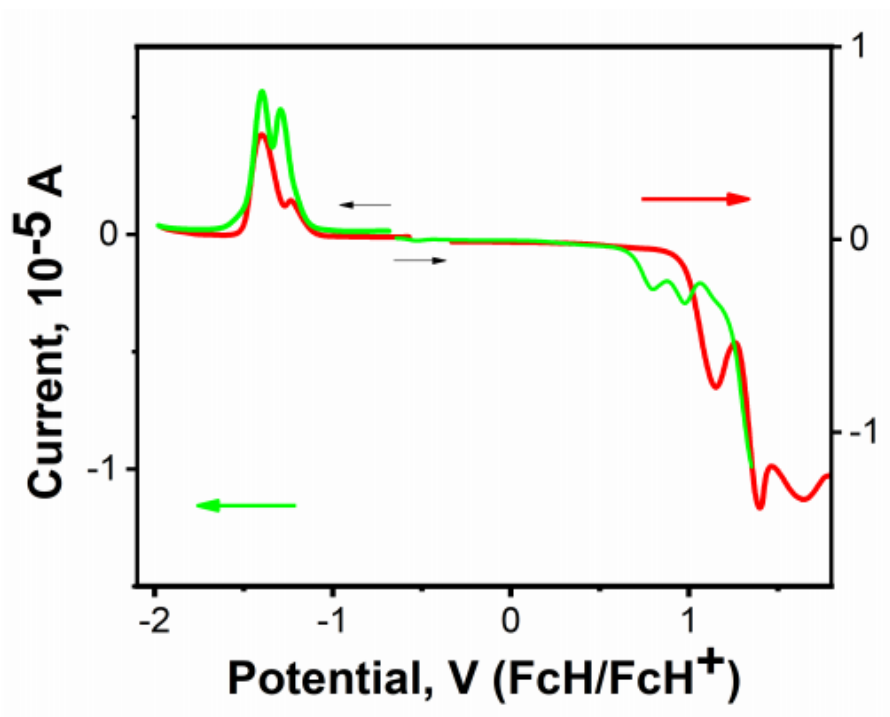


Figure 3.52: DPV spectra of compounds **3.5d** (green) and **3.6d** (red)

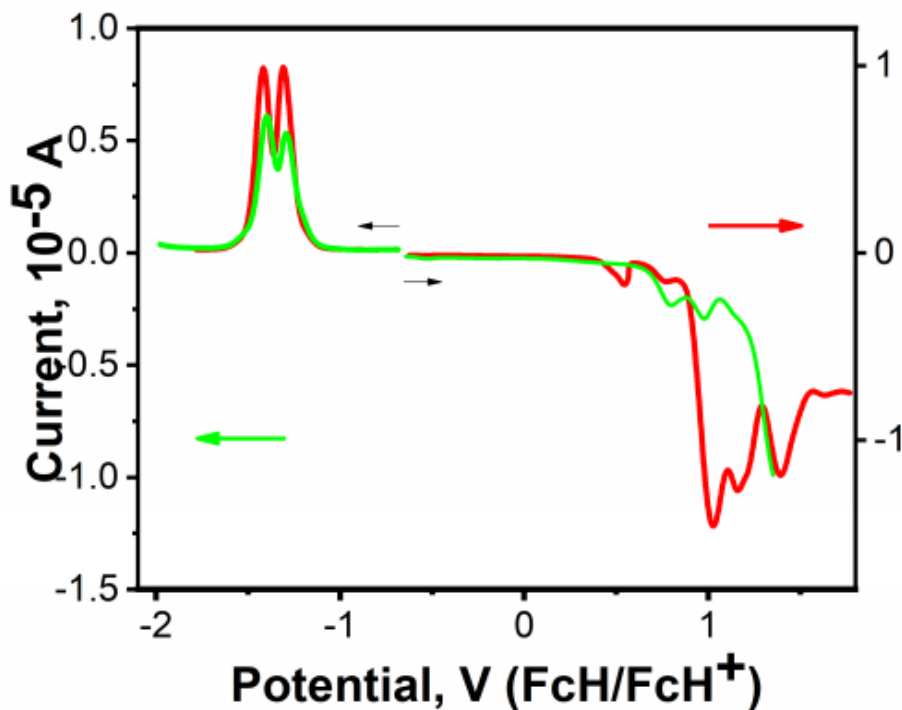


Figure 3.53: DPV spectra of compounds **3.5d** (green) and **3.6e** (red)

Table 3.6. Energetics

	Abs max ( $\pi \rightarrow \pi^*$ )	Ox (catechol)	Red (chromophore)	$\Delta\pi^* \rightarrow \text{CT}$
<b>3.6a</b>	2.36	0.86	-1.20	-0.30
<b>3.6b</b>	1.97	0.82 <sup>†</sup>	-0.83	-0.32
<b>3.6c</b>	1.76	0.81	-1.11	0.16
<b>3.6d</b>	2.55	0.95	-1.30	-0.30
<b>3.6e</b>	2.58	0.95	-1.30	-0.33

All values are in units of eV. Electrochemistry was done in DCM/0.1M TBAP and values are relative to Fc/Fc<sup>+</sup> couple. <sup>†</sup>Estimated as the average of the two oxidation features at 0.74 eV and 0.90 eV. Details and electrochemical data are available above.

To correlate photophysical and electrochemical data on parent compounds **3.5a–3.5d** and catechol-containing compounds **3.6a–3.6e**, we have conducted Density Functional Theory (DFT) and Time Dependent DFT (TDDFT) calculations on all systems. Both TPSSh (10% of

HartreeFock exchange) and B3LYP (20% of Hartree-Fock exchange) exchange-correlation functionals were used to reduce a possibility of the erroneous choice of the computational method. The DFT predicted molecular orbital compositions are shown in Figures 3.53-3.62, comparative energy diagrams are presented in Figure 3.73 and frontier MOs are depicted in Figure 3.74.

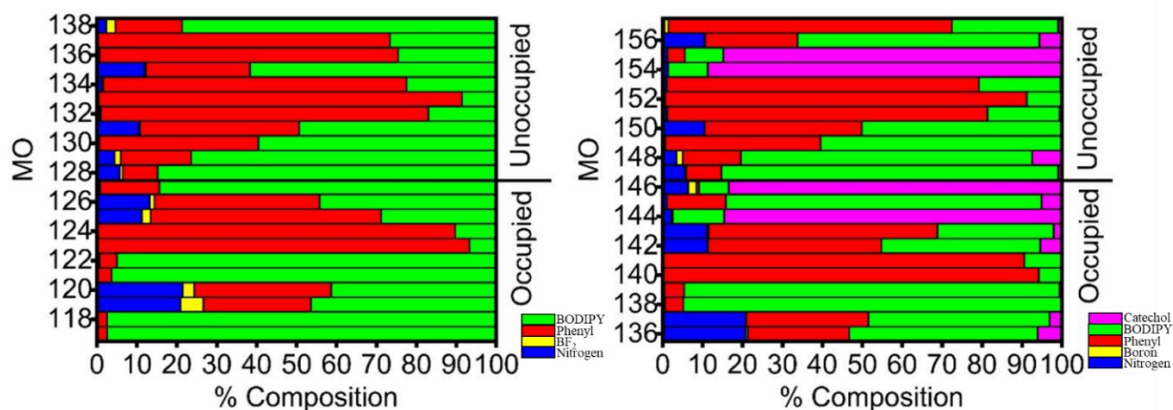


Figure 3.54: TPSSh SP DFT-predicted molecular orbital composition of compounds **3.5a** (left) and **3.6a** (right)

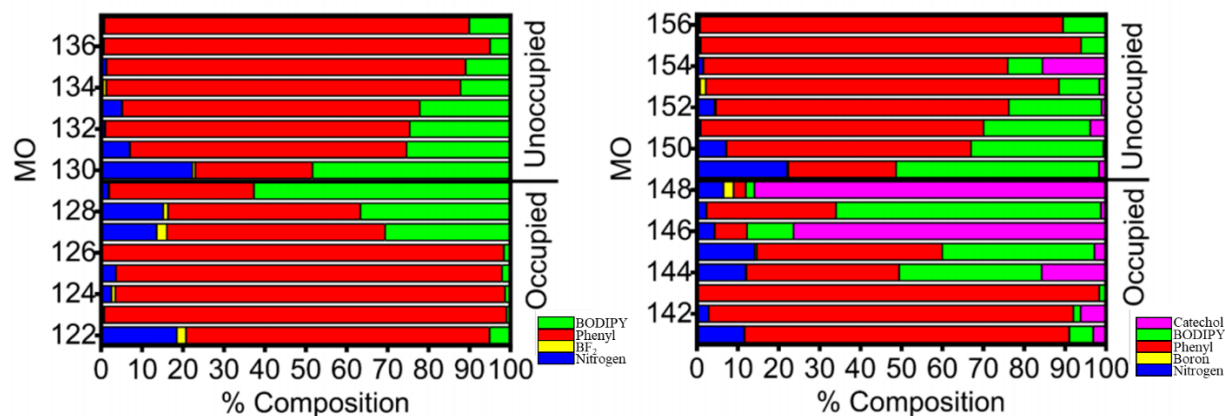


Figure 3.55: TPSSh SP DFT-predicted molecular orbital composition of compounds **3.5b** (left) and **3.6b** (right)

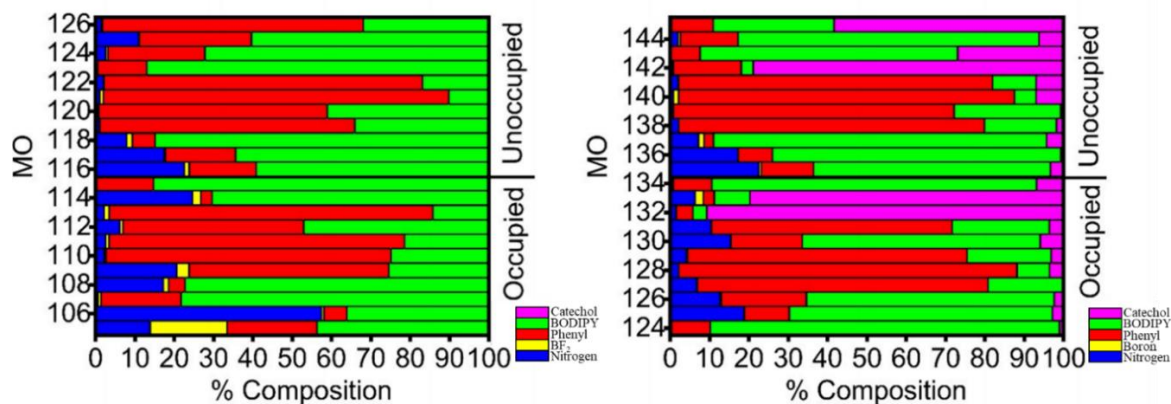


Figure 3.56: TPSSh SP DFT-predicted molecular orbital composition of compounds **3.5c** (left) and **3.6c** (right)

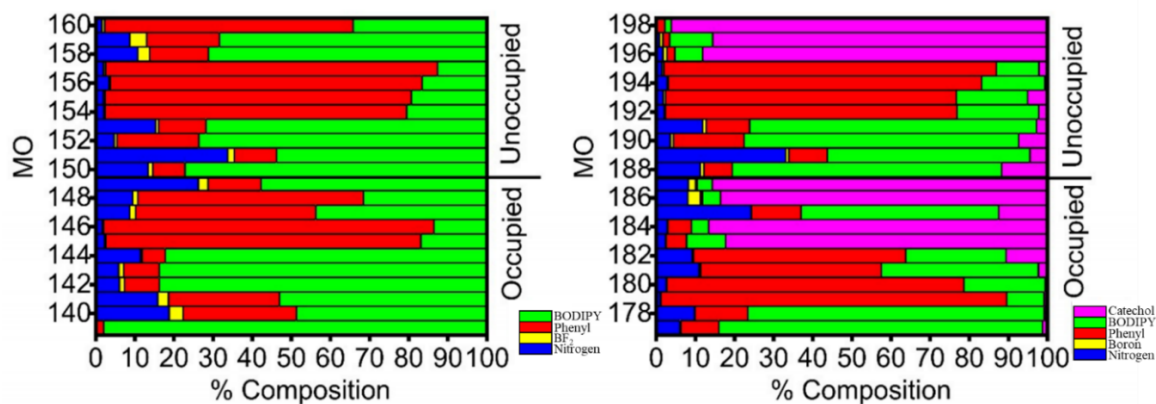


Figure 3.57: TPSSh SP DFT-predicted molecular orbital composition of compounds **3.5d** (left) and **3.6d** (right)

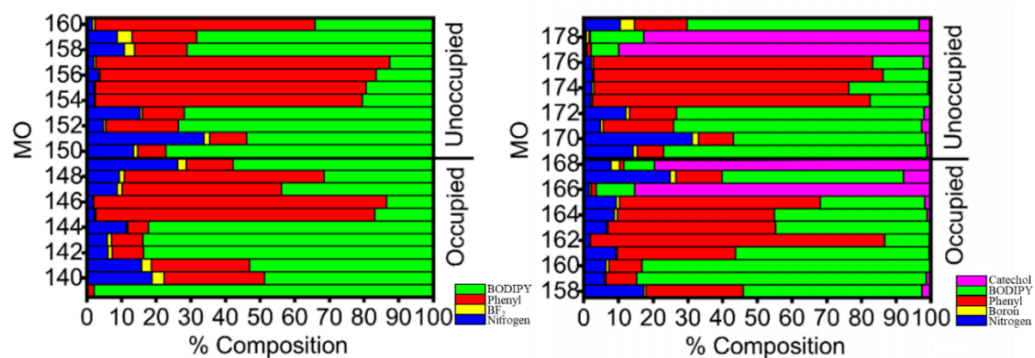


Figure 3.58: TPSSh SP DFT-predicted molecular orbital composition of compounds **3.5d** (left) and **3.6e** (right)

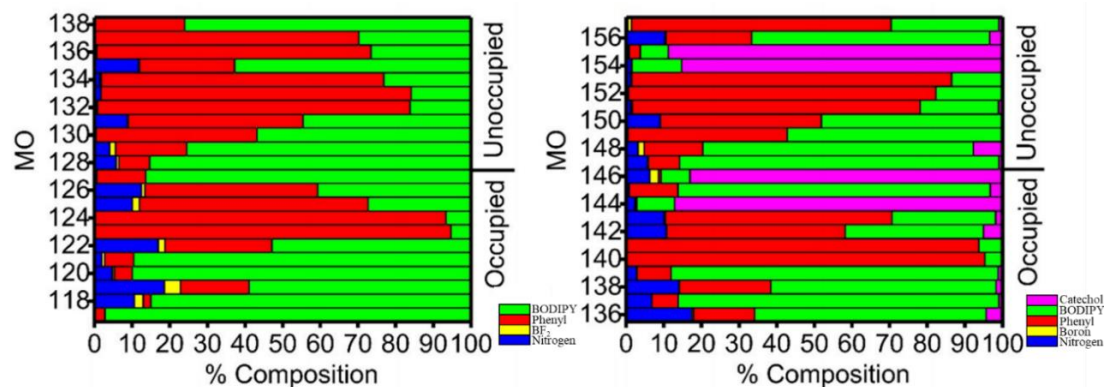


Figure 3.59: B3LYP SP DFT-predicted molecular orbital composition of compounds **3.5a** (left) and **3.6a** (right)

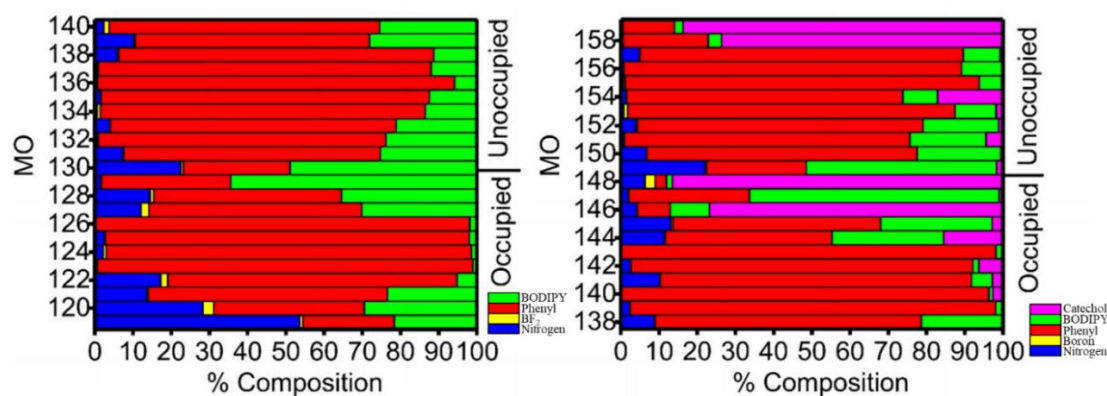


Figure 3.60: B3LYP SP DFT-predicted molecular orbital composition of compounds **3.5b** (left) and **3.6b** (right)

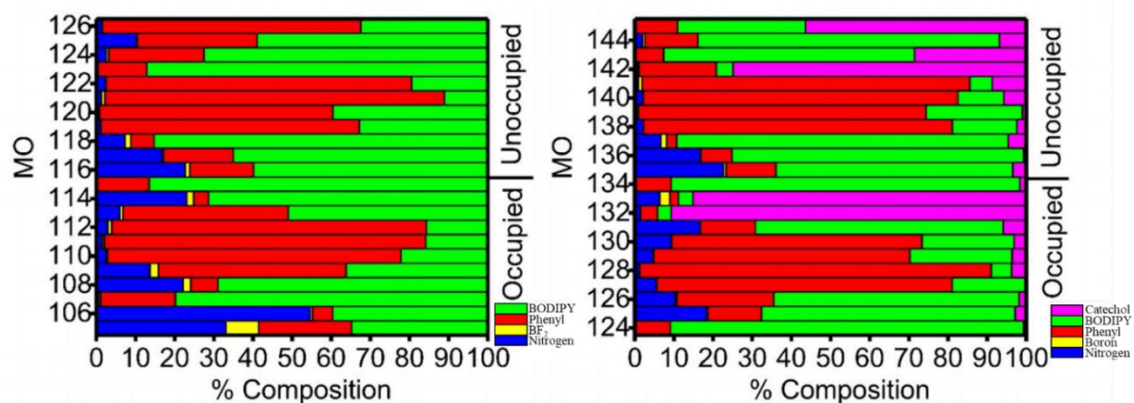


Figure 3.61: B3LYP SP DFT-predicted molecular orbital composition of compounds **3.5c** (left) and **3.6c** (right)

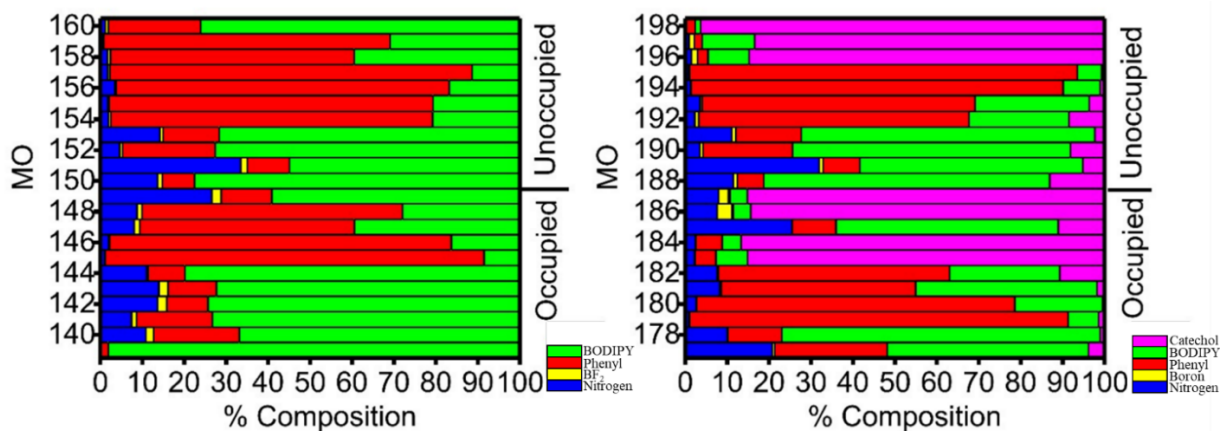


Figure 3.62: B3LYP SP DFT-predicted molecular orbital composition of compounds **3.5d** (left) and **3.6d** (right)

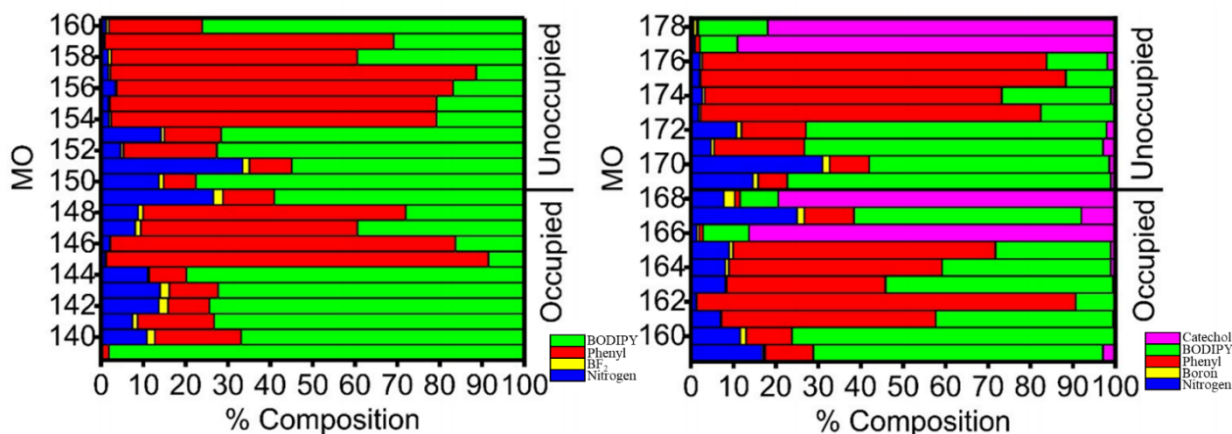


Figure 3.63: B3LYP SP DFT-predicted molecular orbital composition of compounds **3.5d** (left) and **3.6e** (right)

In agreement with the electrochemical data, the LUMOs in all reference compounds **3.5a** – **3.5d** and catechol-containing compounds **3.6a** – **3.6e** are chromophore-centered  $\pi^*$ -MOs. The second excited state for all of these compounds should be dominated by the HOMO-1  $\rightarrow$  LUMO single-electron excitation, which is a standard, chromophore-centered  $\pi$ - $\pi^*$  transition. This second excited state has an energy and intensity close to those observed in the reference compounds **3.5a**–**3.5d**. TDDFT data are also in agreement with a small higher-energy shift of this band in **3.6b** and **3.6c** compared with **3.5b** and **3.5c** as well as low-energy shift in **3.6d** and **3.6e** compared to the

parent **3.5d**. TDDFT predicted intensity for the first, charge-transfer excited state is negligibly small compared to the intense transition associated with a second, chromophore-centered excited state, which explains similarities between experimental UV-vis spectra of the reference and catechol-containing systems.

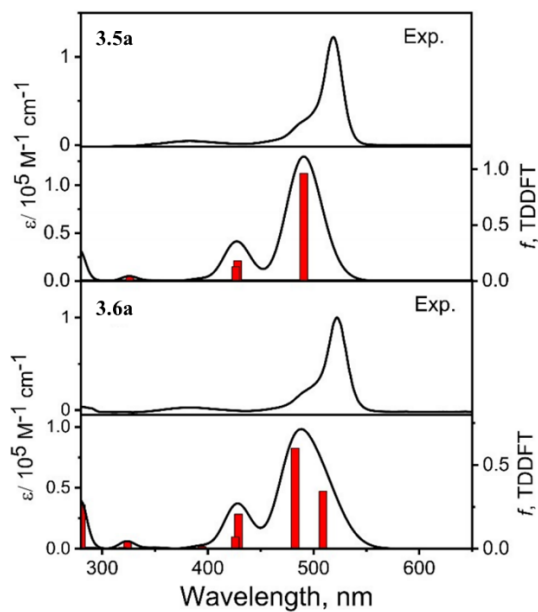


Figure 3.64: TD DFT-predicted and experimental absorption spectra of compounds **3.5a** (top) and **3.6a** (bottom) (TPSSh)

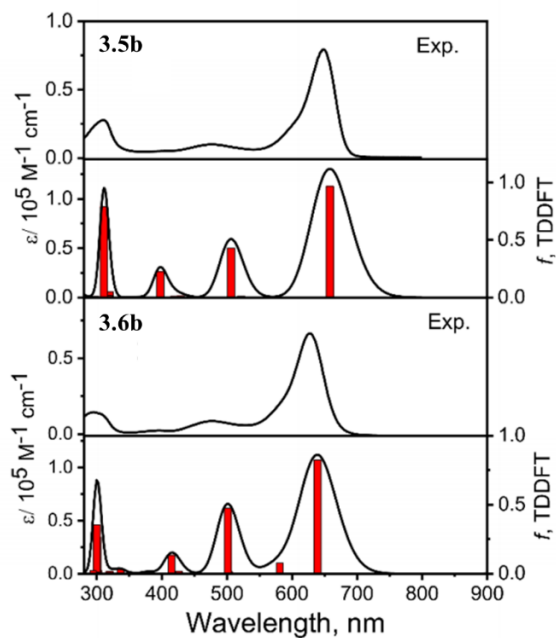


Figure 3.65: TD DFT-predicted and experimental absorption spectra of compounds **3.5b** (top) and **3.6b** (bottom) (TPSSh)

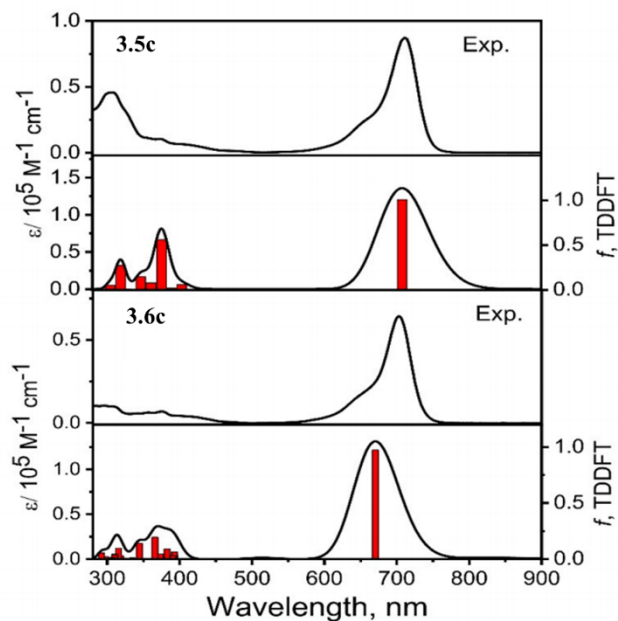


Figure 3.66: TD DFT-predicted and experimental absorption spectra of compounds **3.5c** (top) and **3.6c** (bottom) (TPSSh)

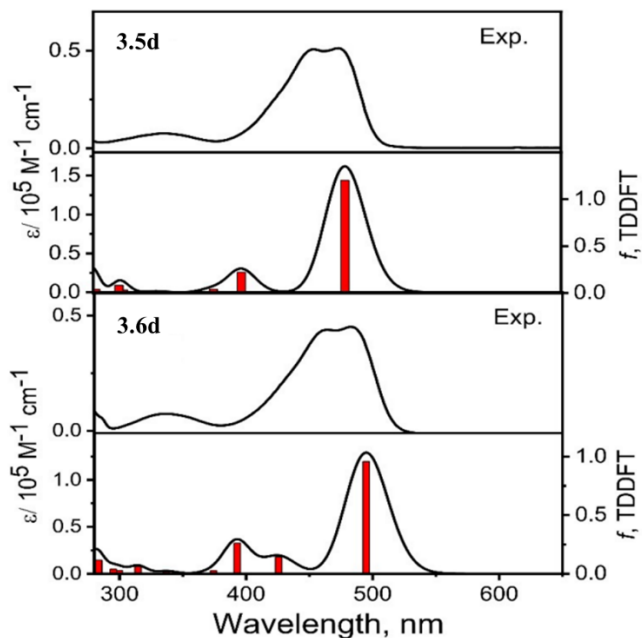


Figure 3.67: TD DFT-predicted and experimental absorption spectra of compounds **3.5d** (top) and **3.6d** (bottom) (TPSSh)

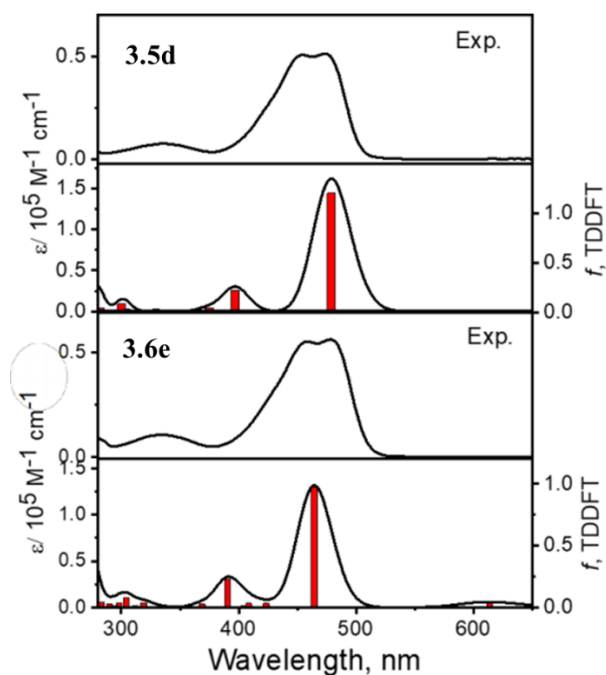


Figure 3.68: TD DFT-predicted and experimental absorption spectra of compounds **3.5d** (top) and **3.6e** (bottom) (TPSSh)

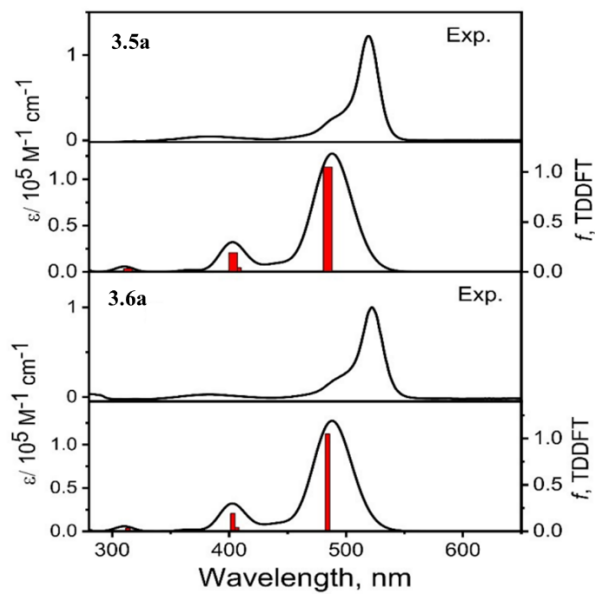


Figure 3.69: TD DFT-predicted and experimental absorption spectra of compounds **3.5a** (top) and **3.6a** (bottom) (B3LYP)

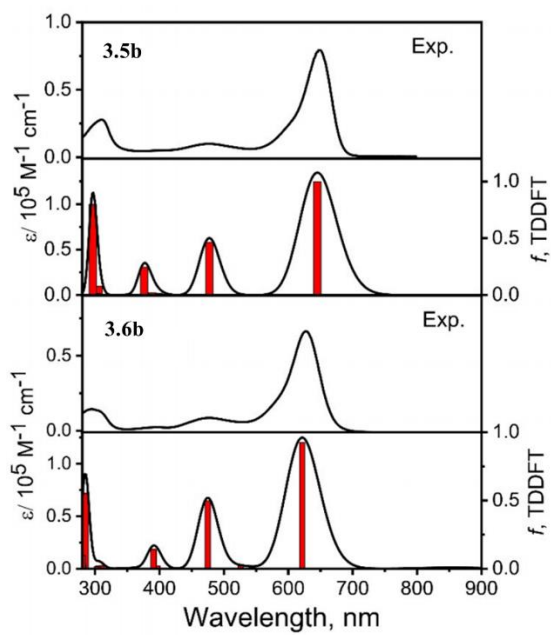


Figure 3.70: TD DFT-predicted and experimental absorption spectra of compounds **3.5b** (top) and **3.6b** (bottom) (B3LYP)

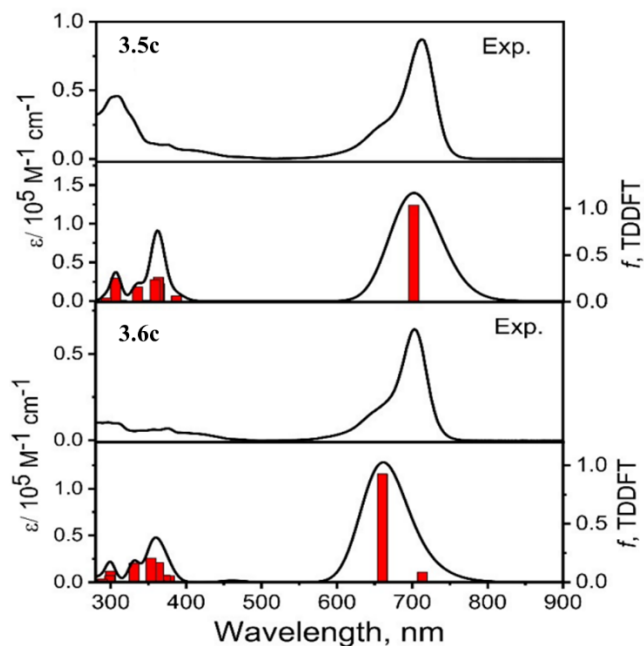


Figure 3.71: TD DFT-predicted and experimental absorption spectra of compounds **3.5c** (top) and **3.6c** (bottom) (B3LYP)

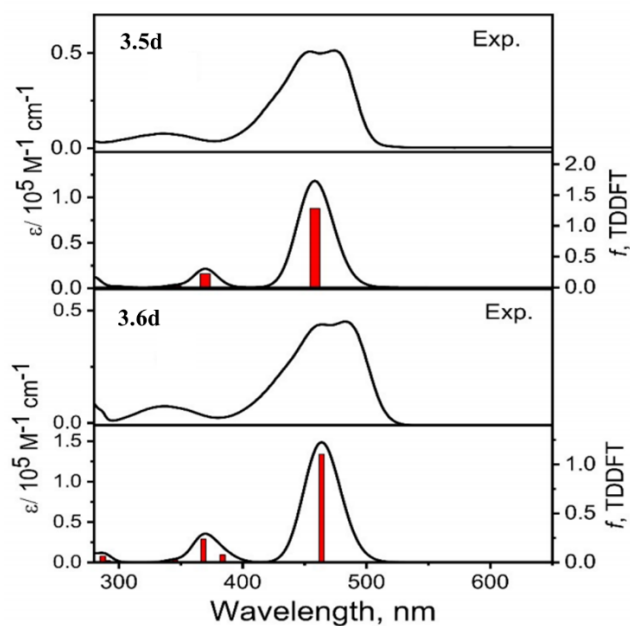


Figure 3.72: TD DFT-predicted and experimental absorption spectra of compounds **3.5d** (top) and **3.6d** (bottom) (B3LYP)

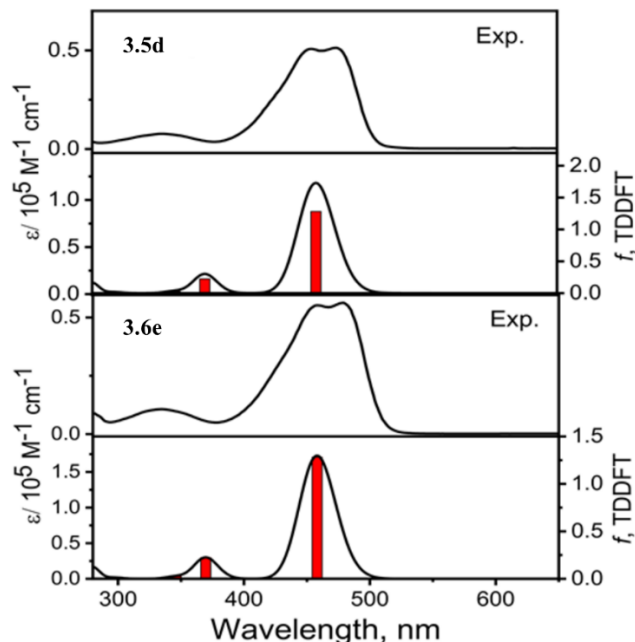


Figure 3.73: TD DFT-predicted and experimental absorption spectra of compounds **3.5d** (top) and **3.6e** (bottom) (B3LYP)

The DFT-predicted electronic structure of the catechol-containing dibenzo-aza-BODIPY **3.6c** is suggestive of an aza-BODIPY centered HOMO and LUMO and catechol-centered HOMO-1. Thus, one might speculate that the first excited state should be dominated by the HOMO  $\rightarrow$  LUMO excitation and the relaxation dynamics for this specific compound should resemble that in a reference compound **3.5c**, which contradicts experimental data. TDDFT calculations for both TPSSh and B3LYP exchange-correlation functionals, however, indicate that the first excited state in **3.6c** consists of both HOMO  $\rightarrow$  LUMO and HOMO-1  $\rightarrow$  LUMO excitations and should be dominated by catechol-to-aza-BODIPY charge-transfer, while the second, more intense transition associated with the most intense band observed in the UV-vis spectrum of this compound also consists of the same two single-electron contributions but will be dominated by the chromophore-centered HOMO  $\rightarrow$  LUMO  $\pi$ - $\pi^*$  excitation. Since charge-transfer transition are predominantly associated with the first excited state, the relaxation dynamics in **3.6c** should be close to the relaxation dynamics observed in the other catechol-containing systems, which correlate well with the experimental steady-state fluorescence and transient absorption spectroscopy data. Overall, TDDFT calculations correctly predicted energies and intensities of the most intense, low-energy transitions in reference as well as catechol-containing compounds of interest. TDDFT also

correctly predicting that the first excited state in catechol-containing systems has catechol-to-chromophore charge-transfer character, which explains fast excited state deactivation dynamics experimentally observed in the corresponding transient absorption spectra. Except for the dibenzo-aza-BODIPY system **3.6c** DFT predicts that HOMOs in all catechol containing compound are catechol-centered, while HOMO-1 is chromophore-centered, which is also in agreement with the electrochemical data. In the case of all reference compounds **3.5a** – **3.5d** and dibenzo-aza-BODIPY **3.6c**, DFT-predicted HOMOs are chromophore-centered  $\pi$ -orbitals, while the HOMO-1 in **3.6c** is a catechol-centered MO in agreement with electrochemical data. Thus, the DFT-predicted electronic structure for all catechol-containing compounds except **3.6c** is indicative of potential low-energy charge-transfer transition dominated by the HOMO to LUMO single electron excitation.

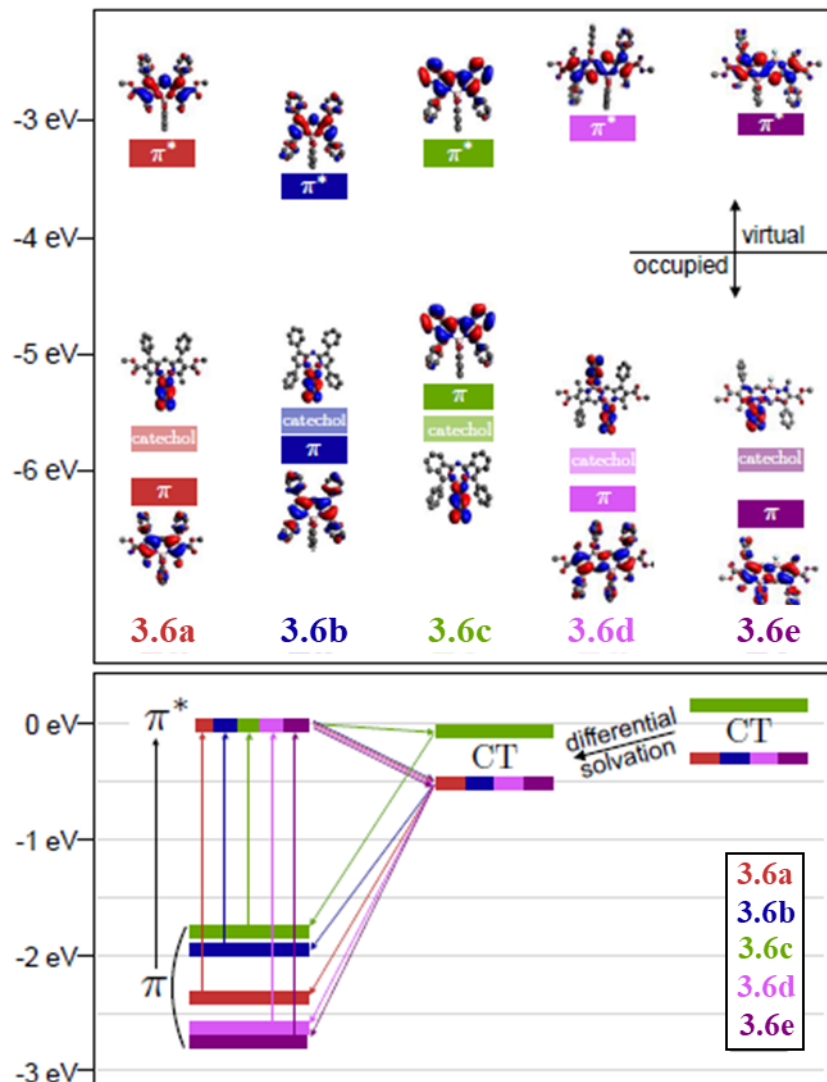


Figure 3.74: **top**: DFT computational predictions of orbital energies for the compounds in Figure 3.29. **bottom**: Energetics relative to the initial optically excited  $\pi^*$  state derived from experimental optical and electrochemical values in table 3.6. Differential solvation represents an estimated difference between solvent polarization energy for the  $\pi^*$  and CT states in toluene.

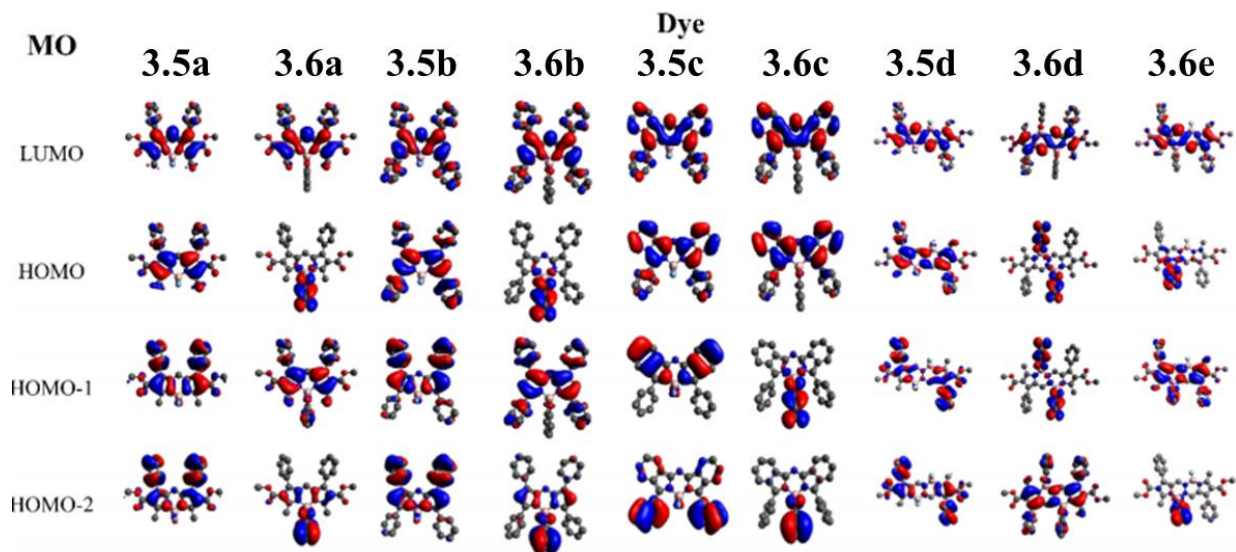


Figure 3.75: TPSSh DFT-predicted frontier molecular orbitals of compounds **3.5a-d** and **3.6a-e**

Relative energetics of the  $\pi \rightarrow \pi^*$ , and charge transfer (CT) states were determined experimentally. The maximum in the absorption spectrum was assigned to the difference between the  $\pi$  and  $\pi^*$  states, and electrochemistry was used to measure the difference in energy between reduction of the  $\pi^*$  and oxidation of the catechol centered orbitals. Experimental results were consistent with the DFT predictions, and are presented in table 3.6 and the bottom of Figure 3.74. The  $\pi^* \rightarrow$ CT conversion had an energy difference of -0.3 eV for all **3.6x** compounds except **3.6c**. Despite transfer to the CT state being 0.15 eV uphill in the case of **3.6c**, the compound exhibited the same rapid excited state deactivation as the other **3.6x** compounds. This can be explained by differential solvation of the  $\pi^*$  and CT states. The CT state was expected to be more polarized than the  $\pi^*$  state. Although time dependent DFT calculations can be unreliable for quantitative prediction of excited state dipole moments, they consistently predicted the dipole moment for the CT state at around 3-4 D larger than the  $\pi^*$  state for the **3.6x** molecules in Figure 3.29. The Kirkwood-Onsager model was used to provide a rough estimate of the differential solvation.<sup>116-118</sup> The solvent polarization energy was expressed in terms of a sphere of radius  $a$  in a dielectric continuum of constant  $\epsilon$  with a dipole moment  $\mu$ ,  $G_p = \frac{\mu^2}{a^3} \left( \frac{2\epsilon+1}{\epsilon-1} \right)$ . For a sphere of radius 6 Å in a solvent with the dielectric constant of toluene ( $\epsilon=2.38$ ), the difference in solvent polarization energy for a change in dipole moment of 2 D  $\rightarrow$  5 D is -0.18 eV. This estimate demonstrates that

differential solvation, even for a very modest increase in molecular polarization in a low dielectric solvent like toluene, is sufficient to bring the CT state below the  $\pi^*$  state in energy for **3.6c**. Thus, following photo-excitation, the CT state is thermodynamically accessible to all of the **3.6x** compounds, which is consistent with the rapid excited state deactivation observed for all of them.

## Experimental Section

**Reagents and materials.** Solvents were purified using standard approaches: toluene was dried over sodium metal; DCM was dried over calcium hydride. Compounds **3.1a-e** and **3.4** were prepared as described earlier<sup>92,107,28</sup>. Fullerene (C<sub>60</sub>), aluminum chloride, and 1,2-dihydroxybenzene were purchased from Sigma Aldrich. Silica gel (60 Å, 60-100 μm) was purchased from Dynamic Adsorbents Inc.

**DFT-PCM and TDDFT-PCM Calculations.** The starting geometries of compounds **3.3a-e** and **3.6a-d** were optimized using a hybrid B3LYP exchange correlation functional.<sup>119</sup> Solvent effects were calculated using the polarized continuum model (PCM).<sup>120</sup> In all calculations, DCM was used as the solvent. In PCM-TDDFT calculations, the first 100 states were calculated for compounds **3.3a-d**, the first 70 states were calculated for compound **3.3e**, and first 30 states were calculated for **3.6a-d**. In all calculations, full-electron Wachter's basis set<sup>121</sup> was utilized for iron atoms, while all other atoms were modeled using 6-31G(d)<sup>122</sup> basis set. Gaussian 09 software was used in all calculations.<sup>123</sup> QMForge program was used for molecular orbital analysis.<sup>124</sup>

**X-ray crystallography.** Useful for X-ray crystallographic experiments single crystals of triad (2,3)-**3.3b** were prepared by the slow evaporation of saturated toluene solution. A Rigaku RAPID-II diffractometer with a graphite monochromator and Cu K $\alpha$  ( $\lambda=1.54187$  Å) radiation was used for X-ray diffraction data collection. All experiments were conducted at -150 °C temperature. Multi-scan absorption correction<sup>125</sup> was applied to the data in all cases. The crystal structure was solved by the direct method (SIR-92)<sup>126</sup> and refined by full-matrix least-squares method based on F<sup>2</sup> using the Crystals for Windows programs.<sup>127</sup> All non-hydrogen atoms were refined anisotropically, while hydrogen atoms were refined using "riding mode" with displacement parameters bonded to a parent atom:  $U_{\text{iso}}(\text{H}) = 1.2U_{\text{eq}}(\text{C})$  ( $U_{\text{eq}} = 1/3(U_{11}+U_{22}+U_{33})$ ).

**Spectroscopy Measurements.** Jasco-720 spectrophotometer was used to collect UV-Vis data for compounds **3.3a-e** and **3.4**. A CARY 50 Spectrophotometer was used to collect UV-Vis data and CARY Eclipse Fluorescence Spectrophotometer was used to collect emission spectra for samples **3.5a-d** and **3.6a-e** in DCM. A CARY 4000 was used to collect UV-Vis data for samples **3.5a-d** and **3.6a-e** in toluene. Electrochemical cyclic voltammetry (CV) and differential pulse voltammetry (DPV) measurements were conducted using a CH Instruments electrochemical analyzer utilizing a three-electrode scheme with platinum working, auxiliary and Ag/AgCl reference electrodes. DCM was used as solvents and 0.05 M solution of tetrabutylammonium tetrakis(pentafluorophenyl)borate (TFAB) was used as electrolyte for samples **3.3a-e** and **3.4** well, 0.1 M solution of tetrabutylammonium perchlorate (TBAP) was used as supporting electrolyte for **3.5a-d** and **3.6a-e**. In all cases, experimental redox potentials were corrected using decamethylferrocene (Fc\*H) as an internal standard. Samples **3.3a-e** and **3.4** NMR spectra were recorded on a Varian INOVA instrument with a 500 MHz frequency for protons and samples **3.5a-d** and **3.6a-e** were recorded on a Bruker Avance instrument with a 300 MHz frequency for protons and 75 MHz frequency for carbons. Chemical shifts are reported in parts per million (ppm) and referenced to tetramethylsilane (Si(CH<sub>3</sub>)<sub>4</sub>) as an internal standard. High-resolution mass spectra were recorded for compounds **3.2a-e**, **3.3a-e**, and **3.6a-e** using a Bruker micrO-TOF-QIII.

**Pump-probe spectroscopy.** A home-built laser system consisting of a Ti:sapphire oscillator (powered by a Spectra Physics Millennia Pro) and regenerative amplifier (powered by a Spectra Physics Empower 15 or Evolution) generated ~60 to 80 fs (FWHM), 0.8-1.0 mJ, **810** nm pulses at a repetition rate of 1 kHz. A portion of this light was directed into a home-built noncollinear optical parametric amplifier (NOPA) to create excitation pulses at **530** nm, **570** nm and **650** nm. Continuum probe pulses of **420-750** nm, and **850-1400** nm, were created by focusing a small fraction of the **805** nm – **815** nm light (~20 μW) into a 2 mm sapphire window and Yttrium Aluminum Garnet (YAG) crystal, respectively. The excitation light was polarized at 54.7 degrees relative to the probe polarization (the magic angle) to isolate the isotropic dynamics of the excited state. Time delay between the excitation and probe pulses was controlled by a mechanical delay stage (Newport UTM150PP.1). Pump and probe pulses were focused and spatially overlapped in 1 mm quartz cuvette containing the sample. The probe beam emerging from the sample was collimated, directed through a monochromator and detected on an array. A Princeton Instruments SP2150i monochromator (150 lines/mm, 500 nm blaze) with an attached 256 pixel diode array

(Hamamatsu S3902-256Q) was used for visible light. A Princeton Instruments SP2150 monochromator (150 lines/mm, 1200nm blaze) with an attached 256 linear pixel InGaAs diode array (Hamamatsu G9213-256S) was used for infra-red light. The pump beam was chopped at half the laser repetition rate while each laser pulse of the probe beam was measured to yield the change in optical density,  $\Delta OD$ . The  $\Delta OD$  was determined for each pulse pair. Typically, 20,000-40,000 pulse pairs were averaged for each time point presented in the pump-probe data. Data shown was collected with pump energies typically between 60 nJ and 150 nJ per pulse. Samples had an optical density of 0.25 to 0.35 at the excitation wavelength. Absorption spectra taken before and after the pump probe experiments were indistinguishable, indicating no evidence of sample degradation.

## Synthesis

### General procedure for the synthesis of compounds 3.2a-f:

To the solution of compound **3.1a-d** (0.2 mmol) aluminum chloride (0.6 mmol, 80 mg) was added in dry DCM (10 mL) under argon atmosphere. The mixture was refluxed for 2 min. After cooling to room temperature 3,4-dihydroxybenzaldehyde (or 2,3-dihydroxybenzaldehyde in the case of compound **3.2f**) (0.8 mmol, 110mg) was added. The resulting mixture was stirred for 2 h at room temperature. Then the solution was slowly quenched with water, organic layer was washed two times with water, dried over  $\text{Na}_2\text{SO}_4$  and evaporated to dryness. The crude product was purified by column chromatography on silica gel using DCM as a solvent.

**Compound 3.2a.** Yield 41 mg (25 %);  $^1\text{H}$  NMR (500 MHz,  $\text{CDCl}_3$ )  $\delta$  9.94 (s, 1H), 7.56 (d,  $J$  = 7.9 Hz, 1H), 7.51 (s, 1H), 7.43 – 7.27 (m, 11H), 7.02 (d,  $J$  = 7.9 Hz, 1H), 7.00 (s, 1H), 6.33 (d,  $J$  = 16.0 Hz, 1H), 4.36 – 4.29 (m, 2H), 4.19 – 4.06 (m, 9H), 3.86 (s, 1H), 3.69 (s, 1H), 2.38 (s, 3H), 1.08 (t,  $J$  = 7.0 Hz, 3H), 1.03 (t,  $J$  = 7.0 Hz, 3H); HRMS (APCI positive) calcd for  $\text{C}_{47}\text{H}_{39}\text{N}_2\text{B}_1\text{O}_7\text{Fe}_1$   $[\text{M} + \text{H}]^+$ : 811.2281, found 811.2333.

**Compound (3,4)-3.2b.** Yield 62 mg (31 %);  $^1\text{H}$  NMR (500 MHz,  $\text{CDCl}_3$ )  $\delta$  10.40 (s, 0.2 H), 9.99 (s, 0.63 H) 7.62 – 7.59 (m, 1H), 7.42 – 7.34 (m, 10H), 7.20 – 7.17 (m, 3H), 7.17 – 7.12 (m, 2H), 7.07 – 7.02 (m, 3H), , 6.35 – 6.29 (m, 2H), 4.33 (s, 1H), 4.33 (m, 3H), 4.18 – 4.11 (m, 14H), 3.87

(s, 2H), 3.78 – 3.72 (m, 2H), 1.07 (m, 6H); HRMS (APCI positive) calcd for C<sub>58</sub>H<sub>47</sub>N<sub>2</sub>B<sub>1</sub>O<sub>7</sub>Fe<sub>2</sub> [M + H]<sup>+</sup>: 1007.2260, found 1007.2228.

**Compound (2,3)-3.2b.** Yield 58 mg (29 %); <sup>1</sup>H NMR (500 MHz, CDCl<sub>3</sub>) δ 10.40 (s, 1H), 7.52 (d, *J* = 8.1 Hz, 2H), 7.42 – 7.34 (m, 10H), 7.20 – 7.16 (m, 3H), 7.10 – 7.07 (m, 1H), 7.03 (s, 1H), 6.35 (d, *J* = 16.0 Hz, 2H), 4.33 (s, 4H), 4.15 (q, *J* = 7.0 Hz, 4H), 4.10 (s, 10H), 3.87 (s, 2H), 3.78 (s, 2H), 1.09 (t, *J* = 7.0 Hz, 6H); HRMS (APCI positive) calcd for C<sub>58</sub>H<sub>47</sub>N<sub>2</sub>B<sub>1</sub>O<sub>7</sub>Fe<sub>2</sub> [M + H]<sup>+</sup>: 1007.2260, found 1007.2315.

**Compound 3.2c.** Yield 53 mg (28 %); <sup>1</sup>H NMR (500 MHz, CDCl<sub>3</sub>) δ 10.36 (s, 1H), 7.51 (dd, *J* = 8.1 Hz, *J* = 1.4 Hz, 1H), 7.41 – 7.34 (m, 10H), 7.21 (s, 0.5 H), 7.17 (s, 0.5 H), 7.14 – 7.12 (m, 1H), 7.10 – 7.05 (m, 1H), 6.96 (s, 1H), 6.63 (d, *J* = 8.9 Hz, 2H), 6.57 (d, *J* = 16.0 Hz, 1H), 6.46 (d, *J* = 8.9 Hz, 2H), 6.39 (d, *J* = 16.0 Hz, 1H), 4.29 – 4.28 (m, 2H), 4.18 – 4.13 (m, 4H), 4.09 (s, 5H), 3.85 – 3.84 (m, 1H), 3.76 – 3.75 (m, 1H), 3.01 (s, 6H), 1.08 (t, *J* = 7.1 Hz, 3H), 1.06 (t, *J* = 7.1 Hz, 3H); HRMS (APCI positive) calcd for C<sub>56</sub>H<sub>48</sub>N<sub>3</sub>B<sub>1</sub>O<sub>7</sub>Fe<sub>1</sub> [M + H]<sup>+</sup>: 942.3018, found 942.3116.

**Compound 3.2d.** Yield 57 mg (34 %); <sup>1</sup>H NMR (500 MHz, CDCl<sub>3</sub>) δ 9.98 (s, 1H), 7.62 (dd, *J* = 8.1 Hz, *J* = 1.4 Hz, 1H), 7.58 – 7.56 (m, 2H), 7.46 – 7.36 (m, 10H), 7.21 – 7.19 (m, 1H), 7.09 – 7.06 (m, 2H), 6.36 (d, *J* = 16.0 Hz, 1H), 5.73 (d, *J* = 7.5 Hz, 1H), 4.39 – 4.38 (m, 2H), 4.20 (q, *J* = 7.1 Hz, 2H), 4.14 (s, 5H), 3.90 (s, 1H), 3.83 (t, *J* = 7.6 Hz, 2H), 3.75 (s, 1H), 1.67 – 1.60 (m, 2H), 1.33 – 1.29 (m, 2H), 1.09 (t, *J* = 7.1 Hz, 3H), 0.89 (t, *J* = 7.4 Hz, 3H); HRMS (APCI positive) calcd for C<sub>49</sub>H<sub>54</sub>N<sub>3</sub>B<sub>1</sub>O<sub>6</sub>Fe<sub>1</sub> [M + H]<sup>+</sup>: 848.3537, found 848.2705.

**Compound 3.2e.** Yield 47 mg (38 %); <sup>1</sup>H NMR (500 MHz, CDCl<sub>3</sub>) δ 9.87 (s, 1H), 7.48 (dd, *J* = 7.9 Hz, *J* = 1.7 Hz, 1H), 7.41 (d, *J* = 1.7 Hz, 1H), 7.40 – 7.35 (m, 6H), 7.27 – 7.26 (m, 3H), 6.98 (s, 1H), 6.97 (d, *J* = 7.8 Hz, 1H), 4.11 (q, *J* = 7.1 Hz, 4H), 2.41 (s, 6H), 1.02 (t, *J* = 7.1 Hz, 6H); HRMS (APCI positive) calcd for C<sub>36</sub>H<sub>31</sub>N<sub>2</sub>B<sub>1</sub>O<sub>7</sub>Fe<sub>1</sub> [M + H]<sup>+</sup>: 615.2303, found 615.2471.

### General procedure for the synthesis of compounds 3.3a-f:

The mixture of catechol-substituted dye (**3.2a-f**) (0.06 mmol), sarcosine (0.6 mmol, 53 mg), and fullerene (0.12 mmol, 86 mg) was refluxed in toluene for 12 h under argon atmosphere.

After cooling to room temperature, the excess of sarcosine and fullerene was filtered out and the solution was evaporated to dryness. The crude product was purified by column chromatography on silica gel using toluene as a solvent.

**Compound 3.3a.** Yield 37 mg (40 %);  $^1\text{H NMR}$  (500 MHz,  $\text{C}_6\text{D}_6$ )  $\delta$  7.80 (d,  $J = 16.0$  Hz, 1H), 7.32 (s, 1H), 7.10-7.08 (m, 2H), 7.00-6.91 (m, 11H), 4.87 (s, 0.44 H,  $\text{H}_{\text{pyrrolidine}}$ ), 4.78 (s, 0.45 H,  $\text{H}_{\text{pyrrolidine}}$ ), 4.65 (d,  $J = 8.0$  Hz, 0.40 H,  $\text{H}_{\text{pyrrolidine}}$ ), 4.60 (d,  $J = 8.0$  Hz, 0.60 H,  $\text{H}_{\text{pyrrolidine}}$ ), 4.35-4.31 (m, 1H), 4.30-4.27 (m, 2H), 4.18-4.14 (m, 6H), 4.07 (s, 1H), 4.00-3.82 (m, 6H), 2.92 (br.s, 1.15 H,  $\text{BDP}_{\text{methyl}}$ ), 2.78 (s, 1.60 H,  $\text{NMe}_{\text{pyrrolidine}}$ ), 2.46 (s, 1.40 H,  $\text{NMe}_{\text{pyrrolidine}}$ ), 2.38 (br.s, 1.30 H,  $\text{BDP}_{\text{methyl}}$ ), 0.77-0.69 (m, 6H); HRMS (APCI positive) calcd for  $\text{C}_{109}\text{H}_{44}\text{N}_3\text{B}_1\text{O}_6\text{Fe}_1$   $[\text{M} + \text{H}]^+$ : 1559.2788, found 1559.2771.

**Compound (3,4)-3.3b.** Yield 49 mg (47 %);  $^1\text{H NMR}$  (500 MHz,  $\text{C}_6\text{D}_6$ )  $\delta$  7.65 (d,  $J = 10.0$  Hz, 1H), 7.61 (d,  $J = 10.0$  Hz, 1H), 7.44 (d,  $J = 7.5$  Hz, 1H), 7.32 (s, 1H), 7.20-7.18 (m, 3H), 7.00-6.94 (m, 10H), 6.90 (s, 1H), 4.82 (s, 1H,  $\text{H}_{\text{pyrrolidine}}$ ), 4.59 (d,  $J = 9.0$  Hz, 1H,  $\text{H}_{\text{pyrrolidine}}$ ), 4.37 (s, 1H), 4.33-4.31 (m, 2H), 4.26-4.23 (m, 8 H), 4.16-4.14 (m, 6H), 3.98-3.91 (m, 6H), 2.61 (s, 3H,  $\text{NMe}_{\text{pyrrolidine}}$ ), 0.80-0.75 (m, 6H); HRMS (APCI positive) calcd for  $\text{C}_{120}\text{H}_{52}\text{N}_3\text{B}_1\text{O}_6\text{Fe}_2$   $[\text{M} + \text{H}]^+$ : 1755.2766, found 1755.2772.

**Compound (2,3)-3.3b.** Yield 53 mg (50 %);  $^1\text{H NMR}$  (500 MHz,  $\text{C}_6\text{D}_6$ )  $\delta$  7.91 (d,  $J = 7.3$  Hz, 1H), 7.84 (d,  $J = 16.0$  Hz, 1H), 7.63 (d,  $J = 16.0$  Hz, 1H), 7.41 (d,  $J = 7.3$  Hz, 1H), 7.31-7.22 (m, 3H), 7.10-7.08 (m, 2H), 7.00 (s, 1H), 6.96-6.95 (m, 3H), 6.91-6.90 (m, 3H), 6.85 (s, 1H), 6.74 (d,  $J = 16.0$  Hz, 1H), 5.64 (s, 1H,  $\text{H}_{\text{pyrrolidine}}$ ), 4.48 (d,  $J = 10$  Hz, 1 $\text{H}_{\text{pyrrolidine}}$ ), 4.35 (s, 1H), 4.26-4.24 (m, 8H), 4.13 (s, 1H), 4.05-3.95 (m, 11H), 3.84 (d,  $J = 10$  Hz, 1H,  $\text{H}_{\text{pyrrolidine}}$ ), 3.78 (s, 1H), 2.47 (s, 3H,  $\text{NMe}_{\text{pyrrolidine}}$ ), 0.83-0.80 (m, 6H); HRMS (APCI positive) calcd for  $\text{C}_{120}\text{H}_{52}\text{N}_3\text{B}_1\text{O}_6\text{Fe}_2$   $[\text{M} + \text{H}]^+$ : 1755.2766, found 1755.2740.

**Compound 3.3c.** Yield 47 mg (47 %);  $^1\text{H NMR}$  (500 MHz,  $\text{C}_6\text{D}_6$ )  $\delta$  8.22 (d,  $J = 10.8$  Hz, 0.2H), 8.11 (d,  $J = 16.8$  Hz, 0.3 H), 7.95-7.92 (m, 1H), 7.83 (d,  $J = 16.2$  Hz, 0.50 H), 7.74-7-70 (m, 1H), 7.61 (d,  $J = 16.8$  Hz, 0.8H), 7.34-7.31 (m, 3H), 7.00-6.91 (m, 10H), 6.83-6.77 (m, 2H), 6.60 (d,  $J = 8.6$  Hz, 1H), 6.35 (d,  $J = 9.0$  Hz, 0.50H), 6.28 (d,  $J = 9.0$  Hz, 1.3H), 5.69-5.69 (m, 1H,  $\text{H}_{\text{pyrrolidine}}$ ),

4.60-4.58 (m, 0.4 H), 4.47 (d,  $J = 9.0$  Hz, 0.57 H,  $H_{\text{pyrrolidine}}$ ), 4.40 (d,  $J = 9.0$  Hz, 0.43 H,  $H_{\text{pyrrolidine}}$ ), 4.30-4.29 (m, 0.67 H), 4.24-4.19 (m, 5H), 4.15-4.14 (m, 0.53 H), 4.06-3.96 (m, 7H), 3.84 (d,  $J = 9.0$  Hz, 0.60 H,  $H_{\text{pyrrolidine}}$ ), 3.80 (d,  $J = 9.0$  Hz, 0.40 H,  $H_{\text{pyrrolidine}}$ ), 2.53 (s, 2H, PhNMe<sub>2</sub>), 2.45 (s, 1.70 H, NMe<sub>pyrrolidine</sub>), 2.39 (s, 1H, PhNMe<sub>2</sub>), 2.35 (s, 1.30 H, NMe<sub>pyrrolidine</sub>), 2.33 (s, 3.00 H, PhNMe<sub>2</sub>), 0.85-0.78 (m, 6H); HRMS (APCI positive) calcd for C<sub>118</sub>H<sub>53</sub>N<sub>4</sub>B<sub>1</sub>O<sub>6</sub>Fe<sub>1</sub> [M + H]<sup>+</sup>: 1690.3524, found 1690.3530.

**Compound 3.3d.** Yield 37 mg (39 %); <sup>1</sup>H NMR (500 MHz, C<sub>6</sub>D<sub>6</sub>)  $\delta$  8.07 (m, 0.46H), 7.93-7.83 (m, 1H), 7.58-7.56 (m, 2H), 7.32-7.25 (m, 3H), 7.05 – 7.00 (m, 8H), 6.87 (d,  $J = 6.7$  Hz, 1H), 6.60-6.56 (m, 0.45H), 5.93 (d,  $J = 7.3$  Hz, 0.60 H,  $H_{\text{pyrrolidine}}$ ), 5.87-5.84 (m, 0.40H,  $H_{\text{pyrrolidine}}$ ), 4.90 (s, 0.53H),  $H_{\text{pyrrolidine}}$ ), 4.79 (s, 0.37H,  $H_{\text{pyrrolidine}}$ ), 4.66 (d,  $J = 9.0$  Hz, 0.38H,  $H_{\text{pyrrolidine}}$ ), 4.59 (d,  $J = 9.0$  Hz, 0.38H,  $H_{\text{pyrrolidine}}$ ), 4.39-4.33 (m, 2H), 4.22-4.20 (m, 6H), 4.11-4.10 (m, 1H), 4.01-3.96 (m, 2H), 3.86-3.84 (m, 0.50H), 3.69-3.67 (m, 0.50H), 3.27-3.22 (m, 1H), 2.90 (s, 1.10H, NMe<sub>pyrrolidine</sub>), 2.77 (s, 1.80H, NMe<sub>pyrrolidine</sub>), 1.44-1.38 (m, 2H), 1.09-1.03 (m, 2H), 0.80-0.77 (m, 3H), 0.71 (t,  $J = 7.3$  Hz, 3H); HRMS (APCI positive) calcd for C<sub>112</sub>H<sub>47</sub>N<sub>4</sub>B<sub>1</sub>O<sub>5</sub>Fe<sub>1</sub> [M + H]<sup>+</sup>: 1596.3105, found 1596.3096.

**Compound 3.3e** Yield 33 mg (40 %); <sup>1</sup>H NMR (500 MHz, C<sub>6</sub>D<sub>6</sub>)  $\delta$  7.05-6.97 (m, 13 H), 6.90 (s, 1H), 4.80 (s, 1H,  $H_{\text{pyrrolidine}}$ ), 4.55 (d,  $J = 9.0$  Hz, 1H,  $H_{\text{pyrrolidine}}$ ), 3.90-3.83 (m, 5H), 2.86 (br.s, 3H, BDP<sub>methyl</sub>), 2.71 (s, 3H, NMe<sub>pyrrolidine</sub>), 2.47 (br.s, 3H, BDP<sub>methyl</sub>), 0.72 (t,  $J = 7.0$  Hz, 6H); HRMS (APCI positive) calcd for C<sub>98</sub>H<sub>36</sub>N<sub>3</sub>B<sub>1</sub>O<sub>6</sub> [M + H]<sup>+</sup>: 1363.2811, found 1363.2803.

#### **Procedure for the synthesis of compounds 3.6a-e and 3.7:**

**Compound 3.6a.** The mixture of BODIPY **3.5a** (200 mg, 0.39 mmol) and dry AlCl<sub>3</sub> (152 mg, 1.16 mmol) was vacuum dried in a Schlenk flask for 30 min. Then the dry DCM (10ml) was added through the septum into the flask and the resulting mixture was refluxed for 1 min under the argon atmosphere. Then the solution of 1,2-dihydroxybenzene (128mg, 1.16mmol) in 10 ml of dry DCM was added through the cannula into the flask. The resulting mixture was stirred for 45 min at room temperature under argon atmosphere. After that time, the reaction mixture was slowly quenched

with water and stirred for another 30 min. The organic layer was separated and washed with water (3x50ml), saturated brine solution (50 mL), dried over MgSO<sub>4</sub> and evaporated to dryness. The crude product was recrystallized from toluene yielding 69 mg (30 %) of **3.6a**. <sup>1</sup>H NMR (300 MHz, CDCl<sub>3</sub>) δ 7.38 - 7.35 (m, 6H), 7.27 – 7.24 (m, 5H), 6.95 (s, <sup>1</sup>H), 6.86 (s, 4H), 4.09 (q, J<sub>H,H</sub> = 7.1 Hz, 4H), 2.45 (s, 6H), 1.02 (t, J<sub>H,H</sub> = 7.1 Hz, 6H); <sup>13</sup>C NMR (75 MHz, CDCl<sub>3</sub>) δ 163.77, 162.53, 151.28, 148.09, 134.48, 132.04, 130.11, 129.71, 128.99, 128.02, 121.73, 120.50, 109.55, 60.47, 14.67, 13.91; HRMS (APCI positive) calcd for C<sub>35</sub>H<sub>31</sub>BN<sub>2</sub>O<sub>6</sub> [M + H]<sup>+</sup>: 587.2354, found 587.2102.

**Compound 3.6b.** The mixture of aza-BODIPY **3.5b** (100 mg, 0.2 mmol) and dry AlCl<sub>3</sub> (134 mg, 1.0 mmol) was vacuum dried in a Schlenk flask for 30 min. Then the dry DCM (10ml) was added through the septum into the flask and the resulting mixture was stirred for 30 min at room temperature under the argon atmosphere. Then the solution of 1,2-dihydroxybenzene (111 mg, 1.0 mmol) in 10 ml of dry DCM was added through the cannula into the flask. The resulting mixture was stirred for 30 min at room temperature under argon atmosphere. After that time, the reaction mixture was slowly quenched with water and stirred for another 30min. The organic layer was separated and washed with water (3x50ml), saturated brine solution (50 mL), dried over MgSO<sub>4</sub> and evaporated to dryness. The crude product was purified by column chromatography on silica gel using toluene as the solvent yielding 30 mg (26 %) of **3.6b**. <sup>1</sup>H NMR (300 MHz, CDCl<sub>3</sub>) δ 8.10 – 8.07 (m, 2H), 7.51 – 7.44 (m, 6H), 7.33 – 7.30 (m, 4H), 7.08 – 7.03 (m, 2H), 6.96 – 6.91 (m, 4H), 6.86 (s, 2H), 6.33 – 6.28 (m, 2H), 6.07 – 6.01 (m, 2H); <sup>13</sup>C NMR (75 MHz, CDCl<sub>3</sub>) δ 150.31, 132.58, 131.53, 129.74, 129.63, 129.34, 128.72, 128.46, 127.46, 120.16, 118.76; HRMS (APCI positive) calcd for C<sub>38</sub>H<sub>26</sub>BN<sub>3</sub>O<sub>2</sub> [M + H]<sup>+</sup>: 568.2197, found 568.1938.

**Compound 3.6c.** The mixture of BODIPY **3.5c** (100 mg, 0.225 mmol) and dry AlCl<sub>3</sub> (400 mg, 3.0 mmol) was vacuum dried in a Schlenk flask for 30 min. Then the dry DCM (10ml) was added through the septum into the flask and the resulting mixture was stirred for 30 min at room temperature under the argon atmosphere. Then the solution of 1,2-dihydroxybenzene (124 mg, 1.12 mmol) in 10 ml of dry DCM was added through the cannula into the flask. The resulting mixture was stirred for 3 h at room temperature under argon atmosphere. After that time, the reaction mixture was slowly quenched with water and stirred for another 30min. The organic layer

was separated and washed with water (3x50ml), saturated brine solution (50 mL), dried over MgSO<sub>4</sub> and evaporated to dryness. The crude product was purified by column chromatography on silica gel using toluene as the solvent yielding 20 mg (16 %) of **3.6c**. <sup>1</sup>H NMR (300 MHz, CDCl<sub>3</sub>) δ 8.14 – 8.11 (m, 2H), 7.53 – 7.48 (m, 2H), 7.37 – 7.34 (m, 2H), 7.30 – 7.22 (m, 7H), 7.09 – 7.03 (m, 2H), 7.00 – 6.94 (m, 4H), 6.32 – 6.26 (m, 2H), 6.02 – 5.96 (m, 2H); <sup>13</sup>C NMR (75 MHz, CDCl<sub>3</sub>) δ 155.89, 150.06, 139.31, 133.77, 132.14, 130.81, 129.32, 129.16, 127.35, 126.98, 124.04, 121.31, 118.83, 109.35; HRMS (APCI positive) calcd for C<sub>34</sub>H<sub>22</sub>BN<sub>3</sub>O<sub>2</sub> [M + H]<sup>+</sup>: 516.1884, found 516.1694.

**Compounds 3.6d, 3.6e.** The mixture of BOPHY **3.5d** (150 mg, 0.24 mmol) and dry AlCl<sub>3</sub> (133 mg, 0.99 mmol) was vacuum dried in a Schlenk flask for 30 min. Then the dry DCM (10ml) was added through the septum into the flask and the resulting mixture was refluxed for 1 min under the argon atmosphere. Then the solution of 1,2-dihydroxybenzene (109 mg, 0.99 mmol) in 5 ml of dry DCM was added through the cannula into the flask. The resulting mixture was stirred for 1 h at room temperature under argon atmosphere. After that time, the reaction mixture was slowly quenched with water and stirred for another 30min. The organic layer was separated and washed with water (3x20ml), saturated brine solution (20 mL), dried over MgSO<sub>4</sub> and evaporated to dryness. The crude product was chromatographed on silica gel column using DCM as the solvent yielding 20 mg (12 %) of **3.6e** and 35 mg (19 %) of **3.6d**.

**Compound 3.6d:** <sup>1</sup>H NMR (300 MHz, CDCl<sub>3</sub>) δ 7.76 (s, 2H), 7.47 – 7.45 (m, 7H), 7.24 – 7.23 (m, 2H), 6.90 (s, 8H), 4.21 (q, J<sub>H,H</sub> = 7.1 Hz, 4H), 2.56 (s, 6H), 1.15 (t, J<sub>H,H</sub> = 7.1 Hz, 6H); <sup>13</sup>C NMR (75 MHz, CDCl<sub>3</sub>) δ 163.73, 155.01, 149.55, 146.22, 140.73, 131.09, 130.18, 128.88, 128.02, 123.50, 120.89, 119.59, 110.63, 60.47, 14.08, 13.94; HRMS (APCI positive) calcd for C<sub>42</sub>H<sub>36</sub>B<sub>2</sub>N<sub>4</sub>O<sub>8</sub> [M + H]<sup>+</sup>: 747.2806, found 747.2673.

**Compound 3.6e:** <sup>1</sup>H NMR (300 MHz, CDCl<sub>3</sub>) δ 7.95 (s, 1H), 7.67 (s, 1H), 7.53 – 7.51 (m, 3H), 7.42 – 7.42 (m, 5H), 7.20 – 7.18 (m, 2H), 6.85 (s, 4H), 4.22 – 4.12 (m, 4H), 2.81 (s, 3H), 2.53 (s, 3H), 1.16 – 1.06 (, 6H); <sup>13</sup>C NMR (75 MHz, CDCl<sub>3</sub>) δ 163.67, 159.30, 155.29, 149.55, 146.29, 140.86, 140.02, 131.37, 130.97, 130.29, 130.18, 129.19, 128.95, 128.29, 128.03, 120.93, 110.64,

60.49, 14.00, 13.91; HRMS (APCI positive) calcd for  $C_{36}H_{32}B_2F_2N_4O_6$   $[M + H]^+$ : 676.2483, , found 676.2179.

**Compounds 3.7.** The mixture of BODIPY **3.5a** (200 mg, 0.39 mmol) and dry  $AlCl_3$  (152 mg, 1.16 mmol) was vacuum dried in a Schlenk flask for 30 min. Then the dry DCM (10ml) was added through the septum into the flask and the resulting mixture was refluxed for 1 min under the argon atmosphere. Then the solution of 3,4-dihydroxybenzaldehyde (160mg, 1.16mmol) in 10 ml of dry DCM was added through the cannula into the flask. The resulting mixture was stirred for 45 min at room temperature under argon atmosphere. After that time, the reaction mixture was slowly quenched with water and stirred for another 30min. The organic layer was separated and washed with water (3x50ml), saturated brine solution (50 mL), dried over  $MgSO_4$  and evaporated to dryness. The crude product was purified by column chromatography on silica gel using DCM as a solvent yielding 95 mg of **3.7** (40 %) of **2.7a**.  $^1H$  NMR (300 MHz,  $CDCl_3$ )  $\delta$  9.87 (s, 1H), 7.48 (dd,  $J = 7.9$  Hz,  $J = 1.7$  Hz, 1H), 7.41 (d,  $J = 1.7$  Hz, 1H), 7.40 – 7.35 (m, 6H), 7.27 – 7.26 (m, 3H), 6.98 (s, 1H), 6.97 (d,  $J = 7.8$  Hz, 1H), 4.11 (q,  $J = 7.1$  Hz, 4H), 2.41 (s, 6H), 1.02 (t,  $J = 7.1$  Hz, 6H); HRMS (APCI positive) calcd for  $C_{36}H_{31}N_2BO_7$   $[M + H]^+$ : 615.2303, found 615.2471.

## Conclusion

Five ferrocene-BODIPY-fullerene triads were prepared along with a reference fullerene-BODIPY dyad. The ferrocene groups were fully conjugated to the BODIPY  $\pi$ -system and the fullerene acceptors were covalently bound at the boron hub via a catecholpyrrolidine linker. The new compounds were characterized by NMR, UV-Vis, steady-state fluorescence spectroscopy, high-resolution mass spectrometry, and in one case X-ray crystallography. The redox processes were investigated by electrochemical (CV and DPV) methods and spectroelectrochemistry. DFT calculations indicate that the HOMO in all triads is delocalized between the ferrocene and BODIPY  $\pi$ -system, the LUMO is always fullerene-centered, and the catechol-centered occupied orbital is close in energy to the HOMO. TDDFT calculations are indicative of the low-energy, very low intensity BODIPY-to- $C_{60}$  and Fc-to- $C_{60}$  charge-transfer bands. Pump-probe spectroscopy, probed throughout the visible and NIR spectral regions, was used to investigate the photophysical properties and potential for excited state charge transfer. The new triads were compared with reference BODIPY-fullerene and Fc-BODIPY dyads. In the BODIPY-fullerene dyad, rapid 4 ps

deactivation of the BODIPY centered  $\pi^*$ -excited state was mediated by the catecholpyrrolidine linker. Subsequent addition of the ferrocene groups created an initial charge transfer state on the Fc-BODIPY that was not deactivated via the catechol, and had a lifetime of 140-400 ps. The ferrocene fragments extended the absorption to longer wavelengths, produced rapid initial charge separation, and subverted the deleterious rapid loss of electronic energy promoted by the catechol linker. However, further transfer of the charge across the catechol bridge to the fullerene was not observed. The catecholpyrrolidine bridge remained a barrier to charge transfer, failing to provide sufficient coupling to the fullerene to out-compete charge recombination between the ferrocene and BODIPY. In all cases, when exciting the Fc-BODIPY antenna, the excited state dynamics of the Fc-BODIPY-ferrocene triads were essentially unperturbed by the presence of the phenyl-fulleropyrrolidine group.

To investigate the rapid excitation state deactivation of BODIPY-fullerene dyad by catechol linking groups a series of five boron-dipyrrromethane (BODIPY) derived chromophores were prepared and characterized. Following excitation to the optically bright  $\pi^*$  state of the BDP chromophore, sub-ps conversion to an optically dark CT state, characterized by a shift of electron density from the catechol to the BODIPY chromophore, was followed by rapid return to the ground state in all complexes investigated. These systems covered a broad range of synthetic modification within the BODIPY core, indicating some generality of the excited state deactivation dynamics in this class of molecules. These results suggest reports of observed fluorescence in analogous systems may indicate the presence of residual BODIPY-F<sub>2</sub> precursor rather than fluorescence from the BODIPY-catechol complex. Sub-ps initial charge separation and the very short lifetime of the penultimate CT state present a substantial hindrance to successful implementation of the catechol as a linker for attachment of other redox partners for the BODIPY chromophore. This raises significant questions about the previous reports and proposed mechanisms for excited state charge separation in BODIPY-catechol-fullerene triad systems.

Accessible chemistry and stability are part of what makes the catechol an attractive linker for covalent attachment of fullerene electron acceptors. However, in the case of BODIPY based antenna, I have shown that it mediates very rapid excited state deactivation. This can be overcome by addition of an electron donor and initial charge separation that precedes the deactivation mechanism. The catechol linker creates a system with competing interests in the two charge transfer steps that prevent this design from producing efficient, long-lived charge separation.

Strong coupling of the ferrocene donor and BODIPY core is required to facilitate initial charge separation prior to catechol mediated deactivation. However, this coupling also facilitates a modest rate of charge recombination in competition with subsequent charge transfer to the fullerene. To promote a long-lived charge transfer state following electron transfer to the fullerene, i.e. inhibit charge recombination, strong coupling to the fullerene is not desirable. In the absence of strong coupling to the fullerene, electron transfer to the fullerene is unable to compete with charge recombination between the BODIPY and ferrocene.

Since we discovered that the catechol leads to rapid deactivation of the excited state of the BODIPY chromophore with absence of an electron donor such as ferrocene I would recommend that future work be directed toward using a different linking group to attach these ferrocene-BODIPYs and fullerenes. Since we surmise that charge recombination with ferrocene is favored without the presence of stronger coupling between our BODIPY and fullerene potential direction could be toward a linking group that provides stronger coupling between BODIPY and fullerene to promote electron transfer to the BODIPY instead of charge recombination.

In order to accelerate the search for the best donor acceptor pair capable of the low energy photoinduced electron transfer with strong absorption in the visible and near infrared spectrum we decided to explore the third general approach for light harvesting donor acceptors as light harvesting arrays. In this approach we screened a large variety of zinc porphyrin and phthalocyanines as electron donors axially coordinated to the pyridine containing terminal acceptors. Two acceptors were studied; pyridyl fullerene and dipyridyl BODIPY. The later one was chosen because of its prominent photophysical light harvesting properties and the first reduction potential being close to C<sub>60</sub> fullerene.

## References

1. S. Fukuzumi, Y. Yamada, *ChemSusChem* **2013**, *6*, 1834-1847.
2. B. Pashaei, H. Shahroosvand, M. Graetzel, M. K. Nazeeruddin, *Chem. Rev.* **2016**, *116*, 9485-9564.
3. M. Urbani, M. Gratzel, M. K. Nazeeruddin, T. Torres, *Chem. Rev.* **2014**, *114*, 12330-12396.
4. I. Pahk, G. Kodis, G. R. Fleming, T. A. Moore, A. L. Moore, D. Gust, *J. Phys. Chem. B* **2016**, *120*, 10553-10562.
5. S. M. Ryno, M. K. Ravva, X. Chen, H. Li, J.-L. Bredas, *Adv. Energy Mater.* **2017**, *7*, 1601370.
6. X. Chen, C. Li, M. Graetzel, R. Kostecki, S. S. Mao, *Chem. Soc. Rev.* **2012**, *41*, 7909-7937.
7. M. Graetzel, R. A. J. Janssen, D. B. Mitzi, E. H. Sargent, *Nature* **2012**, *488*, 304-312.
8. S. Fukuzumi, K. Ohkubo, T. Suenobu, *Acc. Chem. Res.* **2014**, *47*, 1455-1464.
9. S. Fukuzumi, K. Ohkubo, *Dalton Trans.* **2013**, *42*, 15846-15858.
10. G. Yzambart, A. Zieleniewska, S. Bauroth, T. Clark, M. R. Bryce, D. M. Guldi, *J. Phys. Chem. C* **2017**, *121*, 13557-13569.
11. Y. Kuramochi, Y. Kawakami, A. Satake, *Inorg. Chem.* **2017**, *56*, 11008-11018.
12. A. Arrigo, A. Santoro, M. T. Indelli, M. Natali, F. Scandola, S. Campagna, *Phys. Chem. Chem. Phys.* **2014**, *16*, 818-826.
13. J. A. Hutchison, P. J. Santic, P. R. Brotherhood, C. Scholes, I. M. Blake, K. P. Ghiggino, M. J. Crossley, *J. Phys. Chem. C*, **2009**, *113*, 11796-11804.
14. N. Gupta, C. Sharma, M. Kumar, R. Kumar, *New J. Chem.* **2017**, *41*, 13276-13286.
15. T. A. Reekie, M. Sekita, L. M. Urner, S. Bauroth, L. Ruhlmann, J.-P. Gisselbrecht, C. Boudon, N. Trapp, T. Clark, D. M. Guldi, F. Diederich, *Chem. Eur. J.* **2017**, *23*, 6357-6369.
16. G. de la Torre, G. Bottari, T. Torres, *Adv. Energy Mater.* **2017**, *7*, 1601700.
17. G. Bottari, G. de la Torre, T. Torres, *Acc. Chem. Res.* **2015**, *48*, 900-910.
18. M.-E. Ragoussi, M. Ince, T. Torres, *Eur. J. Org. Chem.* **2013**, *2013*(29), 6475-6489.
19. G. Bottari, O. Trukhina, M. Ince, T. Torres, *Coord. Chem. Rev.* **2012**, *256*, 2453-2477.

20. S. A. Majeed, B. Ghazal, D. E. Nevoenen, P. C. Goff, D. A. Blank, V. N. Nemykin, S. Makhseed, *Inorg. Chem.* **2017**, *56*, 11640-11653.
21. D. Molina, M. E. El-Khouly, M. El-Kemary, S. Fukuzumi, F. Fernandez-Lazaro, A. Sastre-Santos, *Chem. Eur. J.* **2016**, *22*, 17800-17807.
22. S. Yamamoto, A. Zhang, M. J. Stillman, N. Kobayashi, M. Kimura, *Chem. Eur. J.* **2016**, *22*, 18760-18768.
23. M. E. El-Khouly, S. Fukuzumi, *Photochem. Photobiol. Sci.* **2016**, *15*, 1340-1346.
24. H. Yang, S. Pan, D. Ma, D. He, Y. Wang, S. Xie, Y. Peng, *J. Luminescence* **2016**, *179*, 588-594.
25. S. Yamamoto, T. Ikeuchi, S. Mori, M. Kimura, *Asian J. Org. Chem.* **2014**, *3*, 1083-1088.
26. T. Ikeuchi, H. Nomoto, N. Masaki, M. J. Griffith, S. Mori, M. Kimura, *Chem. Commun.* **2014**, *50*, 1941-1943.
27. M. Vengris, D. S. Larsen, L. Valkunas, G. Kodis, C. Herrero, D. Gust, T. Moore, A. Moore, R. van Grondelle, *J. Phys. Chem. B* **2013**, *117*, 11372-11382.
28. Y. Ishida, T. Shimada, S. Takagi, *J. Phys. Chem. C* **2013**, *117*, 9154-9163.
29. M. Kimura, H. Nomoto, H. Suzuki, T. Ikeuchi, H. Matsuzaki, T. N. Murakami, A. Furube, N. Masaki, M. J. Griffith, S. Mori, *Chem. Eur. J.* **2013**, *19*, 7496-7502.
30. I. Sanchez-Molina, B. Grimm, R. M. Krick Calderon, C. G. Claessens, D. M. Guldi, T. Torres, *J. Am. Chem. Soc.* **2013**, *135*, 10503-10511.
31. D. Gonzalez-Rodriguez, E. Carbonell, G. M. Rojas, C. A. Castellanos, D. M. Guldi, T. Torres, *J. Am. Chem. Soc.* **2010**, *132*, 16488-16500.
32. H. M. Rhoda, M. P. Kayser, Y. Wang, A. Y. Nazarenko, R. V. Belosludov, P. Kiprof, D. A. Blank, V. N. Nemykin, *Inorg. Chem.* **2016**, *55*, 9549-9563.
33. D. V. Konarev, S. I. Troyanov, R. N. Lyubovskaya, *CrystEngComm* **2015**, *17*, 3923-3926.
34. I. Sanchez-Molina, M. Ince, G. Bottari, C. G. Claessens, M. V. Martinez-Diaz, T. Torres, *Turk. J. Chem.* **2014**, *38*, 1006-1012.
35. X.-S. Ke, T. Kim, V. M. Lynch, D. Kim, J. L. Sessler, *J. Am. Chem. Soc.* **2017**, *139*, 13950-13956.
36. K. L. Mutolo, E. I. Mayo, B. P. Rand, S. R. Forrest, M. E. Thompson, *J. Am. Chem. Soc.* **2006**, *128*, 8108-8109.

37. D. Credgington, S.-W. Liu, J. Nelson, J. R. Durrant, *J. Phys. Chem. C* **2014**, *118*, 22858-22864.
38. D. S. Josey, S. R. Nyikos, R. K. Garner, A. Dovijarski, J. S. Castrucci, J. M. Wang, G. J. Evans, T. P. Bender, *ACS Energy Lett.* **2017**, *2*, 726-732.
39. C. Duan, G. Zango, M. Garcia Iglesias, F. J. M. Colberts, M. M. Wienk, M. V. Martinez-Diaz, R. A. J. Janssen, T. Torres, *Angew. Chem., Int. Ed.* **2017**, *56*, 148-152.
40. J. S. Castrucci, D. S. Josey, E. Thibau, Z.-H. Lu, T. P. Bender, *J. Phys. Chem. Lett.* **2015**, *6*, 3121-3125.
41. D. E. Wilcox, M. H. Lee, M. E. Sykes, A. Niedringhaus, E. Geva, B. D. Dunietz, M. Shtein, J. P. Ogilvie, *J. Phys. Chem. Lett.* **2015**, *6*, 569-575.
42. Sanchez-Molina, C. G. Claessens, B. Grimm, D. M. Guldi, T. Torres, *Chem. Sci.* **2013**, *4*, 1338-1344.
43. R. S. Iglesias, C. G. Claessens, T. Torres, G. M. A. Rahman, D. M. Guldi, *Chem. Commun.* **2005**, 2113-2115.
44. S. Shimizu, S. Nakano, T. Hosoya, N. Kobayashi, *Chem. Commun.* **2011**, *47*, 316-318.  
C. B. KC, G. N. Lim, F. D'Souza, *Chem. Asian. J.* **2016**, *11*, 1246-1256.
45. D. B. Sulas, E. J. Rabe, C. W. Schlenker, *J. Phys. Chem. C* **2017**, *121*, 26667-26676.
46. J. Fernandez-Ariza, R. M. Krick Calderon, J. Perles, M. S. Rodriguez-Morgade, D. M. Guldi, T. Torres, *Chem. Commun.* **2017**, *53*, 8525-8528.
47. K. A. Winterfeld, G. Lavarda, J. Guilleme, M. Sekita, D. M. Guldi, T. Torres, G. Bottari *J. Am. Chem. Soc.* **2017**, *139*, 5520-5529.
48. D. Gao, S. M. Aly, P.-L. Karsenti, G. Brisard, P. D. Harvey, *Dalton Trans.* **2017**, *46*, 6278-6290.
49. A. Cabrera-Espinoza, B. Insuasty, A. Ortiz, *New J. Chem.* **2017**, *41*, 9061-9069.
50. I. Bulut, Q. Huaulme, A. Mirloup, P. Chavez, S. Fall, A. Hebraud, S. Mery, B. Heinrich, T. Heiser, P. Leveque, N. Leclerc, *ChemSusChem* **2017**, *10*, 1878-1882.
51. S. A. Berhe, M. T. Rodriguez, E. Park, V. N. Nesterov, H. Pan, W. J. Youngblood, *Inorg. Chem.* **2014**, *53*, 2346-2348.
52. W.-J. Shi, P.-C. Loc, D. K. P. Ng, *Dyes and Pigments.* **2018**, *154*, 314-319.
53. P. Gautam, R. Misra, M. B. Thomas, F. D'Souza F. *Chem. Eur. J.* **2017**, *23*, 9192-9200.

54. T. Li, T. Meyer, R. Meerheim, M. Hoepfner, C. Koerner, K. Vandewal, O. Zeika, K. Leo, *J. Mater. Chem. A* **2017**, *5*, 10696-10703.
55. M. E. El-Khouly, A. N. Amin, M. E. Zandler, S. Fukuzumi, F. D'Souza, *Chem. Eur. J.* **2012**, *18*, 5239-5247.
56. L. Wang, I.-S. Tamgho, L. A. Crandall, J. J. Rack, C. J. Ziegler, *Phys. Chem. Chem. Phys.* **2015**, *17*, 2349-2351.
57. I.-S. Tamgho, A. Hasheminasab, J. T. Engle, V. N. Nemykin, C. J. Ziegler, *J. Am. Chem. Soc.* **2014**, *136*, 5623-5626.
58. S. Boodts, J. Hofkens, W. Dehaen, *Dyes Pigments* **2017**, *142*, 249-254.
59. F. Meng, Y. Sheng, F. Li, C. Zhu, Y. Quan, Y. Cheng, *RSC Adv.* **2017**, *7*, 15851-15856.
60. J. Wang, Q. Wu, C. Yu, Y. Wei, X. Mu, E. Hao, L. Jiao, *J. Org. Chem.* **2016**, *81*, 11316-11323.
61. L. Zhou, D. Xu, H. Gao, C. Zhang, F. Ni, W. Zhao, D. Cheng, X. Liu, A. Han, *J. Org. Chem.* **2016**, *81*, 7439-7447.
62. C. Zhang, J. Zhao, *J. Mater. Chem. C* **2016**, *4*, 1623-1632.
63. A. Mirloup, Q. Huaulme, N. Leclerc, P. Leveque, T. Heiser, P. Retailleau, R. Ziessel, *Chem. Commun.* **2015**, *51*, 14742-14745.
64. Q. Huaulme, A. Mirloup, P. Retailleau, R. Ziessel, *Org. Lett.* **2015**, *17*, 2246-2249.
65. X.-D. Jiang, Y. Su, S. Yue, C. Li, H. Yu, H. Zhang, C.-L. Sun, L.-J. Xiao, *RSC Adv.* **2015**, *5*, 16735-16739.
66. A. Antoniuk-Pablant, G. Kodis, A. L. Moore, T. A. Moore, D. Gust, *J. Phys. Chem. B* **2016**, *120*, 6687-6697.
67. L. Kavan, J.-H. Yum, M. Graetzel, *Phys. Status Solidi B: Basic Solid State Physics* **2013**, *250*, 2643-2648.
68. L. Kavan, J.-H. Yum, M. Graetzel, *Electrochim. Acta* **2014**, *128*, 349-359. d) S. Cook, R. Katoh, A. Furube, *J. Phys. Chem. C*, **2009**, *113*, 2547-2552.
69. A. Cidlina, M. Miletin, M. Fathi-Rasekh, V. N. Nemykin, P. Zimcik, V. Novakova, *Chem. Eur. J.* **2017**, *23*, 1795-1804.
70. M. Maiuri, J. J. Snellenburg, I. H. M. van Stokkum, S. Pillai, K. WongCarter, D. Gust, T. A. Moore, A. L. Moore, R. van Grondelle, G. Cerullo, D. Polli, *J. Phys. Chem. B* **2013**, *117*, 14183-14190.

71. G. de la Torre, G. Bottari, M. Sekita, A. Hausmann, D. M. Guldi, T. Torres, *Chem. Soc. Rev.* **2013**, *42*, 8049-8105.
72. M.-E. Ragoussi, M. Ince, T. Torres, *Eur. J. Org. Chem.* **2013**, *2013*, 6475-6489.
73. M. Kloz, S. Pillai, G. Kodis, D. Gust, T. A. Moore, A. L. Moore, R. van Grondelle, J. T. M. Kennis, *Chem. Sci.* **2012**, *3*, 2052-2061.
74. C. Romero-Nieto, J. Guilleme, J. Fernandez-Ariza, M. S. Rodriguez-Morgade, D. Gonzalez-Rodriguez, T. Torres, D. M. Guldi, *Org. Lett.* **2012**, *14*, 5656-5659.
75. E. Lager, J. Liu, A. Aguilar-Aguilar, B. Z. Tang, E. Pena-Cabrera, *J. Org. Chem.* **2009**, *74*, 2053-2058.
76. P. Verwilt, H.-R. Kim, J. Seo, N.-W. Sohn, S.-Y.; Cha, Y. Kim, S. Maeng, J.-W. Shin, J. H. Kwak, C. Kang, J. S. Kim, *J. Am. Chem. Soc.* **2017**, *139*, 13393-13403.
77. Z. Biyiklioglu, T. Keles, *Inorg. Chim. Acta* **2017**, *466*, 130-138.
78. K. B. Petrushenko, I. K. Petrushenko, O. V. Petrova, L. N. Sobenina, B. A. Trofimov, *Dyes Pigments* **2017**, *136*, 488-495.
79. Y. Gawale, N. Adarsh, S. K. Kalva, J. Joseph, M. Pramanik, D. Ramaiah, N. Sekar, *Chem. Eur. J.* **2017**, *23*, 6570-6578.
80. V. N. Nemykin, T. S. Blesener, C. J. Ziegler, *Macroheterocycles*, **2017**, *10*, 9-26.
81. B. A. Hussein, J. T. Huynh, P. L. Prieto, C. P. Barran, A. E. Arnold, O. V. Sarycheva, A. J. Lough, B. D. Koivisto, *Dalton Trans.*, **2018**, *47*, 4916-4920.
82. A. Vecchi, N. R. Erickson, J. R. Sabin, B. Floris, V. Conte, M. Venanzi, P. Galloni, V. N. Nemykin, *Chem. Eur. J.* **2015**, *21*, 269-279.
83. D. Sirbu, C. Turta, A. C. Benniston, F. Abou-Chahine, H. Lemmetyinen, N. V. Tkachenko, C. Wood, E. Gibson, *RSC Adv.* **2014**, *4*, 22733-22742.
84. P. Galloni, B. Floris, L. De Cola, E. Cecchetto, R. M. Williams, *J. Phys. Chem. C* **2007**, *111*, 1517-1523.
85. A. Vecchi, P. Galloni, B. Floris, S. V. Dudkin, V. N. Nemykin, *Coord. Chem. Rev.* **2015**, *291*, 95-171.
86. S. J. Dammer, P. V. Solntsev, J. R. Sabin, V. N. Nemykin, *Inorg. Chem.* **2013**, *52*, 9496-9510.
87. A. Vecchi, P. Galloni, B. Floris, V. N. Nemykin, *J. Porphyrins Phthalocyanines* **2013**, *17*, 165-196.
88. S. Ragab, S. Swaminathan, E. Deniz, B. Captain, F. M. Raymo, *Org. Lett.* **2013**, *15*, 3154-3157.
89. C. O. Obondi, G. N. Lim, P. Martinez, V. Swamy, F. D'Souza, *Nanoscale*, **2017**, *9*, 18054-18065.

90. A. Cabrera-Espinoza, B. Insuasty, A. Ortiz, *New J. Chem.* **2017**, *41*, 9061-9069.
91. C. A. Wijesinghe, M. E. El-Khouly, N. K. Subbaiyan, M. Supur, M. E. Zandler, K. Ohkubo, S. Fukuzumi, F. D'Souza, *Chem. Eur. J.* **2011**, *17*, 3147-3156.
92. Y. V. Zatsikha, E. Maligaspe, A. A. Purchel, N. O. Didukh, Y. Wang, Y. P. Kovtun, D. A. Blank, V. N. Nemykin, *Inorg. Chem.* **2015**, *54*, 7915-7928.
93. Y. V. Zatsikha, N. O. Didukh, T. Blesener, M. P. Kayser, Y. P. Kovtun, D. A. Blank, V. N. Nemykin, *Eur. J. Inorg. Chem.* **2017**, *2017*, 318-324.
94. N. O. Didukh, Y. V. Zatsikha, G. T. Rohde, T. S. Blesener, V. P. Yakubovskiy, Y. P. Kovtun, V. N. Nemykin, *Chem. Commun.* **2016**, *52*, 11563-11566.
95. Y. V. Zatsikha, N. O. Didukh, D. Nemez, A. C. Schlachter, P.-L. Karsenti, Y. P. Kovtun, P. D. Harvey, V. N. Nemykin, *Chem. Commun.* **2017**, *53*, 7612-7615.
96. E. Maligaspe, T. J. Pundsack, L. M. Albert, Y. V. Zatsikha, P. V. Solntsev, D. A. Blank, V. N. Nemykin, *Inorg. Chem.* **2015**, *54*, 4167-4174.
97. C. J. Ziegler, K. Chanawanno, A. Hasheminsasab, Y. V. Zatsikha, E. Maligaspe, V. N. Nemykin, *Inorg. Chem.* **2014**, *53*, 4751-4755.
98. Y. V. Zatsikha, C. D. Holstrom, K. Chanawanno, A. J. Osinski, C. J. Ziegler, V. N. Nemykin, *Inorg. Chem.* **2017**, *56*, 991-1000.
99. Y. V. Zatsikha, T. S. Blesener, P. C. Goff, A. T. Healy, R. K. Swedin, D. E. Herbert, G. T. Rohde, K. Chanawanno, C. J. Ziegler, R. V. Belosludov, D. A. Blank, V. N. Nemykin, *J. Phys. Chem. C* **2018**, *122*, 27893-27916.
100. H. M. Rhoda, K. Chanawanno, A. J. King, Y. V. Zatsikha, C. J. Ziegler, V. N. Nemykin, *Chem. Eur. J.* **2015**, *21*, 18043-18046.
101. Y. V. Zatsikha, D. B. Nemez, R. L. Davis, S. Singh, D. E. Herbert, A. J. King, C. J. Ziegler, V. N. Nemykin, *Chem. Eur. J.* **2017**, *23*, 14786-14796.
102. C. A. Wijesinghe, M. E. El-Khouly, J. D. Blakemore, M. E. Zandler, S. Fukuzumi, F. D'Souza, *Chem. Commun.* **2010**, *46*, 3301-3303.
103. C. A. Wijesinghe, M. E. El-Khouly, N. K. Subbaiyan, M. Supur, M. E. Zandler, K. Ohkubo, S. Fukuzumi, F. D'Souza, *Chem. Eur. J.* **2011**, *17*, 3147-3156.
104. V. Bandi, H. B. Gobeze, F. D'Souza, *Chem. Eur. J.* **2015**, *21*, 11483-11494.
105. V. Bandi, S. K. Das, S. G. Awuah, Y. You, F. D'Souza, *J. Am. Chem. Soc.* **2014**, *136*, 7571-7574.
106. R. Cantu, S. Seetharaman, E. M. Babin, P. A. Karr, F. D'Souza, *J. Phys. Chem. A*, **2018**, *122*, 3780-3786.

107. M. Prato, M. Maggini, C. Giacometti, G. Scorrano, G. Sandona, G. Farnia, *Tetrahedron*, **1996**, *52*, 5221-5234.
108. K. G. Thomas, V. Biju, M. V. George, D. M. Guldi, P. V. Kamat, *J. Phys. Chem. A* **1998**, *102*, 5341-5348.
109. R. K. Swedin, Y. V. Zatsikha, A. T. Healy, N. O. Didukh, T. S. Blesener, M. Fathi-Rasekh, T. Wang, A. J. King, V. N. Nemykin, D. A. Blank, *J. Phys. Chem. Lett.* **2019**, *10*, 1828-1832.
110. C. Tahtaoui, C. Thomas, F. Rohmer, P. Klotz, G. Duportail, Y. Mely, D. Bonnet, M. Hibert, *J. Org. Chem.* **2007**, *72*, 269-272.
111. H. Oevering, M. N. Paddon-Row, M. Heppener, A. M. Oliver, E. Cotsaris, J. W. Verhoeven, N. S. Hush, *J. Am. Chem. Soc.* **1987**, *109*, 3258-3269.
112. A. Weller, *Z. Phys. Chem.* **1982**, *133*, 93-98.
113. D. Rehm, A. Weller, *Isr. J. Chem.* **1970**, *8*, 259-271.
114. J. Kroon, J. W. Verhoeven, M. N. Paddon-Row, A. M. Oliver, *Angew. Chem.* **1991**, *30*, 1358-1361.
115. M. P. Shandura, V. P. Yakubovskiy, Y. P. Kovtun, *J. Heterocyclic Chem.*, **2009**, *46*, 1386-1391.
116. Cramer, C. J. *Essentials of Computational Chemistry: Theories and Models*, 2nd ed.; John Wiley and Sons, **2004**.
117. Kirkwood, J. G. *Theory of Solutions of Molecules Containing Widely Separated Charges with Special Application to Zwitterions*. *J. Chem. Phys.* **1934**, *2*, 351-361.
118. Onsager, L. *Electric Moments of Molecules in Liquids*. *J. Am. Chem. Soc.* **1936**, *58*, 1486-1493.
119. A. D. Becke, *J. Chem. Phys.* **1993**, *98*, 5648-5652.
120. G. Scalmani, M. J. Frisch, B. Mennucci, J. Tomasi, R. Cammi, V. Barone, *J. Chem. Phys.* **2006**, *124*, 094107: 1-15.
121. A. J. H. Wachters, *J. Chem. Phys.* **1970**, *52*, 1033-1036.
122. A. D. McLean, G. S. Chandler, *J. Chem. Phys.* **1980**, *72*, 5639-5648.
123. G09 Gaussian 09, Revision D.1, M. J. Frisch, G. W. Trucks, H. B. Schlegel, G. E. Scuseria, et al Gaussian, Inc., Wallingford CT, **2009**.
124. A. L. Tenderholt, QMForge, Version 2.1. Stanford University, Stanford, CA, USA.  
<http://qmforge.sourceforge.net/>
125. R. H. Blessing, *Acta Crystallogr., Sect A* **1995**, *51*, 33-38.

126. A. Altomare, G. Cascarano, G. Giacobazzo, A. Guagliardi, M. C. Burla, G. Polidori, M. Camalli, *J. Appl. Cryst.* **1994**, *27*, 435-436.
127. P. W. Betteridge, J. R. Carruthers, R. I. Cooper, K. Prout, D. J. Watkin, *J. Appl. Cryst.* **2003**, *36*, 1487.

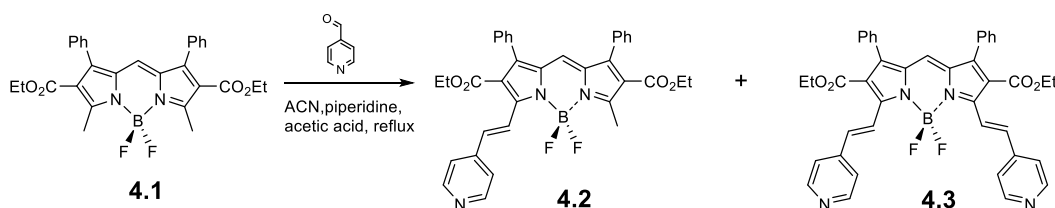
## Chapter 4

# Pyridine-BODIPY a New Type of Non-Fullerene Acceptor for Coordination to Metal Center of Porphyrins and Phthalocyanines

### Introduction

Organic solar cells based on bulk heterojunction active layers designed to create charge separated states with polymers or small molecule electron donors and fullerene acceptors have been studied extensively.<sup>1-9</sup> These compounds typically contain electron-donating chromophores such as porphyrins, phthalocyanines, and ruthenium-(II)-tris(bipyridine) with fullerene as electron acceptors.<sup>10-14</sup> Fullerenes drew special attention as electron acceptors due to their three-dimensional structure, reduction potentials, absorption spectrum range, and small re-organization energy in electron-transfer processes. Covalent attachment of fullerene acceptor to electron donor has been a widely used strategy to form long-lived charge-separated states<sup>15-18</sup> however, self-assembled donor-acceptor conjugates may be the preferred method of formation for these systems as it is most similar to natural photoenergy conversion systems. The benefits of a self-assembling system is self-organization as well as efficient self-repairing assembling-disassembling processes.<sup>19</sup> Self-assembling molecules are formed via weak interactions such as hydrogen bonding,  $\pi$ - $\pi$  interactions or metal coordination. Since  $\pi$ - $\pi$  interactions for donor-acceptor self-assembling systems were previously investigated in chapter 2 using pyrene ligands to promote  $\pi$ - $\pi$  stacking to carbon nanotubes, in this chapter I investigated coordination chemistry in order to determine the effectiveness of metal coordination at forming self-assembling donor-acceptor molecules for generation of charge separated states. A common method for self-assembling fullerene acceptors with electron donors like porphyrin and phthalocyanines is through axial coordination chemistry at the metal center. Coordination can be done through functionalization of the fullerene to contain nitrogenous ligands such as imidazole or pyridine.<sup>20-23</sup> Many different forms of supramolecular complexes have been designed in this way with formation of dyad and triad complexes.<sup>30,31</sup> However due to fullerene's intrinsic drawbacks such as low absorptivity, low solubility, and limited structural modification it has led to lower than required power conversion efficiencies. This has led to development of new non-fullerene small molecule based electron acceptors.<sup>24</sup> Promising candidate chromophores for use as non-fullerene acceptors are BODIPY

and aza-BODIPY due to their excellent absorption and emission properties as well as their capability for structural modifications.<sup>25</sup> BODIPY<sup>26,27</sup> and aza-BODIPY<sup>28,29</sup> compounds have already shown great promise as electron donors and with the correct modifications have also become low-band gap acceptors. In order to mimic this self-assembling process from fullerene complexes we designed a pyridine-BODIPY with two pyridine units substituted at the  $\alpha$ -position of the BODIPY in order to promote coordination to the metal center of a series of electron-donating zinc porphyrins and phthalocyanines (Scheme 4.1). This will hopefully lead to the formation of supramolecular dyads and triads through coordination at the metal center of the porphyrin and phthalocyanine donors (Figure 4.2). Two reference pyridine and phenyl substituted fullerene acceptors (Figure 4.1) were also used to compare with the electron transfer process of the target BODIPY. After initial coordination experiments were completed, another series of electron donor porphyrins were tested to determine if there was a trend for increased coordination of the pyridine group to the metal center of porphyrins and phthalocyanines. A series of cyanated octaethylporphyrins (Figure 4.3) prepared at our collaborator Brueckner's lab were tested to determine if drawing electron density away from the metal center would enhance coordination to the metal center similar to what we observed in previous experiments. Here we present the synthesis, electrochemical and photophysical characterization of the BODIPY-pyridine compounds.



Scheme 4.1: Synthetic pathway for preparation of BODIPY-pyridine compounds

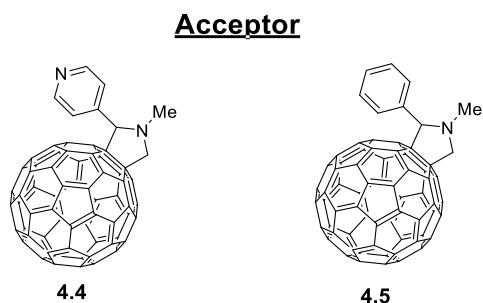


Figure 4.1: Reference compounds fulleropyrrolidine **4.4** and **4.5**

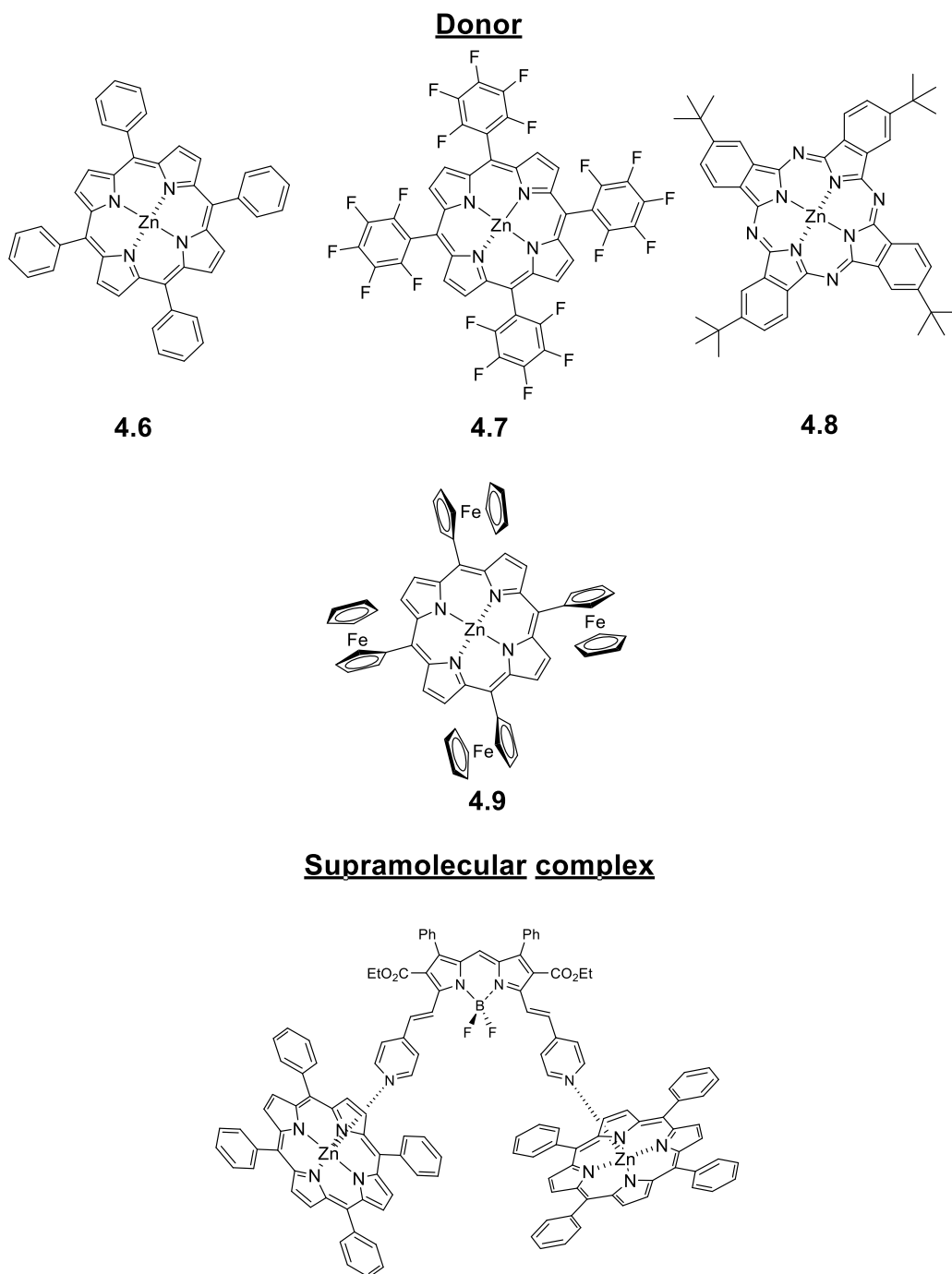


Figure 4.2: (Top) Electron donor porphyrins and phthalocyanine: zinc tetraphenylporphyrin **4.6** fluorinated zinc tetraphenylporphyrin **4.7**, tetra-tert-butyl zinc phthalocyanine **4.8**, and meso-tetraferrocenyl porphyrin **4.9**. (Bottom) Example of potential supramolecular complex with compound **4.3**.

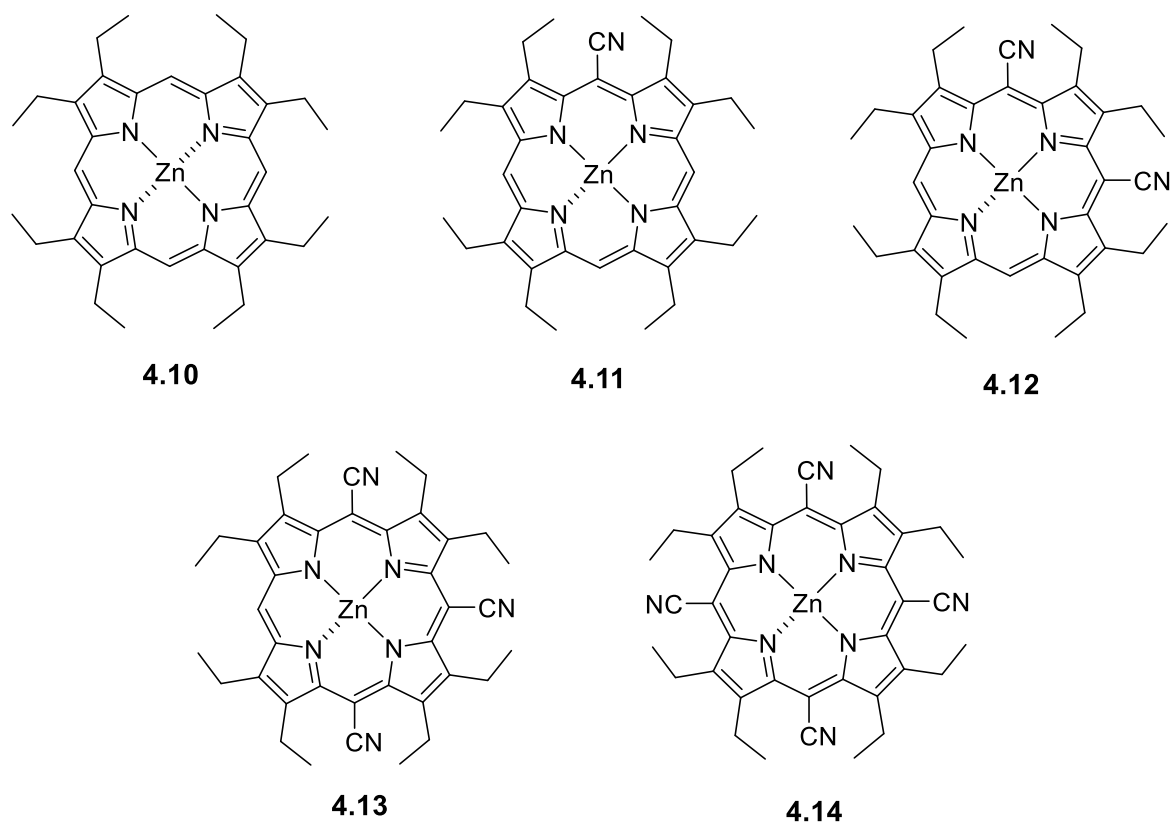


Figure 4.3: Electron donors zinc octaethylporphyrin **4.10**, monocyano zinc octaethylporphyrin **4.11**, dicyano zinc octaethylporphyrin **4.12**, tricyano zinc octaethylporphyrin **4.13**, and tetracyano zinc octaethylporphyrin **4.14**.<sup>33</sup>

### Synthesis and Characterization of Pyridine-BODIPY

Starting from previously reported BODIPY complex **4.1**<sup>32</sup> the synthesis of compounds **4.2** and **4.3** was achieved by a standard Knoevenagel condensation of 3,5-dimethylborondipyrromethane and two moles of 4-pyridylcarboxaldehyde in dry acetonitrile using piperidinium acetate as a catalyst as indicated in Scheme 4.1. The yield of monopyridine-BODIPY for this reaction after purification is very low due to favoring the formation of dipyrindine-BODIPY complex so no experiments were conducted on it. Compound **4.3** was characterized by <sup>1</sup>H and <sup>13</sup>C NMR spectroscopy, high-resolution mass spectrometry, UV-vis, and fluorescence spectroscopy.

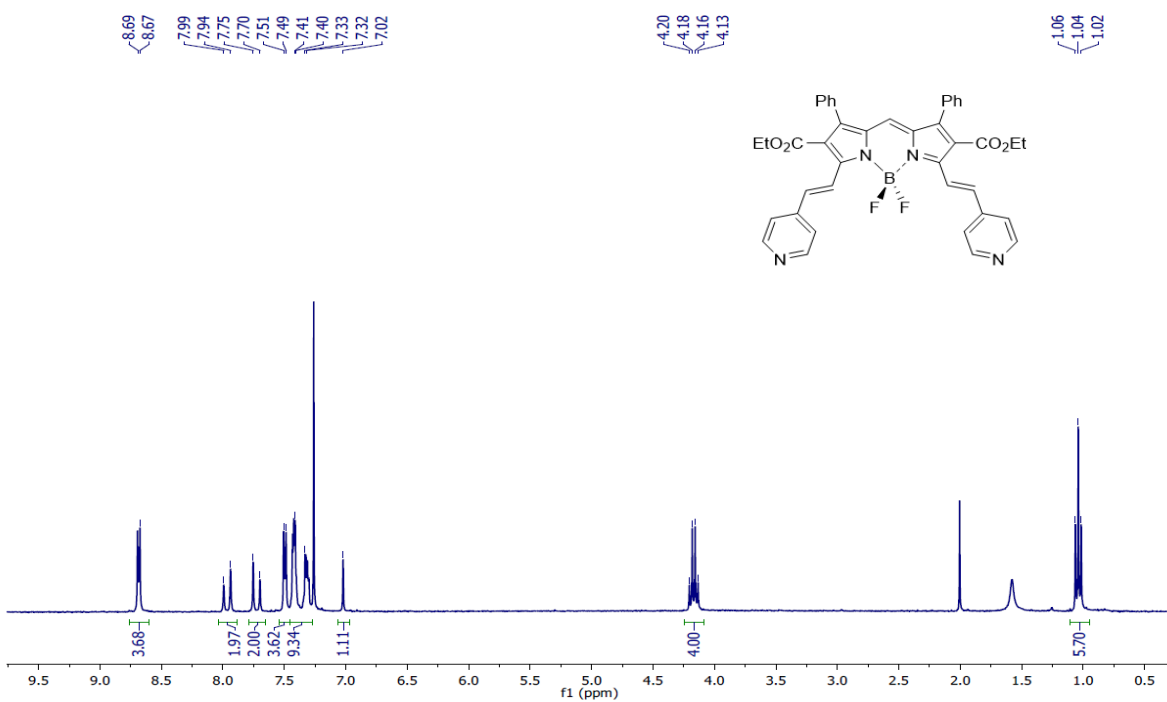


Figure 4.4: <sup>1</sup>H NMR spectrum of compound **4.3** CDCl<sub>3</sub>.

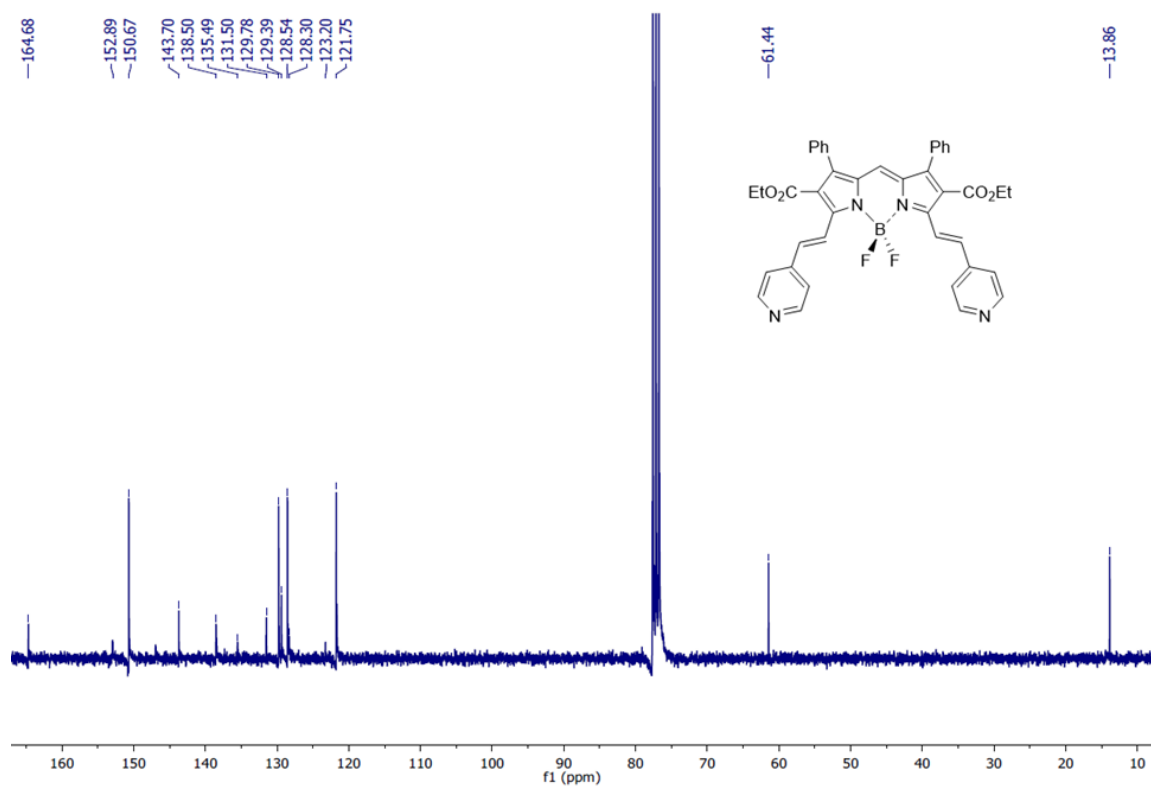


Figure 4.5: <sup>13</sup>C NMR spectrum of compound **4.3** CDCl<sub>3</sub>.

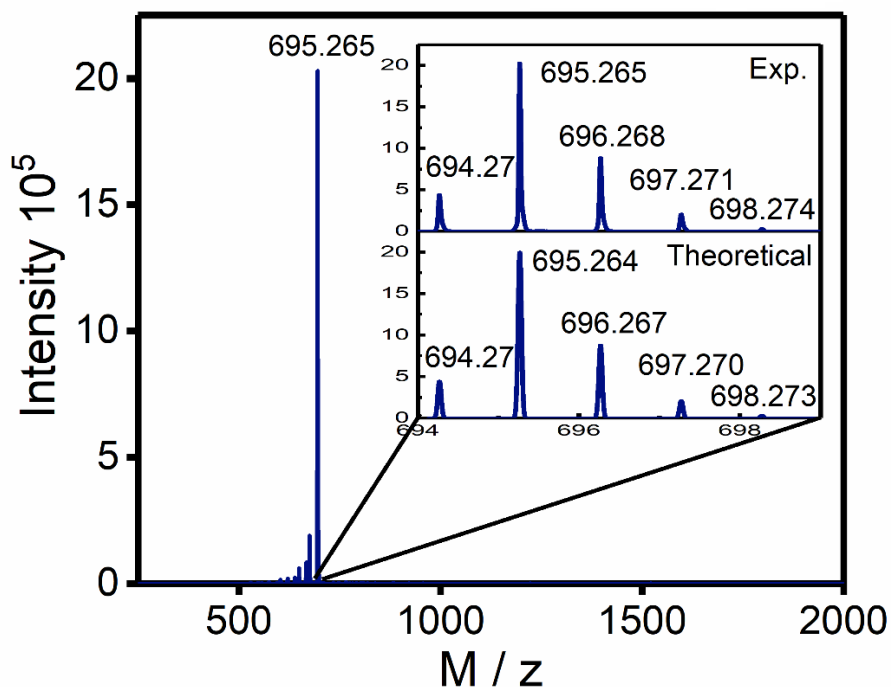


Figure 4.6: HRMS spectrum of compound **4.3**.

The UV-vis spectrum of **4.3** is presented in Figure 4.7 and consists of two distinct peaks. The single narrow band at 343 nm is associated with the pyridine fragments while the lower energy band at 615 nm corresponds to the typical BODIPY absorption. The absorption spectra of our electron donors from the first series of experiments can be seen in Figure 4.8 and consist of typical porphyrin and phthalocyanine absorption spectrum. Porphyrin complexes all have an intense Soret band at higher energy wavelengths and a series of low intensity Q-bands at lower energy wavelengths while the phthalocyanine has a series of low intensity bands at higher energy and an intense band at lower wavelengths. The absorption spectrum for compounds **4.10-4.14** can be seen in Figure 4.9 and consist of typical zinc octaethylporphyrin absorption that experiences a red shift upon each addition of a cyano group to the porphyrin.

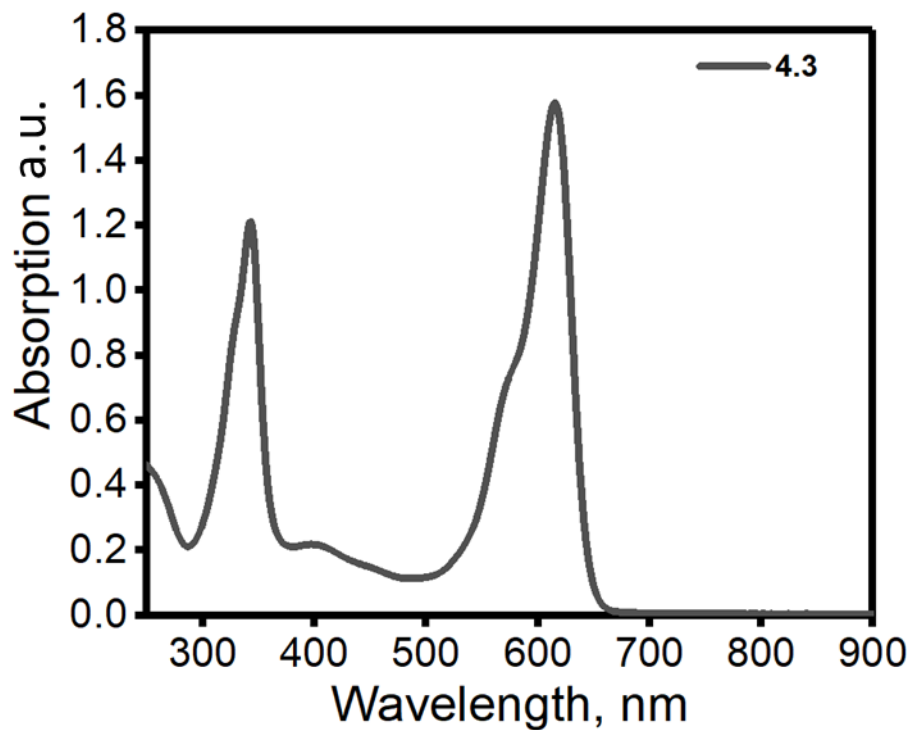


Figure 4.7: UV-Vis spectrum of compound 4.3 in DCM.

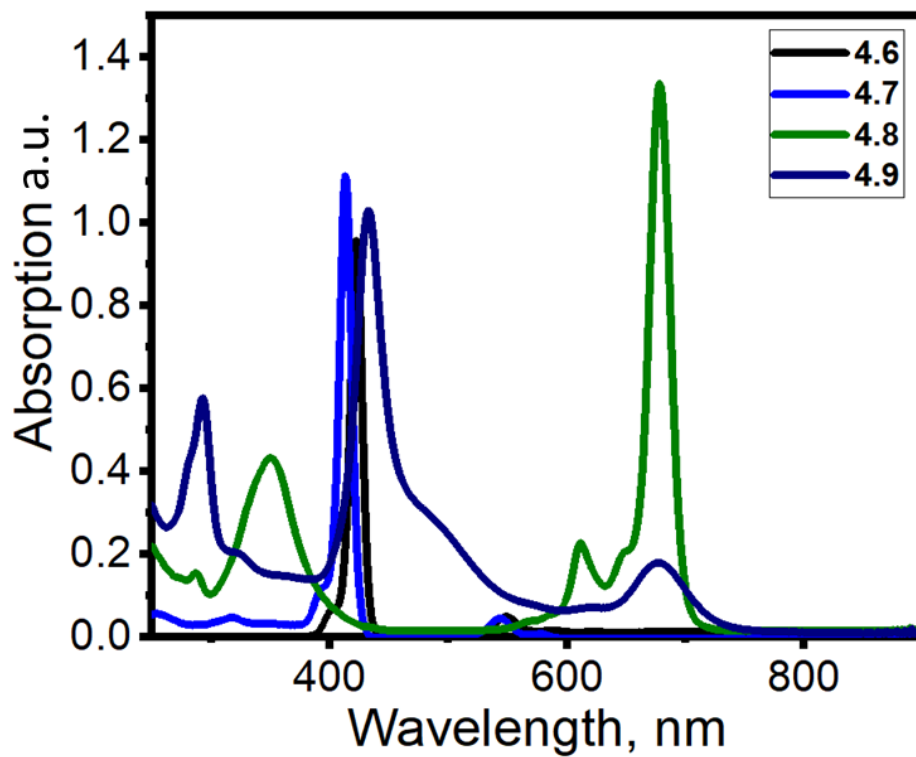


Figure 4.8: UV-Vis spectrum of 4.6, 4.7, 4.8, and 4.9 in DCM.

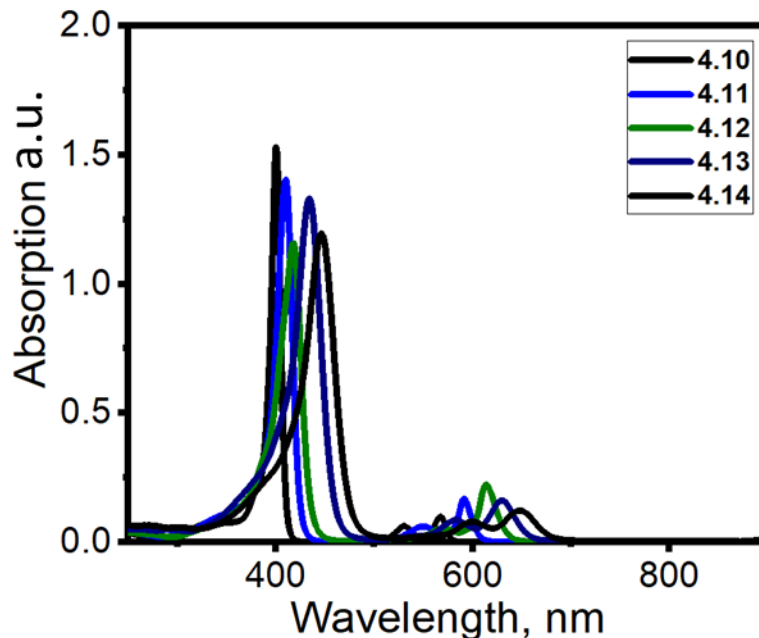


Figure 4.9: UV-Vis spectrum of **4.10**, **4.11**, **4.12**, **4.13**, and **4.14** in DCM.

Steady-state fluorescence spectrum for compound **4.3** is shown in Figure 4.10. The fluorescence spectrum shows typical Stokes shifts of  $\sim 20$  nm. The electron donor's fluorescence spectrum can be seen in Figures 4.11 and 4.12. The fluorescence of the electron acceptor has a partially overlapping fluorescence spectrum with some of the electron donors resulting in complications when testing for coordination using spectroscopy.

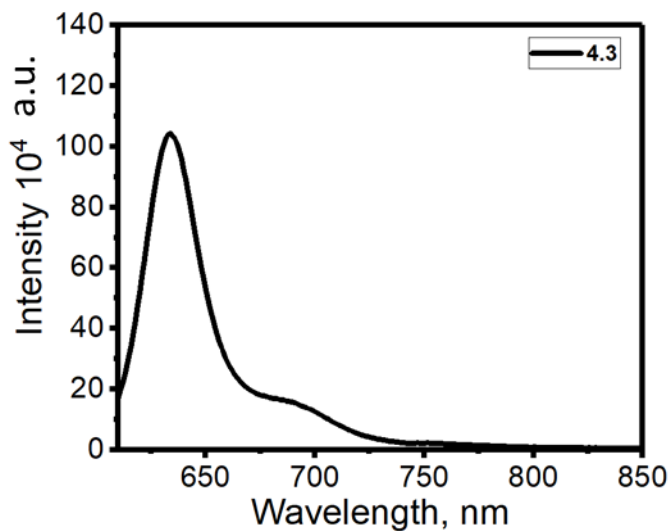


Figure 4.10: Fluorescence spectrum of compound **4.3** at an excitation wavelength of 605 nm in DCM.

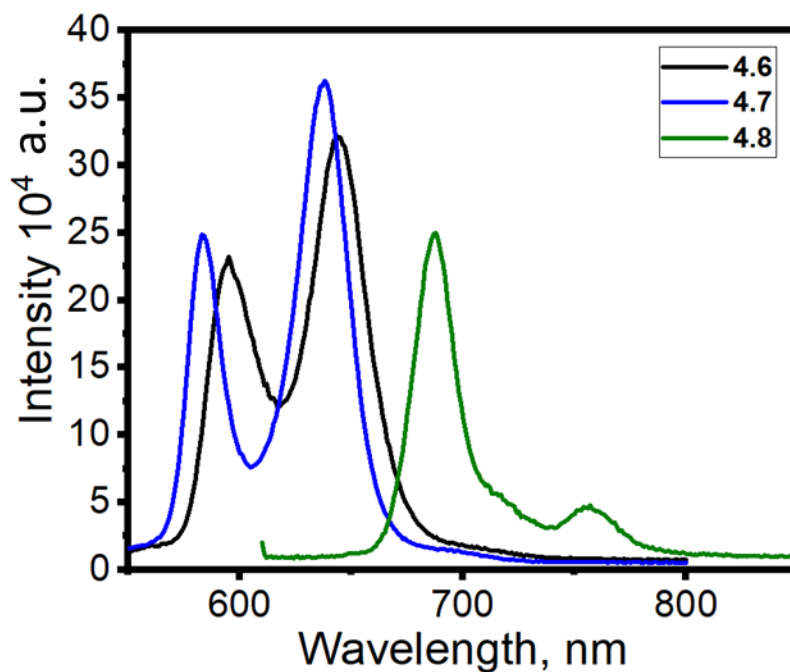


Figure 4.11: Fluorescence spectrum of compounds **4.6** - **4.8** in DCM. Excitation wavelengths are: 420 nm (**4.6**), 540 nm (**4.7**), and 610 nm (**4.8**).

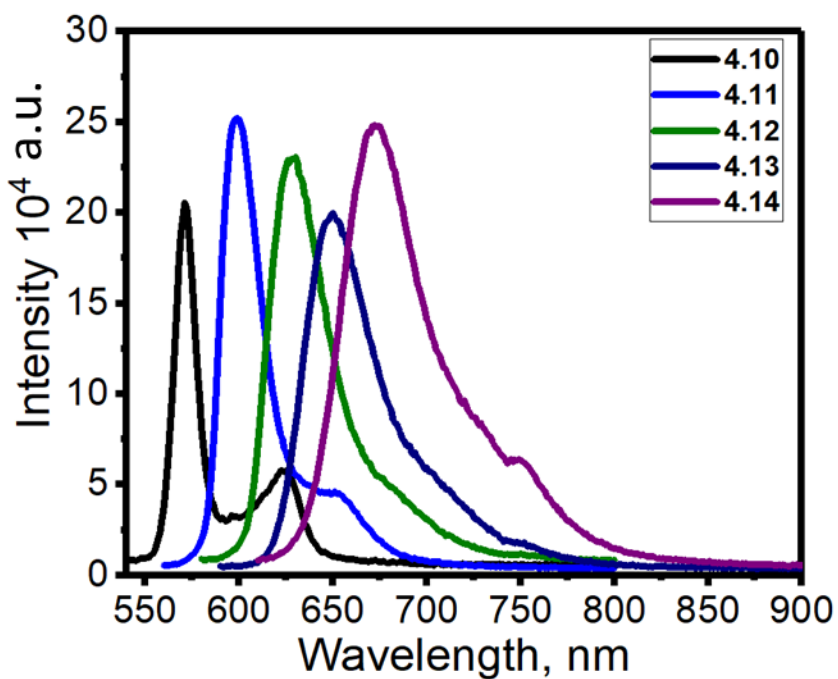


Figure 4.12: Fluorescence spectrum of zinc octaethylporphyrins **4.10** - **4.14** in DCM. Excitation wavelengths are: 530 nm (**4.10**), 550 nm (**4.11**), 570 nm (**4.12**), 580 nm (**4.13**), and 600 nm (**4.14**).

Table 4.1. Selected photophysical properties of acceptor compounds **4.3** – **4.5** and donor porphyrins and phthalocyanines **4.6** – **4.14**.

Compound	$\lambda_{\text{abs}}$ [nm] ( $\epsilon$ [ $\text{M}^{-1}\text{cm}^{-1}$ ])	Emission [nm] ( $\Phi$ )	$\tau$ [ns]
<b>4.3</b>	343 (59313), 615 (76767)	633	
<b>4.6</b>	422 (574000), 512 (3300), 548 (24000), 589 (4200)	594, 644	2.0
<b>4.7</b>	417 (552000), 585 (25100)	583, 638	1.4
<b>4.8</b>	349 (57500), 610 (30200), 648 (25700), 678 (199500)	692, 755	$13 \pm 2$
<b>4.9</b>	320 (34200), 435 (142800), 681 (31500)		
<b>4.10</b>	400, 530, 567	571, 625	
<b>4.11</b>	410 (305,899), 550 (11,115), 590 (35,681)	599	
<b>4.12</b>	418 (150,821), 570 (7,522), 613 (28,863)	628	
<b>4.13</b>	434 (86,393), 583 (5,335), 630 (10,383)	650	
<b>4.14</b>	445 (93,709), 600 (5,953), 647 (9,693)	672	

The redox properties of BODIPY **4.3** were investigated by both cyclic voltammetry (CV) and differential pulse voltammetry (DPV) electrochemical methods. The data is summarized in Table 4.2 and shown in Figure 4.13. In the case of BODIPY compound **4.3** it shows two reduction processes associated with the BODIPY core. The first reduction process is quasi-reversible while the second is irreversible. Electrochemistry was also ran on a solution of **4.3** and **4.8** which resulted in a slight shift of the reduction potential for both the BODIPY and pthalocyanine to higher potentials and the oxidation of the pthalocyanine to shift to slightly lower potential (Figure 4.14).

Table 4.2. Electrochemical data on acceptors and donor

Compound	$E^1_{\text{Ox}}(\text{V})$	$E^1_{\text{Red}}(\text{V})$	$E^2_{\text{Red}}(\text{V})$
<b>4.3</b>		-0.89	-1.72*
<b>4.8</b>	0.011	-1.6	
<b>4.4</b>	1.19	-1.17	-1.53
<b>4.8+4.3</b>	0.16	-0.94	-1.86

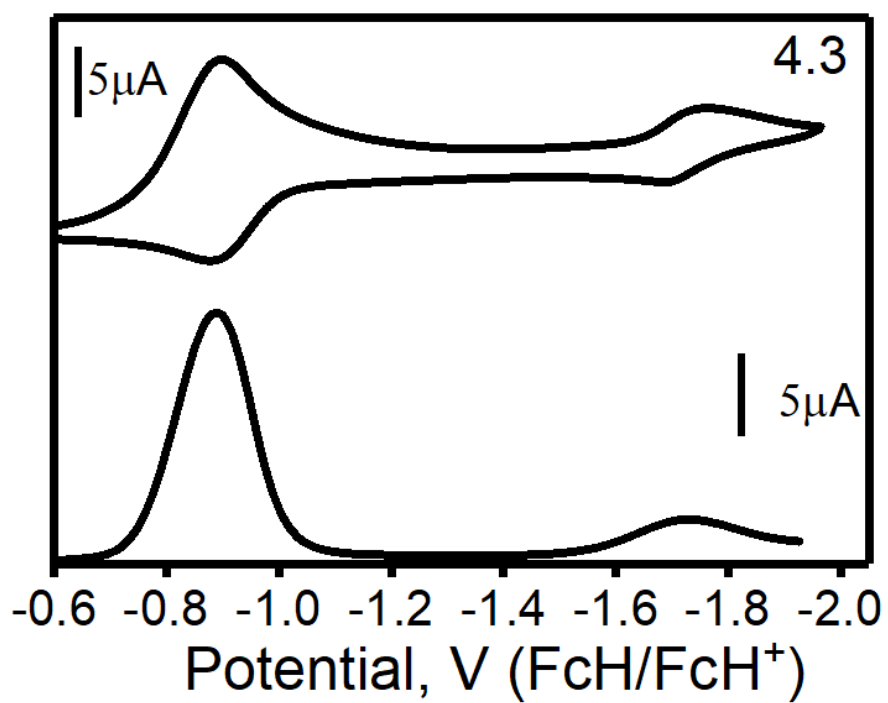


Figure 4.13: CV/DPV of compound 4.3 in DCM.

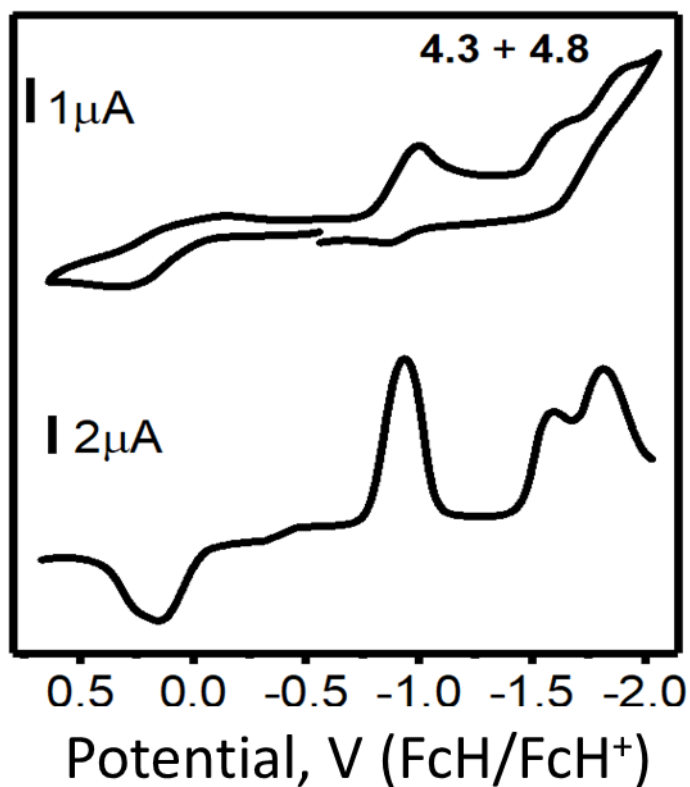


Figure 4.14: CV/DPV of compound **4.3 + 4.8** in a 1:1 ratio in DCM.

### Interaction and complex formation with porphyrins and phthalocyanines

Pyridine substituents attached at the  $\alpha$ -position of the BODIPY core was motivated by the potential to promote coordination complex formation at the metal center of porphyrins and phthalocyanine electron donors similar to what was seen in C<sub>60</sub> pyridine acceptors. Changes in static and time-resolved absorption along with static fluorescence upon titrations of **4.3** and fullerenes with our electron donor porphyrins and phthalocyanines were measured as potential indicators of charge transfer and quantitative evidence of complex formation. All titrations with reference **4.5** resulted in no change in absorption or fluorescence as expected. Titrations of our electron acceptors with the porphyrin and phthalocyanine donors revealed a mixed effectiveness of coordination based on absorption and fluorescence results which can be seen in figures 4.15 – 4.22. There was no significant change in the absorption or reduction in fluorescence during any of the titrations with **4.6** except for loss in fluorescence due to competitive absorption with **4.4** indicating there is not any type of coordination to the metal center. Upon titration of our acceptors **4.3** and **4.4** with **4.7** and **4.8** we observed both a change in absorption and reduction in fluorescence which

are indicators of coordination occurring. Starting with a solution of **4.7** and titrating **4.3** or **4.4** we observe a shift in the absorption maximum of **4.7** from 412 to 423 nm. Fluorescence quenching of **4.7** is also observed when titrating **4.4** when exciting at 540 nm; however, due to slightly overlapping absorption of BODIPY **4.3** and high quantum yields it is difficult to observe the fluorescence quenching of **4.7** and it is not useful in determining coordination of BODIPY and porphyrin. Through the titration of porphyrin **4.7** into a solution of BODIPY **4.3** we are able to observe clear reduction in BODIPY fluorescence upon excitation at 550 and 610 nm respectively. Pthalocyanine experiments with titrations of **4.8** reveals a slight decrease in absorption spectrum and the formation of a new peak at 837 nm when titrating with our pyridine acceptors. There is a drastic decrease in the fluorescence of **4.8** upon addition of **4.4** when exciting at 610 nm as well as the fluorescence of **4.3** upon addition of **4.8** when exciting at 550 nm. Unlike the other donor porphyrins and phthalocyanines **4.9** contains ferrocene which quenches the fluorescence of the porphyrin. Since I observed no fluorescence for compound **4.9** only an absorption titration experiment was possible starting with a solution of **4.9**. The titration experiment beginning with a solution of **4.9** and adding **4.3** results in no change to the absorption spectrum. A titration experiment between a solution of **4.3** and **4.9** was also done to observe the change in the absorption and fluorescence of the BODIPY and no changes were observed. A Stern-Volmer analysis of all titration experiments was carried out with resulting quenching constants shown in table 4.3 and suggests coordination complex formation between electron acceptor and donor compounds.

Table 4.3. Estimated quenching constants for coordination complex formation between electron acceptors **4.3** and **4.4** and electron donors **4.6** – **4.9** and **4.12** - **4.14**.

Compound	<b>4.6</b>	<b>4.7</b>	<b>4.8</b>	<b>4.9</b>	<b>4.12</b>	<b>4.13</b>	<b>4.14</b>
<b>4.3</b>		399613	381132	38405		146373	193795
<b>4.4</b>	8460	178369	350691		41907	81747	144021
<b>4.4</b> Lit.	12000	91000					
<b>4.5</b>	2638		1750				

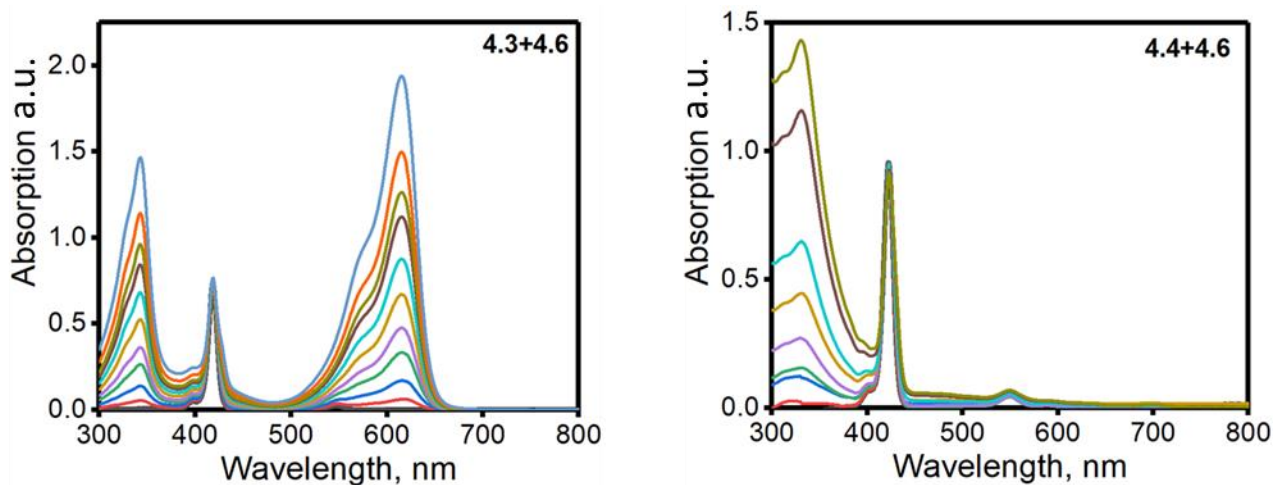


Figure 4.15: (Left) Absorption titration of **4.3** into solution of **4.6**. (Right) Absorption titration of **4.4** into solution of **4.6** in DCM.

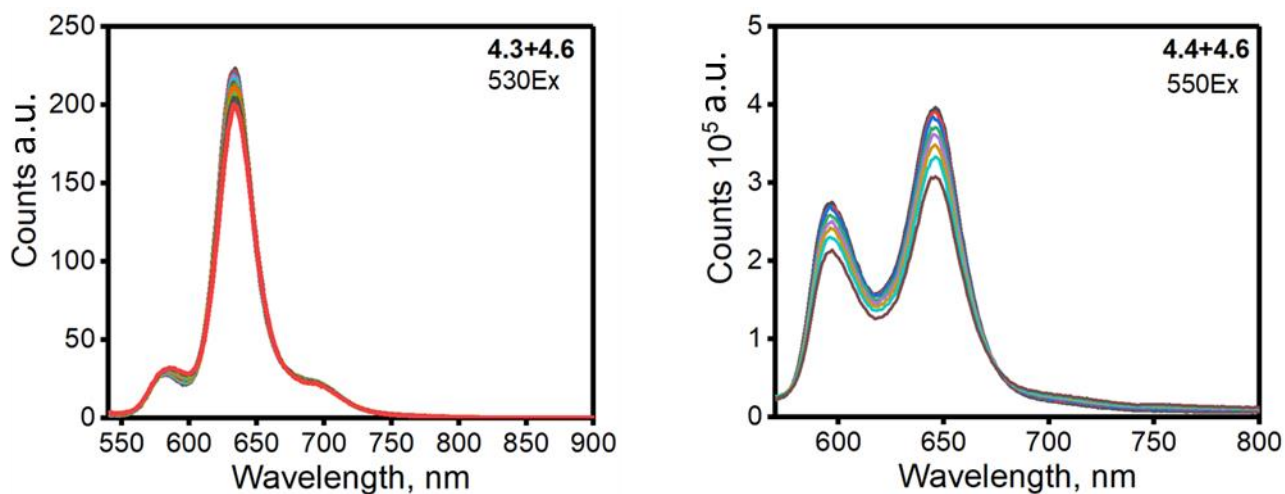


Figure 4.16: (Left) Fluorescence titration of **4.6** into solution of **4.3** excitation: 530 nm. (Right) Fluorescence titration of **4.4** into solution of **4.6** excitation: 550 nm in DCM.

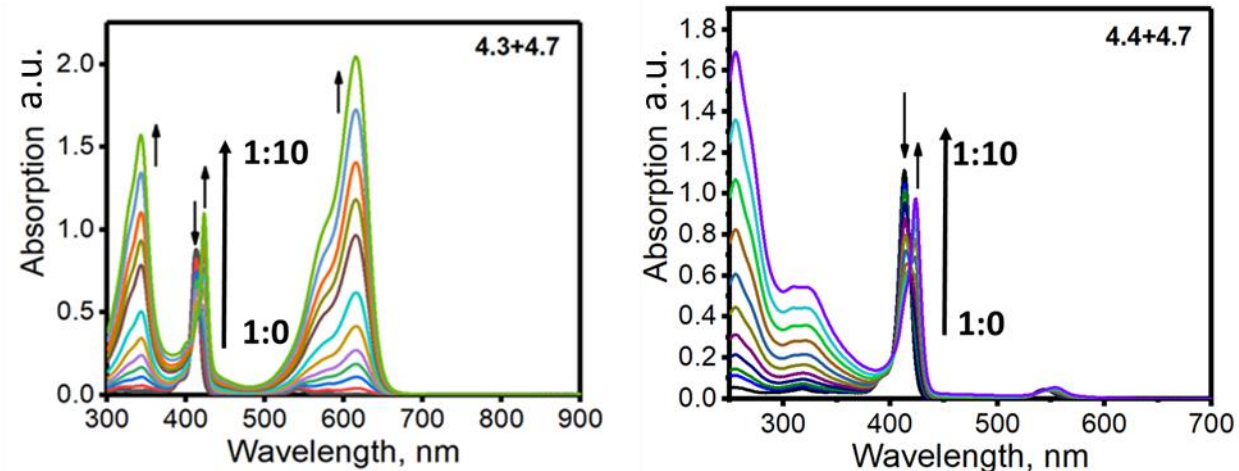


Figure 4.17: (Left) Absorption titration of **4.3** into solution of **4.7**. (Right) Absorption titration of **4.4** into solution of **4.7** in DCM.

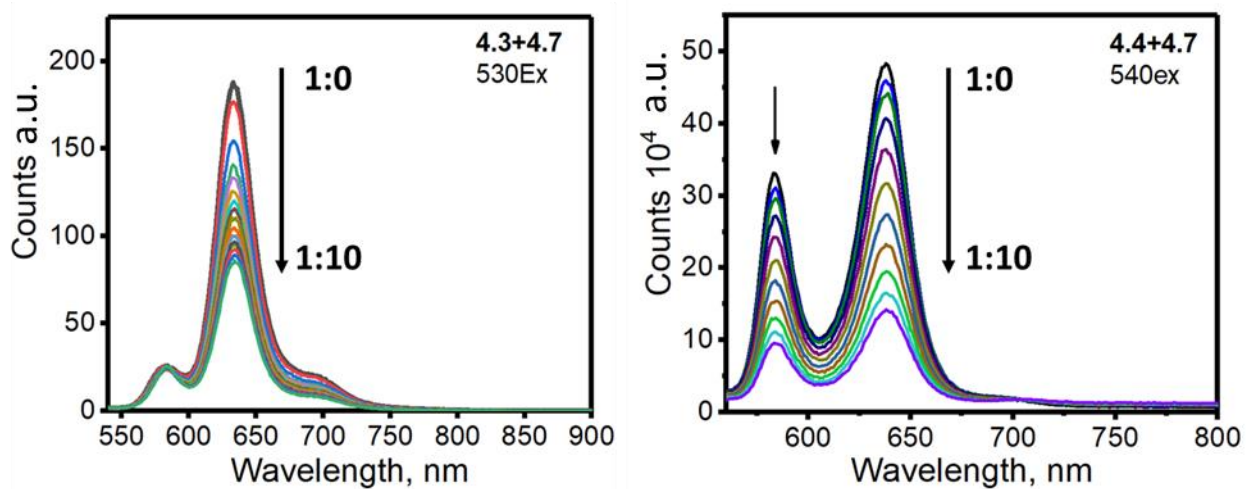


Figure 4.18: (Left) Fluorescence titration of **4.7** into solution of **4.3** excitation: 530 nm. (Right) Fluorescence titration of **4.4** into solution of **4.7** excitation: 540 nm in DCM.

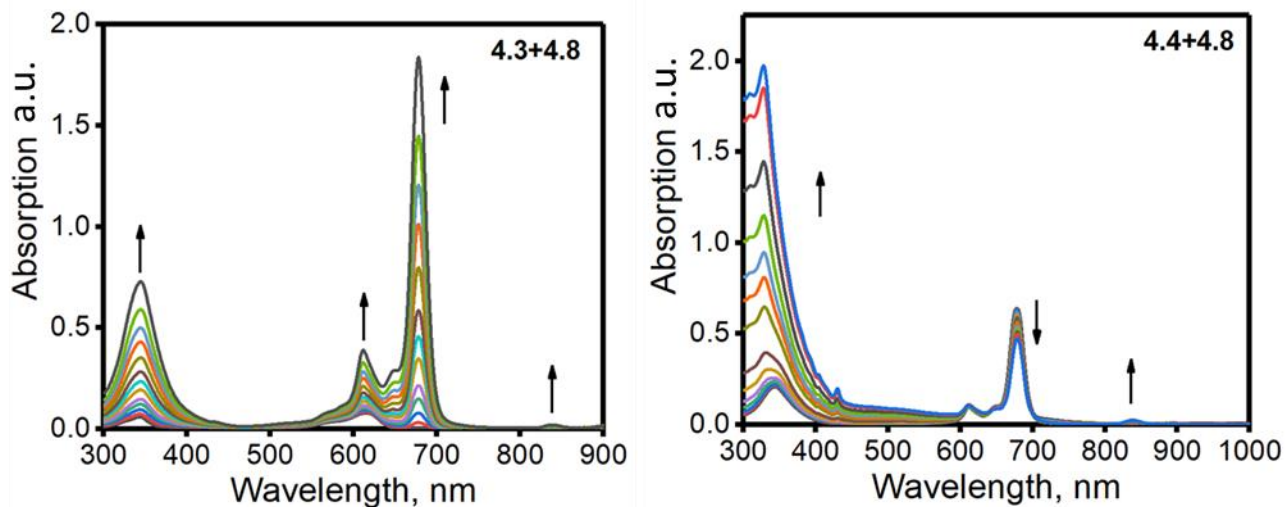


Figure 4.19: (Left) Absorption titration of **4.8** into solution of **4.3**. (Right) Absorption titration of **4.4** into solution of **4.8** in DCM.

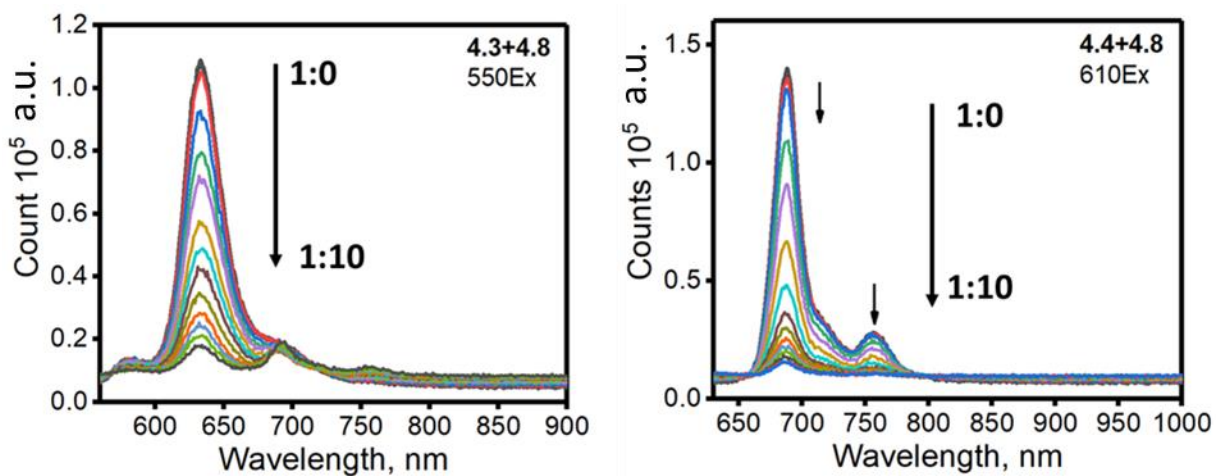


Figure 4.20: (Left) Fluorescence titration of **4.8** into solution of **4.3** excitation: 550 nm. (Right) Fluorescence titration of **4.4** into solution of **4.8** excitation: 610 nm in DCM.

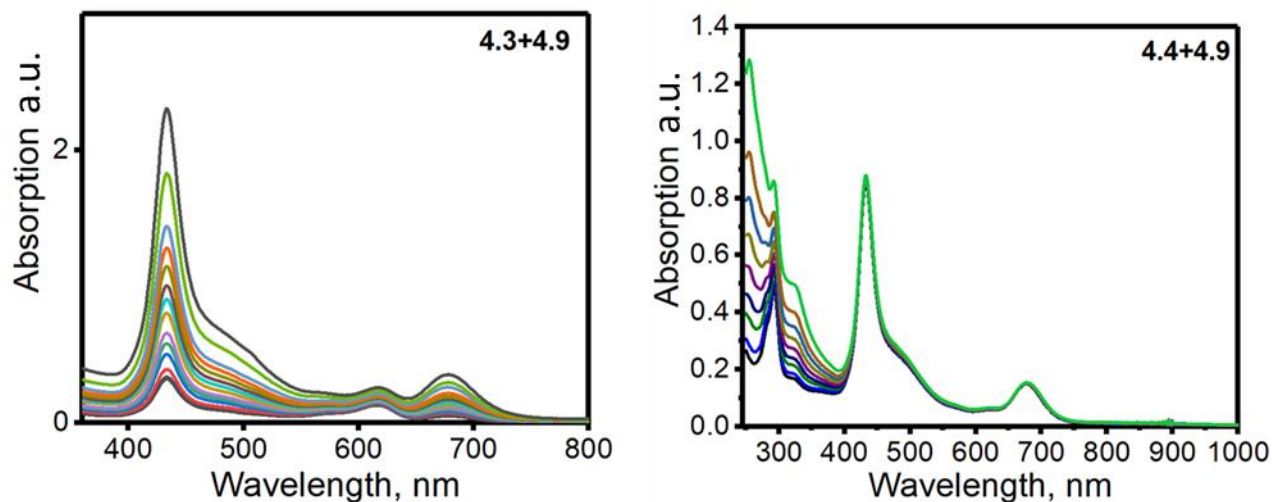


Figure 4.21: (Left) Absorption titration of **4.9** into solution of **4.3**. (Right) Absorption titration of **4.4** into solution of **4.9** in DCM.

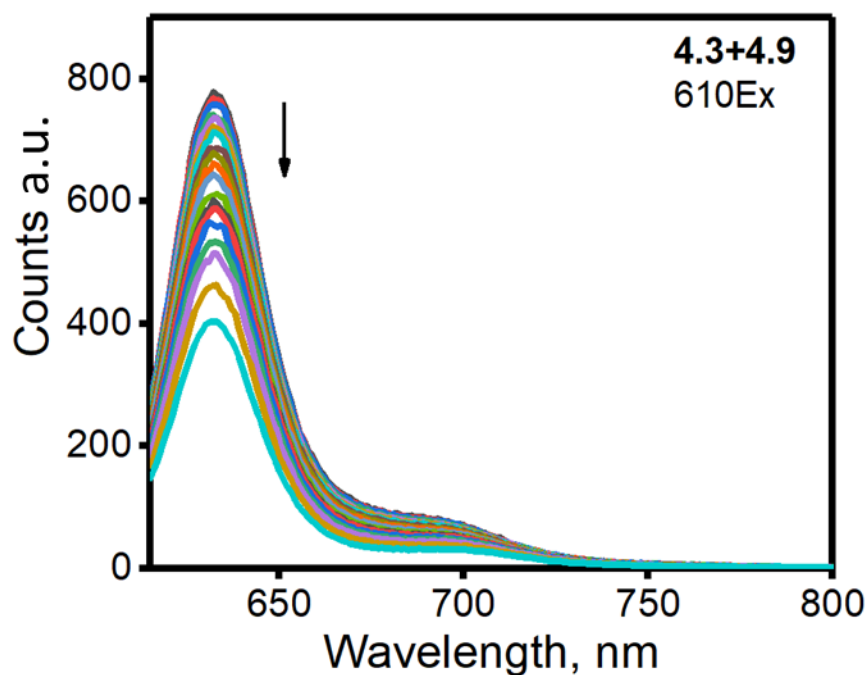


Figure 4.22: Fluorescence titration of **4.9** into solution of **4.3** excitation: 610 nm in DCM

In order to understand the coordination complex formation I observed between the first set of porphyrins and phthalocyanines, additional titration experiments were done between **4.3** and a series of cyanated octaethylporphyrins **4.10** – **4.14** to determine if there is a trend between electrophilicity of the metal center and coordination of pyridine compounds. The zinc metal center

experiences increasing electrophilicity upon addition of cyano groups to the octaethylporphyrin due to their electron withdrawing nature. Titrations of the pyridine acceptor with **4.10** and **4.11** showed no change in the absorption. The fluorescence was difficult to determine if any changes occurred due to overlapping fluorescence spectrum because of competitive absorption. Upon addition of pyridine acceptors with **4.12** we see a very small change in the absorption spectrum and fluorescence. Unfortunately, due to such a slight change in absorption and fluorescence along with overlapping absorptions and fluorescence spectra we can't calculate any quenching constants with **4.3** due to competitive absorption. Titration of **4.13** and **4.14** experience a shift in absorption from 435 to 443 nm and 445 to 457 nm respectively. Similar to **4.7** the absorption and fluorescence spectra overlap when attempting to excite **4.13** and **4.14**. Solutions of **4.3** were made and both **4.13** and **4.14** were added to observe the change in fluorescence of **4.3** at 330 and 595 nm excitation. We observed reduction in fluorescence of **4.3** for both **4.13** and **4.14** with quenching constants reported in Table 4.3. The quenching constants indicate that upon increasing electrophilicity of the metal center of the porphyrin there is greater interaction with our pyridine BODIPY. This indicates the importance of the electrophilicity of the metal center in porphyrins and phthalocyanines to allow for coordination of the pyridine linking group.

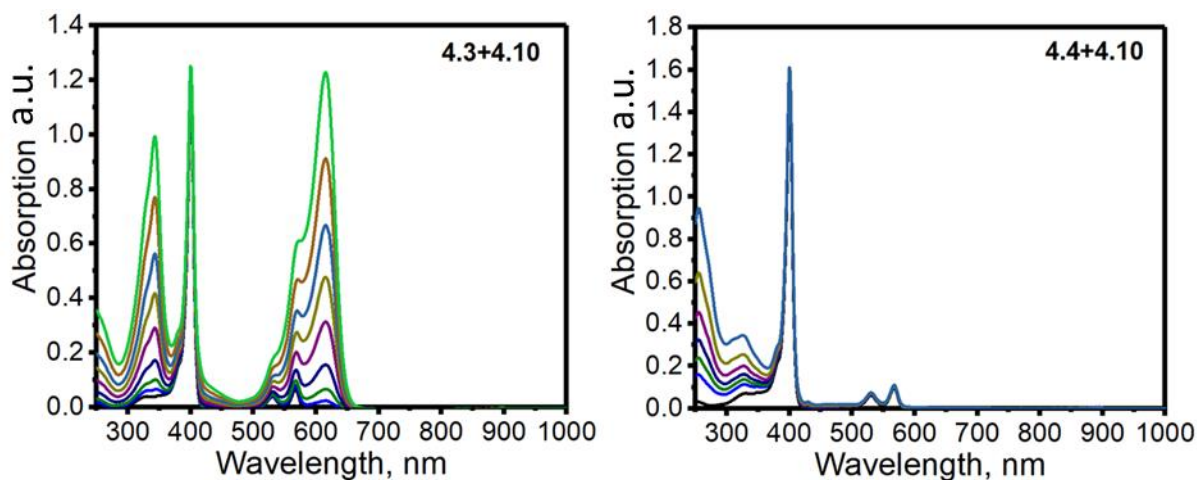


Figure 4.23: (Left) Absorption titration of **4.3** into solution of **4.10**. (Right) Absorption titration of **4.4** into solution of **4.10** in DCM.

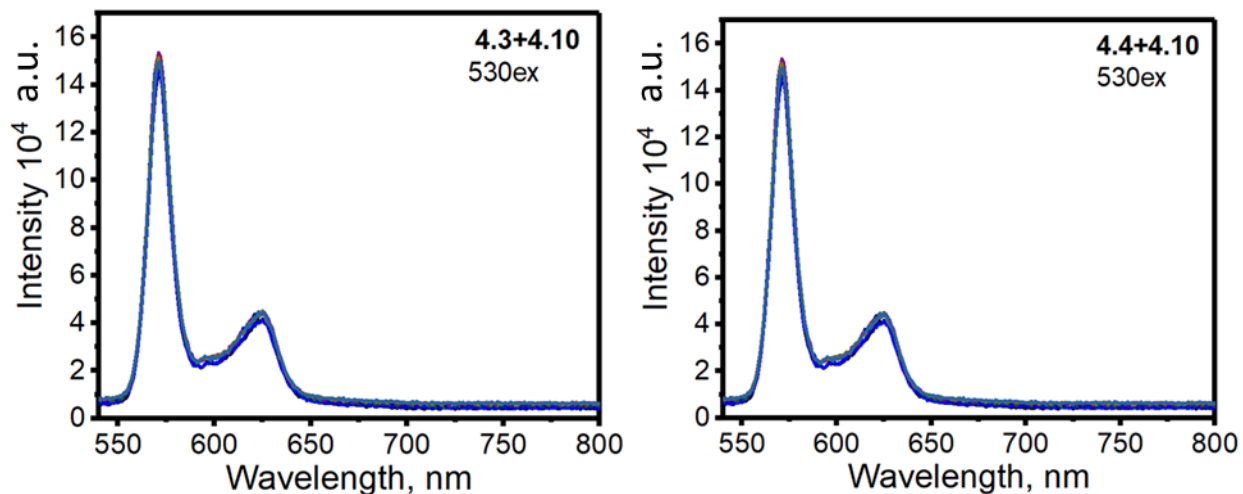


Figure 4.24: (Left) Fluorescence titration of **4.3** into solution of **4.10** excitation: 530 nm. (Right) Fluorescence titration of **4.4** into solution of **4.10** excitation 530 nm in DCM.

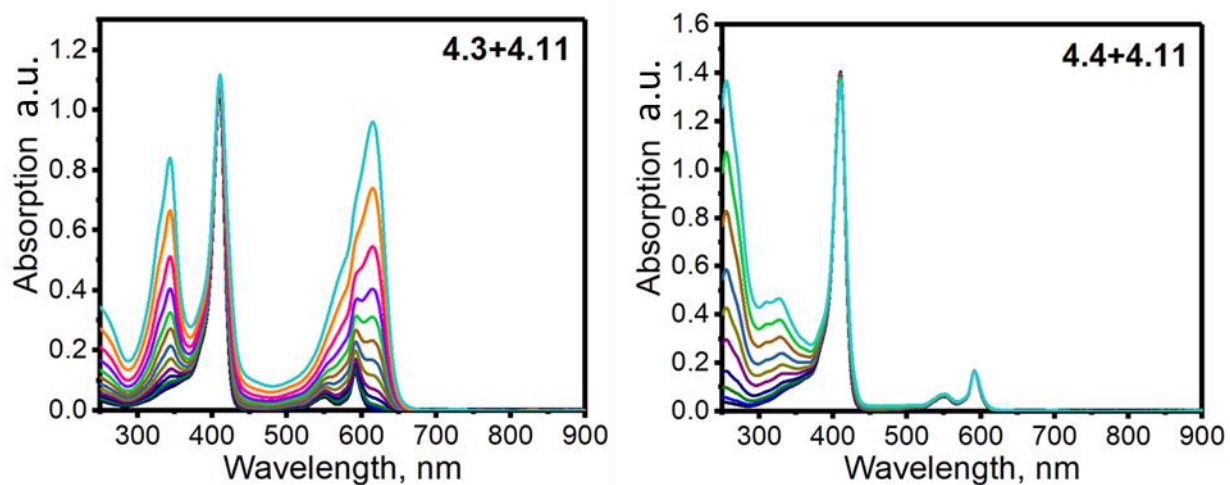


Figure 4.25: (Left) Absorption titration of **4.3** into solution of **4.11**. (Right) Absorption titration of **4.4** into solution of **4.11** in DCM.

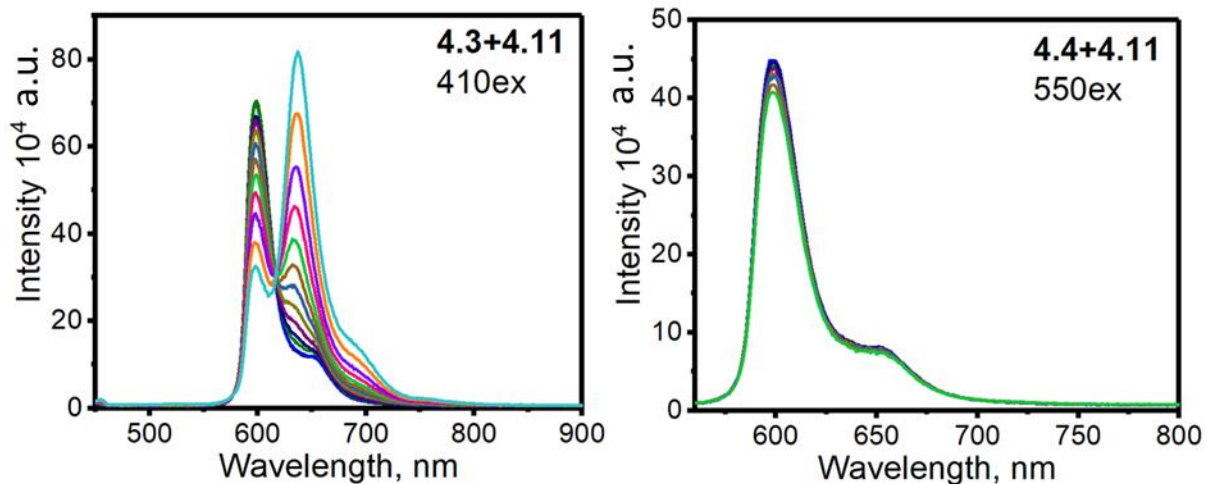


Figure 4.26: (Left) Fluorescence titration of **4.3** into solution of **4.11** excitation: 410 nm. (Right) Fluorescence titration of **4.4** into solution of **4.11** excitation 550 nm in DCM.

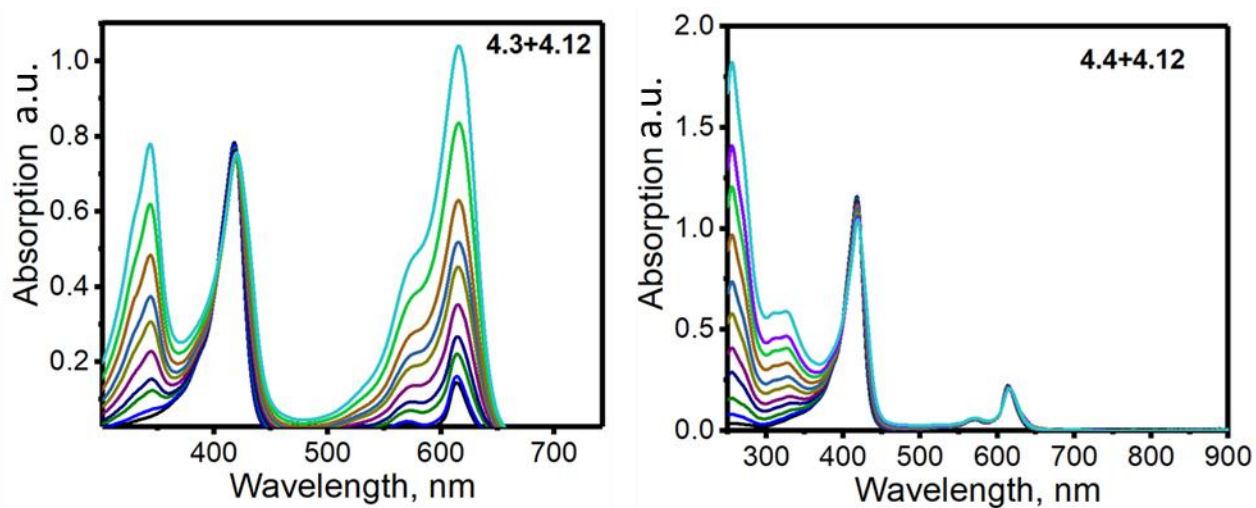


Figure 4.27: (Left) Absorption titration of **4.3** into solution of **4.12**. (Right) Absorption titration of **4.4** into solution of **4.12** in DCM.

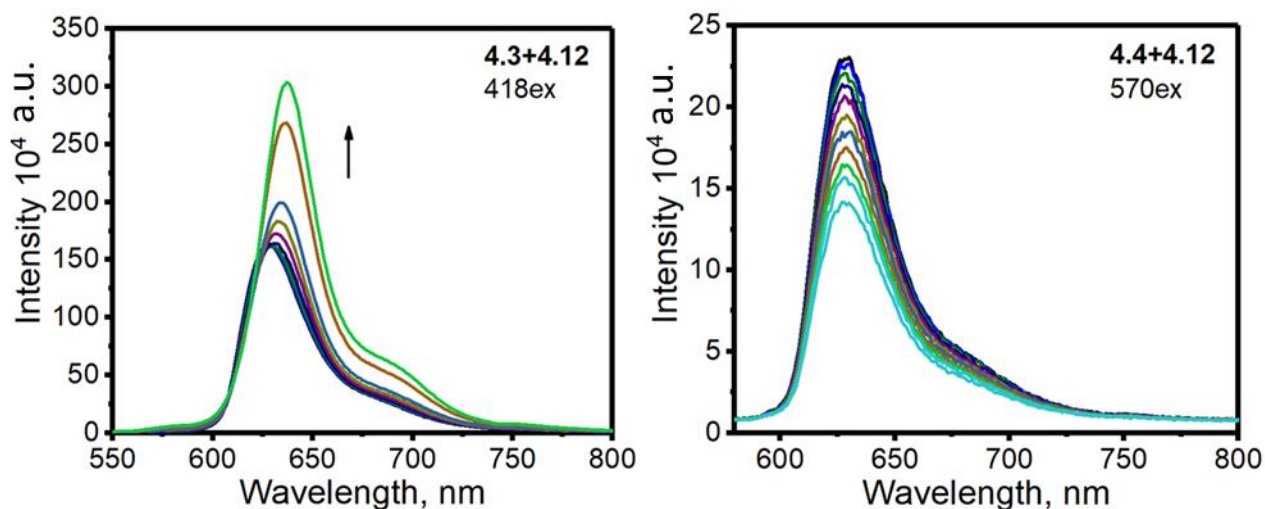


Figure 4.28: (Left) Fluorescence titration of **4.3** into solution of **4.12** excitation: 410 nm. (Right) Fluorescence titration of **4.4** into solution of **4.12** excitation 550 nm in DCM.

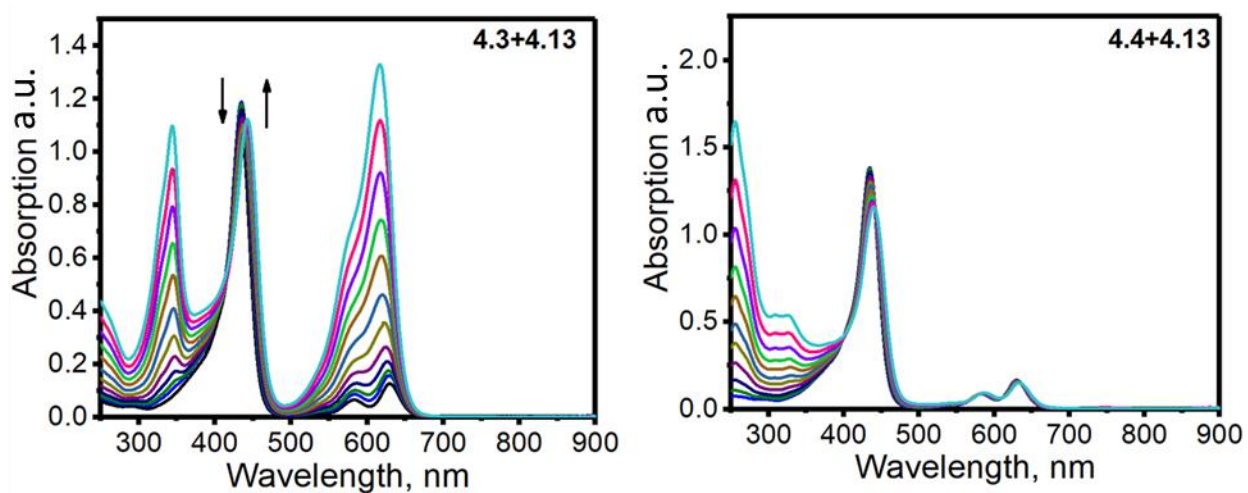


Figure 4.29: (Left) Absorption titration of **4.3** into solution of **4.13**. (Right) Absorption titration of **4.4** into solution of **4.13** in DCM.

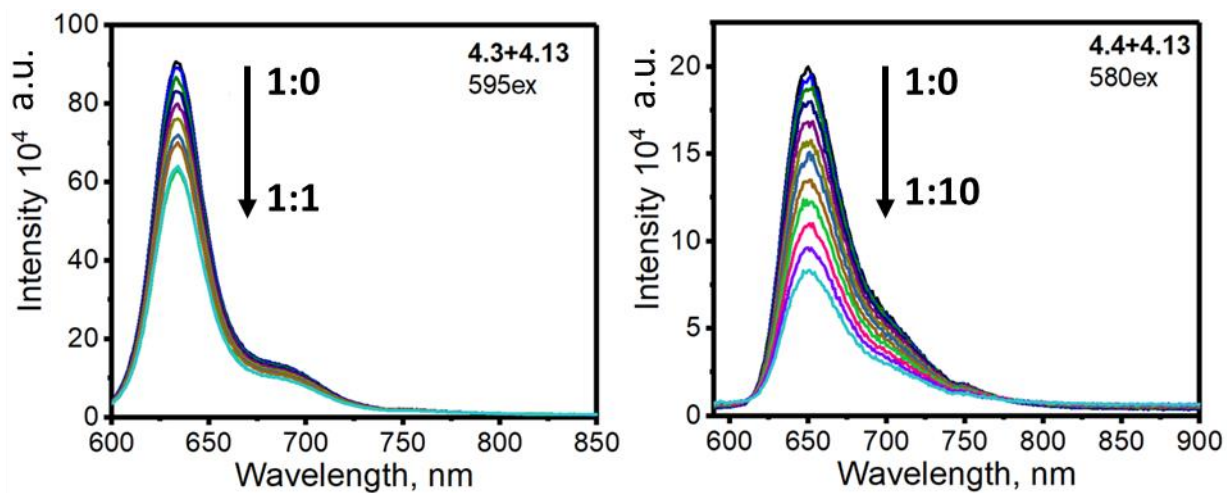


Figure 4.30: (Left) Fluorescence titration of **4.13** into solution of **4.3** excitation: 595 nm. (Right) Fluorescence titration of **4.4** into solution of **4.13** excitation 580 nm in DCM.

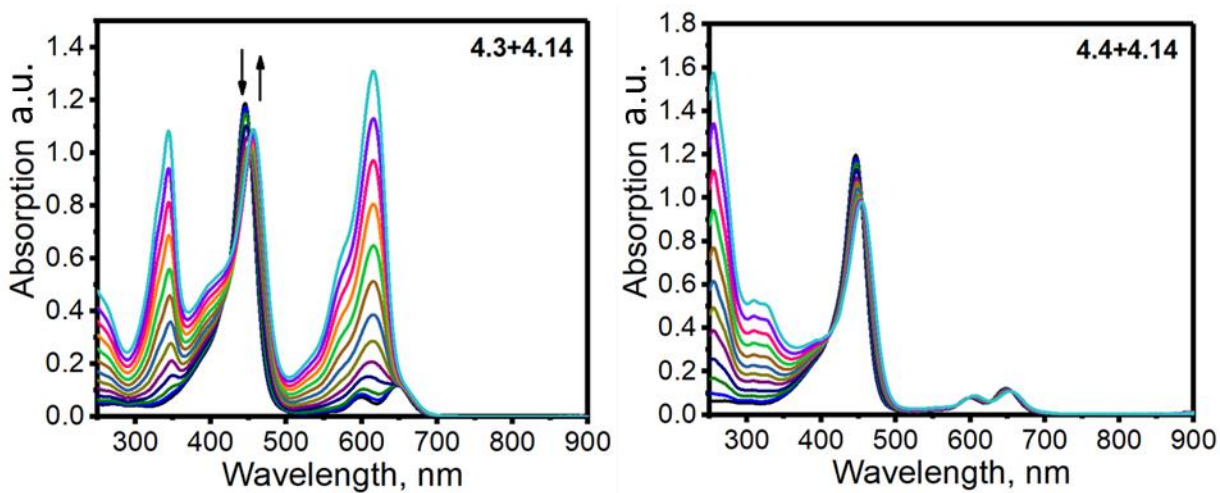


Figure 4.31: (Left) Absorption titration of **4.3** into solution of **4.14**. (Right) Absorption titration of **4.4** into solution of **4.14** in DCM.

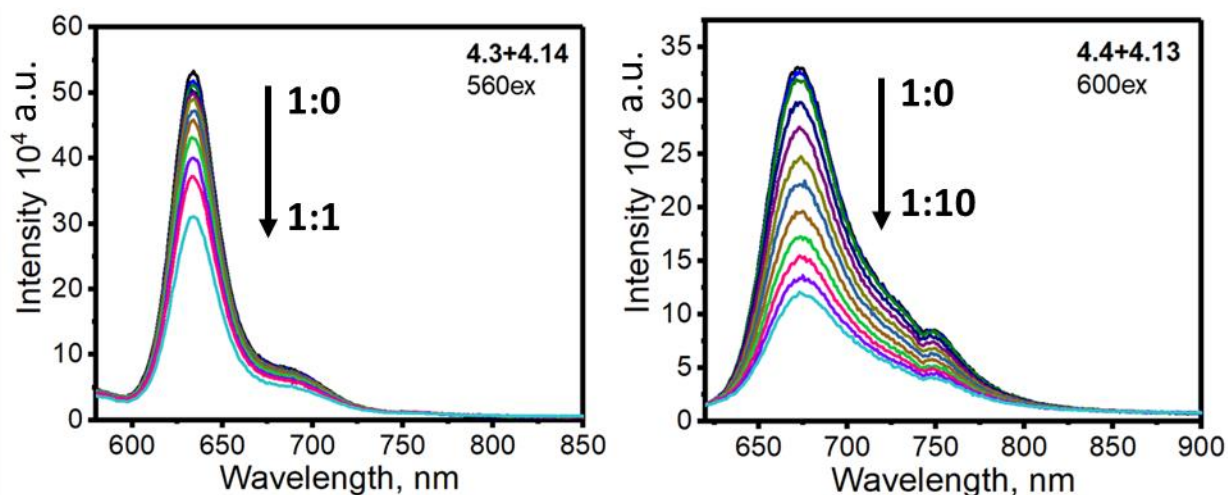


Figure 4.32: (Left) Fluorescence titration of **4.14** into solution of **4.3** excitation: 560 nm. (Right) Fluorescence titration of **4.4** into solution of **4.14** excitation 600 nm in DCM.

Transient absorption spectroscopy was used to investigate the possibility of photoinduced electron transfer between zinc phthalocyanine **4.8** and pyridine acceptors **4.3** and **4.4**. The transient absorption for a solution of **4.3** and **4.8** in a 1:1 molar ratio can be seen in figure 4.33. Transient absorption was measured following excitation at 665 nm and we observe the formation of two new peaks at around 500 and 725 nm which indicates the formation of zinc tetra-tert-butyl phthalocyanine cation-radical. The transient absorption of a solution of **4.4** and **4.8** in a 1:1 molar ratio is shown in figure 4.34. Upon excitation at 665 nm we observed a similar peak formation at 500 and 725 nm. In both cases **4.3** and **4.4** are able to form a charge separated state with **4.8** indicated by the formation of a cation-radical. The formation of charge separated states BODIPY<sup>-</sup>-PcZn<sup>+</sup> meant that the dipyrindine BODIPY acceptor is able to successfully mimic C<sub>60</sub>-pyridine as a new type of non-fullerene acceptor.

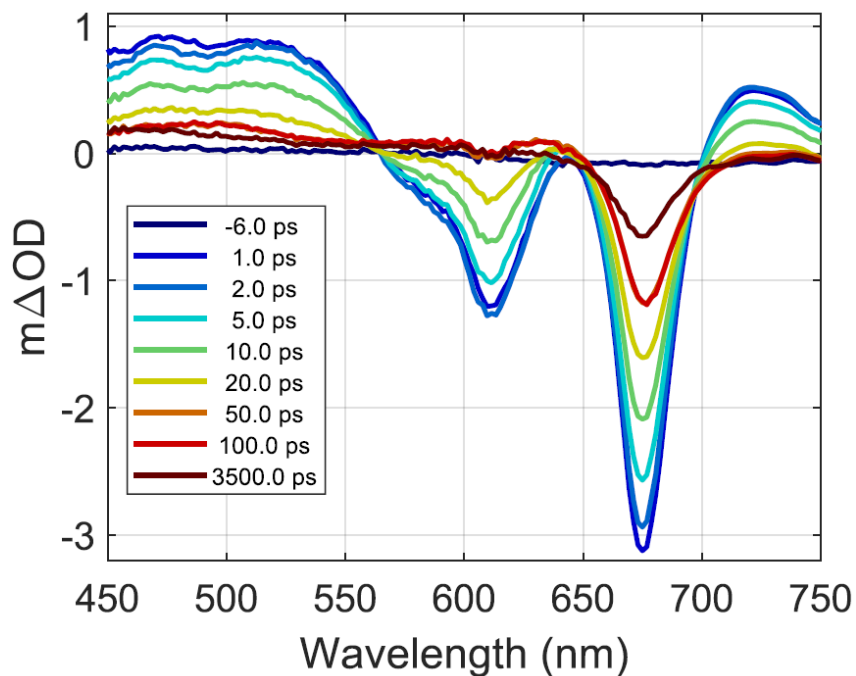


Figure 4.33: Transient absorption of **4.3** and **4.8** 1:1 in DCM at 665nm 100uW.

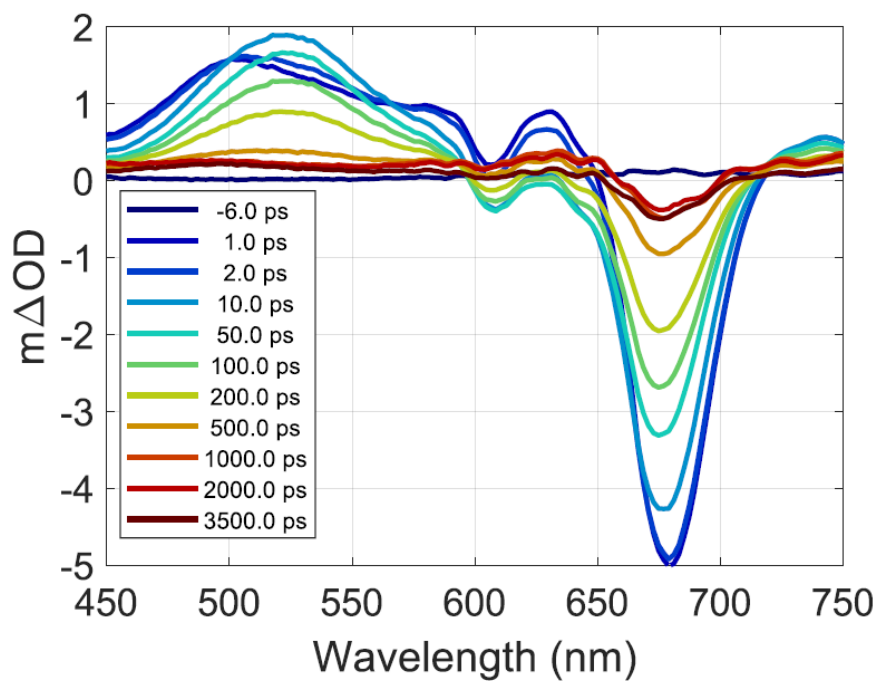


Figure 4.34: Transient absorption of **4.4** and **4.8** 1:1 in DCM at 665nm 100uW.

## Experimental Section

**Reagents and materials.** Solvents were purified using standard approaches: DCM was dried over calcium hydride. Porphyrin and phthalocyanine derivatives **4.6** - **4.9** and fullerene derivatives **4.4** and **4.5** were prepared as described in literature. All Octaethylporphyrins were prepared at the University of Akron by Dr. Ziegler's research group. BODIPY **4.1** was prepared as specified earlier.

**Spectroscopy Measurements.** A Jasco V770 spectrophotometer was used to collect UV-vis data. Steady state fluorescence studies were performed on the HORIBA PT1 QuantaMaster system. Electrochemical cyclic voltammetry (CV) and differential pulse voltammetry (DPV) measurements were conducted using a CH Instruments electrochemical analyzer utilizing a three-electrode scheme with platinum working, auxiliary and Ag/AgCl reference electrodes. DCM was used as solvents and 0.1M solution of tetrabutylammonium perchlorate (TBAP) were used as supporting electrolytes. In all cases, experimental redox potentials were corrected using decamethylferrocene (Fc\*H) as an internal standard. NMR spectra were recorded using a Bruker AVANCE instrument with a 300 MHz frequency for protons and 75 MHz frequency for carbons. Chemical shifts are reported in parts per million (ppm) and referenced to the residual proton resonance of the deuterated solvent ( $\text{CDCl}_3 = \delta 7.26$ ;  $\text{DMSO-d}_6 = \delta 2.50$ ), and carbon spectra are referenced to the carbon resonance of the solvent ( $\text{CDCl}_3 = \delta 77.16$ ;  $\text{DMSO-d}_6 = \delta 39.52$ ). High-resolution mass spectra of all new compounds were recorded using a Bruker microTOF-QIII.

**Synthesis.** Compound 3. The mixture of BDP 1 (300 mg, 0.58 mmol), 4-pyridinecarboxaldehyde (187 mg, 1.74 mmol), piperidine (494 mg, 5.81 mmol), and acetic acid (349 mg, 5.81 mmol) was refluxed in dry acetonitrile (20 mL) in the presence of 4Å molecular sieves for 40 min. After cooling to room temperature, molecular sieves were removed by vacuum filtration, the resulting solution was diluted with water (100 mL) and stirred for 1h. The resulting precipitate was collected by vacuum filtration and air dried. The crude product was recrystallized from acetonitrile yielding 282 mg (70 %) of compound 3 as a dark green precipitate.  $^1\text{H}$  NMR (300 MHz,  $\text{CDCl}_3$ )  $\delta$  8.68 (m, 4H), 7.97 (d,  $J_{\text{HH}} = 16.7$  Hz, 2H), 7.75 (d,  $J_{\text{HH}} = 16.7$  Hz, 2H), 7.51 (m, 4H), 7.41 – 7.32 (m, 10H), 7.02 (s, 1H), 4.20 (q,  $J_{\text{HH}} = 7.1$  Hz, 4H), 1.04 (t,  $J_{\text{HH}} = 7.1$  Hz, 6H);  $^{13}\text{C}$  NMR (75 MHz,  $\text{CDCl}_3$ )  $\delta$  164.7, 152.9, 150.6, 143.7, 138.5, 135.5, 131.5, 129.8, 129.4, 128.5, 128.3, 123.2, 121.7, 61.4, 13.8;

## Conclusion

A synthetic method for preparation of a mono and dipyrindine BODIPY derivatives with pyridine linking groups at the  $\alpha$ -position (**4.2** - **4.3**) was investigated. Full structural and electronic characterization of new dipyrindine BODIPY **4.3** was done using NMR, UV-Vis, fluorescence spectroscopy, and high-resolution mass spectrometry. Substitution of pyridine fragments was motivated by their effectiveness to coordinate to the metal center of porphyrins and phthalocyanines to promote electron transfer between electron donor and acceptors. The UV-vis absorption of **4.3** shows a pyridine absorption band at 343 nm and BODIPY absorption band at 615 nm. The pyridine BODIPY shows regular NIR-emitting BODIPY fluorescence and small Stokes shifts.

Formation of coordination complex between our pyridine BODIPY acceptors and porphyrin and phthalocyanines donors was studied by UV-vis, steady-state fluorescence, and time-resolved transient absorption spectroscopy. Titration experiments between the electron acceptors **4.3** and **4.4** and donors **4.6** – **4.14** resulted in a change in absorption and reduction of measured emission for titrations with donor compounds **4.7** - **4.9** and **4.12** – **4.14**. The changes in absorption and fluorescence indicated coordination complex formation between the pyridine fragment and the zinc metal center. Transient absorption spectroscopy also reveals the appearance of a new absorption feature between **4.3** and **4.8** which supports the presence of a coordinated complex formation. Direct comparison of fluorescence and absorption experiments to control compound **4.5** with no pyridine linking group shows that without the pyridine fragment there is no change to the absorption and fluorescence spectrum indicating the need for the pyridine linking group.

The titration experiments between **4.3** and our cyanated zinc octaethylporphyrins show the importance of the electrophilicity of the metal center to allow for coordination of the pyridine linking group. These results demonstrate the effectiveness for pyridine linking groups to promote coordination complex formation between new electron acceptors with the metal center of porphyrin and phthalocyanine chromophores to promote electron transfer. These results are very exciting as this shows that electron donating linking groups such as pyridine can be used as a platform to rapidly test a wide range of new donor and acceptor molecules that form coordination complexes with porphyrins and phthalocyanines.

The results from these experiments is very promising as these BODIPY-porphyrin and BODIPY-phthalocyanine complexes are the first complexes that I observed the formation of charge separated states in the transient absorption spectroscopy. This makes future work for these set of compounds very exciting as I would like to obtain even better coordination complexes with a wider range of porphyrins and pthalocyanines as well as extend the lifetime of the charge separated state. One possible method for extending the charge separated state lifetimes would be to break conjugation of the pyridine linking group with the BODIPY by using a different synthetic strategy to attach the pyridine linking group that introduces a  $sp^3$  carbon similar to  $C_{60}$  pyridine acceptors. Additionally to obtain better coordination complexes with porphyrin and pthalocyanines a stronger electron donating group then pyridine could be used such as imidazole so that way it can coordinate to less electrophilic metal centers.

## References

1. S. I. Khan, A., M. N. Paddon M. Oliver -Row, Y. J. Rubin, *Am. Chem. Soc.* **1993**, 115, 4919.
2. N. S. Sariciftci, F. Wudl, A. J. Heeger, M. Maggini, G. Scorrano, M. Prato, J. Bourassa, P. C. Ford, *Chem. Phys. Letts.* **1995**, 247, 510.
3. P. A. Liddell, J. P. Sumia, A. N. Macpherson, L. Noss, G. R. Seely, K. N. Clark, A. L. Moore, T. A. Moore, D. Gust, *Photochem. Photobiol.* **1994**, 60, 537.
4. R. M. Williams, J. M. Zwieter, J. W. J. Verhoever, *Am. Chem. Soc.* **1995**, 117, 4093.
5. H. Imahori, K. Hagiwara, M. Aoki, T. Akiyama, S. Taniguchi, T. Okada, M. Shirakawa, Y. Sakata, *J. Am. Chem. Soc.* **1996**, 118, 11771.
6. D. Kuciauskas, S. Lin, G. R. Seely, A. L. Moore, T. A. Moore, D. Gust, T. Drovetskaya, C. A. Reed, P. D. W. Boyd, *J. Phys. Chem.* **1996**, 100, 15926.
7. D. M. Guldi, M. Maggini, G. Scorrano, M. J. Prato, *Am. Chem. Soc.* **1997**, 119, 974.
8. H. Imahori, K. Yamada, M. Hasegawa, S. Taniguchi, T. Okada, Y. Sakata, *Angew. Chem., Int. Ed. Engl.* **1997**, 36, 2626.
9. P. A. Liddell, D. Kuciauska, J. P. Sumida, B. Nash, D. Nguyen, A. L. Moore, T. A. Moore, D. J. Gust, *Am. Chem. Soc.* **1997**, 119, 1400.
10. S. I. Khan, A. M. Oliver, M. N. Paddon-Row, Y. J. Rubin, *Am. Chem. Soc.* **1993**, 115, 4919.
11. N. S. Sariciftci, F. Wudl, A. J. Heeger, M. Maggini, G. Scorrano, M. Prato, J. Bourassa, P. C. Ford, *Chem. Phys. Letts.* **1995**, 247, 510.
12. P. A. Liddell, J. P. Sumia, A. N. Macpherson, L. Noss, G. R. Seely, K. N. Clark, A. L. Moore, T. A. Moore D. Gust, *Photochem. Photobiol.* **1994**, 60, 537.
13. R. M. Williams, J. M. Zwieter, J. W. Verhoever, *J. Am. Chem. Soc.* **1995**, 117, 4093
14. D. Kuciauskas, S. Lin, G. R. Seely, A. L. Moore, T. A. Moore, D. Gust, T. Drovetskaya, C. A. Reed, P. D. W. Boyd, *J. Phys. Chem.* **1996**, 100, 15926.
15. H. Imahori, Y. Sakata, *Adv. Mater.* **1997**, 9, 537.
16. M. Prato, *J. Mater. Chem.* **1997**, 7, 1097.
17. N. Martí'n, L. Sa'nchez, B. Illescas, I. Pe'rez, *Chem. Rev.* **1998**, 98, 2527
18. F. Diederich, M. Go'mez-Lo'pez, *Chem. Soc. Rev.* **1999**, 28, 263
19. A.A. Boghossian, M.-H. Ham, J.H. Choi, M.S. Strano, *Energy Environ. Sci.* **2011**, 4 3834

20. F. D'Souza, G. R. Deviprasad, M. S. Rahman, J.-P. Choi, *Inorg. Chem.* **1999**, 38, 2157.
21. N. Armaroli, F. Diederich, L. Echegoyen, T. Habicher, L. Flamigni, G. Marconi, J.-F. Nierengarten, *New. J. Chem.* **1999**, 77.
22. T. Da Ros, M. Prato, D. M. Guldi, E. Alessio, M. Ruzzi, L. Pasimeni, *Chem. Commun.* **1999**, 635.
23. F. D'Souza, N. P. Rath, G. R. Deviprasad, M. E. Zandler, *Chem. Commun.* **2001**, 267.
24. Y. Z. Lin, X. W. Zhan, *Mater. Horiz.* **2014**, 1, 470–488.
25. H. Lu, J. Mack, Y. Yang, Z. Shen, *Chem. Soc. Rev.* **2014**, 43, 4778–4823.
26. R. Srinivasa Rao, A. Bagui, G. Hanumantha Rao, V. Gupta, S. P. Singh, *Chem. Commun.* **2017**, 53, 6953–6956.
27. I. Bulut, Q. Huaulme, A. Mirloup, P. Chavez, S. Fall, A. Hebraud, S. Mery, B. Heinrich, T. Heiser, P. Leveque, N. Leclerc, *ChemSusChem* **2017**, 10, 1878–1882.
28. T. Li, T. Meyer, R. Meerheim, M. Hoepfner, C. Koerner, K. Vandewal, O. Zeika, K. Leo, *J. Mater. Chem. A* **2017**, 5, 10696-10703.
29. M. E. El-Khouly, A. N. Amin, M. E. Zandler, S. Fukuzumi, F. D'Souza, *Chem. Eur. J.* **2012**, 18, 5239-5247.
30. F. D'Souza, S. Gadde, M. E. Zandler, M. Itou, Y. Araki, O. Ito, *Chem. Commun.* **2004**, (20), 2276-2277.
31. M. E. El-Khouly, S. Gadde, G. R. Deviprasad, M. Fujitsuka, O. Ito, F. D'Souza, *Journal Porphyrins Phthalocyanines* **2003**, 7, 1-7
32. M. P. Shandura, V. P. Yakubovskiy, Y. P. Kovtun, *J. Heterocycl. Chem.* **2009**, 46, 1386-1391.
33. H.J. Callot, A. Louati, M. Gross, *Tetrahedron Letters* **1980**, 21 (34), 3281-3284

## Conclusion

Overall, as shown in chapters 2-4 of this thesis the photoinduced electron transfer in the supramolecular donor acceptor arrays can be tuned by using a variety of approaches. In chapter 2 when non-covalent interactions between the electron donating BODIPYs and aza-BODIPYs and nanocarbon materials are considered we have shown that the extended  $\pi$  surfaces such as carbon nanotubes and graphene have significantly larger interaction energies with my chromophores compared to the traditional  $C_{60}$  and  $C_{70}$  fullerenes. We have also demonstrated that despite all the weak van der Waals force driven interactions BODIPY and aza-BODIPY chromophores can form well-ordered 3D structures with  $C_{60}$  fullerene in the solid state. In contrary to the previous assumptions we have shown that the  $C_{60}$  fullerene will not necessarily interact in the solid state with pyrene groups but instead  $C_{60}$  fullerene electron acceptors will interact with the most electron rich part of the donor. These results indicate that any future work on these types of systems would be best directed toward development of new aza-BODIPYs and BODIPYs that have more electron rich  $\pi$ -systems as pyrene doesn't appear to contribute to stronger non-covalent interaction.

In chapter 3 we have demonstrated that the charge separated states between ferrocene donors and BODIPY chromophores can be reached at an ultra-fast time scale. Nevertheless we were not able to observe the further electron transfer from the reduced BODIPY chromophore to the covalently linked  $C_{60}$  fullerene electron acceptor fragment via catechol bridge. My additional studies on the BODIPY, aza-BODIPY, and BOPHY chromophores linked to the catechol group at the boron hub have also demonstrated that the catechol is an effective fluorescent quencher. The fluorescent quenching mechanism involves charge transfer from the catechol fragment to the photo excited BODIPY, aza-BODIPY, or BOPHY chromophore. Such electron rich linking groups provide additional kinetic and thermal dynamic barriers for the low energy electron transfer in Fc-BODIPY-catechol- $C_{60}$  arrays and prohibits the formation of the  $Fc^+$ -BODIPY-catechol- $C_{60}$  charge separated states from the initial  $Fc^+$ -BODIPY<sup>-</sup>-catechol- $C_{60}$  state. Based on our results it appears that any future work using the catechol as a linking group for BODIPY and  $C_{60}$  fullerene would most likely prove to be a fruitless effort. Thus any future work on these ferrocene-BODIPY- $C_{60}$  triads would be best directed toward finding a new linking group to covalently attach  $C_{60}$  to BODIPY.

Upon screening of the large array of zinc porphyrins and phthalocyanines with pyridine C<sub>60</sub> and dipyrindine BODIPYs in chapter 4 we have demonstrated that the axial coordination trend follows the electrophilicity of the metal center. In particular zinc 2,3,7,8-tetracyano-octaethylporphyrin and zinc tetra-tert-butyl-phthalocyanines were found to form supra molecular assemblies with pyridine containing electron acceptors. We have demonstrated that in the latter case the photoinduced electron transfer with the formation of zinc phthalocyanine cation-radical and acceptor anion-radical that charge separated states can be achieved even upon low energy excitation of the donor chromophore, which makes the coordination approach one of our favorite for the search of light harvesting models in organic photovoltaics. Future work on these axially coordinated BODIPYs and porphyrins or phthalocyanines is the most promising due to the formation of charge separated states. Based on our results I would suggest future work to be to try and improve coordination between our donors and acceptors. This could possibly be done by replacing our pyridine linking group with a stronger electron donating group such as imidazole which would allow for the use of porphyrin and phthalocyanines with lower electrophilicity of their metal center. The life time of the charge separated states of our BODIPY complexes could also possibly be extended if we were to break the conjugation of the  $\pi$ -system of the linking group with the BODIPY chromophore similarly to C<sub>60</sub>-pyridine complexes which have longer lived charge separated states.